

AD 680273

USAAVLABS TECHNICAL REPORT 68-50A
SMALL GAS TURBINE ENGINE COMPONENT
TECHNOLOGY - TURBINE

VOLUME I
PHASE I SUMMARY REPORT
By

T. Schober
W. Franklin

October 1968

U. S. ARMY AVIATION MATERIEL LABORATORIES
FORT EUSTIS, VIRGINIA

CONTRACT DA 44-177-AMC-182(T)
CURTISS-WRIGHT CORPORATION
WOOD-RIDGE, NEW JERSEY

*This document has been approved
for public release and sale; its
distribution is unlimited.*



Reproduced by the
CLEARINGHOUSE
for Federal Scientific & Technical
Information Springfield Va. 22151

378

Disclaimers

The findings in this report are not to be construed as an official Department of the Army position unless so designated by other authorized documents.

When Government drawings, specifications, or other data are used for any purpose other than in connection with a definitely related Government procurement operation, the United States Government thereby incurs no responsibility nor any obligation whatsoever; and the fact that the Government may have formulated, furnished, or in any way supplied the said drawings, specifications, or other data is not to be regarded by implication or otherwise as in any manner licensing the holder or any other person or corporation, or conveying any rights or permission, to manufacture, use, or sell any patented invention that may in any way be related thereto.

Disposition Instructions

Destroy this report when no longer needed. Do not return it to the originator.

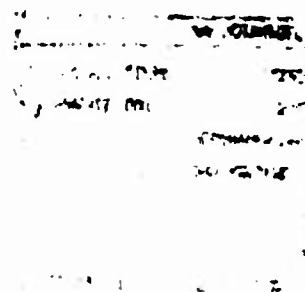
1	
2	
3	
4	
5	
6	
7	
8	
9	
10	
11	
12	
13	
14	
15	
16	
17	
18	
19	
20	
21	
22	
23	
24	
25	
26	
27	
28	
29	
30	
31	
32	
33	
34	
35	
36	
37	
38	
39	
40	
41	
42	
43	
44	
45	
46	
47	
48	
49	
50	
51	
52	
53	
54	
55	
56	
57	
58	
59	
60	
61	
62	
63	
64	
65	
66	
67	
68	
69	
70	
71	
72	
73	
74	
75	
76	
77	
78	
79	
80	
81	
82	
83	
84	
85	
86	
87	
88	
89	
90	
91	
92	
93	
94	
95	
96	
97	
98	
99	
100	



DEPARTMENT OF THE ARMY
U. S. ARMY AVIATION MATERIEL LABORATORIES
FORT EUSTIS, VIRGINIA 23604

Appropriate technical personnel have reviewed
this report and concur with the conclusions
contained herein.

The findings and recommendations outlined herein
have been and will be taken into consideration
in the planning of future programs for turbines
and turbine engines.



Task 1G162203D14413
Contract DA 44-177-AMC-182(T)
USAAVLABS Technical Report 68-50A
October 1968

SMALL GAS TURBINE ENGINE COMPONENT
TECHNOLOGY - TURBINE

Volume I

Phase I Summary Report

By

T. Schober
W. Franklin

Prepared by

Curtiss-Wright Corporation
Wood-Ridge, New Jersey

for

U. S. ARMY AVIATION MATERIEL LABORATORIES
FORT EUSTIS, VIRGINIA

This document has been approved
for public release and sale; its
distribution is unlimited.

SUMMARY

This report describes the design, analyses, and experimental evaluations of a transpiration-cooled single-stage axial flow turbine component capable of operation at an average turbine inlet temperature of 2500°F and suitable for use in a gas generator with a compressor of 8 to 10 pressure ratio and an airflow of 4 pounds per second. Additional design objectives included 90 percent turbine adiabatic efficiency and a turbine work of 140 BTU per pound of airflow.

The turbine component design and the rotating test rig design completed during Phase I will be fabricated and tested in Phase II of this program to demonstrate the performance characteristics and high-temperature capability of the turbine.

Various experimental evaluations were performed to determine airfoil forming characteristics of high-temperature materials, to investigate blade strut fabrication techniques, to perfect strut-to-airfoil attachment techniques, and to prove the high-temperature feasibility of the selected airfoil design.

An eight-blade two-dimensional cascade test was run for approximately 14 hours utilizing blades fabricated to the proposed design and included a 1.5-hour test run at an average gas temperature of 2560°F. The temperature profile produced by the combustor during this run exposed some blades in the cascade to average temperatures as high as 2900°F. All airfoils tested were visually inspected and found to be in satisfactory condition. Cooling airflow checks were also made before and after the test, and results indicate very little change in skin porosity. Blade temperature data obtained during the cascade testing also substantiated the thermal analysis design predictions.

It was concluded during the Phase I period that fabrication techniques, materials, analytical methods, design information, and test facilities were sufficiently advanced to warrant the continued development of this advanced high-temperature turbine component for small gas turbine engines.

FOREWORD

The work reported herein is in partial fulfillment of Contract DA 44-177-AMC-182(T), which was conducted by the U.S. Army Aviation Materiel Laboratories, Fort Eustis, Virginia. It represents the design and evaluation work accomplished during Phase I of subject contract which was continued and completed in Phase II.

TABLE OF CONTENTS

	<u>Page</u>
SUMMARY	iii
FOREWORD	v
LIST OF ILLUSTRATIONS	xi
LIST OF TABLES	xix
LIST OF SYMBOLS	xxi
ABBREVIATIONS	xxiv
1.0 INTRODUCTION	1
2.0 TURBINE AERODYNAMIC ANALYTICAL DESIGN	3
2.1 Turbine Aerodynamic-Thermodynamic Design	4
2.1.1 Thermodynamic Considerations	4
2.1.2 Turbine Performance, Off-Design	5
2.1.3 Efficiency - Design Point	6
2.1.4 Blade Aerodynamic Design	7
2.2 Engine Performance	37
2.2.1 Design Point Performance	37
2.2.2 Off-Design Performance	38
2.2.3 Cycle Analysis Study	39
3.0 TURBINE TEST RIG DESIGN	49
3.1 Rig Design Study	49
3.1.1 Introduction	49
3.1.2 Rig Description	50
3.2 Combustor Design	69
3.2.1 General Description	69
3.2.2 Basic Design Considerations	70
3.2.3 Combustor Design	71
3.2.4 Performance	73
3.3 Turbine Rig Stress and Vibration Analysis	82
3.3.1 Stress Analysis	82

		<u>Page</u>
	3.3.1.1 Inlet Combustor Support	82
	3.3.1.2 Inlet Plate	82
	3.3.1.3 Combustion Chamber Liners . . .	82
	3.3.1.4 Outer and Inner Air-Coolant . . Tubes	84
	3.3.1.5 Exhaust Duct	85
	3.3.1.6 Bearing Support Structure . . .	85
	3.3.1.7 Outer Housing	85
	3.3.2 Vibration Analysis	86
3.4	Turbine Rig Heat Transfer Analysis	110
	3.4.1 Thermal Analysis of Combustor	110
	3.4.2 Turbine Shroud Temperature Distribution . .	111
	3.4.3 Exhaust Duct	111
3.5	Test Equipment Design	122
	3.5.1 Combustor and Turbine Stator Test Rig . . .	122
	3.5.2 Turbine Performance and High-Temperature Test Rig	123
3.6	Instrumentation Design	149
4.0	TURBINE COMPONENT MECHANICAL DESIGN	159
4.1	Turbine Component Design	159
	4.1.1 Introduction and General Arrangement . . .	159
	4.1.2 Stator and Rotor Transpiration-Cooled Blading	159
	4.1.3 Turbine Rotor Assembly	161
4.2	Thermal Analysis	181
	4.2.1 Turbine Rotor Disc and Shaft Assembly . . .	181
	4.2.2 Rotor Blade	182
	4.2.3 Stator Blade	184
4.3	Turbine Component Stress Analysis	210
	4.3.1 Stator Blade	210
	4.3.2 Stator Blade Support Rings	210
	4.3.3 Rotor Blade	210
	4.3.4 Rotor Disc and Shaft	211

	<u>Page</u>
5.0 EXPERIMENTAL EVALUATION	235
5.1 Fabrication Technique	235
5.1.1 Airfoil Forming	235
5.1.2 Strut Fabrication	235
5.1.3 Strut-to-Airfoil Attachments	236
5.1.4 Blade-to-Rotor-Disc Attachment	239
5.2 Cascade Rig Design	253
5.2.1 Cascade Rig and Blade Design	253
5.2.2 Test Equipment and Instrumentation Design	257
5.3 Cascade Rig Test	268
5.3.1 Transverse Temperature Profiles	268
5.3.2 Radial Temperature Profiles	269
5.3.3 Pressure Profiles	270
5.3.4 Blade Cooling Air	270
5.3.5 Stator Cascade Tests	271
5.4 Fatigue Properties	298
5.4.1 Room Temperature Fatigue	298
5.4.2 High Temperature and Thermal Fatigue	300
6.0 TEST PLANS	301
6.1 Combustion Testing	302
6.2 Turbine Stator Tests	303
6.3 Performance Tests	305
6.4 High-Temperature Test	308
REFERENCES	309
DISTRIBUTION	311

LIST OF ILLUSTRATIONS

<u>Figure</u>		<u>Page</u>
1	Turbine Velocity Diagram	19
2	Sketch of Turbine Annulus	21
3	Estimated Overall Turbine Performance Map	22
4	Estimated Overall Turbine Performance Map	23
5	USAAVLABS Estimated Overall Turbine Performance Map	24
6	Adiabatic Efficiency Vs Turbine Blade Loss Coefficient	25
7	Predicted and Cascade Test Values Pressure Distribution Around a Transpiration-Cooled Stator Blade	26
8	USAAVLABS Stator Airfoil Aerodynamic Section - Hub	27
9	USAAVLABS Stator Airfoil Aerodynamic Section - Mean	28
10	USAAVLABS Stator Airfoil Aerodynamic Section - Tip	29
11	USAAVLABS Rotor Airfoil Aerodynamic Section - Hub	30
12	USAAVLABS Rotor Airfoil Aerodynamic Section - Mean	31
13	USAAVLABS Rotor Airfoil Aerodynamic Section - Tip	32
14	Calculated Turbine Stator Blade Static Pressure Distribution	33
15	Calculated Turbine Stator Blade Velocity Distribution	34
16	Calculated Turbine Rotor Blade Static Pressure Distribution	35
17	Calculated Turbine Rotor Blade Velocity Distribution (Preliminary).	36
18	Estimated Optimum Fuel Consumption Performance	41
19	Effect of Combustion Chamber Temperature	42
20	Effect of Combustion Chamber Temperature on HP and SFC	43
21	Effect of Combustion Chamber Temperature on HP and SFC	44
22	Effect of Combustion Chamber Temperature on HP and SFC	45
23	Effect of Compressor Efficiency on ESFC	46

LIST OF ILLUSTRATIONS (Continued)

<u>Figure</u>		<u>Page</u>
24	Effect of Compressor Efficiency on ESFC	47
25	Turbine Test Rig - External Gas Source	55
26	Turbine Test Rig	57
27	Turbine Test Rig	59
28	Turbine Test Rig	61
29	Turbine Test Rig	63
30	Turbine Test Rig	65
31	Turbine Test Rig - Final	67
32	Preliminary Turbine Rig Combustor Basic	78
33	Turbine Test Rig - Combustor Flow Schematic	79
34	Advanced Vaporizing Combustor - Primary Zone Combustion Stability Characteristics	80
35	Combustor Design - Estimated Combustion Efficiency Characteristics	80
36	Turbine Test Rig Estimated Turbine Inlet Radial Temperature Profiles.	81
37	Inlet Combustor Support	90
38	Inlet Plate	91
39	Simplified Inlet Plate	92
40	Summary of Stresses in Inlet Plate.	93
41	Inner Liner	94
42	Thermal Discontinuity in Cone	95
43	Strain - Cycle Curve (Hastelloy X)	96
44	Combustion Chamber Outer Liner	97
45	Liner Section With Rectangular Gradients	98

LIST OF ILLUSTRATIONS (Continued)

<u>Figure</u>		<u>Page</u>
46	Liner Section With Rectangular Gradient	99
47	Combustor Inner Liner	100
48	Combustor Outer Liner	101
49	Summary of Stresses - Inner Air-Coolant Tube	102
50	Summary of Stresses - Outer Air-Coolant Tube	103
51	Exhaust Duct Temperature Distribution	104
52	Revised Exhaust Duct	105
53	Material Properties - Hastelloy X	106
54	Bearing Support	107
55	Housing	108
56	First Critical Speed Vs Support Spring Rate	109
57	Turbine Test Rig Combustor Operating Conditions, Slot Coolant Flow Distribution, and Slot Heights	113
58	Combustion Chamber Outer Liner, Casing, and Cooling Band Temperatures	114
59	Combustion Chamber Inner Liner, Cooling Air Duct, and Cooling Band Temperatures	115
60	Comparison of Analytical and Experimental Metal Temperature Data	116
61	Temperature Distribution in the Turbine Shroud	117
62	Temperature Distribution in the Turbine Shroud (Revised Design)	118
63	Temperature Distribution in the Exhaust Duct	119
64	Temperature Distribution in the Exhaust Duct (Insulated Design)	120
65	Temperature Distribution in the Exhaust Duct (Final Design)	121
66	Test Equipment Installation	131

LIST OF ILLUSTRATIONS (Continued)

<u>Figure</u>		<u>Page</u>
67	Combustor and Turbine Stator Test Stand Schematic	133
68	Rotating Probe and Drive	135
69	Turbine Test Stand Schematic	137
70	Turbine Operating Speed and Turbine Inlet Temperature Vs $N/\sqrt{T_{\text{Inlet}}}$ For Turbine Performance Testing	139
71	Turbine Test Cell Temperature Limitations	140
72	Turbine Horsepower Vs $N/\sqrt{T_{\text{Inlet}}}$	141
73	Turbine Horsepower Characteristics	142
74	Turbine Torque Characteristics	143
75	Turbine Torque Characteristics	144
76	Turbine Required Power Absorption Vs Speed	145
77	Turbine Installation	147
78	Instrumentation Combustor Test Rig	153
79	Instrumentation Combustor and Cascade Test Rig	155
80	Instrumentation Turbine Rotor	157
81	Stator Blade Airfoil Structure	165
82	Average 0.2 Percent Creep Properties of Inco 713C Casting . .	167
83	Rotor Blade Airfoil Structure	169
84	Rotor Blade Airfoil Steady-State Stresses Vs Radius	171
85	Mechanical Properties Mar-M-Alloy 302	172
86	Rotor Blade Cooling Airflow System	173
87	Blade and Disc Assembly	174
88	Disc Thermal Gradient Vs Radius	175
89	Disc Combined Elastic Stress Vs Radius	176
90	Disc Centrifugal Elastic Stress Vs Radius	177

LIST OF ILLUSTRATIONS (Continued)

<u>Figure</u>		<u>Page</u>
91	Blade and Disc Assembly Welded Turbine Rotor Test Rig	178
92	Blade and Disc Assembly Welded Turbine Rotor Test Rig	179
93	Turbine Test Rig - Rotor Blade Disc Assembly	188
94	Temperature Distribution in Turbine Rotor Disc	189
95	Temperature Distribution in Turbine Shaft	190
96	Temperature of Test Rig Turbine Disc Vs Distance From Radial Centerline	191
97	Temperature of Test Rig Turbine Vs Distance From Axial Centerline	192
98	Turbine Rotor Blade Orifice Diameters and Coolant Flows for Rig Engine	193
99	Turbine Rotor Blade - Hub Section Temperature Distribution and Relative Rotor Blade Gas Temperature Profile	194
100	Turbine Rotor Blade - Mean Section Temperature Distribution	195
101	Turbine Rotor Blade - Tip Section Temperature Distribution	196
102	Airfoil Metal Temperature Vs Distance From Leading Edge . . .	197
103	Strut Temperature Vs Distance From Leading Edge	198
104	Turbine Rotor Blade - Tip Cap Temperature Distribution	199
105	Turbine Rotor Blade - Shelf Temperature Distribution	200
106	Orifices for Test Rig Stator Blade	201
107	Rig Engine Stator Blade Temperature Distribution for Maximum Temperature Condition	202
108	Rig Engine Stator Blade Temperature Distribution for Average Temperature Condition	203
109	Gas Temperature Profile, Blade Section Locations, and Temperature Distribution on Upper and Lower Tang	204

LIST OF ILLUSTRATIONS (Continued)

<u>Figure</u>		<u>Page</u>
110	Turbine Stator Blade Upper Shelf Temperature Distribution for Maximum Temperature Condition	205
111	Turbine Stator Blade Lower Shelf Temperature Distribution for Maximum Temperature Condition	206
112	Turbine Stator Blade Upper Shelf Temperature Distribution for Average Temperature Condition	207
113	Turbine Stator Blade Lower Shelf Temperature Distribution for Average Temperature Condition	208
114	Temperature Variation of Representative Points on Shelf . .	209
115	Turbine Stator Blade Thermal Stresses - Tip Section	215
116	Turbine Stator Blade Thermal Stresses - Mean Section. . . .	217
117	Turbine Stator Blade Thermal Stresses - Root Section. . . .	219
118	Goodman Diagram for Turbine Stator Blade	221
119	Stress in Stator Support Ring	222
120	Turbine Rotor Blade Thermal Stresses - Root Section	223
121	Turbine Rotor Blade Thermal Stresses - Tip Section	225
122	Turbine Rotor Blade Thermal Stresses - Mean Section	227
123	Goodman Diagram for Turbine Rotor Blade Strut	229
124	Summary of Stresses for Turbine Rotor Disc	230
125	Turbine Disc Fir Tree Configuration	231
126	Turbine Disc Fir Tree Configuration - Free Body Diagram . .	232
127	Turbine Disc Stress Levels Fir Tree Configuration	233
128	Cascade Rig Blade Strut Castings	242
129	Micrograph of a Typical Land Weld	243
130	Ni V Cb Poroloy Skin Welded to Cast René 41 Strut	243
131	A Micrograph of a Butt Weld at the Blade Leading Edge . . .	244

LIST OF ILLUSTRATIONS (Continued)

<u>Figure</u>		<u>Page</u>
132	A Simulated Trailing Edge Closure Weld (No Filler Wire Was Required in This Specimen)	244
133	A Shoulder Closure Weld Made by Tilting the Shoulder at 5 Degrees to the Beam (No Filler Wire Was Used)	245
134	A Cross Section of the Shoulder Filler Weld	245
135	Fully Welded Convex Side of a Blade	246
136	A Cross Section of a Fully Welded Blade	246
137	A Welded Concave Side of a Stator Blade	247
138	A Composite Picture of an EB Welded Stator Blade	247
139	Weld of Mar-M-302 to Inco 718 1/2-Inch-Thick Specimens	248
140	Photomicrograph of Mar-M-302 and Inco 718	248
141	Photomicrograph of Mar-M-302 Welded to Inco 718 - Aged Condition	249
142	Hardness Survey - Inco 718 EB Welded to Mar-M-302	250
143	Weld of Inco 713 LC to Inco 718 1/2 Inch-Thick Specimens - After Aging	251
144	Longitudinal Section Through Weld of Inco 713 LC to Inco 718 1/2-Inch-Thick Specimens - After Aging	252
145	Cascade Rig Combustor Assembly	259
146	Turbine Cascade Static Pressure Distribution	261
147	Velocity Distribution - Turbine Cascade	262
148	Cascade Rig Test Stand Schematic	263
149	High Temperature Turbine Cascade Rig	264
150	Cascade Rig Combustor Exit Profile Instrumentation	265
151	Temperature Traversing Probe Viewed From Quench Chamber	267
152	Alumina Temperature Traversing Probe in Post-Test Condition	277

LIST OF ILLUSTRATIONS (Continued)

<u>Figure</u>		<u>Page</u>
153	Temperature Profile at Burner Exit	278
154	Baffle Rework	279
155	Temperature Profile at 0.022 Overall F/A Ratio	280
156	Schematic of Temperature Profile and Typical Blade Test Data	281
157	Schematic of Temperature Profile and Typical Blade Test Data	282
158	Baffle Rework	283
159	Schematic of Temperature Profile and Typical Blade Test Data	284
160	Schematic of Temperature Profile and Typical Blade Test Data	285
161	Schematic of Temperature Profile and Typical Blade Test Data	286
162	USAAVLABS Stator Cascade	287
163	USAAVLABS Stator Cascade	288
164	USAAVLABS Stator Cascade	289
165	Vertical Temperature Profile Cascade Rig	290
166	Vertical Temperature Profile Cascade Rig	291
167	Stator Cascade Complete Assembly	292
168	Trailing Edge of 1st Cascade Stator Blades in Post-Test Condition	293
169	Pressure Side of 2nd Cascade Blades in Post-Test Condition	294
170	Leading Edge of 3rd Cascade Blades in Post-Test Condition	295
171	Trailing Edge of 3rd Cascade Blades in Post-Test Condition	296
172	Cascade Stator	297

LIST OF TABLES

<u>Table</u>		<u>Page</u>
I	Overall Turbine Dimensions - Hot	11
II	Turbine Design Data	12
III	Turbine Blade Design Data	13
IV	Turbine Design - Standard Efficiency	14
V	Turbine Design - 1-Percent Efficiency Increase for Shrouds	15
VI	Turbine Design - 90-Percent Prescribed Design Efficiency	16
VII	Comparison of Measured and Calculated Design Point Turbine Efficiency	17
VIII	Design Conditions for Turbine Component and Test Rig. .	75
IX	Combustor Airflow Distribution and Metering Area Schedule	76
X	Turbine Test Rig Combustor - Summary of Design Conditions and Performance	77
XI	Definition of the Analyzed Configurations	87
XII	Component and Resultant Spring Rates	88
XIII	Table of Critical Speeds	89
XIV	Cross Reference Between Instrumentation Required and Instrumentation Supplied	152
XV	Mechanical Stresses in Turbine Rotor Blade	213
XVI	Weld Test Mechanical Properties	240
XVII	Base Material Strengths	241
XVIII	Detail Summary of Blade Time and Temperature	276

LIST OF SYMBOLS

		<u>Units</u>
A	airflow	pound per second
A	area	square foot
Ab	burning zone area	square foot
Ae	effective area	square foot
A _{ref}	reference area	square foot
C	curvature of streamline	1/foot, 1/inch
C _p	curvature, pressure side	1/foot, 1/inch
C _s	curvature, suction side	1/foot, 1/inch
C	chord	inches
C/S	solidity	-
D, d	diameter	inches
DN	diameter speed value for a bearing	mm x rpm
D factor	diffusion factor	-
E	modulus of elasticity	psi
F	fuel flow	pound per second
F/A	fuel-air ratio	-
g	acceleration due to gravity = 32.174	foot per second squared
h	enthalpy	Btu per pound
Δ h	enthalpy drop	Btu per pound
h _o	passage width	inches
H	shear force	pound
i	incidence angle	degrees
I	inertia	foot-pound-second squared
J	mechanical equivalent of heat 778.26	foot-pound per Btu
K	spring rate	pound per inch
L	combustion chamber length	inches
lp	length of primary zone	inches
ld	length of dilution	inches
M	Mach number	
M	mass flow	pound mass per second
M	moment	foot-pound
N	frequency	rpm, cps

		<u>Units</u>
P	absolute pressure	psia, in. HgA
P _S	absolute static pressure	psia, in. HgA
P _T	absolute total pressure	psia, in. HgA
q	dynamic head	psf, psi, in. Hg
r	radius	inches
R	gas constant	Btu per pound - °F
S _a	axial deflection	inches
S	pitch	inches
T	temperature	°R, °F
T _C	coolant temperature	°R, °F
T _G	gas temperature	°R, °F
T _L	local temperature	°R, °F
T ₄	combustor exit temperature	°R, °F
t	thickness	inches
t _e	trailing edge thickness	inches
U	wheel, peripheral speed	fps
V	velocity	fps
V _a	axial velocity	fps
V _a /U	flow coefficient	-
W	weight flow	pound per second
W _c	coolant flow	pound per second
w _t	throat thickness	inches
Y	blade loss coefficient	-
Y _N	nozzle loss coefficient	-
Y _R	rotor loss coefficient	-
α _{N₁}	nozzle outlet gas angle	degrees
α _{R₁}	rotor relative inlet gas angle	degrees
α _{R₂}	rotor relative outlet gas angle	degrees
α _S	stage absolute outlet gas (swirl) angle	degrees

		<u>Units</u>
α	angle	degrees, radius
α	coefficient of thermal expansion	inch per inch per °F
α	angular acceleration	radians per second squared
β	blade inlet angle	degrees
γ	ratio of specific heats	C_p/C_v
δ	deflection	inches
δ	deviation	inches
ϵ, E	strain	inch per inch
E_0	total strain amplitude	inch per inch
η	efficiency	percent
θ	unguided angle	degrees
θ	angular deviation	degrees
ρ	weight density	pound per foot cubed
σ	stress	psi
σ_a	axial stress	psi
σ_a	total stress amplitude	psi
σ_B	bending stress	psi
σ_e	endurance limit at 10^7 cycles	psi
σ_h	hoop stress	psi
σ_θ	tangential stress	psi
σ_r	radial stress	psi
σ_y	yield stress	psi
τ	shear stress	psi
ϕ	angle	degrees
ϕ	torque	foot-pound
ω	work factor $\frac{\Delta h}{U^2/2gJ}$	-

ABBREVIATIONS

USAAVLABS	U.S. Army Aviation Materiel Laboratories
Btu	British thermal unit
cg	center of gravity
C-W	Curtiss-Wright Corporation
DN	bearing parameter diameter and revolutions per minute
EB	electron beam
ESHP	equivalent shaft horsepower
ESFC	equivalent specific fuel consumption
F/A	fuel air ratio
FMB	front main bearing
HP	horsepower
ID	internal diameter
ISA	Instrument Society of America
LC	low carbon
LE	leading edge
NAK	Sodium Potassium mixture
OD	outer diameter
pps	pounds per second
psi	pounds per square inch
psig	pounds per square inch gage
RA	reduction of area
RMB	rear main bearing
RT	room temperature
SR	stress rupture
SST	supersonic transport
TAR	average temperature
TE	trailing edge
TIT	turbine inlet temperature
TS	tensile strength
UTS	ultimate tensile strength
WAD	Wright Aeronautical Division
YS	Yield Strength

IBM Nomenclature

ALFNO	nozzle inlet swirl angle	degrees
ALFN1	nozzle outlet swirl angle	degrees
ALFR1	rotor inlet air angle	degrees
ALFR2	rotor outlet air angle	degrees
ALFS2	absolute outlet rotor swirl angle	degrees
C1	sonic velocity, rotor inlet	foot per second
C2	sonic velocity, rotor outlet	foot per second
DIA1	diameter, rotor inlet	inches
DIA2	diameter, rotor outlet	inches
EPS1	rotor turning angle	degrees
MV1	nozzle outlet Mach number	-
MVR1	rotor inlet Mach number	-
MVR2	rotor outlet Mach number	-
MV2	absolute outlet Mach number	-
PS1	static pressure, rotor inlet	psi
PS2	static pressure, rotor outlet	psi
PTR1	total pressure, rotor inlet	psi
PTR2	total pressure, rotor outlet	psi
REACT	reaction = $(TS1-TS2)/(TTO-TS2)$	-
RH01	density, rotor inlet	pound per inch cubed
RH02	density, rotor outlet	pound per inch cubed
TS1	static temperature, rotor inlet	°R
TS2	static temperature, rotor outlet	°R
TT1	total temperature, rotor inlet	°R
TT2	total temperature, rotor outlet	°R
U1	blade peripheral, inlet	foot per second
U2	blade peripheral, outlet	foot per second
V1	nozzle outlet velocity	foot per second
V2	absolute outlet velocity	foot per second
VA1	axial velocity, rotor inlet	foot per second
VA2	axial velocity, rotor outlet	foot per second
VR1	relative velocity, rotor inlet	foot per second
VR2	relative velocity, rotor outlet	foot per second
VW1	absolute whirl velocity, rotor inlet	foot per second
VW2	absolute whirl velocity, rotor outlet	foot per second

Subscripts

a	axial, amplitude
b	burning zone
B	bending
C	coolant, crushing
D	dilution
e	edge, effective, endurance
G	gas
h	hoop, horizontal, hub
L	local
m	mean, meridional
M	metal
N	nozzle
P	pressure side, primary
r	radial
R	rotor
S	static, suction side, swirl
t	tip, throat
T	thermal, total
V	vertical
VR	velocity, relative to rotor
W, θ	tangential
y	yield
1, 2, 3	stations

1.0 INTRODUCTION

There is a requirement in the field of small gas turbines for advancement of component technology to permit the future development of small, lightweight, high-performance turboshaft engines. This technology will provide background for future aircraft propulsive units, advanced ground vehicle power plants, and stationary power units as well.

Significant work has been done with large turbine engines in improving engine component efficiencies, increasing cycle pressure ratio, increasing turbine inlet temperatures, and developing lightweight high-effectiveness regenerators in order to improve the overall power plant performance. The objective of the current development effort sponsored by the U.S. Army is to advance the state of the art in these same areas to improve the available technology for small engines.

The use of high turbine inlet temperatures (2500°F) has long been a goal of engine designers, because in advanced cycle power plant systems, the horsepower available will more than double, and the specific fuel consumption will be substantially reduced over engines designed with the restrictions of currently available technology. The specific objective of the U.S. Army program reported herein is the development of a single-stage, axial-flow, transpiration-cooled turbine component capable of operation at 2500°F average turbine inlet temperature and improved component efficiency.

The Curtiss-Wright Corporation has developed the technology of a variety of high-temperature components over the past 10 years; in particular, the work conducted on cooled turbine components for the U.S. Navy and the FAA has materially advanced the state of the art. Over 150 hours of full-scale engine tests have been completed at an average turbine inlet temperature of 2500°F and have provided invaluable experience for the work being conducted on this program for small turbine engines.

One of the important aspects to be considered in a high-temperature turbine design is the selection of the blade cooling method. The fundamental thermal characteristics of a blade, average metal temperature, temperature gradients, gas temperature profiles, and coolant requirements are unique functions of the cooling method selected and the design turbine inlet temperature. Transpiration cooling, which was chosen for application to the small turbine under consideration, is a process where cooling air bled from the compressor exit is diffused through a porous structure surrounding the turbine blade into the boundary layer on the hot gas side. Having cooled the porous walls, the coolant then forms a relatively cool film which insulates the gas side airfoil from the hot gas stream and maintains the structure at temperatures substantially below that of the external gas. The cooling action in the transpiration method depends on three factors:

1. Heat sink value of coolant
2. Reduced frictional heat generation due to reduced surface velocity gradients

3. Reduced conductive heat flux into blade surface due to change in temperature profile shape by mass transfer flow

Results of numerous analytical and experimental studies conducted at Government agencies, at private institutions, and at Curtiss-Wright show that the transpiration cooling method is the most efficient in terms of degree of cooling with a given expenditure of coolant in both laminar and turbulent flow regions. In addition, the superiority of transpiration cooling increases as the local gas temperature is raised. Transpiration-cooled blading has been shown also to have the capability of accepting wide ranges in positive and negative gas incidence angles with no detrimental thermal effects at the critical leading edge. The coolant flow and the leading-edge temperature are almost insensitive to a shifting stagnation point at stator or rotor leading edges. It is obvious that this feature is particularly important in the thermal consideration of high-temperature variable-geometry turbine designs.

The advanced technology developed at C-W on transpiration-cooled turbine blades has been applied to the design and evaluation of a small turbine component and incorporated into a rotating test rig during the Phase I period. The detail design analysis (of this turbine component) is the subject of this report and describes the performance characteristics expected during operation and test in Phase II. In addition to the analytical design, various experimental evaluations were made also to confirm the design feasibility:

1. Airfoil forming characteristics
2. Strut fabrication
3. Airfoil-to-strut attachment methods
4. Test of prototype stator blades in two-dimensional cascade.

2.0 TURBINE AERODYNAMIC ANALYTICAL DESIGN

An aerodynamic-thermodynamic design study of a single-stage transpiration-cooled turbine component having the following sea level static performance characteristics as its design goal was completed:

- | | |
|---|-----------------------|
| 1. Turbine work | 140 Btu/pound |
| 2. Temperature, inlet, total average | 2500°F
2960°R |
| 3. Pressure, inlet, total | 112.9 psia |
| 4. Efficiency, adiabatic,
total-to-total, design | 90% |
| 5. Turbine airflow | 4 pounds/second |
| 6. Cooling airflow, rotor blade | 3-5% of total airflow |
| 7. Cooling airflow, stator blade | 3-5% of total airflow |

The design parameters were established to provide a turbine stage capable of driving an 8 to 1 pressure ratio compressor to form the basis of an advanced turbine engine in the 500-1000 horsepower class. The information developed in the analytical study is incorporated into the design of an advanced turbine for experimental testing to demonstrate high-turbine-inlet-temperature technology.

2.1 TURBINE AERODYNAMIC-THERMODYNAMIC DESIGN

2.1.1 Thermodynamic Considerations

At the beginning of Phase I, a study was initiated to define the turbine component to be developed and to review the turbine thermodynamic analysis that had been performed previously. This preliminary analysis assumed that the turbine annulus was unflared (constant O.D. and constant I.D.) and provided a high absolute rotor discharge Mach number of 0.61. This value was considered to be higher than desirable in a turbine of this type; to reduce this outlet Mach number, the rotor exit area was increased from a value of 10.089 square inches to a larger one of 12.252 square inches. In this preliminary stage, it was assumed that the rotor annular area change was achieved by flaring both the inner and the outer walls to achieve the new outlet area. This change in flow passage reduced the outlet Mach number in question to an acceptable value of 0.45.

This basic design concept was then further refined using existing C-W-developed computer techniques for high-temperature turbine technology. The basic objective of this optimization investigation was to establish the best turbine configuration consistent with high efficiency, mechanical considerations, and practicality of manufacture. In all, 20 separate computer design runs were made in this optimization study. Eight trials were performed in the early review and twelve more were made in the final analysis to determine the various characteristics of three turbine configurations being studied.

Many factors require consideration in a design of this type in order to arrive at the optimum configuration for a specific application. For example, to achieve high efficiency in small turbines, minimum tip clearance between rotor tip and engine casing is desirable. While this can be accomplished in a flared passage, it is obviously much more easily accomplished using a straight-across rotor, which also allows use of honeycomb or abradable material in the casing wall for "run in" and maintenance of small tip clearance. The straight-across rotor also provided an improvement in hub/tip ratio, since all the increased leaving area requirement (flare) was achieved by reducing the inner diameter. C-W efficiency assessment procedures indicate that a hub/tip ratio in excess of 0.82 penalizes turbine performance for a required outlet area, reducing the inside diameter to achieve the necessary flare has a greater effect on hub/tip ratio than increasing the outside diameter. Therefore, the I.D. was reduced to achieve a desirable value of this ratio.

When decreasing the hub diameter for other purposes, consideration must be given to the fact that this reduction in diameter increases the rotor blade turning in these root sections and to the possibility that such an increase in turning will produce an impulse or possibly negative reaction condition. Increasing the rotor outlet whirl provides a means of controlling the amount of reaction in such a situation, but it in itself can reduce the rating efficiency as determined by C-W calculation procedures.

After consideration of all these interrelated criteria as well as to those affecting blade mechanical stresses and manufacturing requirements, a final vector diagram (shown in Figure 1) was selected. Figure 2 depicts the turbine

selected, and Table I defines the overall dimensions. From Figure 2, the method to be used for treating the rotor tip clearance should be noted. As indicated previously, it is desirable to have a constant outer diameter so that a minimum clearance can be attained to reduce losses. In addition, it was deemed desirable to make the rotor tip inlet diameter larger than the exit diameter of the stator to insure "capture" and further minimize tip losses.

Table II lists the turbine design point thermodynamic information, and Table III lists the final turbine blade design data. The axial chord lengths indicated here were modified slightly from those presented previously to achieve more desirable chordal solidities.

The turbine design having been optimized for the design characteristics chosen as the goal, it was necessary to determine the conditions for test in the C-W turbine facility. The test point was selected so as to maintain the same $\frac{W}{A} \sqrt{\frac{h}{h_0}}$ with the pressure varying to be compatible with the present air supply pressure capability. It was assumed that the same turbine inlet total temperature of 2500°F would be maintained for both design and test conditions.

The following data are presented to compare the design and test conditions:

	<u>Design</u>	<u>Test</u>
Turbine Inlet Temperature	2500°F	2500°F
Shaft Speed rpm	50,000	50,000
Pressure Ratio	2.35	2.35
Actual Δh (Btu/pound)	140	140
Mass Flow Ent Rotor pps	4.0	3.01
Stator Inlet Pressure psia	112.9	85

2.1.2 Turbine Performance, Off-Design

The predicted turbine performance is shown in Figure 3 in terms of flow capacity and efficiency versus turbine pressure ratio. The efficiency plotted is the so-called "rating" efficiency, and the pressure ratio described is the inlet total to exit total measured in the axial direction. The rating efficiency claims no credit for the whirl (tangential) component of the absolute velocity leaving the turbine. The use of rating efficiency is felt to be consistent with turbine mapping procedures, since the map represents turbine operation at outlet whirls other than design. In the case of a single-stage turbine in a jet propulsion engine, outlet whirl represents energy lost for propulsion. In a multistage turbine, presumably outlet whirl can be utilized by the following stage at the design point so that a true total-to-total pressure ratio would properly express turbine efficiency. However, even in a multistage turbine operating off design,

downstream stage stators operate at other design inlet angle (incidence) and so tend to demonstrate lower their single-stage design efficiencies. Consideration must also be given to the spacing between stages or to struts that might exist between the compressor turbine and the power turbine. Large separations between stages or the use of struts would argue well for the use of rating efficiency.

The 90-percent turbine efficiency design goal discussed previously is assumed to be the total-to-total efficiency, and the equivalent rating efficiency is 89 percent. Rating efficiency is usually about 1-percent less than total-to-total efficiency for moderate rotor exit whirls (10 degrees to 20 degrees). The map of Figure 3 predicts 88 percent rating efficiency at design pressure ratio, with no benefit claimed for shrouds or close-clearance rotors.

Where close clearance can be maintained between rotor tip and casing under hot operating conditions, an additional 1-percent efficiency can be obtained. Since it is intended to test the present turbine at close tip clearances, a potential rating efficiency of 89 percent, or approximately 90 percent total-to-total, has been predicted and established as the efficiency goal.

Additional working curves of the off-design performance discussed above were prepared and are included here as Figures 4 and 5. In one case, the actual value is plotted for the variable parameters; in the other, the same parameters are shown plotted as a percentage of the design value for the turbine under consideration.

2.1.3 Efficiency - Design Point

The IBM program used for designing the turbine discussed herein computes all the velocity diagram quantities at hub, mean, and tip reference radii utilizing the free vortex turbine theory. Provisions for computing the velocity diagrams at two intermediate radii are available if required by blade geometry. The thermodynamic properties of gases at the elevated temperatures in question are computed automatically and are used in gas dynamic equations normally employed in the design of axial flow turbines.

The program also has the additional flexibility of accepting different inlet and exit air weight flows for each blade row; thus, mass addition or subtraction can be accounted for.

Table IV illustrates the kind of information obtained using the previously mentioned C-W computer program (Section 2.1.1). It calculates all the vector diagram information of Figure 1. Tables V and VI are similar calculations in which the efficiency has been revised to determine the effects on various vector diagram parameters. It will be noted that only very small differences exist in the vector diagram quantities, such as stator discharge velocity (V_1), blade angles, Mach numbers, and pressure ratios. This provides an insight into the test instrumentation requirements and the necessity for accuracy to determine actual values of turbine performance.

The efficiency prediction method that is part of the design calculation procedure was developed by C-W using loss rules based on cascade blade data, turbine component data, and engine test data generated at C-W as well as at other U.S. and British sources. The program described uses an iterative procedure to calculate the adiabatic and rating efficiency and can be used, alternatively, with a prescribed turbine efficiency. Table VII compares measured and calculated turbine efficiency for various engines and/or turbine components. The predicted efficiencies utilizing the program described above are in close agreement with the actual measured values.

The stator and rotor loss coefficients are determined using the proposed turbine mean diameter values for the blade cascades which are compared to previous test data. These coefficients are then modified where necessary for other than optimum hub/tip ratio. Blade solidity, shrouds, thickness of blade trailing edge, tip clearances, and so forth can be accounted for by means of separate efficiency movements. As these effects are included, the program recomputes the loss coefficients. Figure 6 shows the effect of varying the stator and rotor loss coefficients on turbine overall total-to-total adiabatic efficiency. This figure clearly indicates that in the case of this particular turbine, efficiency is much more sensitive to stator loss coefficient than rotor coefficient. It reflects the high energy level of the entering gas and the transonic velocities leaving the stator.

The stator loss coefficient calculated for the present design is 0.0780, and the rotor coefficient is 0.1135. Loss coefficient is defined as the difference between the inlet total pressure to a blade row and the outlet total pressure from the blade row divided by the difference between the outlet total from the blade row and the static pressure at blade row outlet, or

$$Y = \frac{P_{T_{in}} - P_{T_{out}}}{P_{T_{out}} - P_{S_{out}}}$$

The turbine mapping program used to get the turbine performance maps (described in Section 2.1.2) utilizes the output of this first program (mean diameter values) as its basic input. Additional modifications to the loss coefficients are made for changes in blade incidence angle as the turbine moves "off-design" over the wide range of operating conditions specified by the map.

2.1.4 Blade Aerodynamic Design

The number of blades were chosen initially based on the method of Reference 1. This method fixes the axial solidity b/s , which with an axial length b leads to a blade number, and with diagram angles leads to a chordal solidity. The final criteria with regard to blade solidity and blade shape are derived from diffusion factor. Diffusion factor is defined as velocity-before-acceleration minus velocity-after-deceleration divided by velocity-before-acceleration. The velocity-before-acceleration is the peak blade surface velocity as determined from a velocity distribution analysis. Suction surface D factor is limited to a value of 0.25.

The velocity and the pressure distribution around a turbine blade are calculated using a third IBM 704 computer program. This program analyzes the "channel" flow between the blades by the stream filament technique. The program is briefly outlined as follows:

The straight lines joining the point of tangency of an inscribed circle in the blade passage are taken to be the potential lines normal to the streamlines. For a two-dimensional irrotational flow, the pressure gradient $\frac{dP}{dh}$ across the blade passage and normal to the streamlines is given by

$$\frac{dP}{dh} = \gamma P \cdot M^2 \cdot C \quad (1)$$

where C is the curvature of the streamline. It is assumed that from one blade surface to the other across the blade passage, the curvature of the streamlines varies linearly. It is clear, of course, that the two blade surfaces represent the bounding streamlines. Hence,

$$C = C_s - \frac{C_s - C_p}{h_o} \cdot h \quad (2)$$

where h_o is the passage width, h is the distance along the potential line measured from the suction side, and C_s and C_p are the curvatures of the suction and pressure side of the passage, respectively. With the help of the isentropic relationship,

$$P_t = P \left(1 + \frac{\gamma - 1}{2} M^2 \right)^{\frac{\gamma}{\gamma - 1}} \quad (3)$$

Equations (1) and (2) yield

$$\frac{V}{V_m} = \exp \left\{ \frac{h_o}{2(C_s - C_p)} (C^2 - C_m^2) \right\} \quad (4)$$

where V_m and C_m are the velocity and the curvature of the mean streamline, respectively.

The total pressure, total temperature, and radial gradient of mass flow at the inlet and the exit are known from turbine performance data. The stream-wise relative total pressure loss and injected mass flow gradient are assumed to be disturbed linearly along the blade passage. From these values, the average velocity for a potential line is arrived at through the relation

$$\frac{1}{h_o} \frac{\sqrt{\frac{T}{P_T}}}{P_T} \cdot \frac{dW}{dr} = \sqrt{\frac{g\gamma}{R}} \left(\frac{v_{av}}{T} \right) \left[1 - \frac{\gamma-1}{2} \frac{v_{av}^2}{A_T} \right]^{\frac{1}{\gamma-1}} \quad (5)$$

Because of exponential variation in velocity across the blade passage, the average velocity arrived at by continuity is different from the mean streamline velocity. To account for this, the following relation is employed in calculating the mean streamline velocity:

$$v_m = v_{av} / \left[1/2 + 1/4 \left(\frac{v_s}{v_m} + \frac{v_p}{v_m} \right) \right] \quad (6)$$

This has been verified graphically with good agreement between values.

With the help of equations (4), (5), and (6), the surface velocities at both the suction and the pressure side are determined. Having the velocities, the pressures are obtained from the isentropic relationships.

The leading-edge portion of the blade is treated by potential flow theory to obtain the velocity and pressure distribution in the neighborhood of the stagnation point.

For subsonic velocities leaving the blade, on the overhang portion, the stream filament method is used by forming a passage between the overhang and a line extending from the trailing edge of the adjacent blade at an angle equal to the main flow air angles. For supersonic velocities leaving the suction side of the blades, however, the velocity distributions are determined from test results of cascades of different solidities for different ratios of exit static pressure to inlet total pressure. This is necessitated by the shocks present as the supersonic suction side flow decelerates to the subsonic main velocity.

Figure 7 shows the comparison of experimentally determined pressure distribution and that computed using Log 905 IBM program.

Figures 8, 9, and 10 show the stator aerodynamic sections at hub, mean, and tip, respectively. Figures 11, 12, and 13 show the rotor aerodynamic shapes at hub, mean, and tip, respectively. Figure 14 gives the stator static pressure distribution, and Figure 15 gives the stator velocity distribution. Figure 16 gives the rotor static pressure distribution, and Figure 17 gives the rotor velocity distribution. In both stator and rotor, pressure differences were made to agree with design momentum differences.

TABLE I
OVERALL TURBINE DIMENSIONS - HOT

BLADE ROW	NOZZLE	ROTOR
Inlet Outer Diameter	6.541 in.	6.581 in.
Exit Outer Diameter	6.541 in.	6.581 in.
Inlet Inner Diameter	5.459 in.	5.419 in.
Exit Inner Diameter	5.459 in.	5.187 in.
Inlet (Hub/Tip) Ratio	0.8346	0.823
Exit (Hub/Tip) Ratio	0.8346	0.788
Inlet Annulus Area	10.1976 in. ²	10.9516 in. ²
Exit Annulus Area	10.1976 in. ²	12.8841 in. ²

NOTE: 1 percent reduction in above annulus areas was used in the vector diagram calculations to allow for boundary layer effects.

TABLE II
TURBINE DESIGN DATA

RPM	50,000					
Weight Flow Entering Stator	3.846 pounds/second					
Total Pressure Entering Stator	16,263 psf					
Total Temperature Entering Stator	3040°R (2580°F)					
Total Temperature Leaving Stator	2960°R (2500°F)					
Enthalpy Drop	140 Btu/pound					
Work Factor (at Mean Section)	4.25					
Turbine Adiabatic Efficiency	0.8826					
Turbine Axial Efficiency	0.8757					
Total Pressure Ratio	2.3596					
Vector Diagram Sect	Nozzle Exit			Rotor Exit		
	HUB	MEAN	TIP	HUB	MEAN	TIP
Diameter (in.)	5.464	6.000	6.536	5.194	5.884	6.574
Total Temp (°R)	2,960	2,960	2,960	2,505	2,505	2,505
Static Temp (°R)	2,428	2,507	2,567	2,434	2,435	2,436
Total Press (psf)	15,500	15,574	15,653	6,905	6,905	6,904
Static Press (psf)	6,410	7,432	8,300	6,076	6,088	6,097
Work Factor, $\frac{\Delta H}{U^2/2gJ}$	-	-	-	5.448	4.250	3.403

TABLE III
TURBINE BLADE DESIGN DATA

Vector Diagram Section	NOZZLE			ROTOR		
	HUB	MEAN	TIP	HUB	MEAN	TIP
Blade Design Sect Dia (in.)	5.464	6.000	6.536	5.56	5.884	6.480
Pitch, S (in.)	0.7458	0.8195	0.893	0.6718	0.711	0.783
Chord, C (in.)	1.26	1.276	1.302	1.24	1.214	1.184
Axial Chord, b (in.)	0.9384	0.9380	0.9380	1.200	1.142	1.040
Solidity, C/S	1.689	1.557	1.458	1.846	1.708	1.512
Axial Solidity, b/S	1.255	1.145	1.050	1.786	1.606	1.328
Maximum Thickness, t_{max} (in.)	0.308	0.300	0.291	0.260	0.238	0.206
t_{max}/C , %	24.4	23.5	22.3	21.0	19.6	17.4
t_{max}/b , %	32.8	32.0	31.0	21.7	20.8	19.8
Trailing Edge Thickness, t_e (in.)	0.03	0.03	0.03	0.03	0.03	0.03
t_e/S , %	4.02	3.66	3.36	4.47	4.22	3.83
Blade Inlet Angle, β (deg)	0	0	0	53.6	46.7	39.4
Incidence, i (deg)	0	0	0	+4	+2.5	-.2
Blade Exit Angle, β_2 (deg)	68.91	66.3	65.24	57.5	58.4	60.0
Deviation, δ (deg)	0	+7.6	+0	-1.5	-1.4	-1.3
Throat Width, ω_t (in.)	0.2557	0.307	0.3576	0.361	0.376	0.3915
Unguided Angle, θ (deg)	5	3.12	5	7.5	8.5	7.33
Number of Blades	23			26		

TABLE IV
TURBINE DESIGN - STANDARD EFFICIENCY

LOG 870. TURBINE DESIGN PROGRAM.

TRECOM TURBINE (H/T)CC EQUALS 1.0 4 28 65

TURBINE OVERALL PERFORMANCE.

ROTATIONAL SPEED.	=50000.0000
WEIGHT FLOW, INLET.	= 4.0000
WEIGHT FLOW, OUTLET.	= 4.1667
PRESSURE RATIO.	= 2.3596
ENTHALPY DROP.	= -140.0000
ADIABATIC EFFICIENCY.	= 0.8826
RATING EFFICIENCY.	= 0.8757
TOTAL PRESSURE, INLET.	= 112.9374
TOTAL PRESSURE, OUTLET.	= 47.8636
TOTAL TEMPERATURE, INLET.	= 2960.0000
TOTAL TEMPERATURE, OUTLET.	= 2504.8671
ANNULUS AREA, ROTOR INLET.	= 10.0956
ANNULUS AREA, ROTOR OUTLET.	= 12.7553
LOSS COEFFICIENT, NOZZLE.	= 0.0780
LOSS COEFFICIENT, ROTOR.	= 0.1135
HUB/TIP DIAMETER RATIO.	= 0.8361
BLADE HEIGHT	= 0.5356
(W*ROOT(T)/P) IN	= 1.9269
(W*ROOT(T)/P) OUT	= 4.3569
(W*N/P)	= 1770.8925
CENTRIFUGAL STRESS.	=41205.5278
YEH LOSS COEFFICIENT, ROTOR.	= 0.2486

RADIAL ELEMENT PERFORMANCE.

DIA1	6.00000	DIA2	5.88400	U1	1308.99998	U2	1283.69263
VW1	2433.24728	V1	2641.76669	VR1	1523.86702	VA1	1028.70740
VW2	250.91928	V2	1037.19217	VR2	1835.16783	VA2	1006.38318
MV1	1.12218	MVR1	0.64732	MV2	0.44706	MVR2	0.79101
ALFN1	67.08280	ALFR1	47.54094	ALFR2	56.74358	ALFS2	14.00000
PS1	51.51271	TS1	2507.17157	RH01	0.05546	C1	2354.12979
PS2	42.16408	TS2	2435.06583	RH02	0.04674	C2	2320.03070
TTR1	2657.84576	TTR2	2653.58841	PTR1	66.92980	PTR2	61.99822
REACT	0.13736	EPSI	104.28452				

DIA1	5.46441	DIA2	5.19397	U1	1192.15276	U2	1133.15138
VW1	2671.73865	V1	2862.93976	VR1	1802.05806	VA1	1028.70740
VW2	284.25436	V2	1045.75696	VR2	1738.34578	VA2	1006.38318
MV1	1.23576	MVR1	0.77784	MV2	0.45086	MVR2	0.74946
ALFN1	68.94170	ALFR1	55.19043	ALFR2	54.62462	ALFS2	15.77242
PS1	44.40947	TS1	2428.17447	RH01	0.04937	C1	2316.74545
PS2	42.07423	TS2	2433.90826	RH02	0.04666	C2	2319.47919
TTR1	2638.88309	TTR2	2629.98093	PTR1	64.50702	PTR2	59.56191
REACT	-0.01090	EPSI	109.81504				

DIA1	6.53559	DIA2	6.57403	U1	1425.84718	U2	1434.23384
VW1	2233.84427	V1	2459.92889	VR1	1308.08957	VA1	1028.70740
VW2	224.58208	V2	1031.13733	VR2	1940.22617	VA2	1006.38318
MV1	1.03233	MVR1	0.54908	MV2	0.44438	MVR2	0.83615
ALFN1	65.27351	ALFR1	38.14786	ALFR2	58.75538	ALFS2	12.57988
PS1	57.54758	TS1	2567.55576	RH01	0.06050	C1	2382.31027
PS2	42.22724	TS2	2435.87842	RH02	0.04680	C2	2320.41776
TTR1	2678.58047	TTR2	2680.13678	PTR1	69.58320	PTR2	64.82981
REACT	0.25123	EPSI	96.90323				

LOG 870. TURBINE DESIGN PROGRAM.

TABLE V
TURBINE DESIGN - 1-PERCENT EFFICIENCY INCREASE FOR SHROUDS

LOG 870. TURBINE DESIGN PROGRAM.			
TRECUM TURBINE EFF. COR. COEF. = .01		4 30 65	
TURBINE OVERALL PERFORMANCE.			
ROTATIONAL SPEED.	=50000.0000		
WEIGHT FLOW, INLET.	= 4.0000		
WEIGHT FLOW, OUTLET.	= 4.1667		
PRESSURE RATIO.	= 2.3372		
ENTHALPY DROP.	= -140.0000		
ADIABATIC EFFICIENCY.	= 0.8919		
RATING EFFICIENCY.	= 0.8850		
TOTAL PRESSURE, INLET.	= 112.9374		
TOTAL PRESSURE, OUTLET.	= 48.3223		
TOTAL TEMPERATURE, INLET.	= 2960.0000		
TOTAL TEMPERATURE, OUTLET.	= 2504.8671		
ANNULUS AREA, ROTOR INLET.	= 10.0956		
ANNULUS AREA, ROTOR OUTLET.	= 12.7553		
LOSS COEFFICIENT, NOZZLE.	= 0.0780		
LOSS COEFFICIENT, ROTOR.	= 0.1135		
HUB/TIP DIAMETER RATIO.	= 0.8361		
BLADE HEIGHT	= 0.5356		
(W*ROOT(T)/P) IN	= 1.9269		
(W*ROOT(T)/P) OUT	= 4.3156		
(W*N/P)	= 1770.8925		
CENTRIFUGAL STRESS.	=41205.5278		
YEH LOSS COEFFICIENT, ROTOR.	= 0.2182		
RADIAL ELEMENT PERFORMANCE.			
DIA1 6.00000	DIA2 5.88400	U1 1308.99998	U2 1283.69263
VW1 2436.15427	V1 2645.11371	VR1 1527.17239	VA1 1030.42657
VW2 247.95501	V2 1024.93915	VR2 1826.18817	VA2 994.49413
MV1 1.12386	MVR1 0.64887	MV2 0.44163	MVR2 0.78687
ALFN1 67.07302	ALFR1 47.56698	ALFR2 57.00451	ALFS2 14.00000
PS1 51.40321	TS1 2506.02341	RHO1 0.05537	C1 2353.59070
PS2 42.69687	TS2 2436.70529	RHO2 0.04730	C2 2320.81158
TTR1 2657.35196	TTR2 2653.09460	PTR1 66.86915	PTR2 62.54013
REACT 0.13246	EPSI 104.57148		
DIA1 5.46441	DIA2 5.19397	U1 1192.15276	U2 1133.15138
VW1 2674.93057	V1 2866.53629	VR1 1805.66025	VA1 1030.42657
VW2 280.89628	V2 1033.40276	VR2 1728.74210	VA2 994.49413
MV1 1.23765	MVR1 0.77961	MV2 0.44538	MVR2 0.74506
ALFN1 68.93256	ALFR1 55.20345	ALFR2 54.88148	ALFS2 15.77242
PS1 44.29653	TS1 2426.83743	RHO1 0.04927	C1 2316.10754
PS2 42.60809	TS2 2435.57495	RHO2 0.04722	C2 2320.27322
TTR1 2638.38928	TTR2 2629.48715	PTR1 64.44801	PTR2 60.08207
REACT -0.01666	EPSI 110.08493		
DIA1 6.53559	DIA2 6.57403	U1 1425.84718	U2 1434.25384
VW1 2236.51303	V1 2462.47211	VR1 1311.09045	VA1 1030.42657
VW2 221.92895	V2 1018.95584	VR2 1931.81111	VA2 994.49413
MV1 1.03385	MVR1 0.55045	MV2 0.43898	MVR2 0.83225
ALFN1 65.26315	ALFR1 38.19317	ALFR2 59.01604	ALFS2 12.57988
PS1 57.44271	TS1 2566.55194	RHO1 0.06042	C1 2381.84451
PS2 42.75928	TS2 2437.49881	RHO2 0.04735	C2 2321.18942
TTR1 2678.08664	TTR2 2679.64301	PTR1 69.52083	PTR2 65.39701
REACT 0.24699	EPSI 97.20921		
LOG 870. TURBINE DESIGN PROGRAM.			

TABLE VI
TURBINE DESIGN - 90-PERCENT PRESCRIBED DESIGN EFFICIENCY

LOG 870. TURBINE DESIGN PROGRAM.

TRECOM TURBINE EFFICIENCY SPECIFIED 90.0% 4 29 65
TURBINE OVERALL PERFORMANCE.

ROTATIONAL SPEED.	=50000.0000
WEIGHT FLOW, INLET.	= 4.0000
WEIGHT FLOW, OUTLET.	= 4.1667
PRESSURE RATIO.	= 2.3175
ENTHALPY DROP.	= -140.0000
ADIABATIC EFFICIENCY.	= 0.9000
RATING EFFICIENCY.	= 0.8931
TOTAL PRESSURE, INLET.	= 112.9374
TOTAL PRESSURE, OUTLET.	= 48.7329
TOTAL TEMPERATURE, INLET.	= 2960.0000
TOTAL TEMPERATURE, OUTLET.	= 2504.8671
ANNULUS AREA, ROTOR INLET.	= 10.0956
ANNULUS AREA, ROTOR OUTLET.	= 12.7553
LOSS COEFFICIENT, NOZZLE.	= 0.0780
LOSS COEFFICIENT, ROTOR.	= 0.
HUB/TIP DIAMETER RATIO.	= 0.8361
BLADE HEIGHT	= 0.5356
(W*ROOT(T)/P) IN	= 1.9269
(W*ROOT(T)/P) OUT	= 4.2792
(W*N/P)	= 1770.8925
CENTRIFUGAL STRESS.	=41205.5278
YEM LOSS COEFFICIENT, ROTOR.	= 0.1909

RADIAL ELEMENT PERFORMANCE.

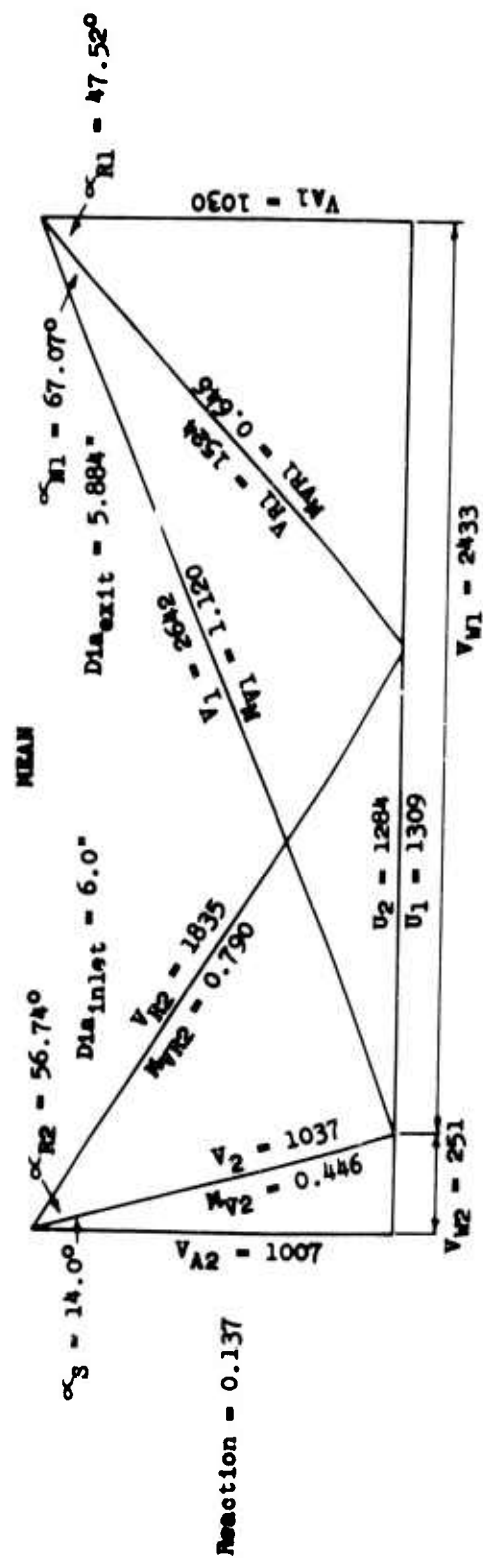
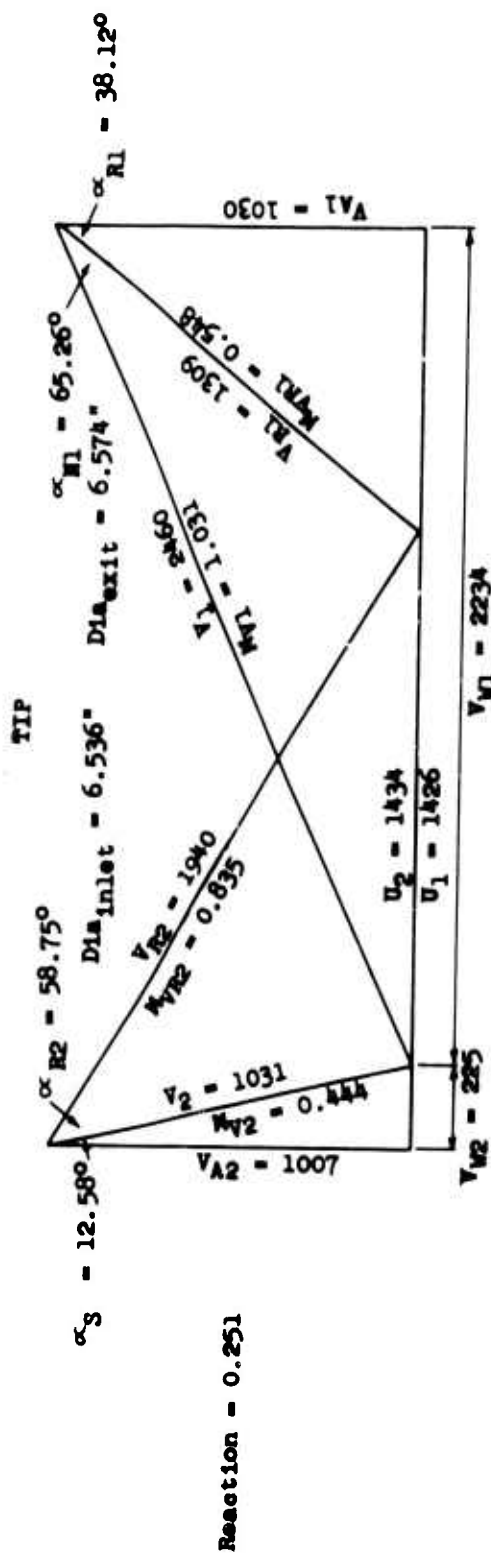
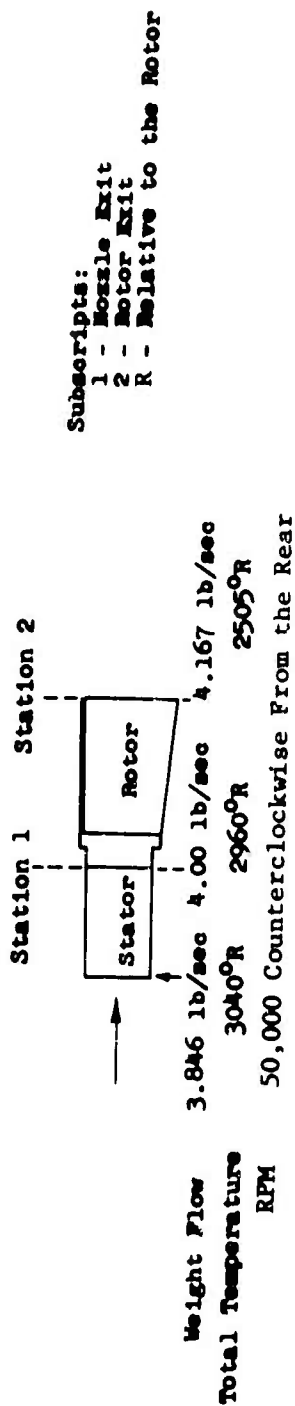
DIA1 6.00000	DIA2 5.88400	U1 1308.99998	U2 1283.69263
VW1 2438.69003	V1 2648.03571	VR1 1530.05995	VA1 1031.93216
VW2 245.36924	V2 1014.25067	VR2 1818.38629	VA2 984.12314
MV1 1.12533	MVR1 0.65023	MV2 0.43690	MVR2 0.78329
ALFN1 67.06439	ALFR1 47.58944	ALFR2 57.23421	ALFS2 14.00000
PS1 51.30765	TS1 2505.01987	RHO1 0.05529	C1 2353.11942
PS2 43.17187	TS2 2438.11954	RHO2 0.04780	C2 2321.48495
TTR1 2656.92120	TTR2 2652.66388	PTR1 66.81627	PTR2 63.02557
REACT 0.12819	EPSI 104.82365		

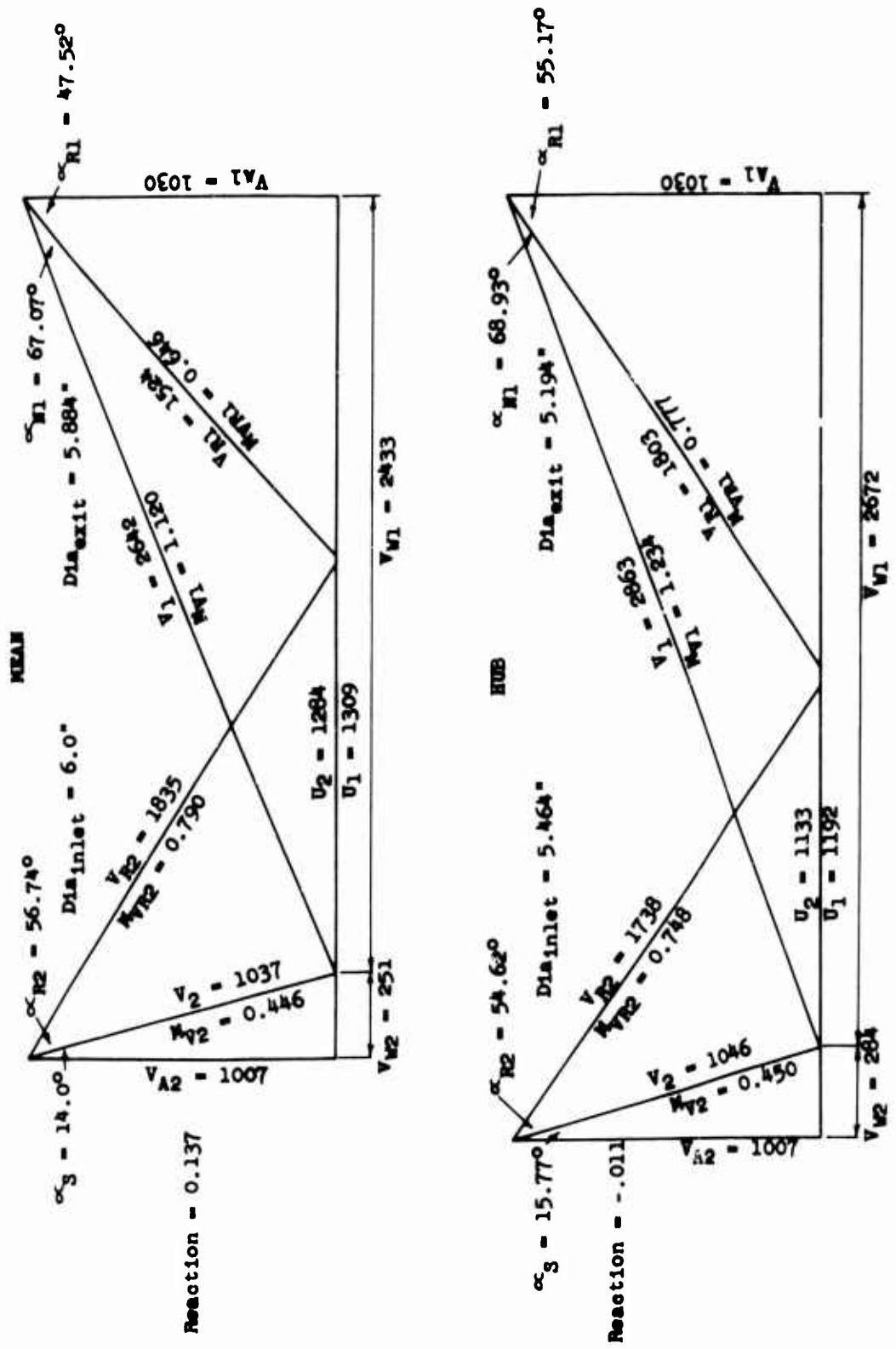
DIA1 5.46441	DIA2 5.19397	U1 1192.15276	U2 1133.15138
VW1 2677.71487	V1 2869.67581	VR1 1808.80591	VA1 1031.93216
VW2 277.96698	V2 1022.62601	VR2 1720.39337	VA2 984.12314
MV1 1.23931	MVR1 0.78116	MV2 0.44061	MVR2 0.74124
ALFN1 68.92449	ALFR1 55.21462	ALFR2 55.10787	ALFS2 15.77242
PS1 44.19800	TS1 2425.66891	RHO1 0.04919	C1 2315.54987
PS2 43.08401	TS2 2437.01260	RHO2 0.04772	C2 2320.95792
TTR1 2637.95850	TTR2 2629.05640	PTR1 64.39656	PTR2 60.54803
REACT -0.02169	EPSI 110.32250		

DIA1 6.53559	DIA2 6.57403	U1 1425.84718	U2 1434.23384
VW1 2238.84100	V1 2465.21649	VR1 1313.71347	VA1 1031.93216
VW2 219.61459	V2 1008.32976	VR2 1924.50359	VA2 984.12314
MV1 1.03518	MVR1 0.55165	MV2 0.43428	MVR2 0.82886
ALFN1 65.25401	ALFR1 38.23236	ALFR2 59.24527	ALFS2 12.57988
PS1 57.35117	TS1 2565.67447	RHO1 0.06034	C1 2381.43732
PS2 43.23363	TS2 2438.89655	RHO2 0.04785	C2 2321.85486
TTR1 2677.65591	TTR2 2679.21222	PTR1 69.46646	PTR2 65.90509
REACT 0.24329	EPSI 97.47764		

LOG 870. TURBINE DESIGN PROGRAM.

TABLE VII COMPARISON OF MEASURED AND CALCULATED DESIGN POINT TURBINE EFFICIENCY							
Turbine	Ω	V/U	α°_s	Dh/Dt	η_{calc}	η_{meas}	Error- $\Delta\eta$
NACA B - 44 (RM E52 C17)	2.06	0.66	0	0.60	0.898	0.894	+0.004
NACA B - 32 (RM E52 C17)	2.11	0.71	0	0.60	0.894	0.889	+0.005
Model							
J-67 LP	2.61	0.83	0	0.70	0.870	0.869	+0.001
J-65 LP W-10	3.28	0.84	15.2	0.74	0.860	0.856	+0.004
J-65 HP W-10	3.00	0.52	30.8	0.75	0.874	0.896	-0.022
T-49 HP	2.64	0.48	16.8	0.73	0.891	0.897	-0.006
T-49 LP	2.64	0.59	13.2	0.68	0.905	0.911	-0.006
T-49 LP	2.32	0.81	0	0.62	0.893	0.896	-0.003
OL 3 HP	3.84	0.58	28.0	0.74	0.897	0.890	+0.007
OL 3 LP	2.64	0.74	7.0	0.63	0.904	0.905	-0.001
SA 7 HP	3.16	0.687	21.8	0.71	0.877	0.864	+0.013
SA 7 LP	2.665	0.747	18.7	0.596	0.886	0.880	+0.006
607007							
J-67 LP	2.71	0.80	6.0	0.70	0.882	0.875	+0.007
607007							
J-67 HP	3.27	0.46	27.0	0.77	0.899	0.900	-0.001

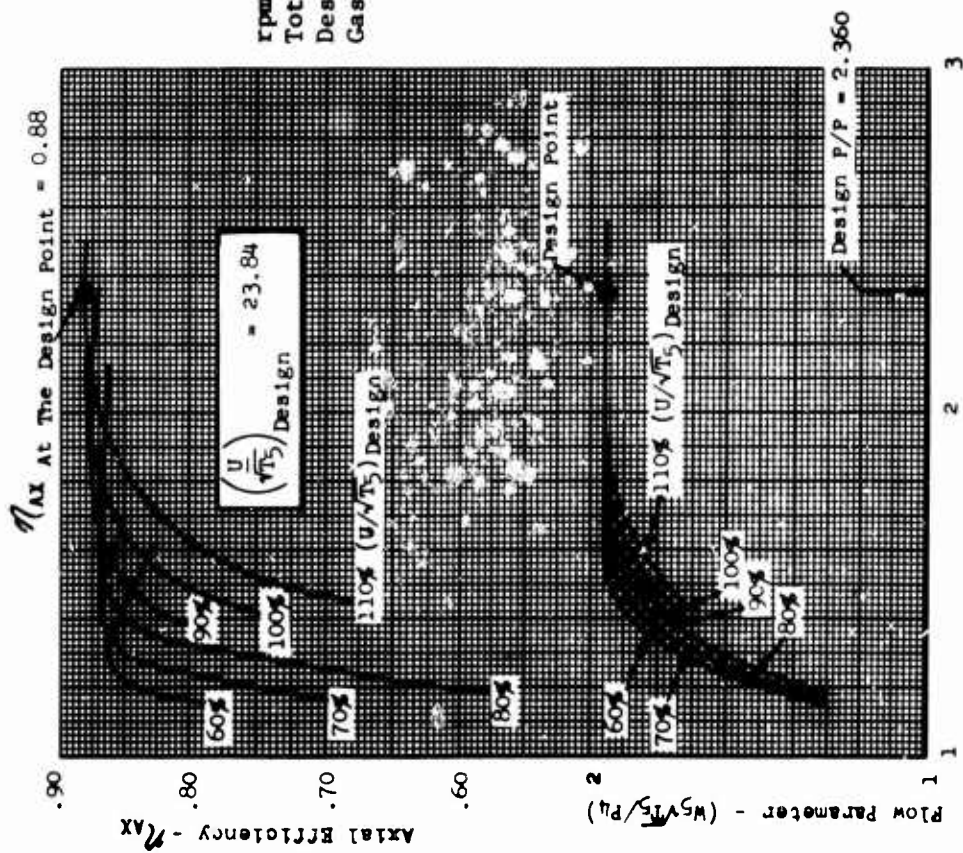




Note: 1% Correction in annulus area has been applied for boundary layer effect at Stations 1 and 2.

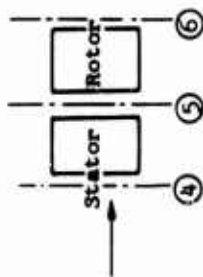
Figure 1. Turbine Velocity Diagram.

B



$$\text{Turbine Axial Pressure Ratio} = \frac{\text{Axial Inlet Total Pressure}_4}{\text{Axial Exit Total Pressure}_6}$$

Figure 3. Estimated Overall Turbine Performance Map.



rpm = 50,000
 Total Temp Engering Rotor = 2960°R(Abs.)
 Design Pressure Ratio = 2.360
 Gas Generator Application

Design Point Data: Gas Generator Application

Inlet Weight Flow	4.0 lb/sec
Actual Work Output	140 Btu/lb
Inlet Temperature, Rotor	2500°F (Stator Absolute Leaving)
Inlet Pressure	229.9 in Hg A
Gas Gen Rotor Speed	50,000 rpm

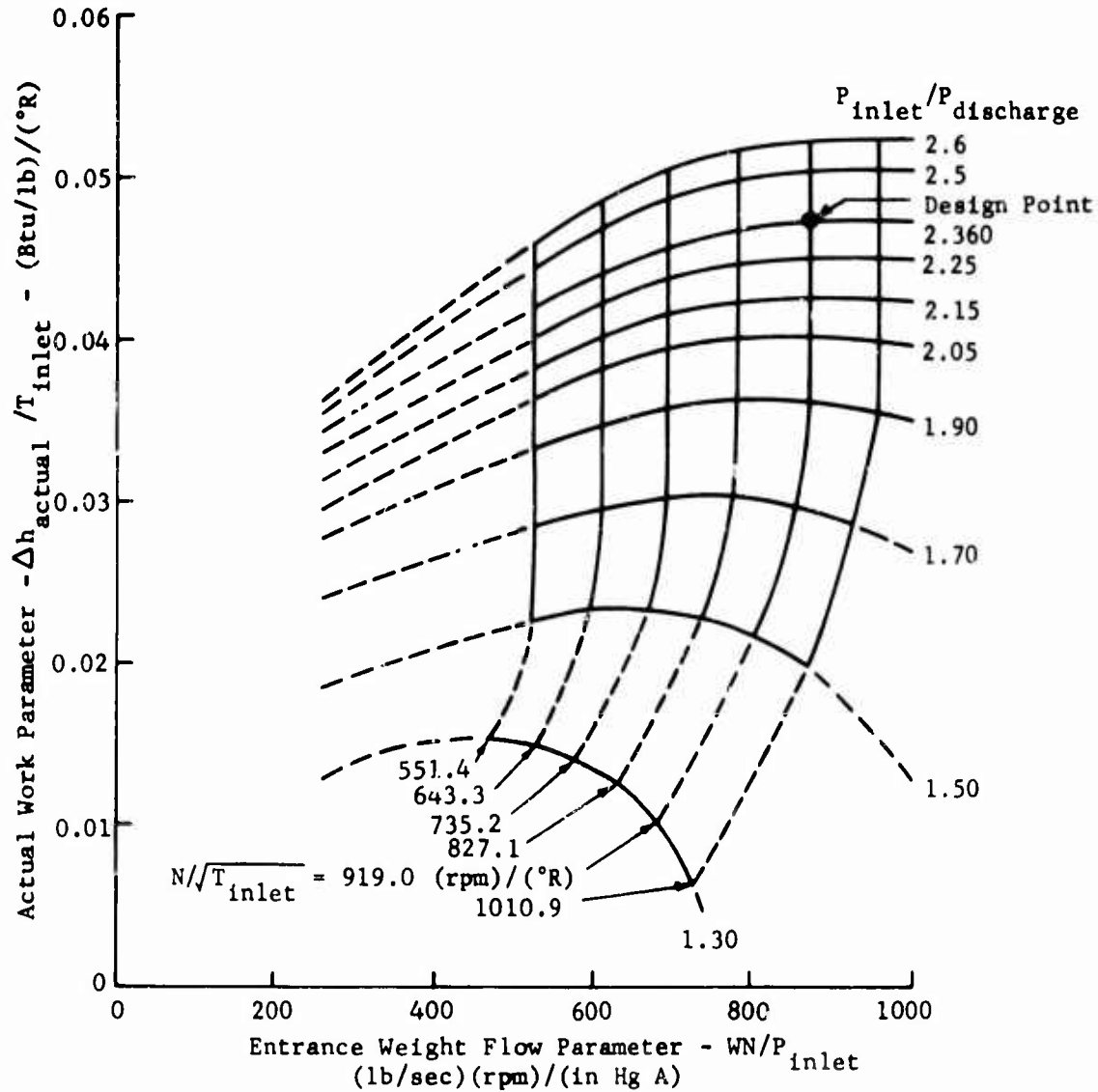


Figure 4. Estimated Overall Turbine Performance Map.

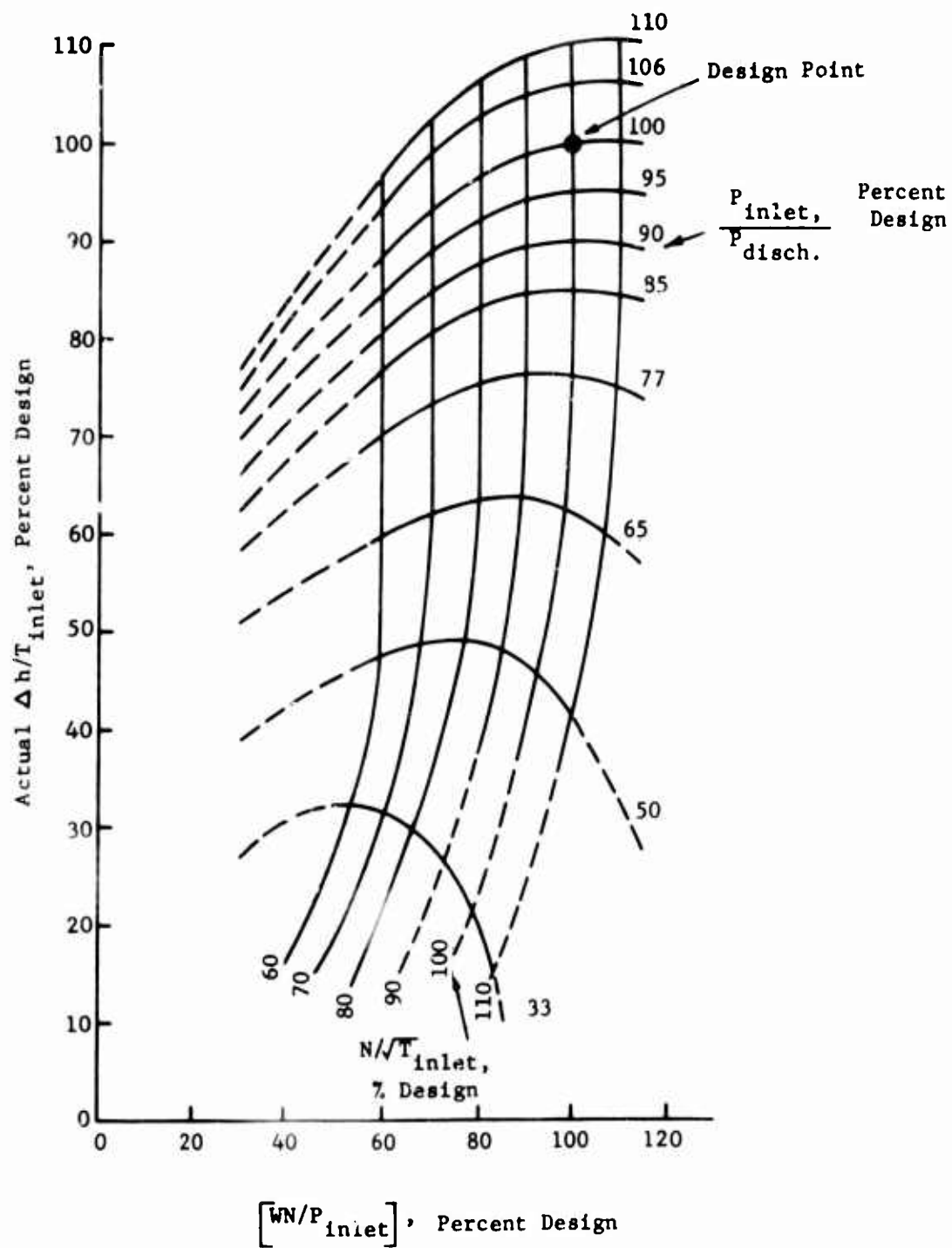


Figure 5. USAAVLABS Estimated Overall Turbine Performance Map.

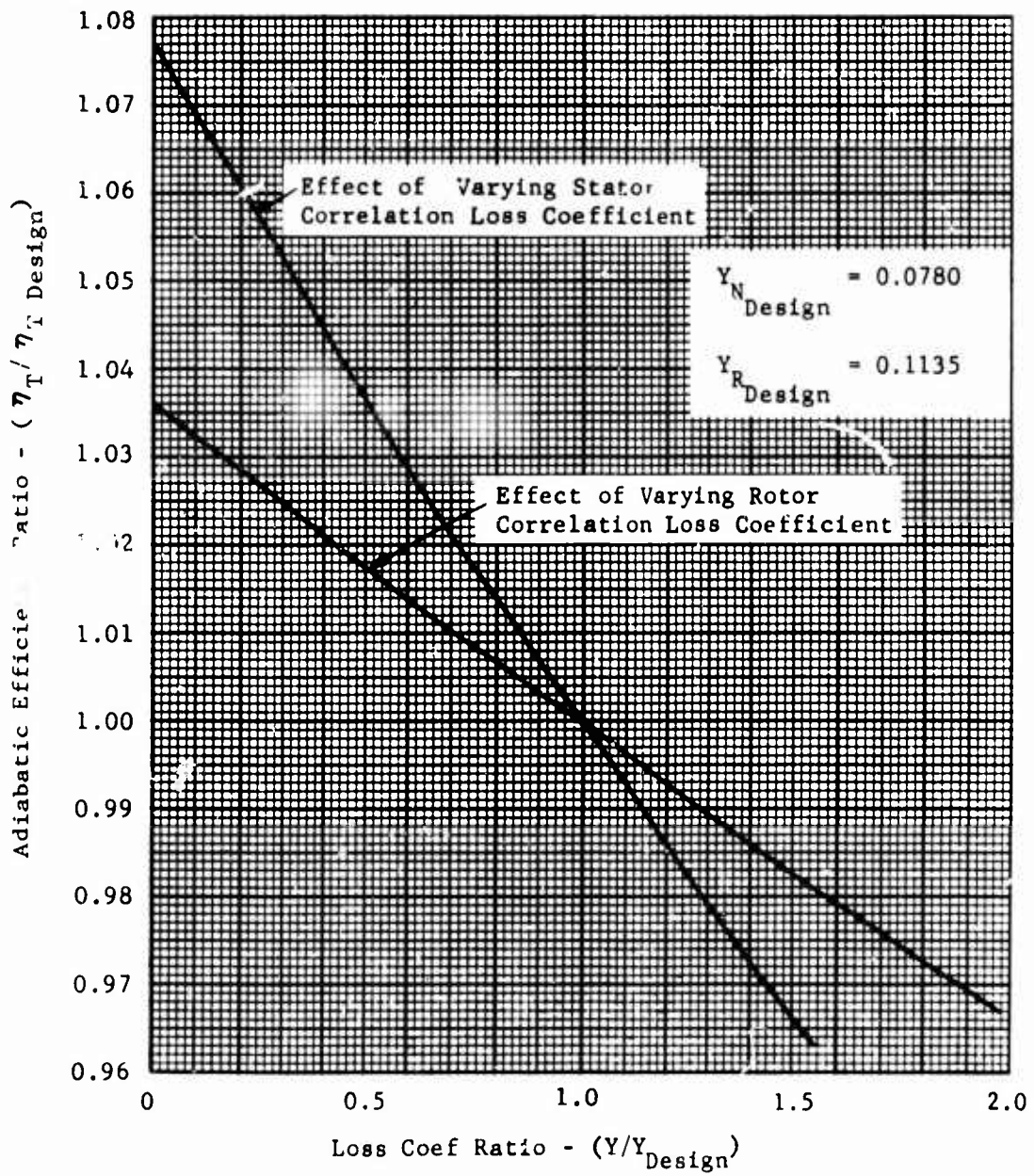


Figure 6 Adiabatic Efficiency Vs Turbine Blade Loss Coefficient.

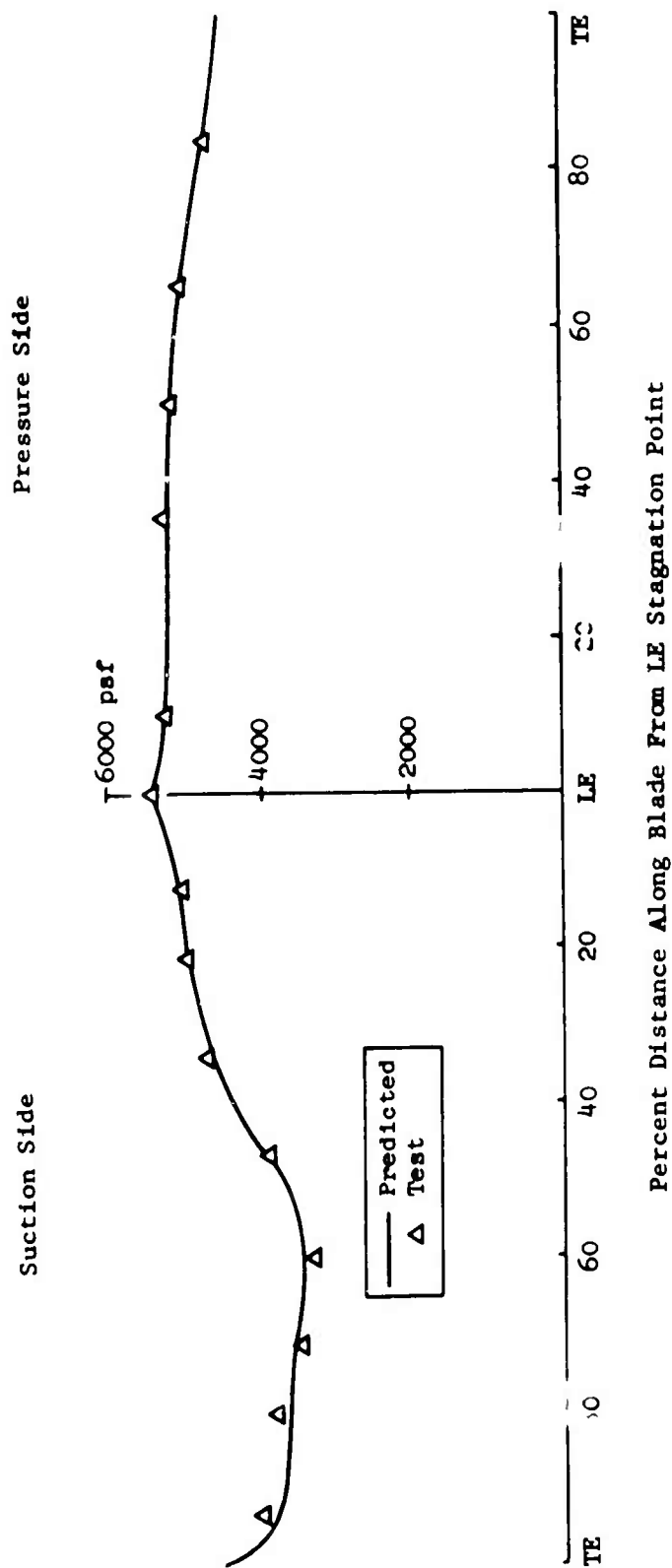
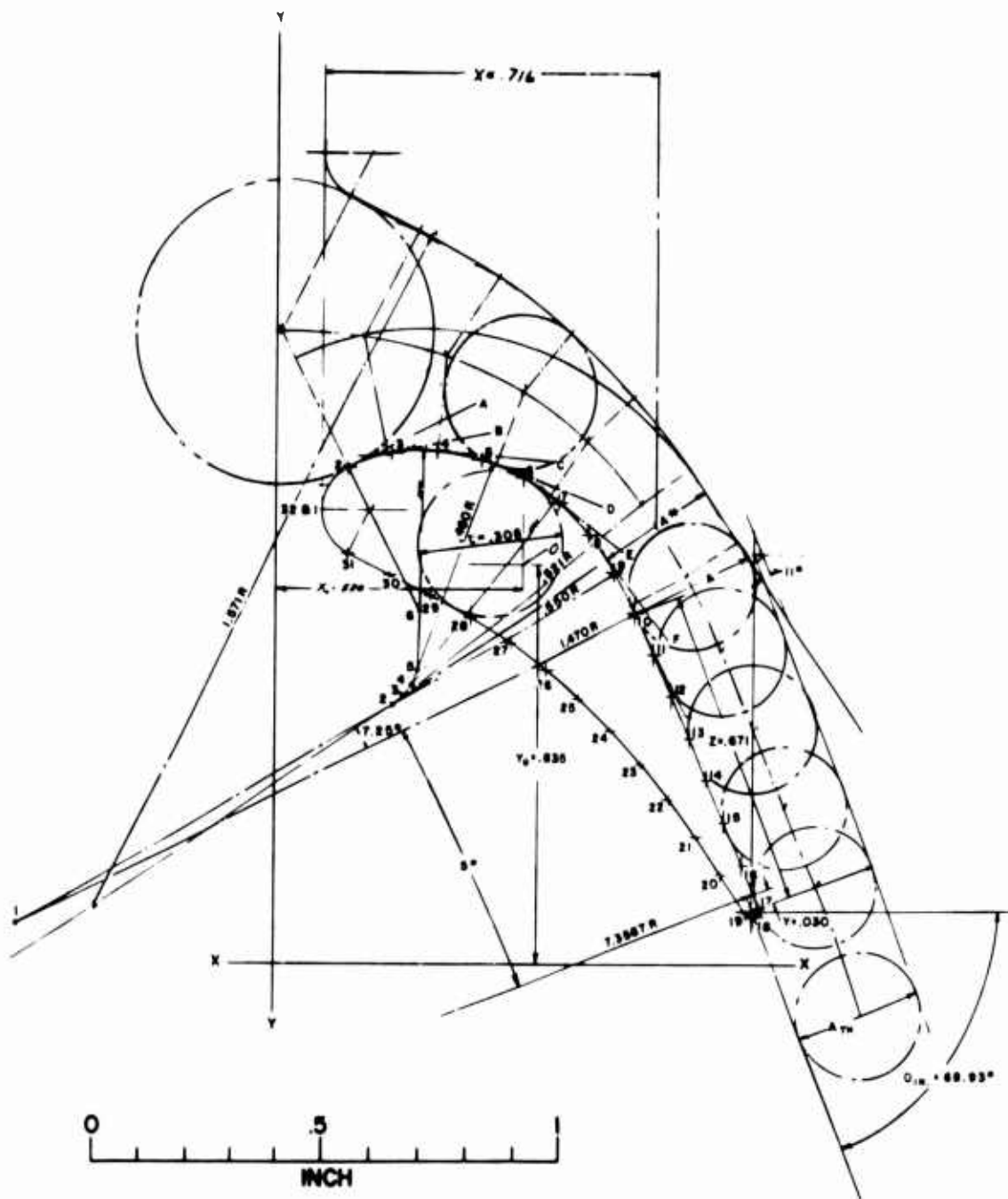


Figure 7. Predicted and Cascade Test Values Pressure Distribution Around a Transpiration-Cooled Stator Blade.



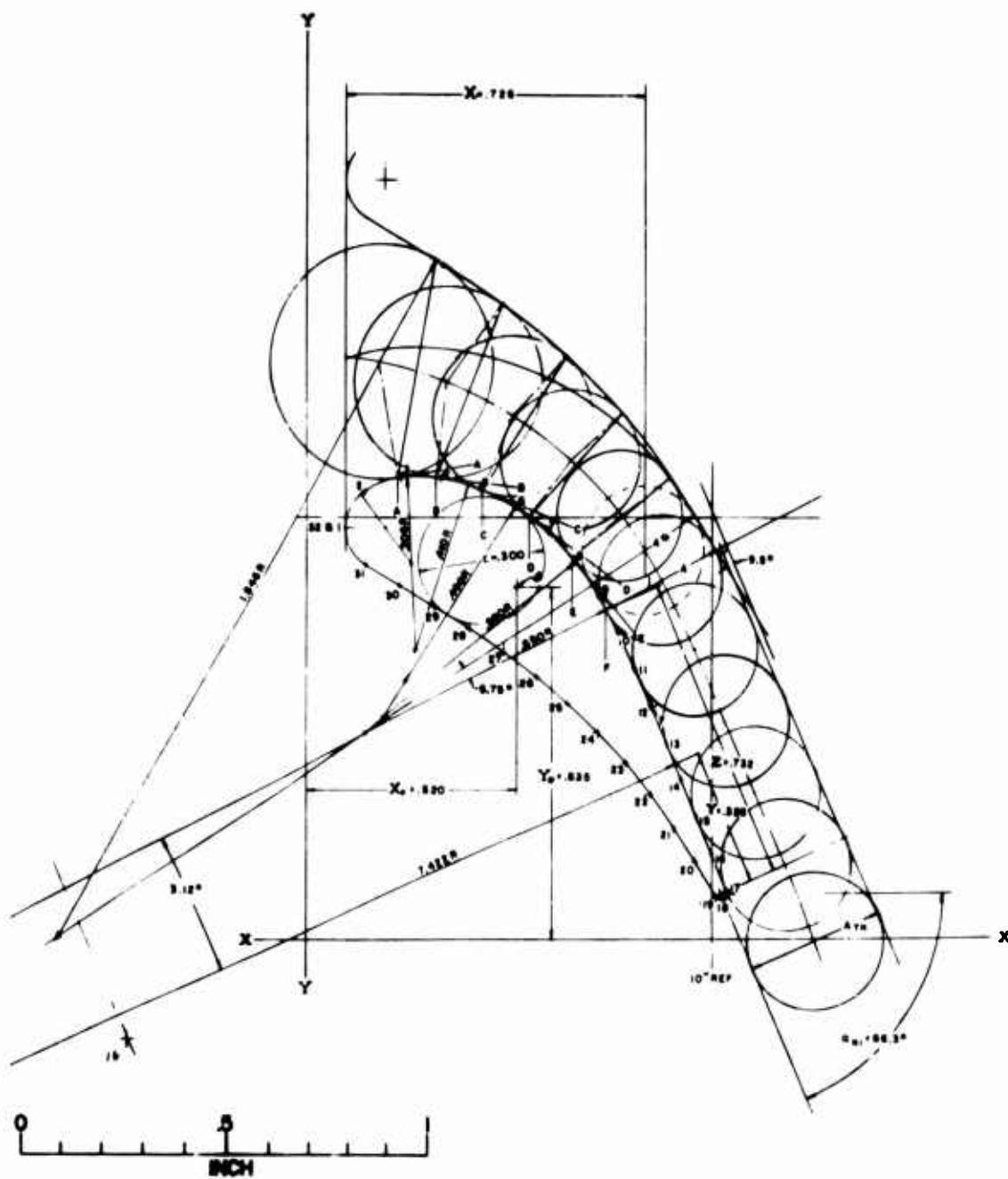
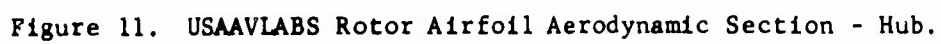


Figure 9. USAAVLABS Stator Airfoil Aerodynamic Section - Mean.





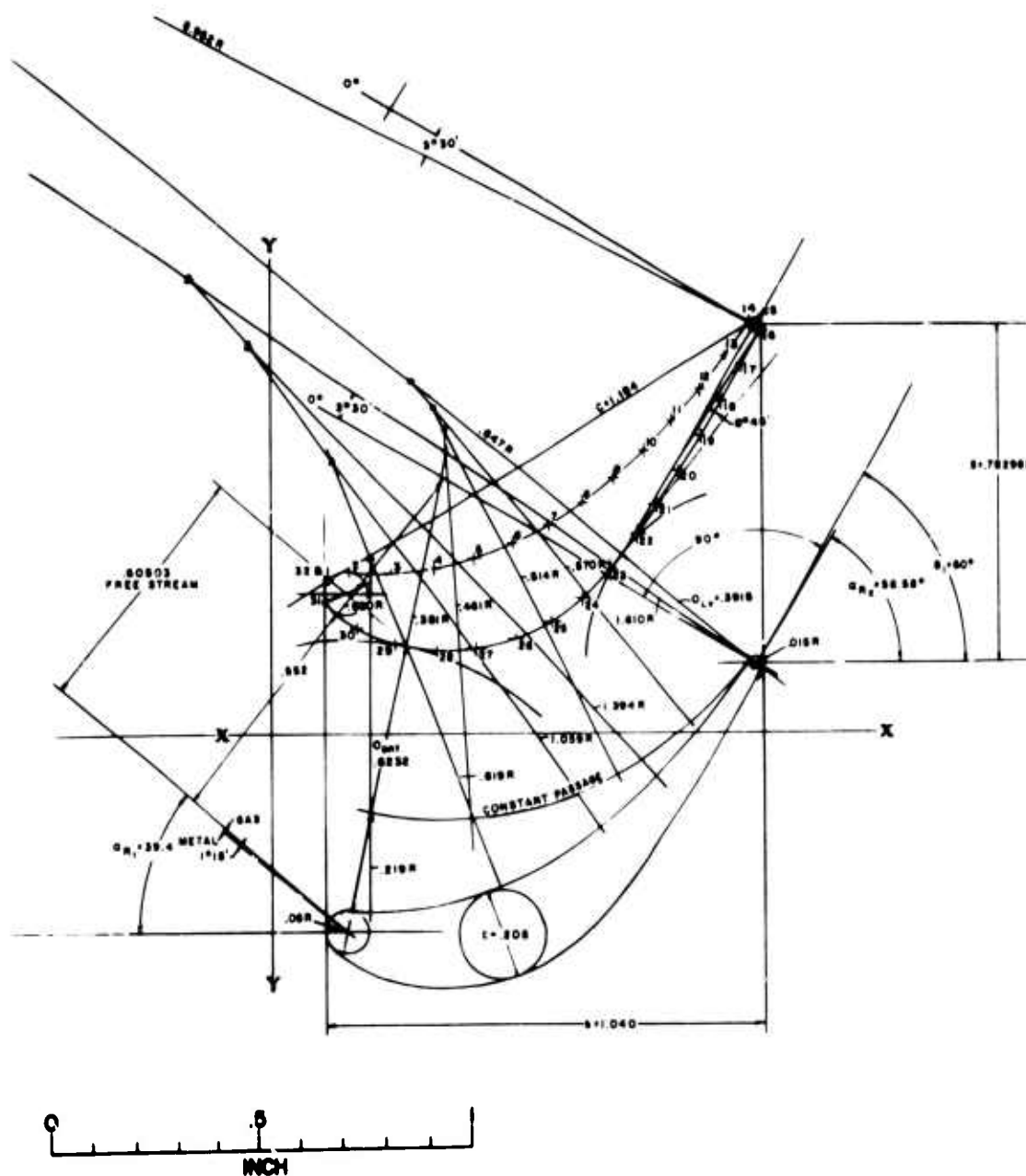


Figure 13. USAFVLAD 1.0-1 at 0.01 Aerodynamic Section - Tip.

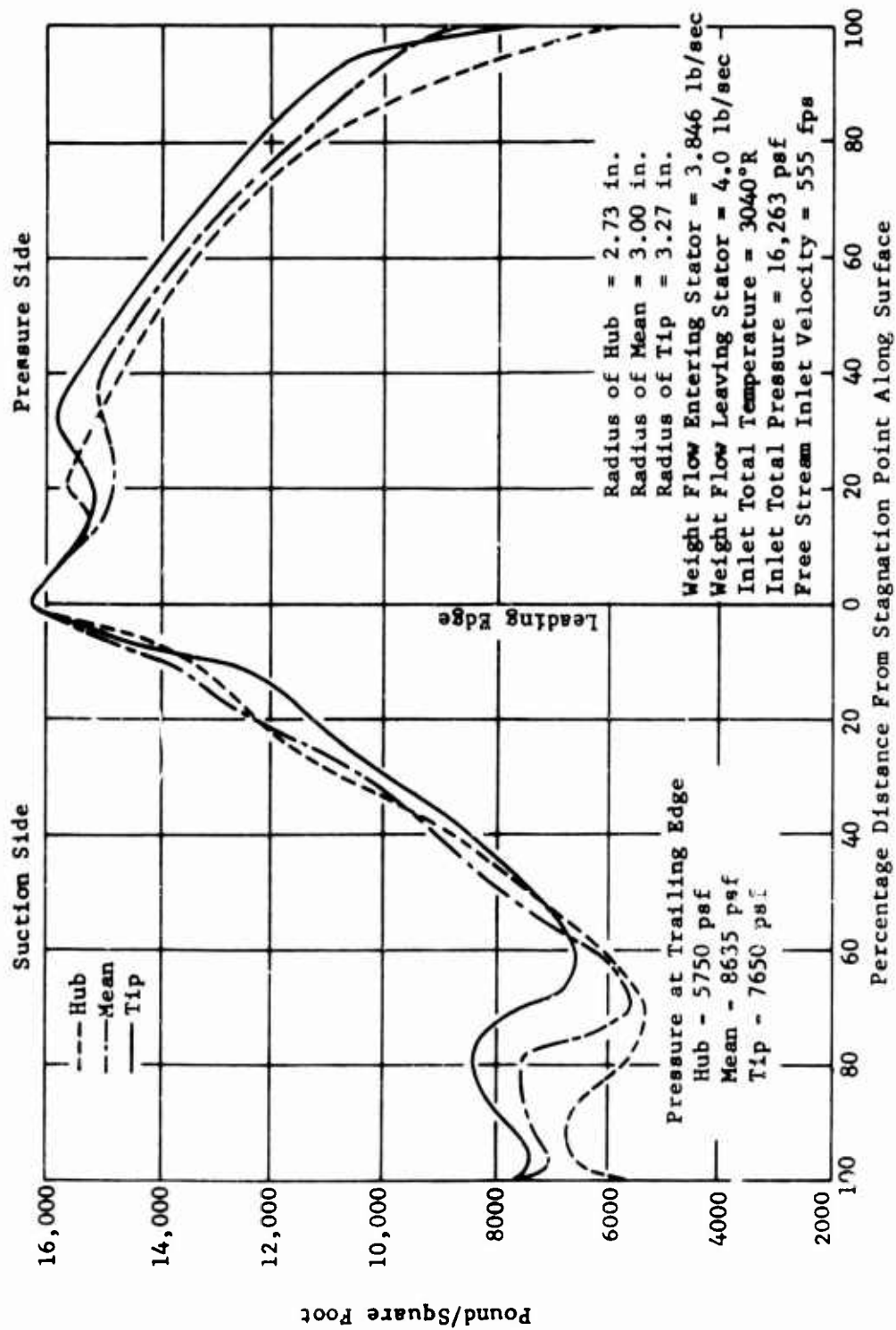


Figure 14. Calculated Turbine Stator Blade Static Pressure Distribution.

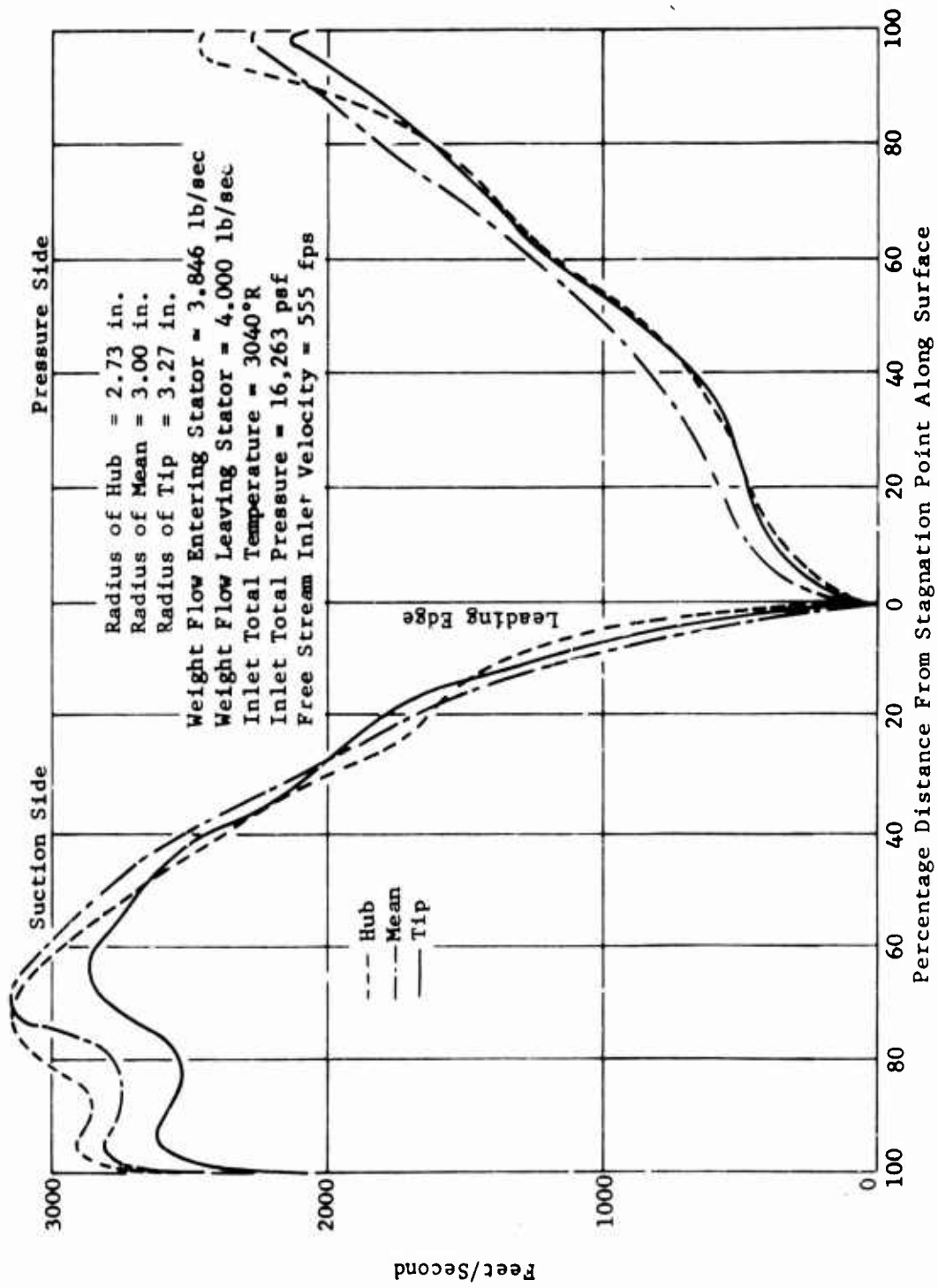


Figure 15. Calculated Turbine Stator Blade Velocity Distribution.

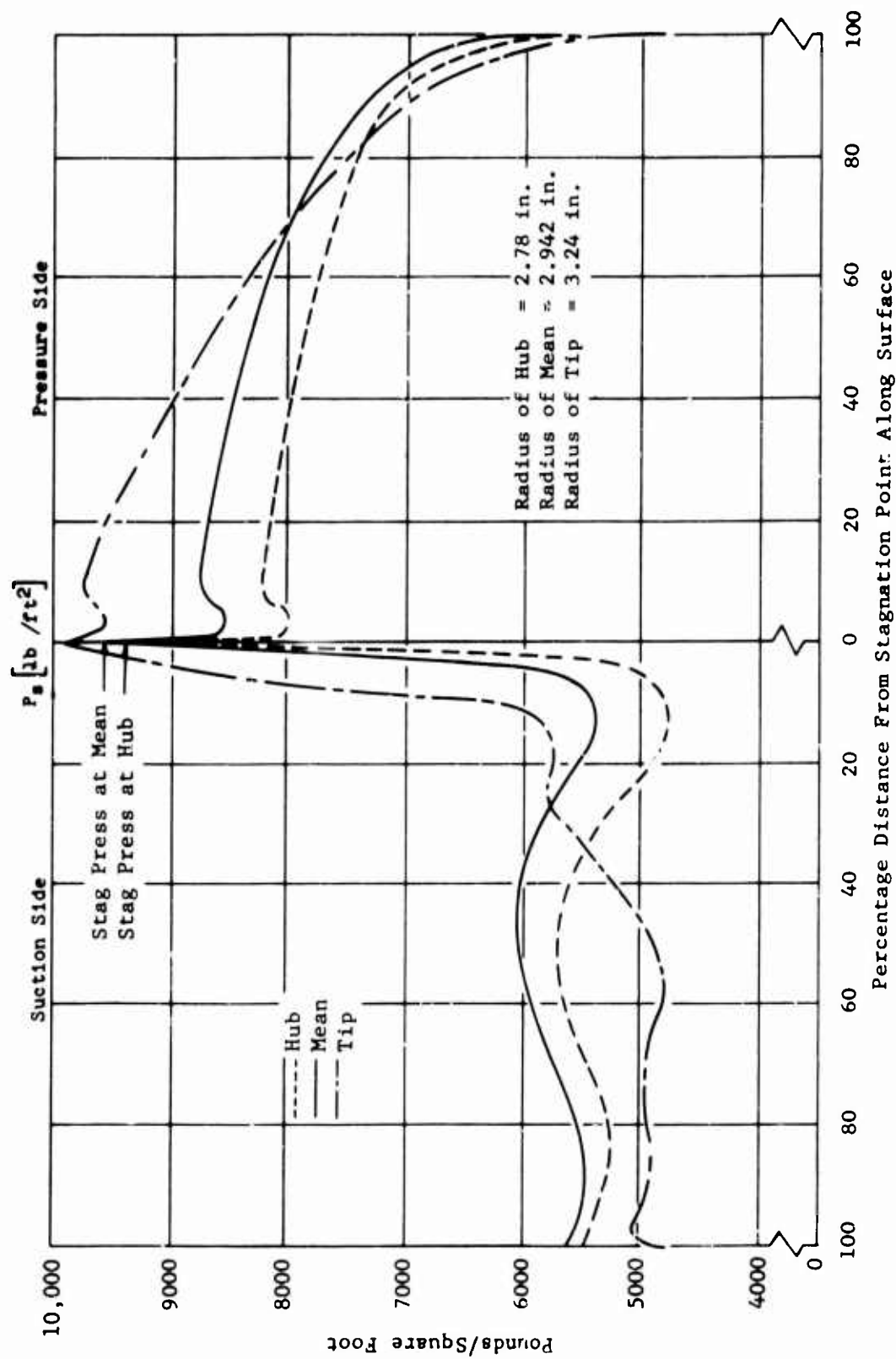


Figure 16. Calculated Turbine Rotor Blade Static Pressure Distribution.

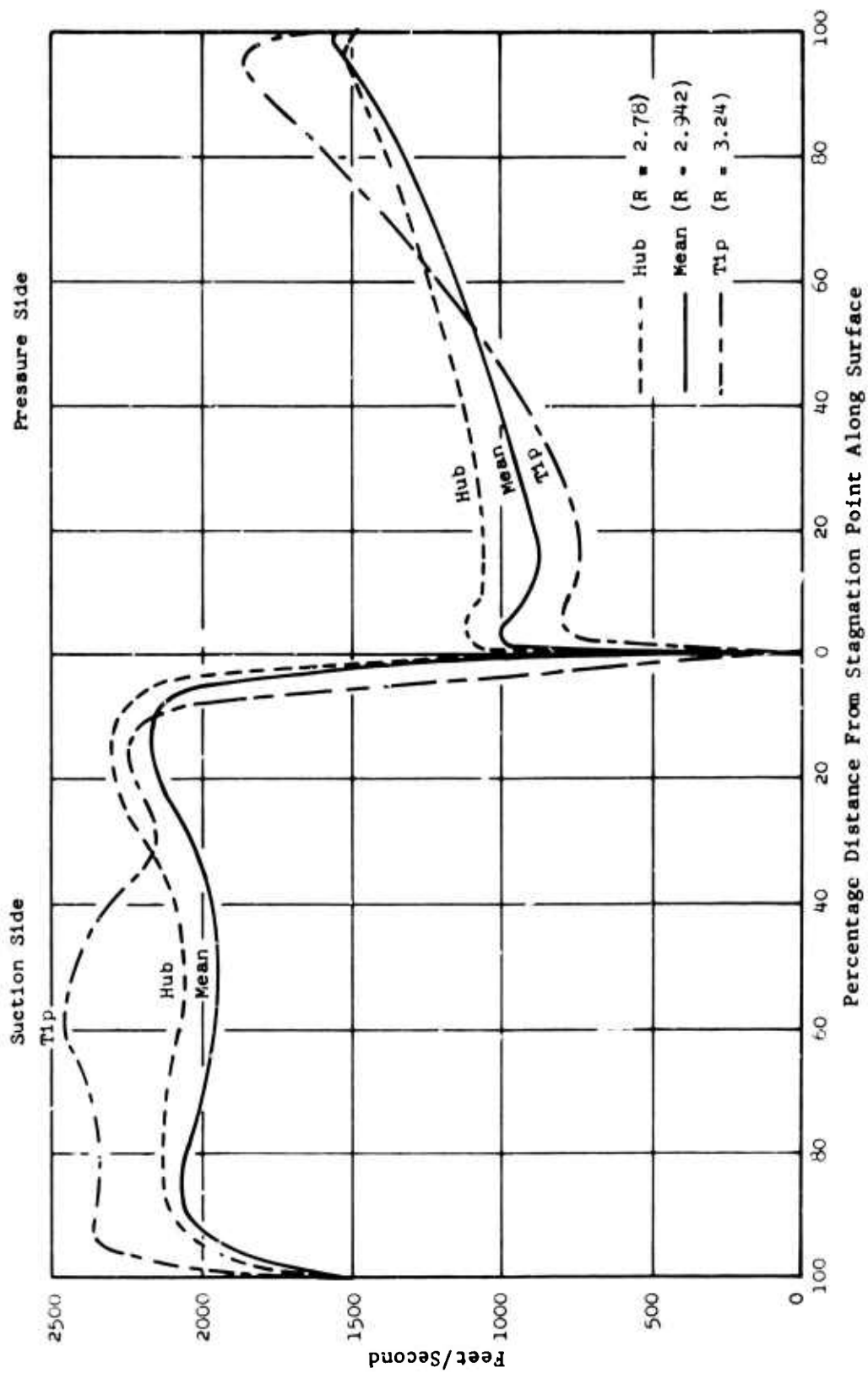


Figure 17. Calculated Turbine Rotor Blade Velocity Distribution (Preliminary).

2.2 ENGINE PERFORMANCE

2.2.1 Design Point Performance

Brief studies were made during Phase I to relate the predicted performance of the gas generator turbine discussed above with other components in a free power turbine engine and to estimate the overall capability of such a system. Of necessity, certain assumptions had to be made on which to base such a study, and the following data are presented to clarify these areas:

Turbine (gas generator)

Weight flow	4.00 pounds/second
Work	140 Btu/pound
Adiabatic efficiency	0.8826
Average inlet temp (leaving stator)	2500°F
Inlet pressure	229.9 in. Hg A
Rotor blade cooling airflow	(4.0% of total weight flow; combustor plus cooling air)

Compressor

Inlet recovery	0.99
Pressure ratio	8:1
Mechanical efficiency	0.99

Combustion Chamber

Fuel lower heating value (JP-4)	18,300 Btu/pound
Pressure recovery	0.97
Combustion efficiency	0.99

Free Turbine (power)

Cooling airflow	None
Adiabatic efficiency	0.913
Diffuser pressure recovery	0.98
Mechanical efficiency	0.98

Nozzle, Exhaust

Velocity coefficient	0.98
Discharge coefficient	0.99
Pressure ratio	1.03

Accessory Power Extraction

None

The following performance data were obtained by design point calculation, using these assumptions:

Compressor inlet pressure	29.62 in. Hg A
Compressor discharge pressure	237.0 in. Hg A
Compressor discharge temperature	621°F
Compressor adiabatic efficiency	0.735
Gas generator turbine pressure ratio	2.36
Gas generator turbine discharge pressure	97.38 in. Hg A
Power turbine pressure ratio	3.097
Jet nozzle area	0.462 square feet
Output shaft horsepower	883 horsepower
Fuel flow	0.123 pound/second
Brake specific fuel consumption	0.5 pound/hour-horsepower

2.2.2 Off-Design Performance

Off-design engine performance was obtained using an IBM computer program over a range of gas generator and free turbine rotor operating speeds to obtain data relating to minimum specific fuel consumption for this engine configuration. For these calculations, the turbine performance map described in Section 2.1 was used for the gas generator rotor, and a free turbine (fixed geometry) performance map taken from Figure 2 of Reference 2 was used for the power turbine rotor. The latter performance map was scaled to provide an adiabatic efficiency of 0.913 (corresponding to 0.80 polytropic efficiency) at the design point. It was felt that this power turbine was compatible in design with the gas generator turbine and would be a realistic representation for study purposes. The compressor performance map utilized was also taken from Reference 2; data for a 9.5:1 pressure ratio axial-centrifugal compressor was scaled to conform with the 8:1 pressure ratio requirement outlined in the design point study described above. Similarly, the compressor efficiency was scaled from 0.805 to 0.735 to agree with design point assumptions for matching the gas generator turbine. The latter efficiency is lower than current state-of-the-art values, which would normally be assessed at approximately 0.80 adiabatic efficiency for engines of this type. Therefore, using the same mass flow and similar

internal conditions with a compressor of current (or advanced) performance, a significant increase in output shaft horsepower could be realized, and an improvement in brake specific fuel consumption could be achieved.

Several assumptions supplementing the design point listing were formulated for off-design operation as follows:

Compressor

Inlet recovery - Inlet pressure loss varies as the square of the airflow.

Turbine (gas generator)

Rotor blade cooling air - Varies with combustion chamber temperature.

Minimum specific fuel consumption data for the study engine are shown in Figure 18 plotted versus output shaft horsepower; combustion chamber temperature, gas generator speed (percent rpm), and power turbine speed (percent rpm) data are also shown. These data represent the loci of minimum SFC points defining the lower boundary of an envelope of generalized operating points obtained by calculating engine performance at various combinations of gas generator and power turbine speeds. It should be noted that approximately proportional relationships exist between internal cycle conditions and output shaft horsepower, tending to minimize engine control problems when projecting this power plant into application studies. As has been pointed out above, the overall minimum SFC of 0.5 pound/horsepower-hour is the value attainable with the compressor efficiency chosen to match the turbine. Such a value would be materially reduced if a more compatible compressor pressure ratio were assumed with the corresponding higher compressor efficiency attainable with advanced technology.

2.2.3 Cycle Analysis Study

Cycle analysis studies were conducted based on internal conditions consistent with the turbine component study to provide an evaluation of the effects of combustion chamber temperature, compressor efficiency, and cycle pressure ratio on engine performance, with and without regeneration.

The following observations may be made:

1. Optimum specific fuel consumption for a constant combustion chamber temperature occurs at a higher cycle pressure ratio for a nonregenerative engine than for a regenerative engine (Figures 19, 20, 21, and 22). For a basic engine capable of operation with and without regeneration, selection of pressure ratio and combustion chamber temperature would have to be a compromise, based on the duty cycle or mission requirements of the power plant (time at maximum power versus time at part throttle).

2. Increasing combustion chamber temperature from 2000°F to 2500°F causes horsepower per pound of air to increase substantially, while more modest improvements in specific fuel consumption are achieved. Selection of the higher operating temperatures becomes pertinent in the design of more advanced gas turbine engines.
3. Increase in compressor efficiency at a given pressure ratio results in performance improvements which become significant for a three-point (0.74 to 0.77 polytropic) increase (Figures 23 and 24). For a gas generator turbine of fixed output, an increase in compressor pressure ratio consistent with design limitations provides further performance improvements when combined with constant or increased compressor efficiency.

The cycle analysis data were calculated using an IBM 704 digital computer. C-W Log 776 - Turboshift Design Point Program - was utilized for these calculations.

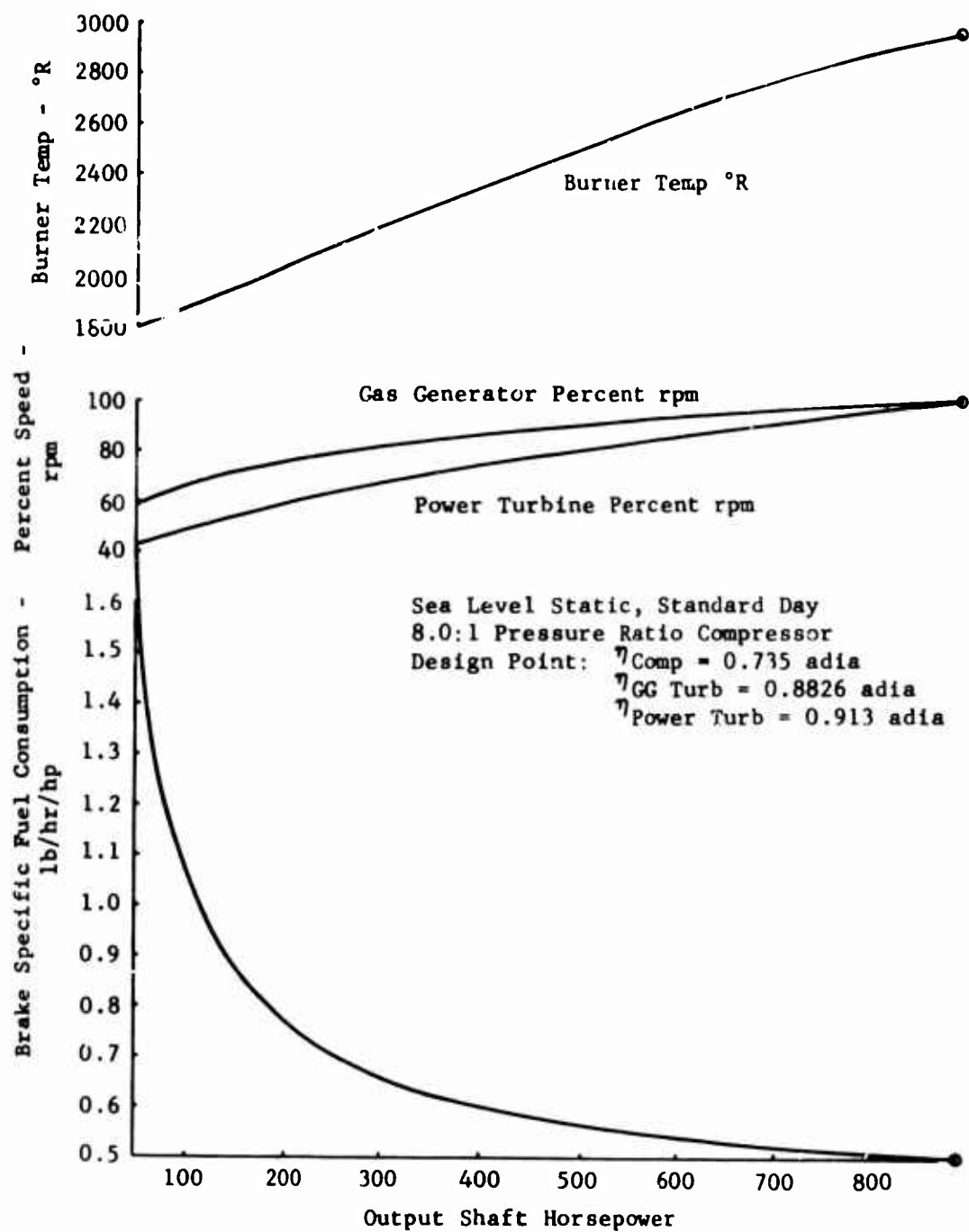


Figure 18. Estimated Optimum Fuel Consumption Performance.

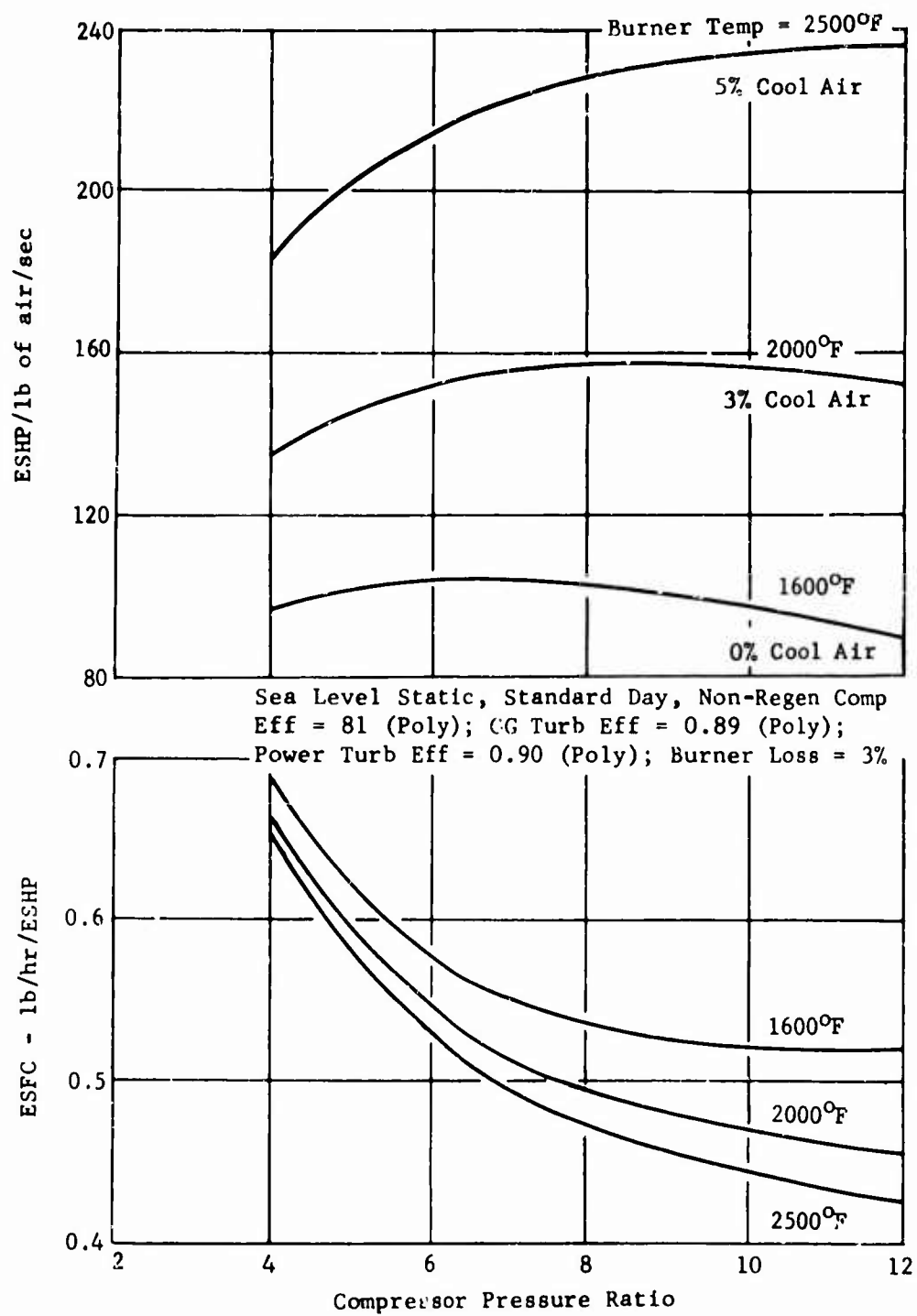


Figure 19. Effect of Combustion Chamber Temperature.

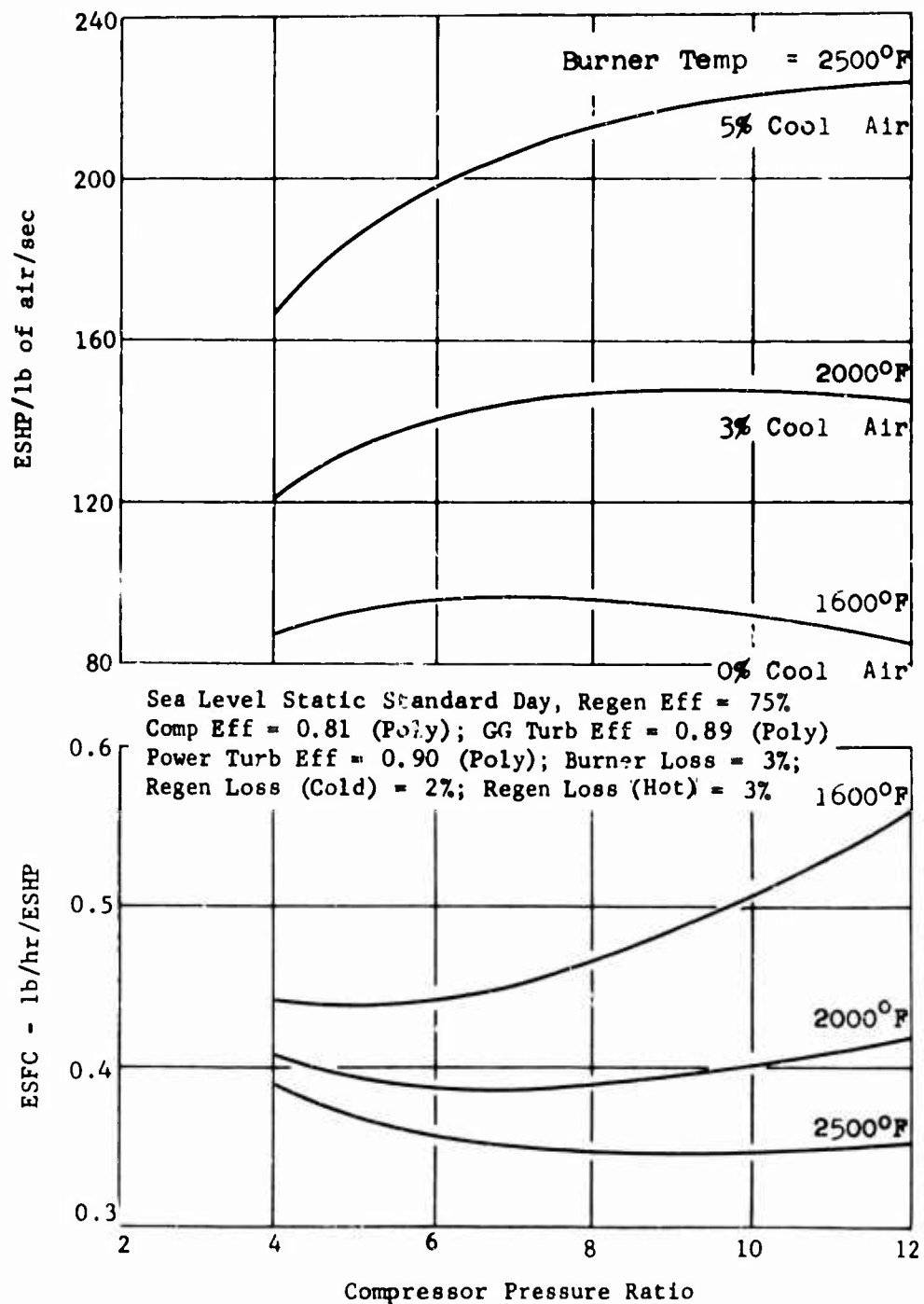


Figure 20. Effect of Combustion Chamber Temperature on HP and SFC.

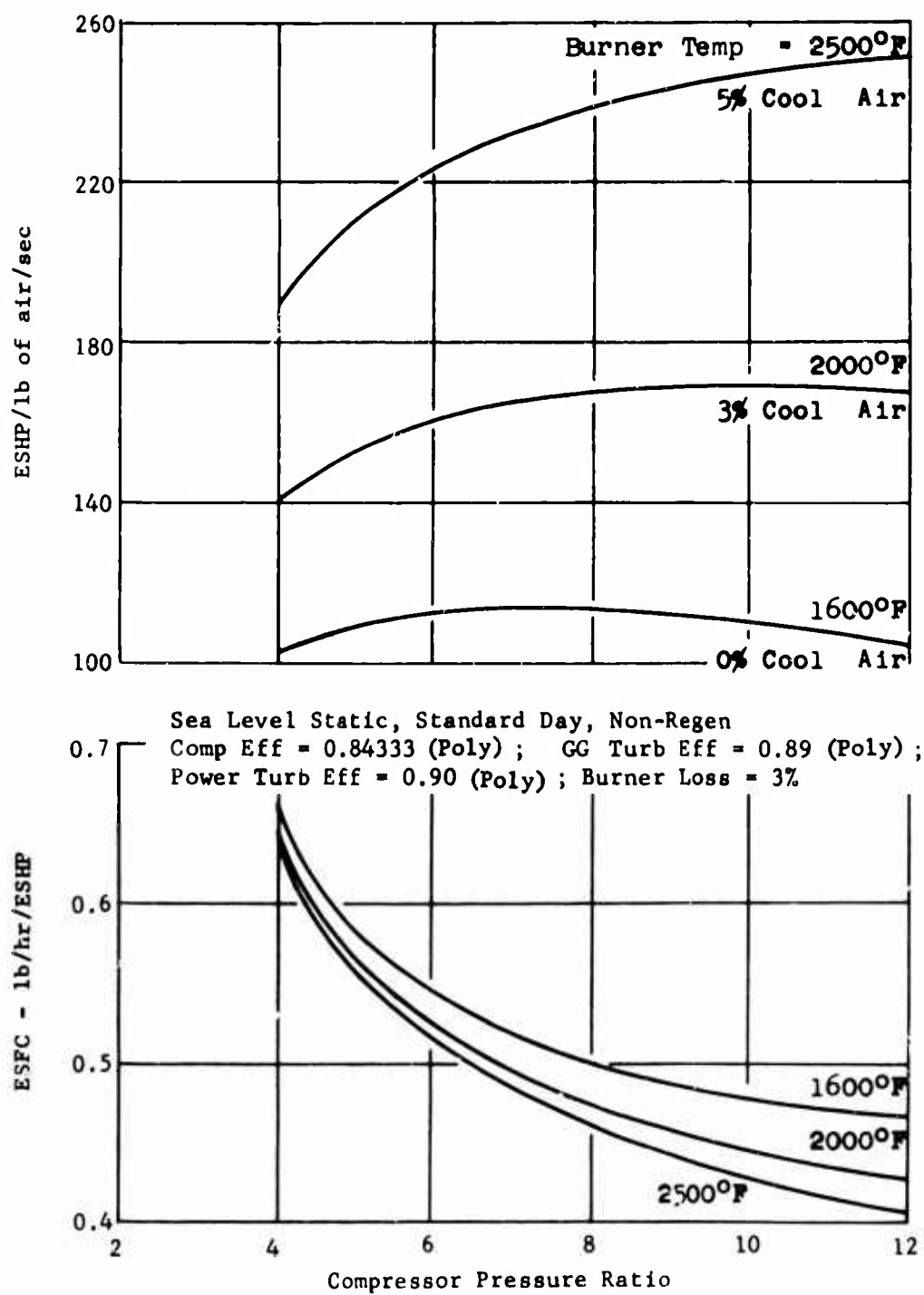


Figure 21. Effect of Combustion Chamber Temperature on HP and SFC.

Sea Level Static, Standard Day, Regen Eff = 75%
 Comp Eff = 0.84333 (Poly); GG Turb Eff = 0.89 (Poly)
 Power Turb Eff = 0.90 (Poly); Burner Loss = 3%;
 Regen Loss (Cold) = 2%; Regen Loss (Hot) = 3%

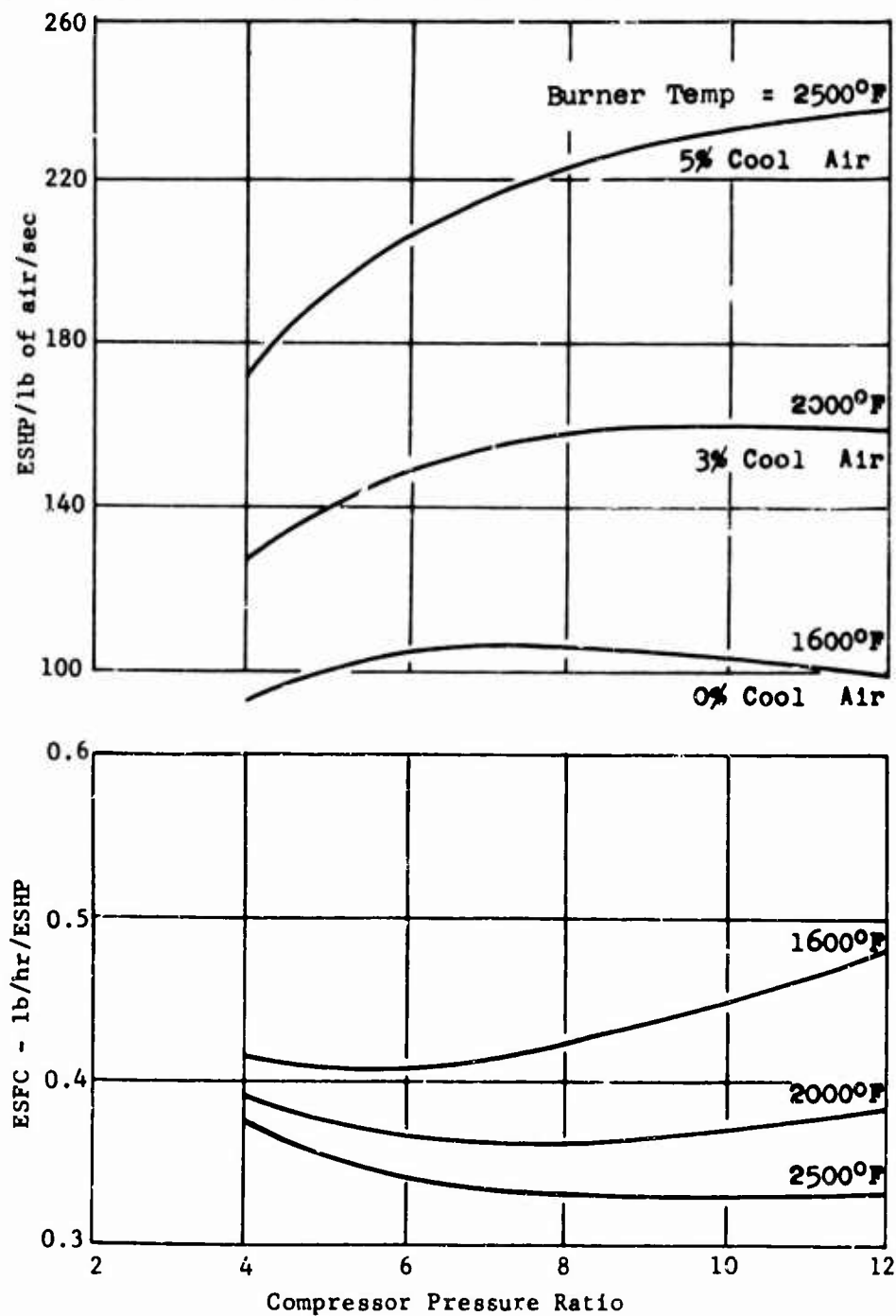


Figure 22. Effect of Combustion Chamber Temperature on HP and SFC.

Sea Level Static, Standard Day, Non-Regen
 Comb Temp = 2500° F; GG Turb Eff = 0.89 (Poly)
 Power Turb Eff = 0.90 (Poly); Burner Loss = 3%
 Coolant Air = 5%

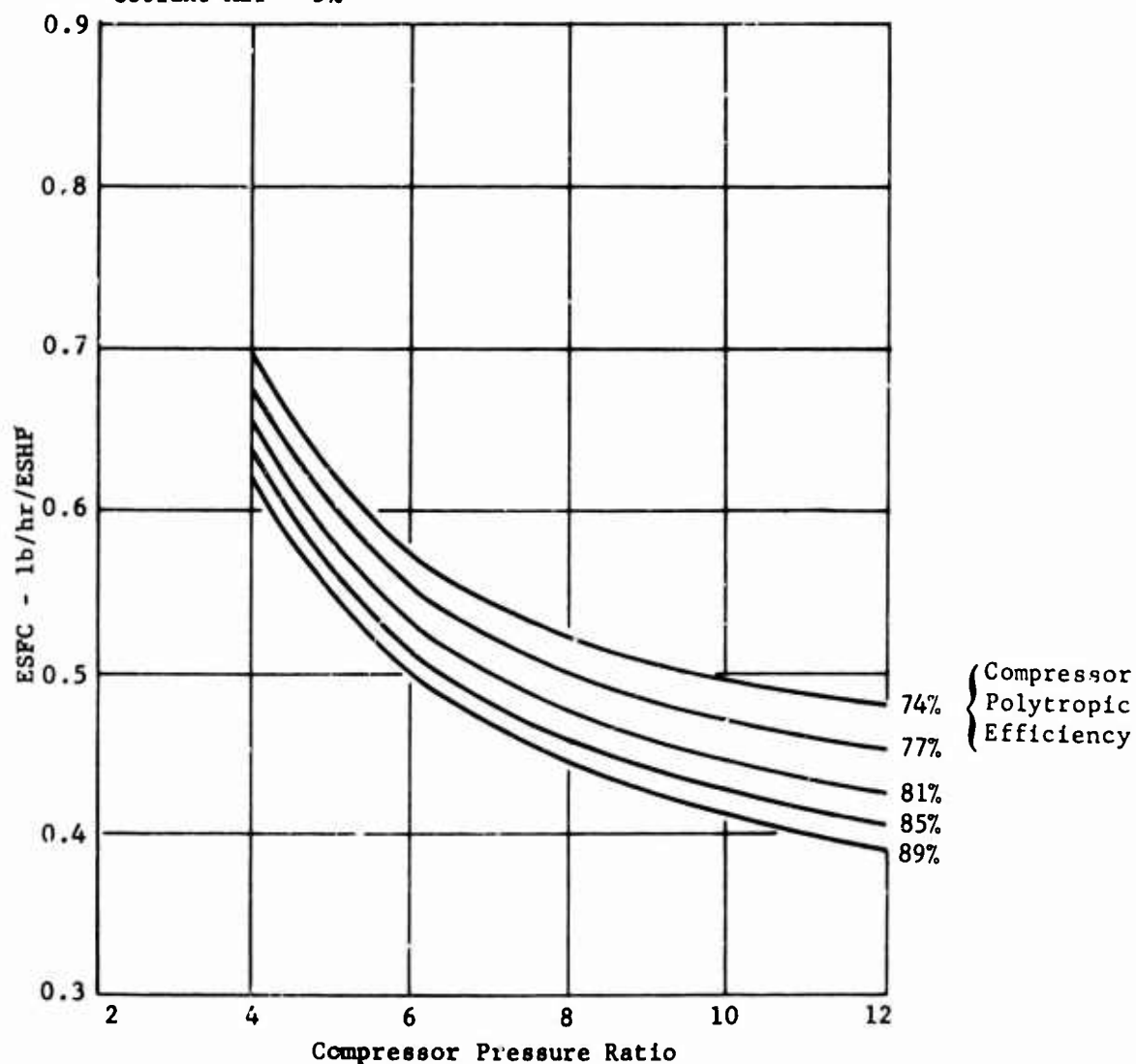


Figure 23. Effect of Compressor Efficiency on ESFC.

Sea Level Static, Standard Day, Non-Regen
 Comb Temp = 2500°F; GG Turb Eff = 0.89 (Poly)
 Power Turb Eff = 0.90 (Poly); Burner Loss = 3%
 Coolant Air = 5%

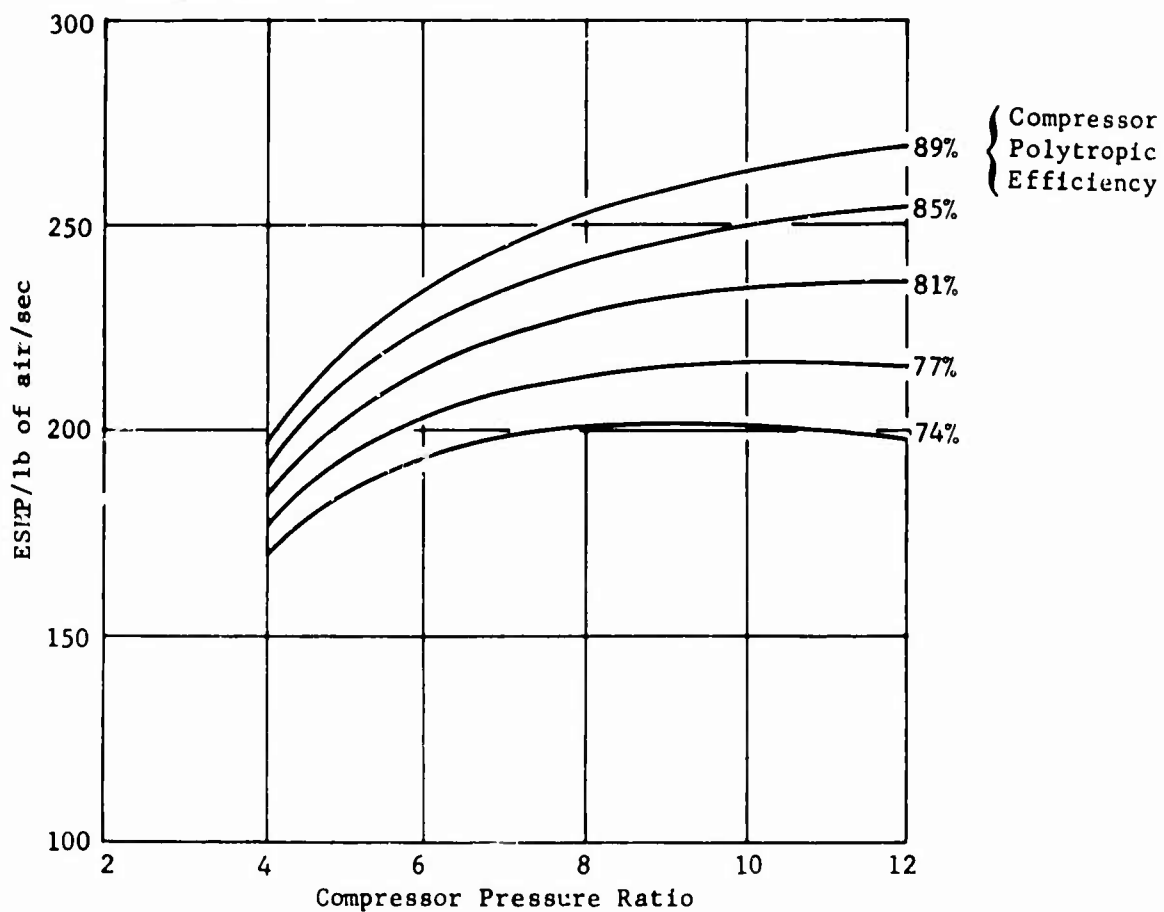


Figure 24. Effect of Compressor Efficiency on ESFC.

3.0 TURBINE TEST RIG DESIGN

3.1 RIG DESIGN STUDY

3.1.1 Introduction

The process of arriving at a final test rig design for an advanced component of this type involves many proposals, trials, and considerations to assure ultimate success during the test period. Figures 25 through 31 show the evolution of the basic rig assembly, with Figure 31 being the final design selected for further development during Phase II. Areas of considerable concern and analysis were the combustion chamber liners, the rotor shroud, the exhaust duct and housing, the critical speed of the turbine, and, of course, the blading which is discussed in Section 4.0. Of similar importance, but requiring less analysis, are the high-speed bearings supporting the turbine shaft, the shaft seal, the rotor cooling air labyrinth seal, the bearing lubrication system, the rotor and stator cooling air supply system, and the combustor support system, including the fuel and air supply.

The combustor liners, cooled by the conventional convective film technique, were patterned after a previous C-W-designed combustor which had close to 50 hours of testing with excellent results. The new liners are similar to this design in that the film cooling flow is metered by orifice holes around the periphery of the liners and the air is directed by cooling bands in a parallel film into the main combustion stream. This orifice and cooling band principle is used rather than the more conventional designs for large engines because the airflow is small and cannot be metered practically by the overlap liner method. The ideal solution to liner design is to keep the thermal gradients along the liner (from one cooling band to the next) to a value that will not cause the liner to buckle and fail. This is accomplished by the selection of the amount of cooling air to be introduced at each cooling band and the axial spacing between bands. Of course the cooling air supply must be judiciously used or the combustion process would be seriously affected.

The rotor shroud configuration was selected after consideration of many schemes. A one-piece shroud had to be eliminated because the thermal growth was too large to maintain tip clearances desired. A segmented shroud was chosen that combines the best features of similar shrouds currently being used on larger C-W engines.

The exhaust duct and housing design is complicated to the extent that the walls, if uncooled, would have large temperature gradients resulting in stresses that would exceed the yield of the material. Although these stresses relieve themselves during operation, the resulting distortions would be detrimental to turbine performance, since the turbine requires close tip clearances. Therefore, an extensive heat transfer and stress analysis was made to determine the best method of cooling this part so that thermal gradients would not cause distortion. Many methods of cooling with air and/or water were investigated: internal cooling combinations, external cooling, internal and external combinations, and insulation of external surfaces.

The turbine critical speed, which is discussed in detail in Section 3.3, is another area that required extensive analysis. An initial effort to design the shaft and support system so that the critical speed would be above the operating range was partially successful. Items that were of concern were the bearing spacing; the overhang of the disc and blades from the bearing; the weight of the disc and blades; the dN values of the bearings; the stiffness of the shaft, bearing, and support housing; and the use of a controlled-gap oil seal. The change from the clamped to welded disc and blade arrangement made it necessary to design the support system so that the first critical speed would be below the operating range. This eased the requirements of the bearings and seal; the bearings were made smaller, and so have lower dN values with adequate life, and the seal was made smaller, thus providing a rubbing seal having an acceptable peripheral speed.

3.1.2 Rig Description

The turbine test rig assembly finally selected was completely designed and detailed on layout drawings, Figure 31, except for the stator blade and the rotor and shaft assembly. The turbine rig basically consists of a combustor, a turbine, and an exhaust section. The combustor is a full annular vaporizing type similar in principle to combustors in the C-W J65 and TJ60 engines. The combustor consists of inner and outer liners, a headplate assembly, and a vaporizer tube. Primary air for combustion enters the forward end of the combustor through 16 (primary) aircups, equally spaced on the headplate and surrounding the vaporizer tube. The air entering the vaporizer tube first passes through a simple swirling device and at the same time mixes with fuel that is injected at this point. In this manner, a uniform rich mixture of fuel and air leaves the vaporizer tube and swirls toward the combustor headplate. Combustion, which is started by a 20-joule ignition system, is completed in the primary zone, which is approximately 5 inches long. At the end of the primary zone, diluent air is injected through 32 slots spaced equally around the outer combustor liner; this air is introduced to reduce the gas temperature to the desired turbine inlet temperature and to establish the desired temperature profile. The combustor as designed has much latitude for testing; it has several features that make it easy to change its configuration or pattern. Among these features are:

1. The headplate has bolting patterns that permit changing the angularity between the igniter and aircups or the aircups and vaporizer inlet air.
2. The aircups can be pressed into the headplate at any selected angularity.
3. The vaporizer is machined so that the fuel introduction location can be selected from three positions (axially) relative to the vaporizer air inlet and so that the number of introduction points can be selected from one to six.

4. The cooling air bands are riveted to the liners for easy removal and replacement in case the orifice sizes or gap heights need changing.
5. The igniter is radially adjustable relative to both the liner and its cooling air shield.

Another extremely important feature is the unrestrained support of the liners that allows thermal growth both axially and radially. Both the inner and outer liners are fixed at the upstream ends, while the inner liner is free to expand at the downstream ends by virtue of its piston ring support. This also blocks the liner cooling air from escaping and makes the outer liner free to expand by virtue of its "fishmouth" support. The diametral dimensions of the fishmouth are selected so that support is obtained on the outer diameter in the cold position and on the inner diameter in the hot or operating position.

A high-energy, 20-joule ignition system, commercially available, is used for igniting the main burner flow, thus eliminating the need for a separate priming system. This concept has been successfully utilized on other C-W combustor rigs.

The combustor liners, both inner and outer, are formed sheet metal cones with cooling bands riveted in place at axial intervals. The ends of the liners are machined rings which reinforce the sheet metal cones and provide means of connection at the upstream end to the headplate and at the downstream end to the stator support rings. The materials selected for the combustor section are noted in the bill of materials contained on Figure 31. Some of the major parts of the combustor and materials selected for each are noted as follows:

<u>Part</u>	<u>Material</u>
Headplate	AISI 310 or 321
Aircups	AISI 310 or 321
Vaporizer	AISI 310 or 321
Combustor Housing	AISI 310 or 321
Inlet Housing	Cast Niresist
Combustor Liners	Hastelloy X

The turbine section (excluding the stator blades and rotor blade and shaft assembly) consists of the stator blade supports (both inner and outer), rotor cooling air labyrinth seal, rotor and stator cooling air tubes, rotor shroud, turbine shaft supports, and support housing. The tubes for the rotor and stator cooling air are located in the center of the combustor. The cooling air is brought in separately through the inlet support casting. The tubes are supported aft by the inner rings centered by the stator blades. The rings also support the labyrinth seal at the rotor. This seal has two stages with an intermediate bleed which reduces the pressure ratio and thus the leakage across the second stage where the leakage cannot be measured during test. This is done by bleeding off the leakage after the first stage. A static test can be made to determine the leakage through the

seal. With the rotor cooling air passage plugged, the total inlet flow can be measured, as well as the flow being bled off between stages; the difference between these flows is the leakage to be expected at the second stage during turbine testing. The advantage of the design is that it allows greater tolerances and labyrinth seal clearances but still has small leakage (calculated to be less than 0.25 percent across the second stage).

The rotor shroud is segmented in four pieces and fastened to a ring that is cooled by approximately 1 percent air from the combustor inlet. The cooling of this support ring enables the rotor tip clearance to be held virtually constant through the operating range (0.010 inch). The four segments are keyed in the support ring in a manner that allows them, when hot, to expand freely in any direction but prevents them from rotating in the event of a rub. The support ring is attached to the exhaust duct; however, its expansion is independent, since it is radially "splined" with 16 lugs. Hastelloy X will be used for the segments which have a honeycomb core brazed to a backup support. To prevent erosion of the honeycomb, an investigation of core filler materials will be made. The support ring will be made of Inconel X, the same as the stator support rings, since both will be subject to high stresses due to thermal gradients.

The turbine shaft support system consists of a nodular cast iron support, two intermediate bearing support rings, two bearings, and a lube jet ring. The forward intermediate bearing support ring is extremely important because of its effect on the critical speed of the system. It is designed to have a low spring rate so that the first shaft critical speed will be below the turbine operating speed range. This ring is designed to house both the oil seal and the roller bearing, thus reducing any concentricity problems for the seal to a minimum. The ring also can be easily reworked or replaced in the event of a desired spring rate change. The rear intermediate bearing support ring is much stiffer and determines the second critical speed which will be above the operating range. The lube jet ring and rear bearing support are drilled in a manner to provide lubrication to the roller and ball bearings, respectively.

The bearings selected are a roller bearing, equivalent to SKF 460650, and a split inner race ball bearing, equivalent to SKF 460651. The roller bearing estimated life at the highest load anticipated at 50,000 rpm will be in excess of 10,000 hours and will have a spring rate varying from 0.488×10^6 pounds/inch at a 13-pound radial load to 0.521×10^6 pounds/inch at a 41-pound radial load. The bearing heat rejection is 46 Btu/minute based on 2 pounds/minute of 7808 oil entering at 150°F. The ball bearing estimated life at its highest load will be 683 hours, with a spring rate approximately constant at 4.65×10^5 pounds/inch over the radial load range and a 200-pound thrust load. The heat rejection estimated for the ball bearing is 70 Btu/minute based on 7808 oil entering at 150°F and flowing 3 pounds/minute. To seal the lubricating oil from the turbine, a Cleveland Graphite No. B-103020 turbine shaft seal has been selected. This design has two carbon elements that are especially suitable for the rubbing speeds encountered here and has a heat rejection rate of approximately 10 Btu/minute.

The exhaust duct and housing section consists of a welded diffuser housing assembly and a heat shield. The welded assembly will be made of Hastelloy X because of its good high-temperature properties and corrosion and erosion resistance to the exhaust gases. The heat shield, which will be made of AISI 321 stainless, serves two purposes: it shields the turbine support housing from exhaust duct radiation, and it forms a high-velocity passage for the auxiliary cooling air that is used to cool the inner wall of the exhaust diffuser. Approximately 0.35 pound/second of cooling air will be introduced at the rear of the exhaust duct which will convectively cool the inner wall as it flows forward and film-cools the same wall as it is introduced into the turbine exit gas stream. This cooling air will be the same temperature as the combustor inlet air so that when it is introduced at the turbine hub it will not cause adverse thermal gradients in the disc. A second source of cooling this housing will be the use of a fine water spray on the outside portion of the exhaust housing between the flanges. This will directly reduce the wall temperature of the exhaust collector to 1300°F, which would otherwise be at a temperature of 1600°F.

Insulation of the flanges was considered in an attempt to reduce the thermal gradients in the housing, but this produced other problems. Thermal gradients in the outer housing were still high; in addition, the exhaust diffuser outer wall temperatures were also high.

The aerodynamic characteristics of the exhaust duct were investigated to determine the exhaust diffuser characteristics and any disturbances brought on by the penetration of cooling air entering at the hub. Since this is a test rig application, the duct losses were not considered. In the diffuser, to prevent separation, an area schedule was selected to provide a minimum of diffusion until the exhaust gases had been turned into the collector. The entering passage area and the entrance geometry for the hub cooling air entering the exhaust duct were selected so that the effect of momentum and penetration could be minimized. The entrance geometry was designed to introduce the cooling air in a direction nearly parallel to the main flow.

It can be seen by reviewing the rig basic as shown in Figures 25 through 31 that other changes have evolved that are not specifically mentioned above. In many instances, these have come about from consideration of assembly and disassembly sequences, for convenience of manufacturing, and for convenience of testing.

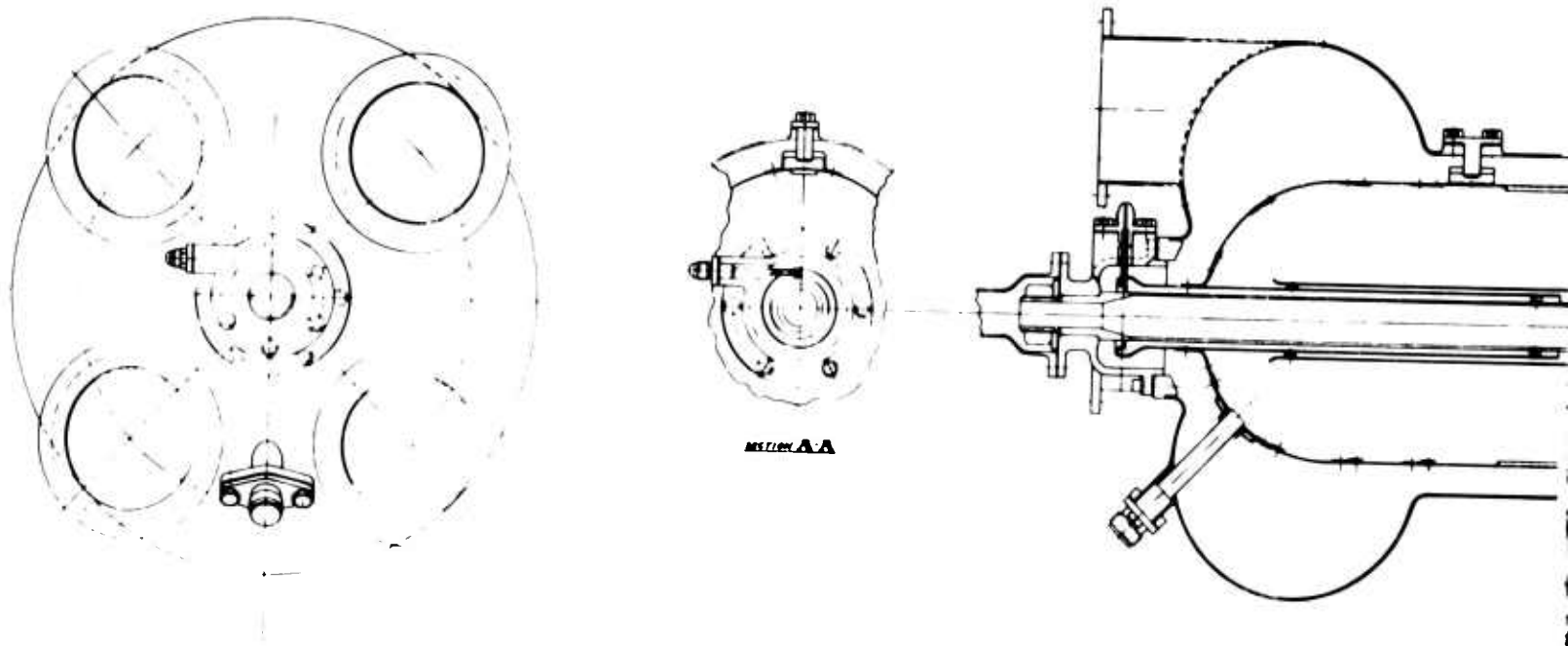
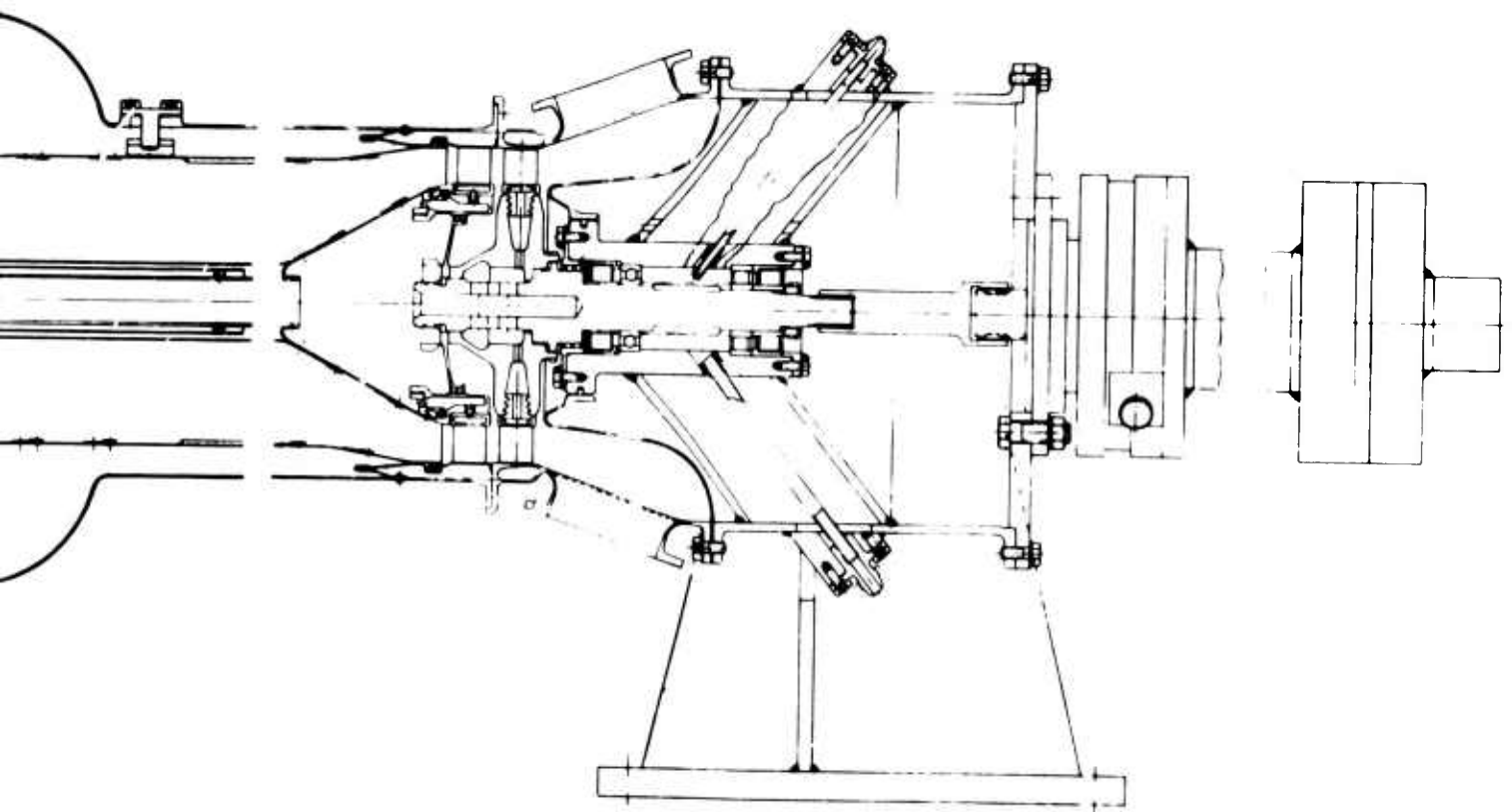


Figure 25. Turbine Test Rig - External Gas Source.



B

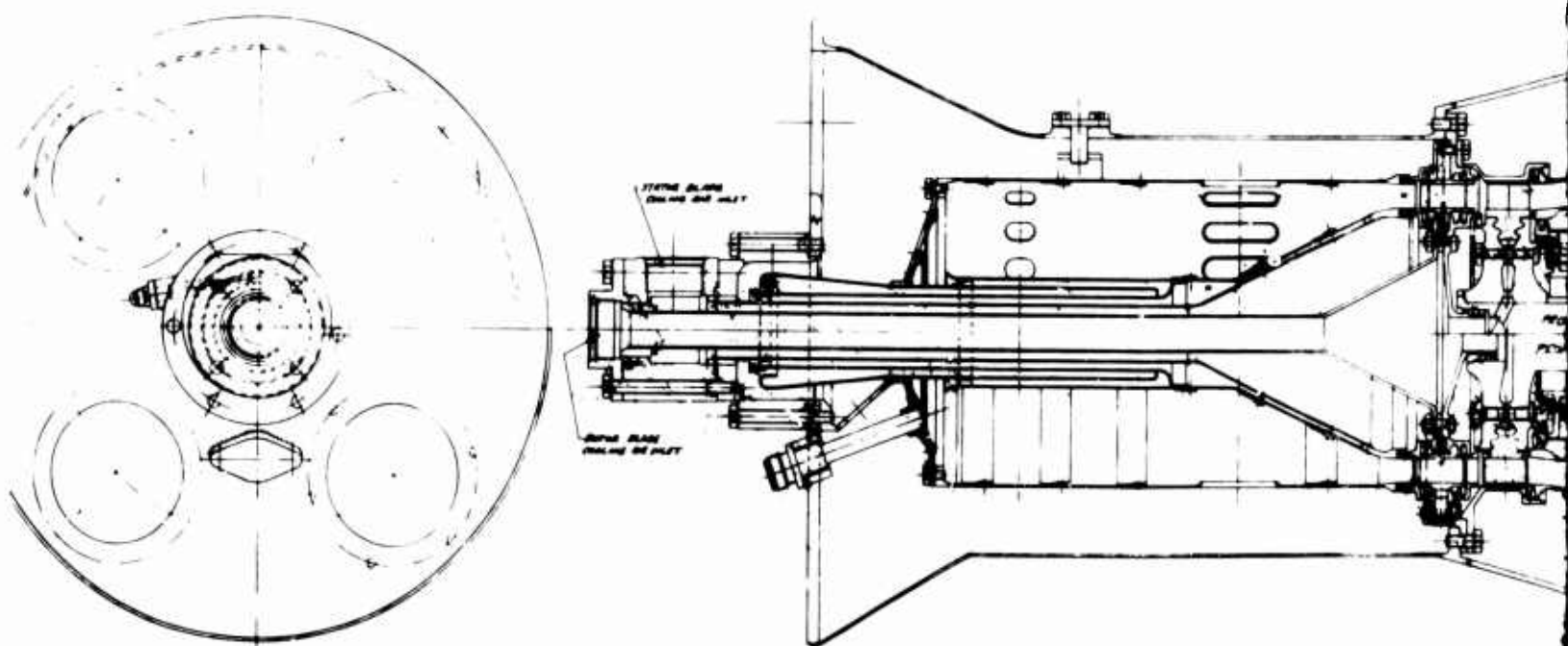
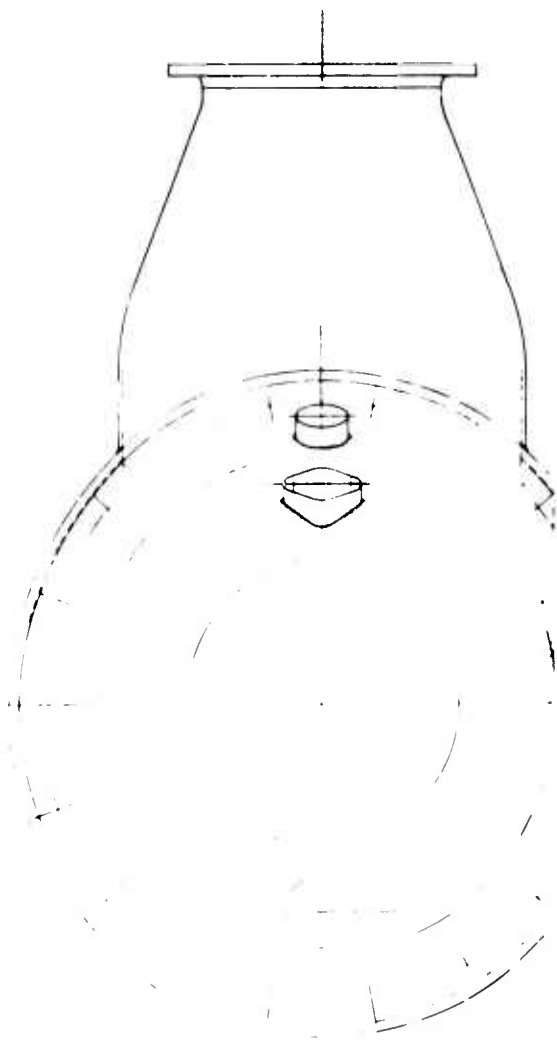
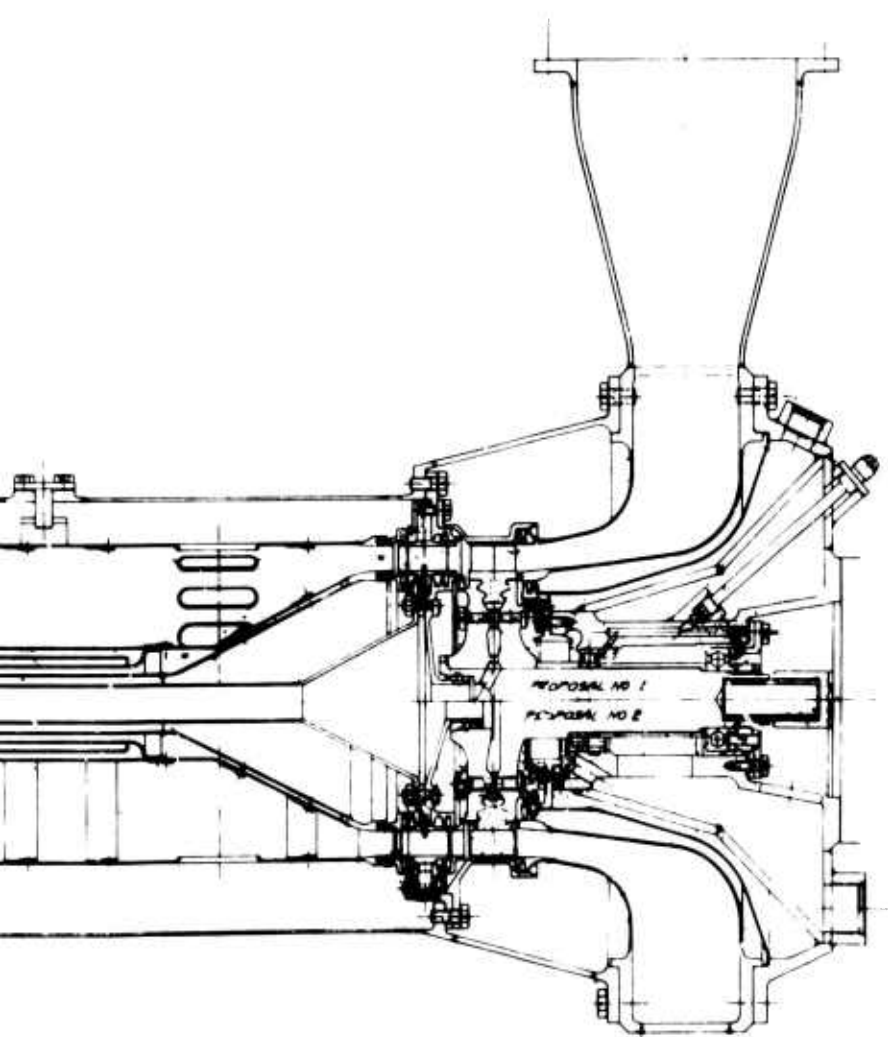


Figure 26. Turbine Test Rig.

A



13

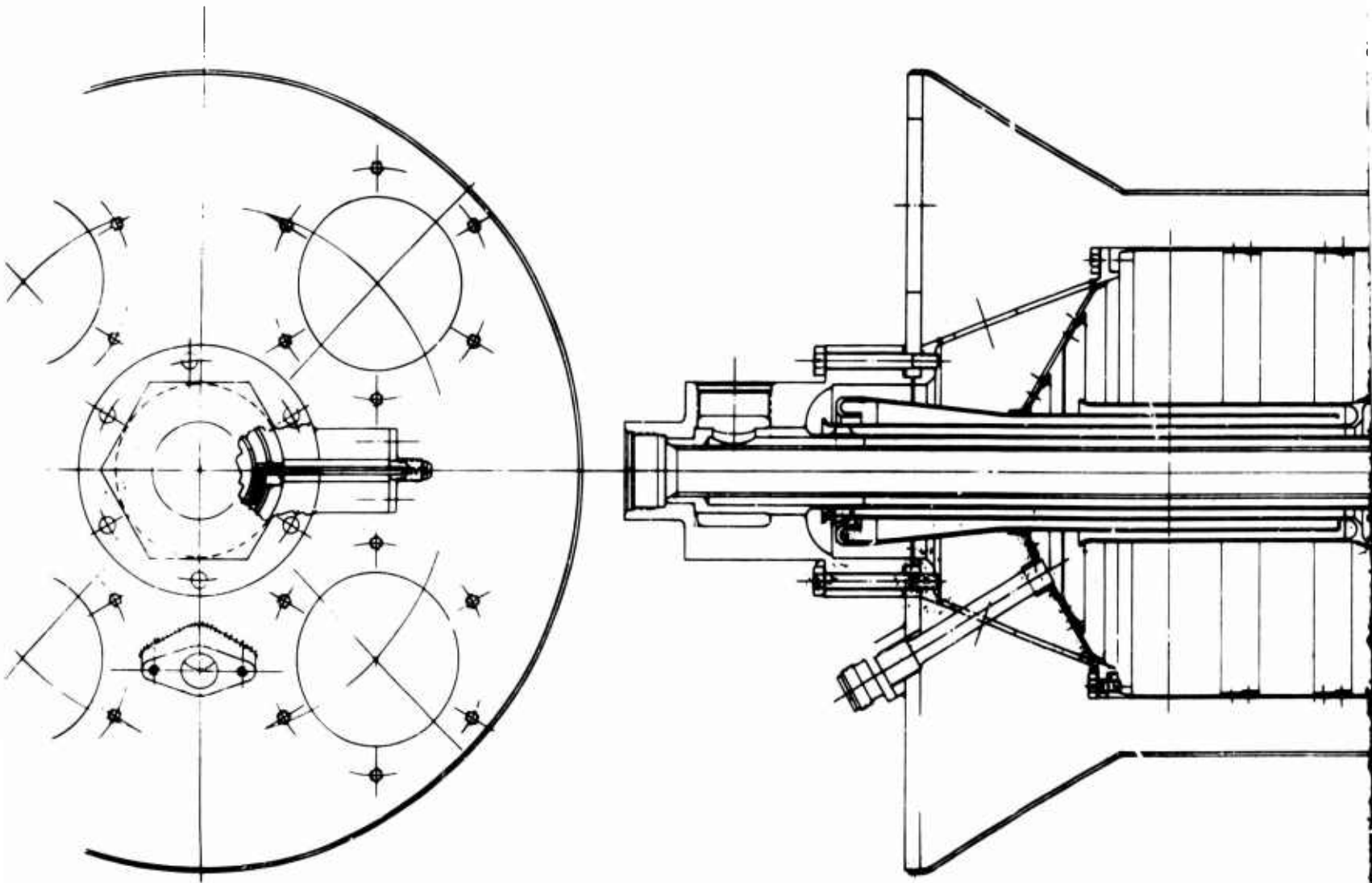
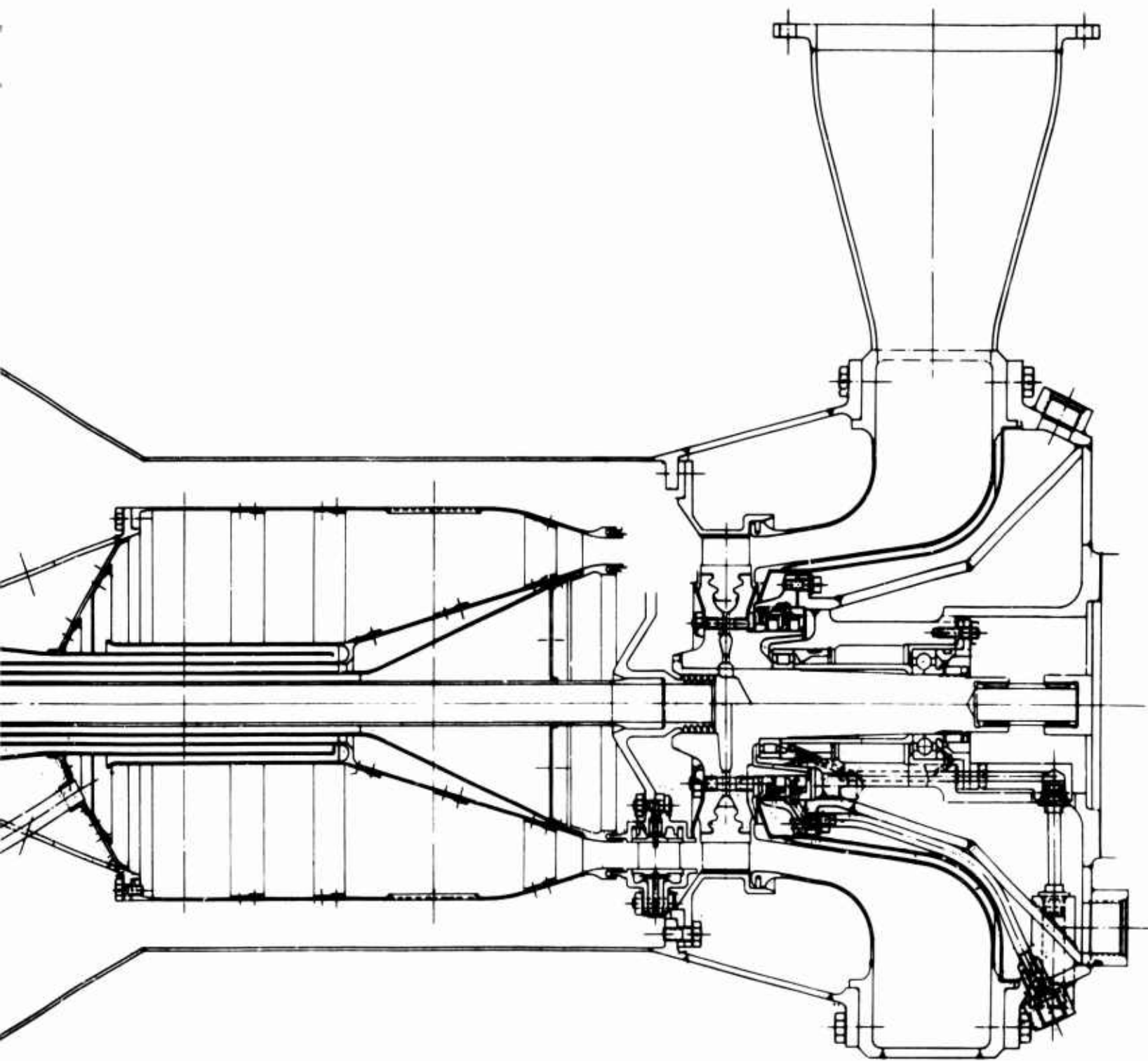


Figure 27. Turbine Test Rig.



13

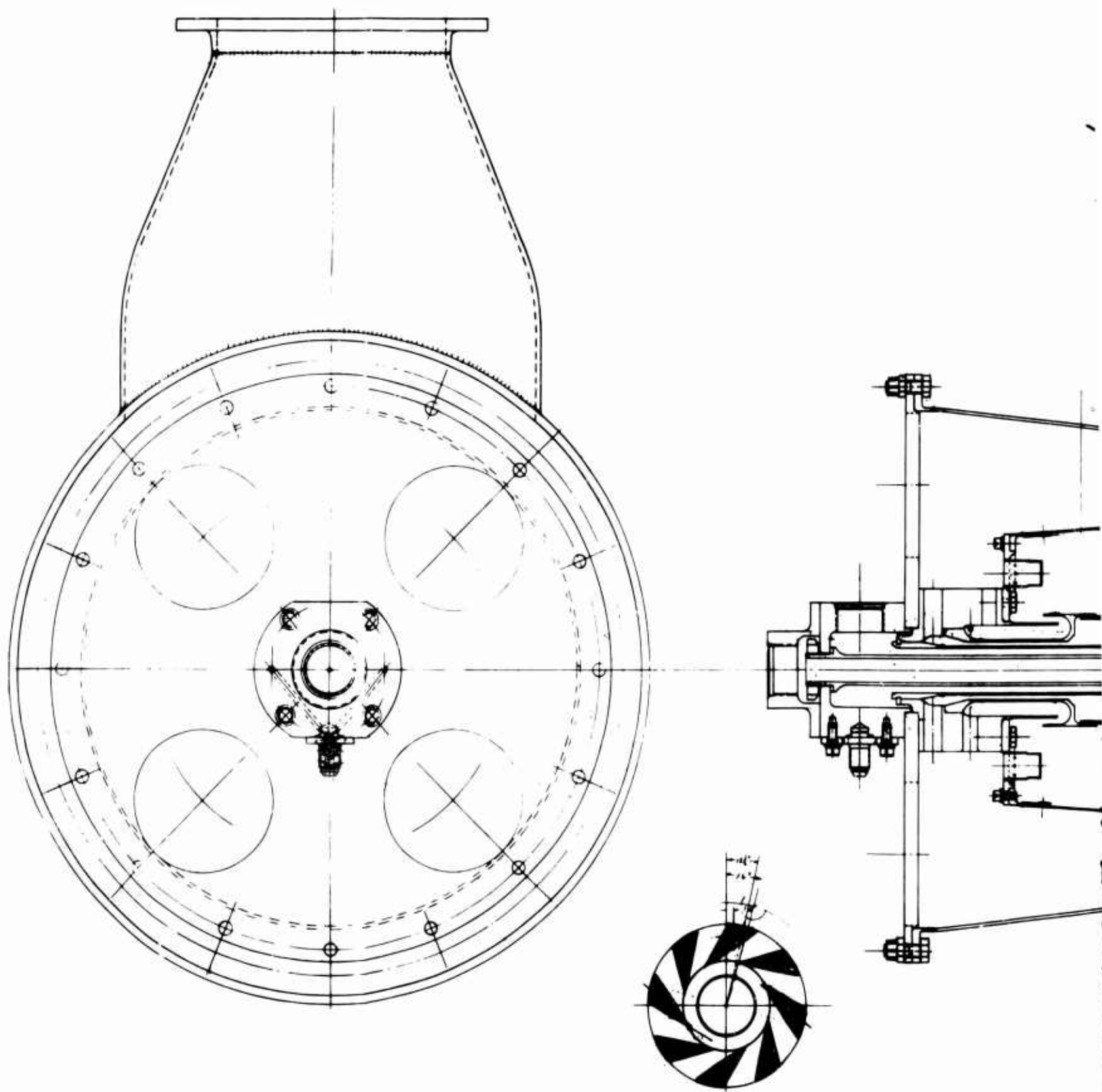
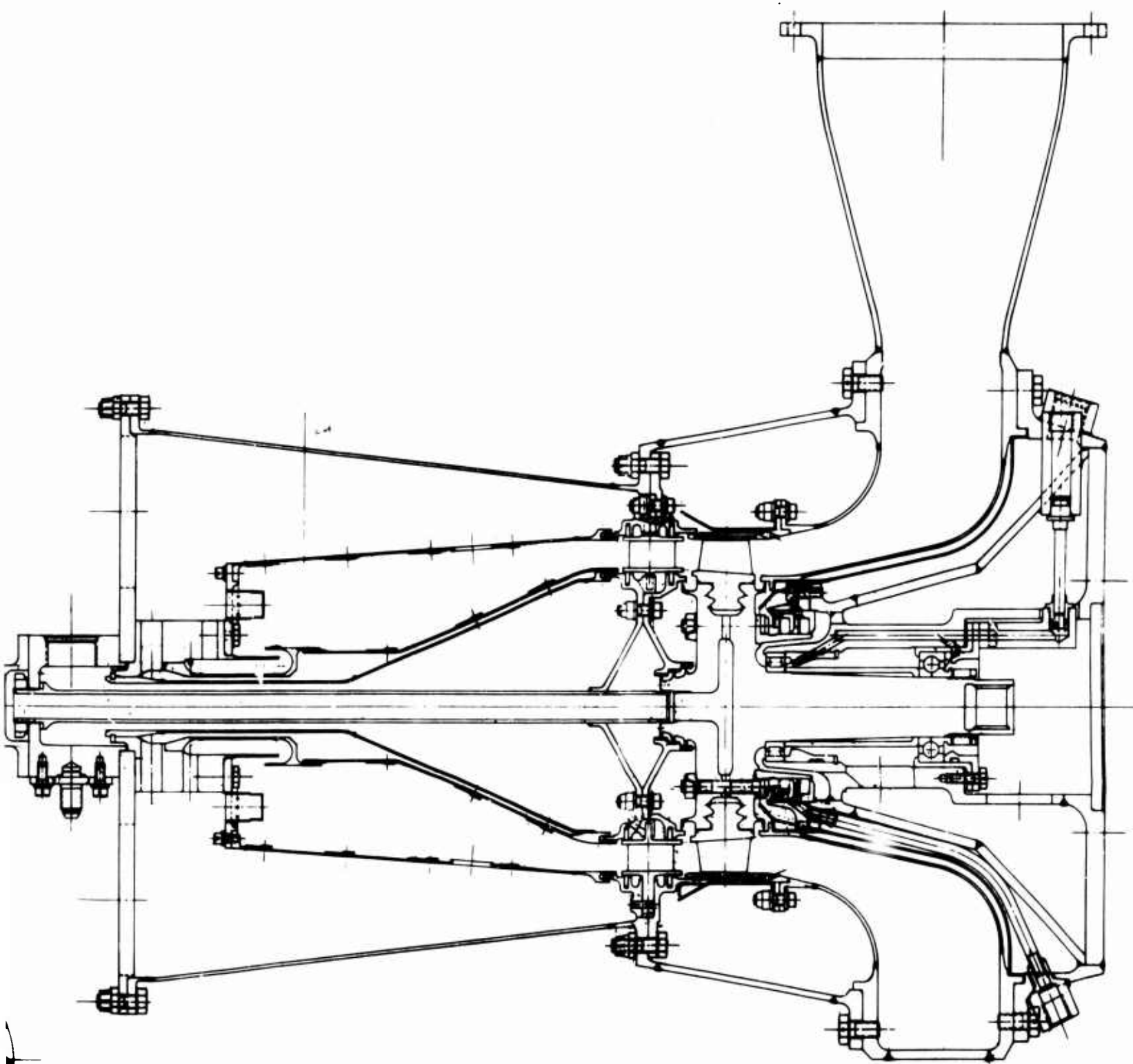


Figure 28. Turbine Test Rig.



13

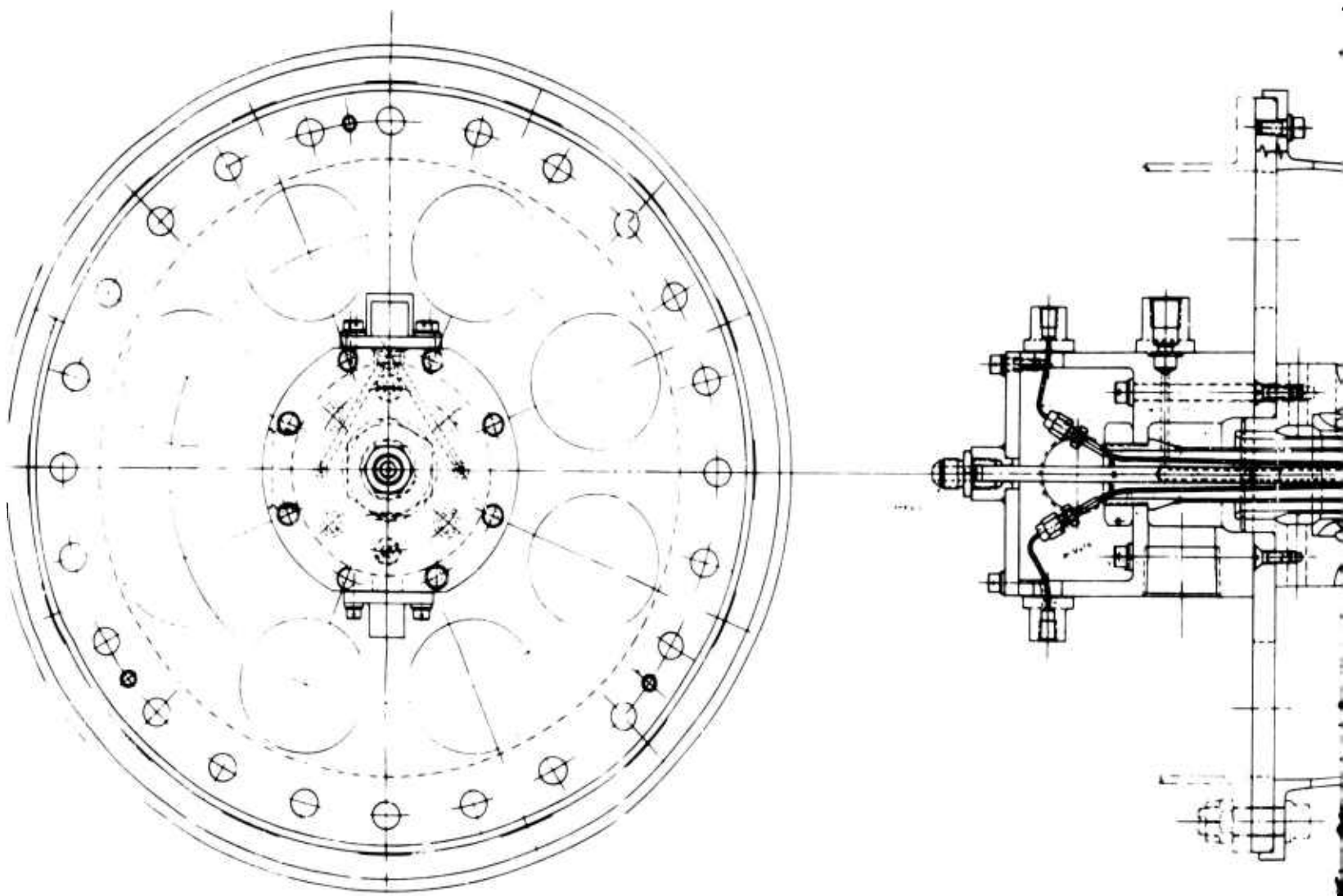
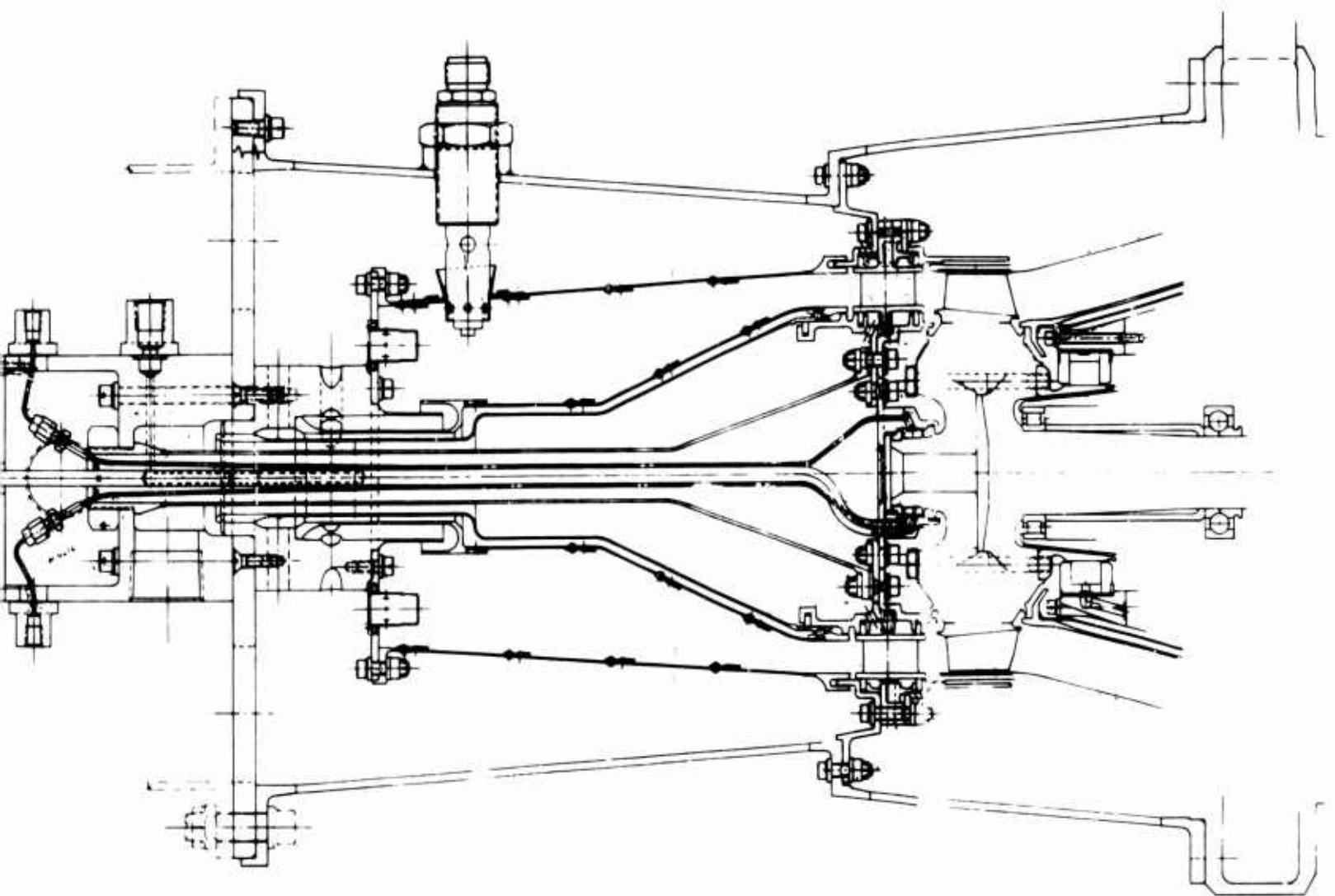


Figure 29. Turbine Test Rig.



B

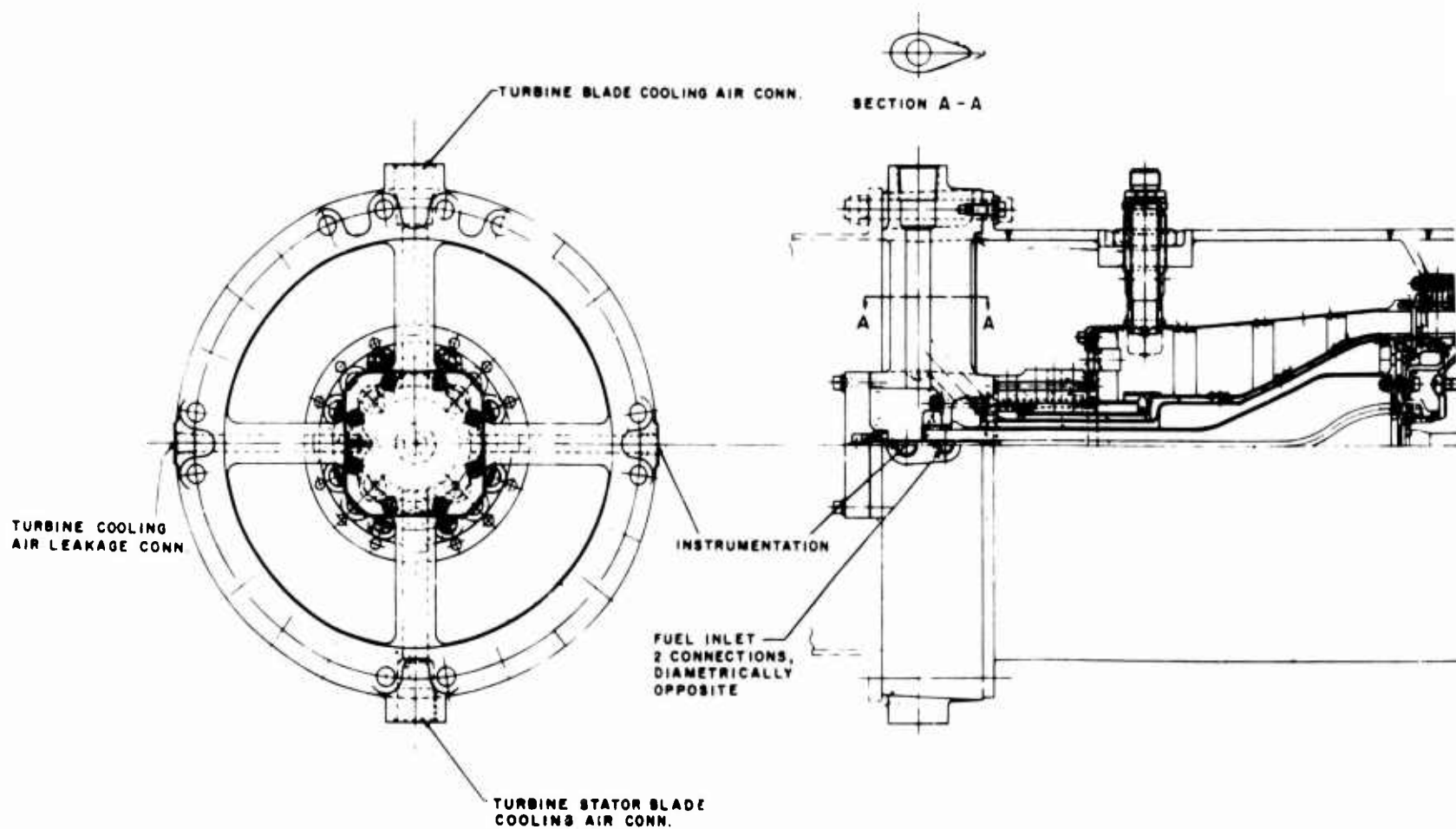
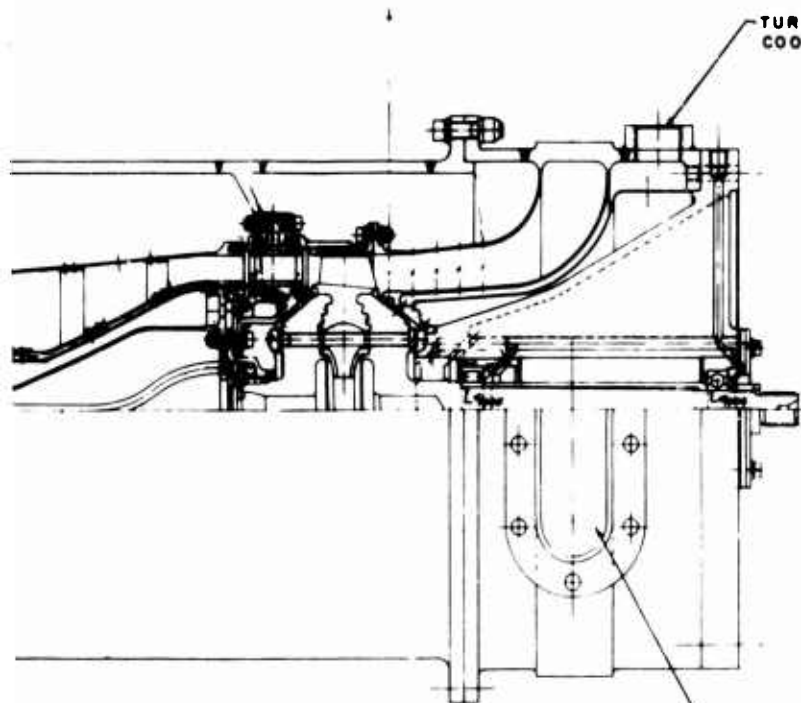
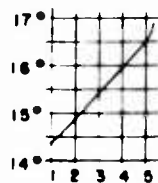
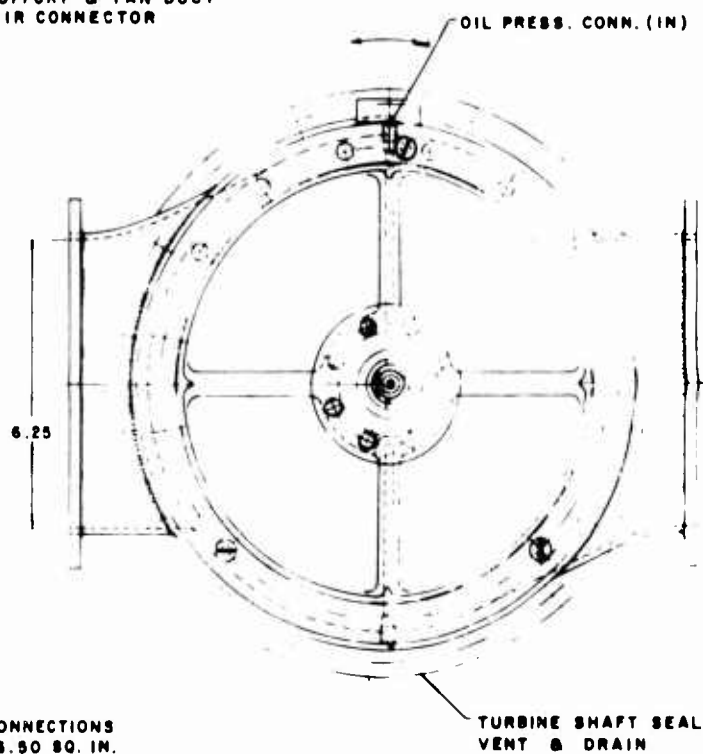


Figure 30. Turbine Test Rig.



TURBINE SUPPORT & FAN DUCT
COOLING AIR CONNECTOR

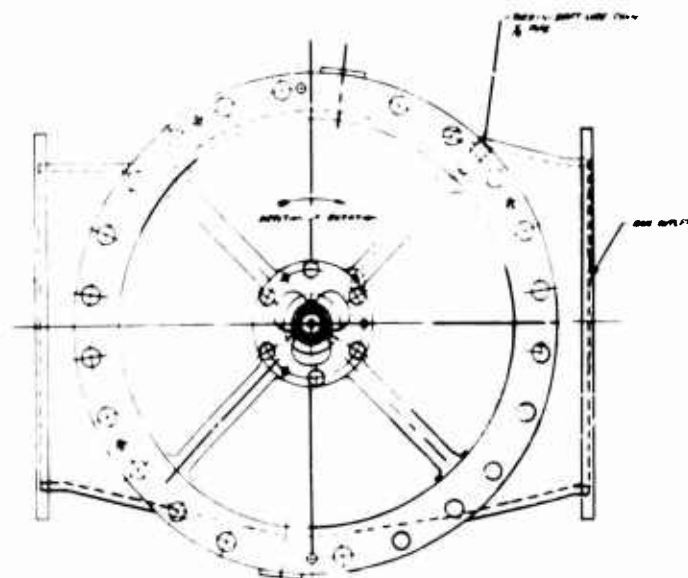
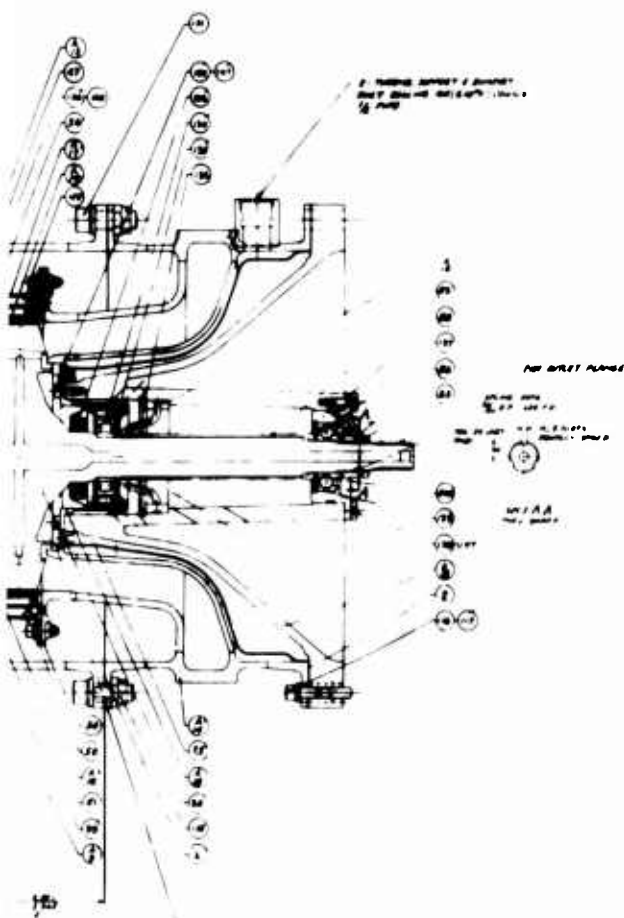
EXHAUST - 2 CONNECTIONS
TOTAL AREA 16.50 SQ. IN.



OIL PRESS. CONN. (IN)

TURBINE SHAFT SEAL
VENT & DRAIN

13



143	MS 1990-27	A17			4
142		A15			1
141		A17			4
140					2
139					1
138	MS 100-000				6
137					1
136	MS 100-000				1
135					1
134					1
133					1
132	MS 100-000				6
131	MS 100-000				20
130	MS 100-000				3
129	MS 100-000				16
128	MS 100-000				20
127	MS 100-000				6
126	MS 100-000				4
125	MS 100-000				20
124	MS 100-000				6
123	MS 100-000				1
122					1
121	MS 100-000				1
120	MS 100-000				1
119	MS 100-000				1
118	MS 100-000				20
117	MS 100-000				8
116	MS 100-000				1
115	MS 100-000				72
114	MS 100-000				2
113	MS 100-000				3
112	MS 100-000				1
111					1
110	MS 100-000				4
109	MS 100-000				4
108	MS 100-000				4
107	MS 100-000				20
106	MS 100-000				16
105	MS 100-000				23
104	MS 100-000				110
103	MS 100-000				2
102	MS 100-000				45
101	MS 100-000				6
100	MS 100-000				3
99					
98					
97					
96					
95					
94					
93					
92					
91					
90					
89					
88					
87					
86					
85					
84					
83					
82					
81					
80					
79					
78					
77					
76					
75					
74					
73					
72					
71					
70					
69					
68					
67					
66					
65					
64					
63					
62					
61					
60					
59					
58					
57					
56					
55					
54					
53					
52					
51					
50					
49					
48					
47					
46					
45					
44					
43					
42					
41					
40					
39					
38					
37					
36					
35					
34					
33					
32					
31					
30					
29					
28					
27					
26					
25					
24					
23					
22					
21					
20					
19					
18					
17					
16					
15					
14					
13					
12					
11					
10					
9					
8					
7					
6					
5					
4					
3					
2					
1					

B

4	AN - 1.015 DIA X .375 LG	AMS 5756			
1	PLUG - .375 DIA X .375 LG	AMS 5756			
4	RIVET - 1/8" DIA X .1875 LG	9031			
2	O RING SEAL	9031			
1	AN - TUBAL 7/8" DIA X .105 LG	9031			
6	SCREW - NO 10-32, 1/2 LG				
1	BEARING-BALL (MT 60681)	9015			
1	RING-TUBAL 7/8" DIA X .105 LG	9031			
1	RING-TUBAL 7/8" DIA X .105 LG	9031			
1	BEARING-BALLER (SR 60680)	9015			
1	SEAL (COPPER BEARING BEARING)	9031			
6	SCREW-NO 10-32, 1/2 LG	CRS			
24	BOLT - 1/2" DIA, 1 1/2 LG	AMS 5757			
3	SCREW-NO 10-32, 1/2 LG	AMS 5757			
16	SCREW-NO 10-32, 1/2 LG	AMS 5757			
20	SCREW-NO 10-32, 1 1/2 LG	AMS 5757			
6	SCREW-NO 10-32, 1/2 LG	AMS 5757			
4	SCREW 1/2" DIA, 1/2 LG	CRS			
24	BOLT - 1/2" DIA, 1 1/2 LG	AMS 5757			
6	SCREW NO 5-40 1/2 LG	CRS			
1	NUT - 1/2" DIA				
1	IGNITER (CINTELLA PART NO 10-111200-1)				
1	PLUG				
1	GASNET				
1	PLUG 1/2" DIA				
24	BOLT - 1/2" DIA, 1 1/2 LG	AMS 5757			
8	LOCKWASHER .250	CRS			
9	SCREW - 1/2" DIA, .625 LG	AMS 5757			
72	NUT - 1/2" DIA PLASTIC STOP (MOUNT)				
2	SCREW-NO 10-32, 2 1/2 LG C-CLAMP	AMS 5757			
8	BOLT-NO 10-32, 1 1/2 LG L-INCH	AMS 5757			
1	NUT - 1.000-1/2" DIA	CRS			
1	O RING SEAL (PART NO 8-110-VITON)	9031			
4	LOCKWASHER NO 6	CRS			
4	SCREW-NO 6-32, 1/2 LG SOCKET NO	CRS			
4	BOLT-NO 6-32, 1/2 LG SOCKET NO	CRS			
4	WIRE 017-0210M	CRS			
16	SCREW-NO 6-32, 1/2 LG SOCKET NO	CRS			
25	DOWEL - 1/8" DIA X 3 1/2 LG	AMS 5758			
110	RIVET				
2	DOWEL - 1/8" DIA X .065 LG	AMS 5758			
45	NUT-SWANK #10-32				
6	PLUG	CRS			
8	DOWEL - 1/8" DIA X .50 LG	AMS 5758			
1	ANAL ASSY TURBINE AIR SEAL				
1	SUPPORT MAIN ASSY				
1	ON VET BODY				
1	SUPPORT ASSY-SHAFT				
1	RETAINER ASSY-BEARING				

SH. 6	AM	-			1	SUPPORT ASSY-TURBINE			
SH. 4	AM	-			4	SHROUD ASSY			
SH. 4	AM	-			1	SUPPORT ASSY- BLADE			
SH. 4	AM	-			1	SEAL ASSY-DOUBLE LABYRINTH			
SH. 3	AM	-			1	DUCT ASSY-COOLING AIR		5797	
SH. 3	AM	-			1	HOUSING ASSY-TURBINE			
SH. 3	AM	-			1	HOUSING ASSY-TURBINE			
SH. 3	AM	-			1	LINER - COMBUSTOR INNER		5797	
SH. 3	AM	-			1	LINER - COMBUSTOR OUTER		5797	
SH. 3	AM	-			1	HEADPLATE ASSY			
SH. 2	AM	-			1	COVER ASSY-COMB SUPPORT			
SH. 2	AM	-			1	SUPPORT ASSY-TURBINE			
SH. 2	AM	-			1	HOUSING ASSY-COMBUSTOR			
SH. 2	AM	-			1	VAPORIZER ASSY-COMB FUEL			
SH. 2	AM	-			1	SUPPORT ASSY-COMBUSTOR			
SH. 2	AM	-			25	STATOR			
SH. 2	AM	-			1	TURBINE			
SH. 2	AM	-			37				
SH. 2	AM	-			36				
SH. 2	AM	-			95				
SH. 2	AM	-			94				
SH. 2	AM	-			93				
SH. 2	AM	-			92				
SH. 2	AM	-			91				
SH. 2	AM	-			90				
SH. 2	AM	-			89				
SH. 2	AM	-			88				
SH. 2	AM	-			87				
SH. 2	AM	-			86				
SH. 2	AM	-			85				
SH. 2	AM	-			84				
SH. 2	AM	-			83				
SH. 2	AM	-			82				
SH. 2	AM	-			81				
SH. 2	AM	-			80				
SH. 2	AM	-			79				
SH. 2	AM	-			78				
SH. 2	AM	-			77				
SH. 2	AM	-			76				
SH. 2	AM	-			75				
SH. 2	AM	-			74				
SH. 2	AM	-			73				
SH. 2	AM	-			72				
SH. 2	AM	-			71				
SH. 2	AM	-			70				
SH. 2	AM	-			69				
SH. 2	AM	-			68				
SH. 2	AM	-			67				
SH. 2	AM	-			66				
SH. 2	AM	-			65				
SH. 2	AM	-			64				
SH. 2	AM	-			63				
SH. 2	AM	-			62				
SH. 2	AM	-			61				
SH. 2	AM	-			60				
SH. 7	AM	-			1	RING-INNER SUPPORT			
SH. 7	AM	-			1	RING-OUTER SUPPORT			

C

1	SUPPORT ASSY - TURBINE			
2	SHROUD ASSY			
3	SUPPORT ASSY - BLADE			
4	SEAL ASSY - DOUBLE LABYRINTH			
5	DUCT ASSY - COOLING AIR	5797		
6	HOUSING ASSY - TURBINE			
7	HOUSING ASSY - TURBINE			
8	LINER - COMBUSTOR INNER	5797		
9	LINER - COMBUSTOR OUTER	5797		
10	HEADPLATE ASSY			
11	COVER ASSY - COMB SUPPORT			
12	SUPPORT ASSY - TURBINE			
13	HOUSING ASSY - COMBUSTOR			
14	VAPORIZER ASSY - COMB FUEL			
15	SUPPORT ASSY - COMBUSTOR			
16	STATOR			
17	TURBINE			
18				
19				
20				
21				
22				
23				
24				
25				
26				
27				
28				
29				
30				
31				
32				
33				
34				
35				
36				
37				
38				
39				
40				
41				
42				
43				
44				
45				
46				
47				
48				
49				
50				
51				
52				
53				
54				
55				
56				
57				
58				
59				
60				
61				
62				
63				
64				
65				
66				
67				
68				
69				
70				
71				
72				
73				
74				
75				
76				
77				
78				
79				
80				
81				
82				
83				
84				
85				
86				
87				
88				
89				
90				
91				
92				
93				
94				
95				
96				
97				
98				
99				
100				
101				
102				
103				
104				
105				
106				
107				
108				
109				
110				
111				
112				
113				
114				
115				
116				
117				
118				
119				
120				
121				
122				
123				
124				
125				
126				
127				
128				
129				
130				
131				
132				
133				
134				
135				
136				
137				
138				
139				
140				
141				
142				
143				
144				
145				
146				
147				
148				
149				
150				
151				
152				
153				
154				
155				
156				
157				
158				
159				
160				
161				
162				
163				
164				
165				
166				
167				
168				
169				
170				
171				
172				
173				
174				
175				
176				
177				
178				
179				
180				
181				
182				
183				
184				
185				
186				
187				
188				
189				
190				
191				
192				
193				
194				
195				
196				
197				
198				
199				
200				
201				
202				
203				
204				
205				
206				
207				
208				
209				
210				
211				
212				
213				
214				
215				
216				
217				
218				
219				
220				
221				
222				
223				
224				
225				
226				
227				
228				
229				
230				
231				
232				
233				
234				
235				
236				
237				
238				
239				
240				
241				
242				
243				
244				
245				
246				
247				
248				
249				
250				
251				
252				
253				
254				
255				
256				
257				
258				
259				
260				
261				
262				
263				
264				
265				
266				
267				
268				
269				
270				
271				
272				
273				
274				
275				
276				
277				
278				
279				
280				
281				
282				
283				
284				
285				
286				
287				
288				
289				
290				
291				
292				
293				
294				
295				
296				
297				
298				
299				
300				
301				
302				
303				
304				
305				
306				
307				
308				
309				
310				
311				
312				
313				
314				
315				
316				
317				
318				
319				
320				
321				
322				
323				
324				
325				
326				
327				
328				
329				
330				
331				
332				
333				
334				
335				
336				
337				
338				
339				
340				
341				
342				
343				
344				
345				
346				
347				
348				
349				
350				
351				
352				
353				
354				
355				
356				
357				
358				
359				
360				
361				
362				
363				
364				
365				
366				
367				
368				
369				
370				
371				
372				
373				
374				
375				
376				
377				
378				
379				
380				
381				
382				
383				
384				
385				
386				
387				
388				
389				
390				
391				
392				
393				
394				
395				
396				
397				
398				
399				
400				
401				
402				
403				
404				
405				
406				
407				
408				
409				
410				
411				
412				
413				
414				
415				
416				
417				
418				
419				
420				
421				
422				
423				
424				
425				

3.2 COMBUSTOR DESIGN

3.2.1 General Description

The object of the design was to provide a combustor for use on the small, high-temperature turbine test rig. The turbine design point was calculated at an 8:1 compressor pressure ratio, 2960°R turbine rotor entry temperature, and 4.0 pounds/second gas flow entering the turbine rotor. Pertinent design and test conditions are summarized in Table VIII.

A reduced scale layout of the combustor is shown in Figure 32. The design is of the full annular vaporizing type and employs axial mixing within the primary combustion zone and transverse injection of diluent air from the outer liner in the dilution, or secondary, zone. A unique feature of the design is the use of a single vaporizer integrated with the inner liner assembly.

A schematic flow diagram is shown in Figure 33. The combustion chamber assembly is mounted within a 10-inch test duct. Primary air for combustion passes through the 16 slotted primary air cups and enters the primary zone as fan-shaped jets. These axial jets divide the primary zone into sectors and create a degree of coarseness in the fuel-air mixture within the primary zone that provides combustion stability over a wide operating range. Strong recirculation patterns conducive to good flame holding are also established. Air for combustion is continually available as required along the edges of the axial jets. The balance of primary air for combustion enters the central annular vaporizer through a swirl guide-vane assembly located upstream of the vaporizer headplate. Fuel is injected into this swirling air as it passes along the vaporizer annulus, and the carburetted, preheated fuel undergoes a reverse turn and is injected into the primary combustion zone toward the vaporizer headplate. The principal objective of the imposed swirl is to provide uniform circumferential fuel distribution around the combustion chamber and to ensure complete wetting of the vaporizer annulus walls. The rich mixture of fuel and air passing through the vaporizer is heated by the combustion process surrounding the vaporizer and is discharged in a state which can be burned immediately. Ignition lag is reduced because the sensitive precombustion stage now occurs within the vaporizer and is protected from random chilling. The name vaporizer implies that the primary function of the component is to prevaporize the fuel. In fact, the essential function is to preheat the fuel and to premix it with air. The quantity of air in the vaporizer annulus is sufficient to avoid fuel cracking and deposition while maintaining maximum carburetion. Combustor performance is not primarily dependent on the degree of fuel prevaporization.

The major portion of the combustor airflow bypasses the headplate and is injected as diluent into the combustion chamber through axial slots located in the outer liner assembly immediately downstream of the primary combustion zone. The balance of the combustor airflow is utilized for convective film-cooling of the inner and outer liners. The film coolant is admitted at five axial locations along each liner through a single row of holes in the liners at each axial location. The coolant passing through

each row of holes impinges on a deflector which is attached to the combustion side of the liner and is discharged tangentially along the liner as a continuous sheet of coolant. This system has been found to provide efficient cooling of the liner while maintaining strict control of coolant flow rate. Such control is of particular concern in the design of small combustors of this type, since metering areas are correspondingly small and tolerance limits could result in unacceptable aberration of the combustor airflow distribution.

In order to provide independent control of the turbine stator and turbine rotor coolant flow rates for test purposes, an arrangement of concentric ducts was located on the combustor centerline. The coolant supply to the stator and the rotor is to be independently controlled and metered upstream of the combustion system.

Ignition is accomplished by means of an air-cooled, 20-joule igniter which protrudes through the outer liner into the primary combustion region. Experience on other test rigs of this type indicates that a primer fuel spray system is not required to supplement the ignition system for this test application.

3.2.2 Basic Design Considerations

The essential function of this combustor is to provide the required gas state conditions at the inlet to the small, high-temperature turbine component under development. In order to provide for turbine design and evaluation most representative of engine application, the combustion system was designed to be compatible with engine requirements, with modifications for test flexibility, and with expeditious procurement.

Assessment of the two principal types of combustion systems, fuel spray atomizing and fuel vaporizing, resulted in the selection of the vaporizing approach for this application based on consideration of the following advantages:

1. Stable combustion over a wide fuel-air ratio range at high efficiency.
2. Well-defined, compact envelope because of improved fuel preparation and advantageous mixing characteristics.
3. Excellent turbine inlet temperature distribution as a result of ability to use a large number of fuel admission points.
4. Relatively low pressure and less complicated fuel supply system required as compared to that needed by spray injection type designs.
5. Fuel metering orifices relatively large and located in a region removed from the combustion process, thus minimizing sensitivity to fuel contamination and eliminating fouling.

6. Minimum maintenance in field use as demonstrated by thousands of J65 military service engines. Recent testing of the TJ60 design and the modified J65 engine operating at 2500°F TIT indicates further improvement in durability and extended operational capability.
7. Reduced radiative heat input to engine components, since vaporizing systems tend to burn with a relatively nonluminous flame.
8. Vaporizing performance relatively insensitive to fuel type and viscosity.

At this point, a choice between the tubular and annular combustion system approaches was required. Annular combustors provide the most efficient use of the available engine volume with clean aerodynamic passages. In general, the tubular approach can impose durability and packaging problems, if complicated transition pieces are required to mate with the annular flow passages of the other engine components. Such transition pieces tend to be bulky, present increased surfaces to be cooled, and impose undesirable temperature distributions upon the turbine. However, tubular combustors usually have the advantage of minimizing the number of fuel introduction points required, which is an important consideration for small engines with low flow rates, since multiple division of low total fuel flow rates can result in a complex fuel metering system with increased sensitivity to blockage due to fuel contamination. In the subject design, the unique use of a single vaporizer integrated with the inner liner assembly of an annular combustion chamber presented a most attractive means of tailoring the annular vaporizing system to the specific requirements of a small gas turbine. In this manner, uniform circumferential fuel distribution is obtained with minimum complexity in the fuel system.

3.2.3 Combustor Design

The test rig combustor design state conditions are shown in Table VIII. The first step in the detail design was to establish the primary zone fuel and air weight flow requirements for the combustion process. The combustion efficiency characteristic assumed in the subject design is that of an advanced vaporizing system. Combustion efficiency is a function of the primary zone fuel-air ratio as shown in Figure 34. Although for test rig purposes the combustion stability range requirements were not as stringent as would be required for engine application, wide stability limits were nevertheless considered desirable. By setting the primary zone weight flow at 43 percent of the total combustor weight flow (Figure 34), wide stability range was obtained and the estimated overall combustor performance shown in Figure 35 was defined. The design point for engine application with a 610°F combustor inlet temperature and a 2500°F turbine rotor inlet temperature is approximately 0.032 overall combustor fuel-air ratio. The weight flow distribution and the combustor entry port area schedule are presented in Table IX.

Previous experience on vaporizing systems indicates that the optimum design-point fuel-air ratio within the vaporizers is approximately 0.25. In

essence, these criteria define the air-fuel ratio sufficient to prevent fuel cracking and deposition while maintaining maximum preheat and carburetion and correspond to a weight flow of about 13 percent into the vaporizer. The detailed thermal analysis of the combustion chamber liner film-cooling requirements was made using an established Thermal Analyzer Computer Program. This analysis, which is described in more detail in Section 3.4.1, indicated a requirement of 6.3 and 21.4 percent of combustor weight flow for convective cooling of the inner and outer liners respectively. The balance of the combustor weight flow (32 percent) was utilized for dilution purposes. This diluent air is radially injected into the chamber through 32 diluent slots located in the outer liner. This number of slots was used in order to maintain regular circumferential phasing with the 16 primary air cups on the vaporizer headplate. The length-to-width ratio of the slots is close to 4:1, which complies with established requirements for high jet penetration and good mixing in the available mixing length.

The required airflow distribution having been determined, a comparative study between combustor pressure loss and chamber cross-sectional area was undertaken using an equation similar to that employed by Reference 3.

$$\frac{\Delta P}{q_{\text{ref}}} = \left(\frac{A_{\text{ref}}}{A_b} \right)^2 \left(\frac{A_b}{A_e} \right)^2 \left(\frac{M_b}{M} \right)^2$$

where

- ΔP = total pressure loss across combustor headplate
- q_{ref} = nominal mean dynamic head of total airflow at inlet density through maximum cross-sectional area of combustion system (A_{ref})
- A_b = cross-sectional area of burning zone of combustion system
- A_e = effective total flow area of entry apertures for air in the vaporizer headplate
- M_b = primary zone mass flow rate
- M = total mass flow rate through combustion system

The use of this type of equation, coupled with the equations of continuity and conservation of total momentum (to estimate the momentum loss, or additional loss in total pressure due to the addition of heat), provided an iterative method of relating overall total pressure loss and vaporizer headplate area. An overall loss of 3 percent of the inlet total pressure was selected. This provided stable flame-holding characteristics, provided an attractive engine cycle, and was consistent with a compact combustor envelope concept. Combustion chamber length, L , may be regarded as the sum of two intermediate lengths: the length of the primary, or combustion zone, l_p , and the length for dilution, or mixing, l_D . Primary

zone length is essentially defined by compliance with two criteria. The first is a thermodynamic requirement that the mean through-flow velocities and length of the primary zone provide sufficient residence time for the fuel to completely burn prior to entering the dilution zone. The second is an aerodynamic requirement to provide a length sufficient to establish mixing patterns within the primary zone. Failure to satisfy both these requirements would result in loss of combustor performance, since unburned fuel would leave the primary zone to be chilled by the incoming diluent air.

Primary zone length in the design of small-scale combustors is generally governed by the residence time criterion. Such was the case in the subject design. Compliance with the residence time criterion resulted in a conservative length for aerodynamic mixing. A primary zone length of 5 inches with a residence time of 4.3 milliseconds was selected for the subject design. This residence time is typical of advanced combustion systems. The dilution, or mixing length, l_p , is conventionally related to the passage height between the liners, h_p , at the plane of diluent air entry (Reference 3). Current combustor development programs at C-W utilizing single-sided diluent air introduction have resulted in satisfactory combustor discharge temperature distribution with dilution length to passage height ratios, l_p/h_p , as low as 1.40. On the subject program, a dilution length of approximately 3 inches was selected, with a conservative l_p/h_p ratio of about 2.5, to minimize combustor development. It should be noted that the conservative combustion chamber length selected imposes an increased burden on liner film-cooling requirements. However, this approach does facilitate combustor modifications for increased turbine inlet temperature levels, should such increases be desirable subsequent to the immediate test program.

3.2.4 Performance

Estimated performance at design point condition is summarized in Table X. Also included in this table are the principal dimensions of the combustor.

An indication of the relative size of the combustor is commonly obtained from these parameters: reference velocity, residence time, and heat release rate. Reference velocity is an empirical figure based on the total flow at inlet density passing through the maximum flow area (A_{ref}) within the combustor casing. In the subject design, this velocity is not significant, since the combustor liners were installed in a section of oversized test ductwork rather than in a minimum-diameter casing. The resultant ratio between the flame tube flow area (A_b) and the reference area (A_{ref}) is approximately 0.25, rather than 0.5 to 0.7 which would be anticipated in engine applications. Primary zone residence time is based on the mean primary zone through-flow velocity and primary zone length. The estimated design-point value of 4.3 milliseconds is representative of an advanced design. Heat release rate per unit of combustion zone volume is more generally used as a measure of combustor size, since it includes fuel flow rate and inlet pressure level. The estimated value of this parameter at the test conditions is 13.4×10^6 Btu/ cubic foot/hour/atmosphere.

The estimated combustor exit total temperature distribution is shown in Figure 36. Two curves are presented in this figure. The first curve represents the mean temperature at any radial location, while the maximum curve represents the maximum local temperature at any radial location. Hence, the mean curve approximates the profile which could be imposed on the turbine rotor, while the maximum curve represents the maximum temperature profile which could be imposed on the turbine stator. The peak value of the mean curve corresponds to a peak mean temperature of 6.1 percent above the overall average exit temperature, while the maximum local temperature is 13.5 percent above the overall average exit temperature. These profiles represent development goals based on test experience on combustors utilizing the same fundamental design criteria and are compatible with the stress limits of the proposed turbine component.

TABLE VIII		
DESIGN CONDITIONS FOR TURBINE COMPONENT AND TEST RIG		
	Turbine Component	Test Rig
Airflow at turbine rotor inlet, W, lb/sec	4.0	3.01
Combustor airflow, lb/sec (excluding turbine coolant)	3.84	2.89
Rotor cooling airflow, % W	4.0	4.0
Stator cooling airflow, % W	4.0	4.0
Combustor inlet temperature, °F	610	610
Turbine cooling air temperature, °F	610	610
Turbine rotor average inlet total temperature, °F	2500	2500
Combustor inlet total pressure, psia	-	87.63
Combustor exit total pressure, psia	116.35	85.0

TABLE IX
COMBUSTOR AIRFLOW DISTRIBUTION AND METERING
AREA SCHEDULE

	<u>Metering Area</u> <u>sq in.</u>		<u>Weight Flow</u>	
	Actual	Effective	lb/sec	% of Total
Combustor Inlet Total	-	-	2.89	100
Outer Liner Passage - Total	5.110	2.493	1.533	53.03
Dilution Slots - Total	2.243	1.346	0.915	31.67
Film Cooling - Total	2.867	1.147	0.617	21.36
1st Film Cooling Annulus	0.801	0.320	0.160	5.536
2nd Film Cooling Annulus	0.550	0.22	0.120	4.152
3rd Film Cooling Annulus	0.550	0.22	0.12	4.152
4th Film Cooling Annulus	0.795	0.318	0.17	5.882
5th Film Cooling Annulus	0.171	0.068	0.047	1.637
Inner Liner - Total	1.233	0.494	0.182	6.30
1st Film Cooling Annulus	0.448	0.179	0.045	1.557
2nd Film Cooling Annulus	0.308	0.123	0.035	1.211
3rd Film Cooling Annulus	0.276	0.111	0.047	1.626
4th Film Cooling Annulus	0.092	0.037	0.025	0.865
5th Film Cooling Annulus	0.109	0.044	0.030	1.038
Vaporizer Headplate - Total	3.541	2.231	1.175	40.67
Vaporizer	1.06	0.901	0.395	13.67
Primary Aircups - Slots	2.37	1.42	0.725	25.09
Primary Aircups - Anti-Carbon Holes	0.090	0.054	0.028	0.96
Headplate Anti-Carbon Holes	0.090	0.054	0.028	0.96

TABLE X
TURBINE TEST RIG COMBUSTOR
SUMMARY OF DESIGN CONDITIONS AND PERFORMANCE

Combustor Inlet Air Conditions:	
Total pressure, in. HgA	178.5
Total temperature, °R	1070
Combustor weight flow, lb/sec	2.89
Density, lb/ft ³	0.221
Combustor Exit Conditions:	
Total pressure, in. HgA	173.1
Total temperature, °R	3040
Peak mean radial total temperature ratio, T_L/T_4 , °R/°R	1.061
Maximum local temperature ratio, $T_{L_{max}}/T_4$, °R/°R	1.135
Basic Dimensions:	
Length (vaporizer headplate to turbine stator LE), in.	8.3
Combustion zone flow area, A_b , ft ²	0.144
Combustion chamber volume, ft ³	0.0785
Test duct total flow area A_{ref} , ft ²	0.5454
Turbine inlet OD, in	6.541
Turbine inlet ID, in	5.459
Combustor fuel-air ratio, F/A	0.0323
Combustion efficiency, %	99
Combustor pressure loss, % of inlet total pressure	3.0
Reference velocity (total flow at inlet density through test duct total flow area, A_{ref}), ft/sec	26
Primary zone residence time, milliseconds	4.3
Overall combustion chamber heat release rate, Btu/ft ³ /hr/atmos	13.4×10^6
Primary zone heat release rate, Btu/ft ³ /hr/atmos	17.8×10^6

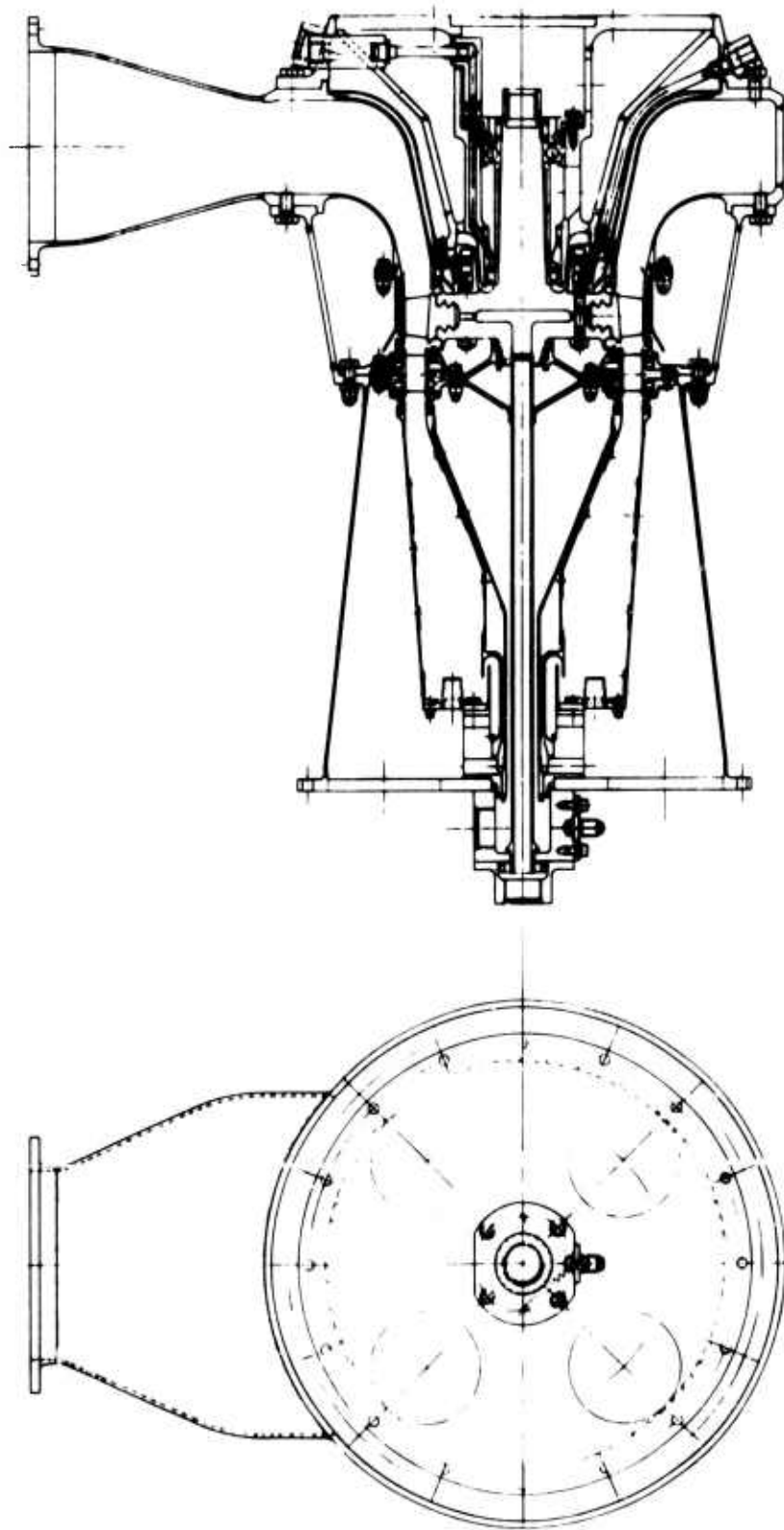


Figure 32. Preliminary Turbine Rig Combustor Basic.

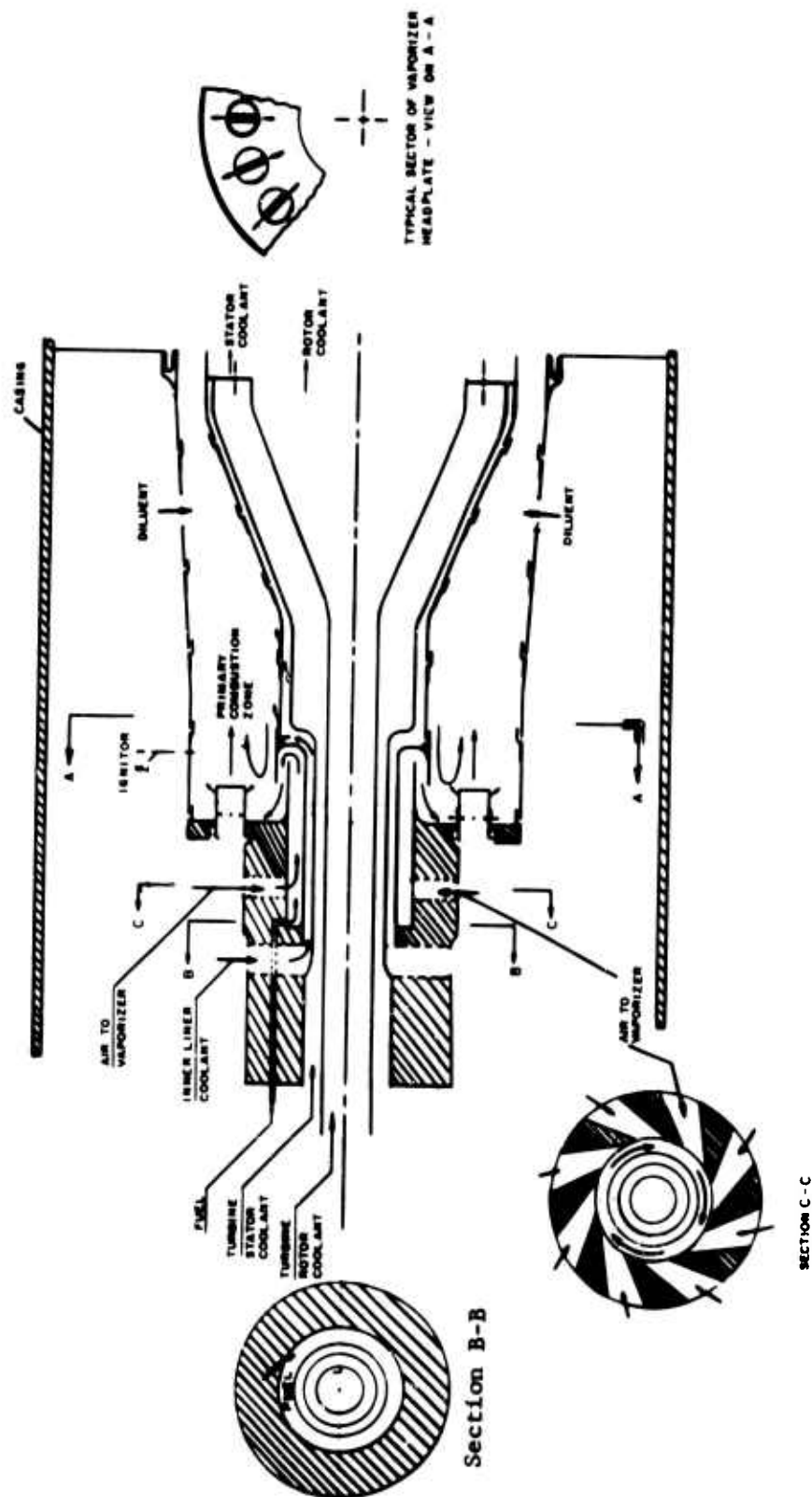


Figure 33. Turbine Test Rig - Combustor Flow Schematic.

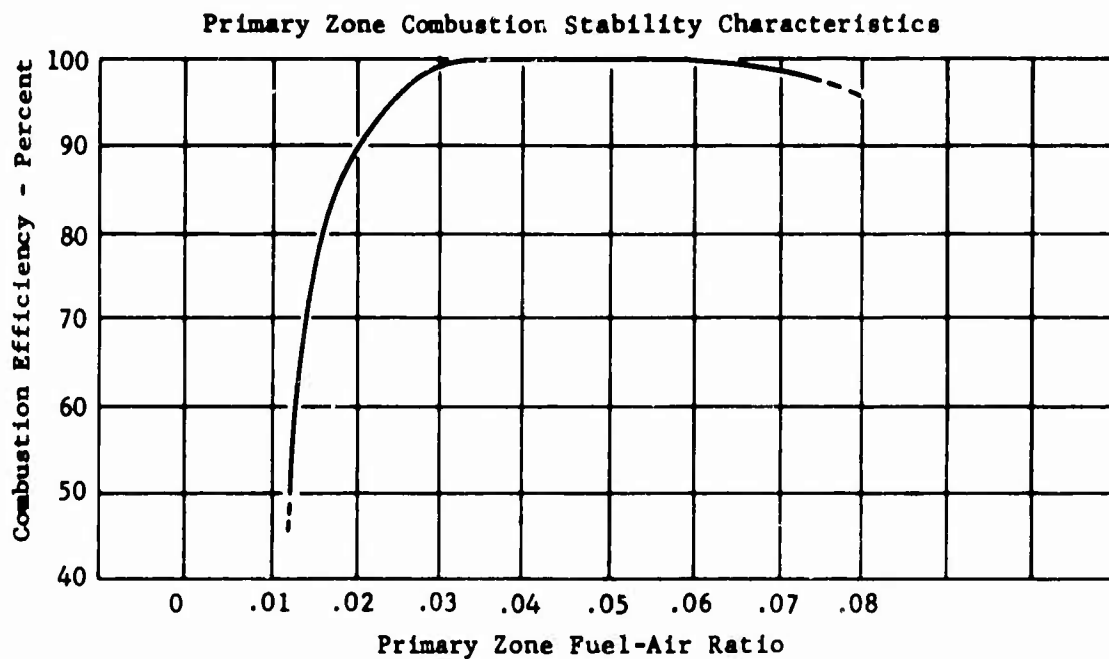


Figure 34. Advanced Vaporizing Combustor.

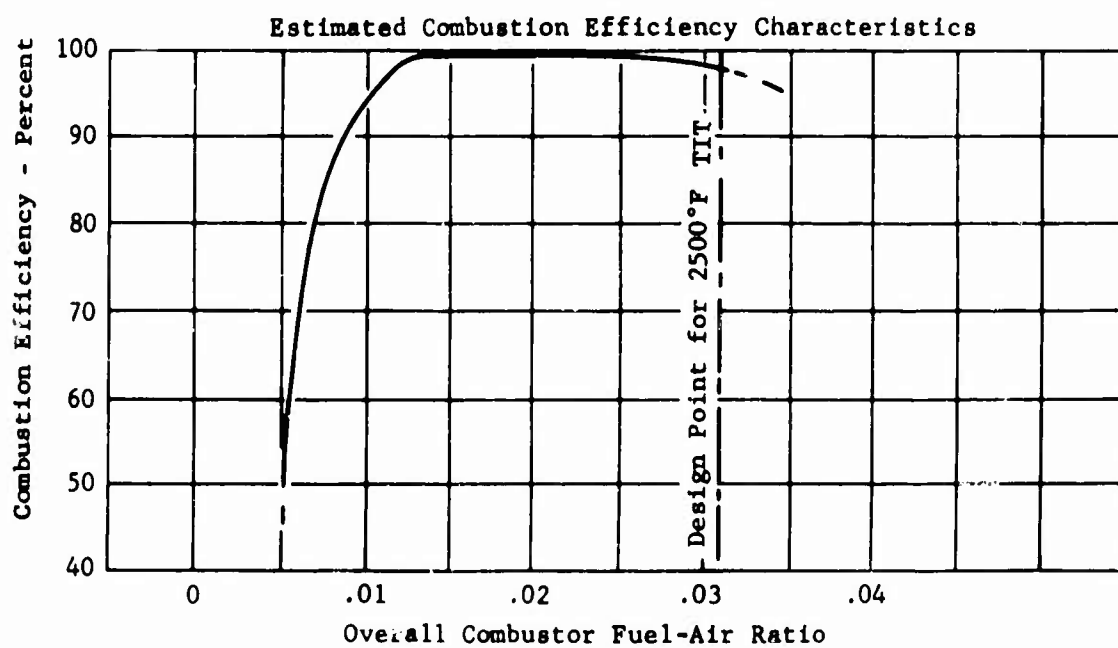


Figure 35. Combustor Design.

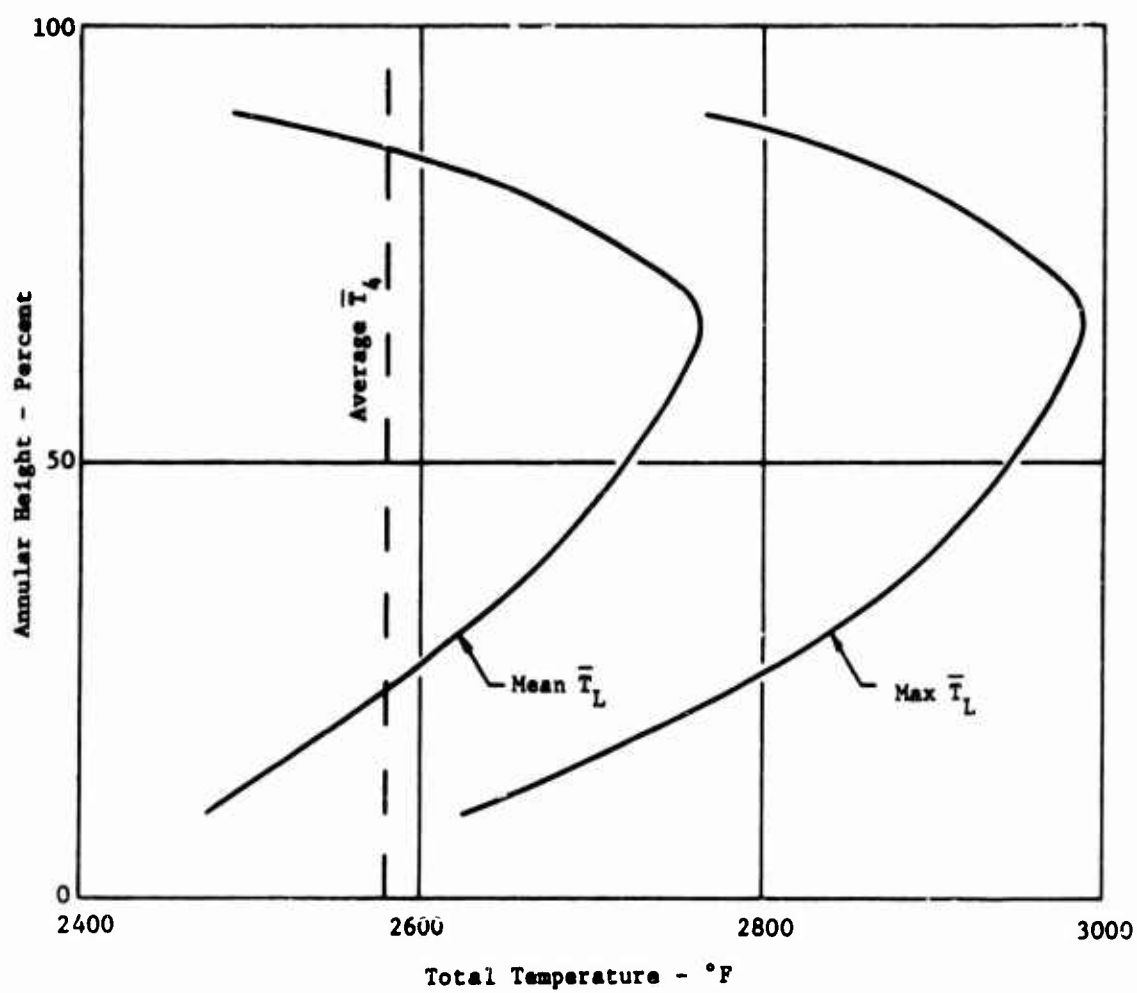


Figure 36. Turbine Test Rig Estimated Turbine Inlet Radial Temperature Profiles.

3.3 TURBINE RIG STRESS AND VIBRATION ANALYSIS

3.3.1 Stress Analysis

3.3.1.1 Inlet Combustor Support

The cast inlet combustor support, consisting of a hub, a rim, and four hollow spokes (Figure 37), is subjected to an axial force from the combustor. To obtain the stresses in the spokes, a compatibility analysis was performed to account for the fact that the vertical and horizontal spokes have different cross sections. Considering the hub as a rigid ring, the spokes were treated as cantilever beams with ends attached to a flexible ring. The rim exerts a restoring moment proportional to the rotation of the spoke; therefore, by assuming the deflection of each spoke to be equal, the force and moment in each spoke were obtained. The stress produced inside the hub by the inner air coolant tube was determined by considering the supporting lip as a plate rigidly fixed at its outer radius and subjected to axial shear of its inner radius. The stress levels, which are shown on Figure 37, are below the material 0.2 percent yield stress of 18,000 psi at 400°F.

3.3.1.2 Inlet Plate

An early design configuration contained an inlet plate (Figure 38) for which stresses and deflections were obtained for two boundary conditions:

1. Inner periphery free and the mating flange at the outer periphery neglected (Figure 39b).
2. Inner periphery clamped and the mating flange at the outer periphery taken into account (Figure 39c).

The above boundary conditions prevailed when the bolts securing the plate to the outer housing flange and to the inner joint block were loose or tight, respectively. In both cases, the plate was assumed to be subjected to a transverse line load at the inner periphery. The maximum axial deflection was found to be 19×10^{-3} inches and 4.5×10^{-3} inches for boundary conditions 1 and 2, respectively. The stresses at various locations of the plate are summarized in Figure 40. They are well below yield strength except at the inner periphery, with the boundary conditions described in item 1. However, since it is unlikely that 11 bolts will accidentally become loose and because the stress is local and does not appreciably exceed yield, the plate is considered to be structurally adequate for rig operation.

3.3.1.3 Combustion Chamber Liners

Inner Liner

In order to expedite required design time, stress analysis of this component was based on an assumed temperature distribution, as shown in Figure 41. This same figure shows that the final temperature distribution does not differ enough to require reanalysis. Stress analysis consisted of theoretically dividing the structure into two free bodies (Figure 42), typical of

adjacent shells, and writing the equations for equilibrium of forces and compatibility of deformations. In order to include the effect of the diffuser ring, shell A was assumed to be twice as stiff as shell B. Comparison of the stresses obtained, with the material (Hastelloy X) stress strain curves at 1200°F and 1800°F, respectively, shows that strain is a better measure of this material's capacity than elastic stress. The calculated stress of 68,000 psi corresponds to a strain of 0.0036 inch/inch. The material stress-strain curve for 1800°F and a strain of 0.0036 inch/inch shows a corresponding stress of 16,000 psi. Since discontinuity-induced stresses are of the fixed strain type, as opposed to constant load, the material will yield to relax the stresses. In order to determine the ability of this liner to withstand proposed test operational life, a low-cycle fatigue analysis was made using the method of Reference 4 for a material reduction in area at failure of 20 percent and 37 percent. A stress concentration factor of 3 was used in the area of the coolant holes, since for the case of a series of holes in a uniaxial stress field, the factor is asymptotic to 3. The above analysis results in a strain (ϵ) of 0.0054 inch/inch, which on Figure 43 shows a minimum number of permissible cycles of 175, which is within the scope of the present test plan.

Outer Liner

The theoretical thermal gradient along the axis of the outer liner is shown in Figure 44. A rigorous analysis using the exact thermal gradient was not considered practical due to the difficulty in ascertaining the true effect of the diffuser rings. A gradient was assumed (Figure 45), and the structure was theoretically separated into three free bodies (Figure 46) consisting of two long cylinders and one short cylinder with a flexural rigidity twice that of the long cylinders. The maximum liner stress occurs at the ends of the long cylinders, and the maximum strain is 0.0077 inch/inch. Low-cycle fatigue life was determined using the same method described previously and can be seen to be 70 cycles on Figure 43 for a maximum strain of 0.0077 inch/inch. Since this liner is subjected to an external pressure (3 psi), it was also checked for instability. The critical buckling pressure was found to be 77 psi, which is greatly in excess of the expected operating environment.

Poroloy Combustion Chamber Liners

An analysis was made to determine the feasibility of using a porous material (Poroloy)* for combustion chamber liners. The inner liner geometry is shown in Figure 47 and was analyzed for 3.0 psi internal pressure at 1300°F uniform temperature throughout the liner.

The analysis included the pressure and discontinuity stresses at details A-A and B-B shown in Figure 47 and the axial critical buckling stress in the liner. In this analysis the following assumptions were made:

1. The flanges are infinitely rigid relative to the shell. This is conservative in that deflection of the flanges will relieve discontinuity stresses in the shell.

* Bendix Filter Div., South Bend, Indiana

2. Friction forces between the flange and piston ring will not restrain the liner in the axial direction.

The outer liner geometry is shown in Figure 48 and was analyzed for 3.0 psi external pressure and 1300°F uniform temperature throughout the liner. Stresses were calculated at section A-A of Figure 48 for both the shell-flange transition and the weld. An elastic deformation compatibility analysis was employed. The critical buckling pressure was determined using methods prescribed in Reference 5. The following assumptions were made:

1. The liner is cylindrical.
2. The flanges are infinitely rigid relative to the shell. The shell is free to deform only in the axial direction.
3. The stress concentration factor for the slots in the shell is 1.5.

From a structural viewpoint, Poroloy liners are adequate for this type of application; however, in view of the experimental nature of this material, the following recommendations are made:

1. The outer liner thickness be increased to 0.040 inch to provide a margin of safety of 2.1 for buckling.
2. A program be pursued to obtain further mechanical properties of porous materials at operating temperature anticipated in a small combustor.

3.3.1.4 Outer and Inner Air-Coolant Tubes

The outer and inner air-coolant tubes used to form a passage to carry air to the plenum chamber and to conduct coolant to the center of the disc were analyzed for stresses due to pressure differential across the shells and an axial load. Discontinuity stresses were determined by dividing the tubes into cylindrical or conical free bodies and by using the method of compatible deformation. The inner tube was considered to be a cone attached to a fixed-ended short cylinder at the large end and a long cylinder leading into a shouldered, threaded ring section at the small end (Figure 49). The outer tube was considered to be a cone attached at its large end to a transition section which makes the junction with a vertical bulkhead and, at its small end, transitions into a small diameter cylinder, Figure 50. At this end the shell is free of restraint, and there is no mechanical stress. Each tube was considered to be at a constant temperature and free of thermal stress. Stresses were found to be low except in the inner tube at the junction of the small end of the cone with the cylinder (Figure 49). Here, discontinuity stresses reach 90 percent of yield. However, this stress is local and will not be a problem under steady load. The possibility of the inner tube's buckling under external pressure was considered. In this analysis, the stiffening effect of axial tension was conservatively neglected. The critical buckling pressure was found to be 160 psi, which is well in excess of the design pressure of 60 psi.

3.3.1.5 Exhaust Duct

The bell-shaped shells forming the exhaust duct must withstand elevated temperatures due to exhaust gases and internal pressure. The original design configuration is shown in Figure 51. The stresses on the inner shell due to pressure were very low; however, the outer shell stresses were high, and a recommendation to increase thickness from 0.05 inch to 0.10 inch was made. Subsequent to this analysis, a design change was incorporated such that the configuration is as shown in Figure 52. The receipt of temperature data showed that high stresses occurred as a result of temperature differences between the housing and exhaust duct shells. In order to reduce the stresses due to these thermal gradients, the housing material was changed to that of the exhaust duct (Hastelloy), and the housing stiffness was decreased by reducing flange and shell thickness. In addition, local areas will be insulated and/or spray cooled to reduce stresses to acceptable levels shown in Figure 53.

3.3.1.6 Bearing Support Structure

The primary structural design criterion of the bearing support is the spring rate which must be determined in order to calculate critical speed. The spring rate is defined as the ratio of the applied load at a point to the resulting deflection at that point. To obtain the spring rate at the forward bearing position (Figure 54), the flange is assumed to be perfectly rigid and the support is considered as a cantilever beam. Both bending and shear deformation were considered in determining the spring rate. The thrust bearing is in the plane of the flange and is connected to it by four ribs, or spokes. The spring rate at this bearing was obtained by considering the deformation of the ribs only. The spring rate at the forward bearing is 2.1×10^6 pounds/inch. The spring rate at the thrust bearing is 17.2×10^6 pounds/inch.

3.3.1.7 Outer Housing

The outer housing is formed by bolting together three flanged cylinders of the same radii and thicknesses. The stator support is bolted between two of these sections (Figure 55). The housing and flanges must withstand a tensile axial force, an internal pressure, and temperature gradients. The most severe thermal gradients occur in the vicinity of the exhaust liners and are discussed in that section of the report. The discontinuity stresses produced at a flange by the tensile axial force and the internal pressure were found by compatibility analysis. The flange was treated as a hollow disc with a rigidly fixed outer edge, which was taken as the center line of the bolt holes, and an inner edge joined to a long cylinder. By finding the forces and moments that make the deformations of the disc and cylinder compatible, the stresses induced by pressure and axial force were determined. The stator support was treated as a disc with an axial shear at its inner edge and its outer edge rigidly fixed to the housing flanges. The stress levels for all the above components are well below material yield, as shown in Figure 55.

3.3.2 Vibration Analysis

Continuous attention was given to the vibration aspects of the various design configurations during the first phase of the work. This work consisted primarily of determining the critical speeds of the turbine shafts.

For the sake of analysis, the shaft was divided into a number of sections conveniently located, and the geometrical properties of these sections were computed. Isotropic spring rates representing the elasticities of the bearings and casings at both front and rear supports were next assumed. After the geometry was defined, the information was used in a digital computer program.

This computer program not only establishes the critical speeds of the system by considering the inherent random eccentricity and gyroscopic forces, but readily computes the shear forces, moments, deflections, first derivatives of the deflection, and normalized deflections.

The analysis is based on the procedure for finding forced deflections of an elastic rotor on flexible supports when the center of gravity of one or more rotating masses does not lie on the axis of rotation, and a modified Prohl's method is used. Four equations can be written for the portion of the shaft between sections n and $n + 1$, expressing the equilibrium of forces and moments and the compatibility of deflections and slopes of the elastic curve. Assuming now a rotating speed, the program checks whether the given boundary conditions are satisfied. If these conditions are not satisfied, another rotational speed is assumed and the step-by-step integration procedure is repeated. The critical speeds occur at those rotational speeds at which both the difference equations and the boundary conditions are satisfied.

Since the effective spring rates could be determined only after the configuration was agreed upon, a parametric critical speed study was undertaken to facilitate the selection of the best design; the resulting critical frequency versus front main and rear main bearing support curves were plotted. A typical curve is shown in Figure 56.

Based on the analysis, it was concluded that the first critical speed is primarily controlled by the front main bearing support spring rate, whereas the rear main bearing support spring rate is more important from the point of view of the second critical speed. The parametric study further indicated that by considering support spring rates having practical values and considering the rather wide operational range of 20,000 - 55,000 rpm of the rig, the first critical speed cannot be obtained above this range; furthermore, a resonant condition would be found within this speed range.

Geometric description of the analyzed configurations, the computed component spring rates, the total resultant spring rates, and the corresponding critical speeds are shown in Tables XI, XII and XIII, respectively.

Inasmuch as an extended operation might be required at any of the speeds between 20,000 and 55,000 rpm, having a condition where a critical speed was within this range was considered to be intolerable.

After several possibilities were considered, it was decided that the design criterion for reducing the first critical speed below the operational range while bringing the second critical above 55,000 rpm would result in a resonance-free speed span and consequently would provide safe and noiseless rig testing. Accordingly, a flexible front main bearing support was designed to obtain a low first critical speed while maintaining the rear main bearing support relatively stiff to control the second critical speed. The shaft and support design submitted with this report depicts this philosophy.

In spite of the fact that the interchangeable soft front main bearing support provides enough flexibility to keep unexpected excitations and responses under control, additional refinement of the analysis will be conducted during the second phase of the work as the turbine component details are finalized to more accurately predict vibration phenomena, to eliminate rough operation, and to prepare various spring sizes for various operating conditions. The critical speeds will be redefined, and, in addition, the system will be analyzed for synchronous whirl, for amplitude responses, and for deflections caused by the loss of a turbine blade. It is felt that these precautions will help to prevent unnecessary shutdowns and to maintain efficient testing.

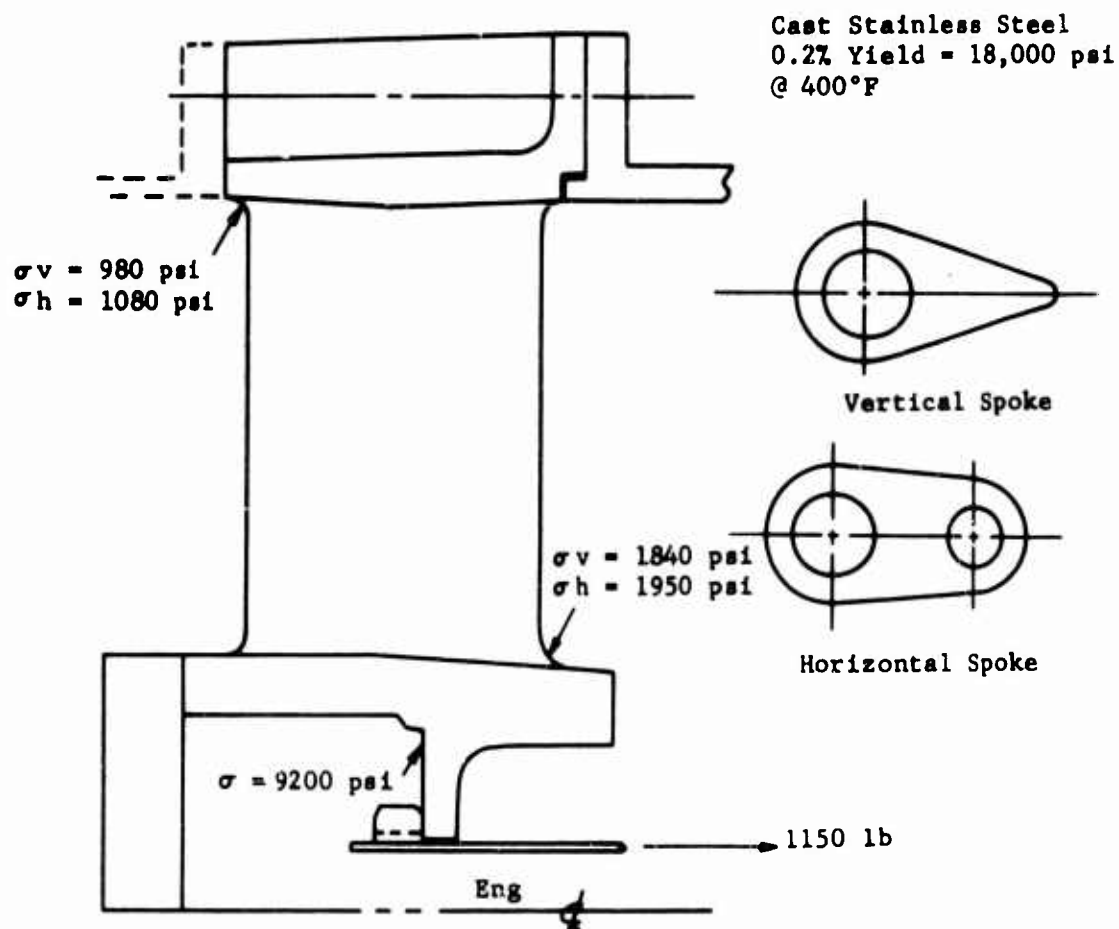
TABLE XI
DEFINITION OF THE ANALYZED CONFIGURATIONS

Config- uration No.	Weight of Turbine (lb)	Overhang Length (in.)	Span Between Bearings (in.)	Total Length Between Center Lines of RMB and Turbine (in.)
1	8.400	1.800	3.25	5.050
2	6.600	1.025	3.000	4.025
3	10.50	0.897	3.25	4.147
4*	10.50	-	16.750	16.750
5	10.50	1.500	3.250	4.750
6	12.50	2.750	5.500	8.250
7	7.00	0.897	7.353	8.250
8	8.00	1.000	7.250	8.250
9	8.33	2.000	6.250	8.250
* No Overhang				

TABLE XII							
COMPONENT AND RESULTANT SPRING RATES							
Configuration No.	Spring Rate of FMB $\times 10^6$ (lb/in.)	Spring Rate of FMB $\times 10^6$ Support $\times 10^6$ (lb/in.)	Resultant Spring Rate of FMB and Support $\times 10^6$ (lb/in.)	Spring Rate of FMB $\times 10^6$ (lb/in.)	Spring Rate of FMB $\times 10^6$ Support $\times 10^6$ (lb/in.)	Resultant Spring Rate of FMB and Support $\times 10^6$ (lb/in.)	Spring Rate of FMB $\times 10^6$ Support $\times 10^6$ (lb/in.)
1**	-	-	1.000	-	-	1.000	-
2	2.750	2.714	1.366	1.000	2.714	0.731	2.714
3*	2.500	2.714	1.301	1.000	2.714	0.730	2.714
4	2.500	2.714	1.301	1.000	2.714	0.730	2.714
5*	2.500	2.714	1.301	1.000	2.714	0.730	2.714
* Parametric study was made.							
** Parametric study was made. Spring rates were picked up for comparison.							

TABLE XIII
TABLE OF CRITICAL SPEEDS

Config- uration No.	FMB Resultant Spring Rate $\times 10^6$ (lb/in.)	RMB Resultant Spring Rate $\times 10^6$ (lb/in.)	First Critical Speed (rpm)	Conclusion
1	1.000	1.000	33,000	Critical speed is in the operational range.
2	1.366	0.731	64,200	Lightweight con- figuration.
3	1.300	0.730	51,760	Critical speed is in the operational range.
4	1.300	0.730	30,840	Critical speed is in the operational range.
5 a	1.300	0.730	43,160	Critical speed is in the operational range.
5 b	0.100	0.100	13,275	Spring rates were determined to bring critical speed be- low 15,000 rpm.
6 a	1.300	0.730	15,900	Critical speed is below the opera- tional range.
6 b	1.30	0.325	15,970	Critical speed is below the opera- tional range.
7	1.30	0.956	64,605	Critical speed is above the opera- tional range.
8	0.722	0.365	44,360	Critical speed is in the operational range.
9	1.086	0.325	21,920	Critical speed is in the operational range.



Notation:

σ_v - Bending stress in vertical spoke
 σ_h - Bending stress in horizontal spoke

Figure 37. Inlet Combustor Support.

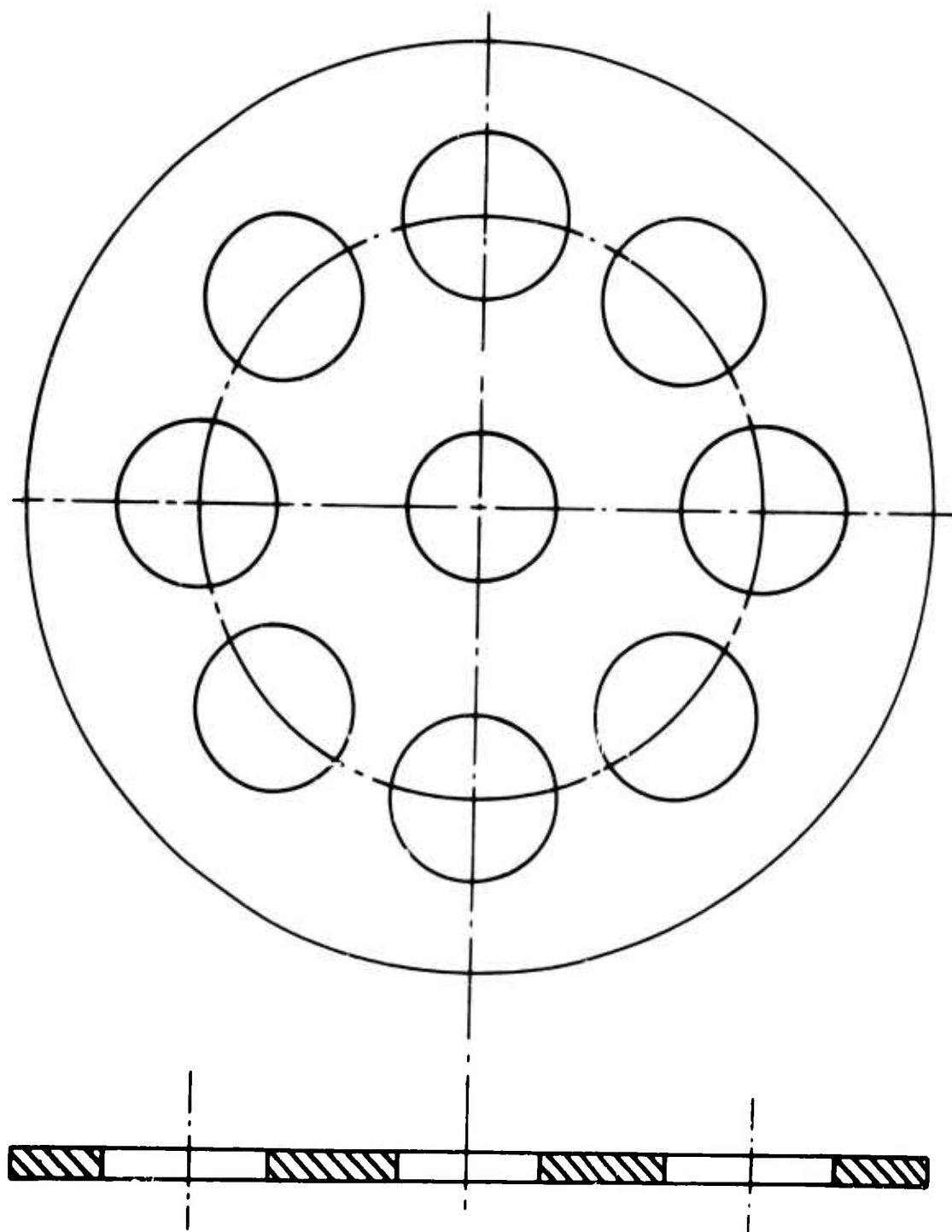


Figure 38. Inlet Plate.

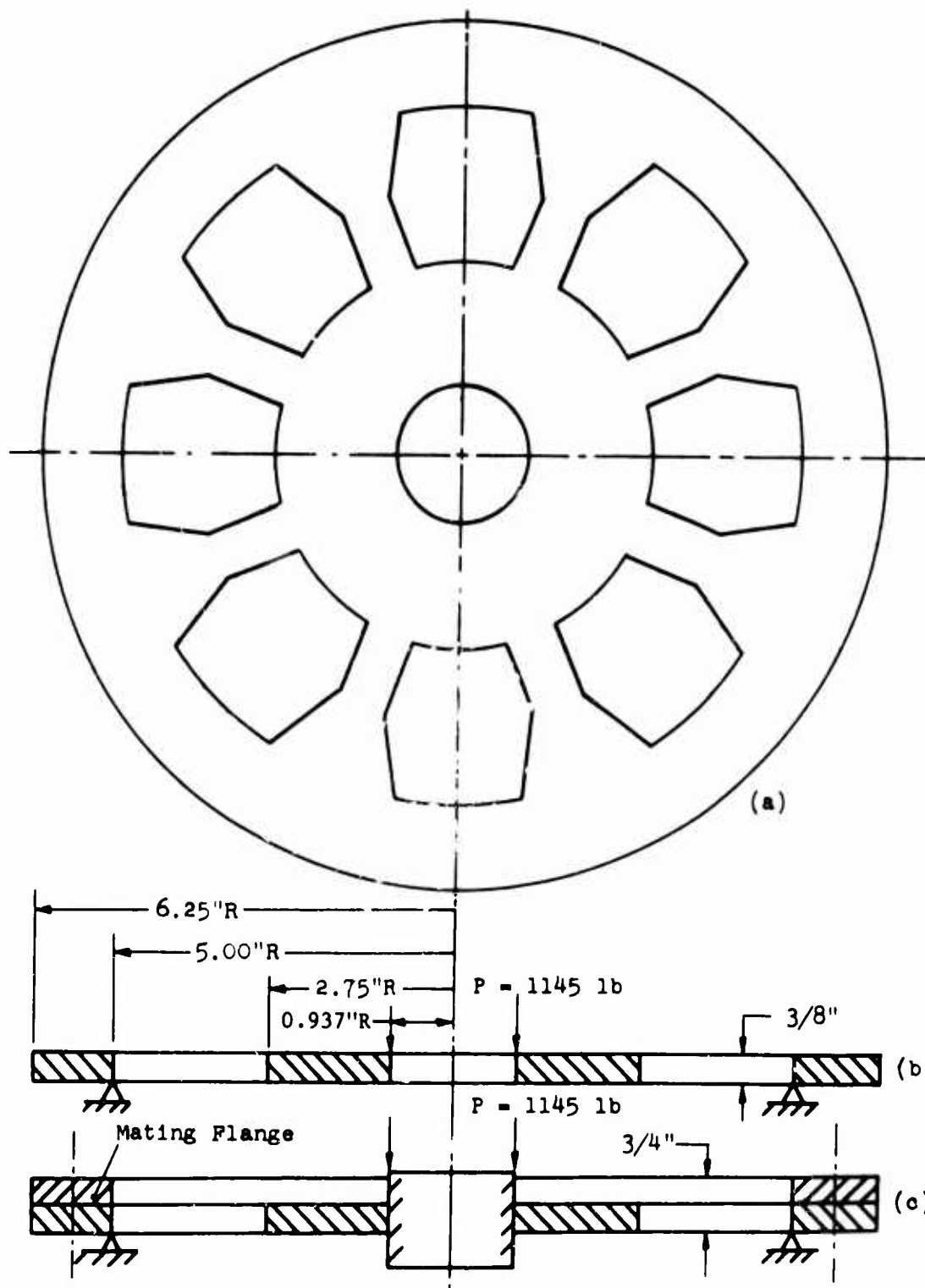
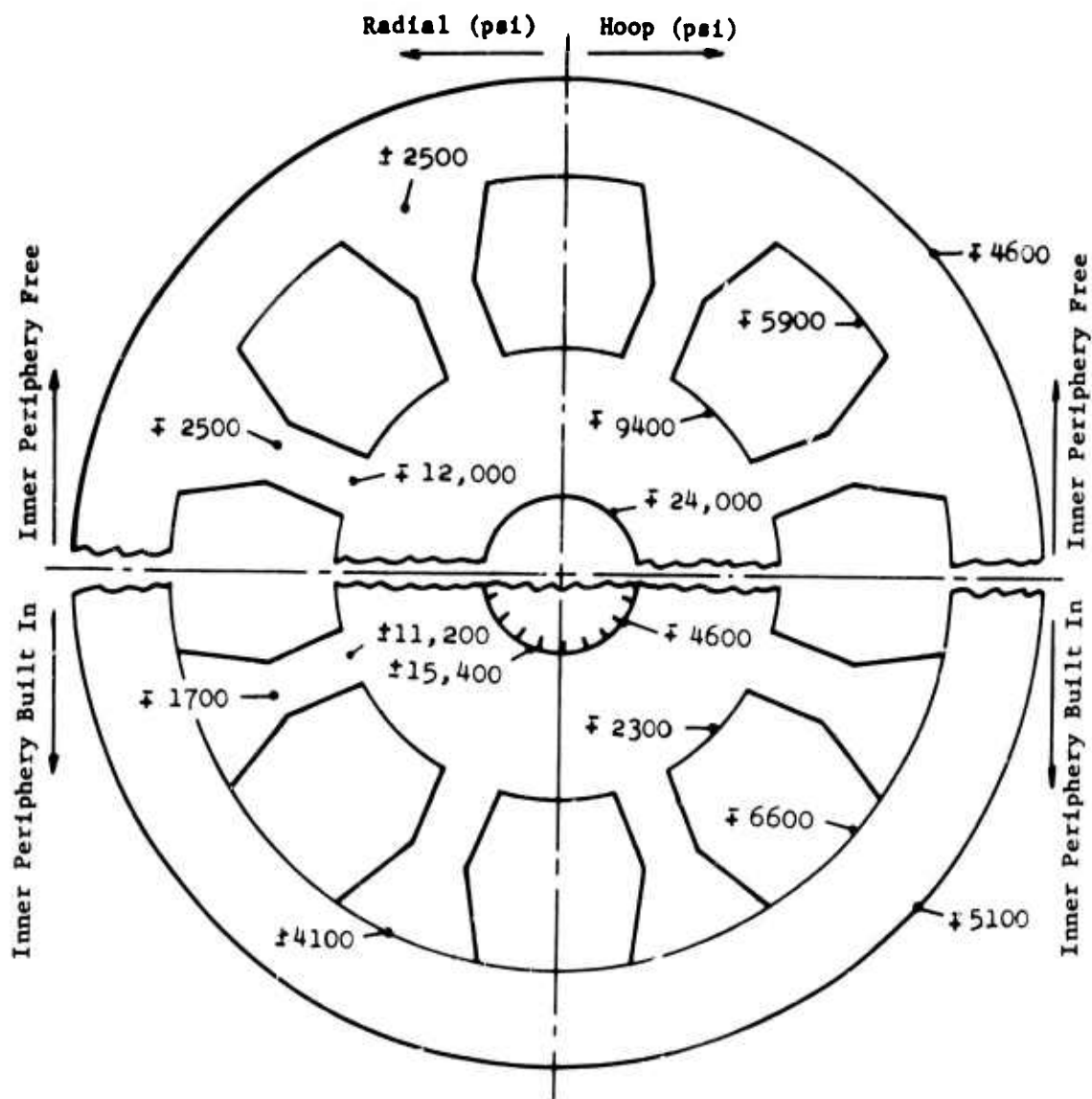


Figure 39. Simplified Inlet Plate.



Yield Stress at 600°F, $\sigma_y \approx 20,000$ psi
(Plate Material AISI 321)

Figure 40. Summary of Stresses in Inlet Plate.

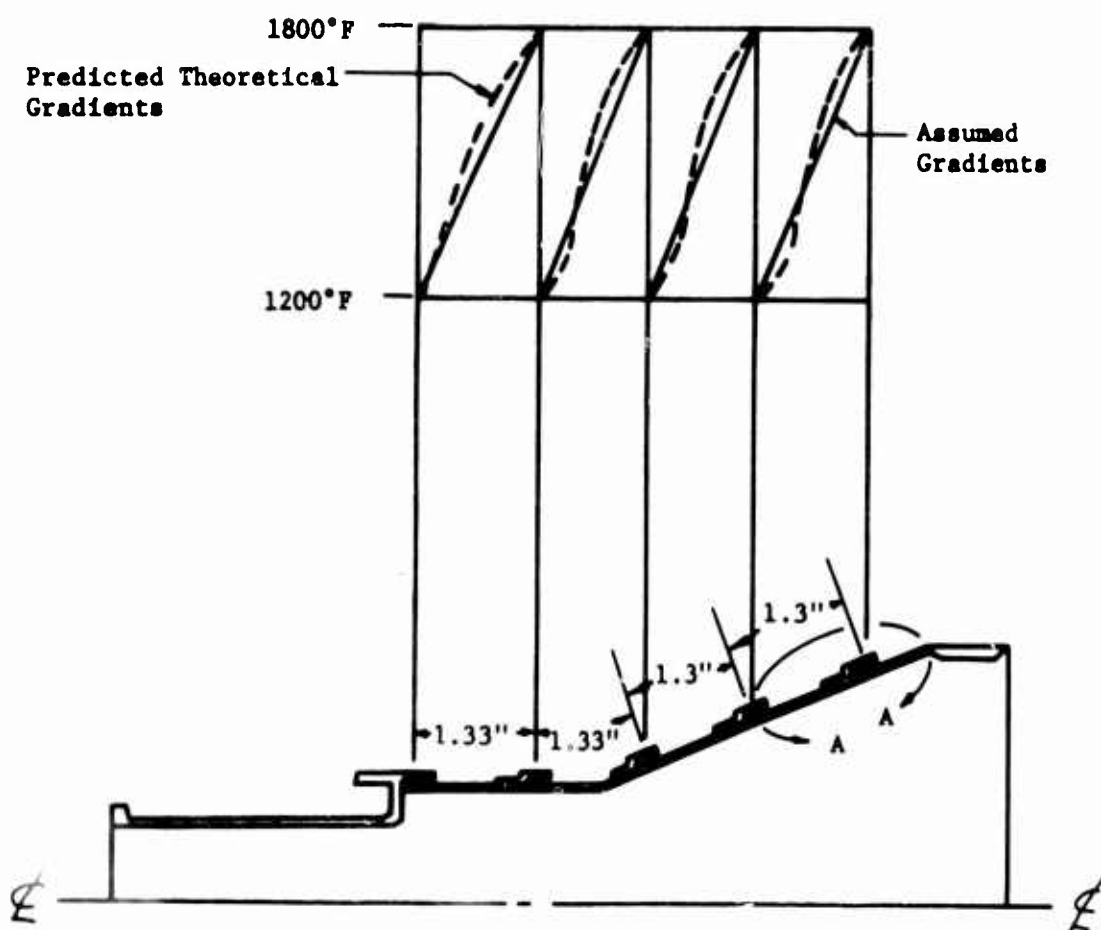


Figure 41. Inner Liner.

A = Shell A
 B = Shell B
 H = Shear Force
 M = Moment
 r = Radius

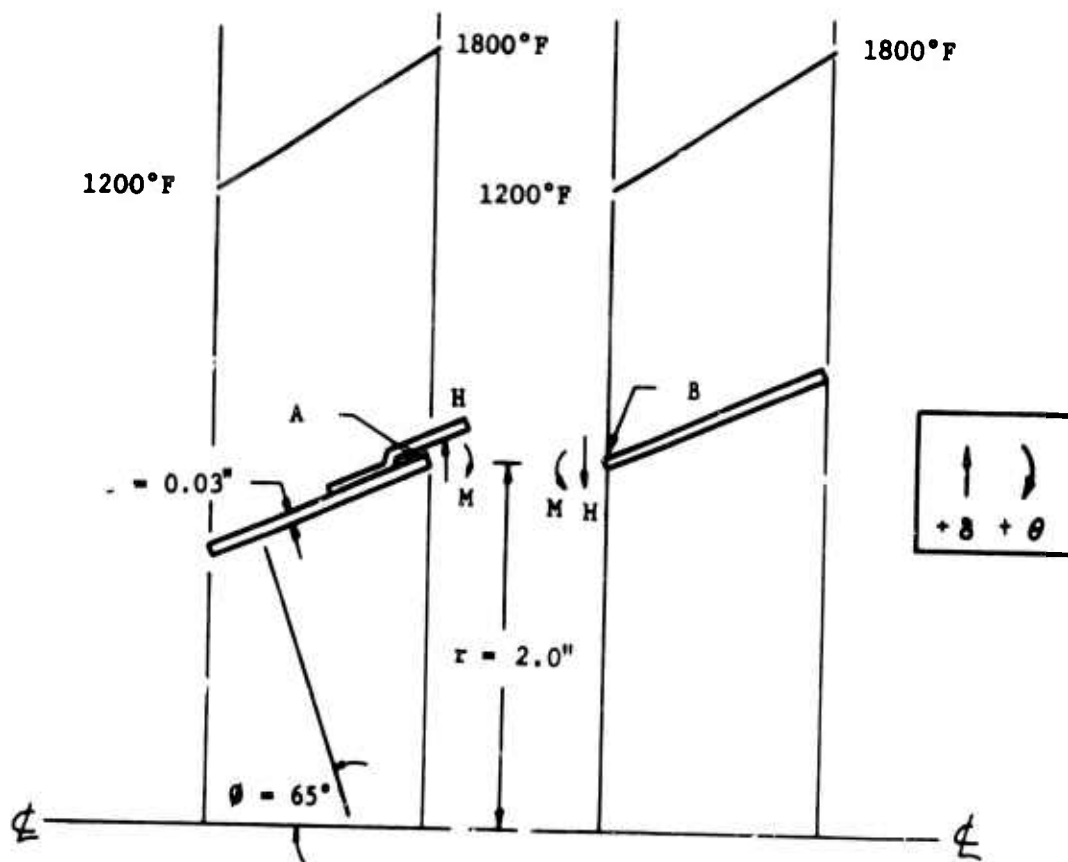


Figure 42. Thermal Discontinuity in Cone.

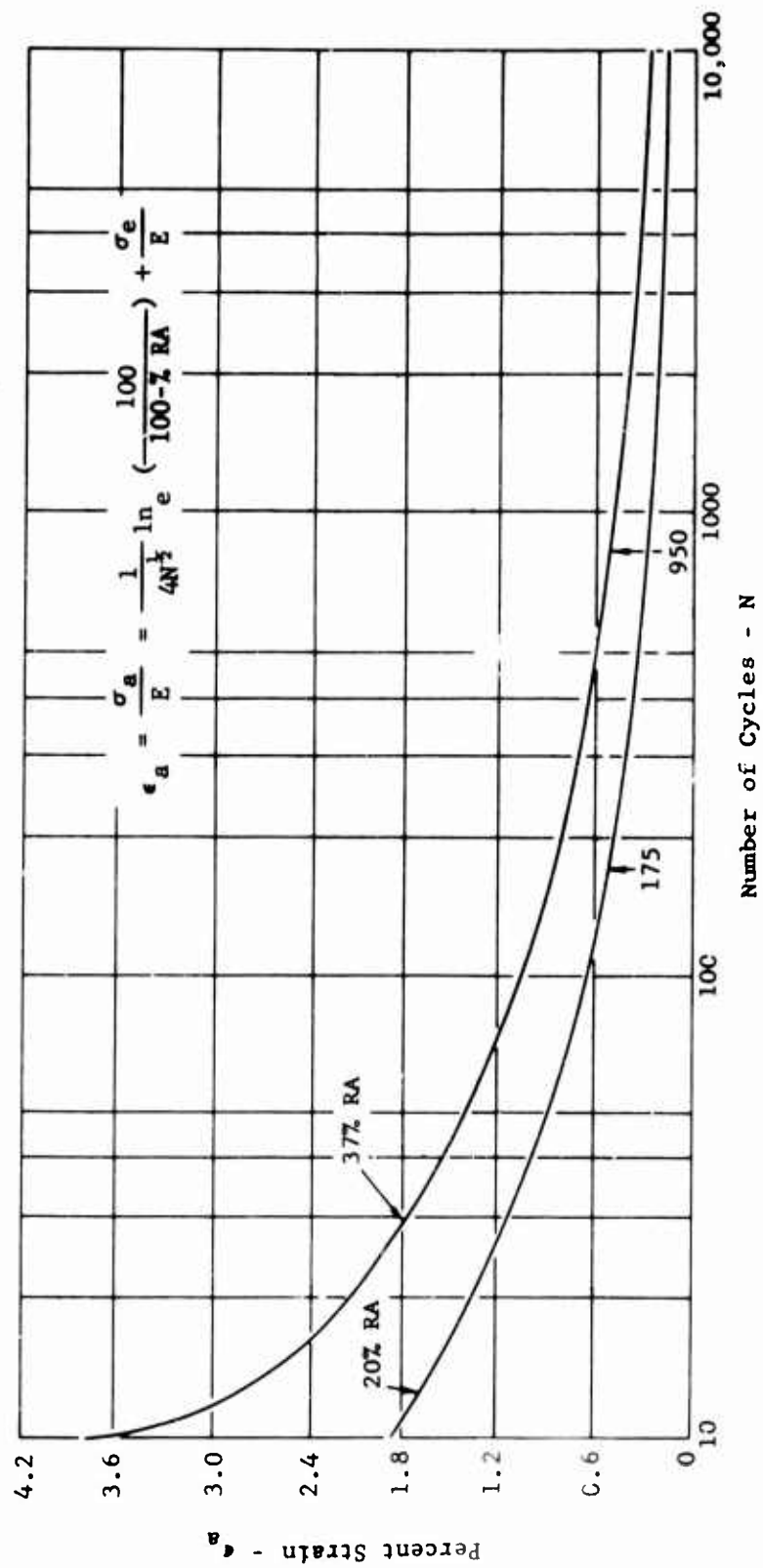


Figure 43. Strain - Cycle Curve (Hastelloy X).

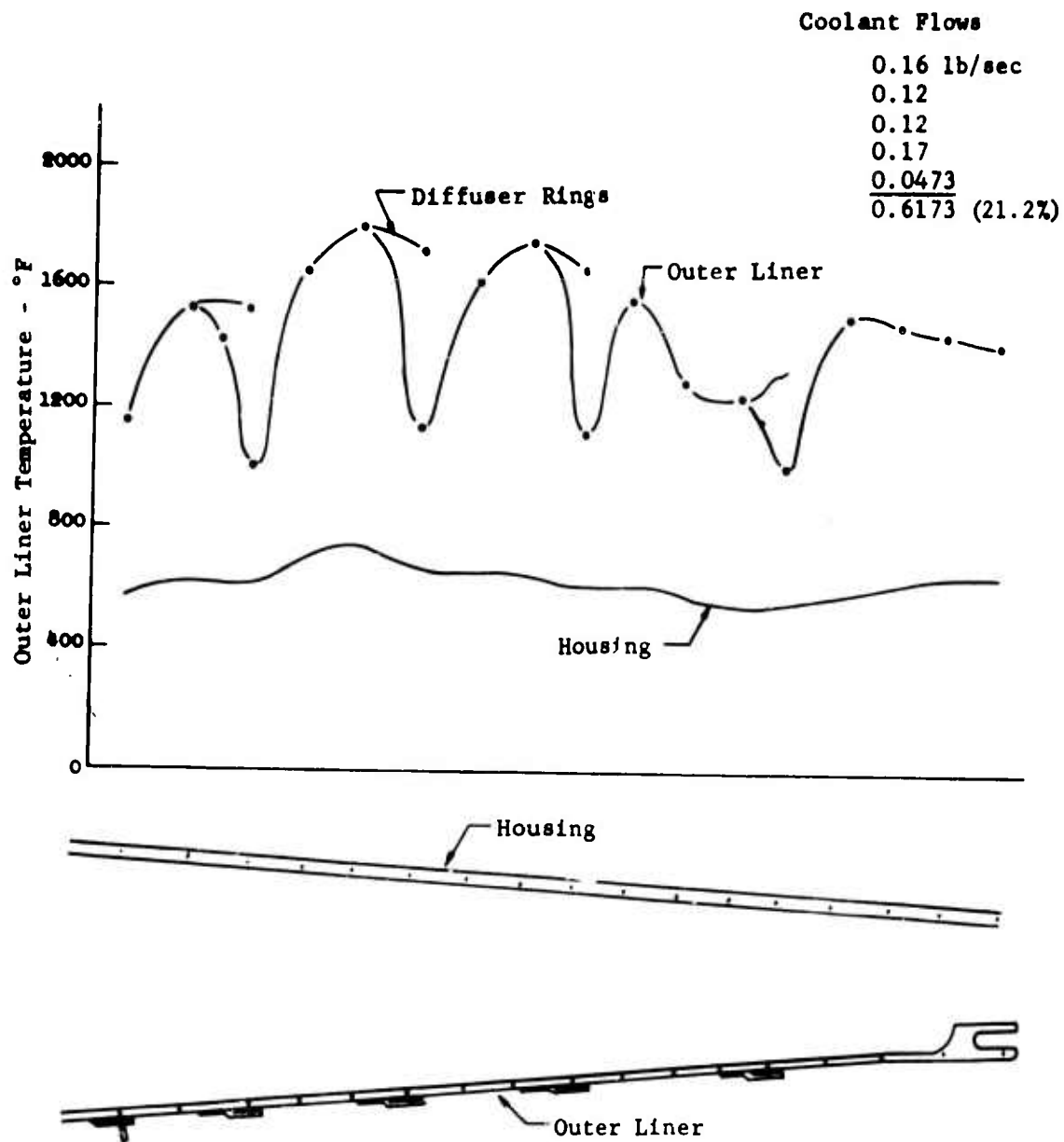


Figure 44. Combustion Chamber Outer Liner.

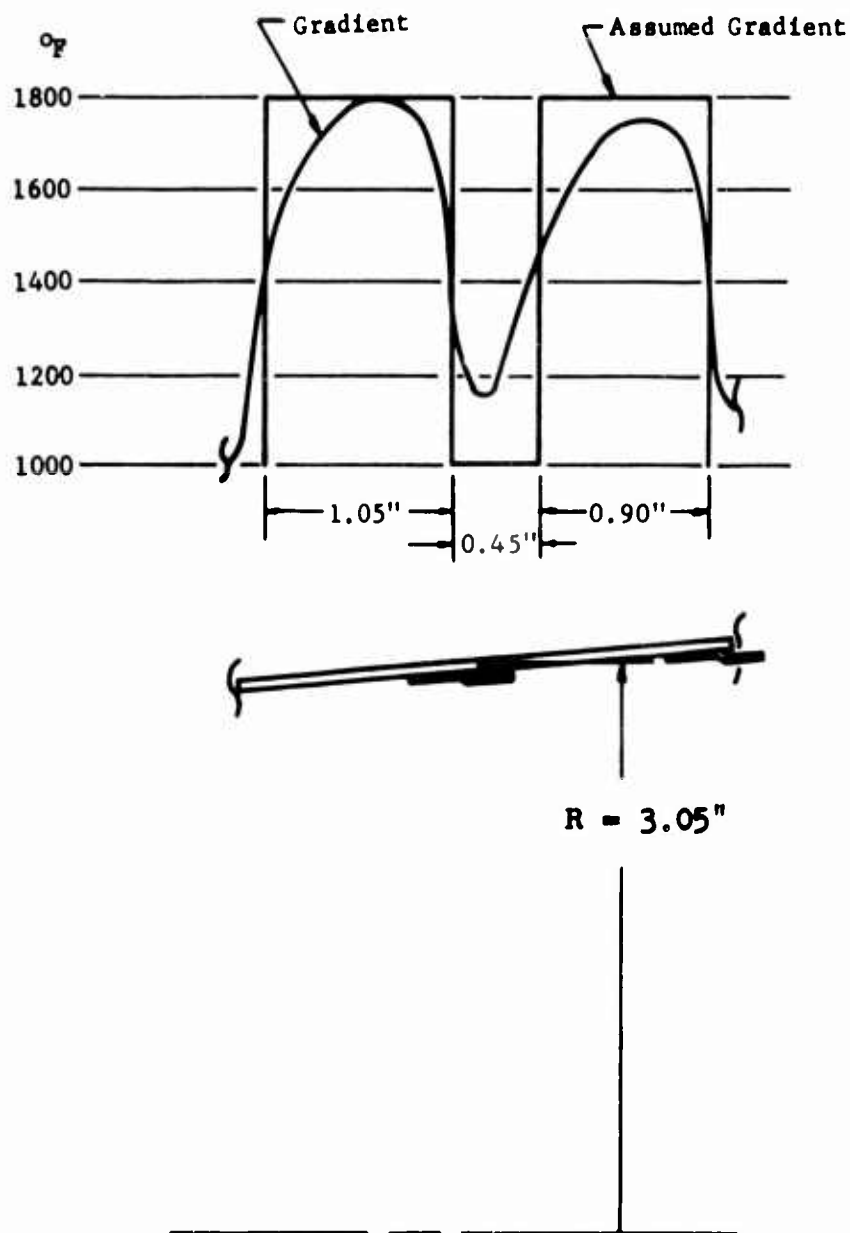
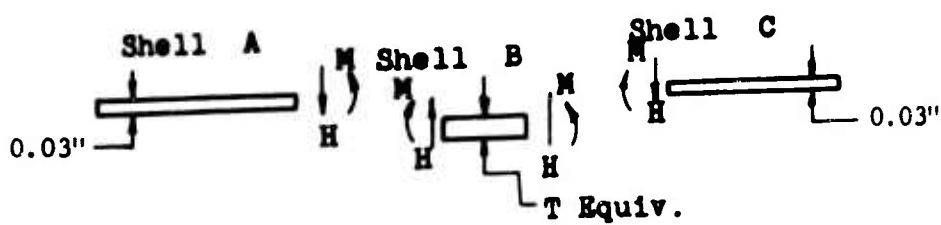


Figure 45. Liner Section With Rectangular Gradients.

1000°F to 1800°F

$$+\delta \mid +\theta($$



Free Body

Figure 46. Liner Section With Rectangular Gradient.

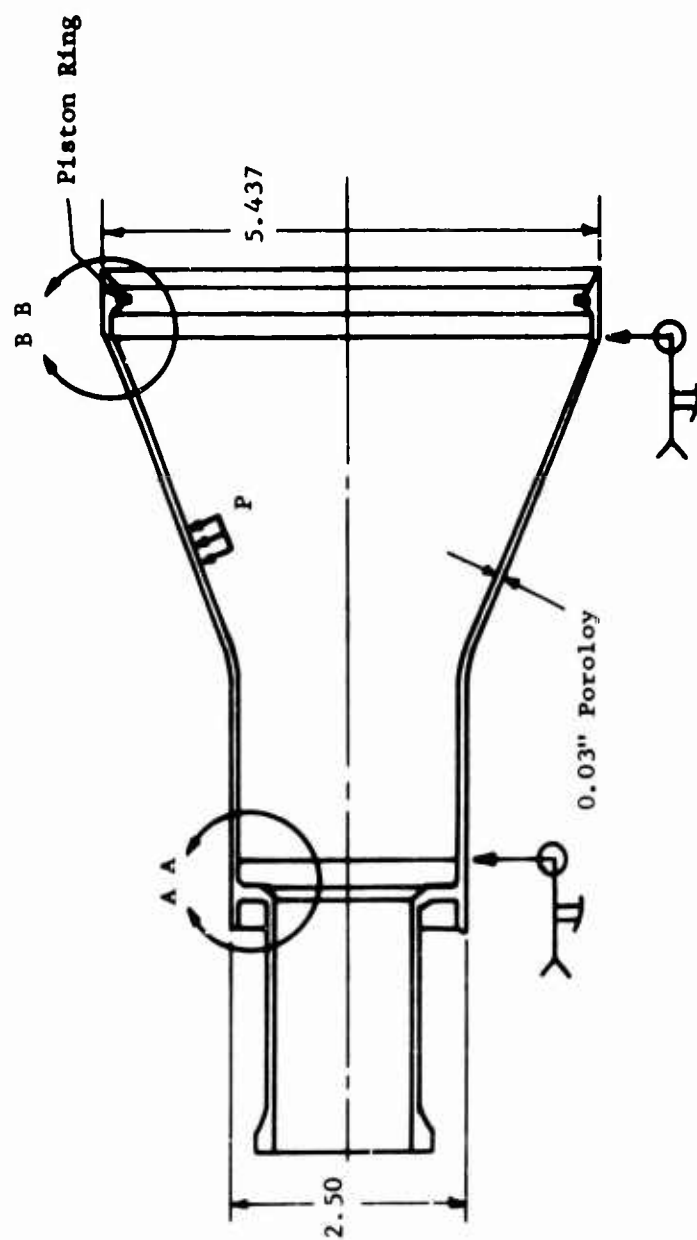


Figure 47. Combustor Inner Liner.

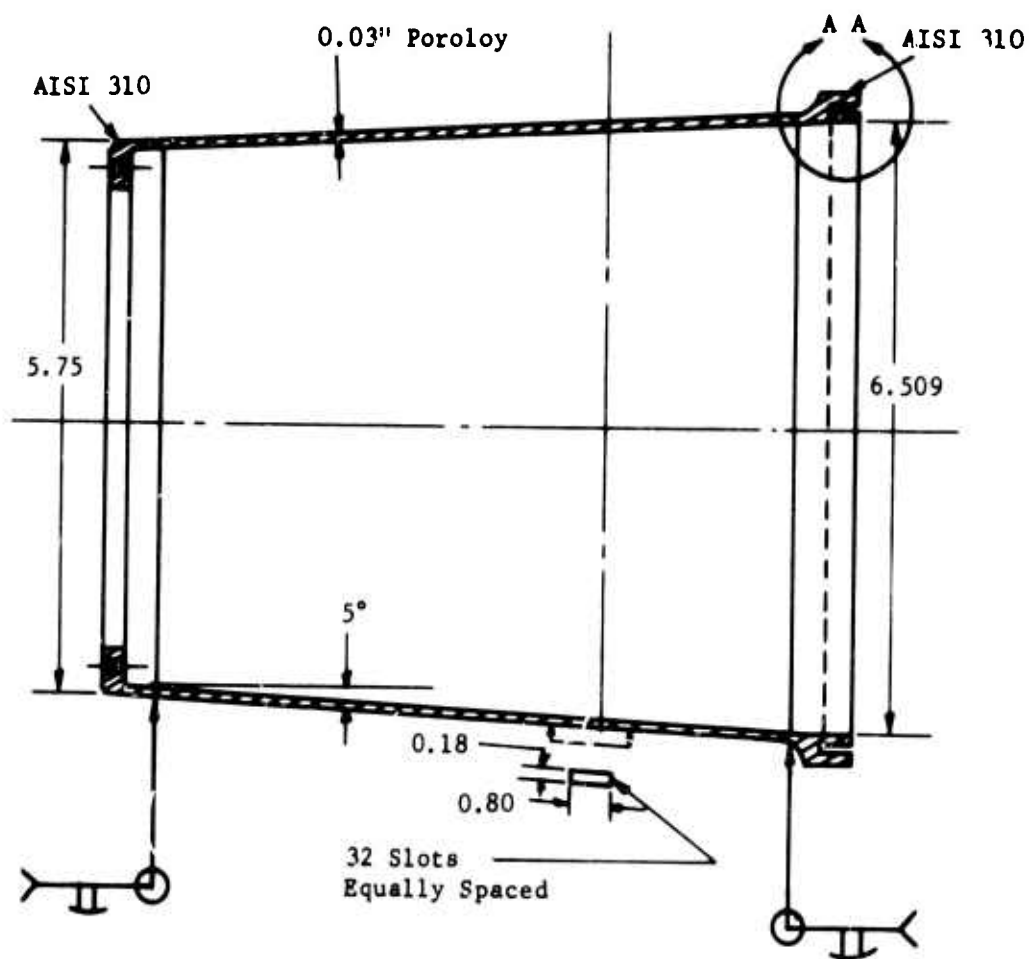


Figure 48. Combustor Outer Liner.

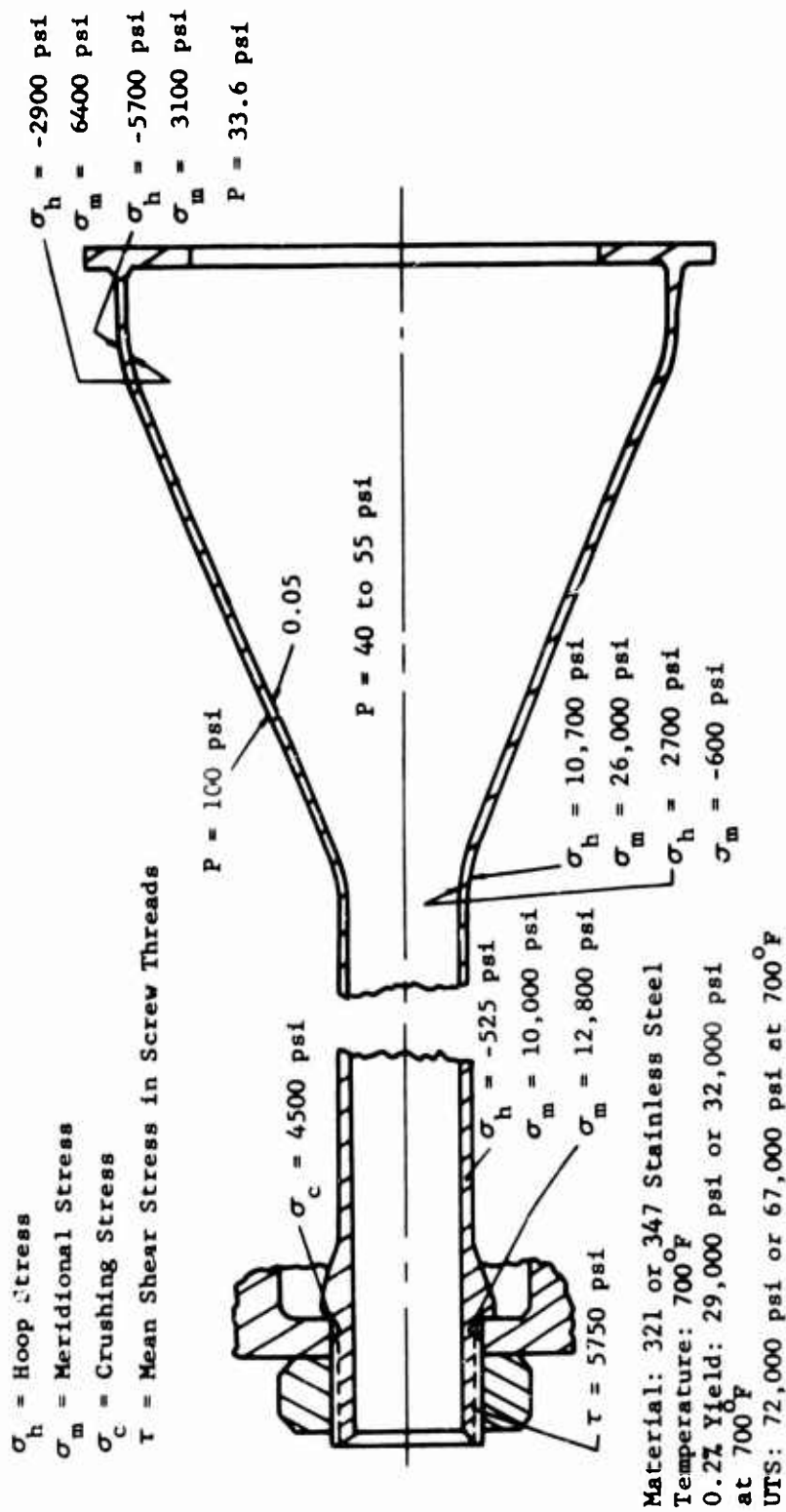


Figure 49. Summary of Stresses - Inner Air-Coolant Tube.

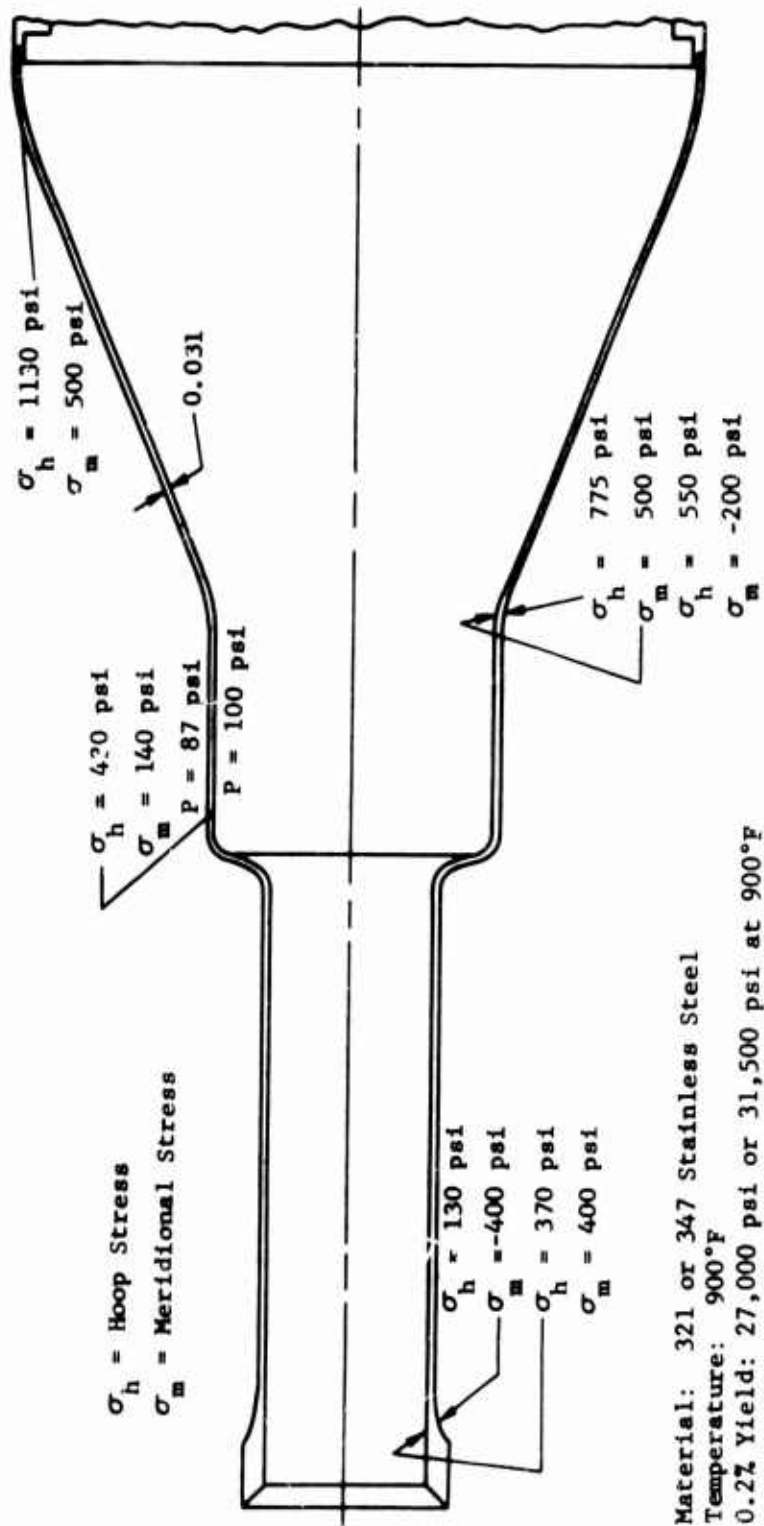


Figure 50. Summary of Stresses - Outer Air-Coolant Tube.

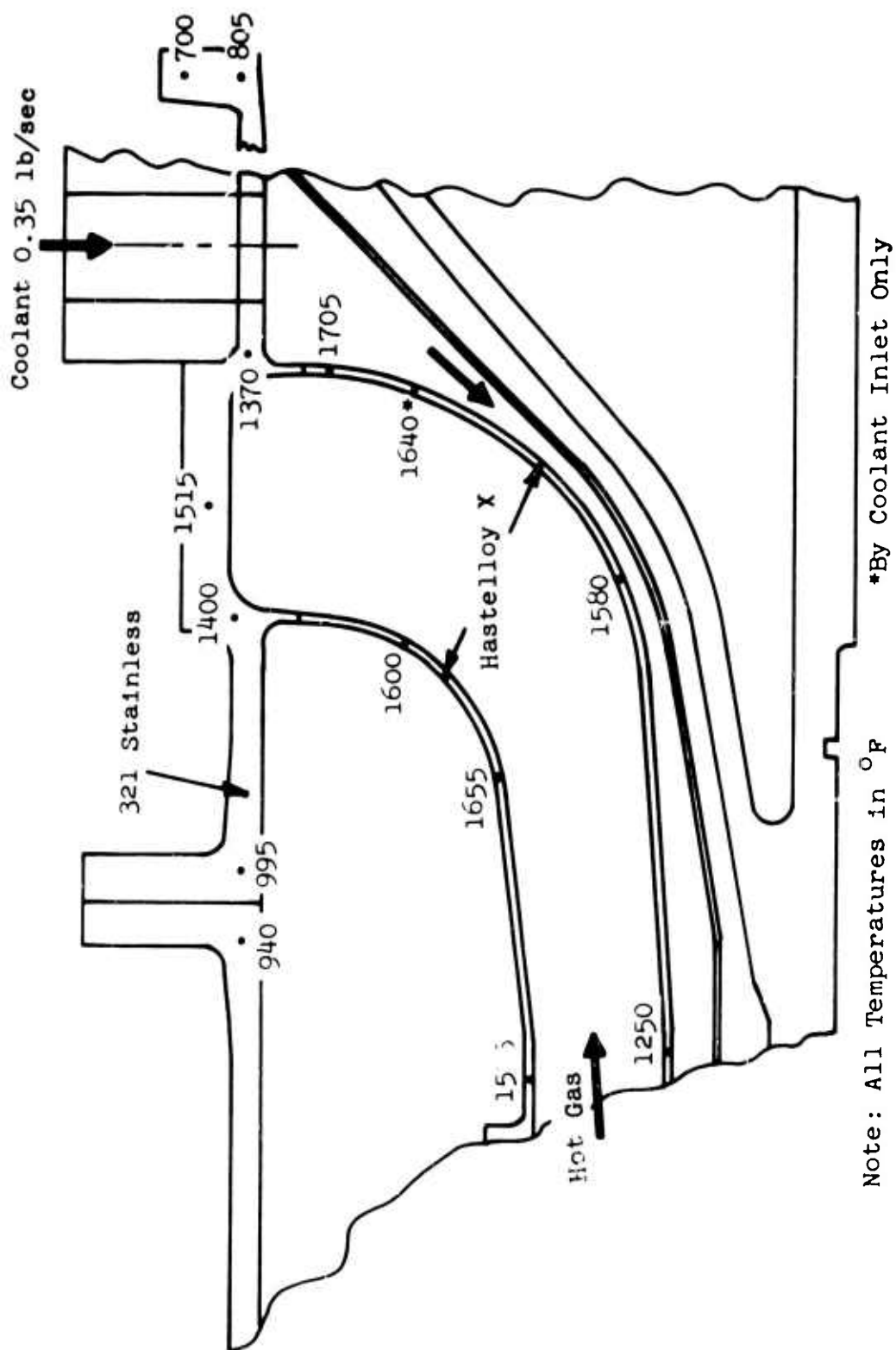


Figure 51. Exhaust Duct Temperature Distribution.

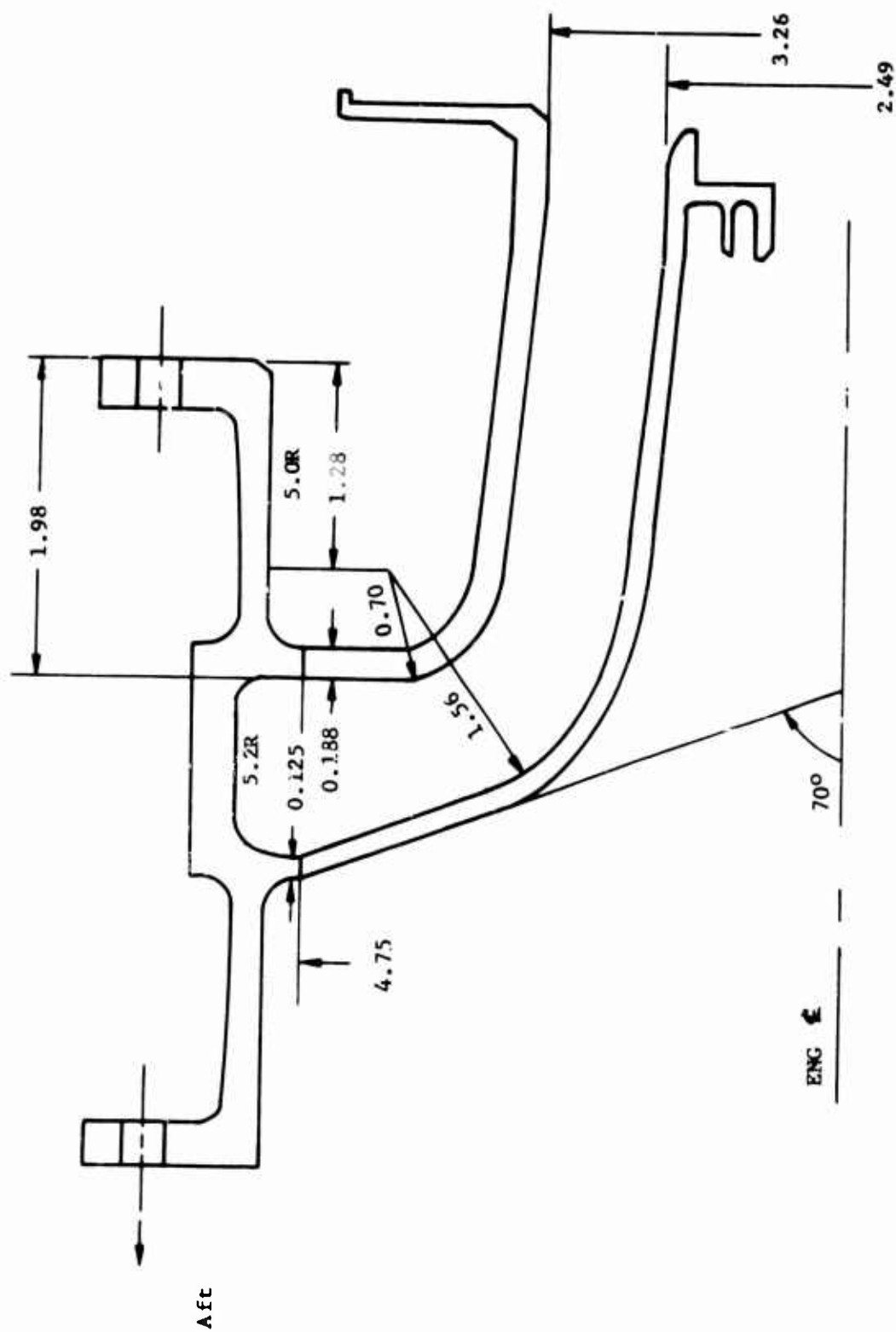


Figure 52. Revised Exhaust Duct.

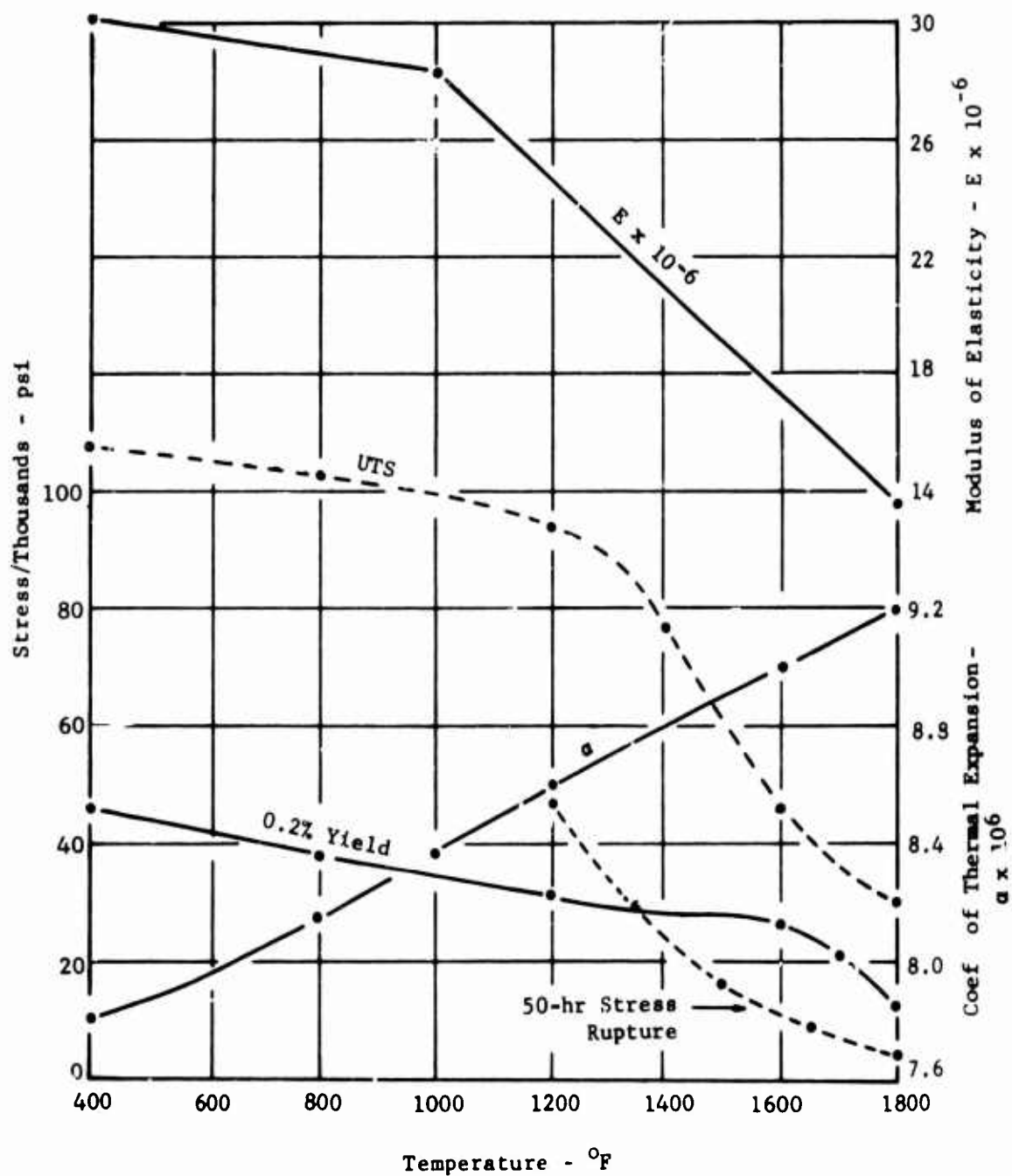


Figure 53. Material Properties - Hastelloy X.

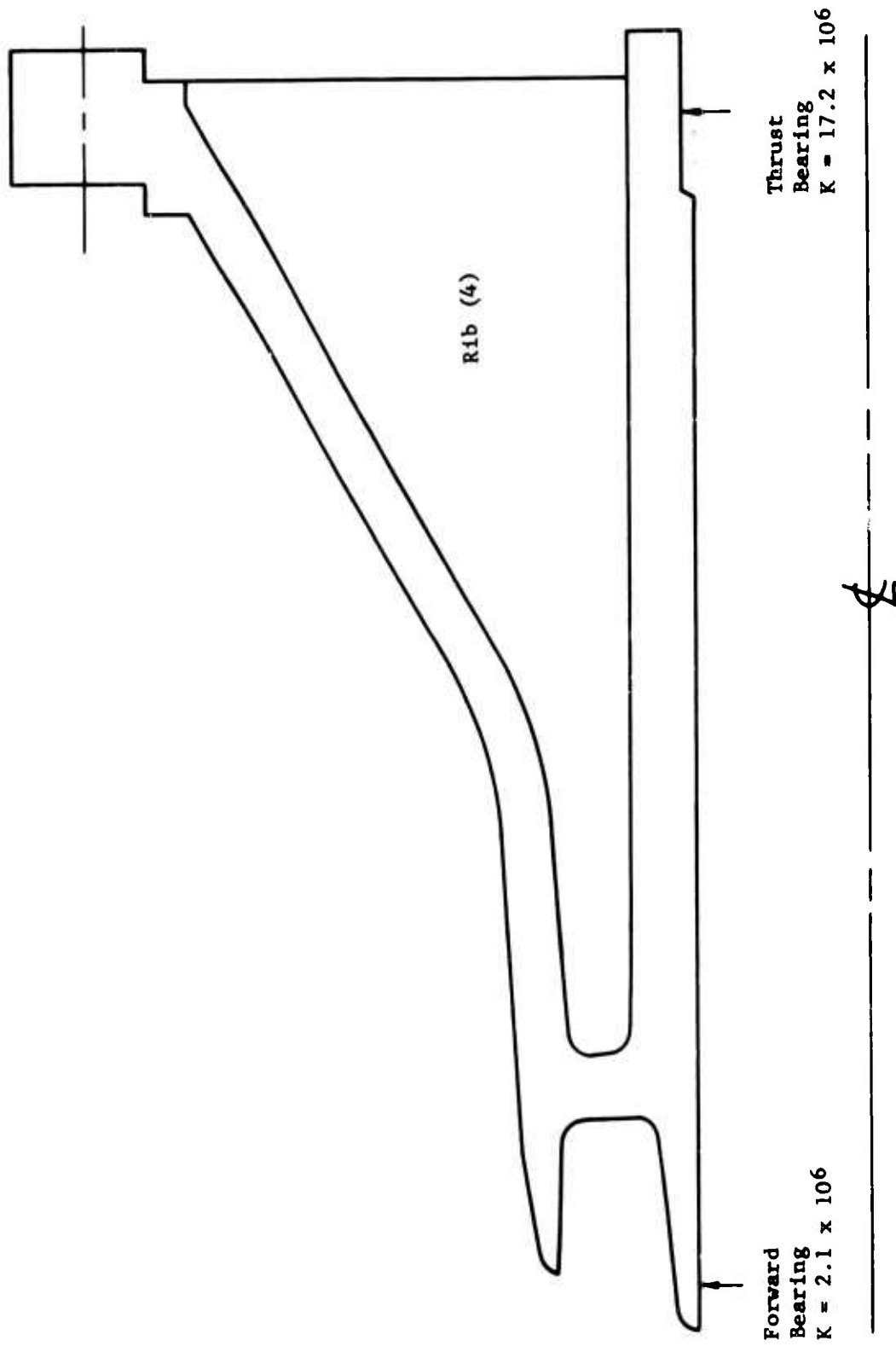
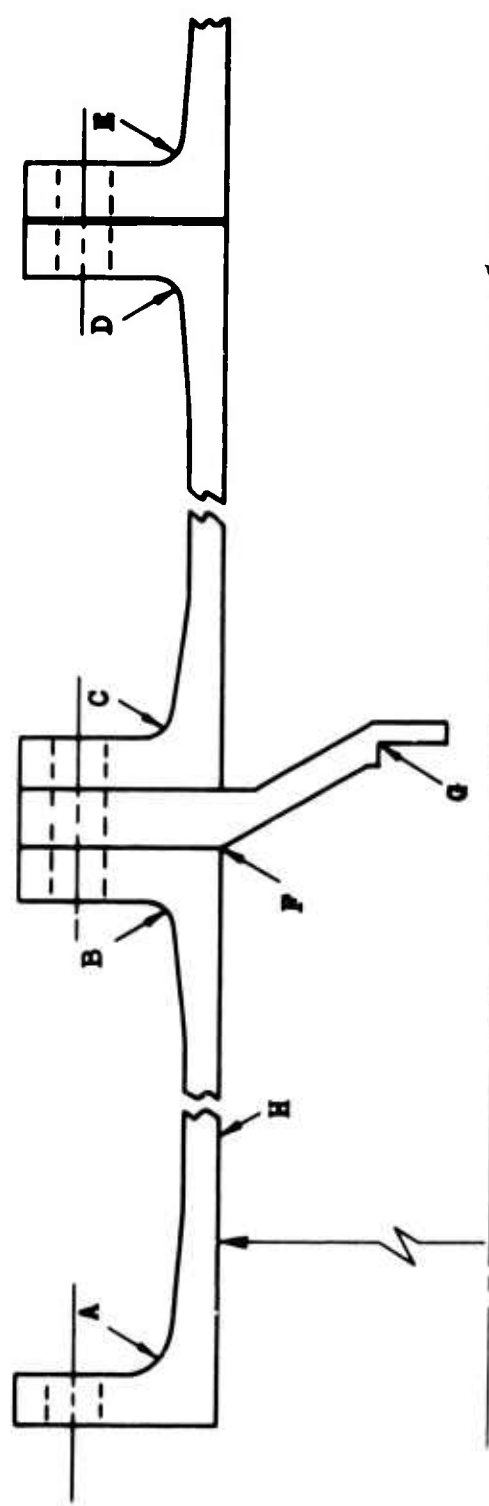


Figure 54. Bearing Support.



Stress	Flanges								Stator Support		Housing
	A	B	C	D	E	F	G	H			
Tangential	1080	1080	990	990							1980
Axial	1730	2190	1070	1300	1300	3220	2010				1080
Bending											
Total Axial	2810	3270	2060	2290	2290						

Material: Stainless Steel (AISI 304)
 0.2% Yield at 1000°F = 30,000 psi

Figure 55. Housing.

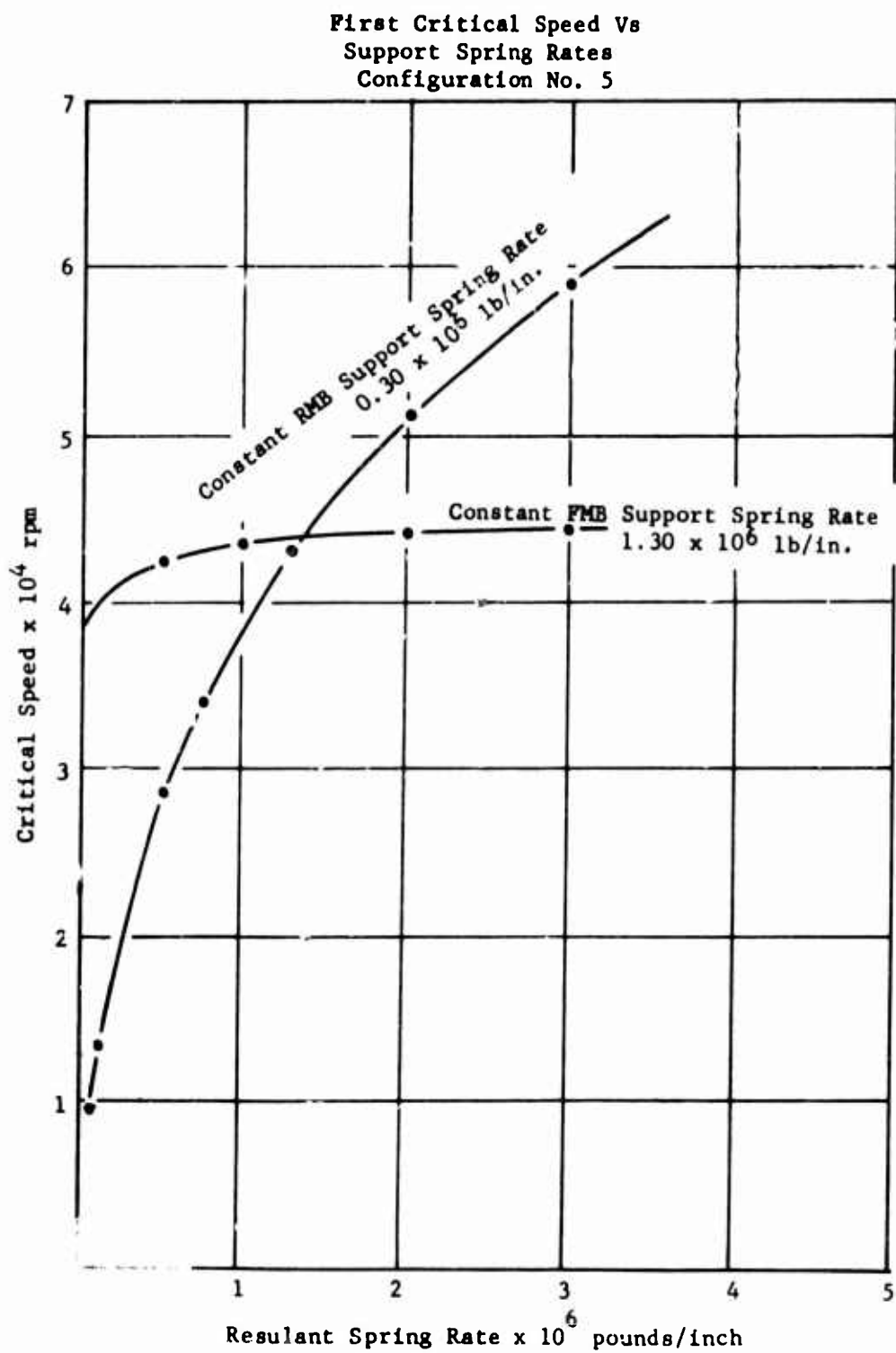


Figure 56. First Critical Speed Vs Support Spring Rate.

3.4 TURBINE RIG HEAT TRANSFER ANALYSIS

3.4.1 Thermal Analysis of Combustor

The purpose of this analysis was to determine the slot geometry and coolant flow rates required to maintain the liner metal temperature distribution compatible with stress requirements.

The results of the analysis are shown in Figures 57, 58, and 59. Figure 57 shows the optimized slot geometry and coolant flow rates. The design point steady-state temperature distribution of the combustor liners and casings is presented in Figures 58 and 59.

This optimization was carried out utilizing an established Thermal Analyzer Computer Program. The analytical procedure determines cooling effectiveness by means of a detailed examination of the thermal and fluid mechanisms involved. Specifically, fluid velocity profiles near the wall and resulting changes caused by momentum and thermal interchanges between the injected coolant and the gas stream are determined to obtain an analytical approach to film-cooling thermal behavior.

The following heat fluxes were considered in the steady-state analysis:

1. Luminous radiation from flame to liners.
2. Convective heat transfer from flame to liners.
3. Conduction within liners.
4. External convection cooling of liner by coolant.
5. Radiation from liners to casing or cooling air duct.
6. External convection cooling of casing or cooling air duct.
7. Convection cooling and radiation heating within film-cooling slots.

Thermal radiation from the flame may be determined by use of the Stefan-Boltzman relation, provided that an appropriate value is used for the effective flame emissivity. Experimental values have been provided by Reference 6 for such emissivities, which are applicable to typical aircraft combustion chamber operating conditions. This information includes data for high-pressure operation and provides an effective flame emissivity of 0.38 for the subject design point operating conditions.

A separate analysis was undertaken to determine in more detail the temperature distribution in the vicinity of the orifices. This analysis showed that the wall temperature gradients in the vicinity of the orifices would be small because the air leaving the orifices quickly acquires a uniform velocity distribution. Since wall temperatures depend upon heat transfer rates which, in turn, depend upon air velocities, a relatively uniform wall temperature distribution is established immediately downstream of each row of orifices.

This method of predicting liner temperatures has previously been applied to various combustion chambers, and the results compared favorably with test data. Typical agreement between predicted and observed liner temperatures is shown in Figure 60. These data are for the NAK burner, where operating conditions are similar to those of the USAAVALABS combustion chamber.

3.4.2 Turbine Shroud Temperature Distribution

One of the primary considerations in the successful operation of the turbine component design in Phase I is the maintenance of a turbine rotor shroud concentric with the rotor assembly and having a minimum radial clearance for optimum efficiency. To achieve such a design required significant design study of mechanical features and methods of cooling. The solution selected provides for air-cooling the shroud support ring to a relatively low temperature to prevent radial expansion and hanging the shroud segments from this ring. The segments will be at higher temperatures than the support ring, and their radial expansion is constrained by the cooler support ring, thereby making it possible to hold close rotor tip clearances.

Various schemes were investigated and are shown in Section 3.1. However, it was not until the design concept shown in Figure 61 was made that a significant advance was made from a temperature distribution standpoint. This figure indicates the calculated temperatures in all portions of the assembly. The turbine inlet temperature used for these results was 2500°F, and the coolant air temperature was assumed to be 610°F. A coolant air-flow of 0.039 pound/second was required.

A further modification was made to simplify manufacturing, and the results of this change can be clearly seen on Figure 62. The temperature distribution noted was considered to be acceptable from a stress standpoint, and the design was incorporated as part of the rig assembly.

3.4.3 Exhaust Duct

An intensive investigation was made of the thermal characteristics of the exhaust duct, which is designed to receive the gases discharging axially from the turbine component and to direct them radially outward to a collector duct for discharge into the test facility exhaust system. The duct is supported by an outer ring which becomes part of the rig housing. A thermal analysis of this complete structure to determine temperature gradients was made for a series of designs and design modifications. The analysis took into account the following:

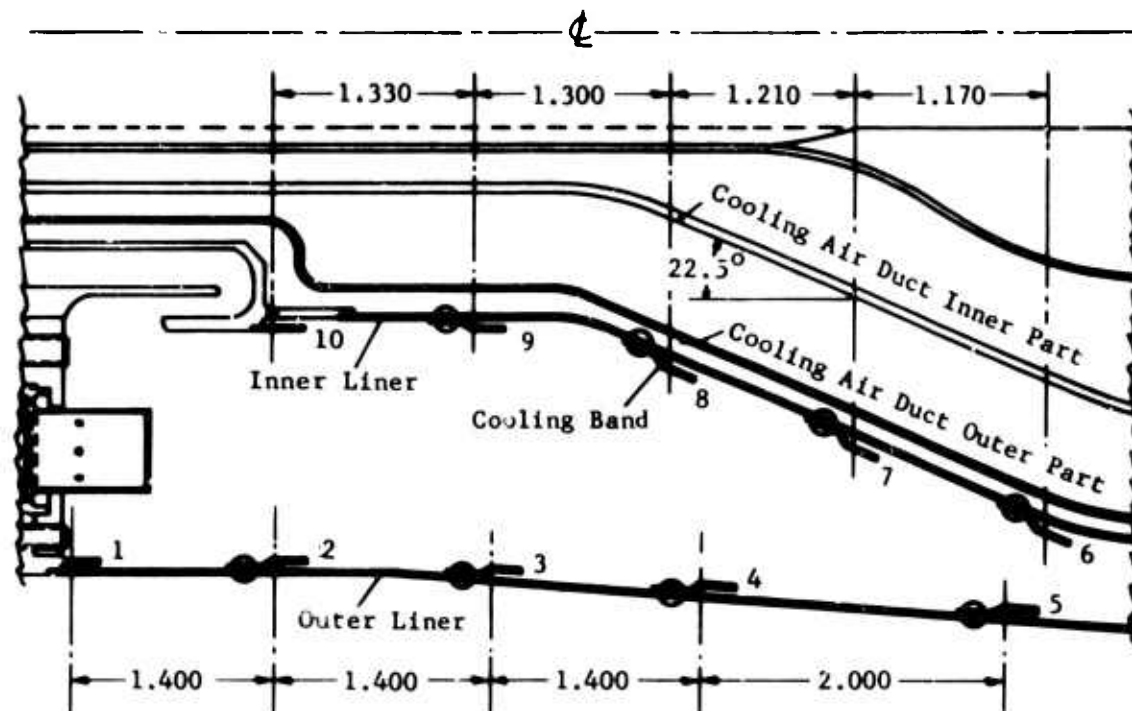
1. Radiation from the hot gas to the duct walls.
2. Nonluminous radiation from the outer duct wall to the casing.
3. Radiation from the casing to the ambient air.
4. Film-cooling in the duct.
5. Forced convection around the inner duct wall.
6. Natural convection from the casing to the ambient air.
7. Conduction.
8. Radiation from the outer duct wall to the inner duct wall.
9. Natural convection within the annular space between the outer duct wall and the casing.

By the use of a flow divider, the exhaust duct cooling air (0.35 pound/second) is split into two parts. The cooling air below the flow divider impinges on the back side of the turbine rotor disc and enters the gas stream as a convective film on the outside of the inner duct wall. The cooling flow above the flow divider convectively cools the inside surface of the inner duct wall and then likewise impinges on the back side of the turbine rotor disc and enters the gas stream as a convective film on the outside of the inner duct wall.

Figure 63 depicts one of the earlier designs and indicates the wall temperatures. In this design, 20 percent of the exhaust duct cooling air flows above the flow divider. A stress analysis of this part indicated unacceptable stress levels with this configuration. In order to reduce the stresses, the thickness of the duct walls was increased, and insulation was added to the flanges. Figure 64 shows the results of this analysis. Because of the insulation, high temperatures (1707°F) were reported on the outer duct wall, and unacceptable stresses were obtained.

In the design which finally evolved, the insulator was removed from the flanges, the coolant flow was increased along the wall, and the duct housing was "fog-water" cooled. Figure 65 shows the temperatures for the exhaust duct and housing using "fog-water" cooling. The analysis of the "fog-water" cooled portion of the exhaust duct housing assumes that (1) all the water injected through the fog nozzles hits the duct housing surface and vaporizes and (2) the water is homogeneously distributed. In order to obtain the temperatures shown in Figure 65, approximately 7-1/4 gallons of water/hour/square foot of surface will be needed. The exact amount of water will have to be determined experimentally.

A similar temperature distribution could be obtained using air jets instead of "fog-water" cooling to cool the duct housing. Less than 0.05 pound/second of air would be needed. Further analysis would be required to determine more accurately the amount of cooling air and the resulting temperature distribution.



Slot Number	1	2	3	4	5	6	7	8	9	10
Slot Height (inches)	.020	.020	.020	.020	.020	.015	.015	.015	.020	.020
Coolant Flow (lb/sec)	.16	.12	.12	.17	.0473	.03	.025	.047	.035	.045

Operating Conditions

Combustor Inlet Air Temperature	610°F
Combustor Inlet Pressure	87.63 psia
Combustor Airflow	2.89 lb/sec
Primary Zone Temperature	3970°F
Secondary Zone Temperature	2500°F
Inner Liner Airflow	6.3%
Outer Liner Airflow	21.2%

Figure 57. Turbine Test Rig Combustor Operating Conditions, Slot Coolant Flow Distribution, and Slot Heights.

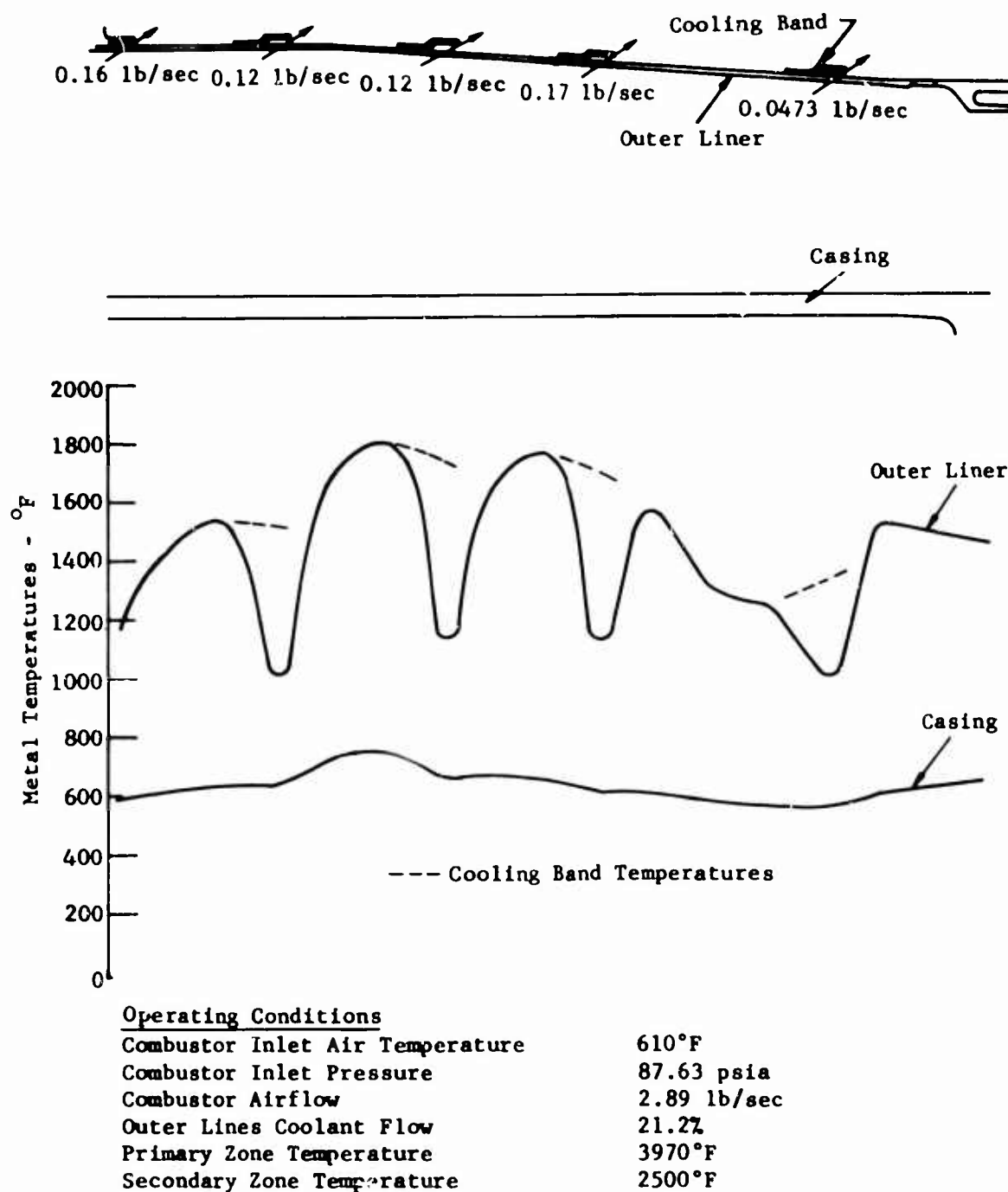
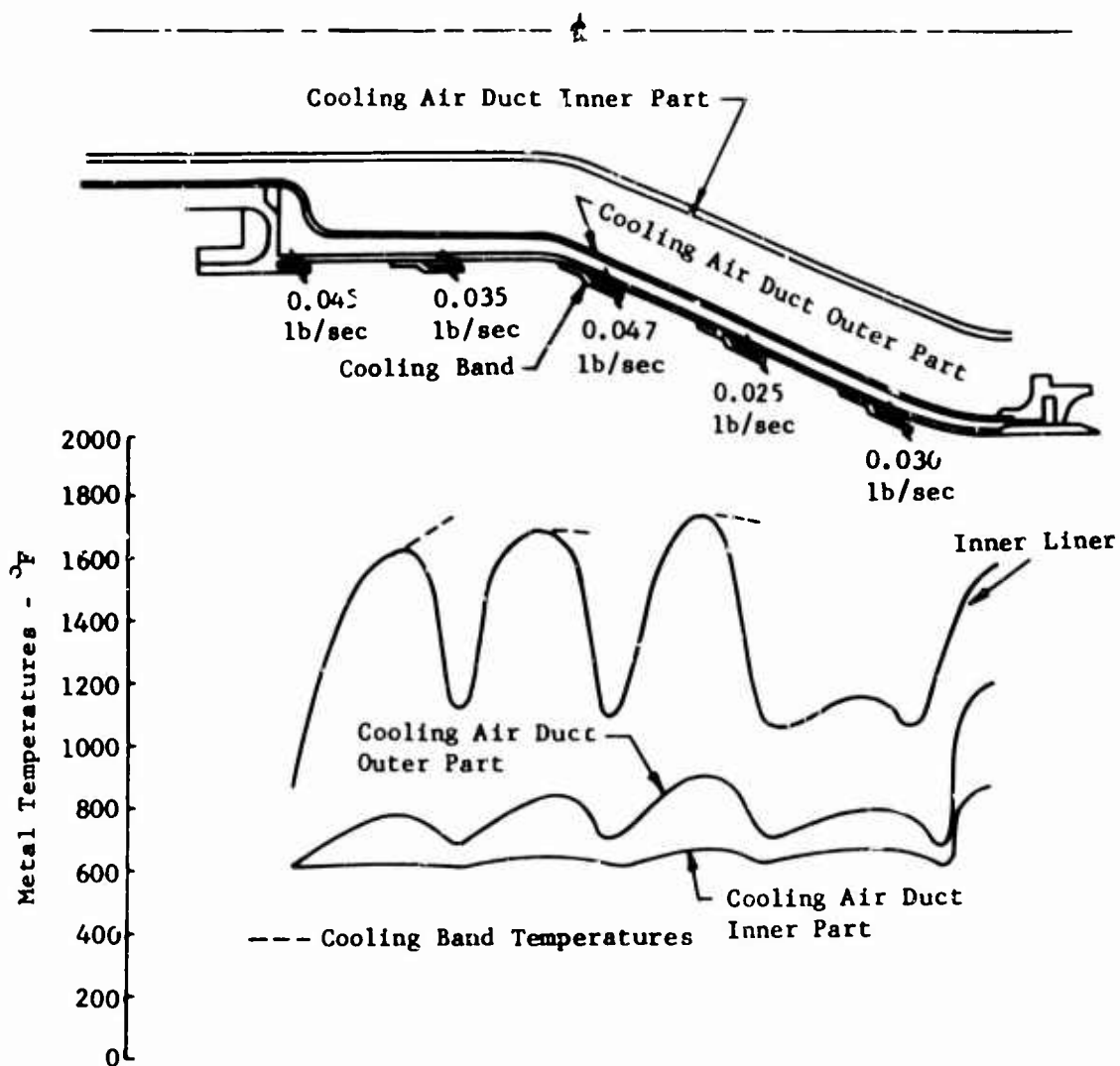


Figure 58. Combustion Chamber Outer Liner, Casing, and Cooling Band Temperatures.



Operating Conditions

Combustor Inlet Air Temperature	610°F
Combustor Inlet Pressure	87.63 psia
Combustor Airflow	2.89 lb/sec
Inner Liner Coolant Flow	6.3%
Primary Zone Temperature	3970°F
Secondary Zone Temperature	2500°F

Figure 59. Combustion Chamber Inner Liner, Cooling Air Duct, and Cooling Band Temperatures.

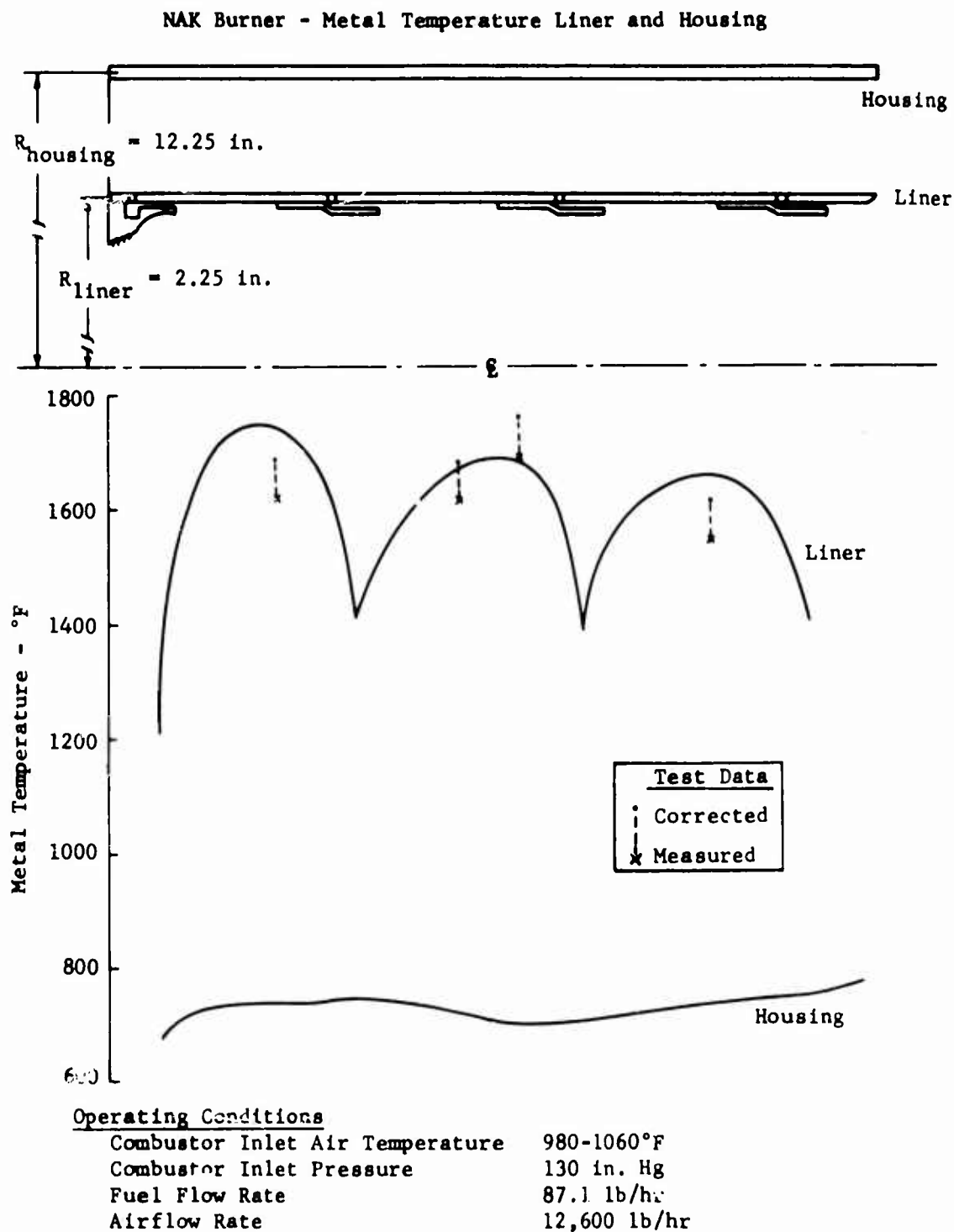


Figure 60. Comparison of Analytical and Experimental Metal Temperature Data.

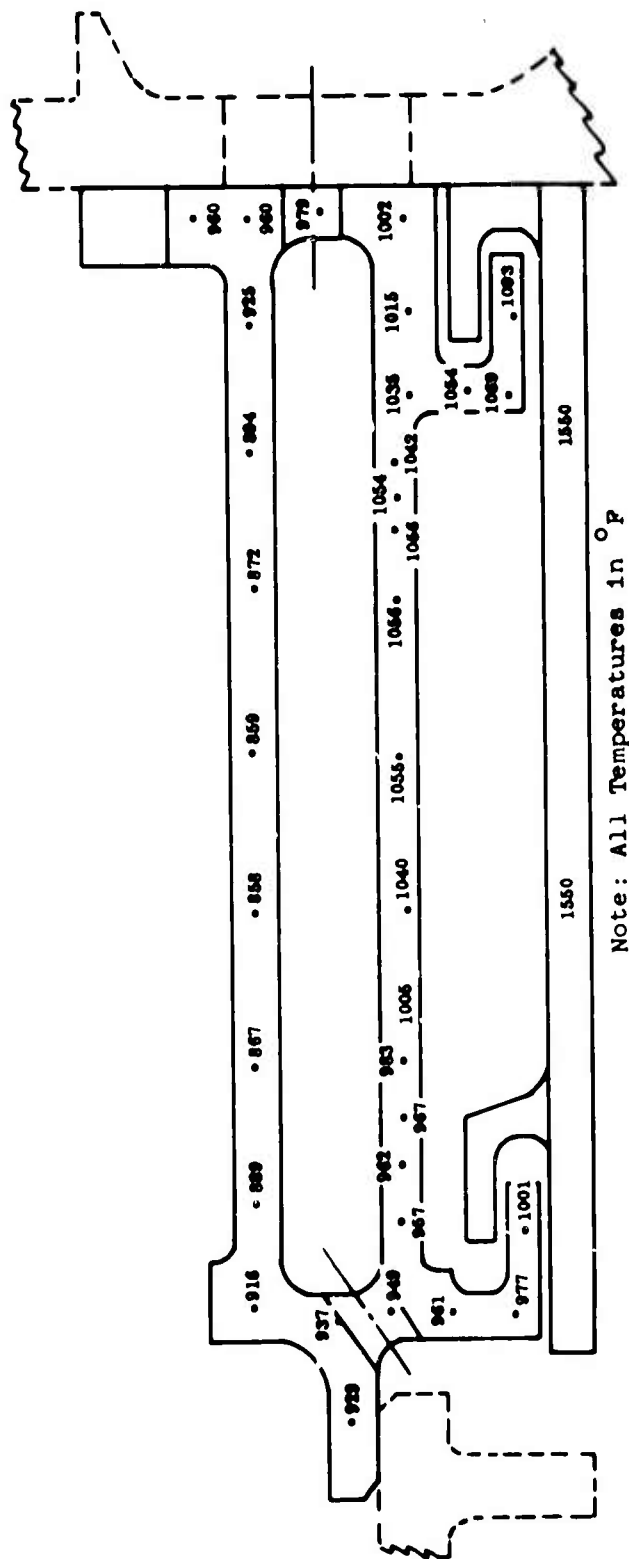


Figure 62. Temperature Distribution in the Turbine Shroud (Revised Design).

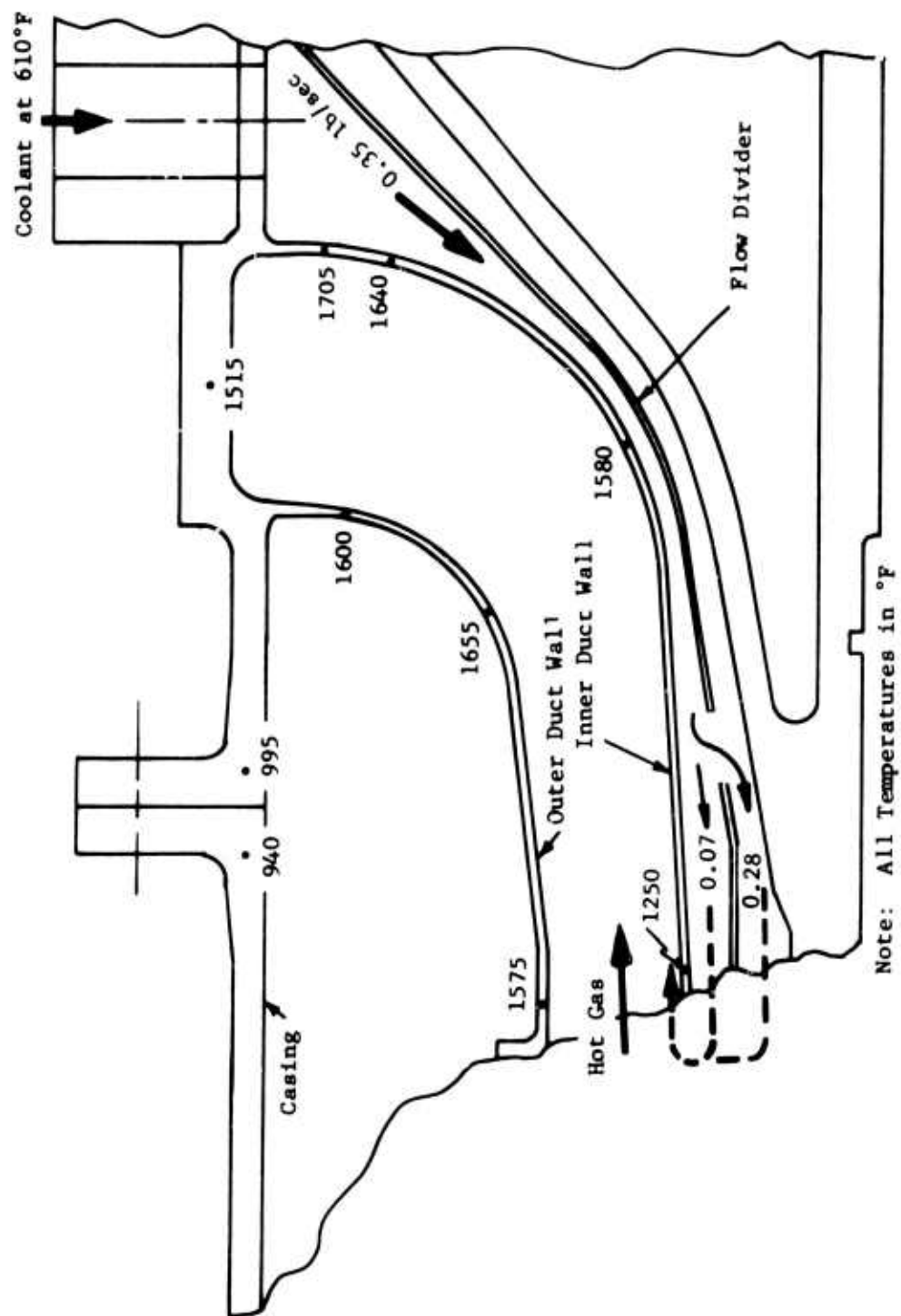


Figure 63. Temperature Distribution in the Exhaust Duct.

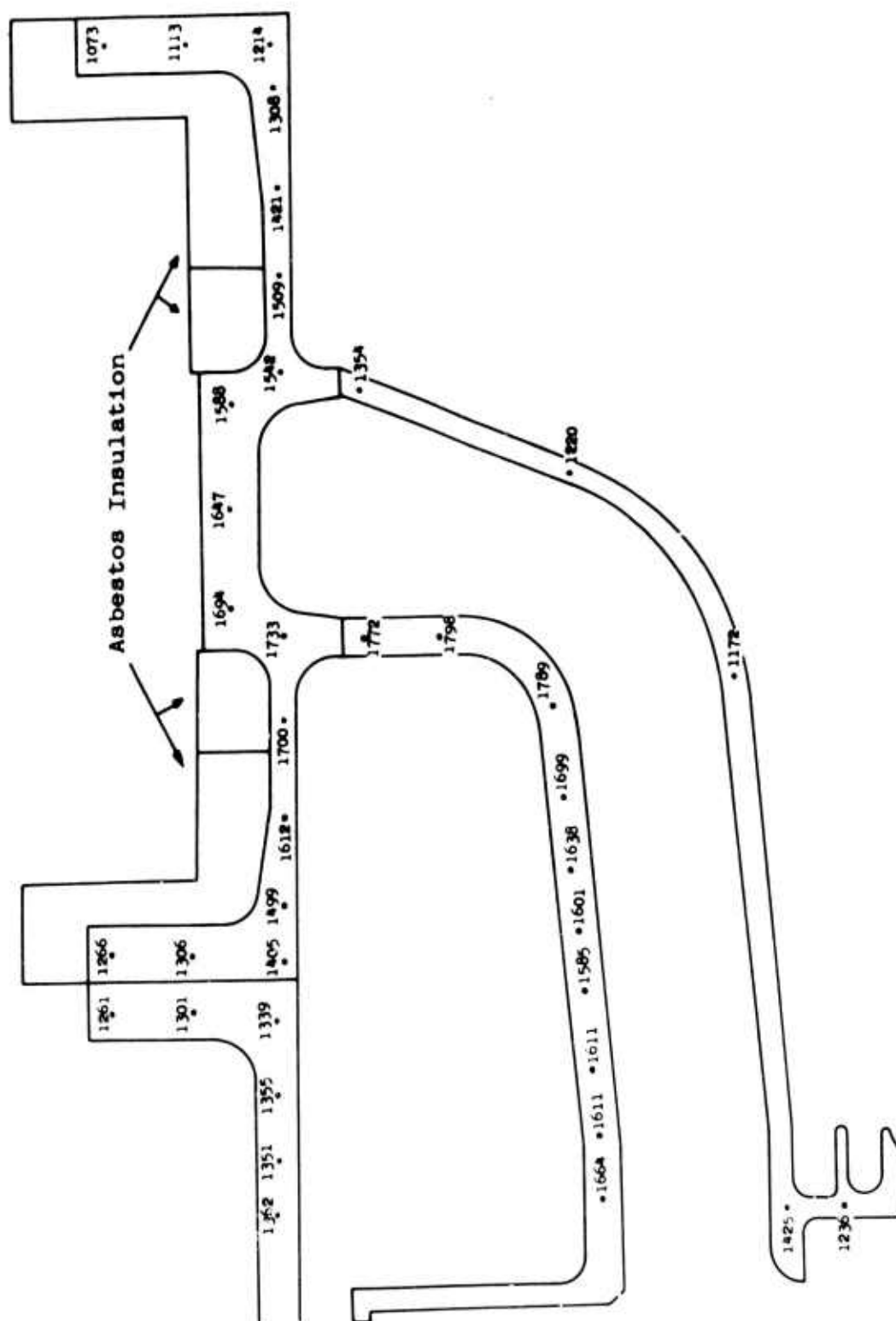


Figure 64. Temperature Distribution in the Exhaust Duct - Insulated Design.

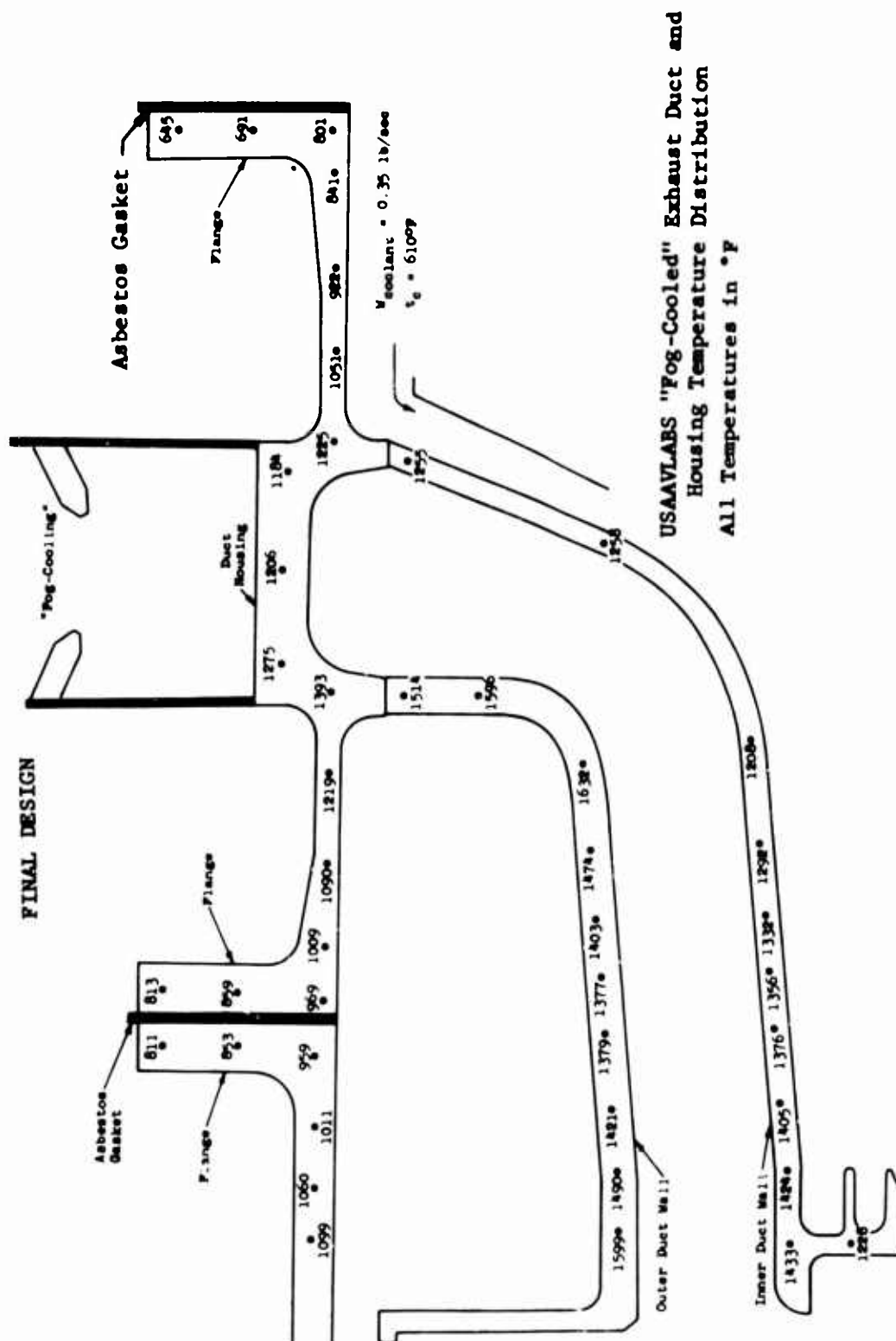


Figure 65. Temperature Distribution in the Exhaust Duct - Final Design.

3.5 TEST EQUIPMENT DESIGN

The test equipment and facility design for the Phase II portion of the contract series of tests was divided into two distinct tasks. The testing of the turbine rig will concentrate initially on the development of the annular combustor designed specifically to provide the high-temperature gas for operation of the turbine component. Next, the stator vanes will also be tested separately from the rotating component to determine their heat transfer characteristics and preliminary aerodynamic performance. Task one was the design of a test rig to accommodate the test and development of these two nonrotating components. Task two was the design of a facility to accommodate the complete rotating single-stage high-temperature turbine for both cold air performance testing and high-temperature endurance testing.

3.5.1 Combustor and Turbine Stator Test Rig

The basic design for this rig is patterned after the test equipment utilized in the Phase I portion of the contract for the two-dimensional cascade tests. In fact, various parts, ducts, controls, etc., used in this early rig will be utilized again where possible in the new rig. Figure 66 shows the arrangement of this combustor and turbine stator rig in the test facility. The facility that will be used is the same one that has been used for the two-dimensional cascade mentioned previously and reported in Section 5.2 of this report. The general arrangement of components is shown schematically on Figure 67. A basic facility air supply will be used as the source for all airflow requirements, including main stream flow, blade cooling airflow, and secondary cooling airflow, for rig hardware and internal test equipment. All airflows of particular concern will be monitored and measured using flat-plate, sharp-edged orifices constructed, installed, and calibrated per (ASME) standards. Flow indication will be accomplished using liquid level manometers, and control will be established through remotely operated, air-controlled valves. The blade cooling airflow circuit will be equipped with electrical heaters to provide the desired cooling air inlet temperature. Positive filtration to the 5-micron level will be provided in series with the heater circuit to make certain of the air cleanliness level and thereby prevent one possible variable from affecting the test results.

The main air supply to the primary combustor will be preheated using a hydrocarbon fuel to simulate the air inlet temperature normally seen by such a combustor when receiving air from a high-pressure-ratio compressor. The fuel supply and fuel system will be the same as those currently being used in the cascade rig which utilizes a JAECO (Warrington, Pennsylvania) positive displacement pump as the key element.

In addition to the cooling requirements anticipated within the rig where air is utilized as the cooling fluid, a further cooling requirement is handled in the exhaust system by the use of water spray. Water is also used to provide an effective means of cooling for the rotating probe, where care is taken that it does not interfere with the main stream airflow. The present test facility exhaust system will be used to discharge the combustion gases to the atmosphere. A valve in this exhaust line will provide a

means of back pressuring the system for attainment of the desired mass flows and upstream pressures.

The rotating probe mentioned above has been designed to obtain pressure and temperature traverses either immediately downstream of the combustor during combustor tests or downstream of the full stator assembly during stator tests. Figure 68 shows the design and assembly of this rotating probe in position downstream of the combustor and/or turbine stator during tests. Both air and water will be used to maintain a moderate metal temperature throughout the assembly in order to maintain structural integrity. The probe head will be capable of traversing 360 degrees circumferentially to measure both temperature and pressure profiles. Figure 68 indicates the method of driving this probe to obtain the 360-degree circumferential rotation.

In general, the system as designed will easily withstand the full operating pressures and temperatures anticipated during operation. Water quench facilities have been added to the exhaust system in a quench chamber to reduce the full combustor flow from 2500°F average temperature to 600°F before discharging through the back pressure valve and into the standard exhaust system.

3.5.2 Turbine Performance and High-Temperature Test Rig

The second facility design is required to provide a means of testing the complete turbine stage to determine both aerodynamic and thermodynamic performance, as well as its operating characteristics at the design gas temperature of 2500°F. A schematic diagram of the required facility components is shown in Figure 69. The basic difference in facility requirements for this series of tests is the necessity for providing a mechanism for absorbing the shaft power generated by the turbine under test. Schematically, this system is shown by a gearbox and a water brake which are driven by the turbine. A regulated pressure water supply is required for operation of the water brake and is accomplished using a constant-level water supply tank with a regulated gas blanket maintaining the proper head. This provides a constant water flow to the brake, thereby improving the stability and control of the system.

The other features of the facility are very similar to those designed into the combustor-turbine stator rig. An additional cooling air supply has been added, however, with a separate control and measurement system to provide the necessary cooling flow to the transpiration-cooled rotor blades.

Specifications were drawn up for the proposed power absorber system based on the turbine design characteristics and predicted performance discussed previously. The basic criteria established for performance testing which define the lower power absorption range are indicated below.

Turbine Power and Torque

Basic Criteria - Turbine Performance Testing

1. Minimum allowable physical speed = 15,000 rpm.
2. Turbine discharge pressure, atmospheric.
3. Evaluate performance at pressure ratios up to 2.6 from N/\sqrt{T} of 50 percent to 110 percent.
4. Set pressure ratio by adjusting inlet pressure.
5. Set N/\sqrt{T} by holding speed constant and varying inlet temperature where possible. Maximum T inlet = 1600°F; minimum T inlet = 200°F (to prevent icing of blades). (See Figure 70.)
6. Maximum allowable airflow = 4 pounds/second (see Figure 71 for inlet temperature and pressure limitation).

Basic Criteria - High Temperature Testing

1. Maximum turbine inlet pressure = 85 psia.
2. Maximum turbine inlet average temperature = 2500°F.
3. Maximum turbine speed = 55,000 rpm.
4. Test turbine from N/\sqrt{T} of 50 percent to 110 percent up to pressure ratio of 2.6 maximum.

Basic Data Assumed

1. Preliminary turbine performance map is discussed in Section 2.1.
2. Zero speed torque is equal to twice design speed torque.

The following expressions were developed to further define the power absorption characteristics:

1. Horsepower:
$$\text{Horsepower} = 1.415 \cdot W \cdot \Delta h \quad (8)$$

W = Airflow - pound/second
 Δh = Turbine enthalpy drop - Btu/pound
 P = Inlet pressure - psia
 T = Temperature - degrees Rankine ($^{\circ}\text{F} + 460$)
 N = Speed - rpm

Multiplying and dividing horsepower equation by P, T, and N, the following equation results:

$$\frac{\text{Horsepower}}{P_{\text{inlet}} \sqrt{T_{\text{inlet}}}} = 1.415 \times \frac{\left(\frac{WN}{P} \right) \left(\frac{\Delta h}{T} \right)}{\left(\frac{N}{\sqrt{T}} \right)} \quad (9)$$

@ design conditions:

$$\frac{WN}{P} = 100 \text{ percent} = 1770$$

$$\frac{\Delta h}{T} = 100 \text{ percent} = 0.0473$$

$$\frac{N}{\sqrt{T}} = 100 \text{ percent} = 920$$

Expressing horsepower equation in terms of percent, (10)

$$\frac{\text{Horsepower}}{P_{\text{inlet}} \sqrt{T_{\text{inlet}}}} = 1.415 \times \frac{\frac{1770}{100} \left(z \frac{WN}{P} \right) \left(\frac{.0473}{100} \right) \left(z \frac{\Delta h}{T} \right)}{\frac{920}{100} \left(z \frac{N}{\sqrt{T}} \right)}$$

$$\therefore \frac{\text{Horsepower}}{P_{\text{inlet}} \sqrt{T_{\text{inlet}}}} = 0.001288 \times \left| \frac{\left(z \frac{WN}{P} \right) \left(z \frac{\Delta h}{T} \right)}{z \frac{N}{\sqrt{T}}} \right| \quad (11)$$

Figure 72 shows horsepower vs N/\sqrt{T} . Figure 73 shows this relationship plotted parametrically.

2. Torque:

$$\phi = \frac{\text{Horsepower (5250)}}{N} \quad (12)$$

$$\text{Horsepower} = 1.415 \, W \Delta h \quad (13)$$

$$\therefore \phi = 7430 \frac{W \Delta h}{N}$$

By multiplying and dividing by P and T,

$$\frac{\phi}{P_{\text{inlet}}} = 7430 \left[\frac{\left(\frac{WN}{P} \right) \left(\frac{\Delta h}{T} \right)}{\left(\frac{N}{\sqrt{T}} \right)^2} \right] \quad (14)$$

In terms of percent,

$$\frac{\phi}{P_{\text{inlet}}} = 0.737 \left[\frac{\left(z \frac{WN}{P} \right) \left(z \frac{\Delta h}{T} \right)}{\left(z \frac{N}{\sqrt{T}} \right)^2} \right] \quad (15)$$

Refer to Figure 74 for the parametric plot.

Calculation of Torque and Horsepower

Turbine Performance Testing

(Refer to Figure 70 for speed and temperature vs N/\sqrt{T} .)

Sample calculation

@ max conditions

$$P_{\text{inlet}}/P_{\text{downstream}} = 2.6; \text{ atmospheric discharge}$$

$$P_{\text{inlet}} = 2.6 (15) = 39 \text{ psia}$$

$$@ \frac{N}{\sqrt{T}} = 80\%, T = 1155 \text{ }^{\circ}\text{R}, N = 25000 \text{ rpm}$$

$$\sqrt{T} = \sqrt{1155} = 34$$

$$\text{from Figure 74; } @ \frac{N}{\sqrt{T}} = 80\% \text{ and } P_{\text{inlet}}/P_{\text{downstream}} = 2.6$$

$$\frac{\text{Horsepower}}{P_{\text{inlet}} \sqrt{T_{\text{inlet}}}} = 0.1370$$

$$\therefore \text{Horsepower} = .1370 (39) (34) = 181.5$$

$$\text{from Figure 74; } \frac{\phi}{P_{\text{inlet}}} = 0.976; \quad \phi = 0.976 (39) = 38.0 \text{ ft/lb}$$

Starting Torque

Assume start-up turbine with preheat of 600°F

Assume pressure ratio of 2.6 with atmospheric discharge

$$\therefore P_{\text{inlet}} = 39 \text{ psia}$$

Check for flow:

$$\frac{W\sqrt{T}}{P_{\text{inlet}}} = 1.924$$

$$\therefore W = \frac{1.924 (39)}{\sqrt{1060}} = 2.31 \text{ lb/sec}$$

which is less than max allowable W of 4 lb/sec satisfactory

$$@ 100\% \frac{N}{\sqrt{T}}, N = 920 \sqrt{1060} = 30,000 \text{ rpm}$$

$$\frac{\phi}{P_{\text{inlet}}} = 0.815 \quad \phi = 39 (0.815) = 32 \text{ ft/lb}$$

$$\therefore \text{Starting Torque} = 2 (32) = 64 \text{ ft/lb @ } N = 0$$

Figure 75 illustrates the estimated torque characteristics based on the parametric plot, Figure 74.

Maximum Allowable Power Absorber Inertia

Assume acceleration from 0 to 25,000 rpm

$$\text{Average torque} = \frac{38.6 + 64}{2} = \frac{102.6}{2} = 51.3 \text{ ft/lb}$$

$$\phi = I \alpha \quad (16)$$

where I = moment of inertia about axis of rotation -
lb/ft²

α = angular acceleration - rad/sec⁻²

$$\alpha \left[\frac{\text{rad}}{\text{sec}^2} \right] = \left(\frac{\pi}{30} \right) \text{ N/Sec} \quad (17)$$

Assume acceleration time = 30 sec to go from 0 to 25,000 rpm

Assume negligible friction

$$\therefore \alpha = \frac{\pi (25,000)}{30 \cdot 30} = 87.2 \text{ rad/sec}^2$$

$$I = \frac{J}{\alpha} = \frac{51.3}{87.2} = 0.588 \text{ ft/lb/sec}^2$$

$$= 19.0 \text{ lb/ft}^2$$

From the above analysis, Figure 76 was drawn to define the two distinct operating ranges required for performance testing and high-temperature testing. Specifications (References 7, 8, and 9) were established from this information and used for selecting the optimum power absorption system. This consists of a 6:1 single-stage high-speed reducer manufactured by the Cotta Gear Company and a water brake manufactured by Taylor Dynamometer Company consisting of ten stages and operating at a maximum speed of 9,200 rpm. The brake is rated at 900 horsepower but is capable of increased absorption for moderate periods of time. This hydraulic dynamometer was selected for its unusual design features, particularly the ten absorber stages, which offer great flexibility in operation. The stages can be employed singly or in combination to provide the particular absorber capacity required for any particular test. Absorber stages can be added or subtracted by simply closing a valve to a particular stage. In addition to the flexibility of operation, this feature should materially improve the control characteristics as well.

The remaining features of this facility are shown in the installation drawing, Figure 77. These other details closely resemble the systems used for the previous rig and will not be repeated here.



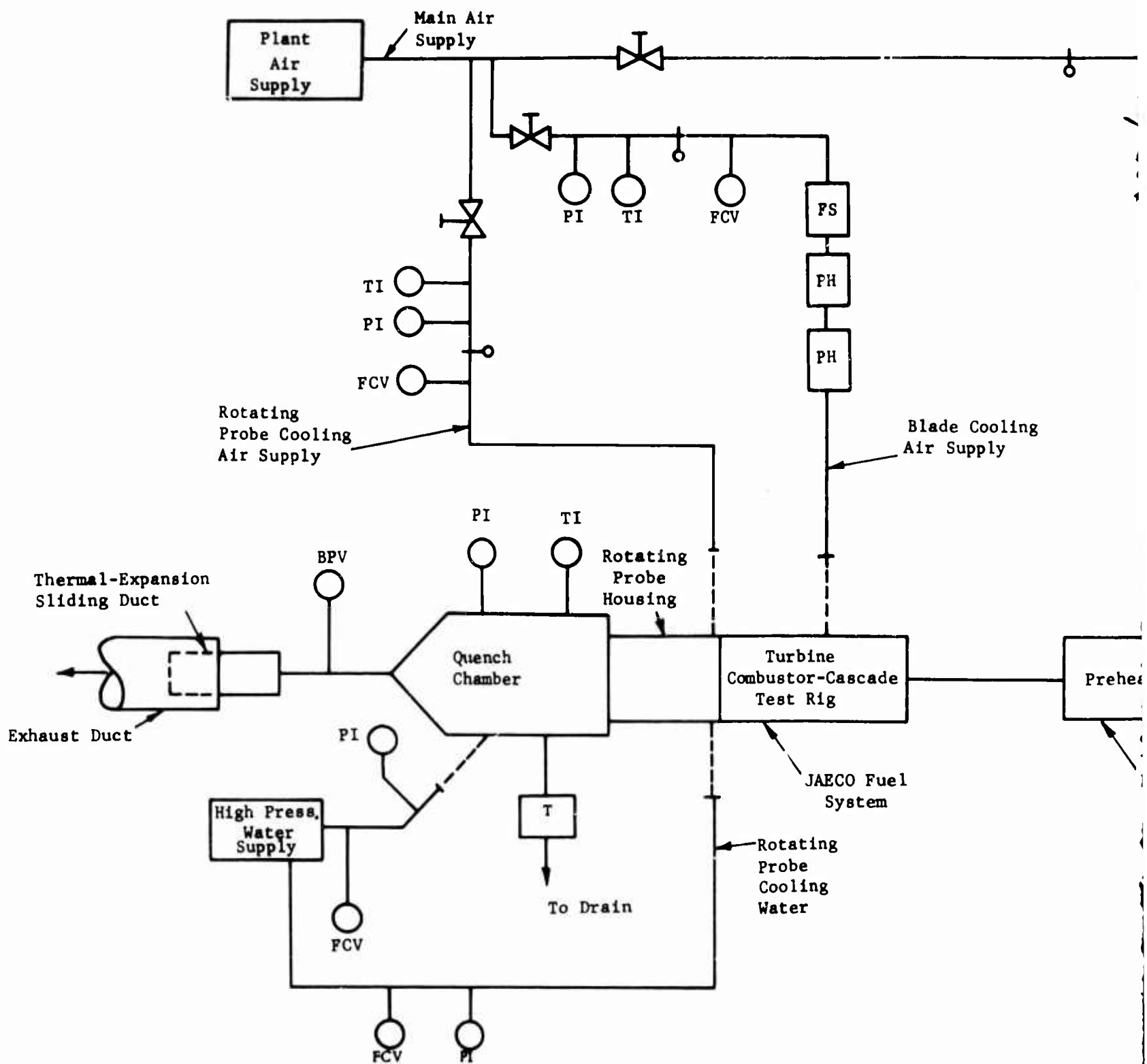
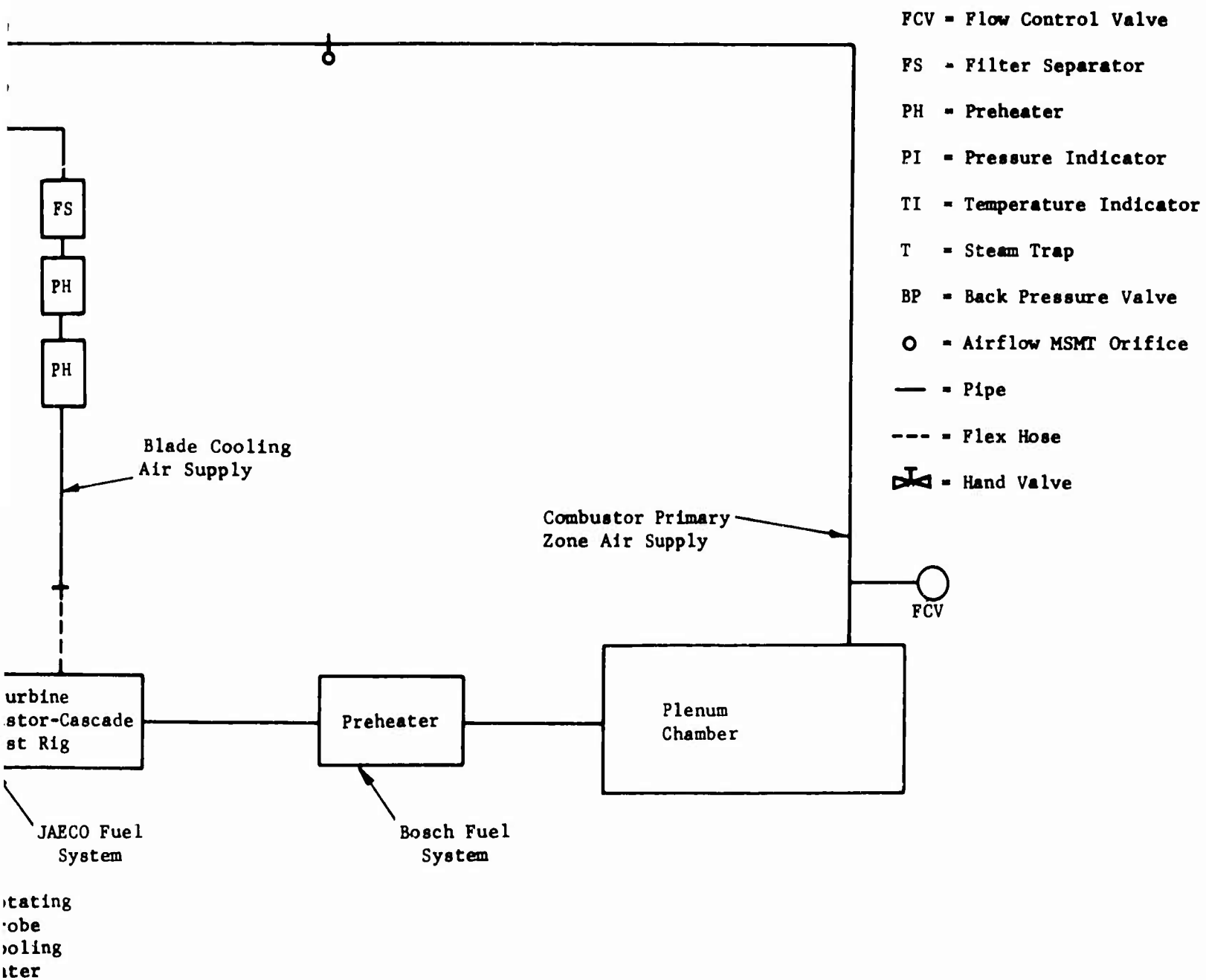
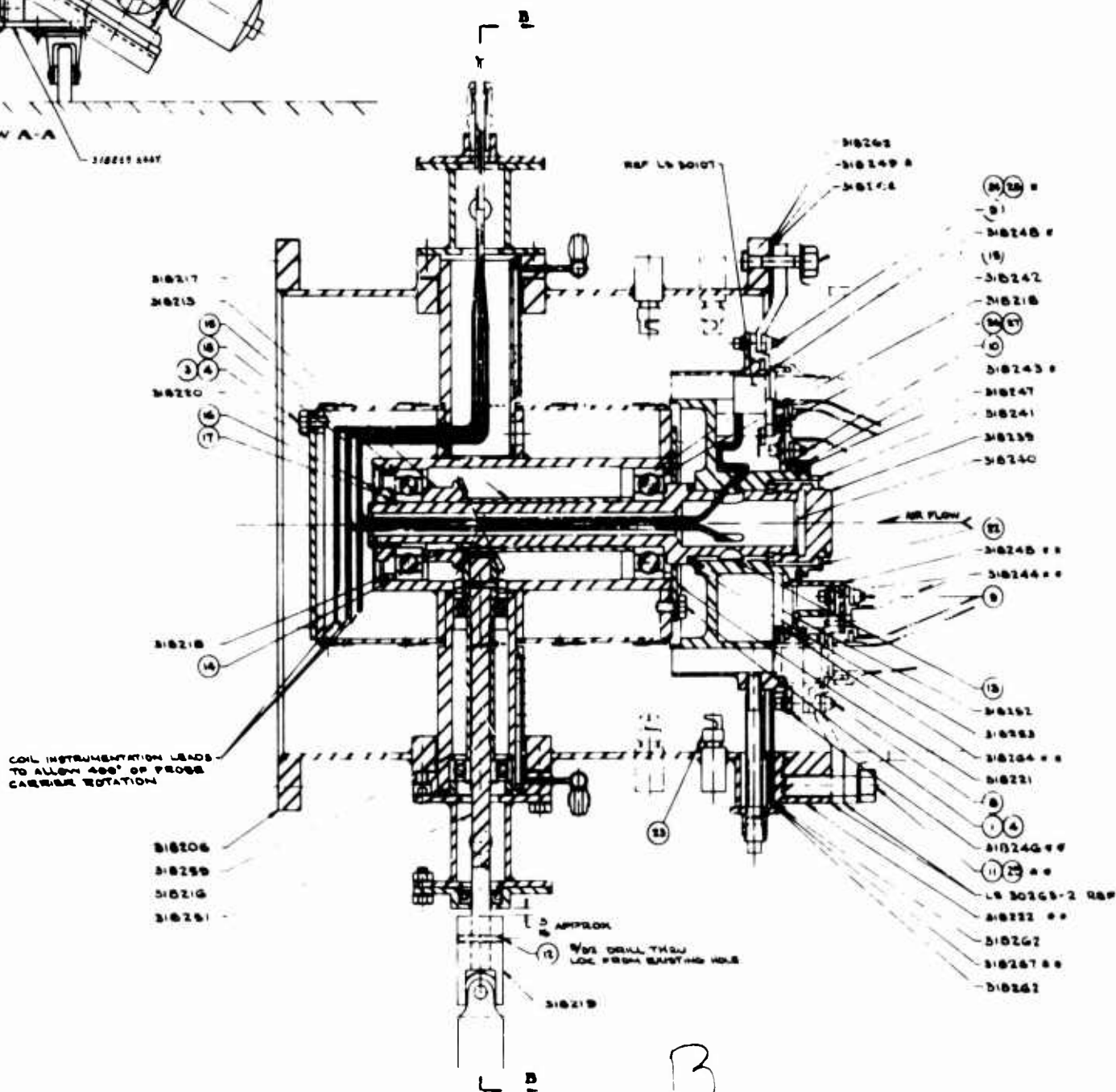
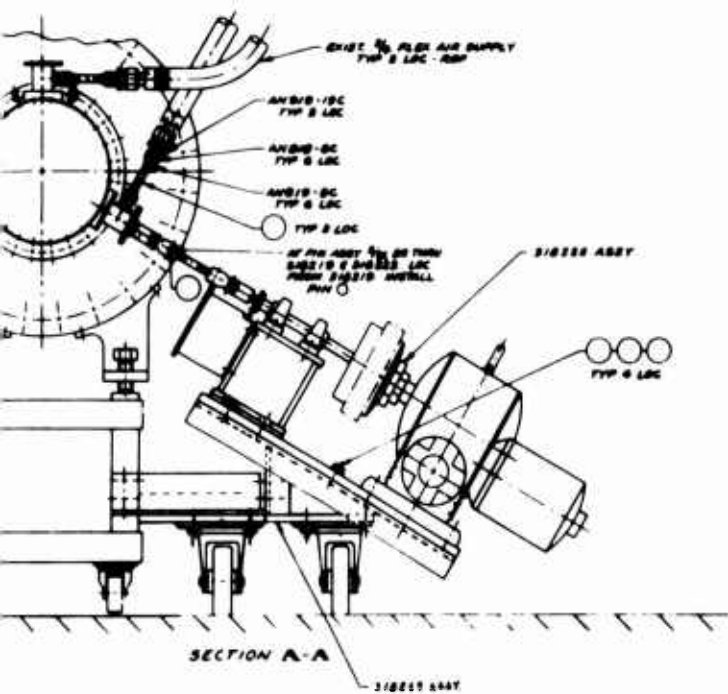


Figure 67. Combustor and Turbine Stator Test Stand Schematic.



B



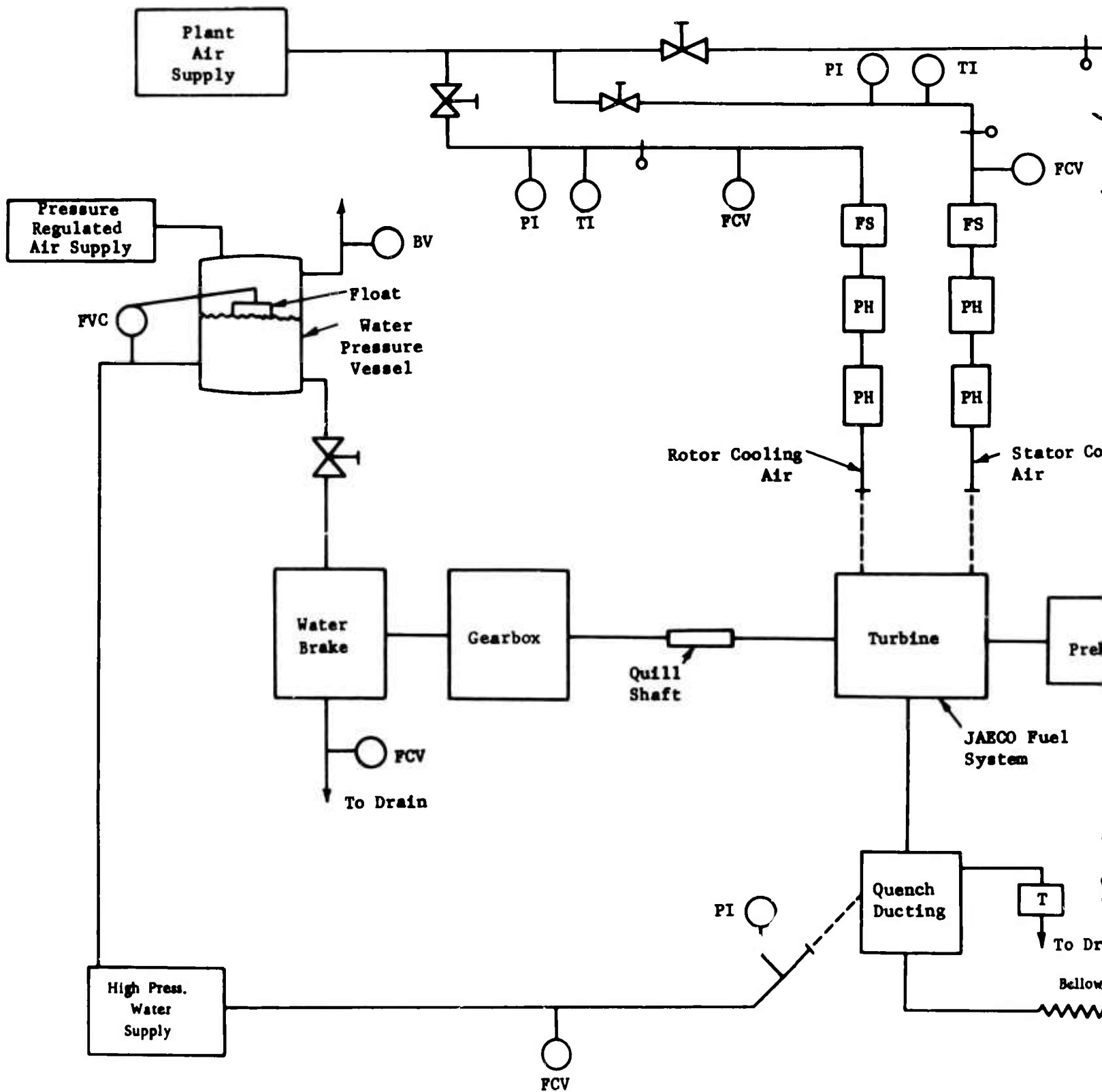
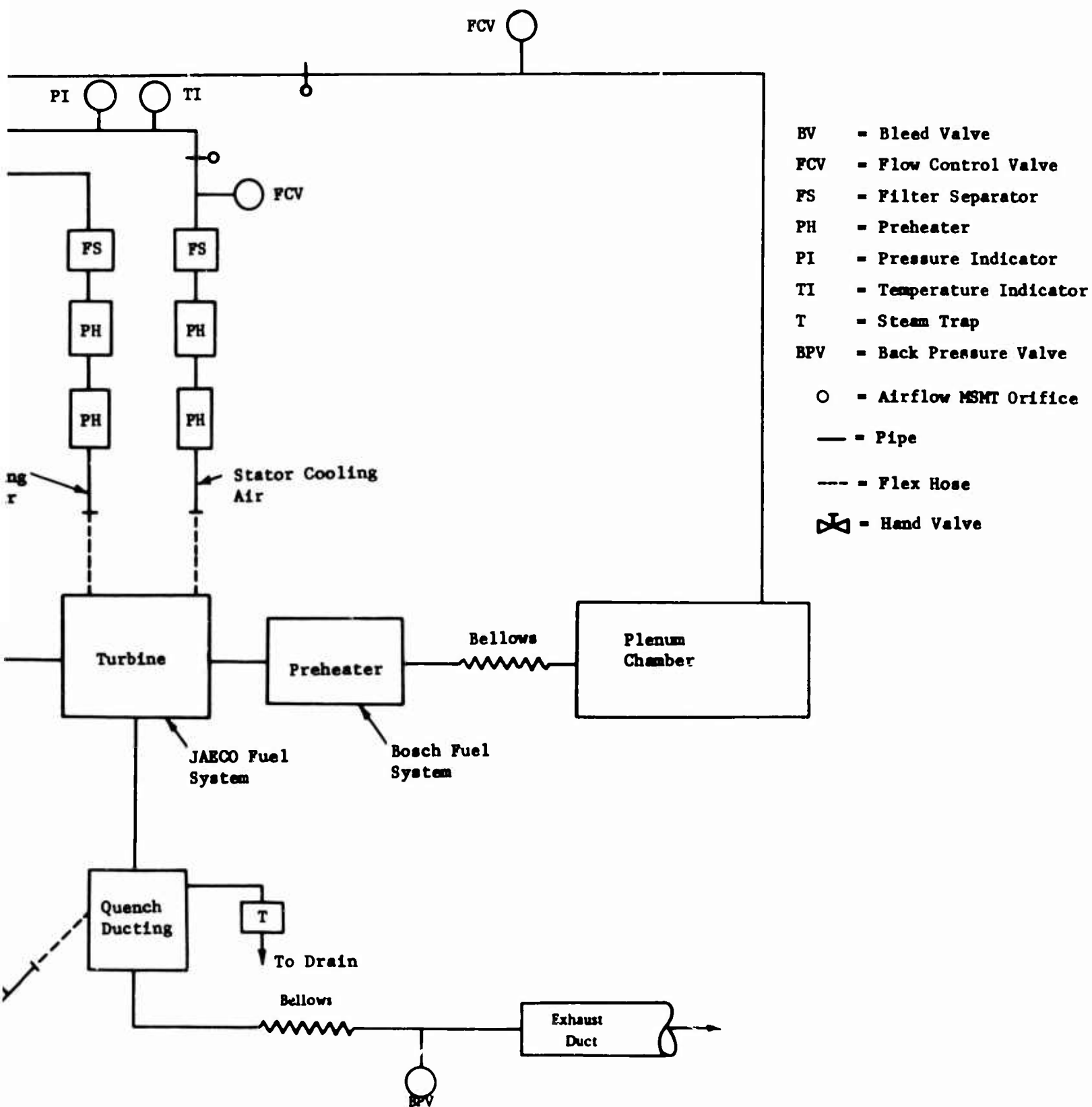


Figure 69. Turbine Test Stand Schematic.

A



E

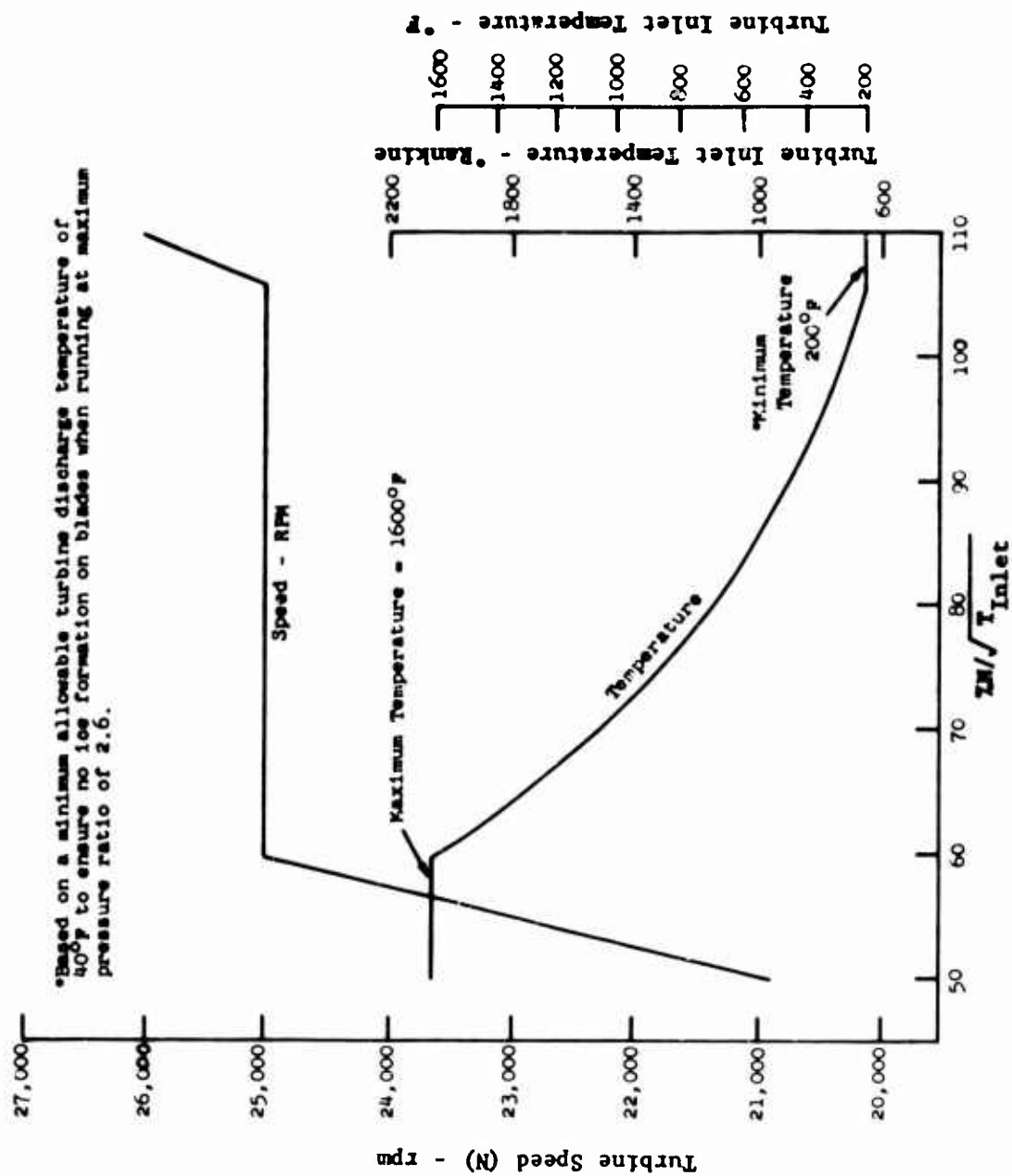


Figure 70. Turbine Operating Speed and Turbine Inlet Temperature Vs $N/\sqrt{T_{Inlet}}$ For Turbine Performance Testing.

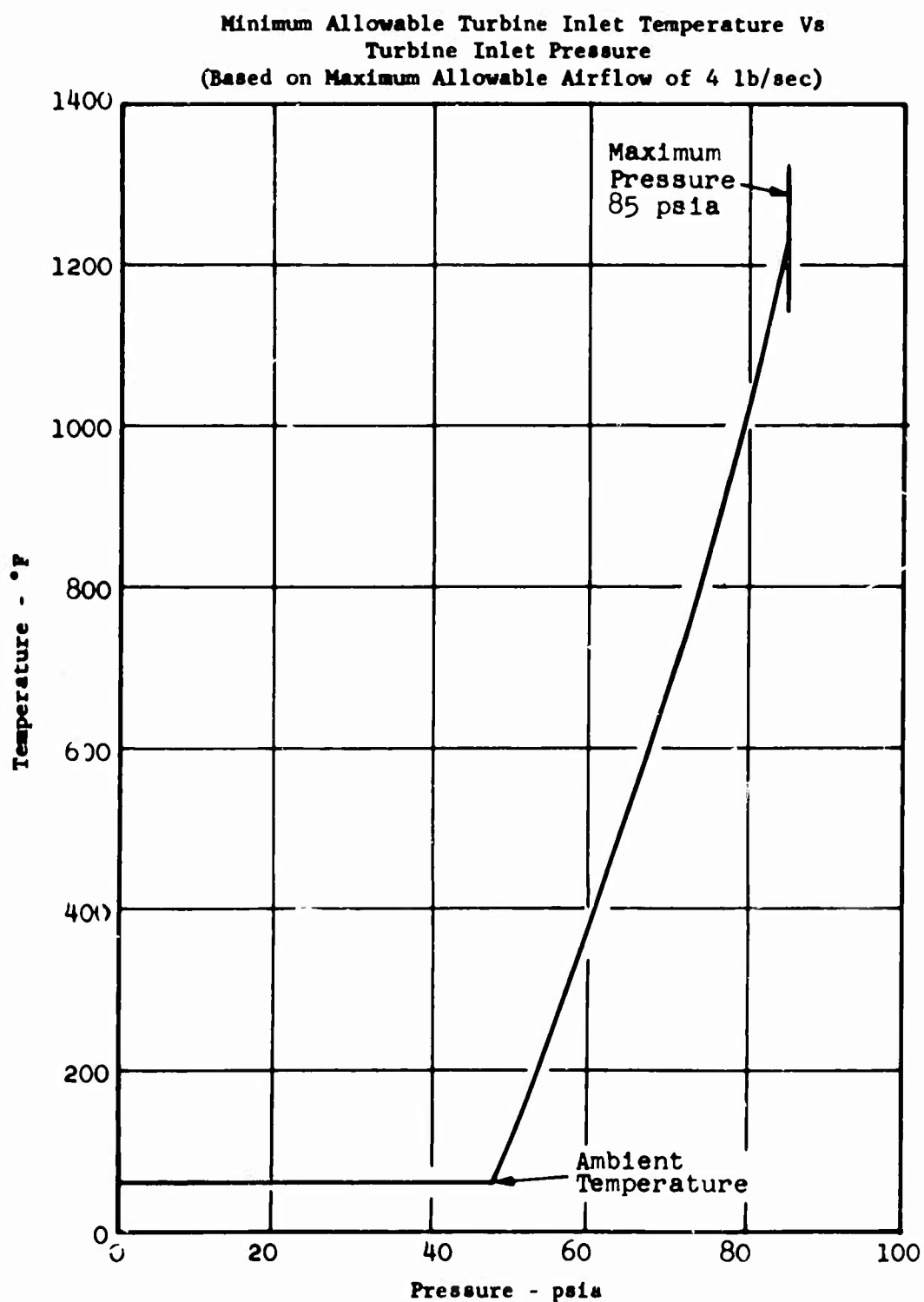


Figure 71. Turbine Test Cell Temperature Limitations.

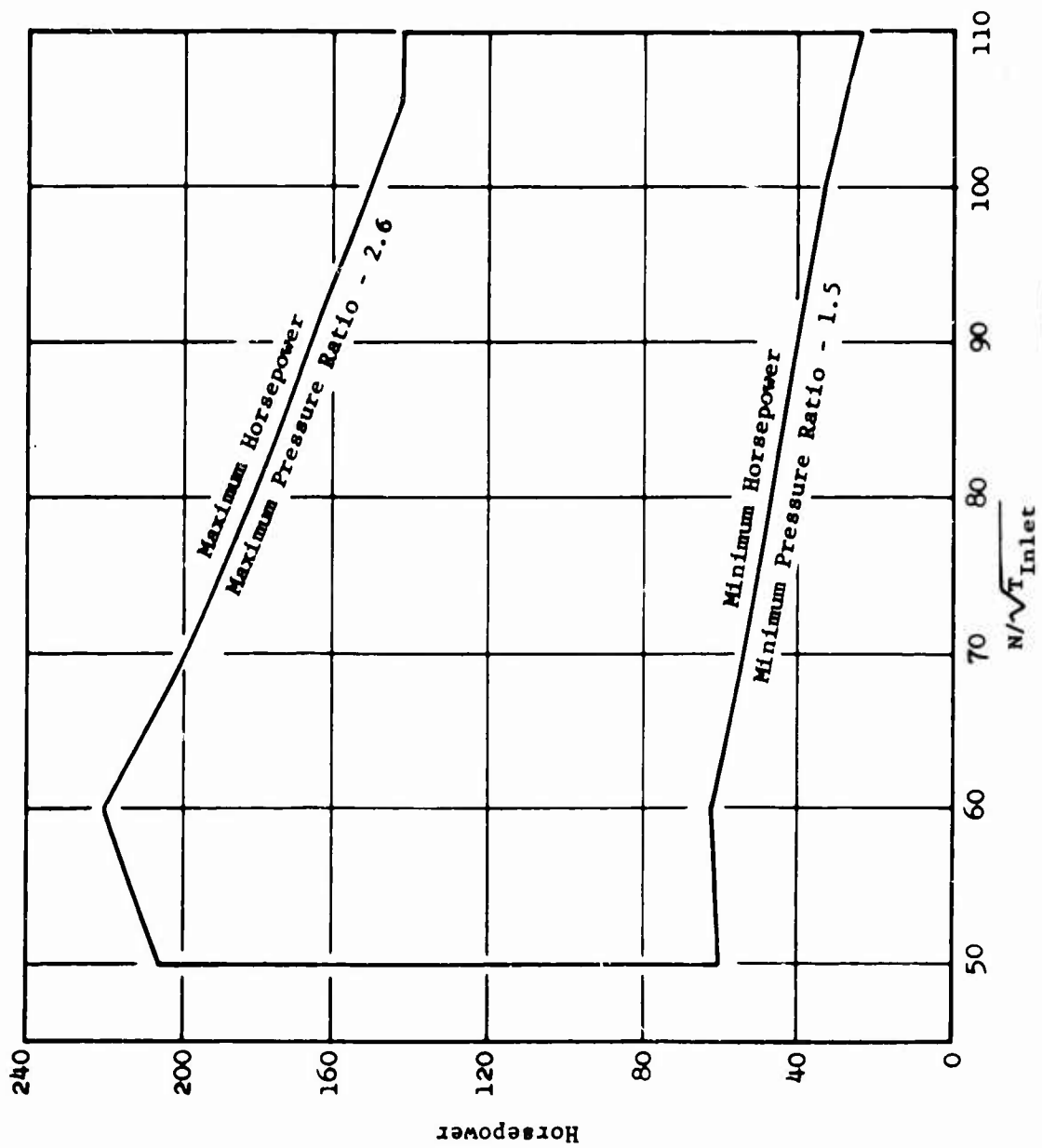


Figure 72. Turbine Horsepower Vs $N/\sqrt{T_{Inlet}}$.

Based on Figure 1 of October 15, 1964, Technical Report
Rig 9404 Preliminary Turbine Performance Map

$$HP/P_{Inlet}\sqrt{T_{Inlet}} = 0.001288 \left(\frac{WN}{P} \right) \left(\frac{\Delta h}{T} \right) / \left(\frac{N}{\sqrt{T}} \right)$$

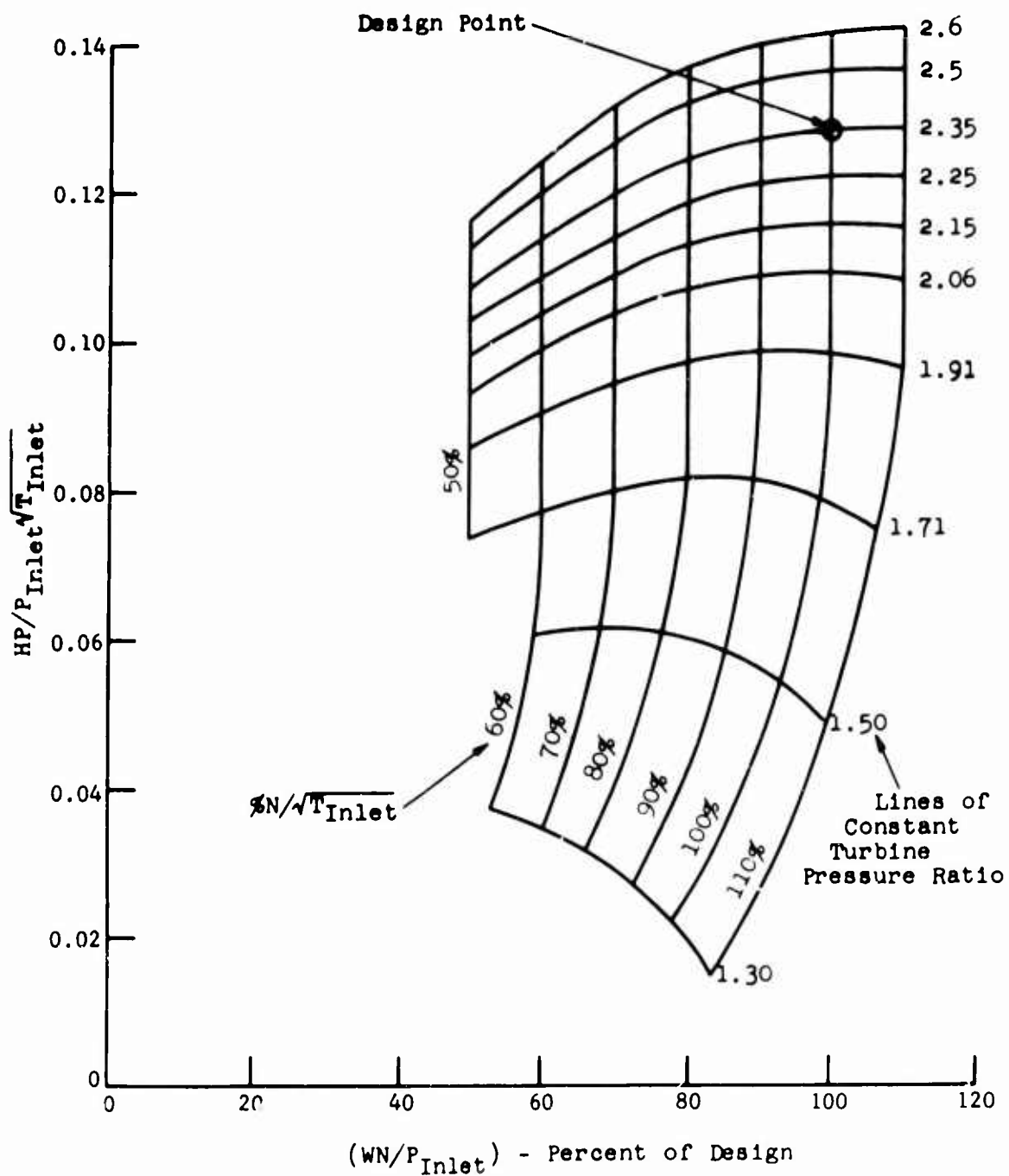


Figure 73. Turbine Horsepower Characteristics.

Based on Figure 1 of October 15, 1964, Technical Report
Rig 9404 Preliminary Turbine Performance Map

$$\text{Torque}/P_1 = 0.737 \left(\frac{WN}{P} \right) \left(\frac{\Delta h}{T} \right) / \left(\frac{N}{\sqrt{T}} \right)^2$$

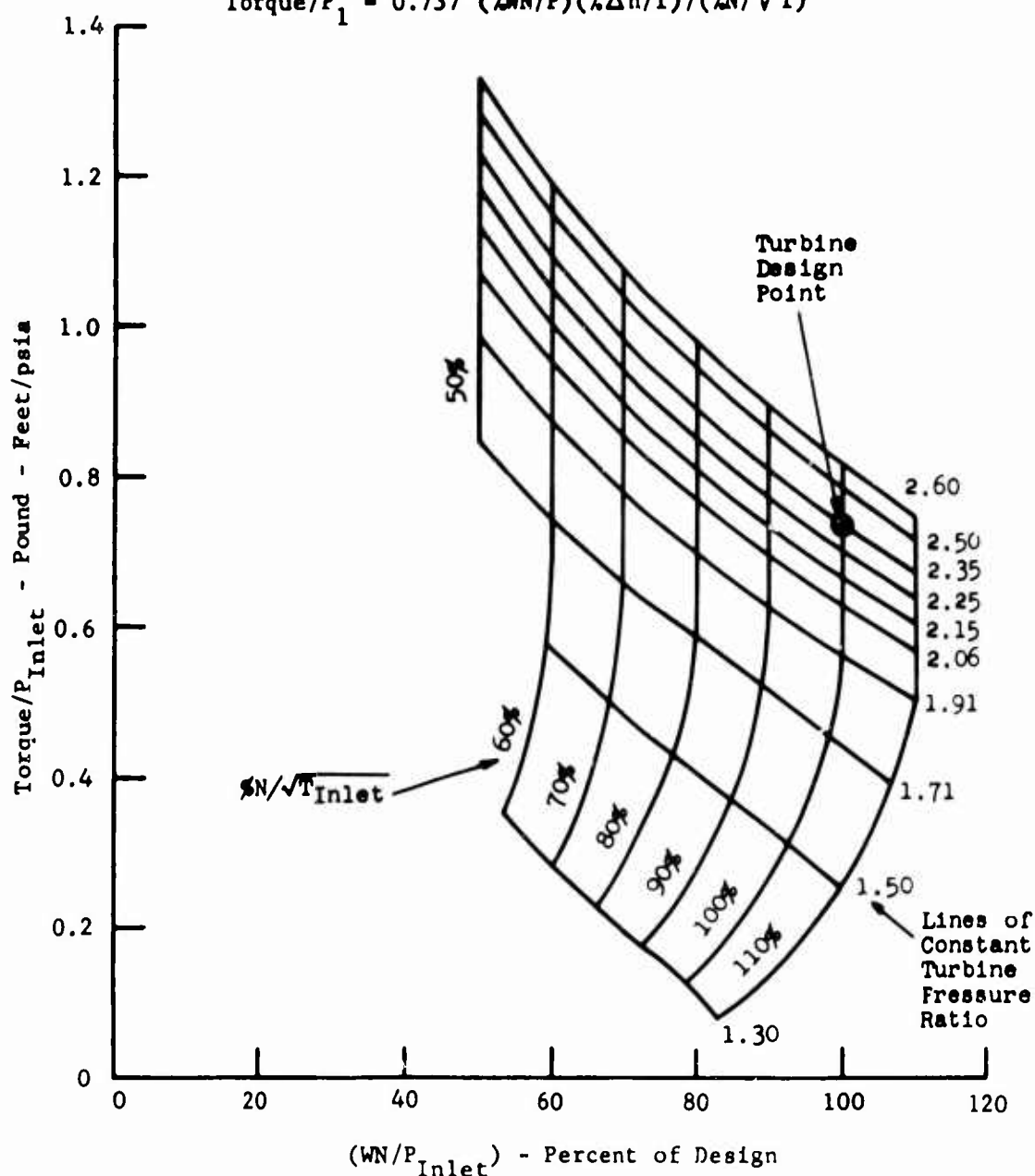


Figure 74. Turbine Torque Characteristics.

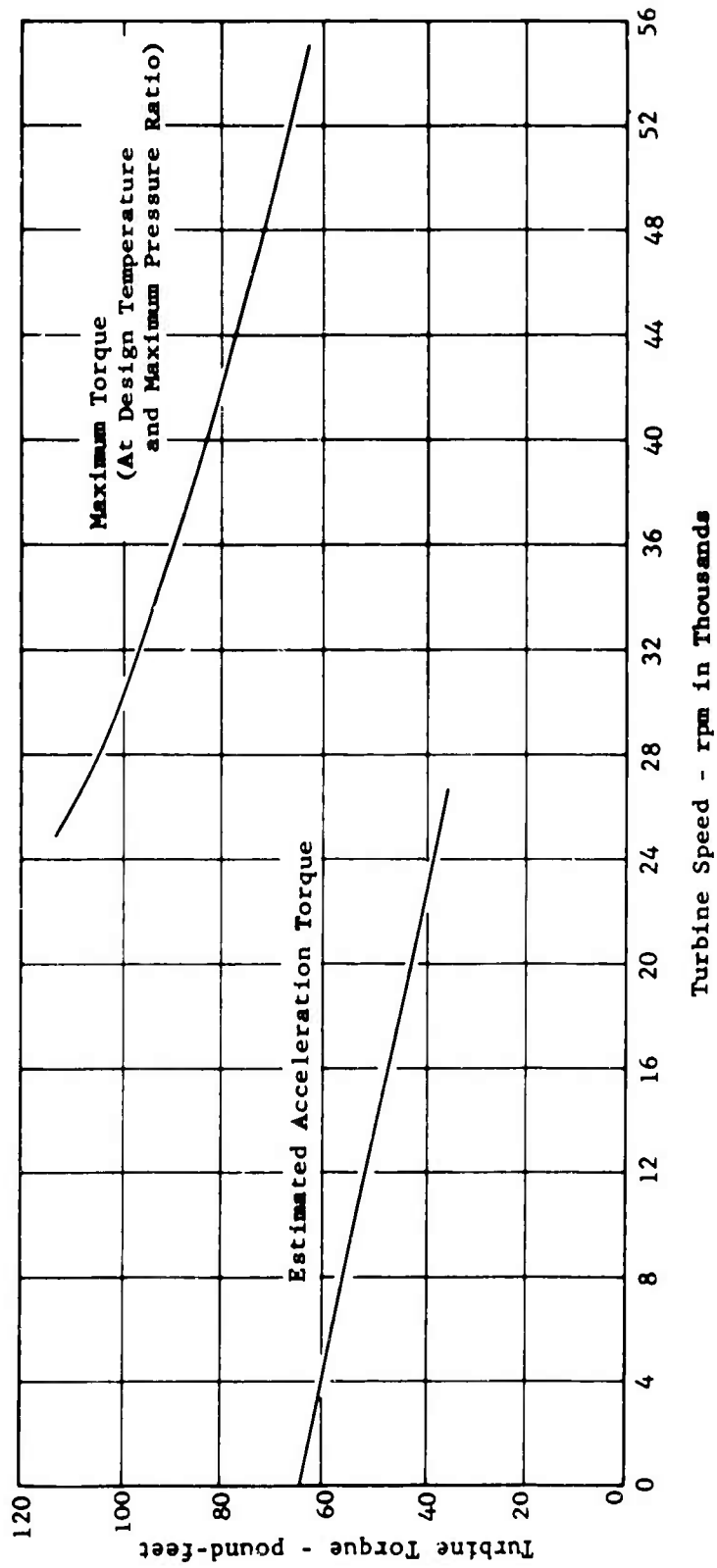


Figure 75. Turbine Torque Characteristics.

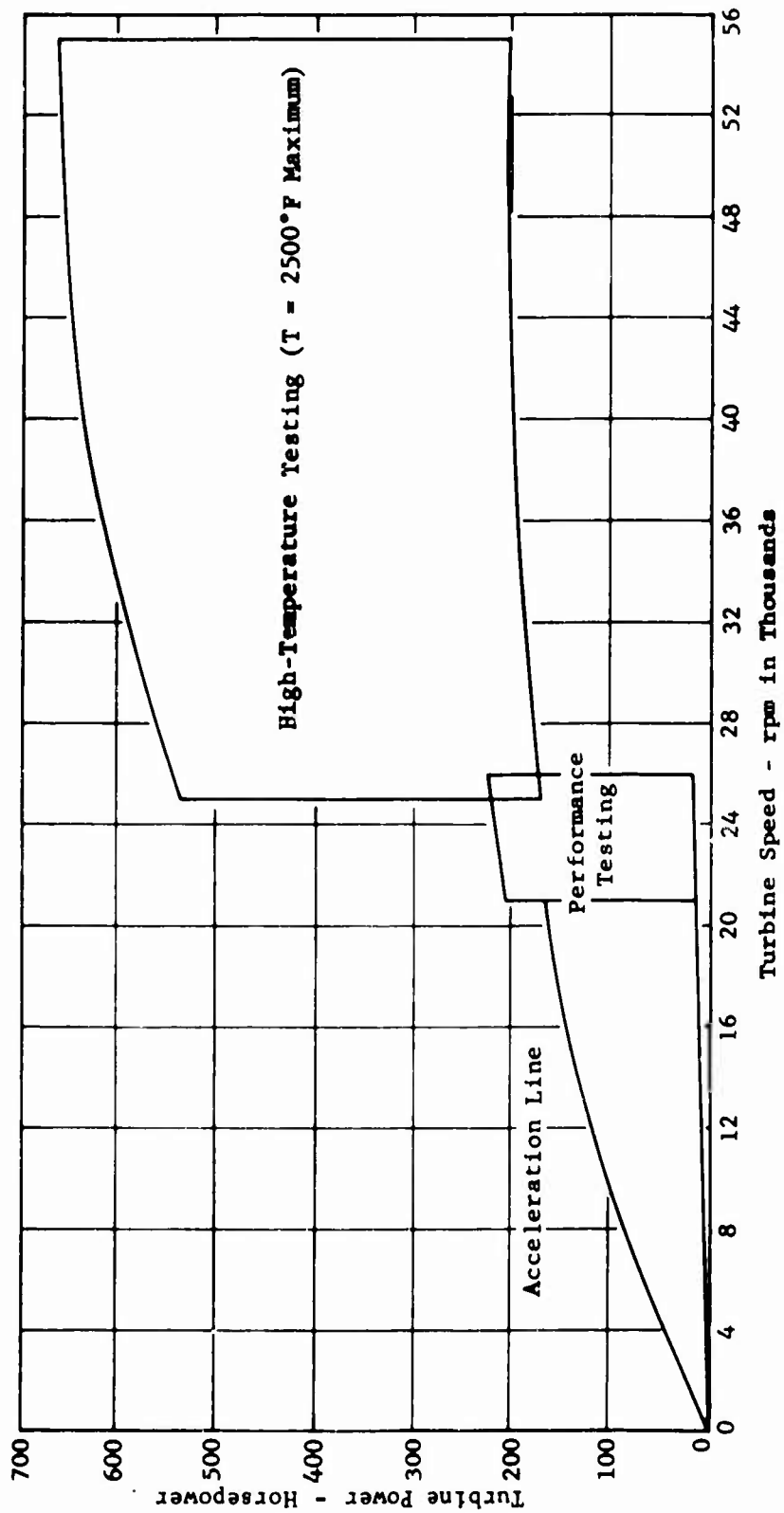


Figure 76. Turbine Required Power Absorption Vs Speed.

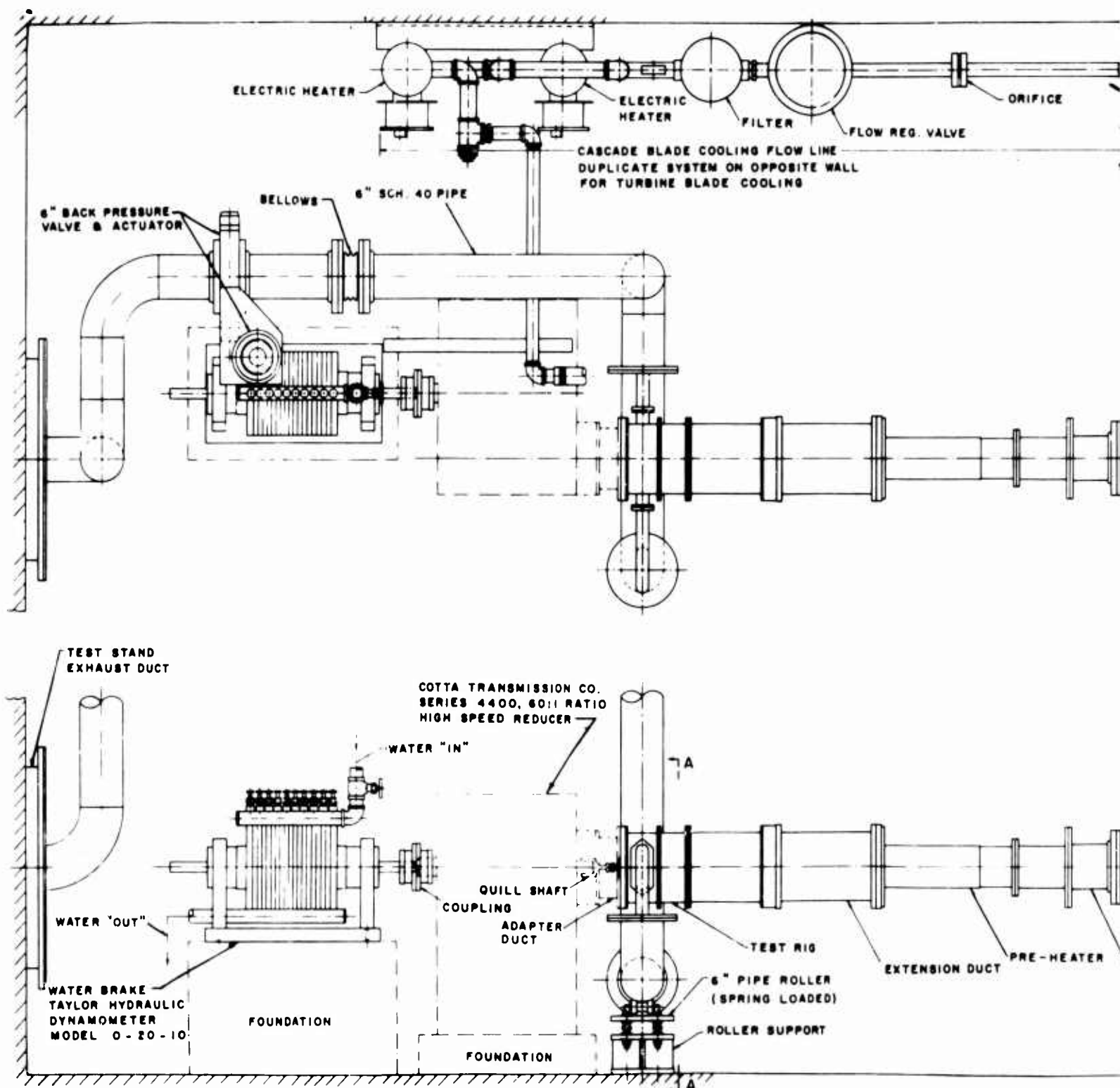
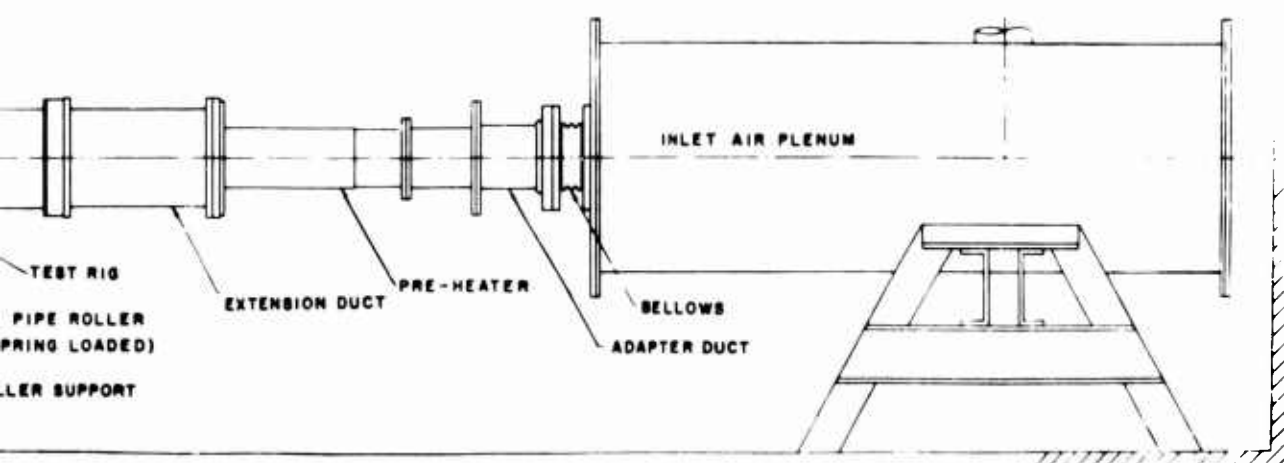
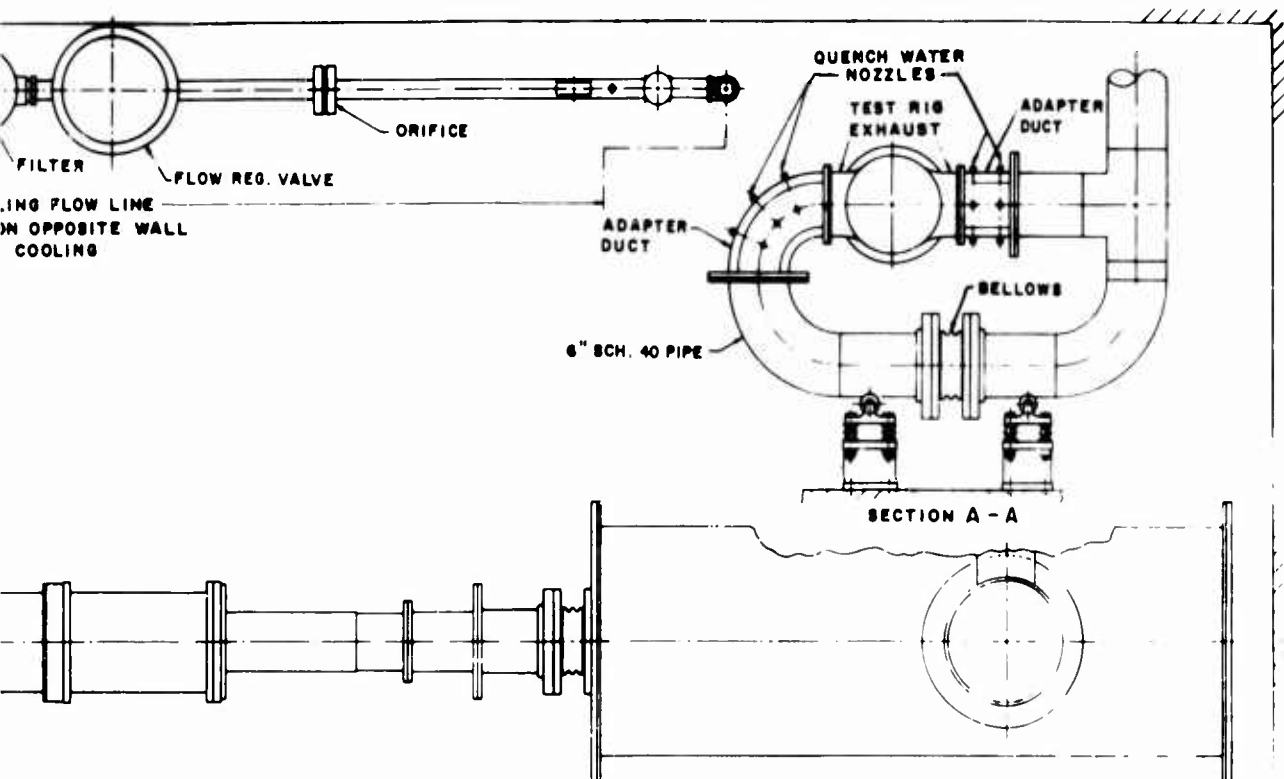


Figure 77. Turbine Installation.

A



B

3.6 INSTRUMENTATION DESIGN

Instrumentation for the full-round rigs has been designed to utilize as much of the existing equipment used for the two-dimensional cascade rig as possible; indeed, many of the techniques used are the same.

The full-round combustor rig instrumentation, Figure 78 and Table XIV, provides many temperature and pressure tapings in the combustor area and its immediate surroundings, such as inlet air, cooling and diluent air, and discharge passages.

The combustor liner temperatures are measured with surface thermocouples welded to the outside surfaces of the walls with their leads routed out either through one of the yokes of the inlet housing or across the diluent air plenum to the duct wall, depending on whether the thermocouples are reading inner or outer liner temperatures. The temperatures in these areas of the rig dictate the use of Instrument Society of America calibration K thermocouples (Chromel/Alumel) of the swaged type in an Inconel sheath; 0.040-inch-diameter wire was chosen as representing the best compromise between ruggedness and minimum interference with cooling and cooling airflows.

Combustor static pressures are measured with 1/16-inch tubing, which produces slightly greater flow interference in the cooling air passages but which allows a quicker response to pressure changes than could be achieved with tubing the same size as the thermocouples.

Both pressure and temperature leads are carried some 2 or 3 feet beyond the test rig before the change is made to extension leads. This arrangement allows the use of low-temperature material, glass insulated thermocouple extensions, and plastic tubing pressure leads; and it also eliminates any error signals that might be fed into the thermocouple leads by making connections in a high-temperature area where thermal errors can be introduced and oxidation can occur.

Also provided for the combustor rig is a rotating probe carrying both temperature and pressure profile instrumentation. The heads are mounted 130 degrees apart and will sweep through a full circle. The probe may be driven remotely to predetermined angles, may be rotated in both forward and reverse directions, and may be moved manually to any desired location in order to follow a profile exactly. The drive has a single speed of 1/2 rpm, providing a complete 360-degree traverse of either probe head in 2 minutes.

The turbine stator testing will utilize a portion of the combustor thermocouples and pressure tapings to prove the consistency of combustor operation.

Instrumentation of two sets of four turbine stator blades located approximately 180 degrees apart will follow the general practice of the two-dimensional cascade rig, with thermocouples inserted into the blade spar from the OD shelf and others passed through the spar at an angle to measure skin temperature from the ID shelf. Shelf temperature will also be picked up by means of thermocouples embedded in the material.

The general design philosophy of the rotating probe follows that of the traversing mechanism used in the Phase I rig. The probes make a sweep of the exit area from either the combustor or the stator to establish a profile. The same probe mechanism will be used for both duties, with the axial shift secured by means of spacers.

At the combustor exit, the flow is axial and subsonic; here, the vanes developed for the cascade rig will be used. The flow out of the stator ring is supersonic and is at an angle of approximately 60 degrees to the axis of the engine. At this station, a specially designed probe head must be used, mounted in a carrier adjusted to present it to the gas stream at the correct angle. The angle setting will be determined by use of a yaw probe.

In the rotating phase of testing (see Figure 79), the combustor instrumentation will be retained and the rotating probe will be removed to make way for the turbine rotor. Some additional skin and gas temperatures and static pressures will be provided, notably in the cooling air ducts leading to the rotor.

Thermocouples will be installed in the turbine rotor blades.* Chromel/Alumel swaged wire thermocouples, 0.025 inch in diameter, will be used, and these will be run out through the hollow turbine shaft to a high-speed slip ring as shown in Figure 80.

Two holes will be drilled in the wheel by the electrical discharge machining, one prior to attachment of the blades and one after the blade is attached. The first hole will run diagonally from the front face of the wheel, through the material of one of the impeller vanes cast into the wheel, and out to the hollow shaft near the upstream bearing. The second hole will be on a circular arc starting at the front face of the wheel near the end of the first hole and running up into the blade to a specified height, either midspan or near the root. This curved hole will be made using a special adapter which will translate the normal linear stroke of the linear discharge machine through a system of levers to the arc required.

The thermocouple will be fed into the rotor from its front face. The junction section will be precurved and fed into position first, and the lead out will be held straight and passed down the diagonal hole and out to the slip ring in its turn. The short length of ceramo wire that runs between the two holes on the face of the wheel will be secured with a clip.

After assembly, the thermocouple will not be spark welded into the bottom of the hole in the blade, but will be held in position by centrifugal force. This arrangement makes it possible to replace rotor thermocouples in the event of failure.

* During actual buildup, thermocouples were not installed in the rotor blades. Instead, temperature indicating paints and frequent visual and boroscopic examinations were used to monitor rotor condition.

The slip ring will be of the type developed by the Boeing Company using deionized water for cooling, insulation, and lubrication. It will have eight rings to allow four thermocouples to be used, and it will be mounted at the nondriving end of the hollow high-speed shaft of the speed-reducing gearbox. The input and output terminals of the slip ring are widely separated (about 3 inches apart), and steps will be taken to enclose the slip ring in an insulating cover so as to minimize temperature differences.

Shaft speed will be sensed for overspeed cut-out-control purposes by a magnetic pickup at the end of the turbine shaft. A castellated nut is used to retain the bearing races, and the passage of the ten castellations will be detected by the magnetic pickup, which is fed to an amplifier and indicator system having a preset overspeed cut-out arrangement.

CROSS REFERENCE BETWEEN INSTRUMENTATION REQUIRED AND INSTRUMENTATION SUPPLIED			
TABLE XIV			
TABLE A - COMBUSTOR DEVELOPMENT TESTS			
Instrumentation Required	Item number on Figure 76	Instrumentation Required	Item number on Figure 76
Temperature		Pressure	
Combustor liners	(25) ID, T_g : 7, 9, 11, 14, 17, 19, 21, 22, 24, 26, 28, 30, 32	Combustor liner cooling passages and fuel vaporizer tubes	(9) Cooling passages: P_g : 3, 12, 13, 14, 15, 18
Outer housing	OD, T_g : 4, 6, 8, 10, 12, 15, 18, 20, 23, 27, 29, 33	Combustor inlet air	Vaporizer tube, P_g : 5, 10, 11
Inner shell	T_g : 1, 13, 34	Burner plate	P_g : 1, 2
Burner plate	T_g : 5, 16, 25, 31	Outer cooling chamber	P_g : 6, 7, 8, 9
Inlet air	(2) T_g : 2, 3	Discharge wall	(2) P_g : 4, 17
Discharge air	(2) T_g : 1, 2		(4) Inner: P_g : 19, 21
	(3) Rotary probe (Drawing No. LS-30107)	Discharge air	Outer: P_g : 20, 22
		Combustor outer liner	(3) Rotary probe (Drawing No. LS-30107)
			(1) P_g : 16
TABLE B - FULL CASCADE TESTS			
Instrumentation Required	Item number on Figure 79	Instrumentation Required	Item number on Figure 79
(Additional to A)		Pressure	
Blade strut and skin	(18) Blade struc, T_g : 58, 59, 60, 61, 62, 64, 67, 68, 69, 70, 71, 73	Blade shroud cooling air	(2) P_g : 52, 53
Blade shroud	Blade skin, T_g : 63, 65, 66, 72, 74, 75	Blade skin cooling air	(2) P_g : 50, 51
	(8) ID, T_g : 50, 52, 54, 56	Blade row exit	(2) P_g : 54, 55
	OD, T_g : 51, 53, 55, 57	Stator exit, yaw	Drawing No. 318178
Blade shroud cooling air	(2) T_g : 50, 51	Stator exit	(3) Rotary probe (Drawing No. LS-30107)
Blade skin cooling air	(2) T_g : 52, 53		
Stator exit	(3) Rotary probe (Drawing No. LS-30107)		
TABLE C - PERFORMANCE TESTS			
Instrumentation Required	Item number on Figure 79	Instrumentation Required	Item number on Figure 79
(Additional to A and B)		Pressure	
Temperature		Combustor inlet air	(2) P_g : 100, 101
Rotor discharge	(1) Yaw probe (Drawing No. 318178)	Turbine discharge wall	(4) Inner: P_g : 103, 104
Rotor blade cooling air	(2) T_g : 100, 101		Outer: P_g : 102, 105
		Rotor blade cooling air	P_g : 100, 101
TABLE D - HIGH-TEMPERATURE TESTS			
No additional instrumentation			
TABLE E - OTHER INSTRUMENTATION			
(1) Pickup No. 3015 HT			

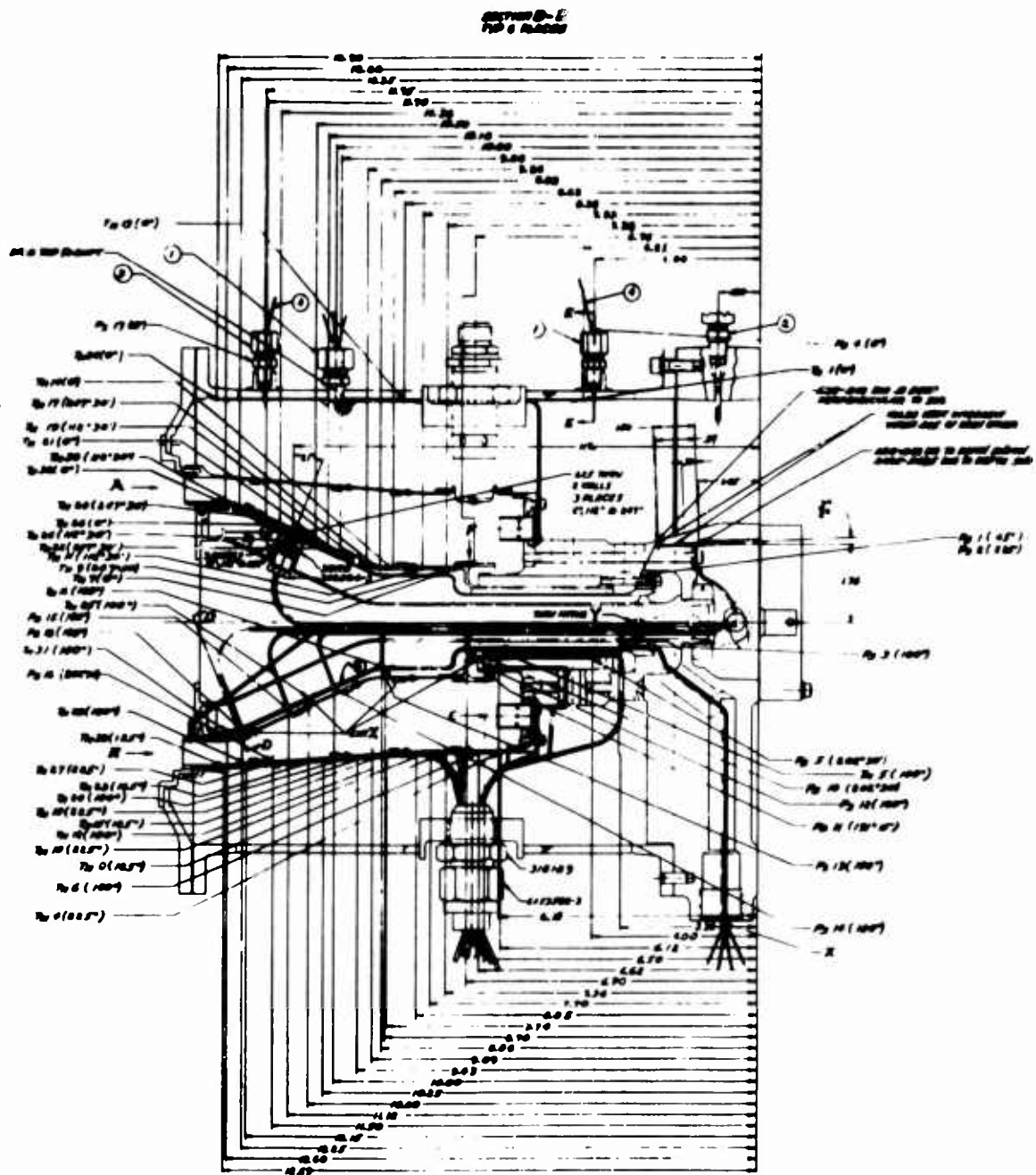
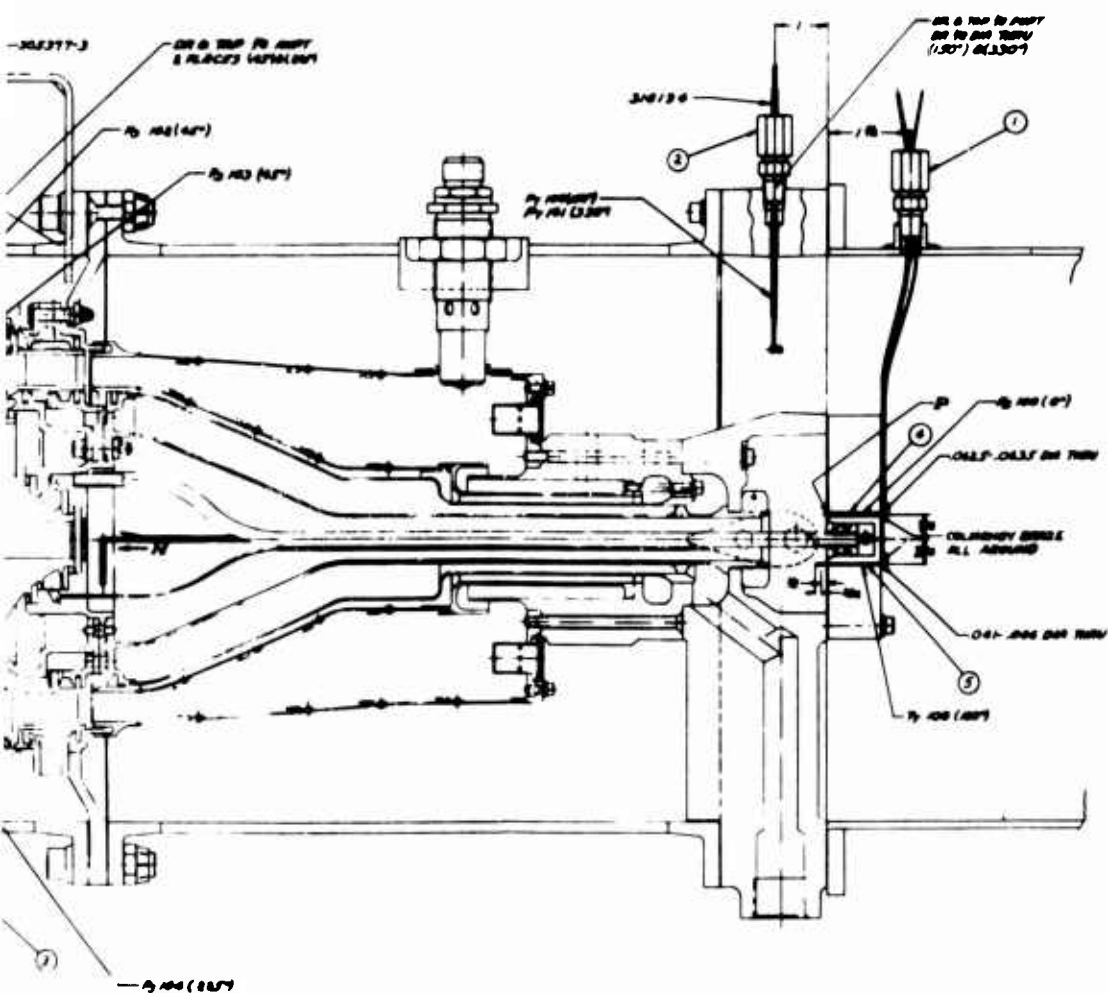
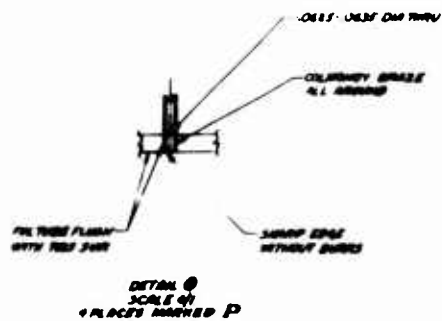


Figure 78. Instrumentation Combustor Test Rig.



NOT REPRODUCIBLE



: and Cascade Test Rig.

DOUBLE

B

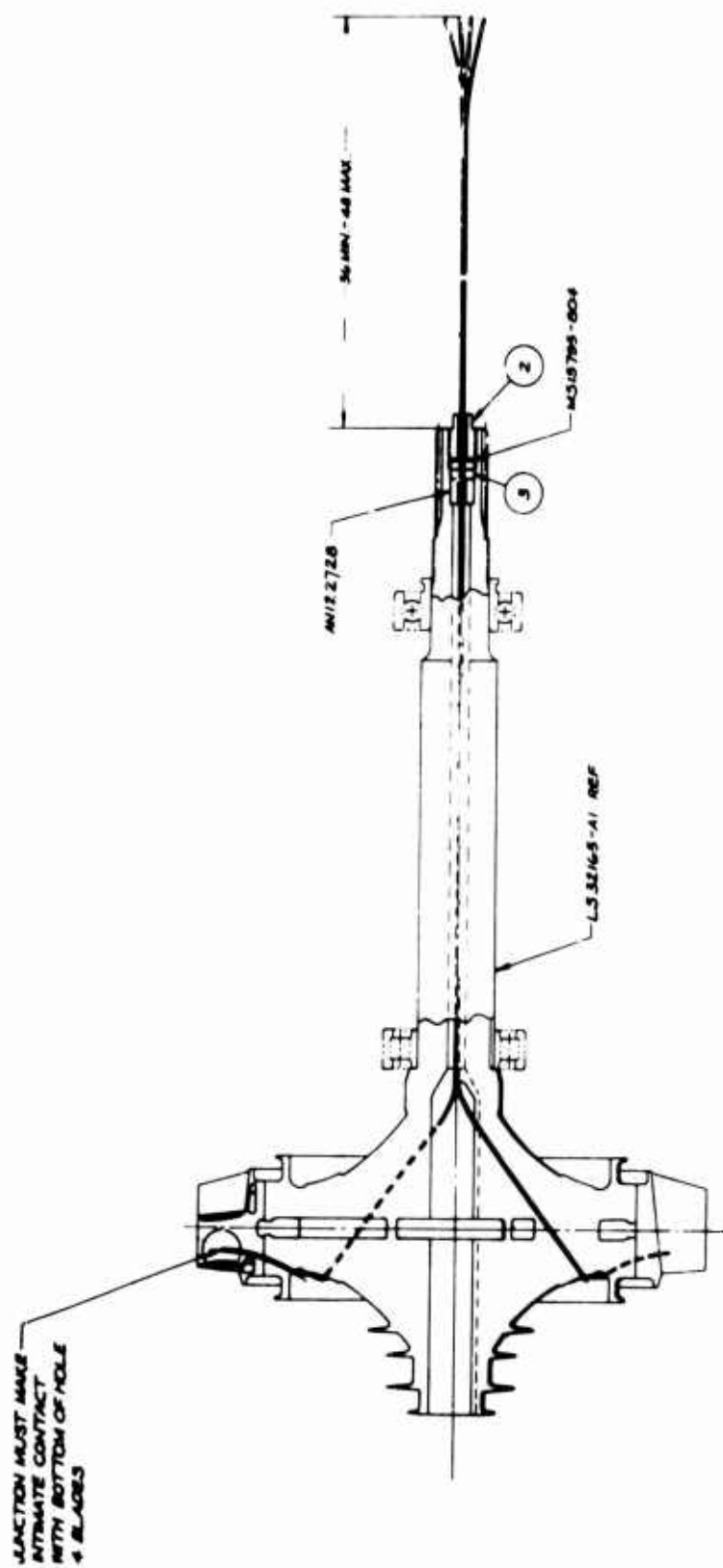


Figure 80. Instrumentation Turbine Rotor.

4.0 TURBINE COMPONENT MECHANICAL DESIGN

4.1 TURBINE COMPONENT DESIGN

4.1.1 Introduction and General Arrangement

The turbine rig was designed to demonstrate the capability of using transpiration-cooled turbine technology for a small (2-5 pps) gas turbine engine. Initial design effort was directed toward the establishment of single-stage transpiration-cooled blading for both stator and rotor for a high-temperature, high-work turbine utilizing previous C-W design information. Experience derived from the design, fabrication, testing, and development of the eight-blade cascade rig reported in Section 5.2 provides practical demonstration of these techniques. Concurrent with this design effort, a preliminary layout design of the complete turbine component, including stator blade support system, cooling air supply system to the stator blades, rotor blade disc attachment, disc, and cooling air supply system to the rotor blades, was undertaken. This latter design effort had two distinct phases which eventually led to the final configuration. The initial design phase included a turbine rotor blade fir-tree attachment to a split disc, and the second or final design included an EB welded turbine blade-disc configuration which showed great promise (Figure 31).

The turbine rig airfoil structure is very similar to the one previously designed into the cascade blade. Fundamentally, the basic concept is used with slight modifications to form a supersonic stator blade and to form a high-work rotor blade. Each stator blade is individually cantilevered from the outer support structure, and the integral shells of each blade at both ends form the cylindrical gas passage walls. Provisions are made to introduce cooling air to the blade spar from underneath the inner, or unsupported, blade end. The inner ring assembly is positioned by individual stator blade tangs which extend radially inward, and provides for the source of stator blade cooling air, as well as a stepped labyrinth seal system which prevents leakage from the rotor blade cooling air feed system. The turbine rotor blade is cantilevered from the periphery of the turbine disc, where it is EB welded to the disc. Welding the blades to the disc provides an integrated turbine rotor shaft assembly which is overhung from the two-bearing mainshaft support system. Cooling air for the rotor blades is fed through the hollow disc and turned radially outward by means of low work inducers to the shelf cavity of each rotor blade and then is metered at each blade to the airfoil cooling air passages.

4.1.2 Stator and Rotor Transpiration-Cooled Blading

Stator and rotor blade design is based on the aerodynamic data presented in Section 2.1. Initial stator blade effort was concentrated in the design of the aerodynamic passage, where great care was taken to avoid excessively high suction side velocities upstream of the converging-diverging nozzle. Downstream of the nozzle throat, special attention was given to the rate of curvature on the suction side.

Stator blade airfoil pressure and velocity profiles were generated utilizing the aerodynamic passages discussed above. These data, along with the definition of the airfoil spar cross section, the gas inlet temperature profile, and the cooling air temperature and pressure, formed the necessary input data for the blade thermal design and heat transfer analysis.

The turbine rig stator blade airfoil closely resembles the cascade blade in size and shape except for slight hub to tip section twist; therefore, a very similar structural design of the spar was utilized. This meant that the cooling passages, the spar land width, and the airfoil trailing-edge design could be made similar to the cascade blade. This final stator blade airfoil is illustrated in Figure 81.

Each stator blade is individually cantilevered from the outer support assembly by means of a stem extending above the outer cylindrical blade shelf, thus affording blade interchangeability.* The integral shelves of each blade at both ends of the airfoil form the gas passage walls. As in the cascade blade, provisions are made to introduce cooling air to the blade spar from underneath the unsupported inner blade and through orifices in the shelf which are fed from a common cooling air annular supply chamber located within the inner ring assembly. The annular cooling air supply chamber is sealed from the hot gas passage with piston ring type seals located on the inside surface of the inner blade shelves and away from the hot gas passage. A similar sealing arrangement is used at the outer blade shelf location, and combustion chamber diluent air is used to cool the blade attachment. Blade shelf-to-shelf sealing is accomplished by close-fitting lap-joints. It should be noted that these methods of sealing have been successfully used by C-W on larger engine turbine stator blades.

Utilizing the previously mentioned thermal design data, a complete heat transfer analysis was undertaken, and the resulting blade section temperature distributions are presented in Section 4.2. Also included are the sizes of cooling air passage orifices whose locations are specified on the detailed blade design layout.

Stresses due to the aerodynamic loading of the rig stator blade airfoil are low and well within the 0.2 percent creep strength properties of the Inco 713 material (Figure 82) which has been selected for this application. Utilizing the airfoil temperature distributions discussed previously, thermal stresses were calculated and found to be acceptable for the expected turbine rig test and are discussed in Section 4.3.

As indicated above, the turbine rig stator blade spar will be cast of Inco 713 material, and either Ni55 or Ni V Cb skin materials can be utilized. These blade material combinations have been used by C-W in other applications, and no fabrication problems for this blade assembly are foreseen.

*Construction changed after initial tests. See Volume II.

Rotor blade airfoil pressure and velocity profiles were generated after completion of the passage analysis utilizing the aerodynamic passages discussed in Section 2.1; these data, along with the definition of the airfoil spar cross section, the gas inlet temperature profile, and the cooling air temperature and pressure, formed the necessary input data for the blade thermal design and heat transfer analysis. Since, in general, the turbine rig rotor blade airfoil is similar in size and shape to the cascade stator blade and turbine rig stator blade, a similar structural design of the spar was utilized. However, because the rotor blade rotates, the tip structure of the blade was reduced and the root structure was increased to provide an acceptable tip-to-hub structural area ratio and centrifugal stress variation. This modification did not appreciably affect the airfoil spar and airfoil design; therefore, the cooling air passages, the spar land width, and the airfoil trailing edge design could be made similar to the cascade blade and turbine rig stator. The final rotor blade airfoil structure is illustrated in Figure 83.

Utilizing the previously mentioned thermal design data, a complete heat transfer analysis was undertaken; the resulting blade section temperature distributions are presented in Section 4.2.

Stresses due to the aerodynamic loading of the rig rotor blade airfoil are low, but due to the high shaft speed, the airfoil centrifugal stresses considering the skin material as dead load are reasonably high. Airfoil steady-state stresses versus radius were calculated and are shown in Figure 84. When these stress levels are correlated with their respective temperatures, it can be shown that this blade design affords ample margins for the expected turbine rig test program. The Mar-M-302 material selected for this blade has excellent high-temperature properties, as shown on Figure 85. In addition, thermal stresses were calculated utilizing the above temperature distribution data and were found to be at an acceptable level for the rig test program scheduled.

The turbine rig rotor blade, as mentioned above, is made of cast Mar-M-302 cobalt-base alloy, and the skin material is made of N155 or Ni V Cb material. The choice of this blade spar material is based on test results at C-W which have shown it to be readily weldable to cast Inco 718 disc material, which will be discussed later. Although other nickel-base alloys would also provide an acceptable blade, these alloys present problems in EB welding to acceptable disc alloys. EB welding techniques in this area continue to progress, and it may be possible in the future to have an alternate material with improved life for the turbine rotor blade. The fabrication techniques for the selected rotor blade materials are established, and no problems are foreseen in manufacturing these parts as designed.

4.1.3 Turbine Rotor Assembly

Early in the design of the turbine rig, it was decided that the rotor blade cooling air system should be as leakproof as possible. In other words, it should limit the possible points through which cooling air could leak from the system and thereby reduce the cooling air weight flow to that which was actually required to cool the blade. It was decided that a split disc

arrangement could best fill this requirement. Thus, with the cooling air exiting at the OD of the split disc system, each blade was fitted with a shelf cavity for the purpose of supplying air directly to the airfoil coolant passages by means of metering orifices located in the shelf region of the blade.

Initial turbine rotor assembly configurations incorporated a circumferential two-tooth, fir-tree, and bolted split disc configuration (Figure 86). Design stress analysis of this arrangement soon indicated that a fir tree with high tooth pressure angles rotating at the design shaft speed would cause excessive separating loads on the two disc attachment rims. These loads would then in turn cause failure of the bolts holding the disc halves together.

Still attempting to retain a circumferential fir-tree configuration, an arrangement was designed to reduce the fir-tree pressure angle and thereby limit separating loads on the two disc attachment rims, (Figure 87). Stress analysis of this configuration indicated that the fir tree with a little more material would work, but that the centrifugal loading of the disc rim was excessive and required a great deal of additional material to reduce the disc rim bending stresses to acceptable limits; see Section 4.3. In view of the large amount of material at the disc rim required to make this configuration acceptable, it was decided to investigate other design approaches for the following reasons:

1. High assembly weight
2. Design of adjacent structure complicated by large assembly cross section
3. Complication of supplying cooling air to stator blade

With the development of the design complexities of the circumferential fir-tree turbine rotor assembly configuration, attention focused on alternate approaches. One of the most direct methods of attaching blades to a disc is to integrate the blade and disc into a single unit weldment. A survey was made of blade and disc alloys capable of withstanding the high temperatures of the application, and the most promising combinations were EB welded. In general, the nickel-base super alloys presented more problems than the cobalt-base super alloys. From many possible materials, two combinations emerged as the best for this application: Mar-M-302 cast blade with Inco 718 cast disc and Inco 713 cast blade with Inco 718 cast disc. The former combination has been selected for the initial turbine rotor assembly, while the latter requires more welding development, but expectations are that eventually these materials will provide an improved turbine rotor assembly. Welding of the selected materials has been accomplished successfully with excellent results, and work has progressed toward perfecting the weld joint for the initial turbine rotor assembly.

After selection of a blade-disc welded attachment design, final disc stresses were obtained utilizing an average radial thermal gradient for the disc (Figure 88), which was based on heat transfer analysis of the final blade-disc configuration discussed in Section 4.2. The final disc stresses are presented in Figures 89 and 90. Fabrication of this turbine rotor assembly (shown in Figures 91 and 92) will require little development to accomplish the EB welding of the blades to the disc rim, except in the area of fixturing. The methods for fabricating the blade and disc details are well within the state of the art, as demonstrated by the successful work accomplished on the cascade prototype blades during the Phase I period.

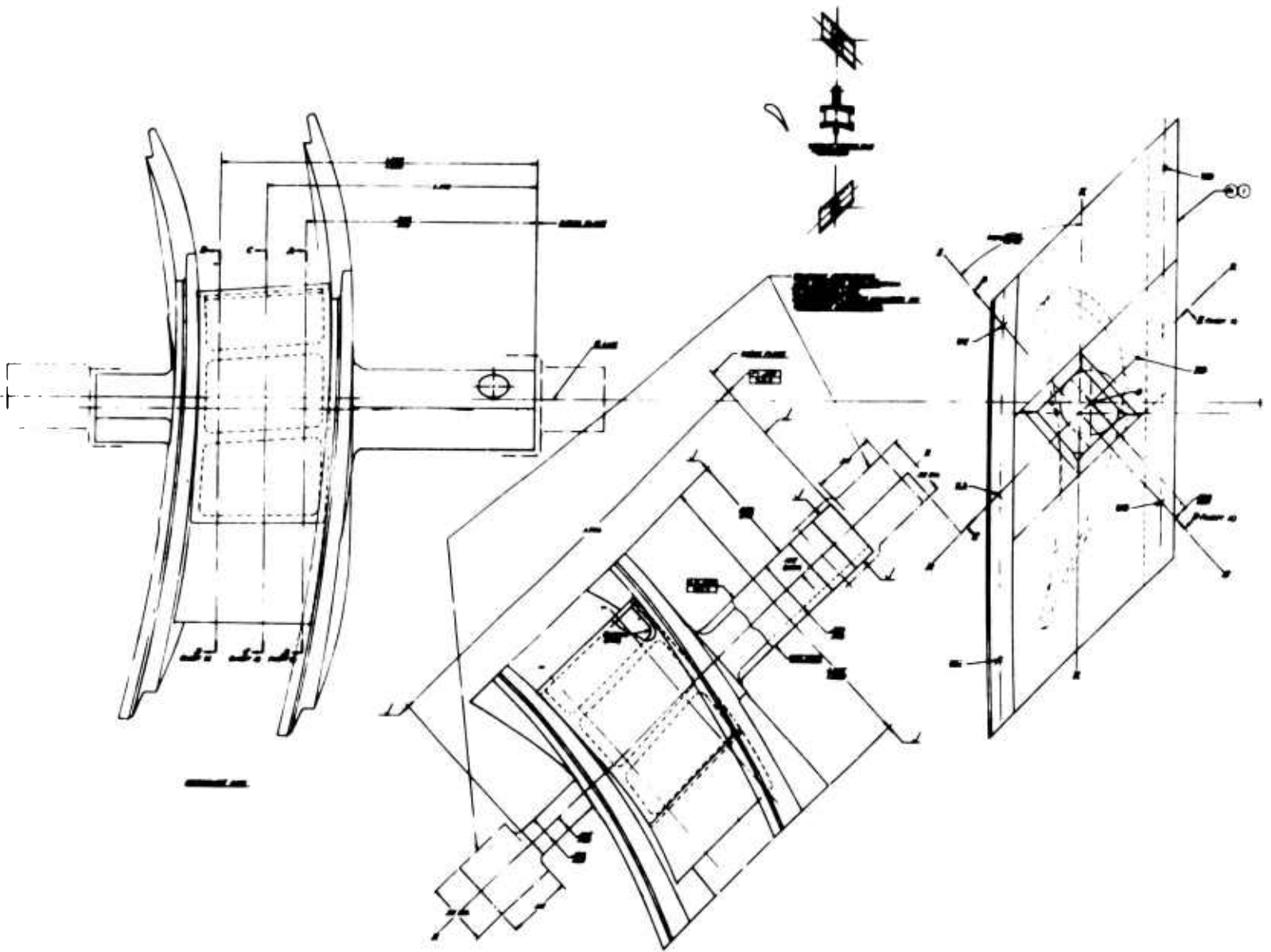
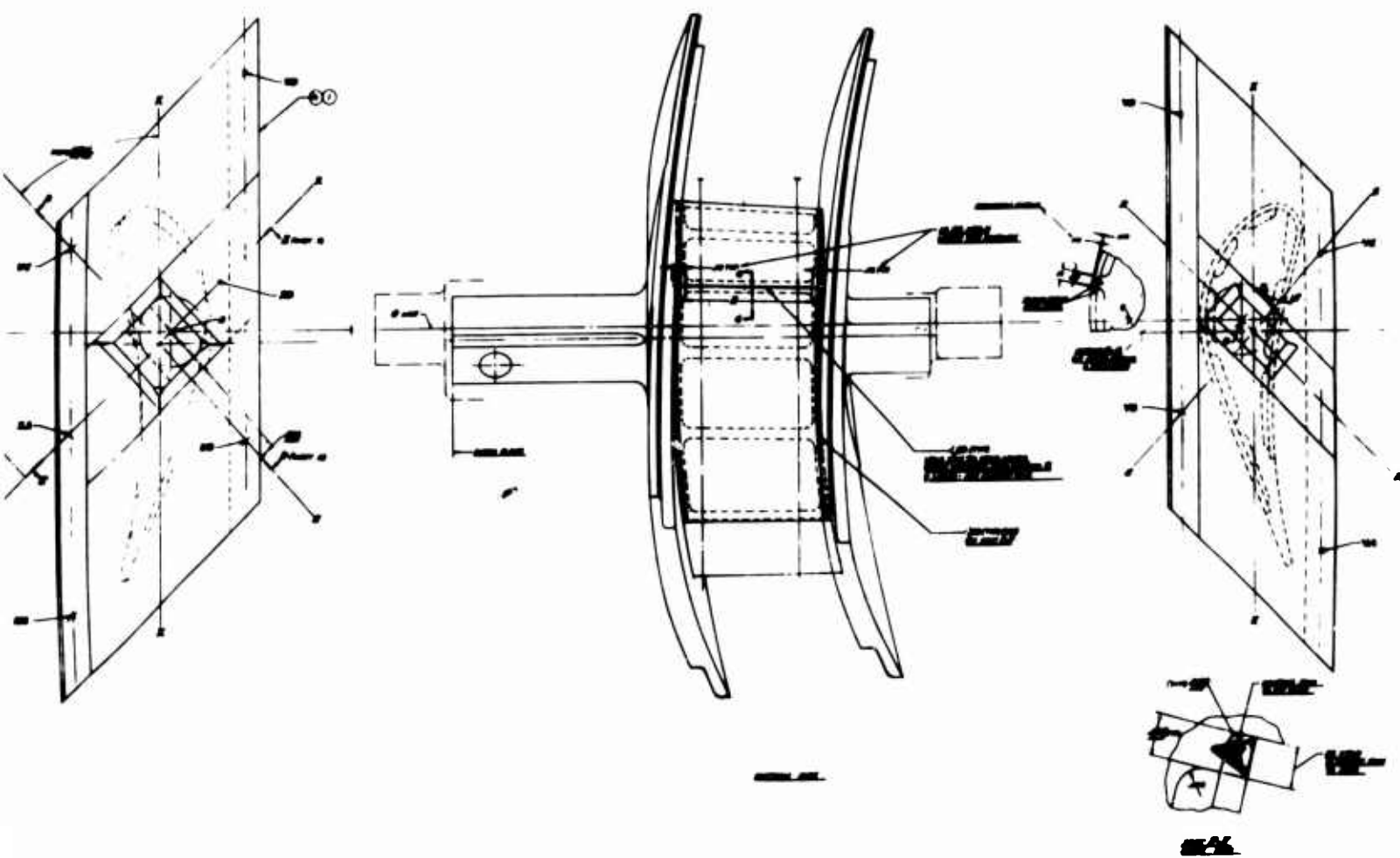


Figure 81. Stator Blade Airfoil Structure.

A

165

NOT REPRODUCIBLE



B

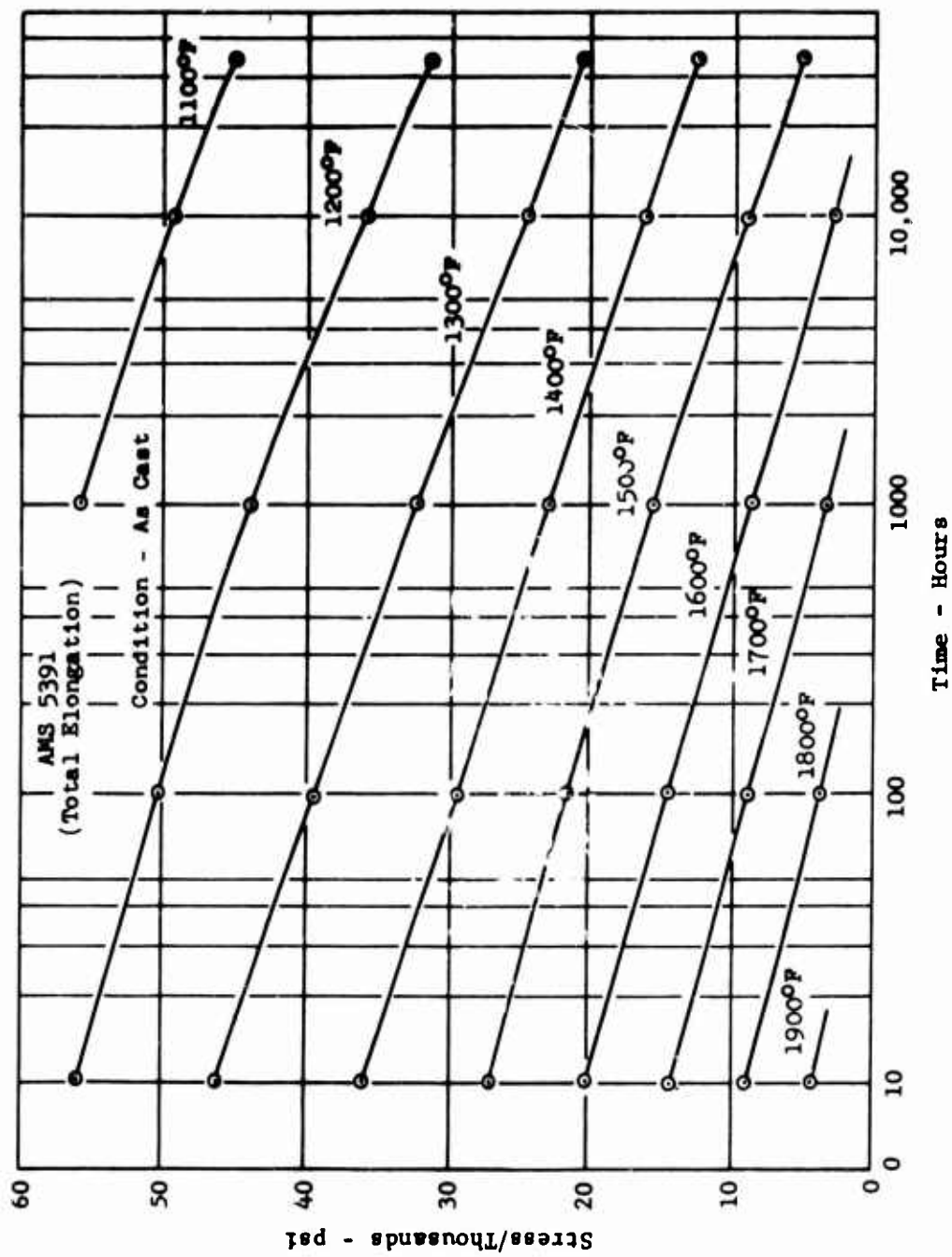


Figure 82. Average 0.2 Percent Creep Properties of Inco 713C Casting.

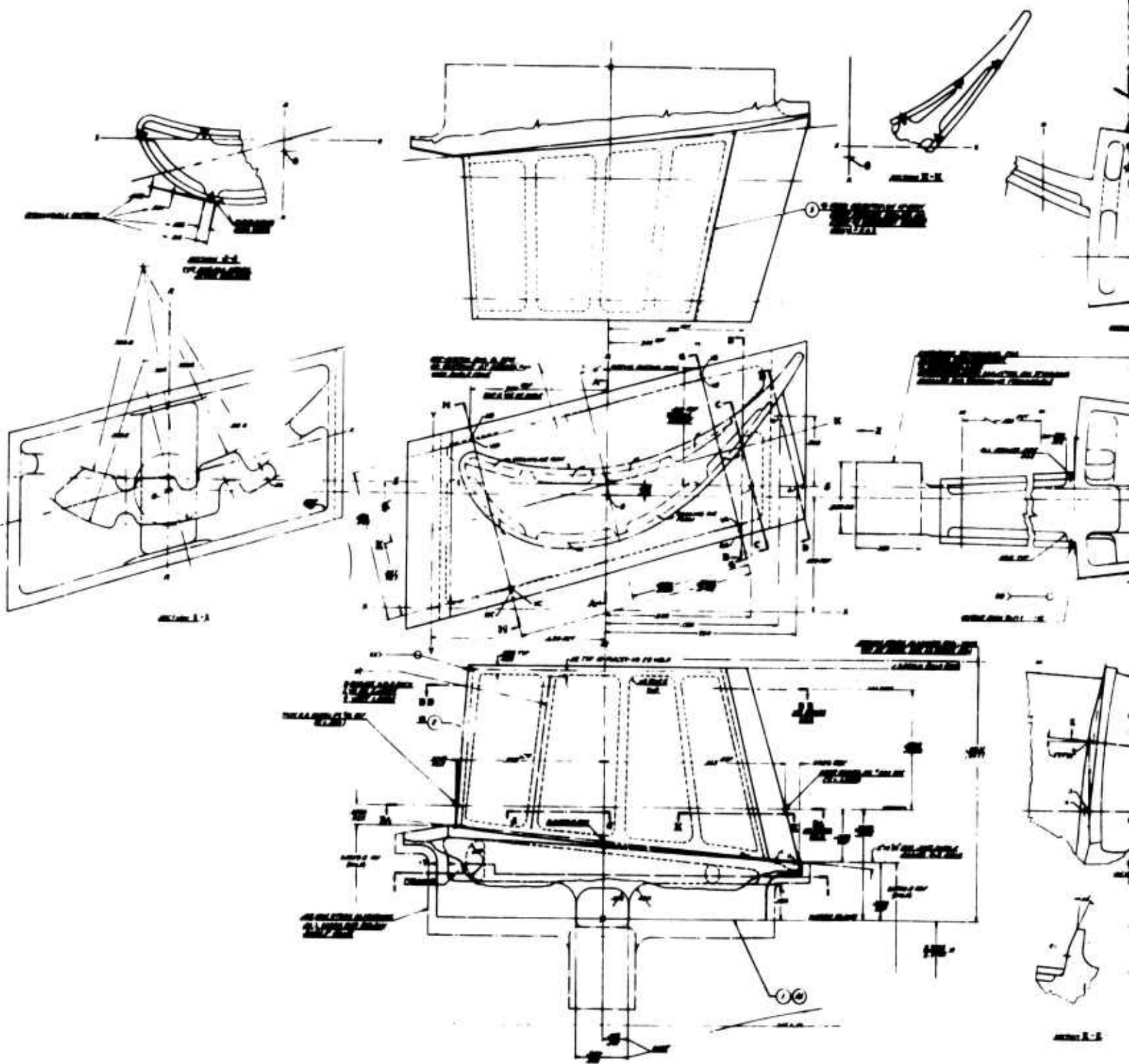
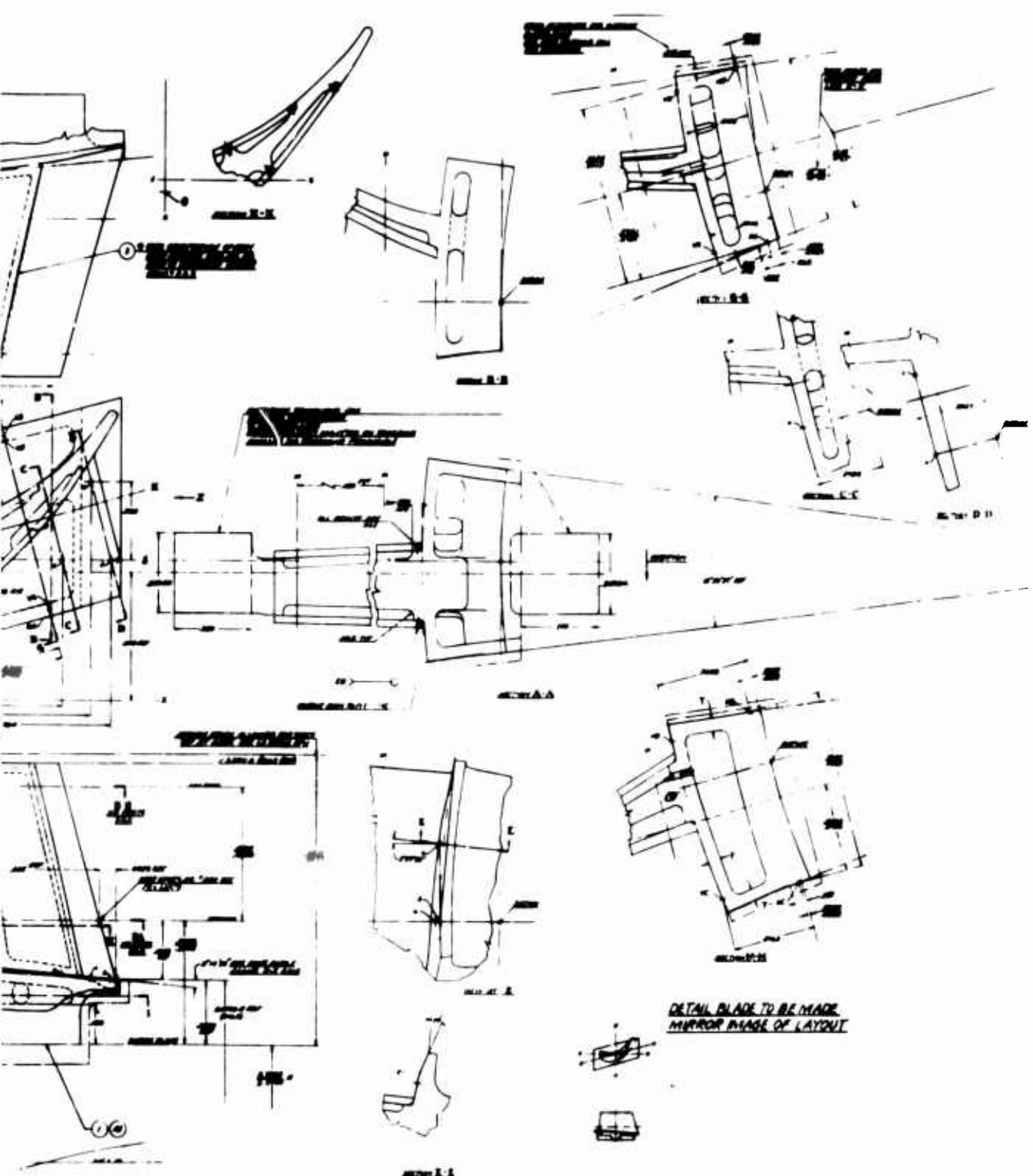


Figure 83. Rotor Blade Airfoil Structure.



5

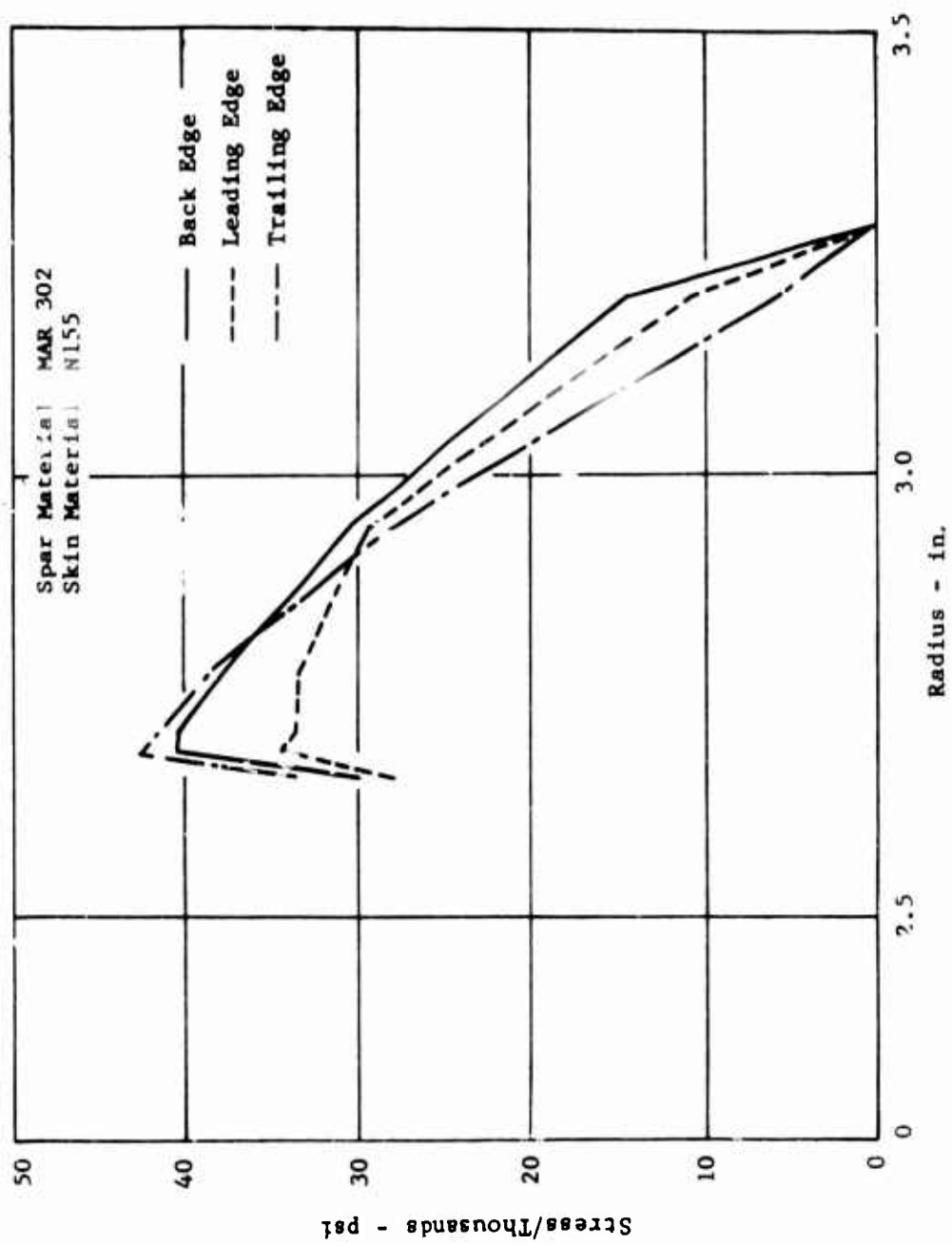


Figure 84. Rotor Blade Airfoil Steady-State Stresses Vs Radius.

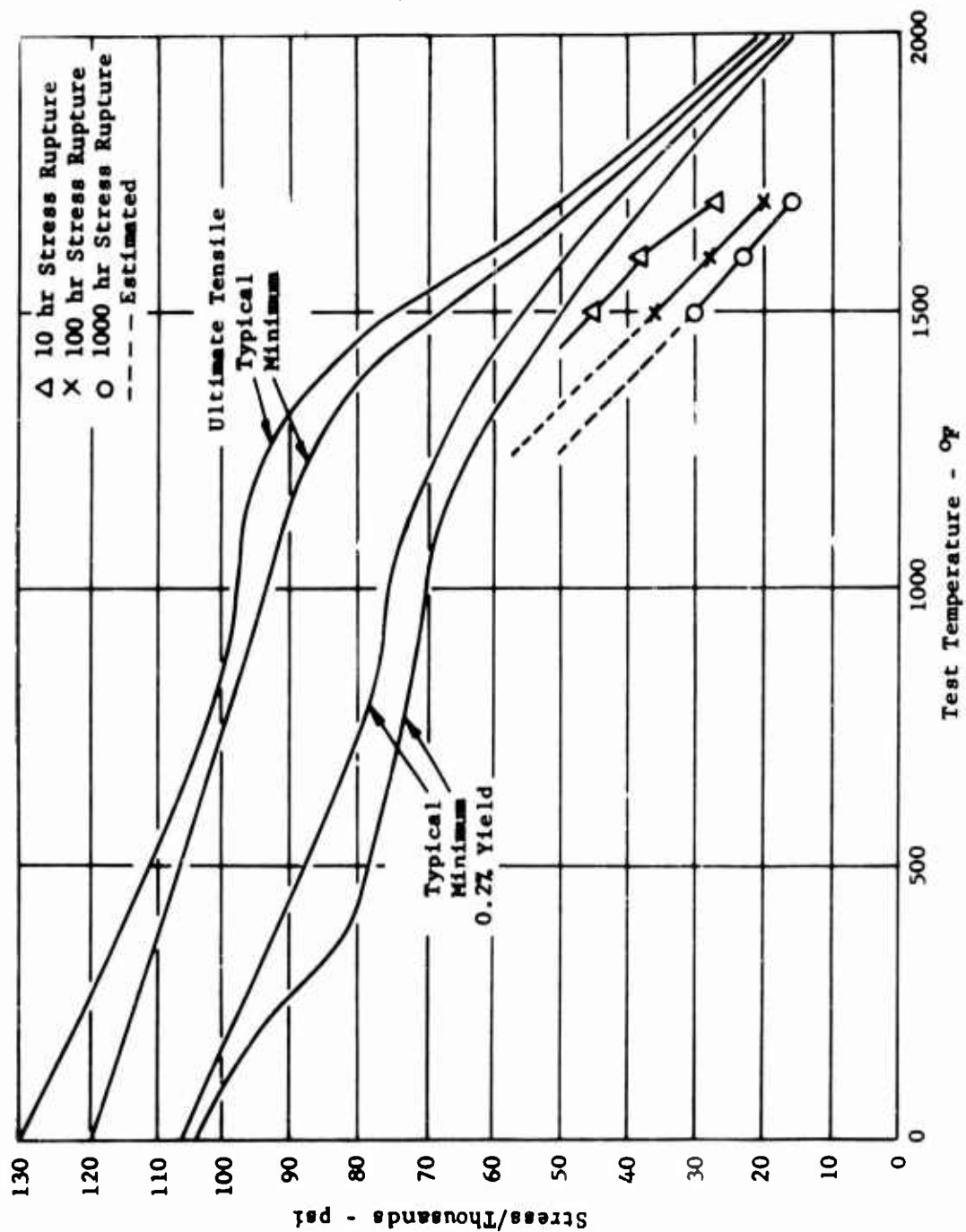


Figure 85. Mechanical Properties Mar-M-Alloy 302.

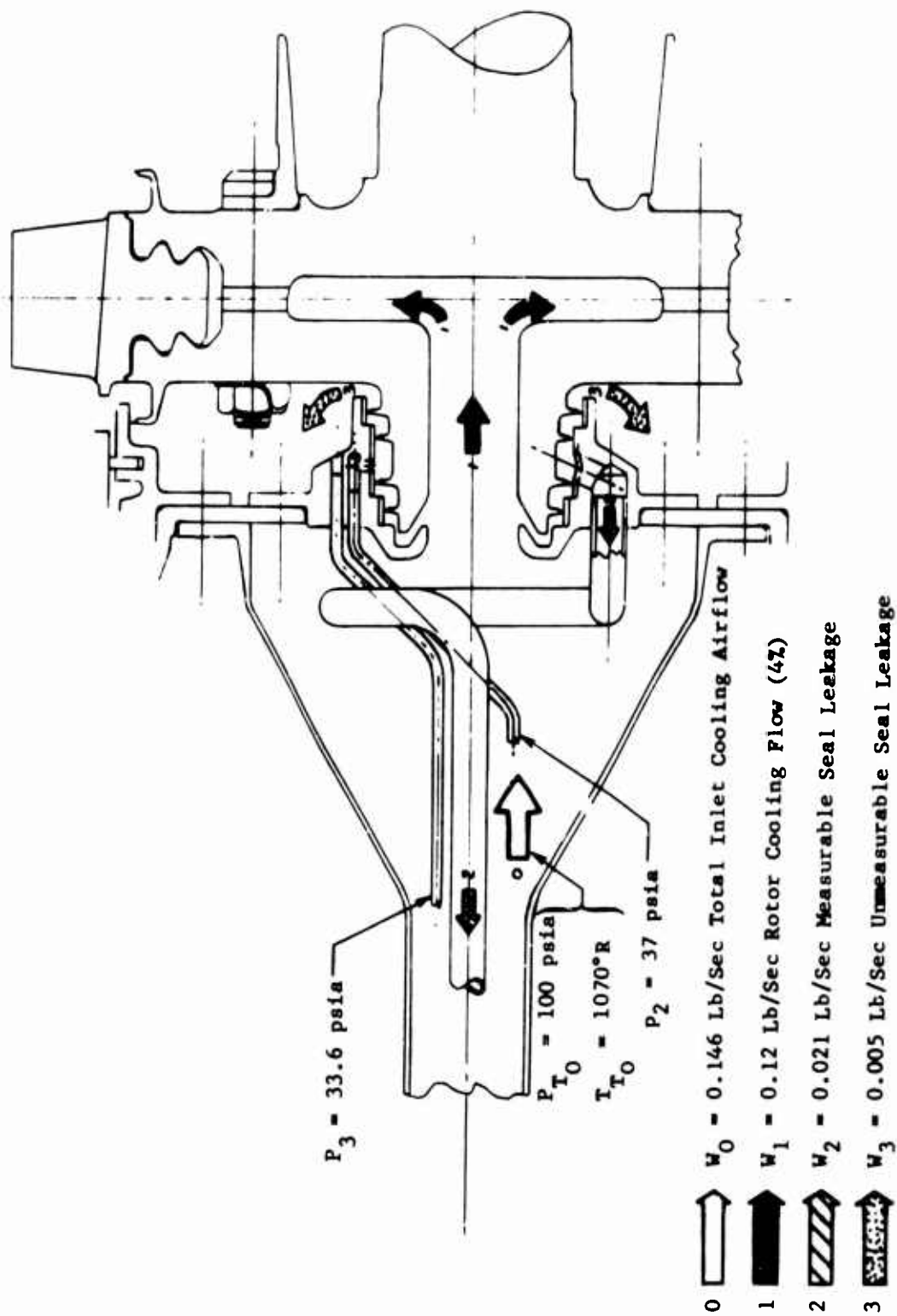


Figure 86. Rotor Blade Cooling Airflow System.

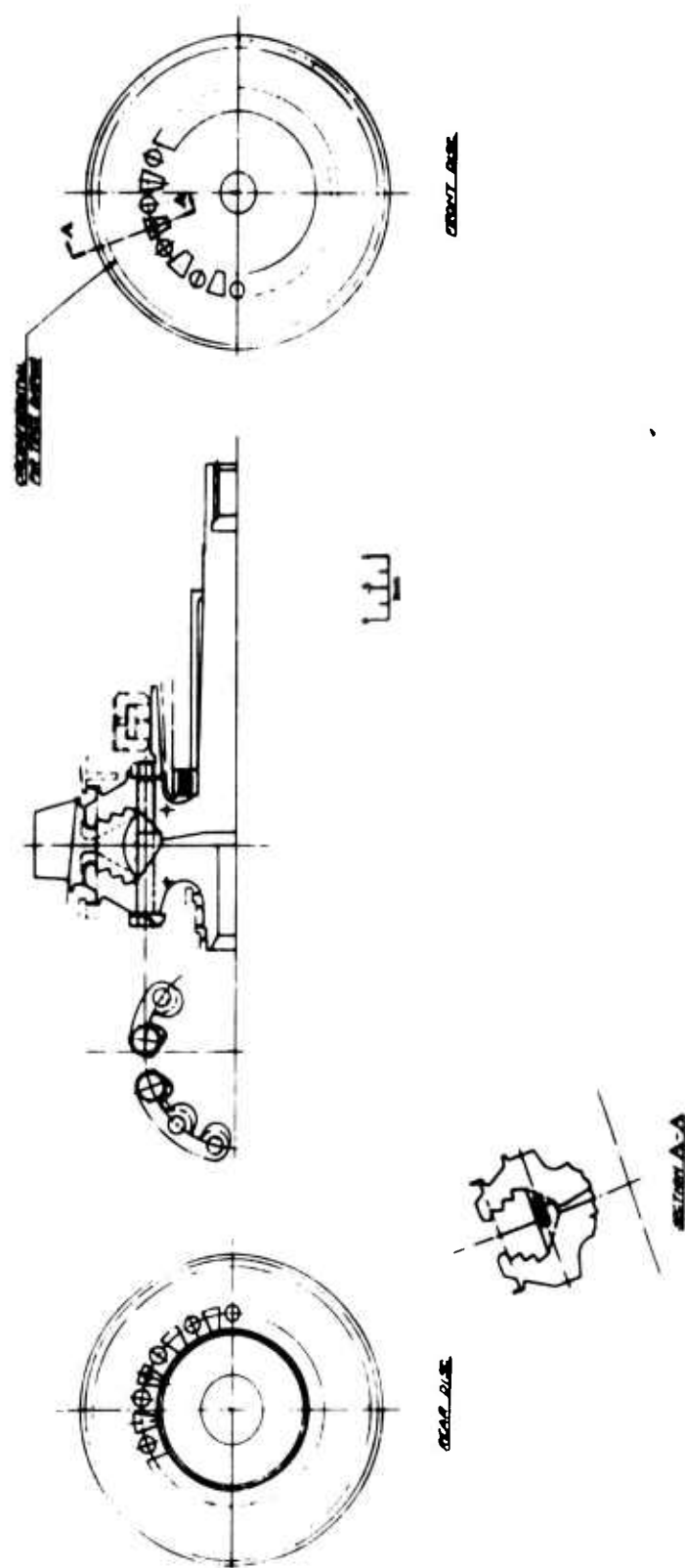


Figure 87. Blade and Disc Assembly.

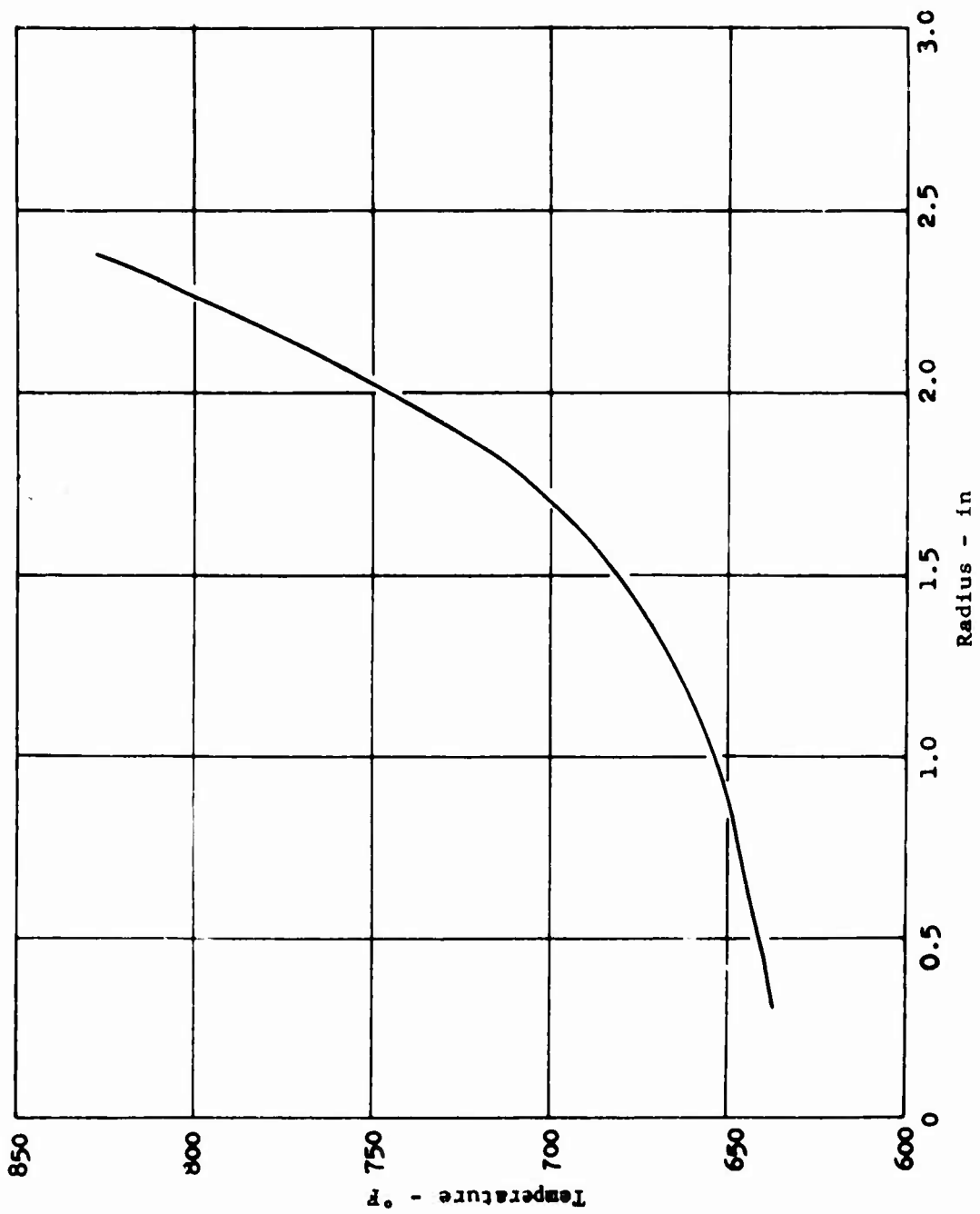


Figure 88. Disc Thermal Gradient Vs Radius.

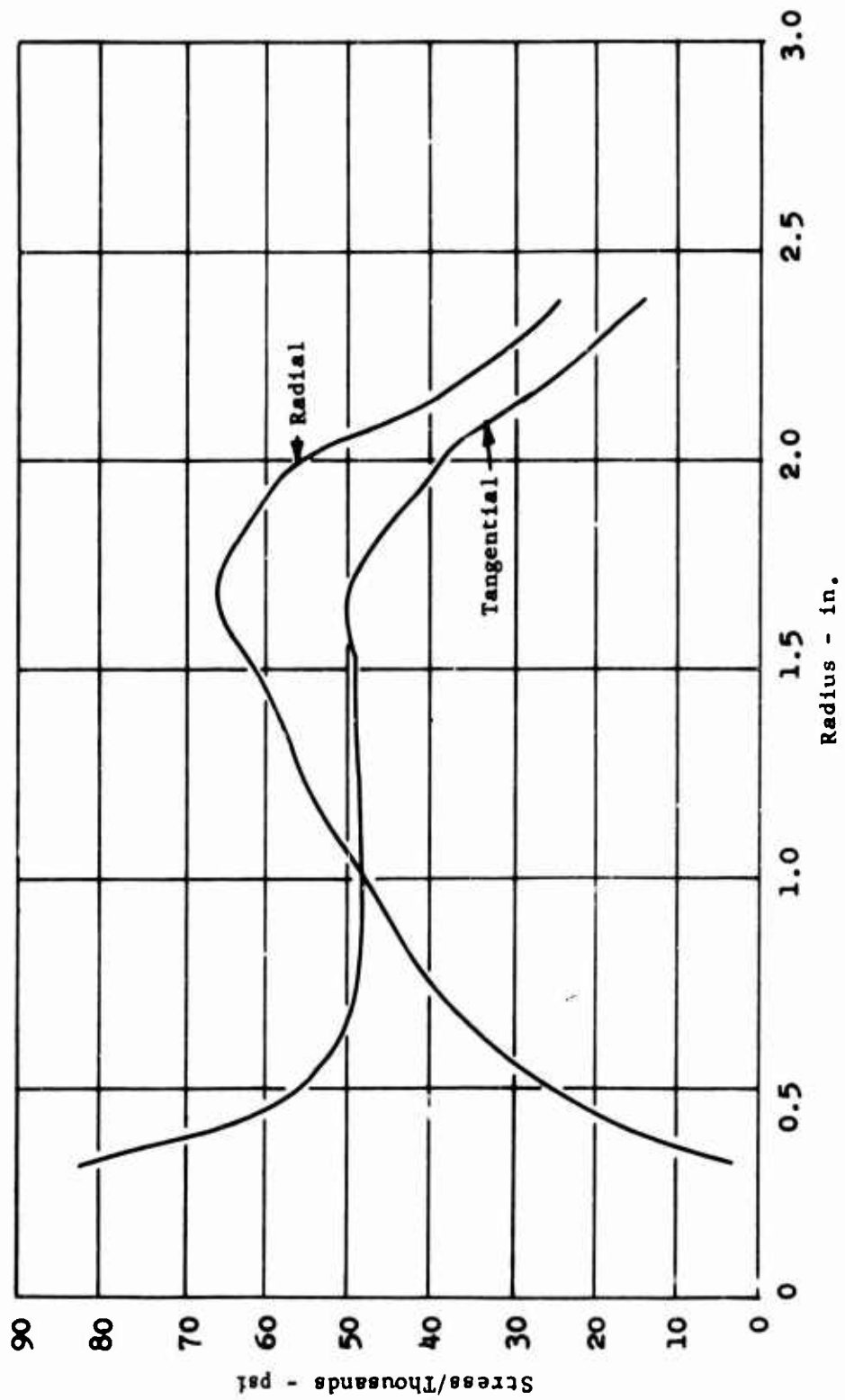


Figure 89. Disc Combined Elastic Stress Vs Radius.

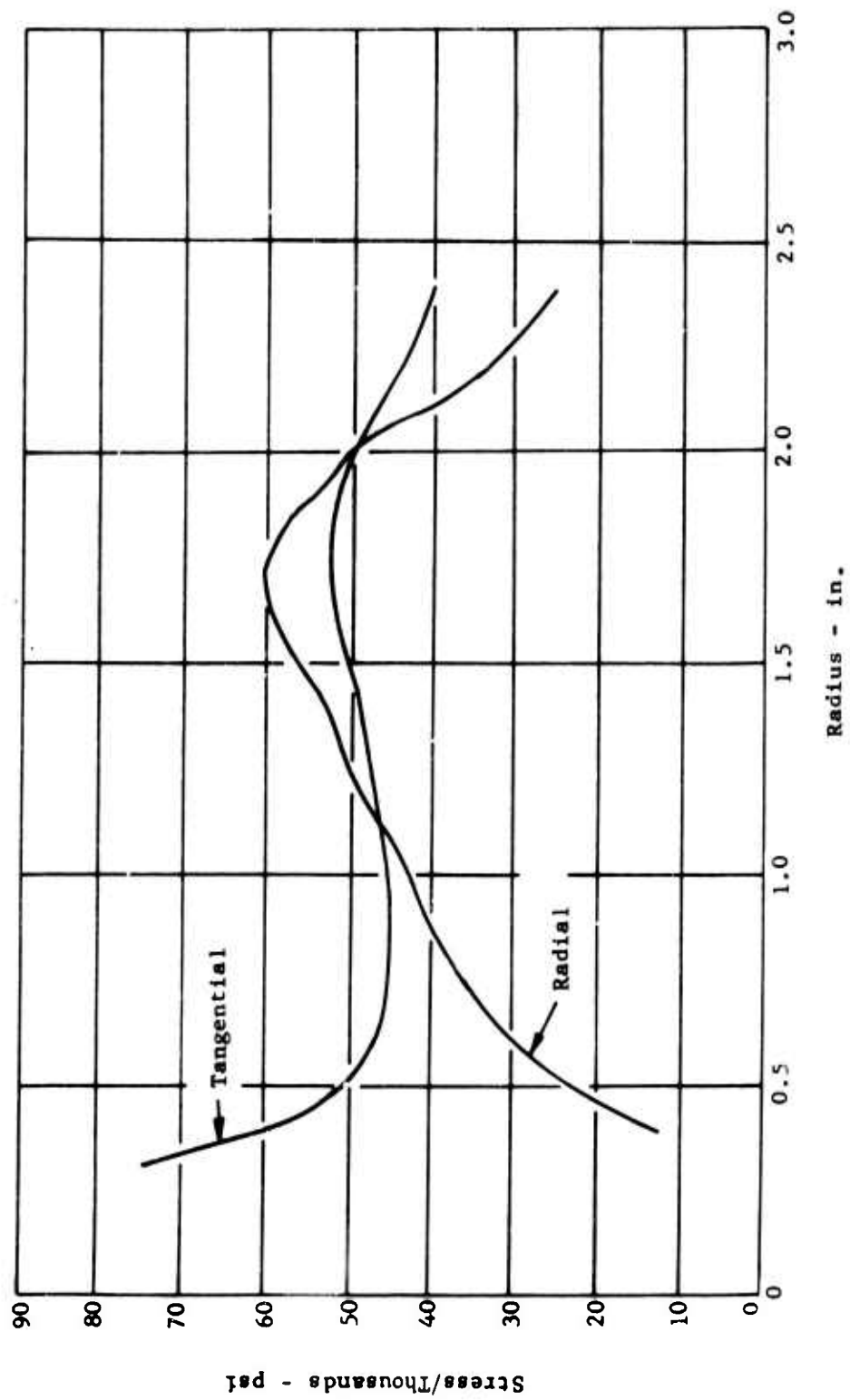
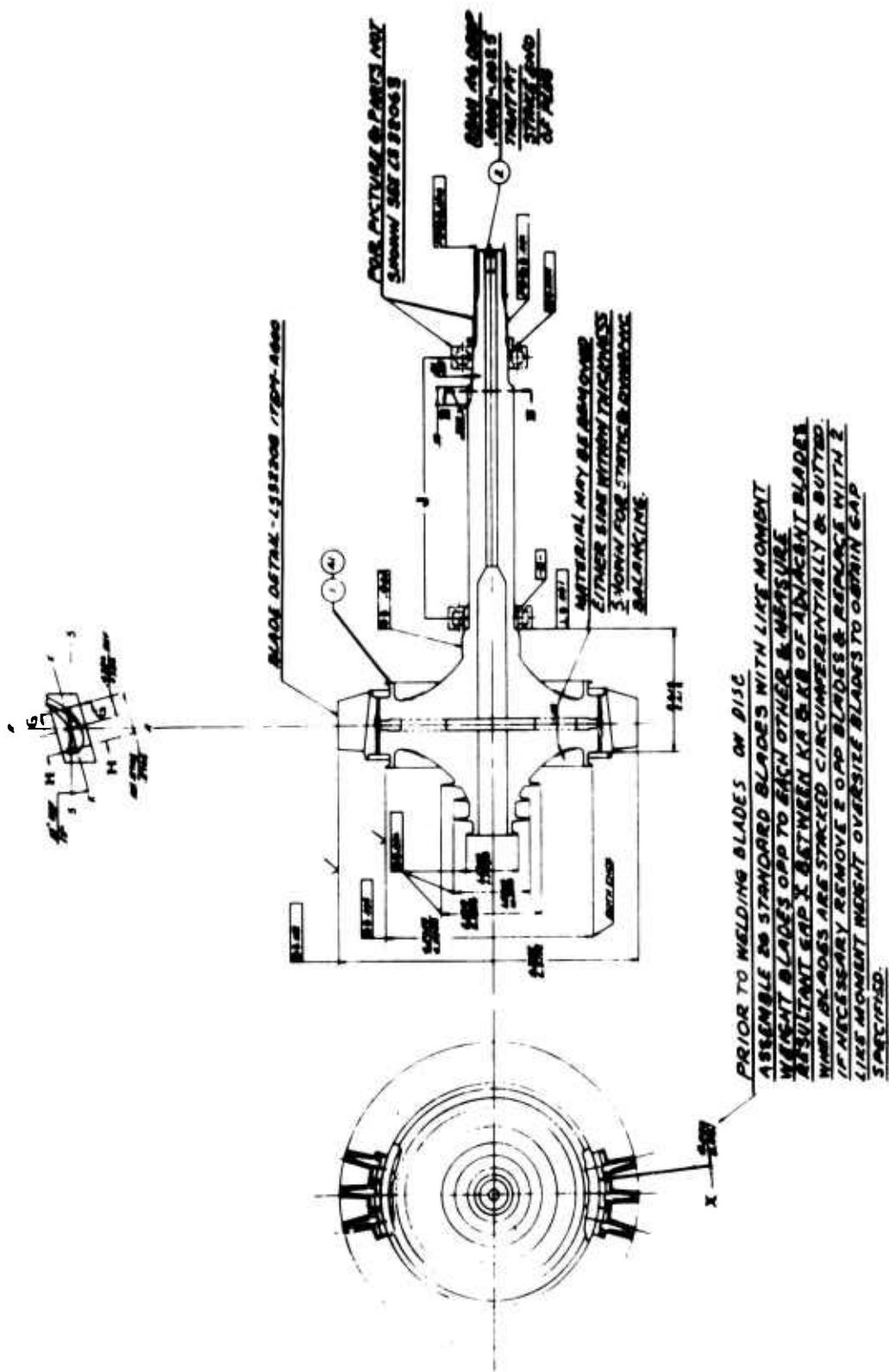


Figure 90. Disc Centrifugal Elastic Stress Vs Radius.



BB

~~NO NEW STUDY ALLOWANCE~~
~~ADDITIONAL ALGOS~~
~~NO NEW STUDY ALLOWANCE~~

AS CAST

CLARENCE
FRANKLYN JENCKA
(ALCANT)

ION. A-B

15

4.2 THERMAL ANALYSIS

4.2.1 Turbine Rotor Disc and Shaft Assembly

A thermal analysis was performed for the turbine rotor disc and shaft assembly to determine the temperature distributions in the various areas of concern. This information is required for determining the thermal stresses involved due to the resulting temperature gradients and for dimensioning the critical parts for operation at the design turbine inlet temperature of 2500°F.

The analysis was performed with the aid of an IBM computer and the following conditions:

1. Disc and shaft configuration are shown on Figure 93.
2. Turbine test rig assembly are shown on Figure 31.
3. Materials of construction are:
Disc and shaft - Inco 713 LC
Rotor blade and shelf - Mar-M-302
4. Rotor blade cooling air is supplied at 610°F.
5. Rear cavity cooling air is supplied at 610°F.
6. The predicted heat rejection rates are 46 Btu/minute from the #1005 roller bearing, 70 Btu/minute from the #1004 ball bearing, and 10 Btu/minute from the CGB#B-103020 seal. Oil enters the bearings at 150°F and leaves the roller bearing and the ball bearing at 196° and 197°F respectively.
7. Leakage flow past the front lower labyrinth seal configuration on the upstream side of the disc is 0.00289 pound/second, and 0.35 pound/second of coolant impinges on the downstream face of the rear outer labyrinth seal of the disc.
8. Disc has a normal running speed of 50,000 rpm.
9. Cooling air for the rotor blades (0.004866 pound/second/blade) flows through the hollow disc and past an impeller blade which increases the rotor blade cooling air pressure moderately.
10. The coolant temperature remains constant; that is, the coolant is neither heated nor cooled by contact with the disc and shaft. This assumption was found to be quite good and has been checked by means of an energy balance which indicated that the temperature of the coolant varied by less than 5°F.

11. The coolant temperature rise past the impeller is negligible.
12. Axial conduction across the impeller blades is negligible.

The configuration analyzed is shown on Figure 93. This drawing also locates the bearings and seals in the assembly and shows the areas in which cooling air makes contact with the assembly. Figures 94 and 95 show the detailed temperature distributions for the turbine rotor disc and the rotor shaft respectively.

Figure 96 describes the variation in disc temperature relative to the distance from the vertical or radial centerline for selected locations along the horizontal or axial centerline. This figure clearly indicates the small axial thermal gradients that exist in the design and verifies assumption number 12 above.

It was found also that the thermal gradients are a maximum at the outer radius of the disc and decrease toward the disc centerline (Figure 97). This is as expected, since the major heat input to the disc comes through the rotor blade attached at the disc outer diameter. A final thermal network system was employed in this region to obtain the desired thermal definition.

4.2.2 Rotor Blade

Various objectives for the thermal design of these transpiration-cooled blades are specified in order to provide the required blade life while operating in the anticipated high-temperature environment and are listed below for reference:

1. Maintain temperatures in the blade skin at or below 1300°F.
2. Maintain uniform blade strut temperatures at or below 1350°F except for the exposed trailing-edge region, where the maximum permissible temperatures are limited by the allowable stress levels of the materials being used.
3. Maintain the blade tip at or below 1500°F.
4. Maintain the blade shelf at or below 1400°F.
5. Determine the coolant distribution and minimum amount of cooling air necessary to meet the above objectives.
6. Specify cooling air orifice sizes necessary to achieve the required coolant flow distribution.

The framework within which the thermal design was established is detailed below:

1. Rotor blade configuration, Figure 83.

2. Turbine test rig rotor blade and disc assembly, Figure 92.
3. Turbine test rig assembly, Figure 31.
4. Materials of construction:
 - Blade strut, tip and shelf - cast Mar-M-302
 - Blade skins, N155 and N1 V Cb
5. Porous skin 0.020 inch \pm 0.002 inch thick with a uniform permeability of 3.6×10^{-11} square inch.
6. Main gas stream velocity and pressure distribution external to the blade as discussed in Section 2.1.
7. Main gas stream turbine inlet temperature profile, Figure 100.
8. A nominal engine speed of 50,000 rpm.
9. Coolant air supplied clean and particle free, at 75 psia and preheated to 610°F.
10. Cooling air leakage flow at leading edge of shelf 0.0001' pound/second/blade and leakage flow at rotor shroud of 0.0029 pound/second.

Figure 98 shows the required coolant flow distribution and the coolant passage orifice sizes, assuming round orifices, necessary to obtain this distribution. The orifice sizes are calculated on the basis of compressible flow theory with discharge coefficients for round orifices based on experiments performed at C-W during Phase I and reported previously. If slots are substituted for round orifices, actual values of discharge coefficients will need to be determined experimentally and the orifice sizes will need to be adjusted in order to maintain the specified flows to each channel.

Figures 99, 100, and 101 show detailed temperature distributions for the hub, mean, and tip sections of the blade; the relative rotor blade gas temperature profile; and the blade section location. These figures indicate that, with the exception of the stagnation point and the trailing edge, the blade's thermal objectives have been achieved. At the trailing edge, the temperatures as shown in Figures 99, 100, and 101 could have been reduced further, but the large coolant flows needed to obtain lower temperatures would have required excessively large flow areas and would have weakened the blade structurally.

The high temperatures at the leading edge are due to the fact that near the stagnation point, the heat transfer coefficient is very large and the blade is unable to maintain a sufficient film blanket layer of transpired coolant to protect the blade from the hot combustion gas. In addition, the leading edge land is larger than usual due to the double EB weld, thereby exposing a relatively greater amount of surface area to the hot gas. In order to decrease the temperatures in this region using the present design, a

substantial increase in coolant flow to Passages 1 and 8, which are on either side of the leading edge land, would be needed.

Figure 102 shows the airfoil metal temperature around the periphery of the blade for the hub, mean, and tip sections as a function of distance from the leading edge. The low temperatures obtained at approximately 1.3 inches from the stagnation point on the suction side (775°F) and 0.85 inch from the stagnation point on the pressure side are due to the large amount of coolant transpired through Passages 4 and 5, Figure 98 respectively, in order to cool the trailing edge of the blade. Figure 103 shows the variation in strut temperatures along a mean camber line for all three design sections.

The temperatures for the blade tip and shelf sections shown in Figures 104 and 105 are dependent primarily on the gas boundary layer temperature. On the blade tip, a gas boundary layer temperature of 1500°F around the periphery and 1350°F at the tip can be expected. The 1350°F at the tip includes the effect of the 1 percent (0.0029 pound/second) of coolant injected in order to help cool the turbine rotor shroud. The gas boundary layer temperature at the shelf (1300°F) is influenced by the 0.1 percent coolant leakage (0.000289 pound/second) past the front inner lab seal configuration of the rotor disc assembly.

4.2.3 Stator Blade

The heat transfer analysis of the stator blades determined the coolant flow orifice sizes needed to maintain temperatures and the temperature gradients of the blade porous skin and its strut material within allowable limits, when using a minimal amount of coolant. The various objectives for the blade thermal design which are specified to provide the required blade life while operating in the anticipated high temperatures are as follows:

1. Maintain porous skin temperature at or below 1300°F.
2. Maintain strut and shelf temperature at or below 1500°F.
3. Maintain strut temperature gradients small enough to keep thermal stresses within allowable limits.
4. Find the flow of coolant required in each channel to meet objectives 1 through 3.
5. Size each channel orifice to pass the required coolant flows.

The parameters under which the thermal design was established are listed below:

1. The blade configuration is as shown on Figure 81.
2. The rig engine assembly is as shown on Figure 31.

3. The metal used for strut, shelves, and tangs is cast Inco 713 and in the porous skin, Ni V Cb.
4. The porous skin is 0.020 inch \pm 0.002 inch thick and has a permeability of 3.6×10^{-11} square inch.
5. Hot gas velocity and pressure distributions around the blade are illustrated in Section 2.1, Figures 12 and 13.
6. Hot gas radial temperature profiles for the average temperature conditions and for the anticipated maximum temperature conditions are shown on Figure 109.
7. Cooling air is supplied upstream of the blade entrance orifices at 100 psia and 610°F.
8. Any air leakage at shelf seals or between blade shelves is not included in this analysis.
9. Pressure loss coefficients, for the flow through the blade entrance orifices, are determined from experimental data. This is true of all of the orifices, except the large noncircular one for channel 3, Figure 106. The velocity through this orifice is low enough so that the orifice loss is negligible.
10. Temperature effects due to radiation from the combustion chamber flame and walls are assumed to be negligible. With a luminous flame, the "viewing angle" with which the blade "sees" the flame front affects the amount of radiation to the blade. With proper burner construction, the flame front ends well upstream of the inlet to the blades, making this "viewing angle", and consequently, the luminous radiation effects are relatively small.

In this analysis, the temperatures of the hot gas flowing past the nonporous sections of the blade represented by the skin attachments are lower than the main stream gas temperature because of the effect of the film blanket layer from the immediate upstream transpiration section. For the nonporous trailing edge, the gas stream temperatures are lower not only because of the film blanket layer from the transpiration sections immediately upstream of the trailing portion of the blade (Passages 4 and 5, Figure 98), but also because of the film blanket layer from the next preceding upstream sections (Passages 3 and 6). The decrease in the hot gas temperature due to the blanket layer from Passages 3 and 6, however, is small compared to the decrease due to blanket layer from the immediate upstream Passages 4 and 5.

Using this analysis in conjunction with the parameters previously stated, it was determined that the original blade material, René 41, experienced temperatures and temperature gradients with consequent thermal stresses that would induce premature blade failure. Changing to cast Inco 713 for the strut, shelf, and tang material resulted in acceptable, allowable stresses.

The analysis of the stator blades yielded the following results which are consistent with the objectives previously enumerated. The porous skin temperatures are all below the 1300°F maximum allowable. The strut material is below the 1500°F level stipulated for this material except for two sections, one near the leading edge and one near the trailing edge where the temperature is somewhat higher. However, these conditions did not produce excessive thermal stresses due to thermal distortions and have been accepted for this design. The cooling air requirement, at the specified conditions which include the extreme gas temperature gradient assumed for all blade locations, is 0.008147 pound/second/blade, which is a total of 0.01874 pound/second for the 23 stator blades. This is 6.22 percent of the total engine airflow of 3.01 pound/second.

Figure 106 shows the required coolant flow distribution and cooling passage orifice sizes to achieve this result. The orifice sizes are based on the test results of Reference 10.

The blade temperature distributions given for both the maximum and the average combustor exit profiles are given on Figures 107 and 108. These profiles are discussed below. The higher temperatures at the leading-edge portion of the blade are due mainly to the land proximity to the stagnation point, where the heat transfer rate is very large and the land is unprotected by a film blanket layer of transpired coolant. In addition, the leading-edge land is larger than the center-body lands due to the double EB weld, thereby exposing a relatively greater solid surface to the hot gas.

The higher temperatures in the trailing-edge portion of the blade are due to the large solid areas which are protected from the hot gas only by a film blanket layer of transpired coolant. The coolant flows to Passages 3 and 4 which are on either side of the trailing edge, have increased to thicken and extend this film blanketing layer.

The combustor is characterized by having circumferential temperature peaks at various circumferential locations. These peaks form the maximum temperature conditions which the blades are expected to experience. Rotor blades run through all circumferential conditions fairly rapidly, and average conditions prevail for all rotor blades. Unlike rotor blades, the stator blades must operate continuously in whatever circumferential location they are placed, and those in a location where maximum conditions exist must be designed to withstand these conditions. The maximum and average temperatures assumed for stator design are shown in Figure 109. Combustor work is in progress to alleviate or eliminate the circumferential hot regions.

The shelf temperature distributions are shown in Figures 110 and 111 for the maximum temperature conditions and in Figures 112 and 113 for the average temperature conditions.

Tang temperatures are shown in Figure 109. A negligible difference in the metal temperatures shown results from using either the maximum temperature condition or the average temperature condition. Figure 114 shows the variation of representative metal node temperatures with shelf gas temperature at average combustion exit conditions. These curves indicate an upper limit of 1685°F for the gas boundary layer if the maximum shelf temperature is to be 1500°F.

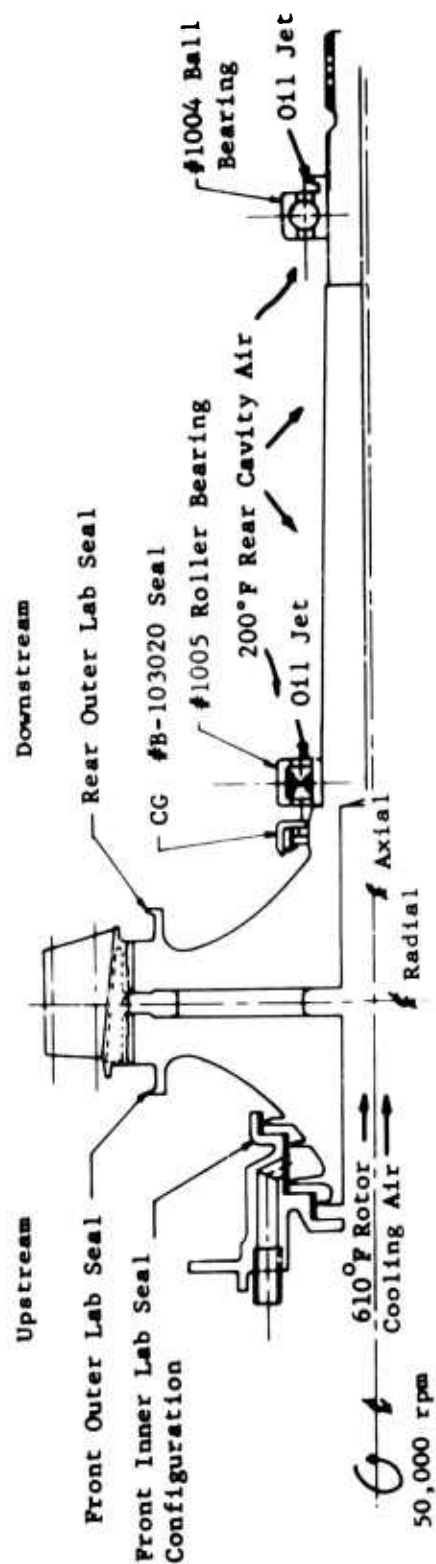


Figure 93. Turbine Test Rig - Rotor Blade Disc Assembly.

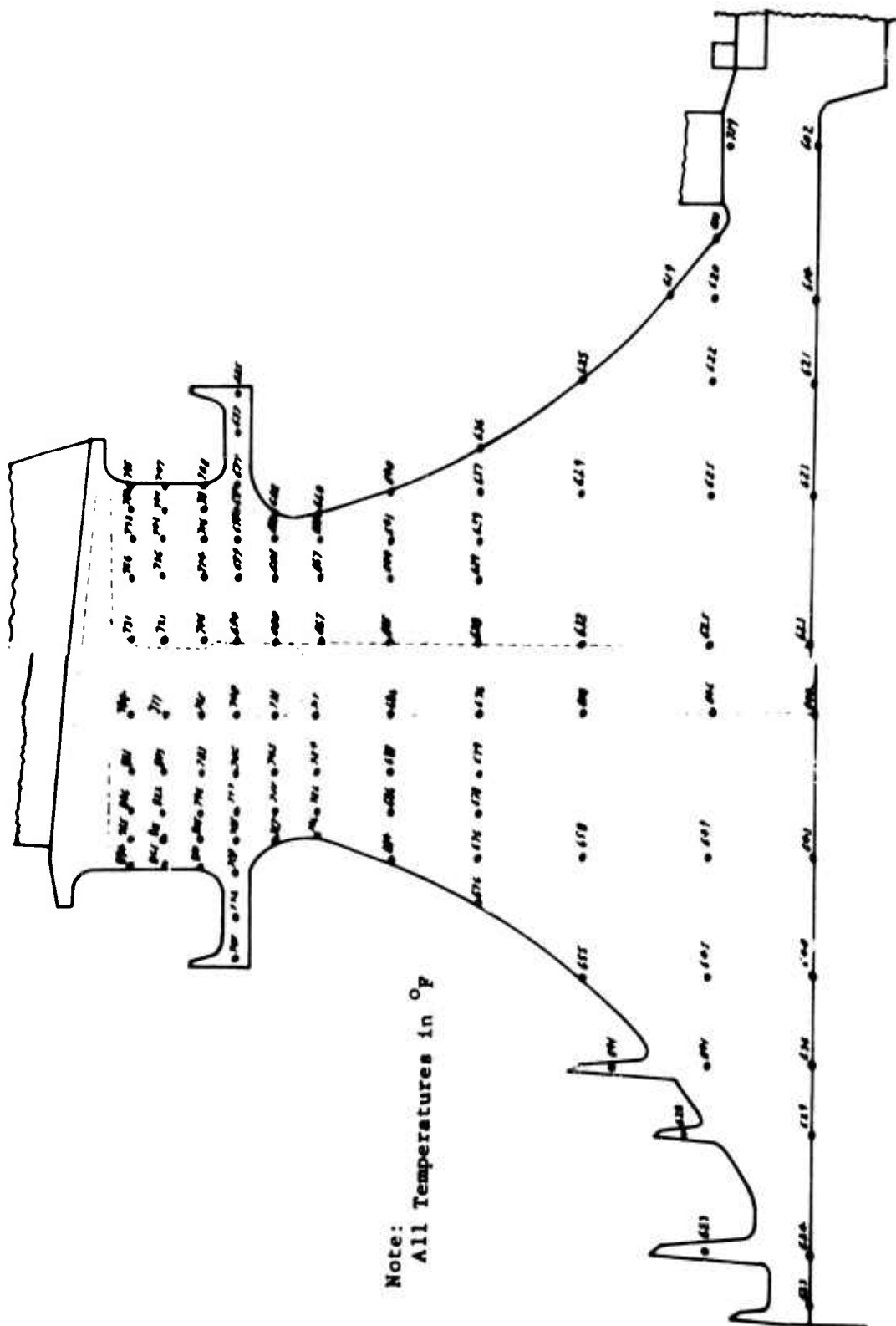
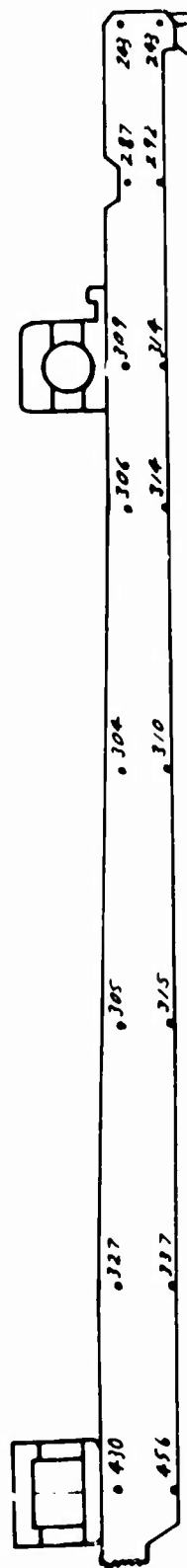


Figure 94. Temperature Distribution in Turbine Rotor Disc.



Note:
All Temperatures in °F

Figure 95. Temperature Distribution in Turbine Shaft.

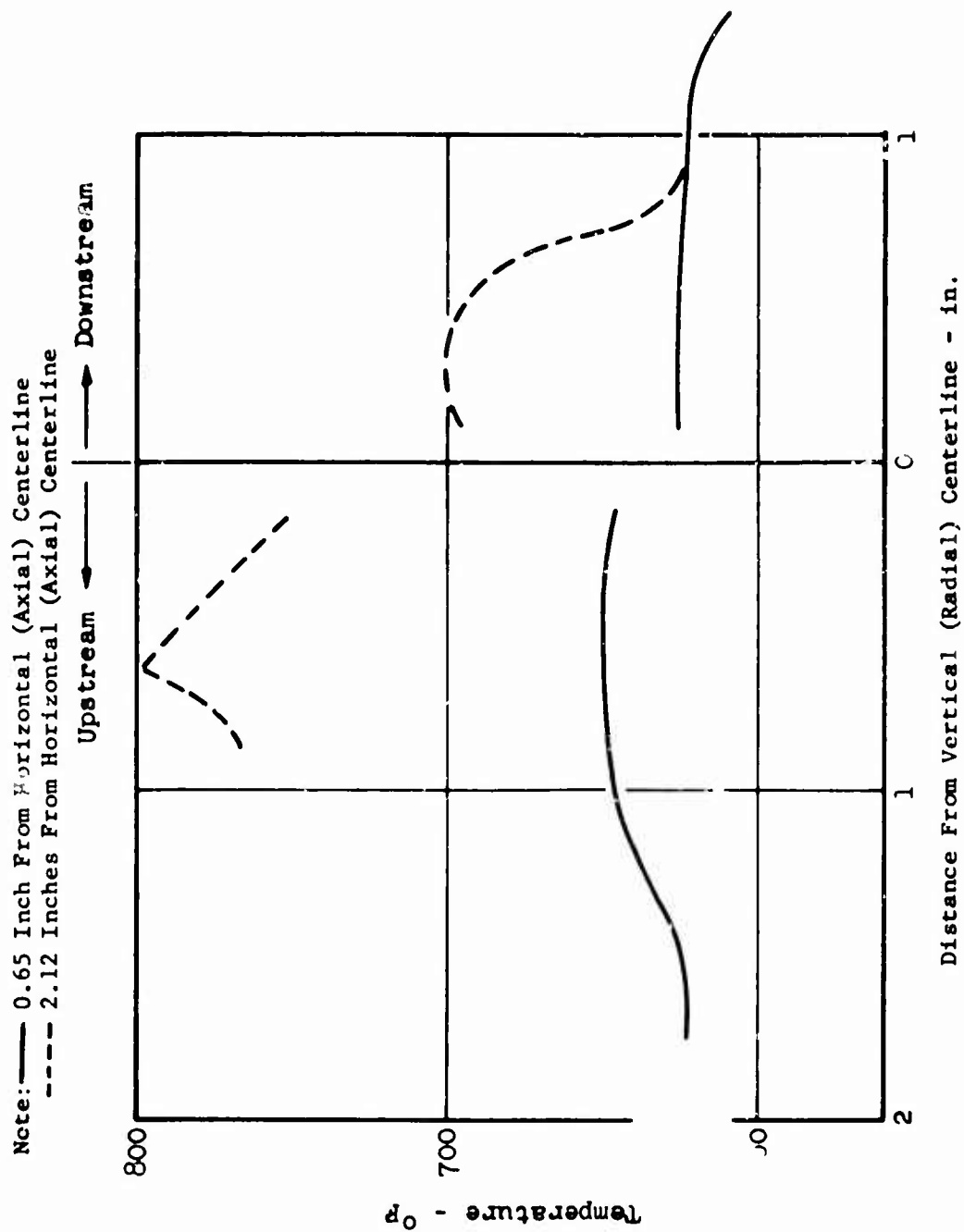


Figure 96. Temperature of Test Rig Turbine Disc Vs Distance From Radial Centerline.

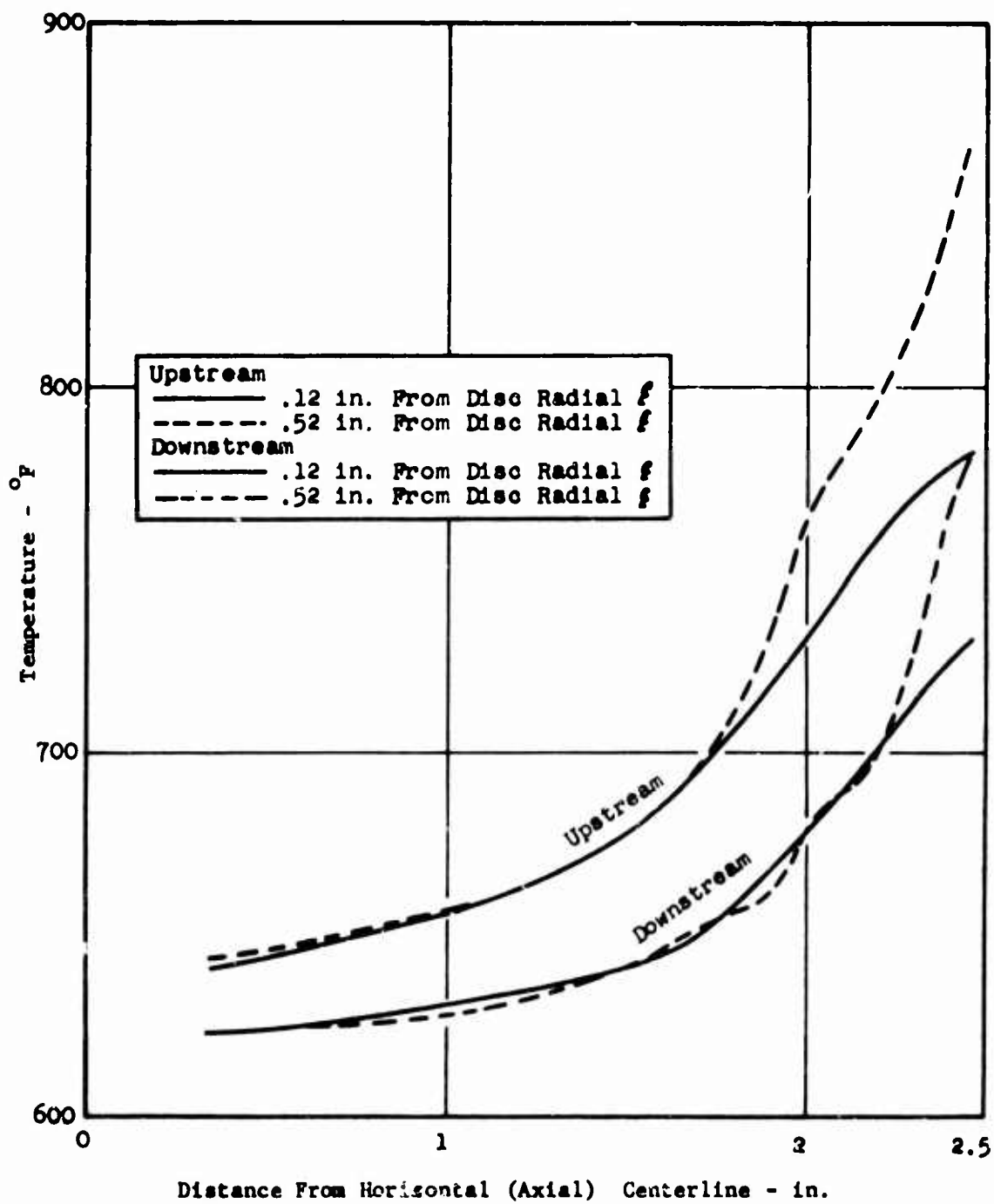
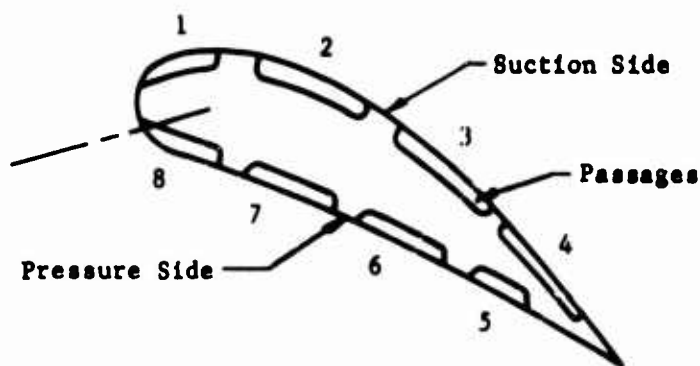


Figure 97. Temperature of Test Rig Turbine Disc Vs Distance From Axial Centerline.



Schematic - Blade Section
Passage Number Identification

Passage Number	Orifice Diameter	Coolant Flow
1	0.0230 in.	1.7415 lb/hr
2	0.0214	1.5029
3	0.0218	1.5662
4	0.0520	6.0499
5	0.0420	3.7450
6	0.0180	1.0416
7	0.0180	0.5539
8	0.0180	0.9179

Total Coolant Flow = 17.5196 lb/hr-blade
Percent Total Engine Airflow = 4.38

Note: 1. Orifice Tolerance 0.0005 in.
2. Coolant Flows Based On Round Orifices

Figure 98. Turbine Rotor Blade Orifice Diameters and Coolant Flows for Rig Engine.

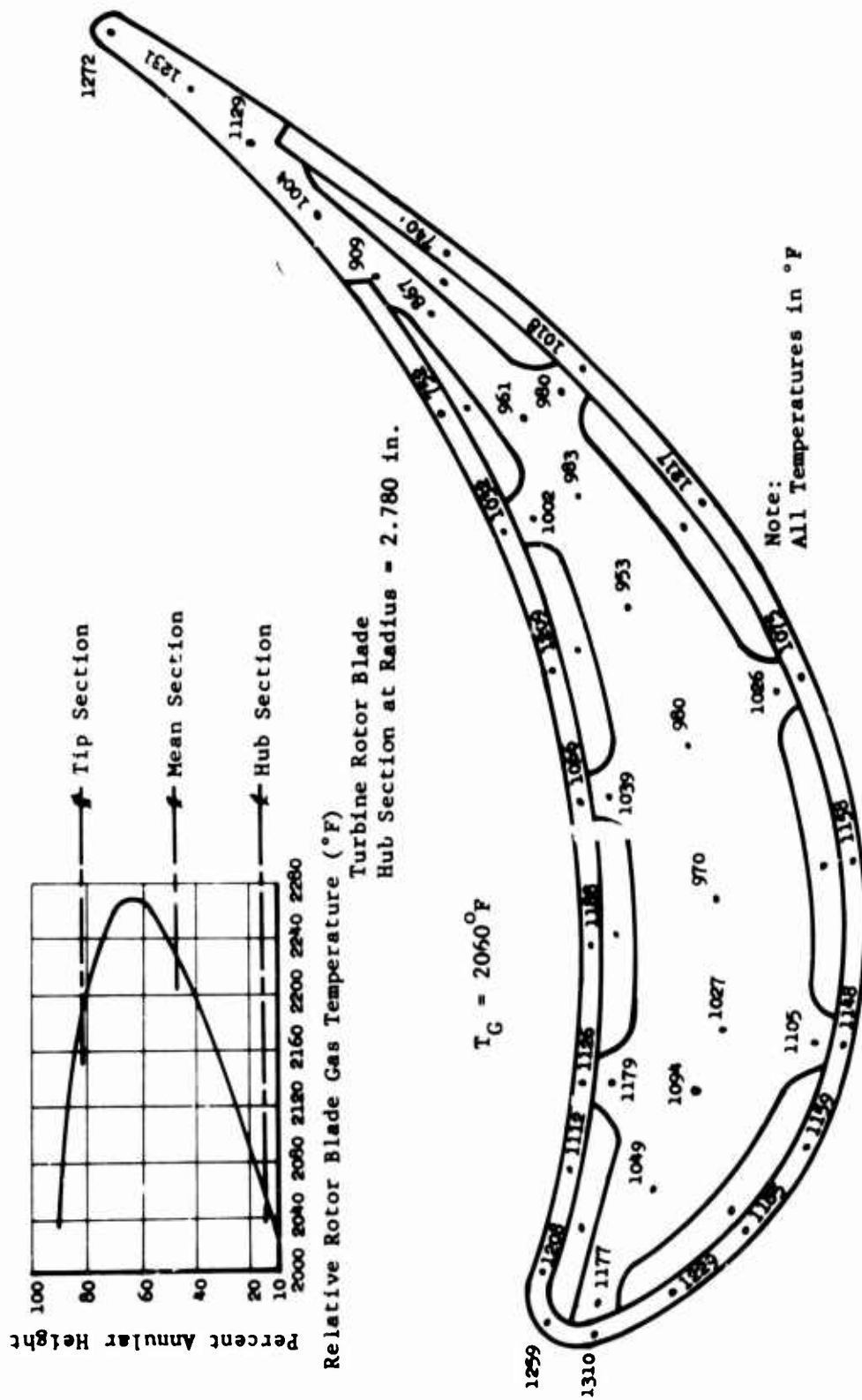


Figure 99. Turbine Rotor Blade - Hub Section Temperature Distribution and Relative Rotor Blade Gas Temperature Profile.



Figure 100. Turbine Rotor Blade - Mean Section Temperature Distribution.

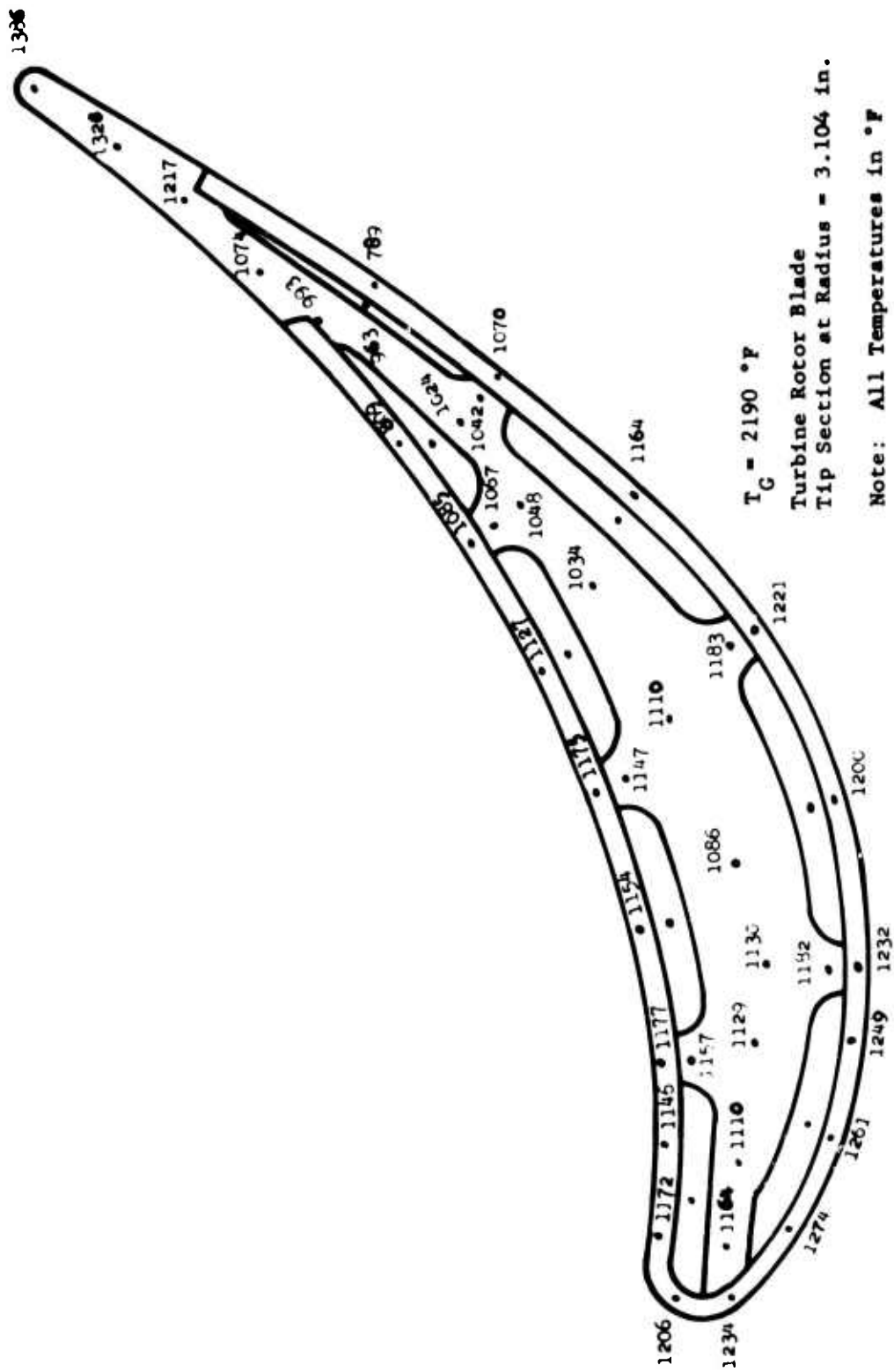


Figure 101. Turbine Rotor Blade - Tip Section Temperature Distribution.

Airfoil Metal Temperature Vs Distance From the Leading Edge Along the Airfoil Surface for the Hub, Mean, and Tip Sections of the Rig Engine Turbine Rotor Blade.

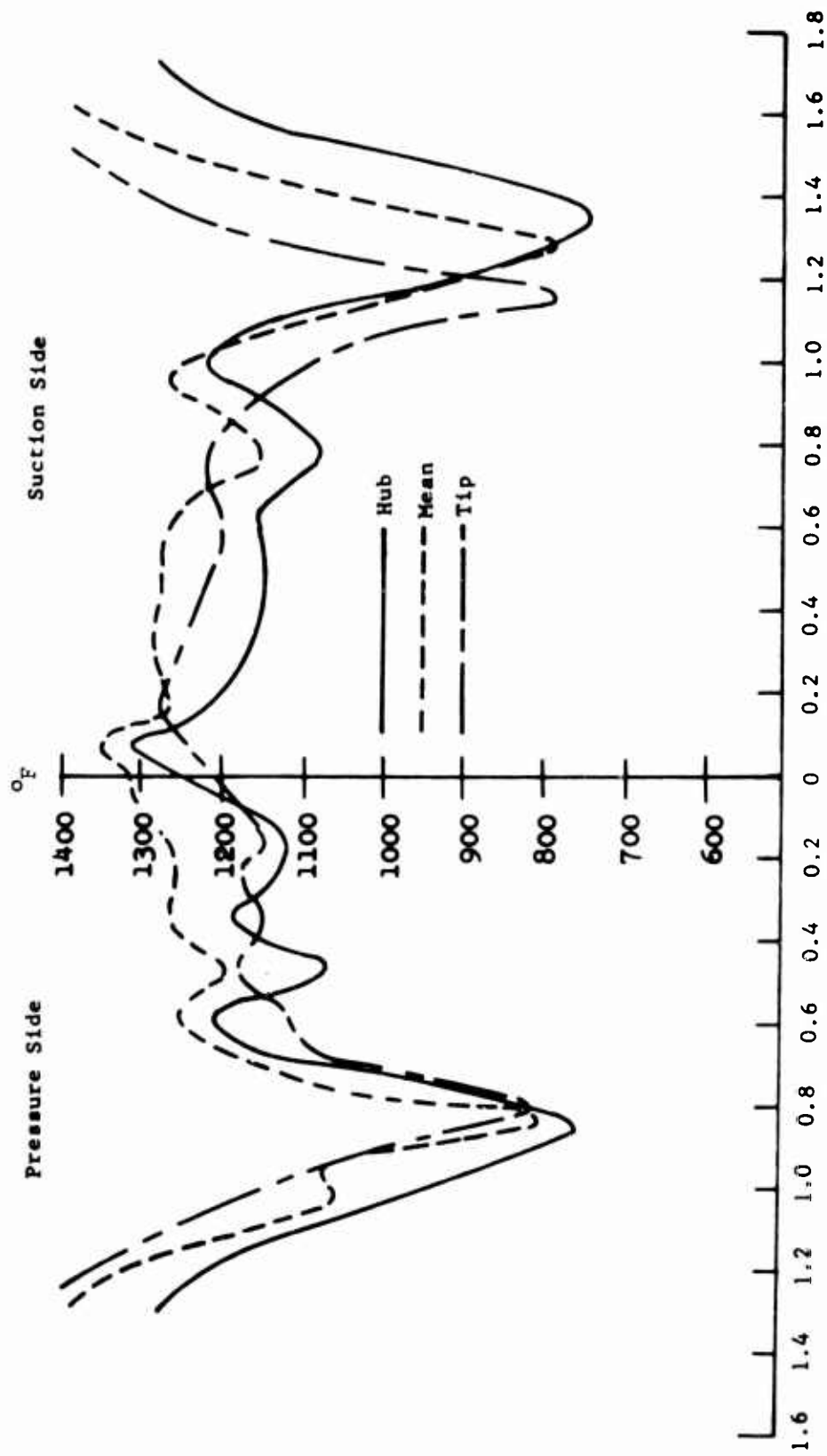


Figure 102. Airfoil Metal Temperature Vs Distance From Leading Edge.

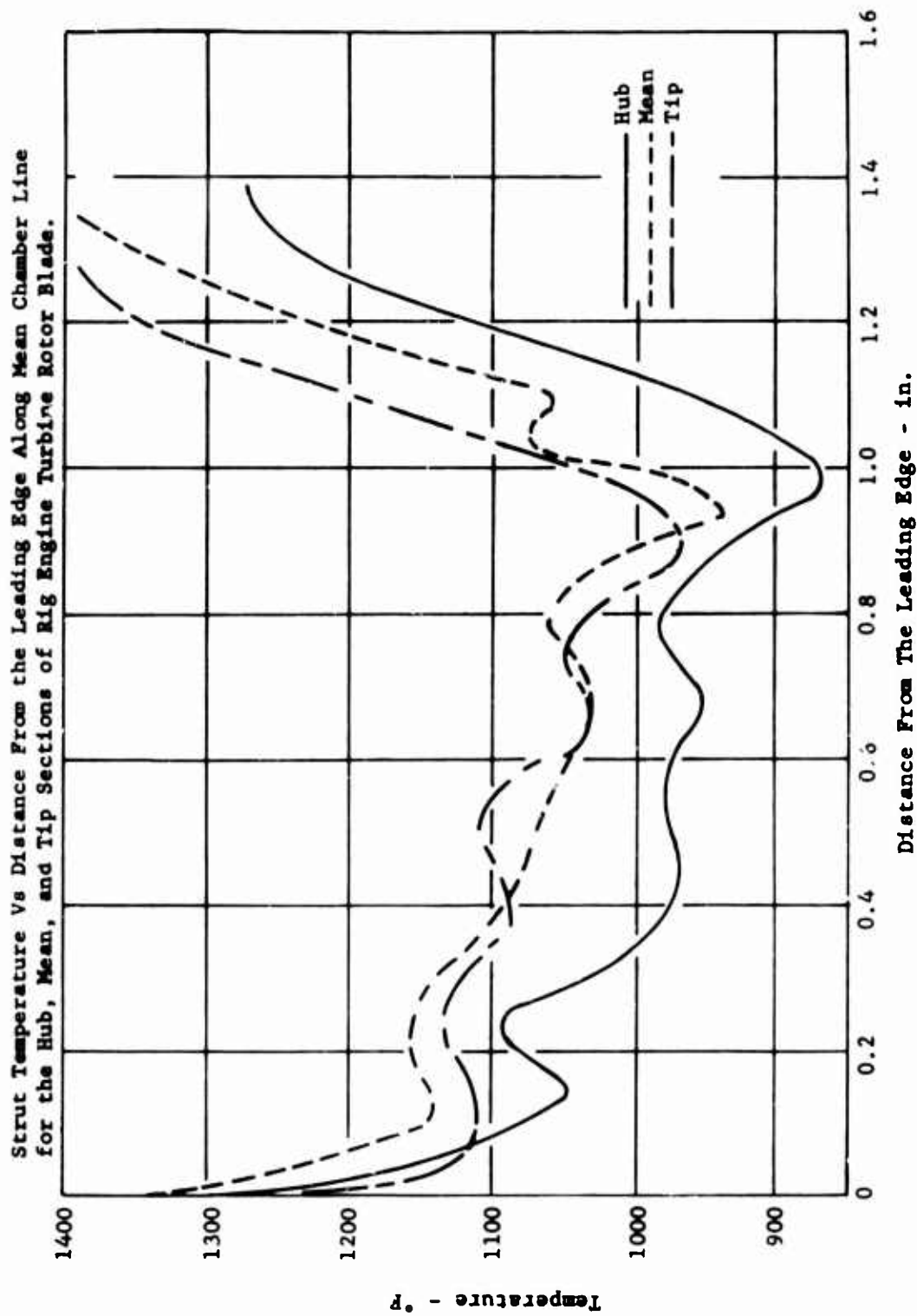


Figure 103. Strut Temperature Vs Distance From Leading Edge.

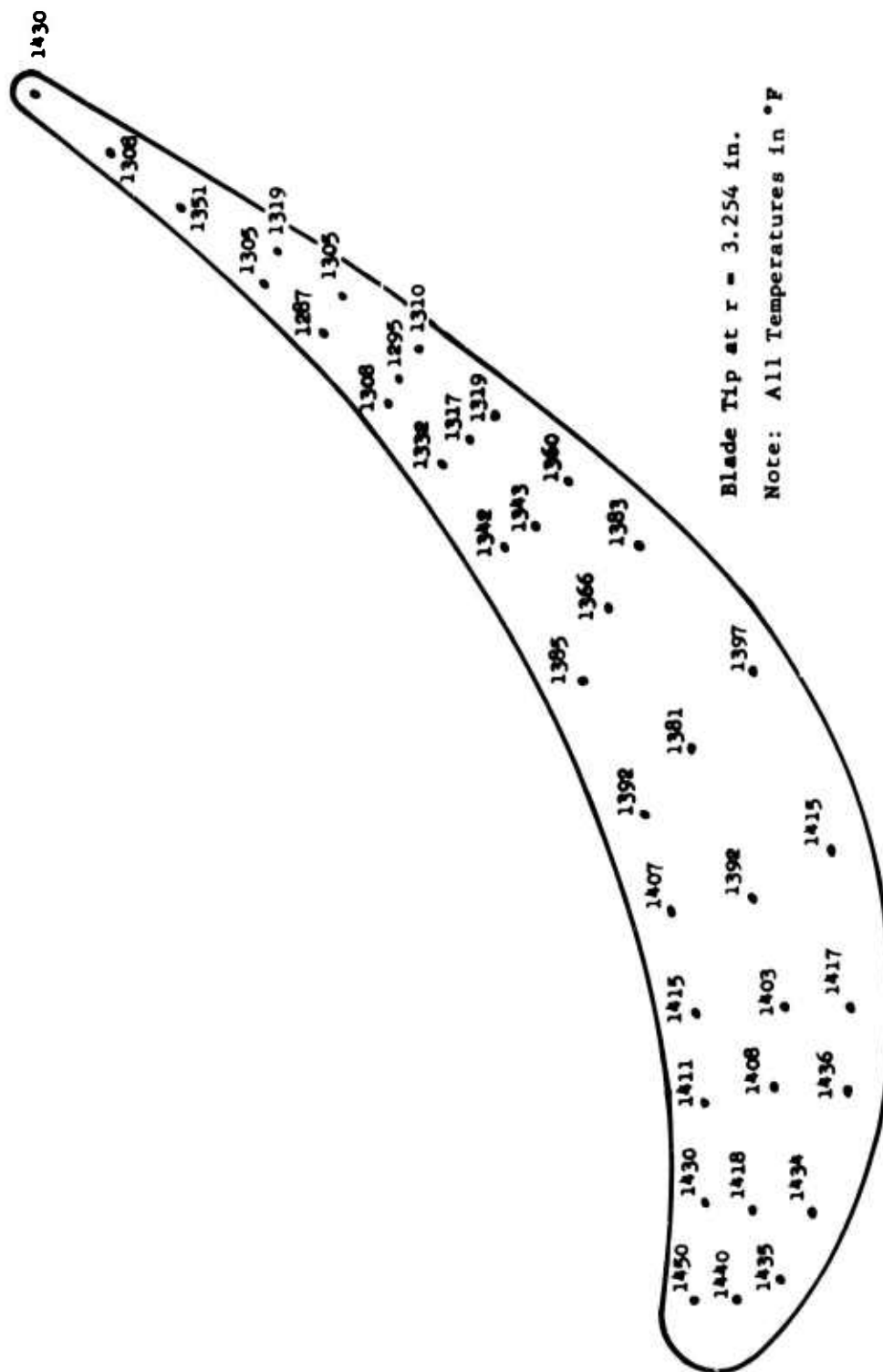


Figure 104. Turbine Rotor Blade - Tip Cap Temperature Distribution.

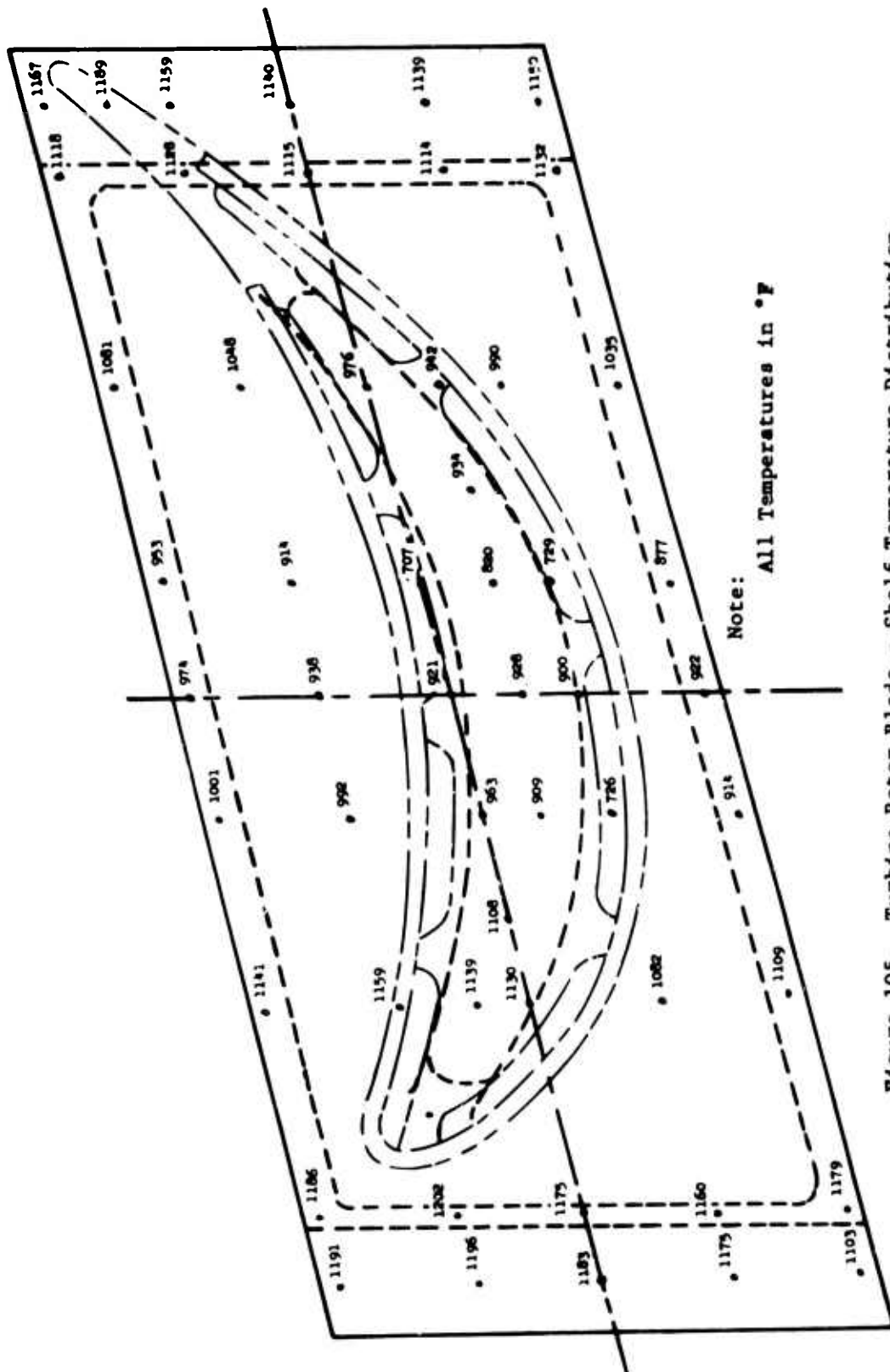
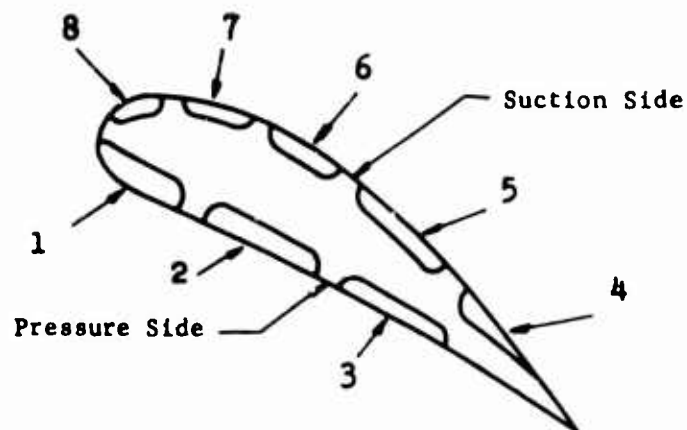


Figure 105. Turbine Rotor Blade - Shelf Temperature Distribution.

Schematic-Blade Section
Coolant Passage Number Identification



Passage Number	Orifice Dia Inch	Coolant Flow lb/sec
1	0.0300	0.000459
2	0.0345	0.000640
3	*0.0950	0.001710
4	2- 0.0400	0.002030
5	0.0315	0.001055
6	0.0300	0.000820
7	0.0300	0.000656
8	0.0300	0.000777

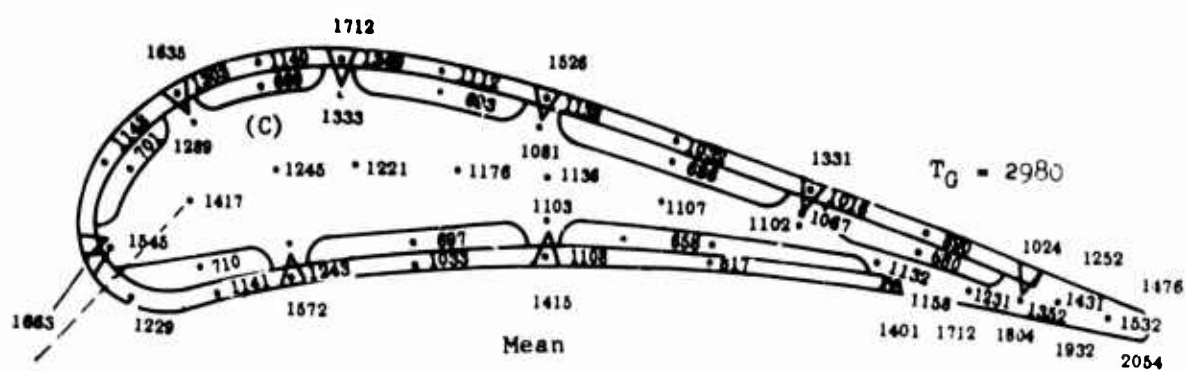
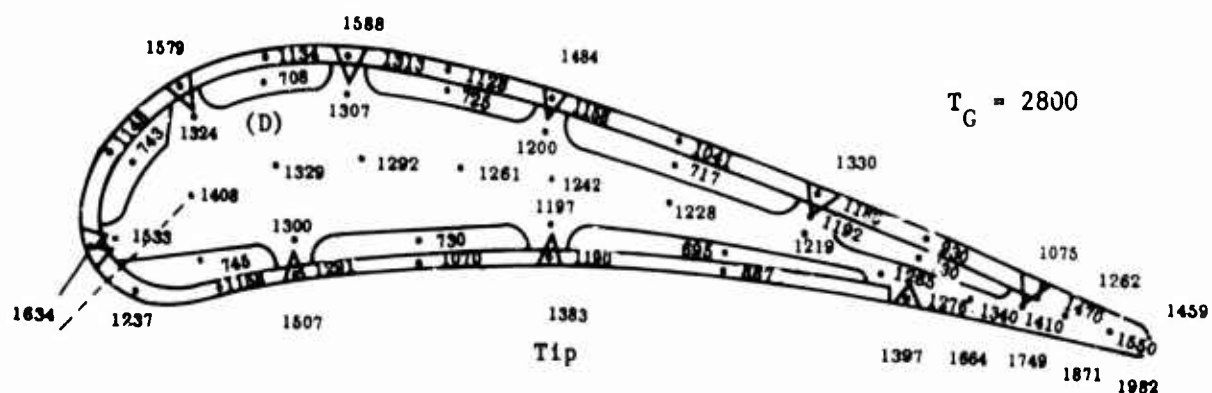
Total Coolant Flow = 0.008147 lb/sec-blade
Percent Total Engine Airflow= 6.22%
3.01 lb/sec 23 Blades
*Equivalent

Maximum Flow in Channels 3 and 4
Credit for Flow From Channels 2 and 5

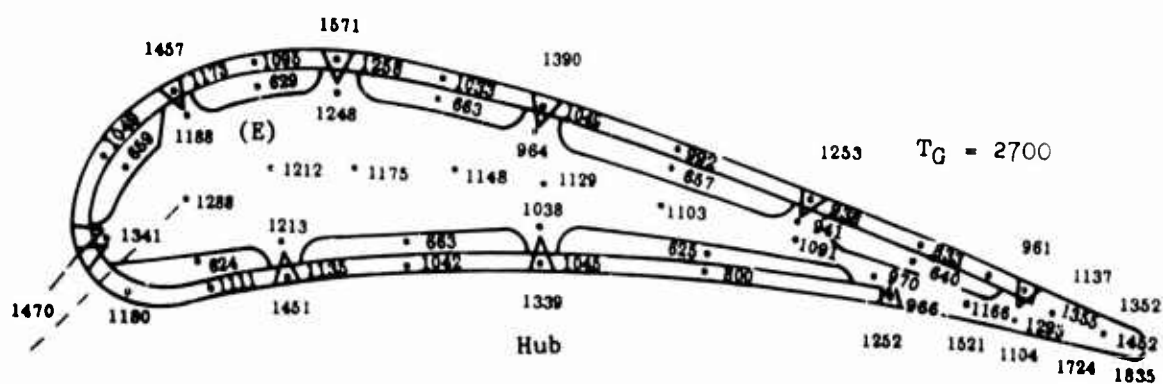
Notes:

- (1) Orifice Tolerance ± 0.0005 inch
- (2) Orifices Sized for Square Edge Inlets
- (3) Blade per Dwg LS-29972

Figure 106. Orifices for Test Rig Stator Blade.

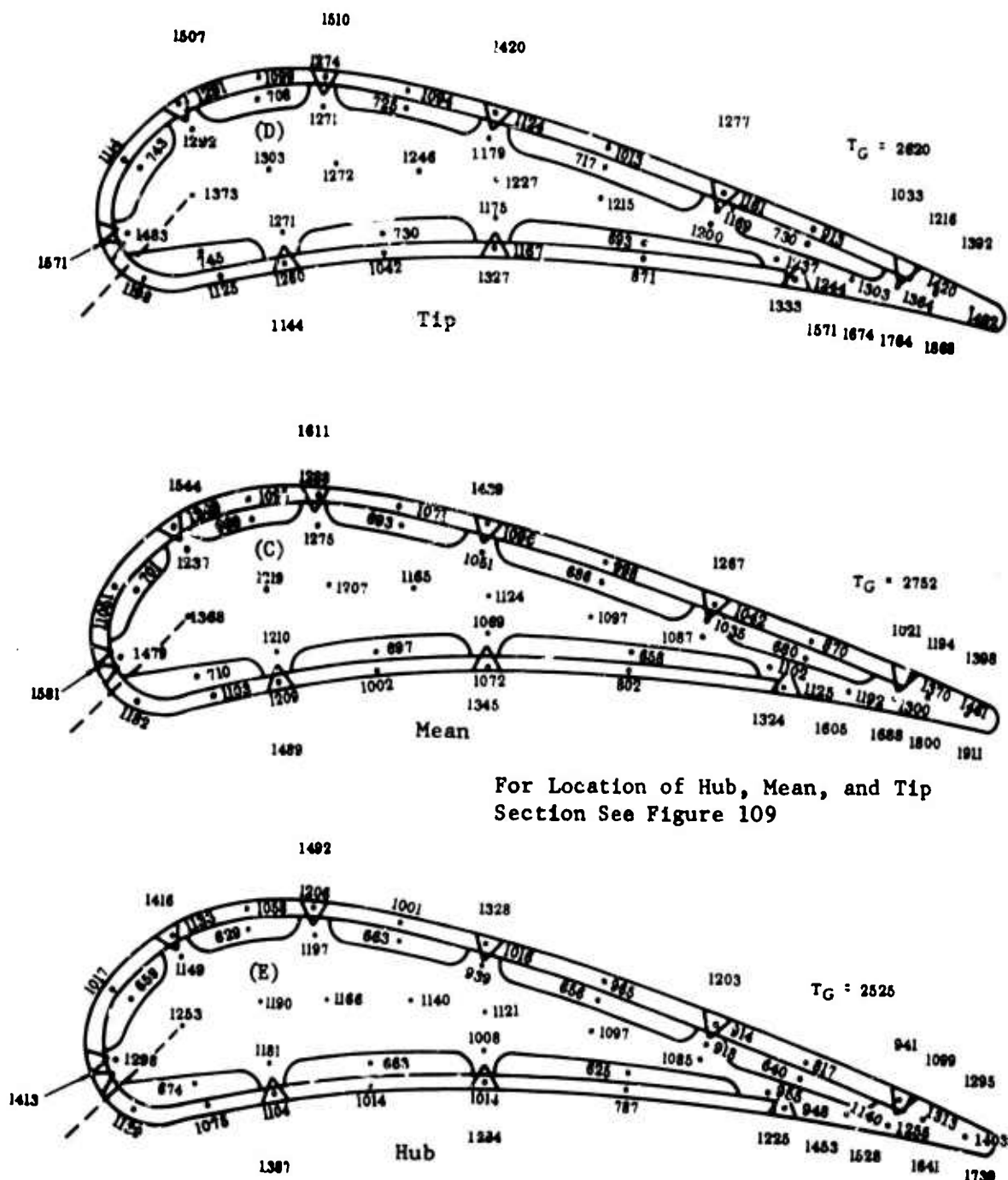


For Location of Hub, Mean, and
Tip Sections See Figure 109



Note:
All Temperatures in $^{\circ}\text{F}$
 T_G at Shelves = 1600°F

Figure 107. Rig Engine Stator Blade Temperature Distribution for Maximum Temperature Condition.



For Location of Hub, Mean, and Tip
Section See Figure 109

Note:
All Temperatures in $^{\circ}F$
 T_G at Shelves = $1600^{\circ}F$

Figure 108. Rig Engine Stator Blade Temperature Distribution
for Average Temperature Condition.

T_G at Shelf = 1600°F

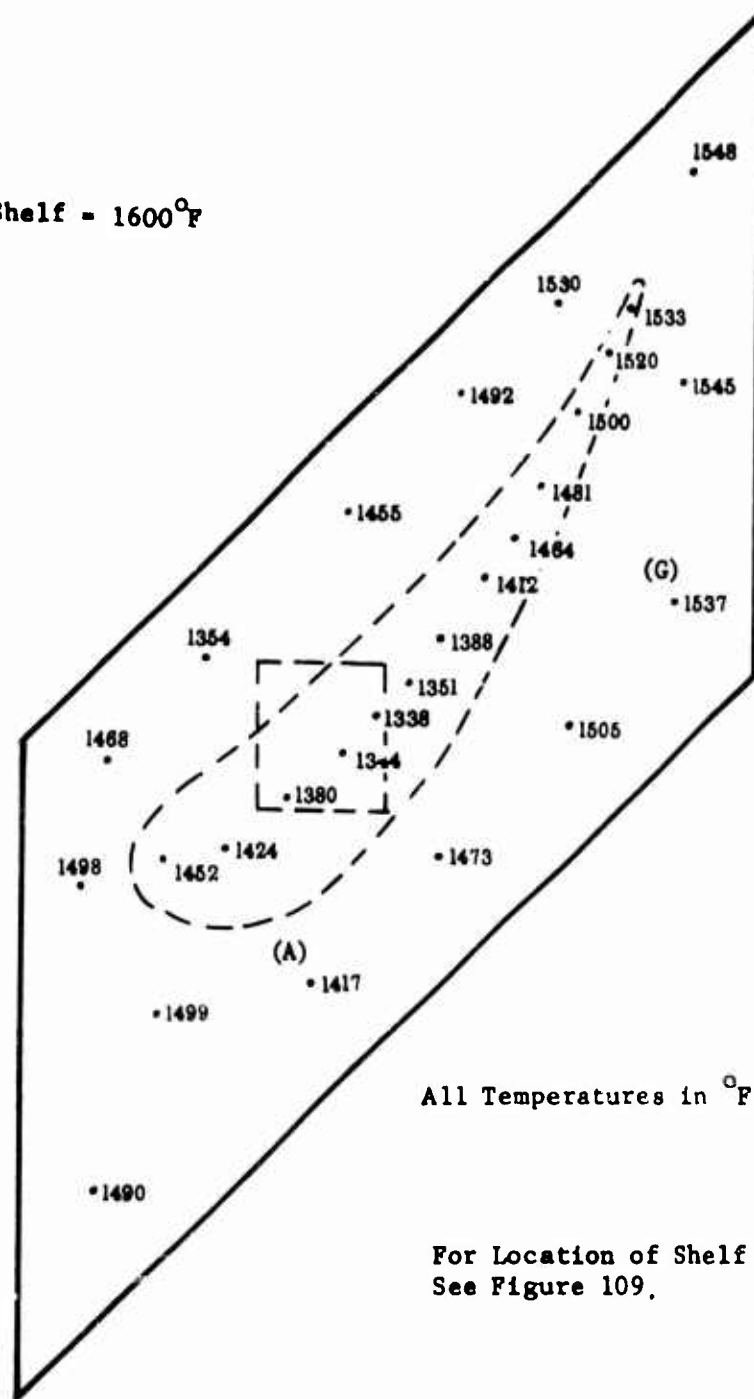


Figure 110. Turbine Stator Blade Upper Shelf Temperature Distribution for Maximum Temperature Condition.

T_G at Shelf = 1600°F

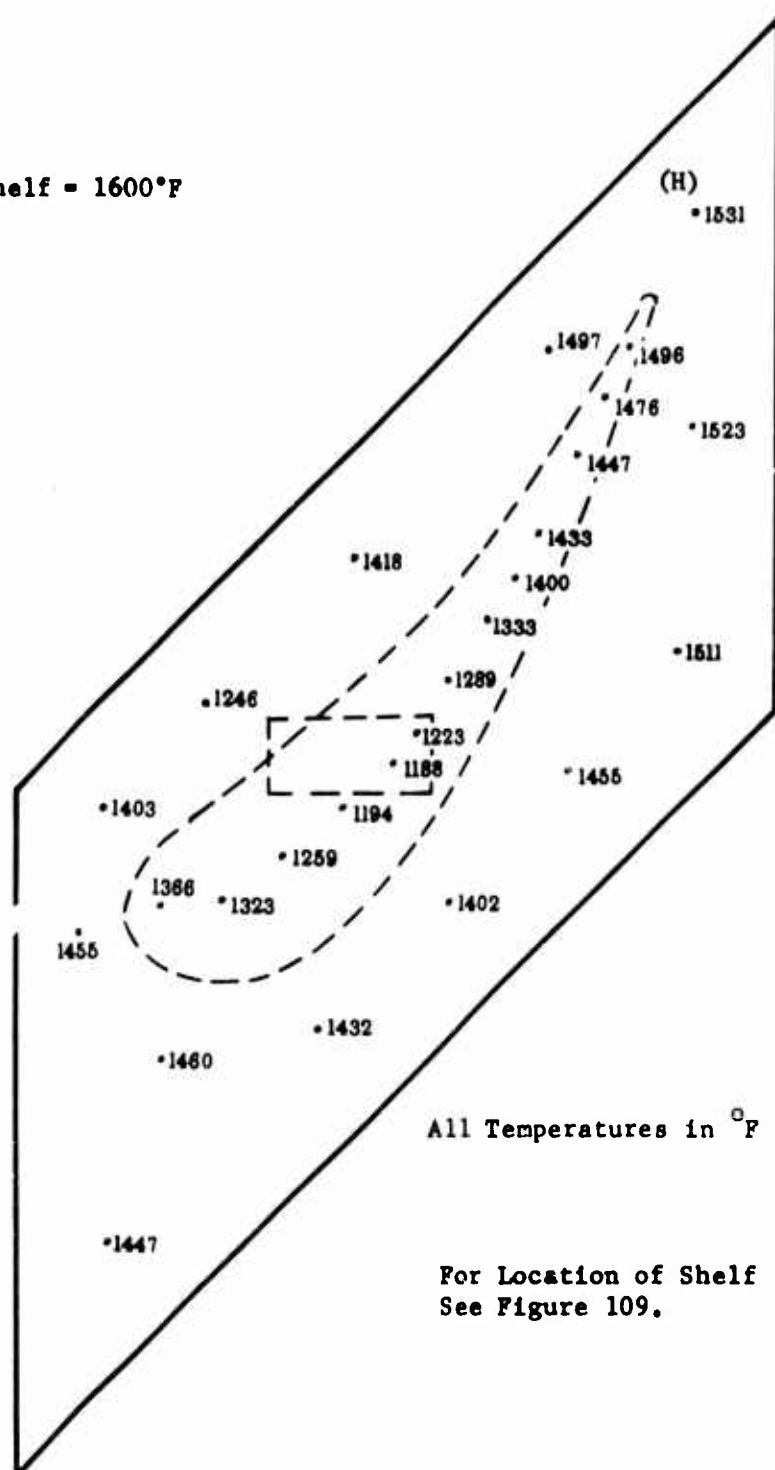


Figure 111. Turbine Stator Blade Lower Shelf Temperature Distribution for Maximum Temperature Condition.

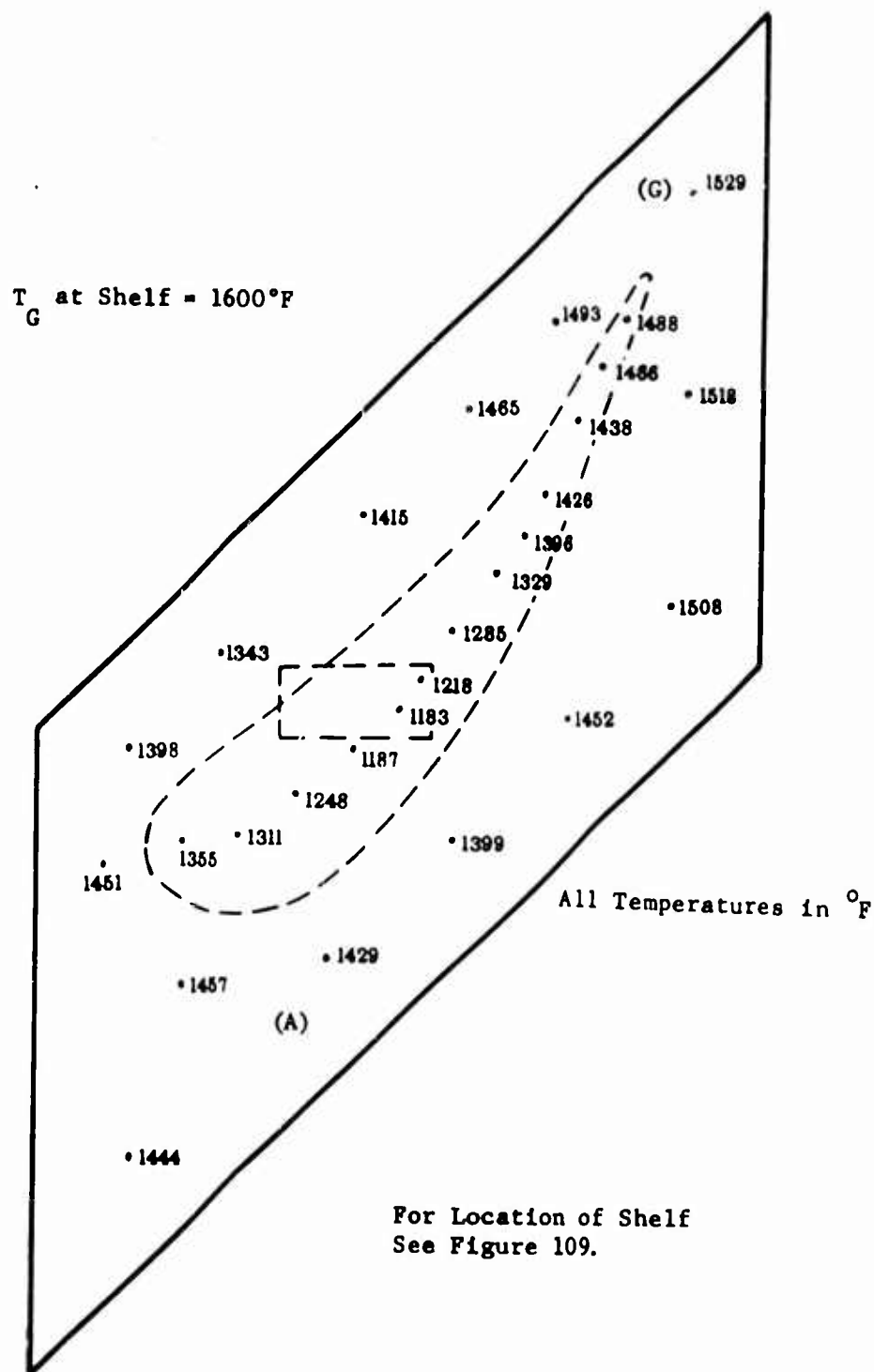


Figure 112. Turbine Stator Blade Upper Shelf Temperature Distribution for Average Temperature Condition.

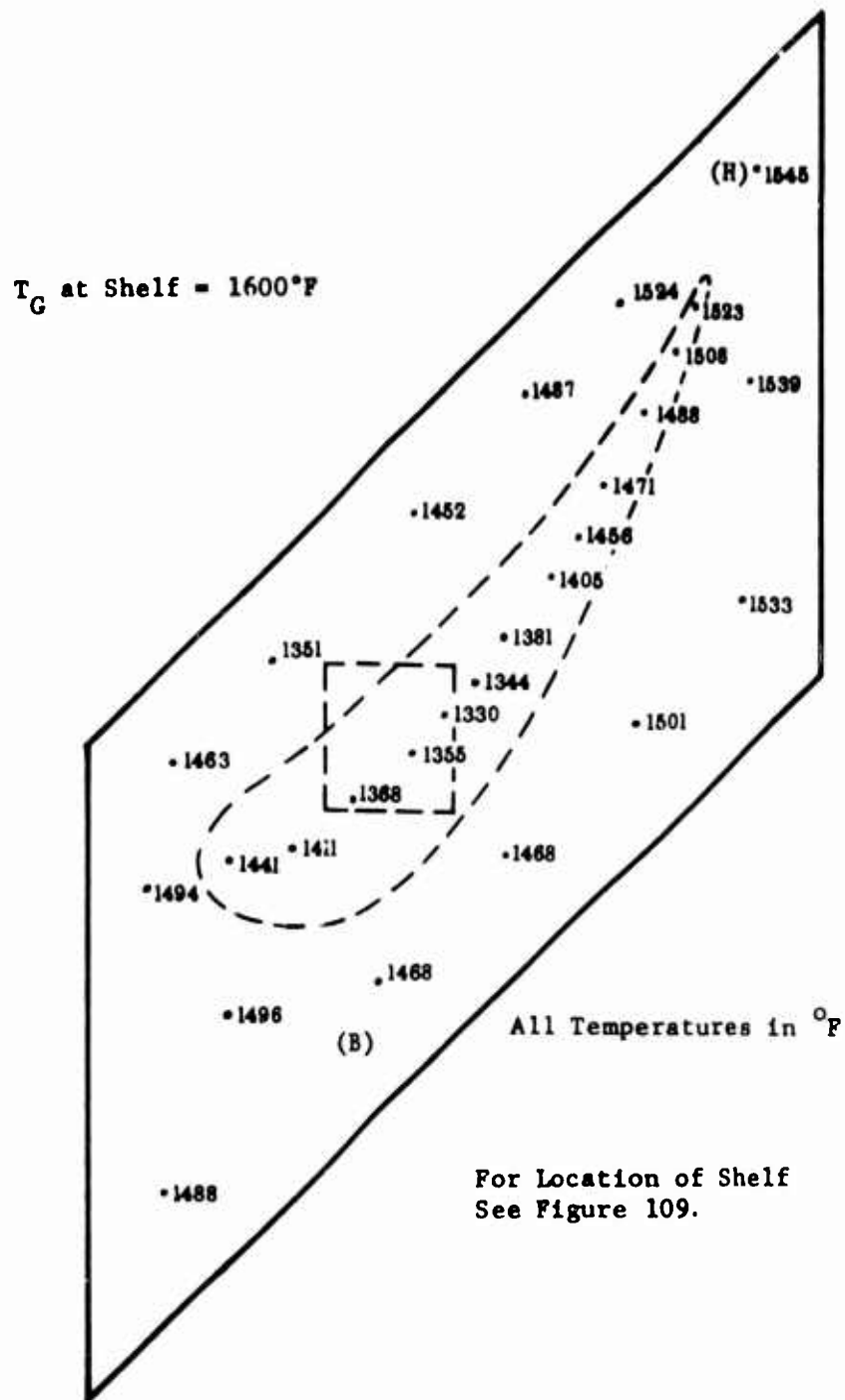


Figure 113. Turbine Stator Blade Lower Shelf Temperature Distribution for Average Temperature Condition.

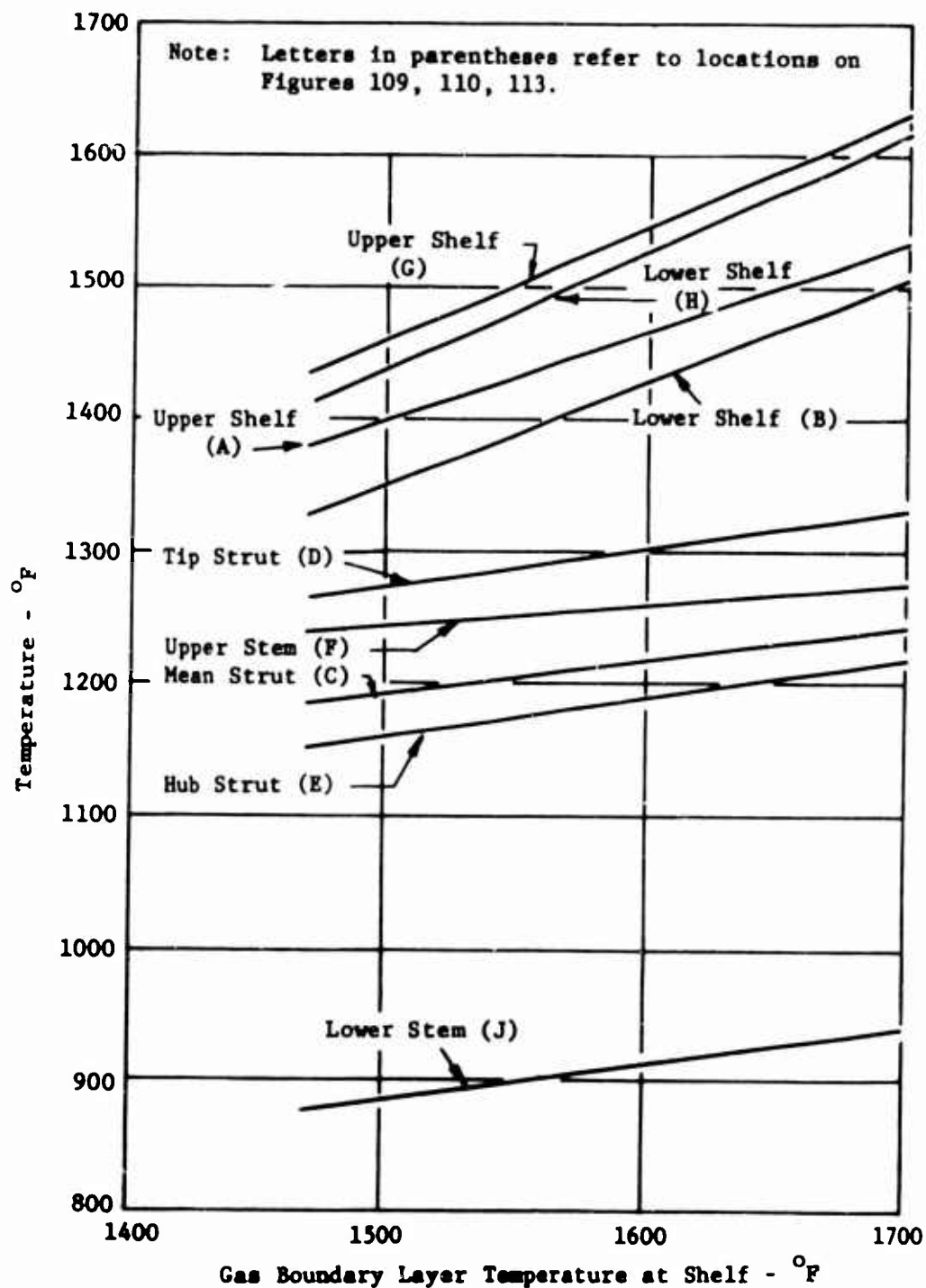


Figure 114. Temperature Variation of Representative Points on Shelf.

4.3 TURBINE COMPONENT STRESS ANALYSIS

4.3.1 Stator Blade

The transpiration-cooled stator blade was analyzed by treating the blade as a beam. Stresses due to gas loads and steady-state temperatures are shown in Figures 115, 116, and 117 and were calculated at three cross sections of the airfoil spar defined as root, mean, and tip. The peak stresses occurring at each of these sections is shown in Figure 118, which is a modified Goodman diagram of the blade spar material, Inco 713 C, at 1550°F. These steady-state stresses are the algebraic sums of the mechanical stresses due to gas bending and the thermal stresses due to steady-state temperature gradients. Thermal stresses have significance in the determination of blade life due to high- or low-cycle fatigue. However, in order to evaluate low-cycle fatigue life, i.e., the number of startup and shutdown cycles required to cause cracking, it is necessary to determine not only the steady-state thermal stresses but the transient thermal stresses as well (Reference 11). Because of the small number of required test hours, such an analysis was not conducted for this blade.

The following conclusions can be made, though, as a result of the limited analysis actually carried out:

1. The static strength of the blade strut is adequate .
2. The high-cycle fatigue life of the blade strut is satisfactory .
3. The stator blade will not fail in creep rupture .

4.3.2 Stator Blade Support Rings

The inner and outer stator support rings shown in Figure 119 were stress analyzed using pressure difference loads and accounting for thermal gradients in addition to the mechanical loads induced by the stator vanes. Stresses due to the latter are small compared to the stresses due to pressure loads and temperature gradients. The location and magnitude of the peak stresses are also shown in Figure 119. These stresses are well below the acceptable 0.2 percent yield strength of René 41, 118,000 psi, the material from which the rings are manufactured.

4.3.3 Rotor Blade

The transpiration-cooled turbine blade was analyzed for stresses due to gas loads, steady-state temperatures, temperature gradients and centrifugal loads. The blade was analyzed as a twisted beam of varying cross section in the determination of the stresses due to mechanical loads (rotation and gas bending), Table XV. Thermal stresses, Figures 120, 121, and 122, were computed utilizing C-W computer program Log 970. This program, based on an analysis presented in Reference 12, analyzes an unrestrained beam subjected to a set of force systems which satisfy equilibrium and produce deformations which are compatible with the requirement of plane cross sections remaining plane after bending. Figure 123 is a modified Goodman

diagram of the blade strut material at an operating temperature of 1400°F. Also presented on this figure are the peak steady-state stresses occurring at three sections defined as root, mean, and tip and the corresponding gas bending stresses. These stresses are the combined stresses due to gas bending, centrifugal force, and steady-state temperature gradients shown in Figures 120, 121, and 122. The comments concerning low-cycle fatigue made for the stator blade are applicable here also.

4.3.4 Rotor Disc and Shaft

Stresses in the disc and shaft at the operating speed of 50,000 rpm arise from

1. The applied blade load of 373,000 pounds/blade at the outer periphery.
2. Disc body forces due to rotation.
3. Thermal stresses due to radial temperature gradients in the disc.
4. Shear stresses due to the torque that the shaft is required to transmit.
5. Bending stresses due to cantilevering of the disc with respect to the mounts.
6. Discontinuity stresses arising as a result of change in geometry from disc to shaft.

A computer program developed at C-W for calculating the stresses in discs with variable thickness was utilized to determine stress levels. Each half of the split disc was run separately because each had a distinct temperature profile.

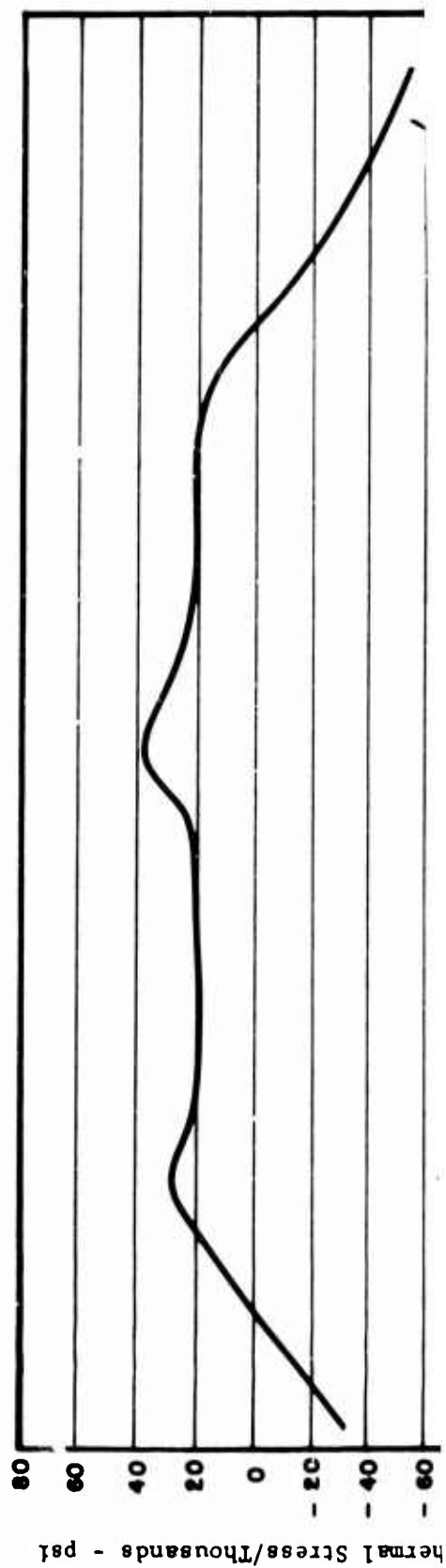
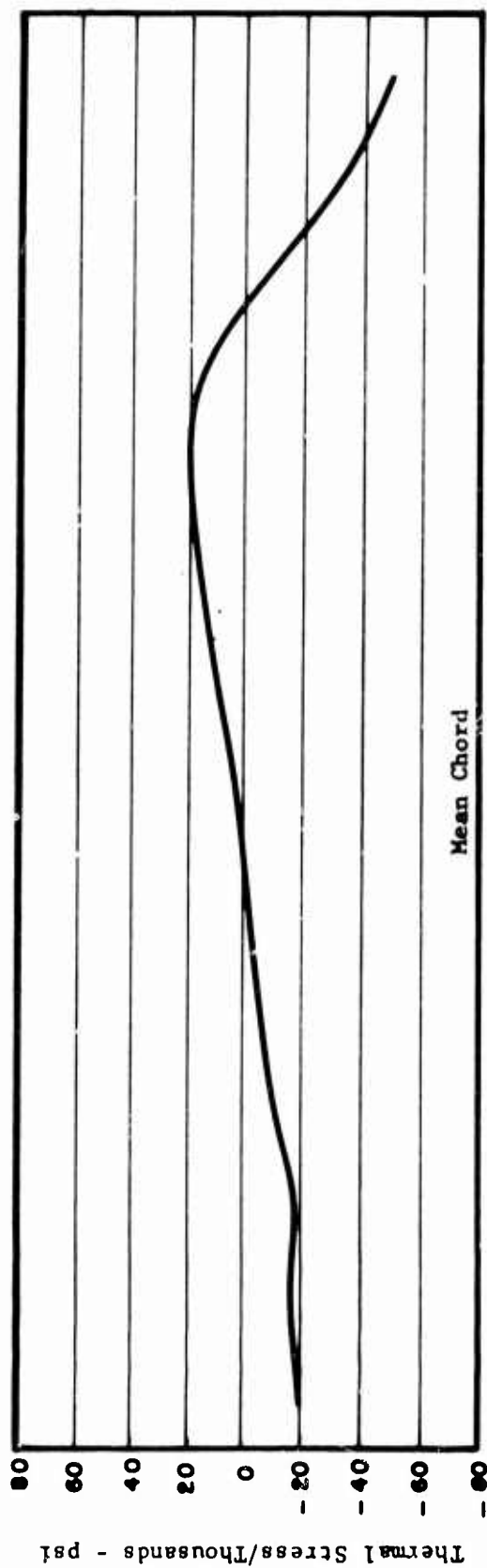
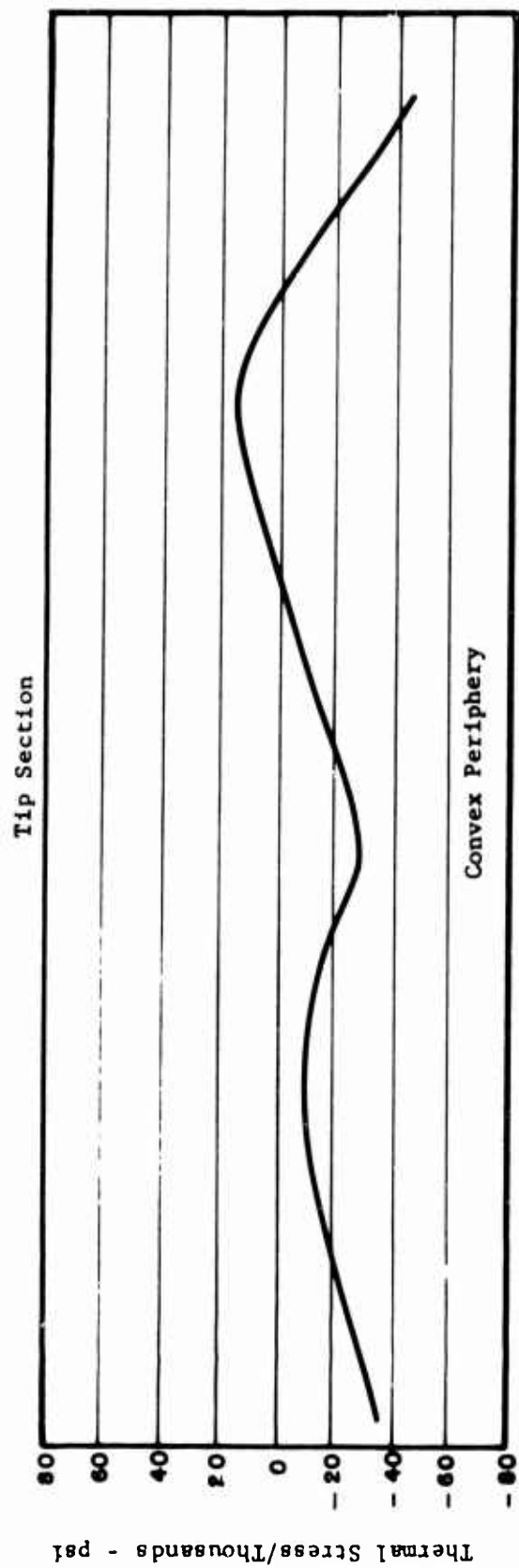
Figure 124 shows the stress levels of the disc and shaft. The highest stress occurs at the bore and is equal to the 0.2 percent yield stress of the material (Inco 718 cast) at temperature for the front segment and 96 percent of yield for the rear segment. The average tangential stress is equal to 58 percent of yield for both segments. In this analysis, the centrifugal effect of the impeller vanes between disc segments was taken into account by increasing the density by a factor related to the mass of the vanes at the appropriate radial station. At the periphery, the effect of the blade weld restraint was considered. In the impeller vane webs, the shear caused by the differential growth of the two disc segments caused by temperature differences was calculated. These effects were found to be small. The existence of a full slot between disc halves from the bore up to the radius at which the impeller vanes begin creates an out-of-plane bending condition in that area due to the asymmetry of the half-disc segment. Calculation of this effect gives a bending stress of 7000 psi at the bore and lesser values proceeding radially outward. In the rear shaft, the total bending stress due to weight and cg unbalance at the forward bearing is 1200 psi. At the same cross section, stress due to torque is 6100

psi, while at the spline end of the shaft the shear stress is 35,500 psi. A compatibility problem arises at the disc-shaft intersection because of disc growth under centrifugal load, which is 0.001 inch for a bore radius of 0.3125 inch for an unrestrained disc. Since the shaft has virtually no growth due to its own body force, shears and moments exist at the disc-shaft interface maintaining compatible deformations. In the compatibility analysis, unit loads were applied separately to the common surface of the two elements to determine relative stiffness; this revealed that the disc is nine times as stiff, indicating a shaft radial growth of 0.0009 inch. Since the bearing seat is adjacent, a radial growth of the inner race support of 0.0006 inch is indicated.

Disc - Blade Attachment - Early Design

During the early design phase of the turbine test rig, a circumferential fir tree type of attachment was considered for disc-to-blade attachment. Because of its complex geometry, the disc, Figure 125, could not be analyzed using the existing computer program; therefore, the analysis was performed as follows. The upstream half of the disc was divided into a number of free bodies subjected to the known centrifugal and the discontinuity forces as shown in Figure 126. The unknown forces were found from the conditions of equilibrium of forces and compatibility of displacements. Having found the forces, the stresses were then calculated and are summarized in Figure 127. The stresses in the downstream disc are similar. The stresses in the outer regions of the disc considerably exceed the yield stress of the material (150,000 psi). This is largely due to the S-like shape of the discs' cross section, which causes very high discontinuity moments. Succeeding calculations were made to determine a structurally adequate disc employing the fir tree design. The minimum permissible size became so prohibitive that the fir tree type of attachment was discarded in favor of the previously discussed welded assembly.

TABLE XV							
MECHANICAL STRESSES IN TURBINE ROTOR BLADE (PSI)							
Radius	Centrifugal Stress	Bending Stress			Total Steady-State Mechanical Stress		
		Leading Edge	Back Surface	Trailing Edge	Leading Edge	Back Surface	Trailing Edge
3.200	11,700	-600	3010	-6000	11,100	14,710	5,700
2.942	29,800	-450	810	-1720	29,350	30,610	28,080
2.780	36,700	-3210	970	1490	33,490	37,670	38,190
2.710	38,800	-4840	1420	2510	33,960	40,220	41,310
2.690	39,400	-4890	1270	3180	34,510	40,510	42,580
2.660	30,200	-1990	360	3460	28,210	29,840	33,660



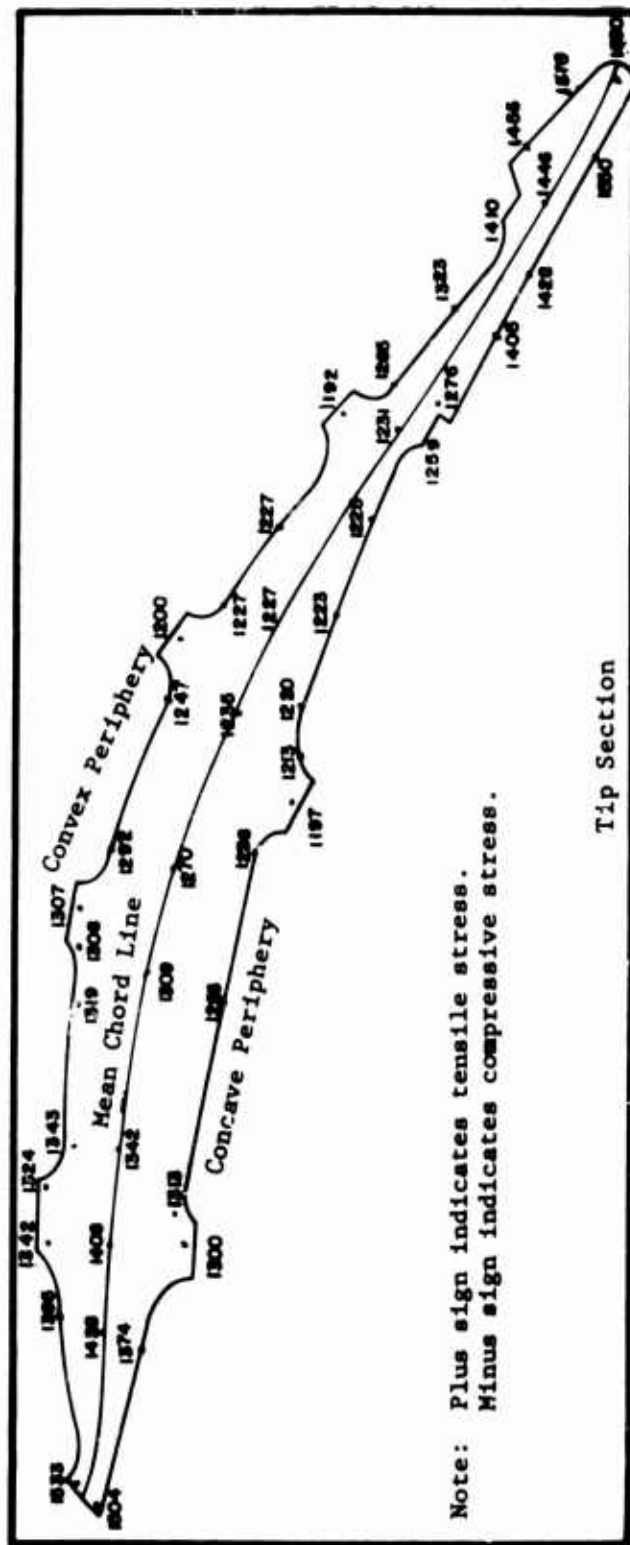
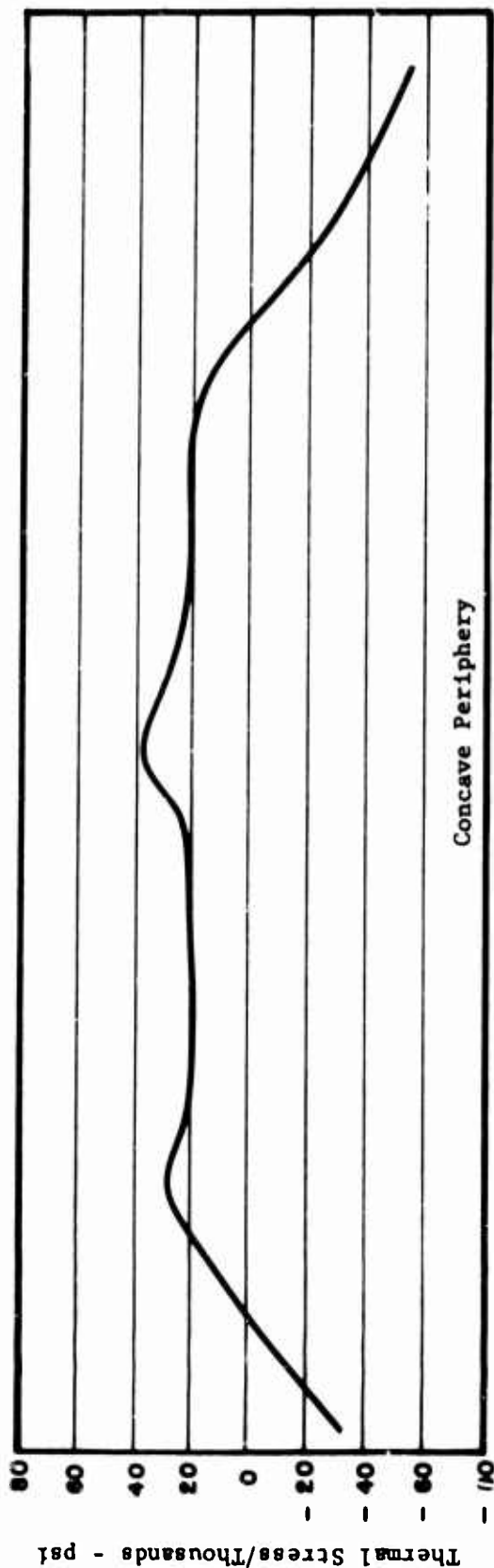
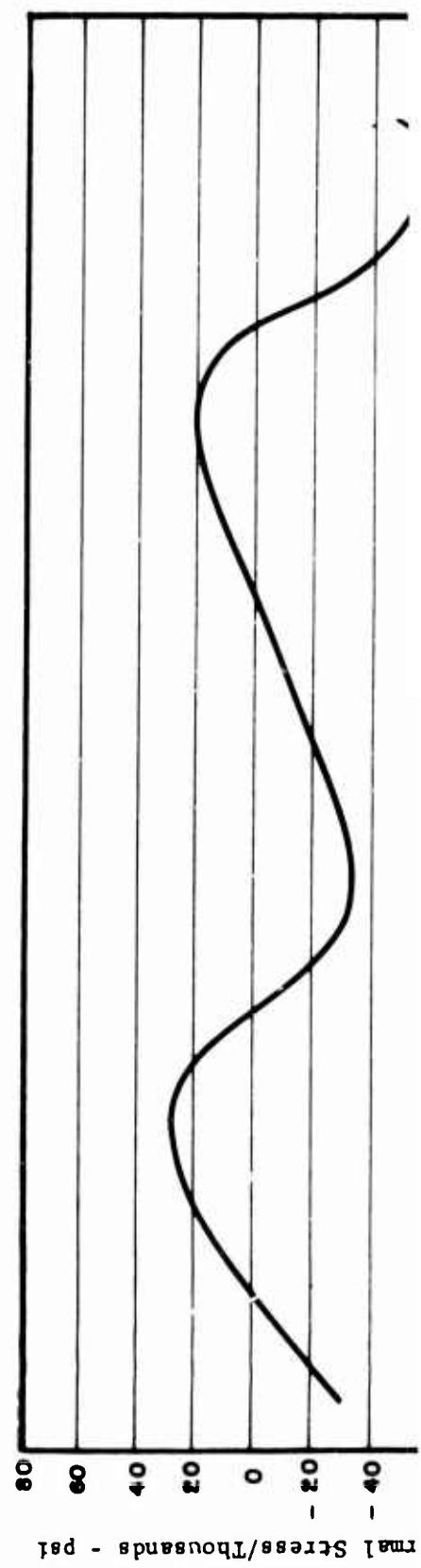
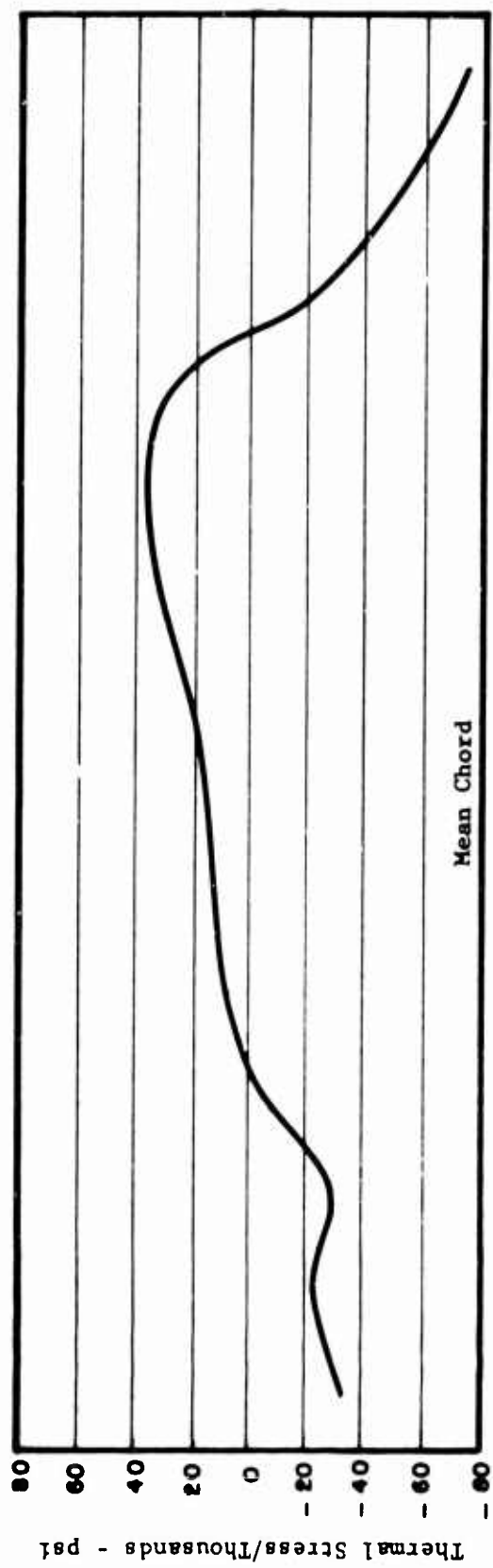
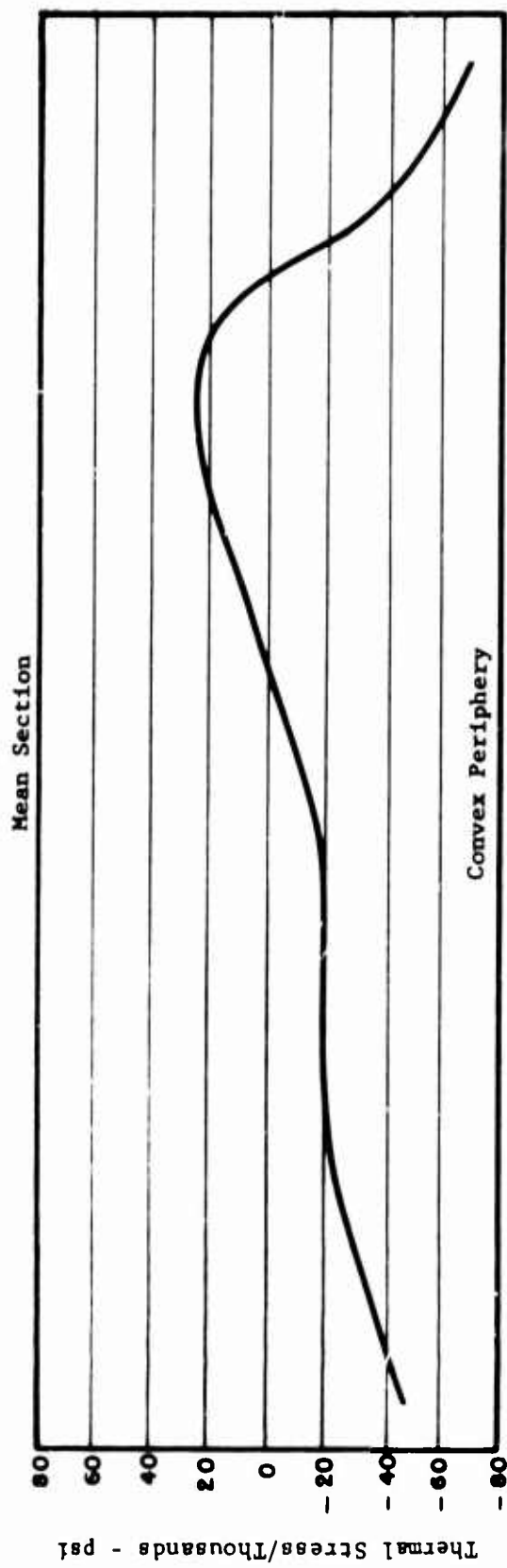


Figure 115. Turbine Stator Blade Thermal Stresses - Tip Section.

B



F

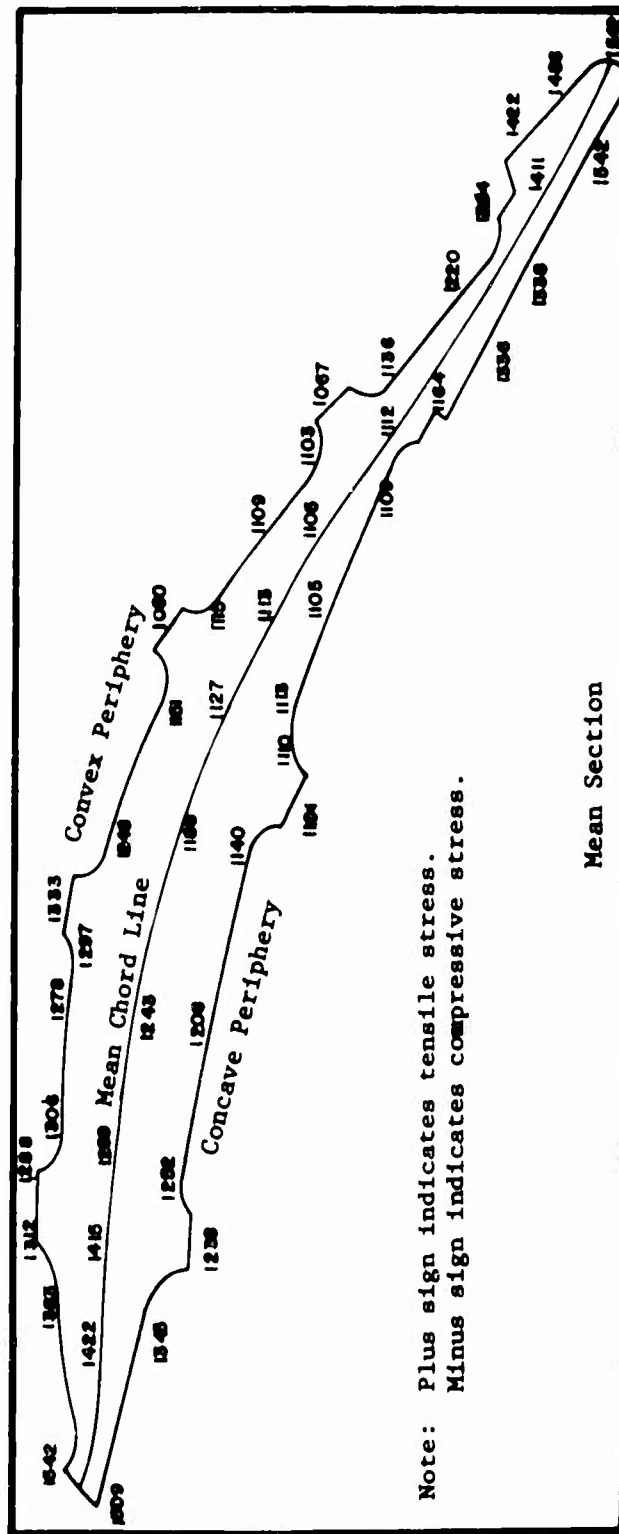
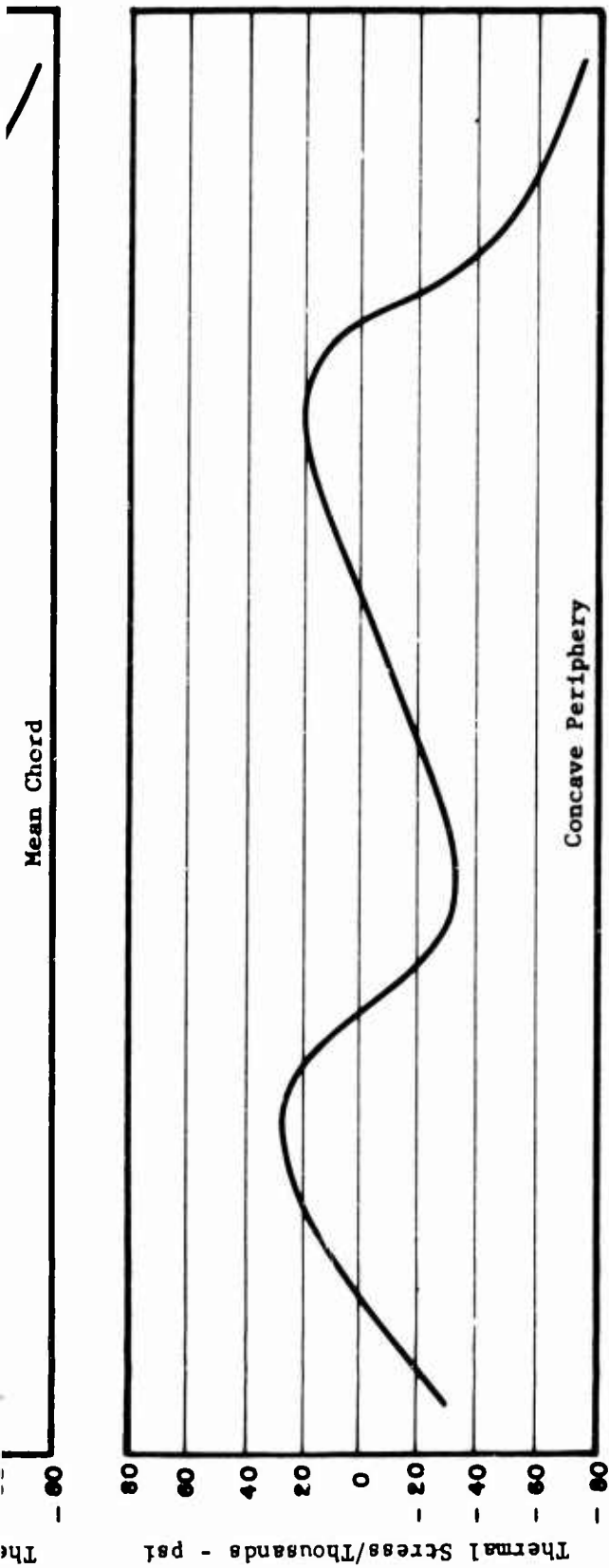
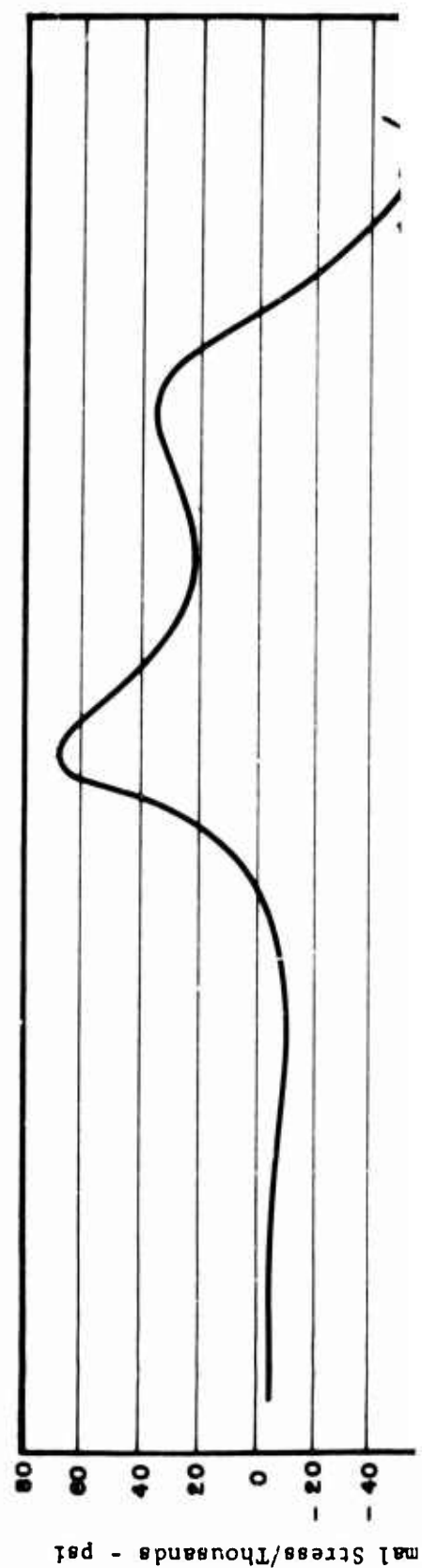
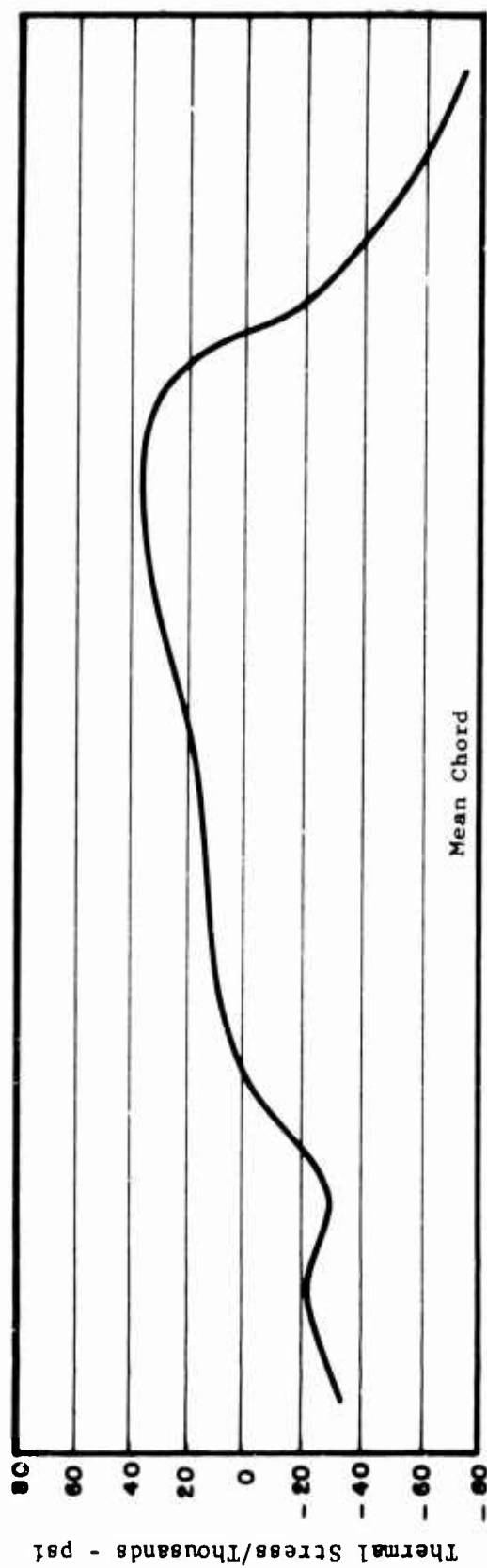
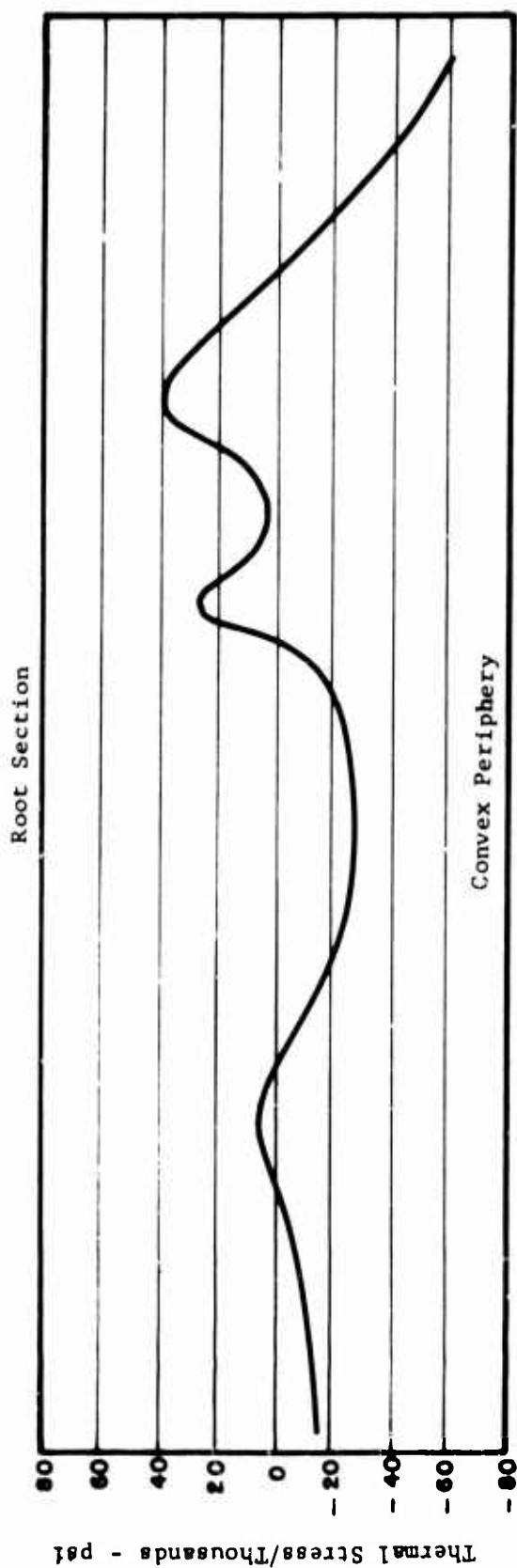


Figure 116. Turbine Stator Blade Thermal Stresses - Mean Section.

B



A

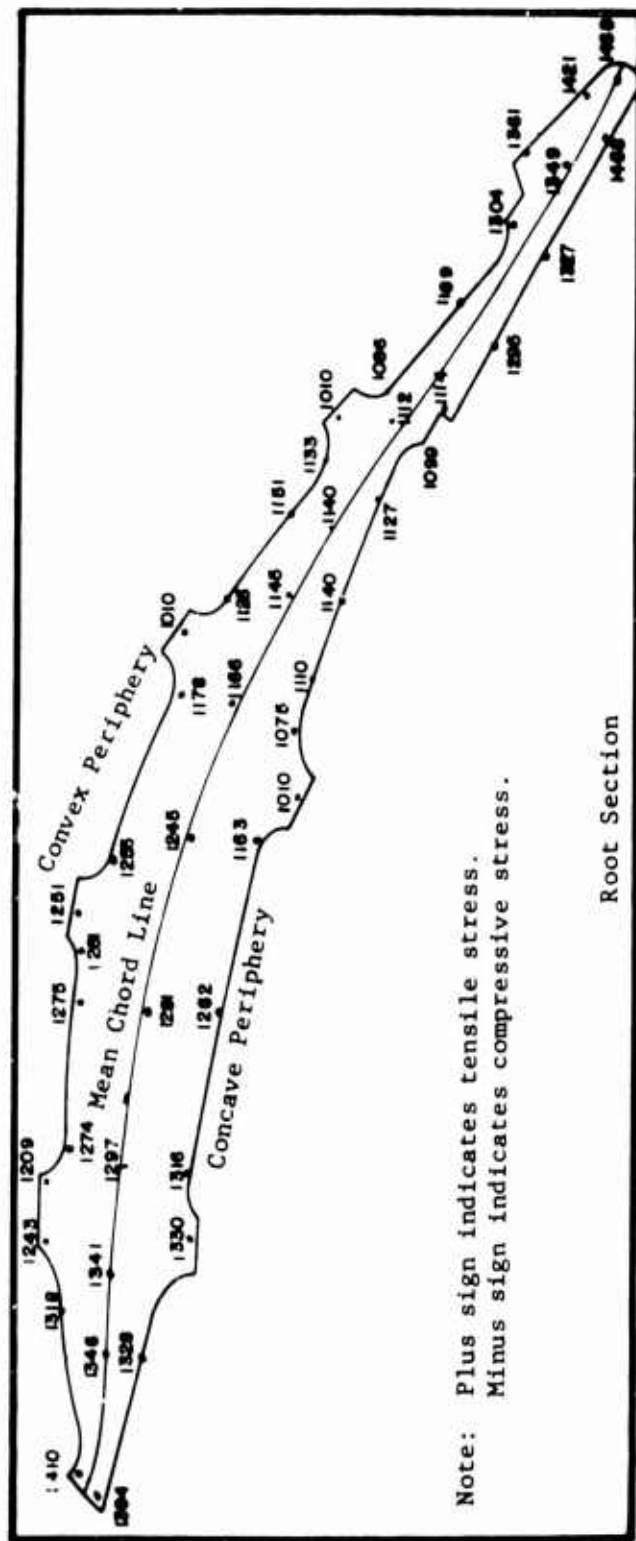
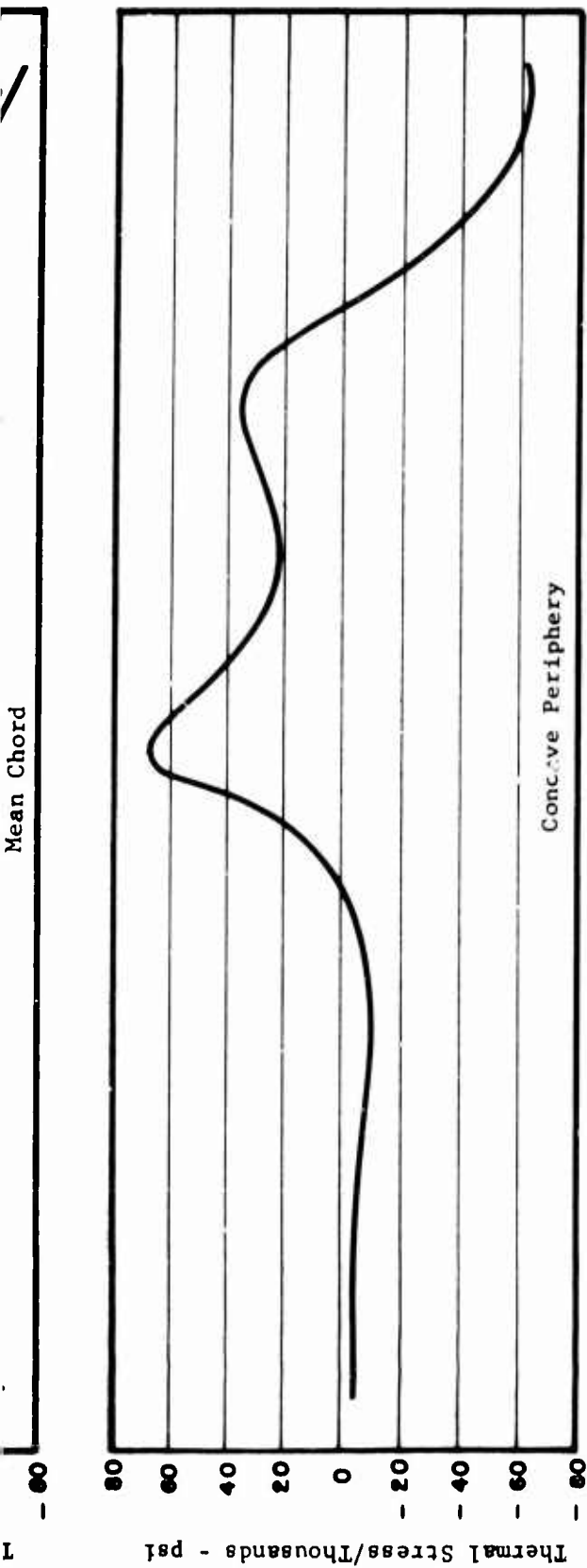


Figure 117. Turbine Stator Blade Thermal Stresses - Root Section.

B

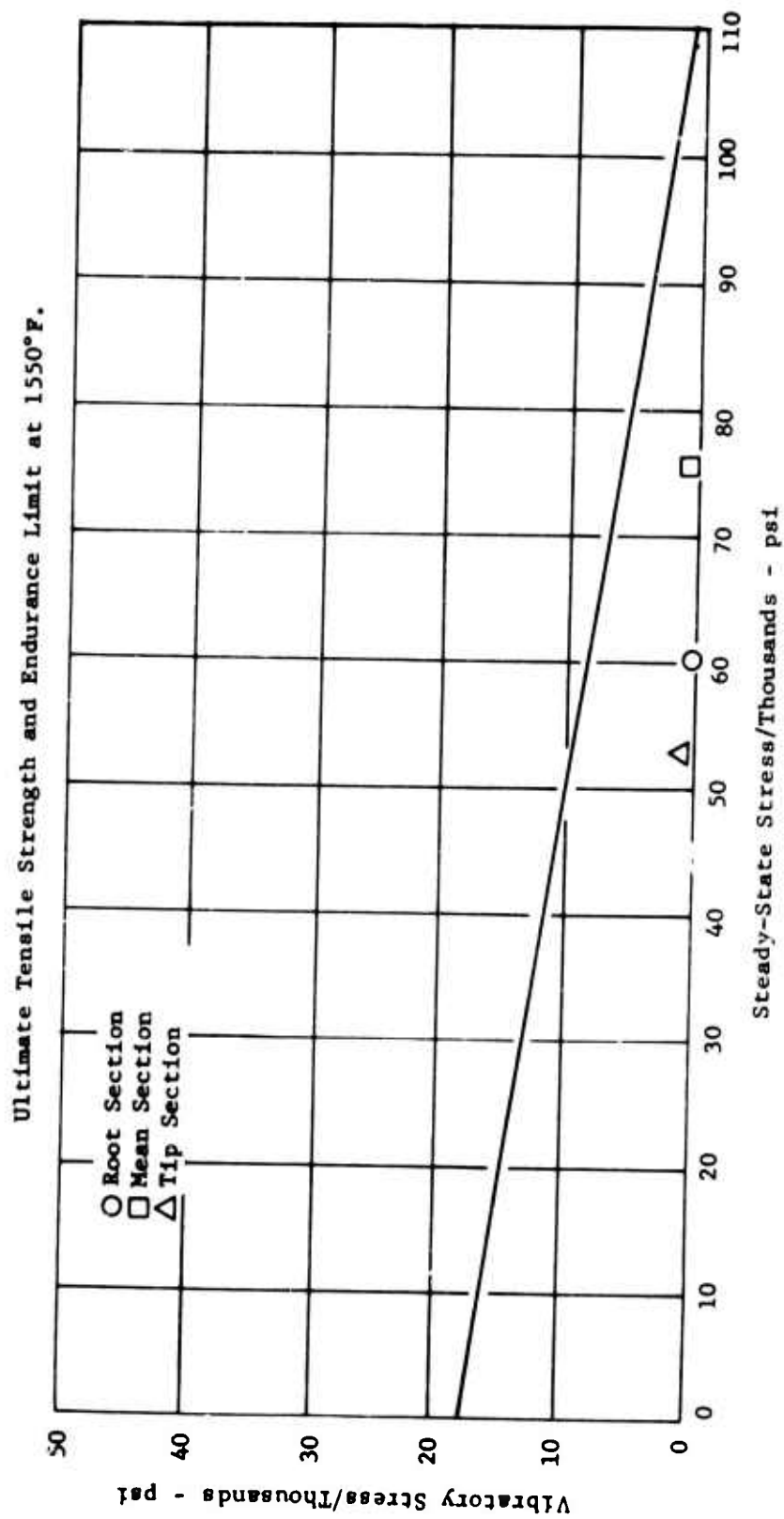
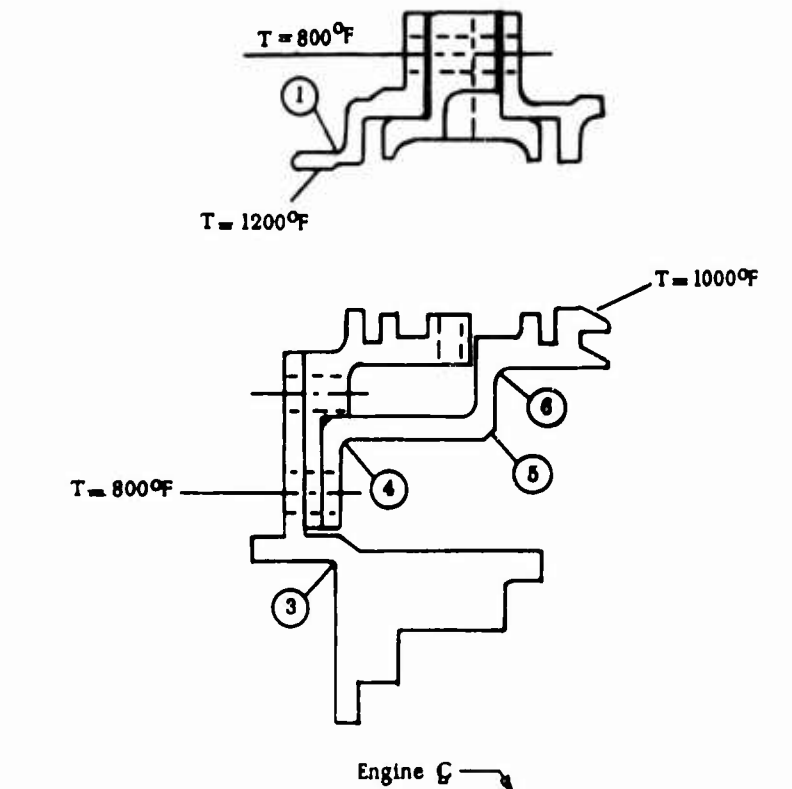


Figure 118. Goodman Diagram for Turbine Stator Blade.

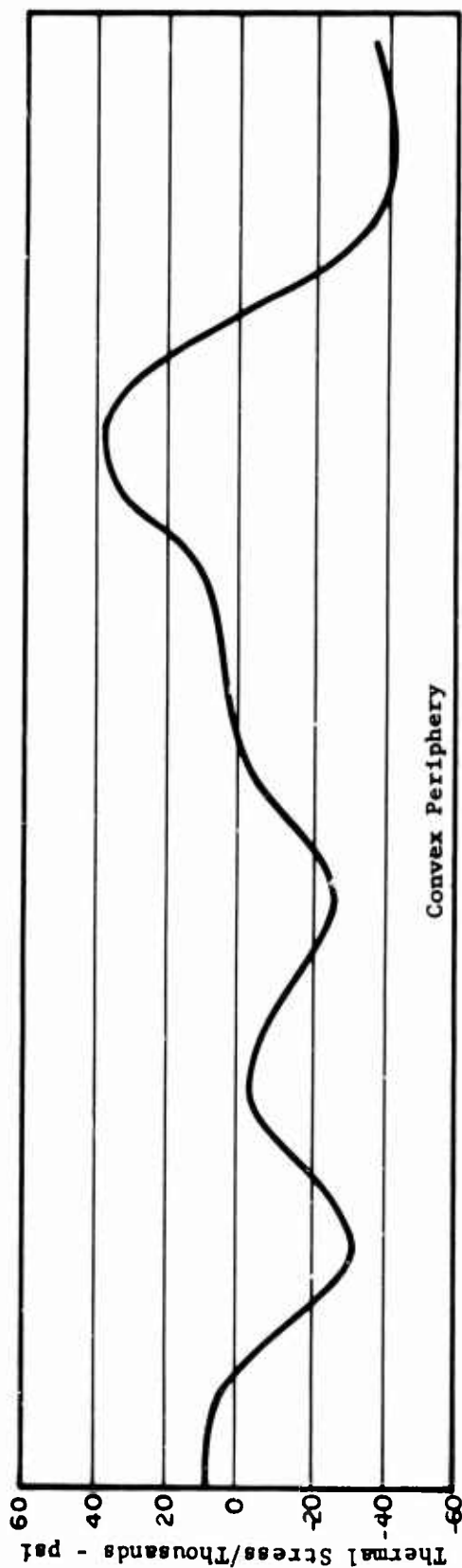


	Outer	Inner			
Stress	1	3	4	5	6
Bending	70.6	1.0	11.1	45.6	50.6
Hoop	-69.6				

Stress in ksi - René 41 at 1200°F - 0.2% Yield Stress = 118,000 psi

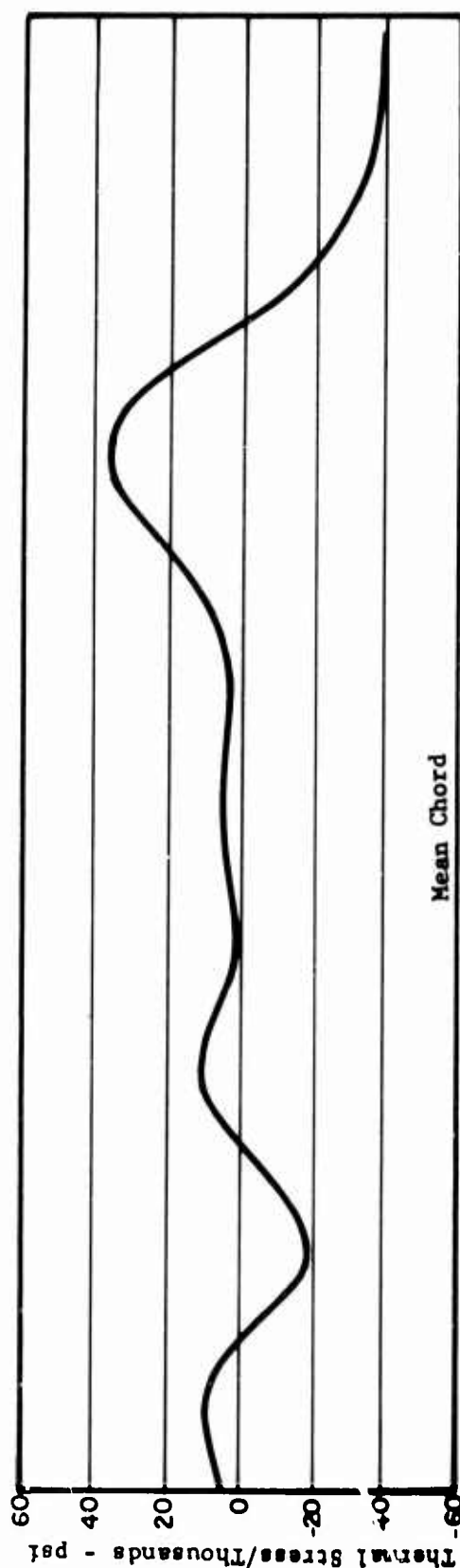
Figure 119. Stress in Stator Support Ring.

Root Section

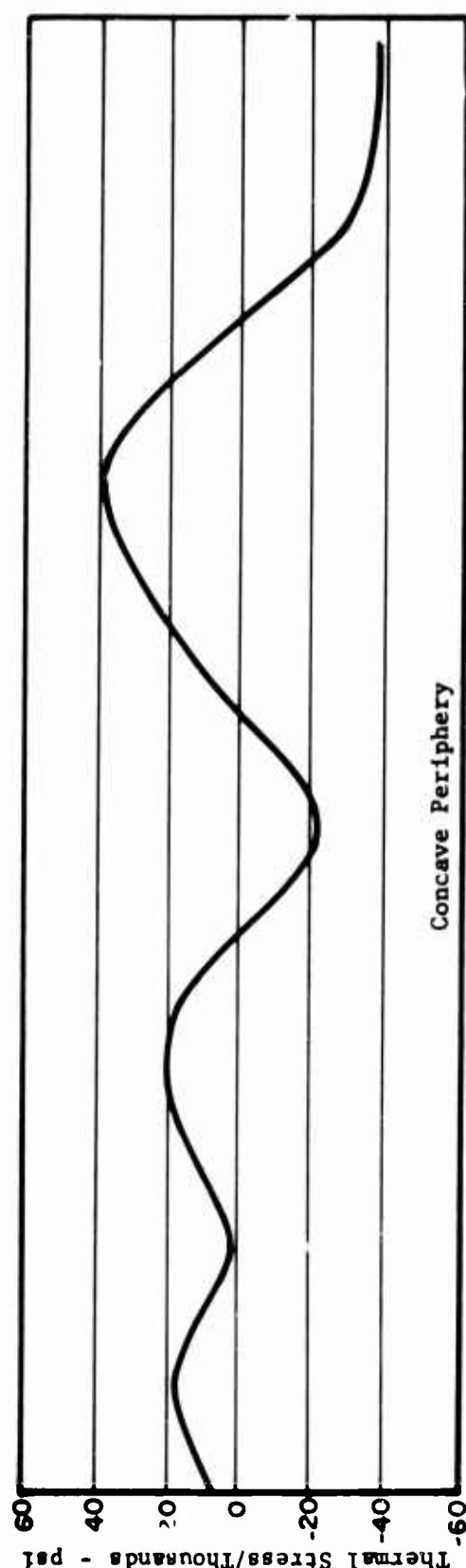


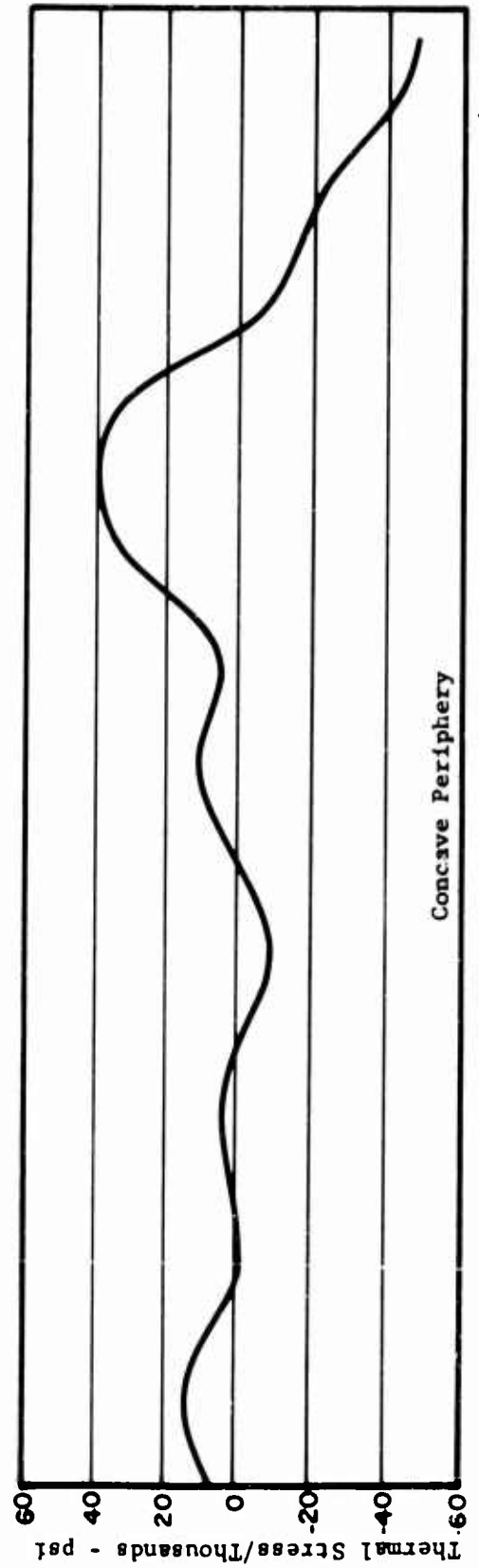
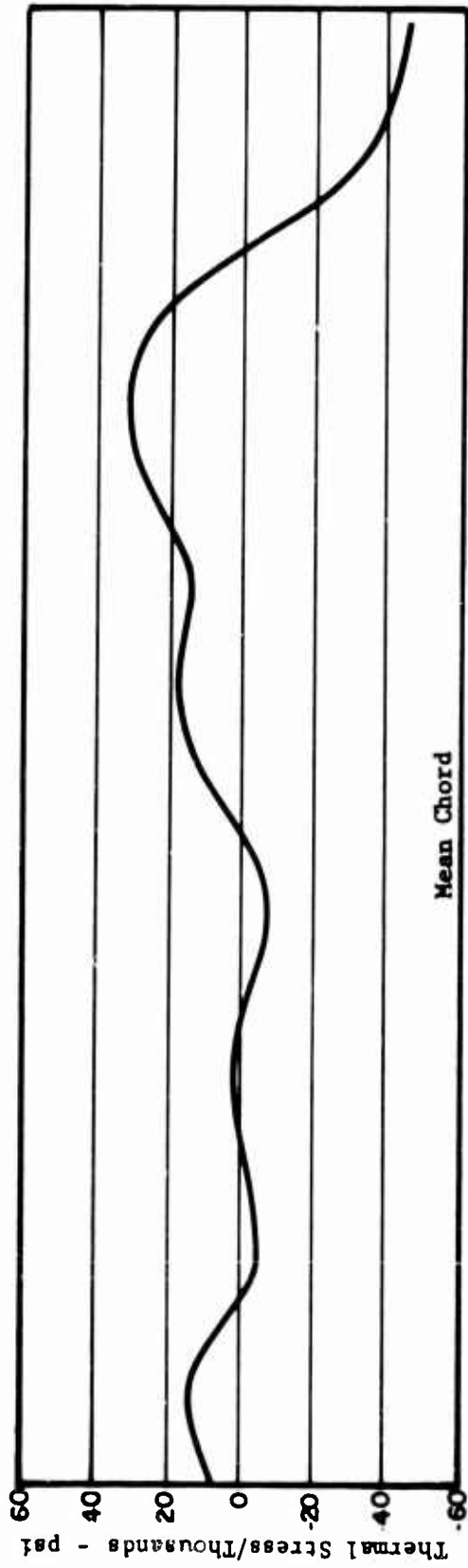
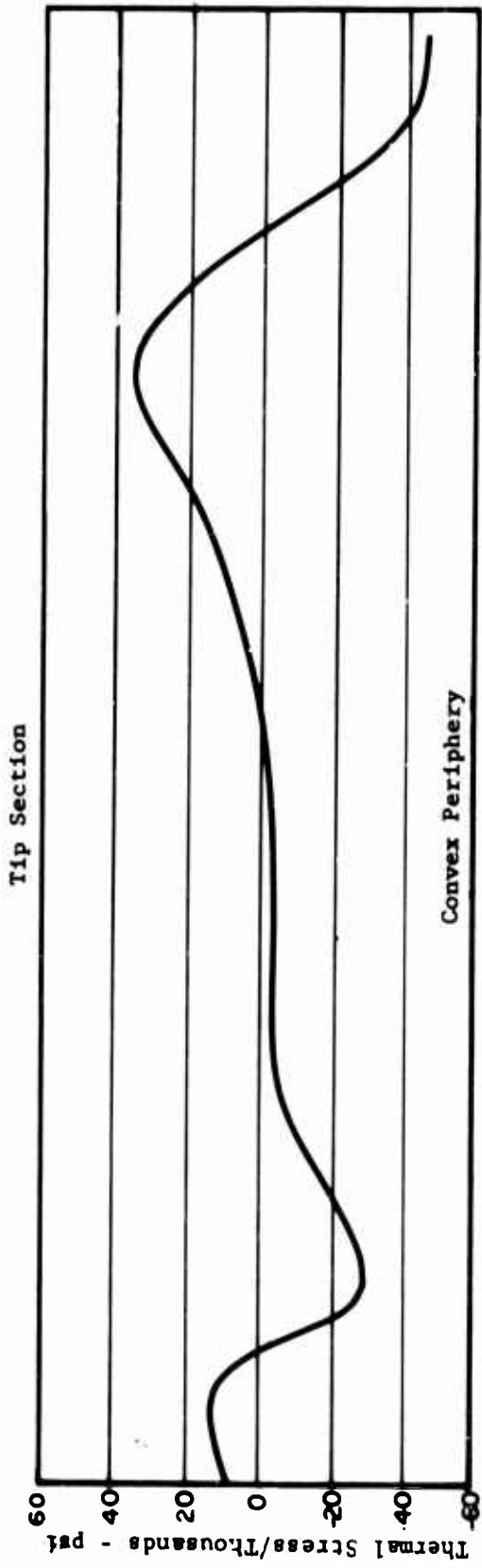
Convex Periphery

Mean Chord



Concave Periphery





A

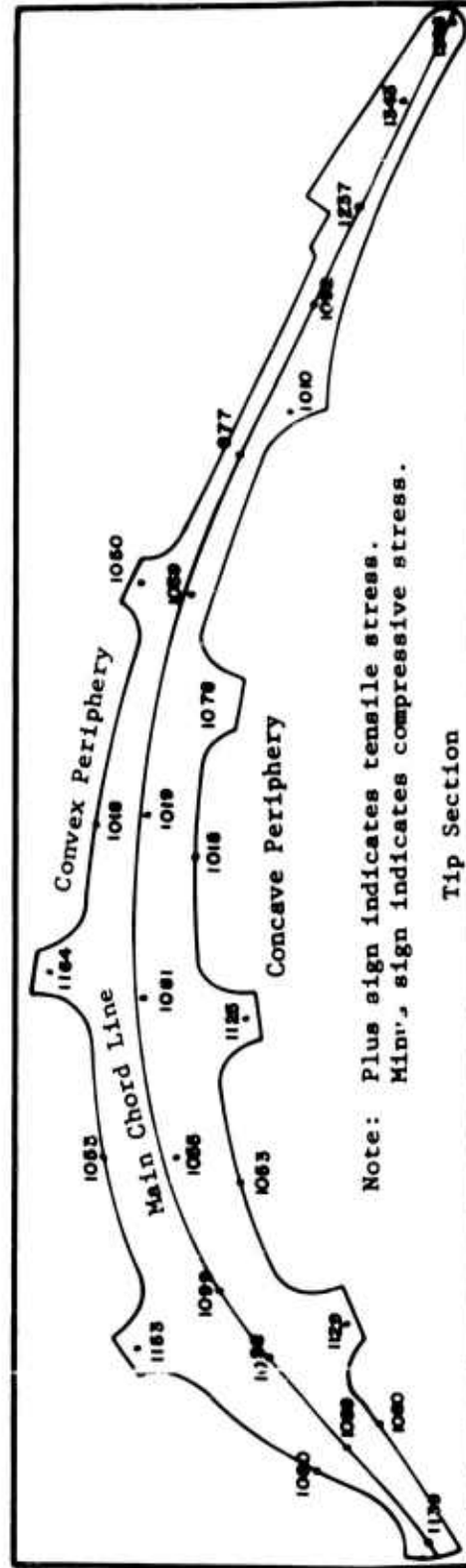
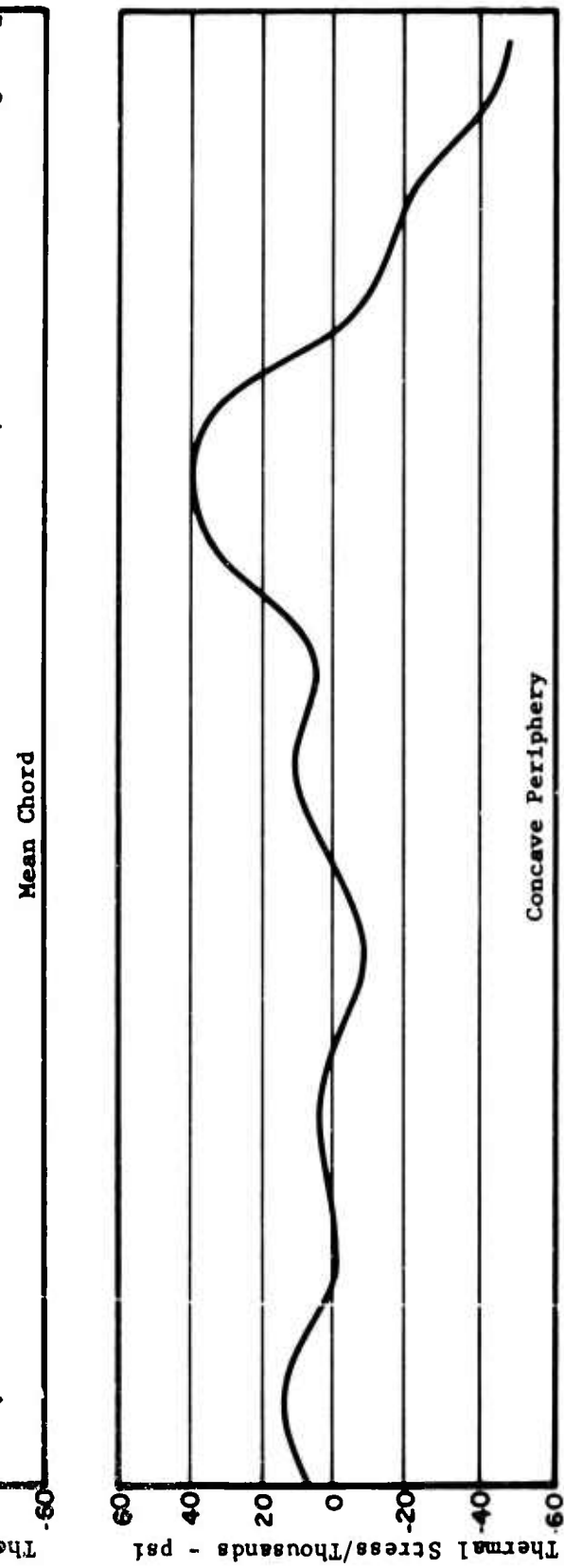
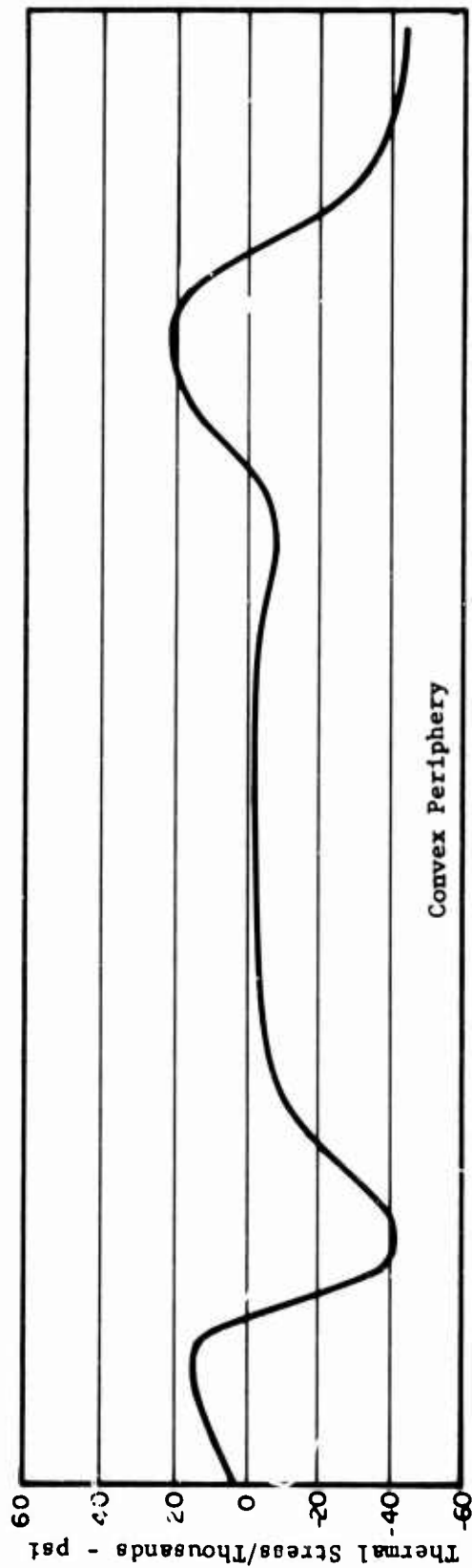


Figure 121. Turbine Rotor Blade Thermal Stresses - Tip Section.

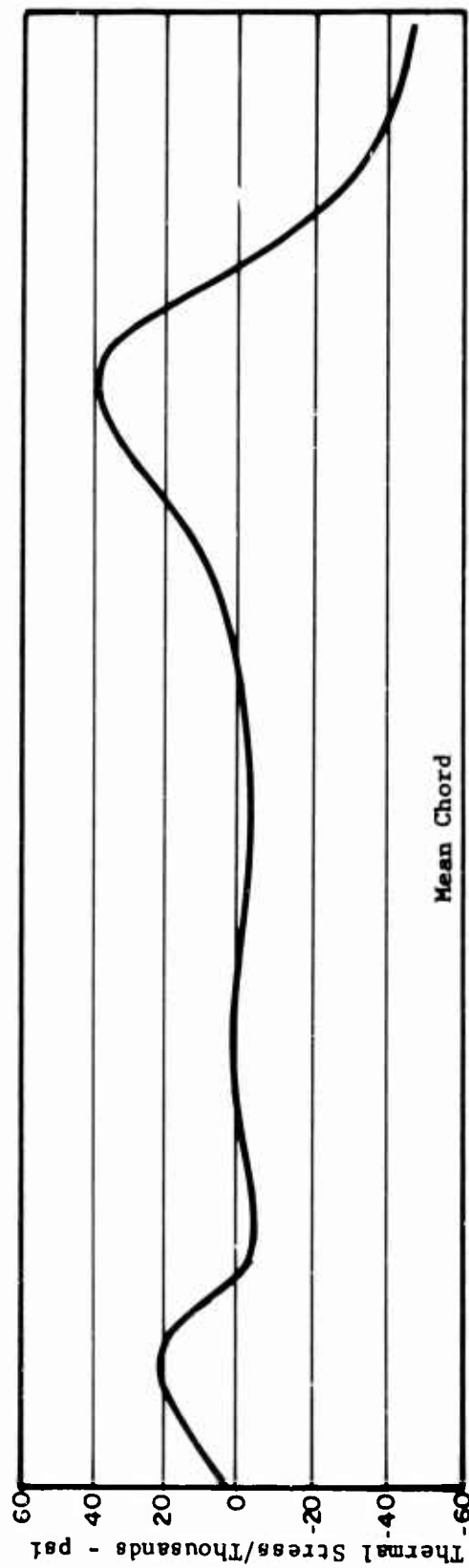
B

Mean Section

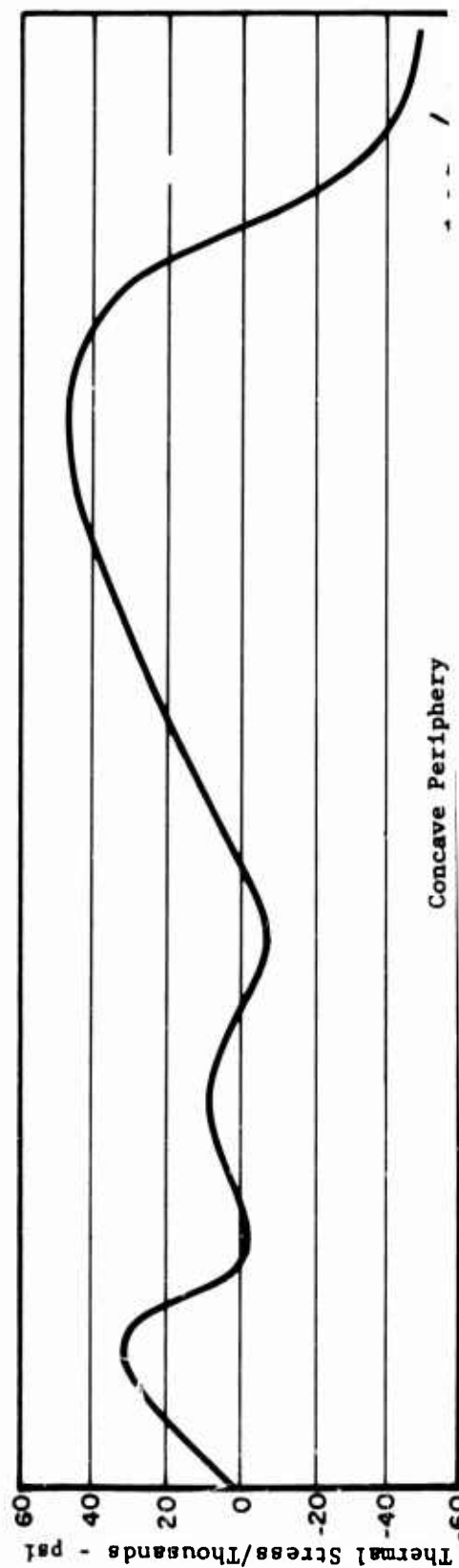


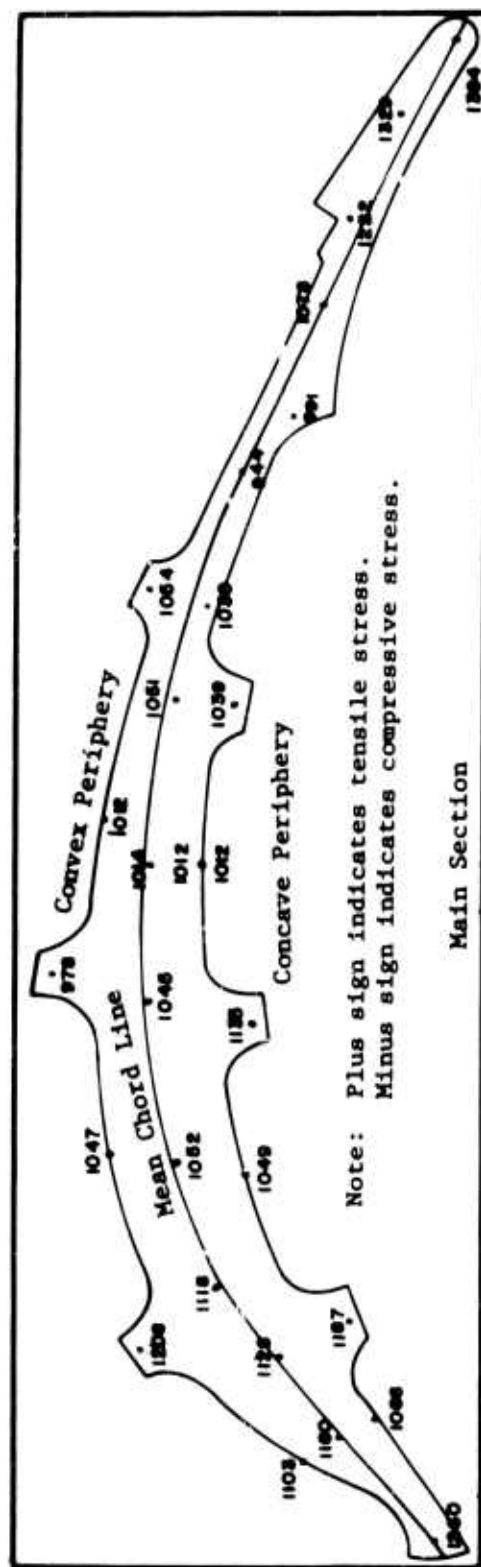
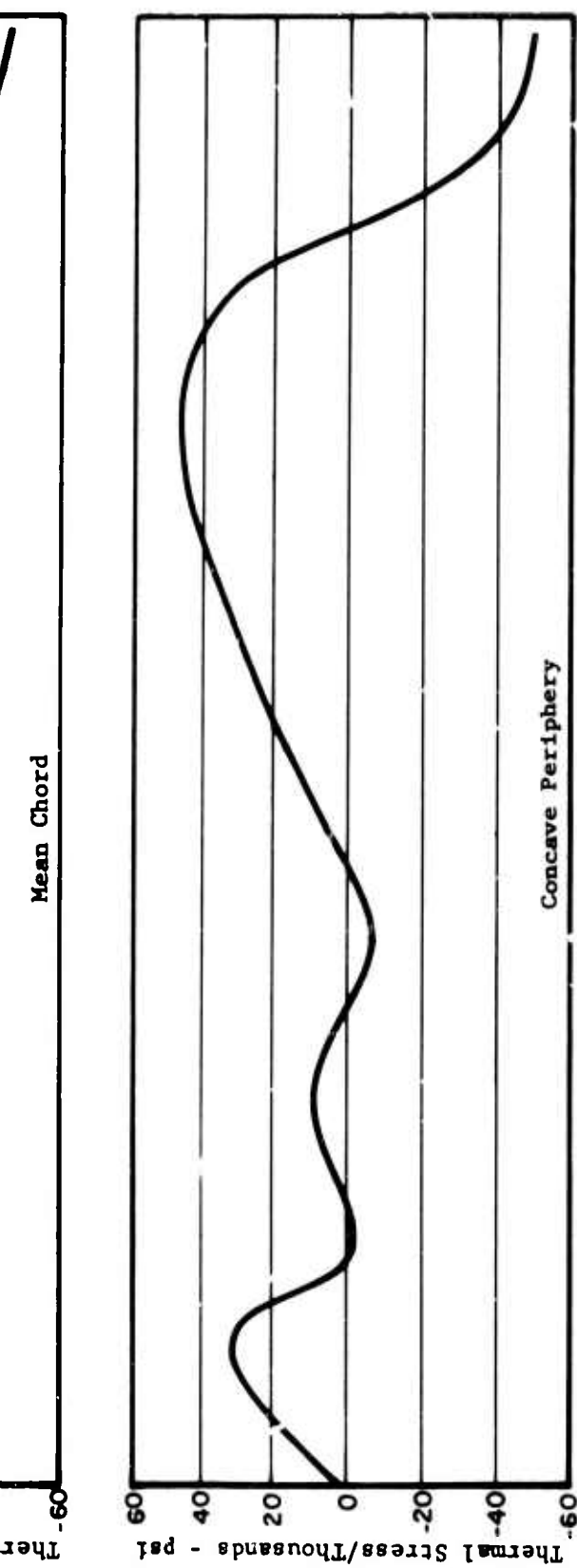
Convex Periphery

Mean Chord



Concave Periphery





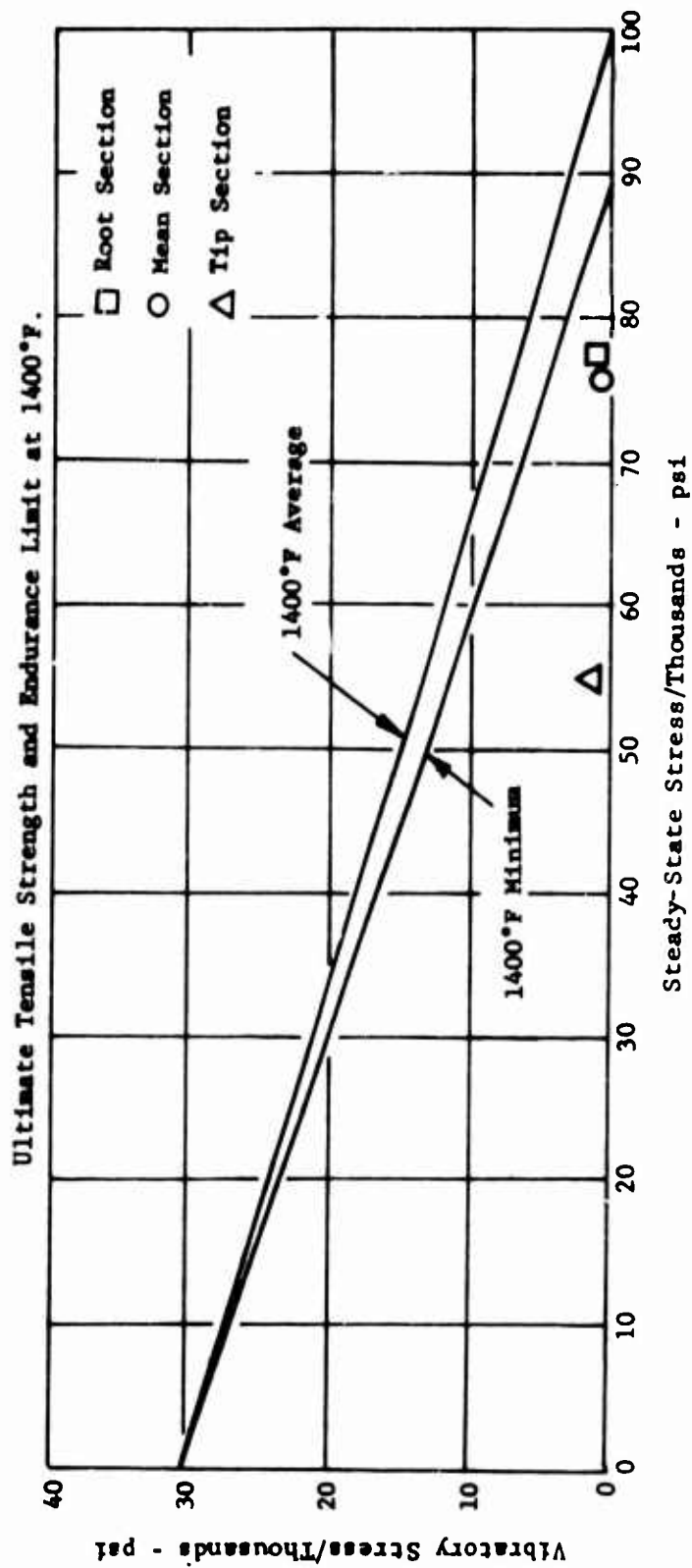


Figure 123. Goodman Diagram for Turbine Rotor Blade Strut.

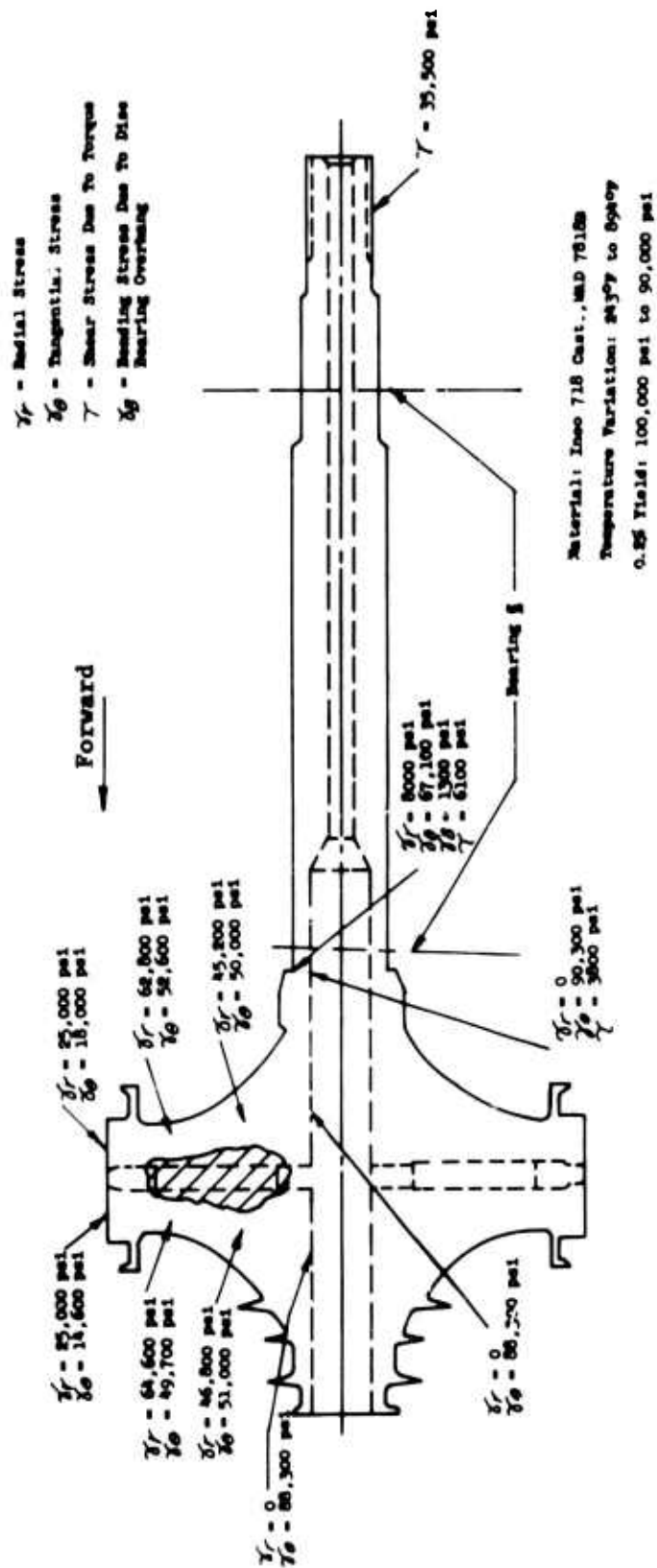


Figure 124. Summary of Stresses for Turbine Rotor Disc.

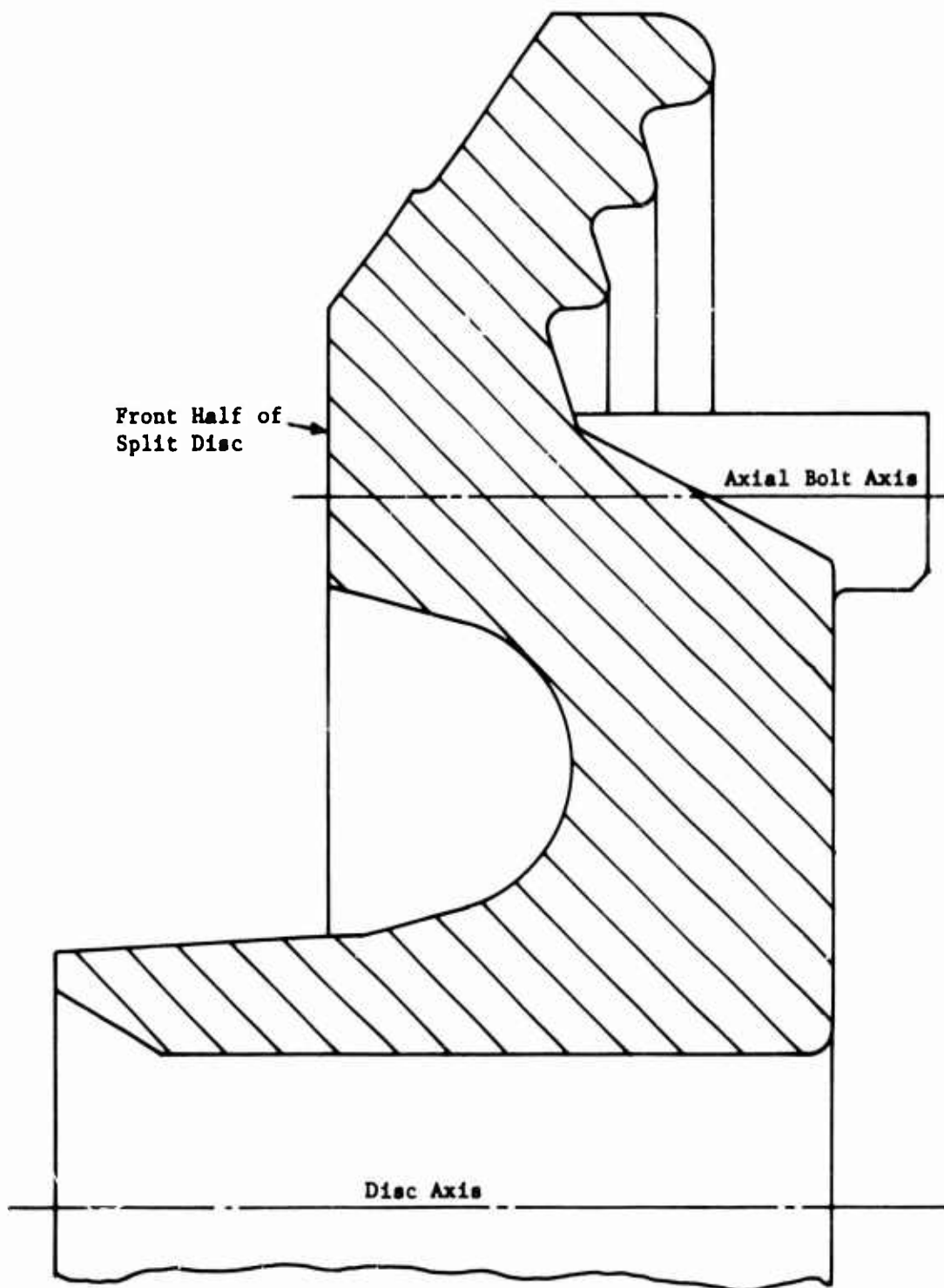


Figure 125. Turbine Disc Fir Tree Configuration.

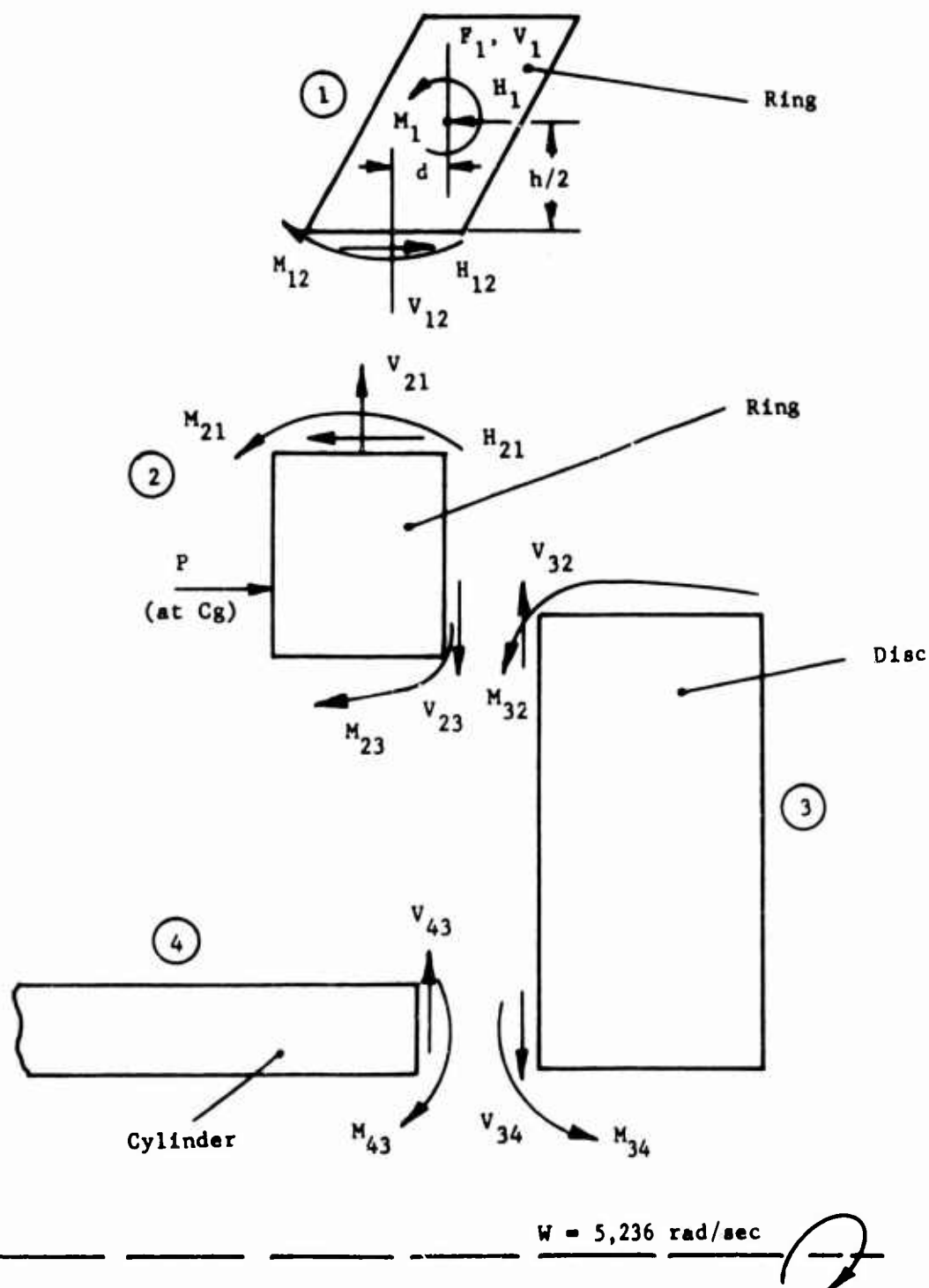
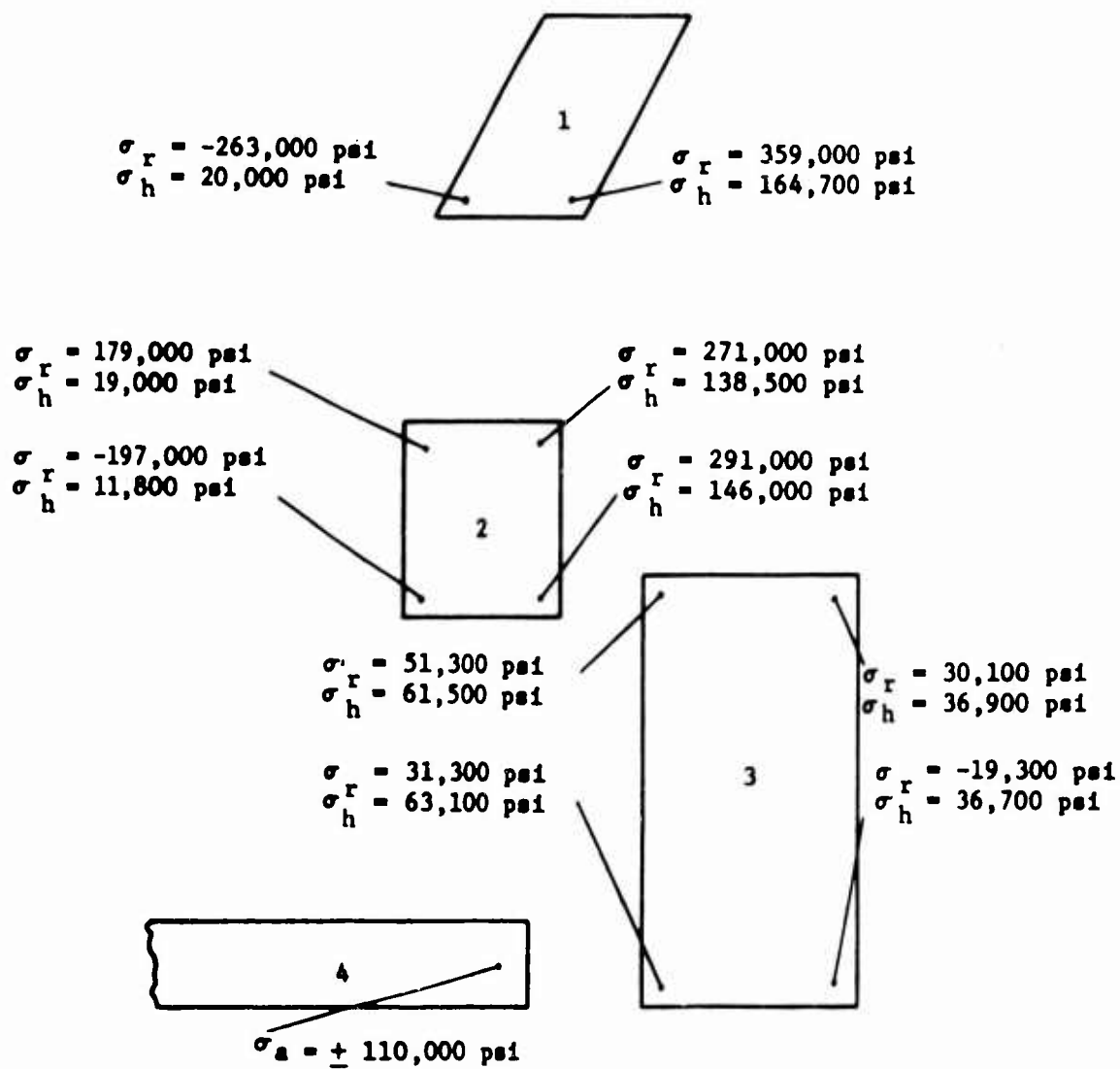


Figure 126. Turbine Disc Fir Tree Configuration - Free Body Diagram.



Disc Axis

Disc Material: René 41 Forged
Yield Stress: $\sigma_y \approx 150,000 \text{ psi}$

Note:
 σ_r - Radial Stress
 σ_h - Hoop Stress
 σ_a - Axial Stress

Figure 127. Turbine Disc Stress Levels Fir Tree Configuration.

5.0 EXPERIMENTAL EVALUATION

5.1 FABRICATION TECHNIQUE

5.1.1 Airfoil Forming

Skin forming was accomplished satisfactorily for the Ni55 and Ni V Cb materials. Blades with these skins have been subjected to 14 hours of testing with gas temperatures ranging from 1378°F to 2900°F without any detrimental effects. The techniques developed for the cascade rig blades are readily adaptable to the stator blades of the full round rig.

The method used in fabricating the stator airfoil parallels the normal production procedures in that a cylindrical mandrel is used for winding and sintering. The part is then hand rolled, to obtain the required thickness as well as strength and permeability characteristics. The skin is finally cut in two pieces along the diameter and turned end for end so as to orient the mesh air passages in the same direction on each side of the blade.

The rotor blade skins, because of blade twist, are more adapted to fabrication from porous sheet stock. The material is cut and then formed on dies for each side of the blade. Orientation of the mesh air passage is maintained as in the stator blades. Techniques and experience gained on the larger transpiration-cooled blades of other programs are applicable to the small turbine rig blade; thus, this accounts for the high confidence level and success in forming the smaller blades. Test specimens of the porous skin on the cascade blades were flow checked, and the anticipated uniform flow characteristics were verified. Bend tests of specimens also were performed to confirm formability and fatigue strength.

During the early stages of the airfoil forming investigation, use was made of an elliptical or formed mandrel. This offers interesting possibilities on the shape of the airfoil surface. Further study of this technique would be warranted for production forming or for more complicated airfoils.

5.1.2 Strut Fabrication

The blade struts of the cascade rig were precision cast of high-strength René 41. Five representative spar castings were subjected to a complete layout inspection prior to machining and were found to be dimensionally acceptable. The airfoil sections of these castings were almost perfect; contour variations were substantially below the blueprint allowable tolerance. Figure 128 shows three of these spar castings (the two lines on each airfoil were scribed during inspection). Material strength, determined from test bars of the material heat lot, was well above specification values both at room temperature and at 1200°F.

The stator spars for the full round rig are similar to those for the cascade in that the airfoil section remains as cast and only the shelf and sealing surfaces are ground. The cooling air holes on the shelf as well as the instrumentation holes for the thermocouples are formed by an electrical

discharge process. Fabrication techniques for the stator blades will be essentially the same as for the cascade with the addition of curved shelves.

The rotor blade spars are ground as with the stators only in the shelf area. The grinding, however, is much simpler since the blades merely butt together rather than overlap. A final tip grinding operation will be required after the blades and disc are welded together.

5.1.3 Strut-to-Airfoil Attachments

The objective of this phase of the program was to establish manufacturing feasibility, to develop proper electron beam weld settings, and to evaluate fixtures and techniques to weld transpiration-cooled blades.

Conclusions

1. The electron beam welding process, when carefully controlled, is an excellent method for joining mesh to solid struts.
2. Metallurgically sound welds were obtained between cast René 41 struts and N155 Poroloy or Ni V Cb Poroloy skin material combinations, as found in cascade stator blades.
3. Dimensionally acceptable welds were made on the four joint configurations found on the stator and rotor blades:
 - a. Skin-to-skin butt weld at the leading edge.
 - b. Land welds.
 - c. Closure butt welds at the trailing edge.
 - d. Closure welds at the shoulders.
4. A program to weld a complete stator blade using tooling designed and fabricated at C-W was successful, and the production welding of stator blades for the first static rig has been completed as of this date.
5. A high-voltage, low-amperage electron beam welder of the Hamilton-Zeiss type was found to be the best adaptable machine for this application.

The feasibility of electron beam welding of porous skin to a solid strut having been effectively proven, the areas of major concentration in turbine blade welding development were:

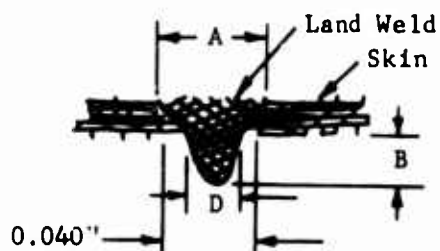
1. To establish skin-strut material compatibility.
2. To optimize weld settings and techniques for welding the four typical joints on a blade.

The initial welding development was conducted on a Sciaky electron beam welder, but application considerations resulted in the choice of a Hamilton-Zeiss machine, which is more adaptable for the precise welding required in the blade configuration.

The stator blade material combinations investigated were cast René 41 strut (WAD 7813) with 0.020-inch-thick Ni55 and Ni V Cb Poroloy skins. Both combinations proved to be weldable, and the typically sound weld microstructures of both are shown in Figures 129 and 130.

The following is the analysis of the four joints characteristic of the blade design:

Land Welds



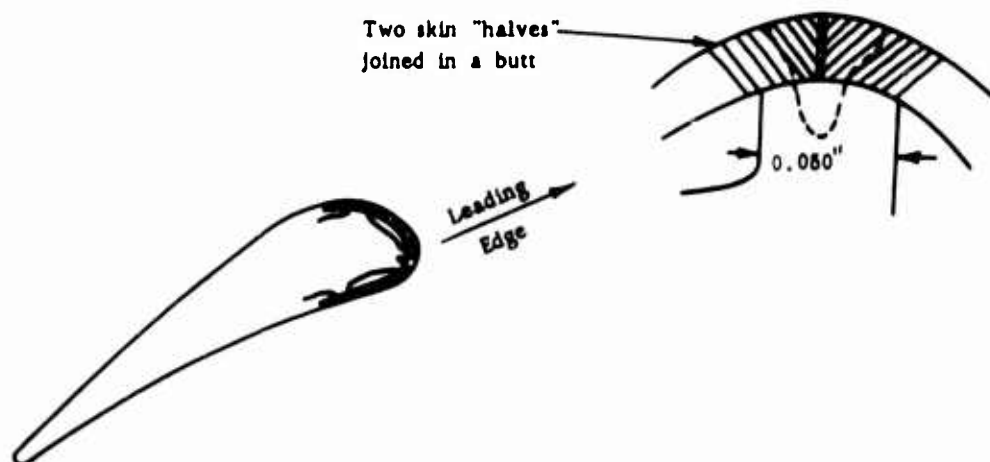
"C" is weld surface depression.
Joints marked ✓ are called
"Land Joints" in this report.
"B" is land weld penetration

The requirement was to determine the beam settings and to develop a technique to obtain a weld nugget that will (a) be contained within the 0.040-inch land surface, (b) have a minimum reproducible depth of penetration, and (c) exhibit a reasonably flush weld surface. The weld settings to accomplish this were developed from a series of trials, and the resulting weld configurations from four samples were measured:

<u>Dim/Spec No.</u>	<u>FLD-3</u>	<u>FLD-4</u>	<u>FLE-1</u>	<u>FLE-2 (Leading Edge)</u>
A	0.046	0.049	0.053	0.051
B	0.016	0.017	0.020	0.016
C	0.003	0.0016	0.0018	0.0023
D	0.016	0.017	0.017	0.017

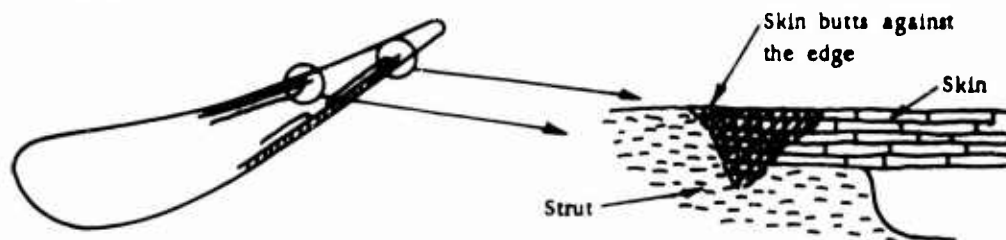
Although the weld width dimension A exceeds the width of the land, an improvement at the present time would be at a sacrifice to the minimum skin-strut weld interface and surface depression. Although the worst condition found is sample FLE-1, which overlaps the land by approximately 0.006 inch on each side, it is only 0.003 inch over the welding specification requirement.

Leading Edge



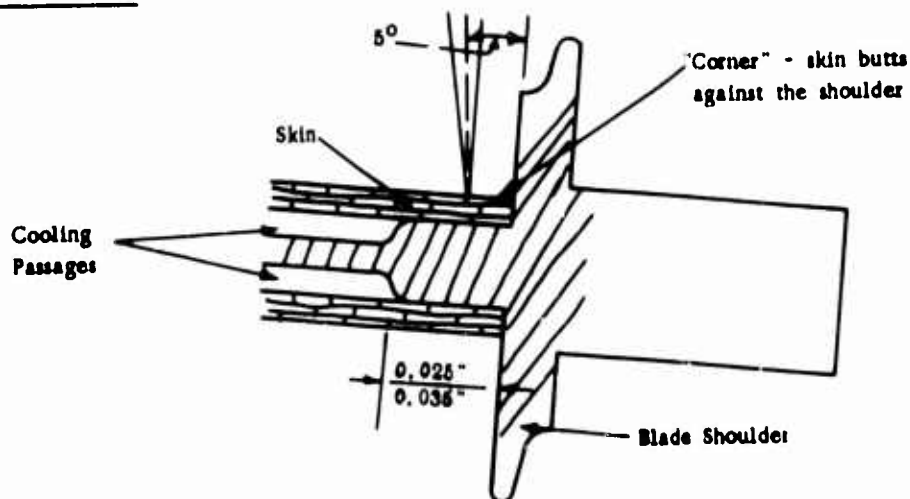
As shown above, the leading edge of the blade is made by butting two pieces of formed skin together. Two approaches were considered: one was to weld the two skins individually, and the other was to weld the two skins simultaneously to the land. The latter was chosen, and the result is shown in Figure 131. The weld was made by fusing the joint with one pass, followed by three low power cosmetic passes which raised the weld surface. The same pass sequence was used for the land welds.

Trailing Edge



The skin butts against the solid strut on both sides of the blade. The weld surface quality is a function of skin fit-up. If the skin mates well with the step, the resulting weld is as shown in Figure 132; but in most cases, a gap is created from the cumulative shrinkage of land welds, and the use of filler wire to fill the gap is necessary. If the skin is too long, it is almost impossible to trim it back for a good fit for welding. The additional weld passes that are made on the poorly-fitted joints cause buckling of the trailing edge. The solution to this problem is to carefully cut the skins to the proper length prior to welding, allowing 0.005 inch shrinkage for each weld.

Shoulder Welds



The shoulder closure welds as seen in Figures 133 and 134 present a very sensitive problem. The technique developed for welding the shoulders is as shown above; i.e., the blade is tilted at approximately 5 degrees to the beam, and the weld is made by directing the beam on the corner. Four or five straight-line passes in sequence were necessary to complete one shoulder. The problems arise when the skin is not in intimate contact with the shoulder or when the land welds, which terminate at the shoulder, have excessive craters. (There is a characteristic tendency to form a deep crater when the beam runs off the part and into a shield or a mask.) The resulting closure welds have localized depressions and cracks. Any additional weld passes to correct this situation tend to buckle the shoulders. A solution to this problem is threefold:

1. Cut the skins squarely, do not chamfer, and make them to fit snugly at the shoulders.
2. Eliminate weld craters by sloping out the beam.
3. If absolutely necessary, use Hastelloy X filler wire, but do not make more than one weld pass.

Figures 135 through 138 show a fully welded cascade rig stator blade. A cross section of the blade (Figure 137) shows the accurate centering of welds and uniform depth of penetration made possible by the excellent tooling designed by C-W. The composite picture of the welded turbine blade (Figure 138) demonstrates the excellent, versatile application of the electron beam process.

5.1.4 Blade-to-Rotor-Disc Attachment

Mar-M-302 blade material was successfully welded to Inco 718 by the electron beam process. The material samples used were 1/2 inch thick, and thus simulated the maximum weld thickness in the blade and disc assembly. Figure 139 shows a cross section of the weld at a magnification of five.

Figure 140 is a composite picture showing the weld and heat-affected zone in the "as welded" condition at a magnification of one hundred. Figure 141 shows the effect of aging on the microstructure. These photos indicate the excellence of the electron beam welding technique.

Tensile test specimens of 0.252-inch diameter were machined from the welded test assembly to determine mechanical properties across the weld. The results given in Table XVI show the minimum and the maximum yield strengths of five samples taken at each of the temperatures shown. The tests were continued to ultimate tensile rupture, and all specimens were fractured in the weaker Mar-M-302 base material.

TABLE XVI WELD TEST MECHANICAL PROPERTIES					
Test Temp (°F)	Ultimate Tensile (ksi)	.2% Yield (ksi)	Elongation (%)	Reduction in Area (%)	Efficiency (Weld Strength to Base Metal for 5 Specimens)
Room Temp	124.6	99.2	3.0	2.0	YS Eff Range 94% - 98.5%
	116.4	102.0	3.0	1.6	TS Eff Range 91.5% - 97.5%
700	94.6	72.4	4.5	1.6	YS Eff Range 88% - 100+%
	101.2	86.5	2.0	1.6	TS Eff Range 90% - 100+%
850	97.6	71.0	2.2	1.6	YS Eff Range 90% - 100+%
	109.0	89.2	2.0	0.8	TS Eff Range 94% - 100+%
1000	88.7	69.2	4.0	1.2	YS Eff Range 92% - 100+%
	103.2	84.2	3.0	2.8	TS Eff Range 90.5% - 100+%

Efficiencies were calculated from typical base material values shown in Table XVII.

TABLE XVII			
BASE MATERIAL STRENGTHS			
Material	Temp	YS (ksi)	TS (ksi)
Mar-M-302	RT	104	128
	700	83	105
	850	79	100
	1000	75	98
Inco 718	RT	124	167

The test panels were heat treated after welding as follows: 8 hours aging at 1325°F, furnace cooled to 1150°F and held at 1150°F for 8 hours, then air cooled. A hardness check was made across a typical welded joint in the as-welded and after-aging condition. Figure 142 shows the hardness reading across the weld and verifies the soundness of the joint.

Further evaluation of the blade and disc welding will include stress-rupture tests of welded specimens and development of techniques to weld blade samples onto a solid disc. Other blade material will also be evaluated, namely, Inco 713 LC. This material has already been successfully welded to Inco 718, as shown in Figures 143 and 144, and further mechanical tests are planned similar to those described above. In this way, the latest state-of-the-art material and welding techniques will be incorporated in the rig hardware.

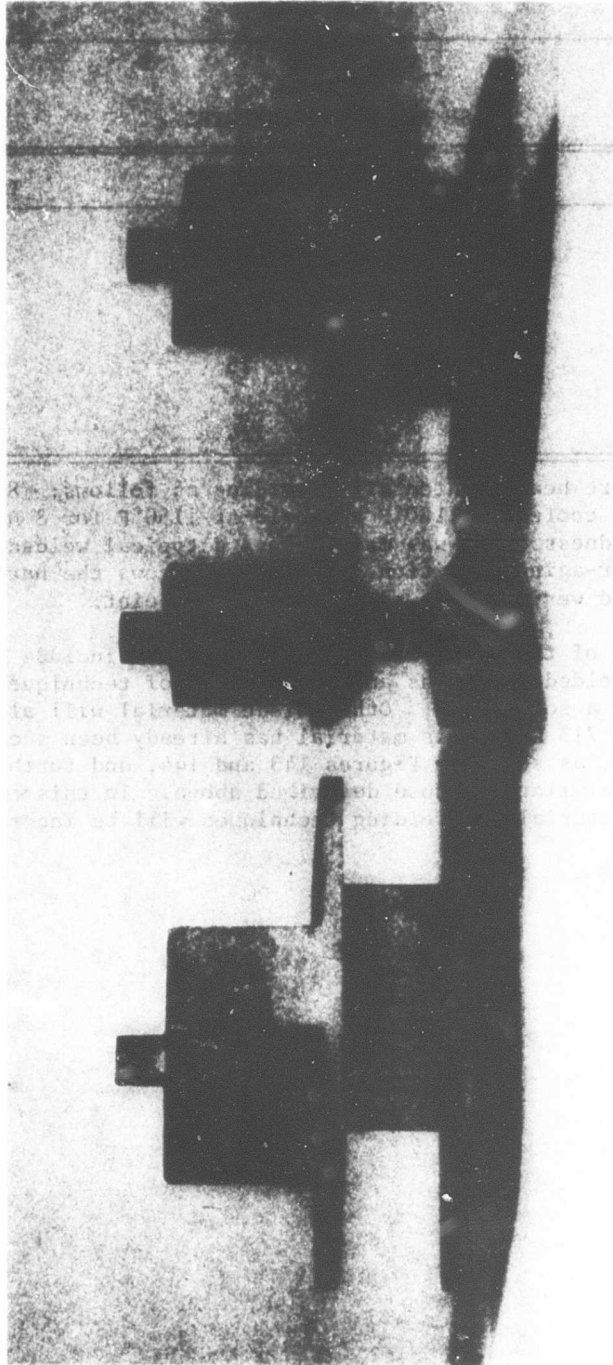


Figure 128. Cascade Rig Blade Strut Castings.

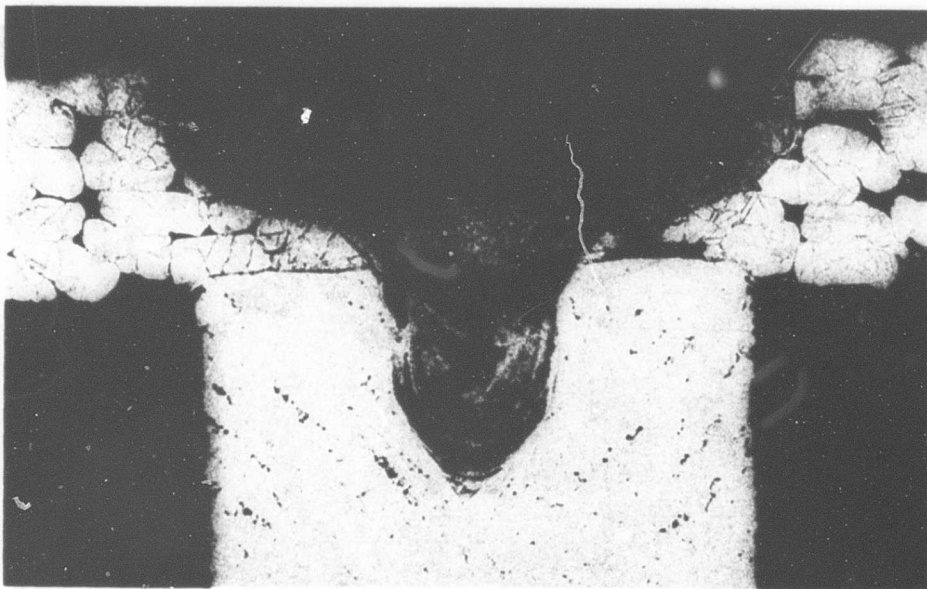


Figure 129. Micrograph of a Typical Land Weld. (The Strut Is Cast René 41, The Skin Is N155 Poroloy.)



Figure 130. Ni V Cb Poroloy Skin Welded to Cast René 41 Strut.

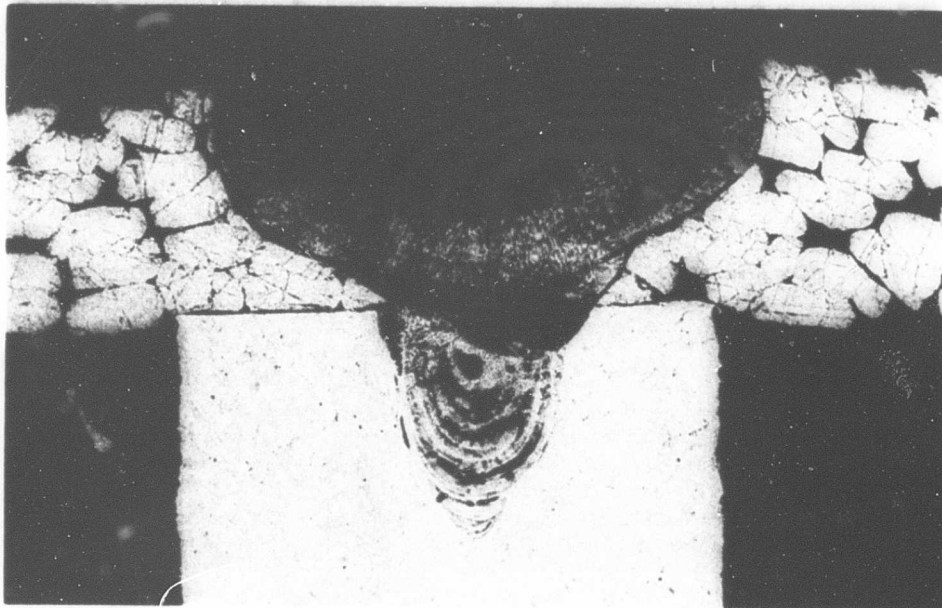


Figure 131. A Micrograph of a Butt Weld at the Blade Leading Edge. (The Skins Are Welded Together and to the Leading Edge Simultaneously.)

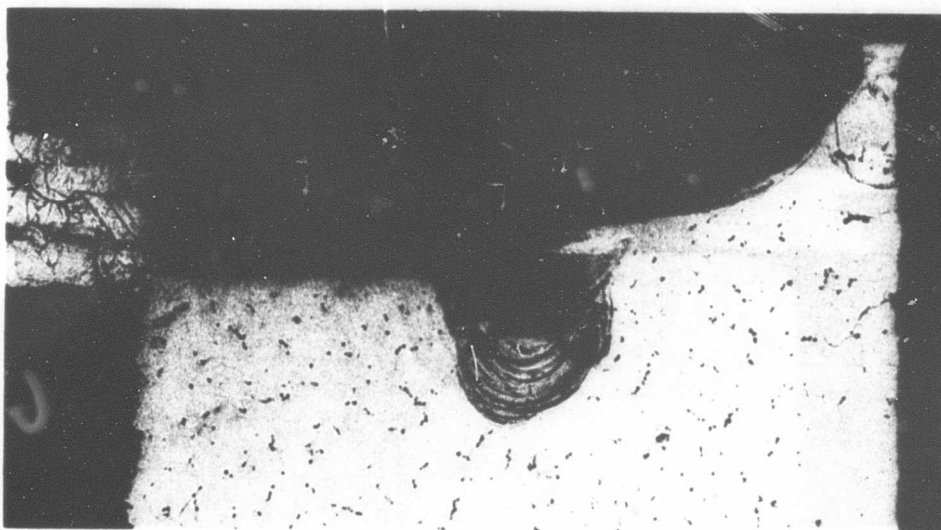


Figure 132. A Simulated Trailing Edge Closure Weld. (No Filler Wire Was Required in This Specimen.)

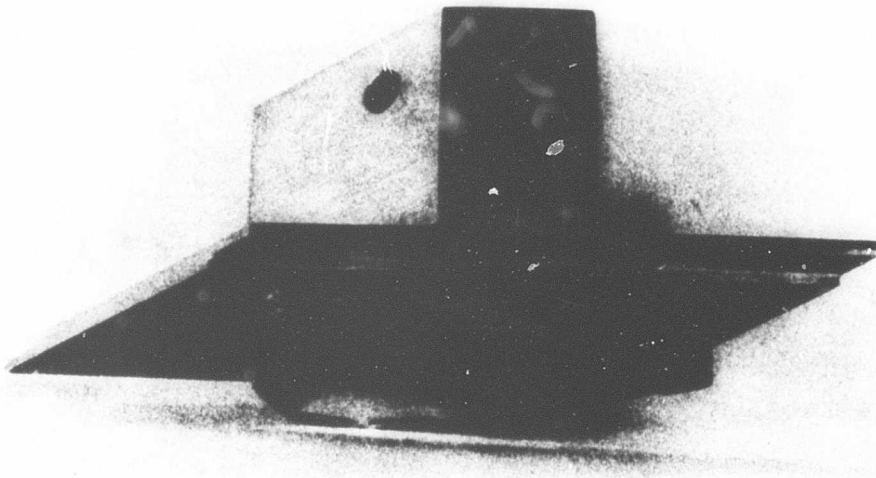


Figure 133. A Shoulder Closure Weld Made by Tilting the Shoulder at 5 Degrees to the Beam. (No Filler Wire Was Used.)



Figure 134. A Cross Section of the Shoulder Filler Weld.

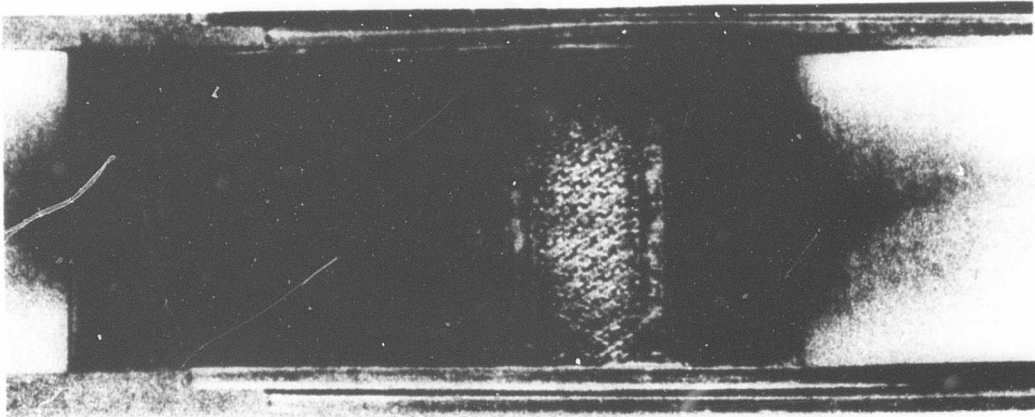


Figure 135. Fully Welded Convex Side of a Blade.

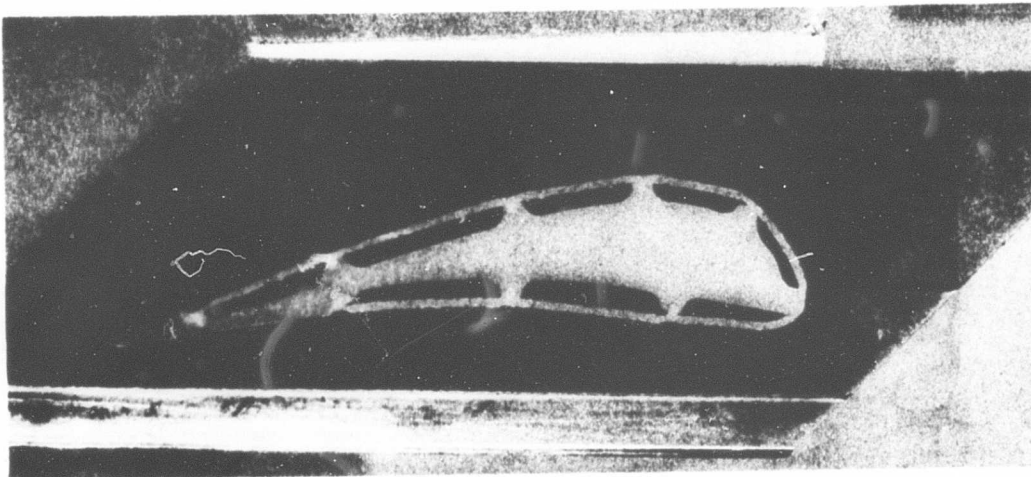


Figure 136. A Cross Section of a Fully Welded Blade.

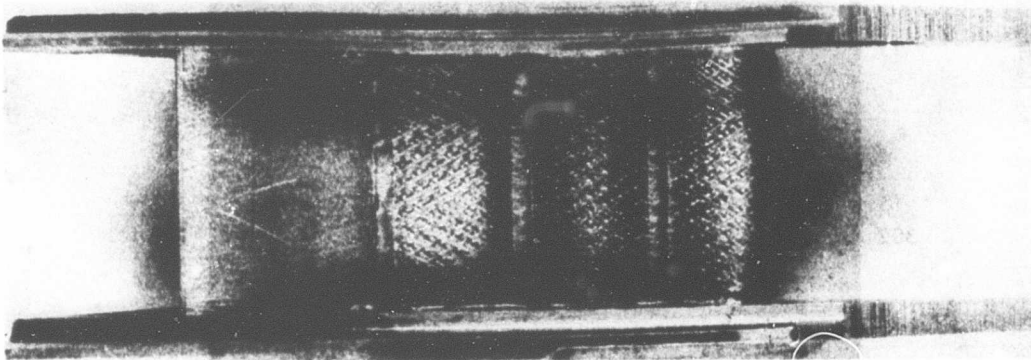


Figure 137. A Welded Concave Side of a Stator Blade.

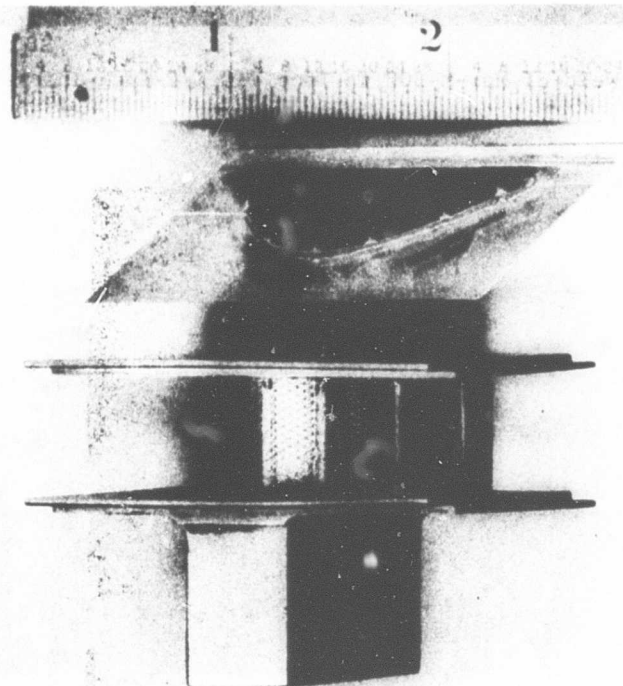


Figure 138. A Composite Picture of an EB Welded Stator Blade. (Note the Size of the Blade.)

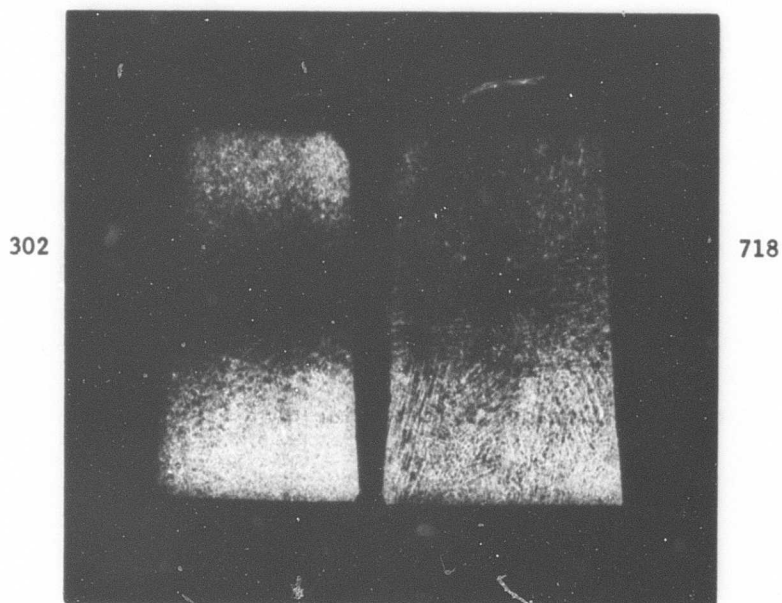


Figure 139. Weld of Mar-M-302 to Inco 718 1/2-Inch-Thick Specimens.

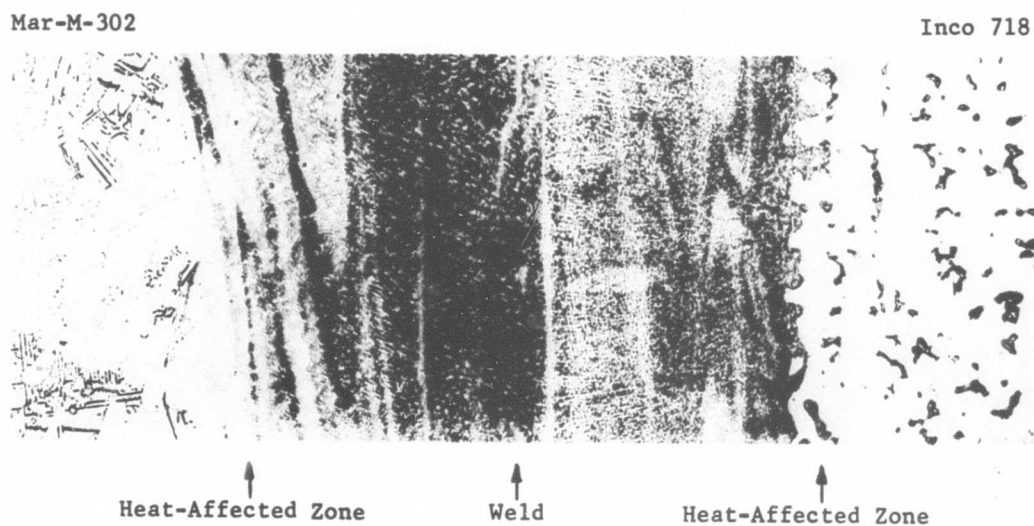


Figure 140. Photomicrograph of Mar-M-302 and Inco 718.

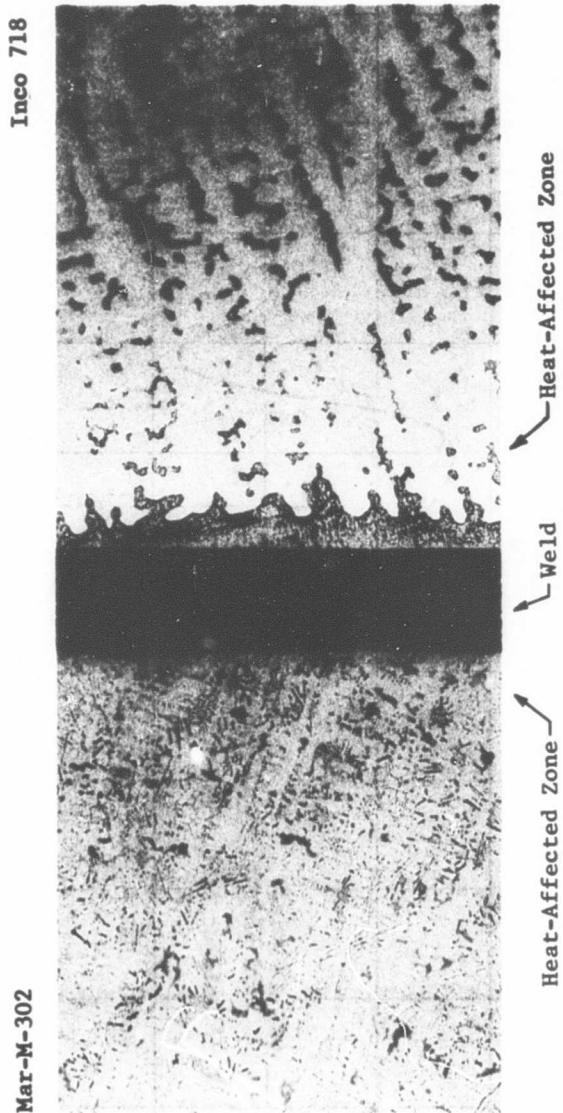


Figure 141. Photomicrograph of Mar-M-302 Welded to Inco 718 - Aged Condition.

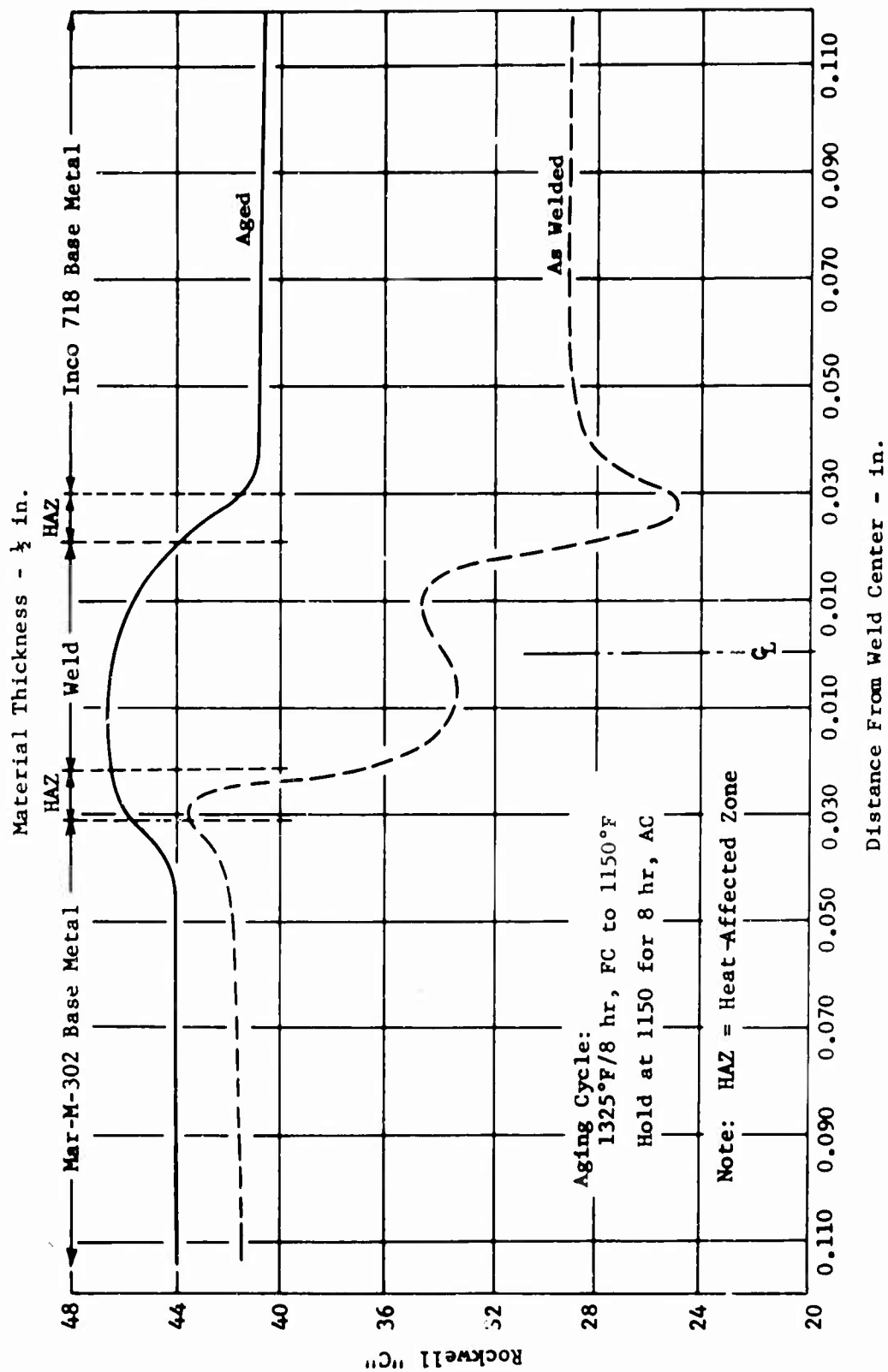
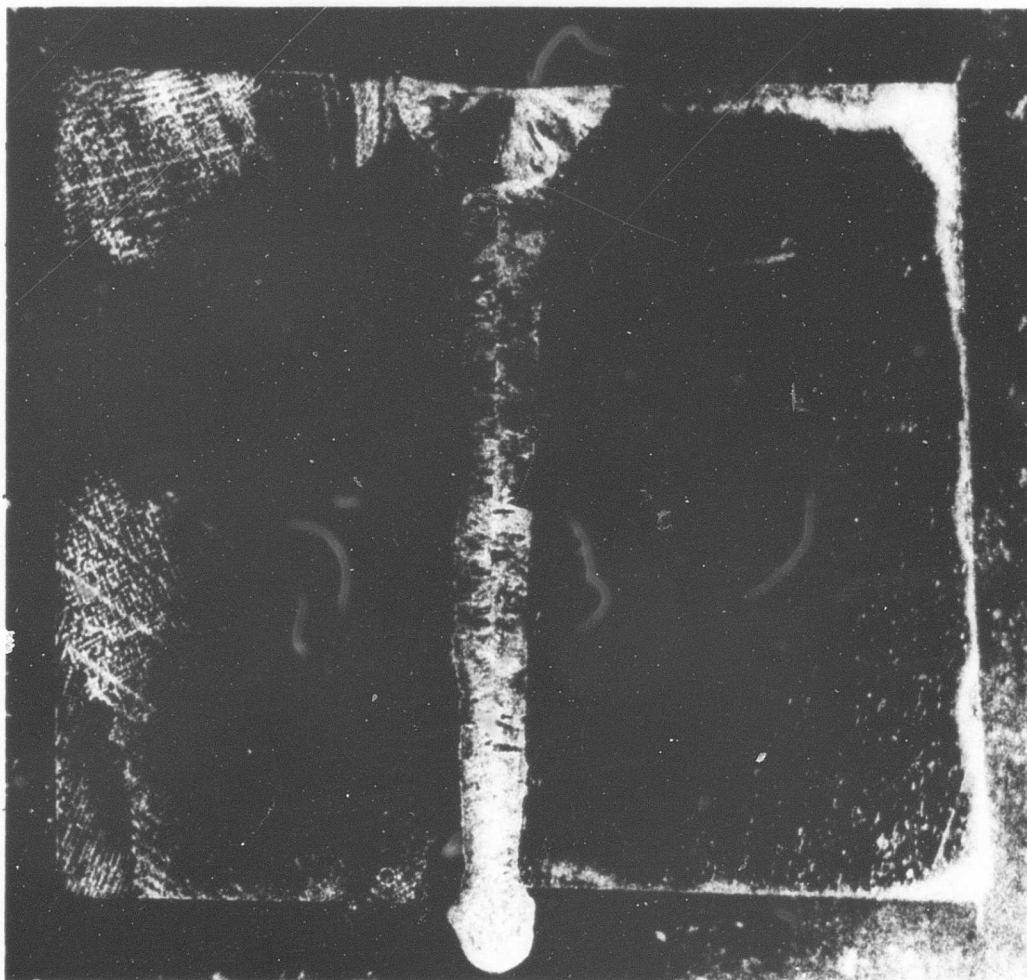


Figure 142. Hardness Survey - Inco 718 EB Welded to Mar-M-302.

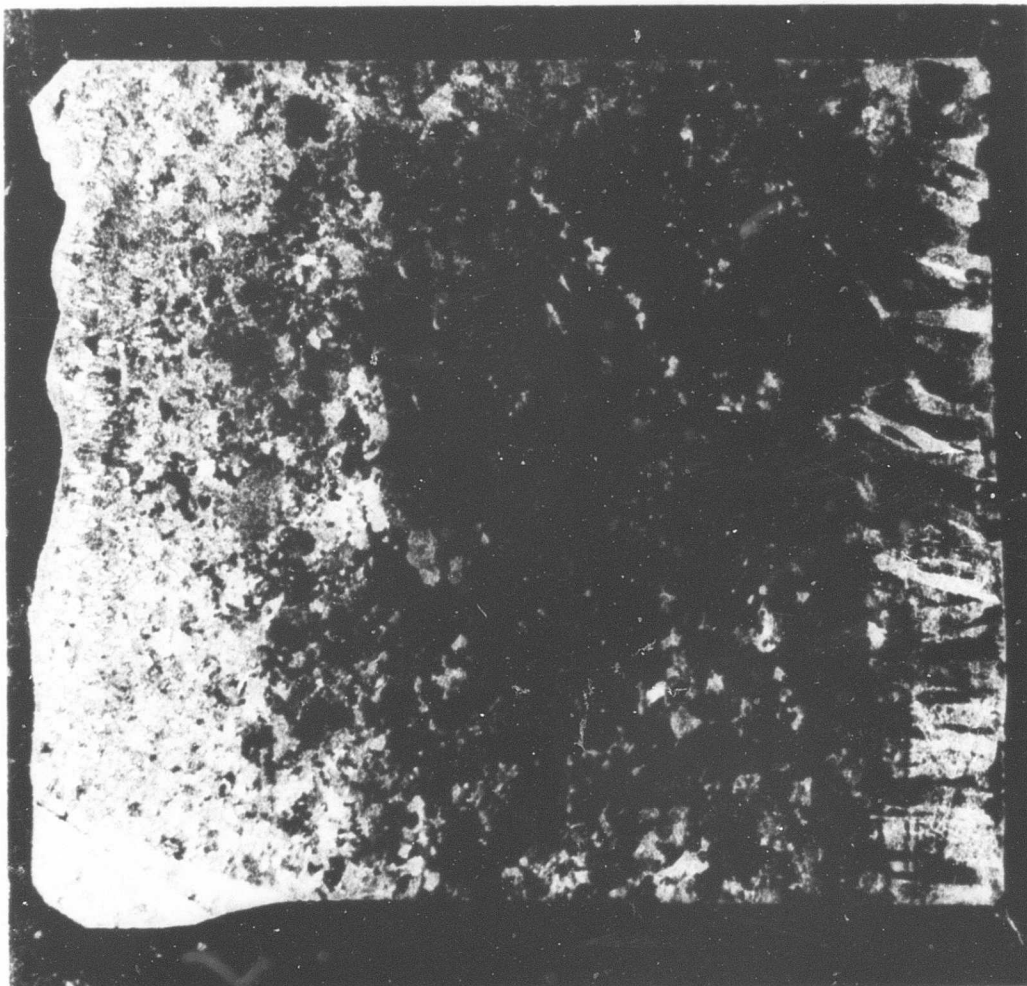
Inco 718

Inco 713LC



Mag. 11X

Figure 143. Weld of Inco 713 LC to Inco 718 1/2-Inch-Thick Specimens - After Aging.



Mag. 11X

Figure 144. Longitudinal Section Through Weld of Inco 713 LC to Inco 718
1/2-Inch-Thick Specimens - After Aging.

5.2 CASCADE RIG DESIGN

5.2.1 Cascade Rig and Blade Design

Cascade Rig - Combustor

The cascade rig combustor and blade holder have been completely designed and detailed on drawings LS 29955, sheets 1-5, and LS 29982. (See Figure 145.) The rig has a rectangular combustor made up of graphite walls supported suitably by a steel frame that will allow thermal expansion in any direction. The primary section has a headplate with vaporizer tubes and air cups in a 4-inch-long graphite panel duct of 1.8-inch by 7.46-inch (flow) cross section. This primary section is cantilevered forward from a bulkhead in an existing 10-inch-diameter duct and is supplied with compressed air at the desired inlet temperature and pressure. The secondary section consists of a graphite panel duct tapering to a (flow) cross section of 0.54 inch by 7.46 inches which is the passage section for an eight-blade cascade. This section contains adjustable film cooling slots on the upper and lower walls to permit variation of the temperature profile entering the cascade. The secondary section is cantilevered aft from the same bulkhead as above and is provided with secondary air for film cooling. The overall burner length (primary and secondary) is about 8 inches. The combustor can be tested and profile adjusted without installation of the eight-blade cascade. The mounting provisions for the blade assembly can be used for mounting instrumentation to measure exit profile conditions.

The blade cascade consists of machined supports that are mechanically attached to hold eight blades in position aft of the combustor, thus simulating installation of the stator blades in the turbine rig. Because the cascade section is rectangular, flat strip seals are necessary and are spring loaded to seal the cooling air at the back of the shelves.

The materials used for the rig were chosen to assure dependable operation of the high-temperature components. AISI 310 or 321 stainless was selected for the bulkheads, headplate, aircups, vaporizer tubes, combustor walls support brackets, and blade holder. Hastelloy X is used for the two louver plates for upper and lower film cooling. The wave springs for loading the blade shelf seals are Inconel X. The combustor wall material is silicon-carbide-coated RVC graphite. To initiate testing sooner, however, a Rokide-Z-coated ATJ graphite was used with limited success. The main problem involved with the graphites is the selection of an erosion-resistant coating that has a thermal expansion similar to the graphite. The silicon-carbide-coated RVC graphite is a newly developed combination by Union Carbide Corporation having thermal coefficients (coating and graphite) that are nearly identical over a wide temperature range.

A one-dimensional steady-state heat transfer analysis was performed to determine the temperature distribution within the cascade rig in the primary combustion zone. The resulting conservative estimates indicate that there will be no thermal failures: 2900°F graphite combustor wall, 1300°F combustor support brackets, 750°F rig housing. A two-dimensional analysis considerably more complex and time consuming, taking into account the end

effects of the combustor and bulkhead, and would more accurately estimate the temperature distribution but was considered to be unnecessary for the results required. Stress analysis of the graphite combustor parts indicates that a stress of 400 psi might be developed in bending on the top and bottom walls for a 5-psi pressure differential. The RVC graphite has a flexural strength of 2000 psi; thus, there is a large margin of safety over the possible mechanical and thermal loads.

Cascade Rig - Stator Assembly

The cascade rig was designed to illustrate that established C-W transpiration-cooled turbine technology for a relatively large, high-temperature turbine could be applied to turbine components for a small gas turbine engine. Initial design effort was directed toward the establishment of an eight-blade cascade assembly arrangement to fit snugly, as a complete unit, to the cascade rig combustion chamber rectangular exhaust opening. Within this assembly, each cascade blade is individually cantilevered from the upper support structure by means of a stem extending above the upper blade shelf; the integral shelves of each blade at both ends of the constant cross-sectional airfoil form the gas passage walls. Provisions are made to introduce cooling air to the blade spar from underneath the unsupported blade end through orifices in the shelf, which, in turn, are fed from a common cooling air chamber located in the lower support structure. The cooling air chamber is sealed from the hot gas passage with flat spring-loaded seals located behind the blade shelves and away from the main stream of the hot gases. It was intended that this design arrangement simulate the piston ring sealing configuration that is incorporated in the turbine rig design. Blade shelf-to-shelf sealing is accomplished by close-fitting lap joints.

Cascade Blade Design

Initial cascade blade design effort, utilizing the stator mean section vector diagrams similar to Figure 1, was concentrated in the design of the aerodynamic passage. Great care was taken to avoid excessively high suction side velocities upstream of the converging-diverging nozzle. In addition, downstream of the nozzle throat, special attention was given to the rate of curvature on the suction side. The design of the aerodynamic gas passage, and the ratio of nozzle exit area to throat area, is based on experience obtained at C-W during recent turbine engine programs. Airfoil pressure along with velocity profiles (Figures 143 and 147) were generated utilizing this aerodynamic passage, the airfoil span cross section, the gas inlet temperature profile, and the cooling air.

At this time in the blade design, several important design factors were established which are worthy of discussion:

1. Cascade Blade Attachment - Individual blade interchangeability was incorporated in the cascade rig. A locating stem for each blade was used and a loose-fit locating dowel arrangement was incorporated into the stem to permit positive location and yet allow the composite blade assembly freedom to grow thermally in any direction.

2. Size of Cooling Air Passages - Because of the extremely small size of the blade, the chordwise and spanwise arrangement of the cooling air passages became an early design consideration. Based on C-W experience with larger transpiration-cooled turbine blades, the most important design consideration is the chordwise and spanwise external pressure gradient that the individual waffles, or cooling air passages, experience. Because the cascade blade is a constant cross section, the necessary consideration of the spanwise pressure gradient is eliminated; therefore, the resulting cooling air passage chordwise width was primarily only a function of the chordwise external pressure gradient. As a practical consideration, the blade span was used as the other dimension. It is also to be noted that data obtained by scaling down previously successful C-W large high-temperature turbine stator blade waffle, or cooling air passage sizes, were used as additional background information in arriving at the final cascade blade passage design.
3. Airfoil Trailing Edge - In most of the previous C-W transpiration-cooled blade designs, the skin material and cooling air passages are continued to the airfoil trailing edge; however, during the past year, successful running has been achieved with the passages adjacent to the trailing edge blanked off and this region cooled only by the persistence of the film emanating from the upstream cooling air passages. Because of the high performance goals set for this turbine rig, it was necessary to keep the trailing edge thickness-to-pitch ratio within specific aerodynamic limits. This was achieved by terminating the skin-upstream of the airfoil trailing edge and forming a flush surface with the solid trailing edge region of the airfoil.
4. Welding Skin to Spar - Because of the small size of the cascade blade, the spar lands must also be kept small, or in proportion to the adjacent transpiration skin area, such that the solid portion created by the weld joint is not over-temperatured. Through advanced EB techniques developed by C-W, 0.020-inch standard thickness skins were successfully welded repeatedly to land width of 0.040 inch. In addition, at the airfoil leading edge where the pressure and suction side skins are joined, only 0.050 inch is required for successful skin attachment. It should be noted that two skin pieces are required due to the distinct directional flow characteristics of the skin material; C-W testing has shown that improved blade cooling and film boundary layer persistence can be achieved if the skin material is orientated such that cooling airflow exists through the skin material in the direction of the hot gases. Another distinct design feature incorporated in the cascade blade is the skin attachment weld at the shelf line. Again, a very small land is required so as not to create a bulk of material which cannot effectively be cooled by the adjacent transpiration skin area. Through EB welding development, it was found that only a 0.030 inch land was required; and by properly contouring the skin and by controlling the fit to the shelf surface, the skin material could be attached and also create a smooth fillet of weld material.

5. Thermal Design and Heat Transfer Analysis - As previously described, the blade cooling air enters through the lower shelf by means of orifices; these orifices meter air directly to the individual passages. A complete summary of blade temperatures and orifice detail data is discussed in the heat transfer section.
6. Stress Analysis - Stresses due to the aerodynamic loading of the blade are low and well within the strength properties of René 41 material. Utilizing the airfoil temperature distributions from the heat transfer analysis, thermal stresses were calculated and found to be acceptable for the expected cascade test program. Further details are found in the stress analysis section.
7. Materials - During the early design period, several different spar materials were suggested; some of those considered were René 41, Inco 713C, Inco 713LC, Mar-M 322, Mar-M 302, and In 100. To date, C-W has had experience with all these materials. The cascade spar material, René 41 (cast), was chosen primarily because of excellent EB welding and casting characteristics; it also possesses satisfactory strength at a temperature to 1500°F. It is to be noted that several of the above-mentioned materials are acceptable for this application; Inco 713C and Inco 713LC both fulfill the design requirements. Initial blade design called for an N-155 material because the bulk of C-W development has been with this material; however, recently, Ni V Cb has shown slightly superior qualities at higher temperatures. Consequently, some blades were also fabricated and subsequently tested to evaluate this material further.
8. Fabrication - With all cascade blades now fabricated, only two difficulties were encountered. (1) EB welding of the skin to the spar was initially accomplished at too high a setting, which caused excessive stretching of the skin material as it was attached to the spar and thus caused a poor fit at the last weld joint near the trailing edge of the airfoil; this was corrected by making minor adjustments in the EB welding technique. (2) Finishing of the shelf lap joints prior to skin attachment caused a great deal of distortion of the sealing surfaces in the initial group of blades; however, with the reduction of the arc intensity as mentioned above, the later blade sealing surfaces showed a great deal of improvement. It should be noted here that the blade castings were of excellent quality; therefore, this indicates that the finished piece prior to skin attachment is easily produced by existing manufacturing methods (i.e., precision casting, lost wax method).

Initial feedback data from the cascade test have indicated that stator blade shelf sealing may be a problem with the turbine rig. To date, high-temperature filler materials are being used to seal the lap joint sealing surfaces with a high degree of success. Additional design and test evaluation effort in this area is continuing, however, to assure adequate sealing in the full round rig.

5.2.2 Test Equipment and Instrumentation Design

Test Equipment

A schematic diagram of the test stand setup for Phase I blade cascade testing is indicated on Figure 148, and Figure 149 shows an external view of the actual hardware. Airfoil measurements of combustor primary zone airflow, combustor diluent airflow, and blade cooling airflow were accomplished using flat-plate, sharp-edged orifices constructed and installed per ASME standards. The airflow calibration coefficients were obtained from Reference 13. Flow read-out was by means of liquid level manometers.

Control of airflow was accomplished by using remote manual valve air operators. Back pressure on the system was adjusted by a remotely operated butterfly valve. Operation of the rig consisted of adjusting airflows and back pressure. Main, diluent, and blade cooling airflow had separate control valves.

The blade cooling airflow circuit was equipped with electrical heaters to heat the air to simulated compressor discharge temperature. A 5-micron filter in series with the heater assured delivery of cooling air free from dirt, scale, or contamination from the stand duct work.

Downstream of the combustor-cascade rig, a quench chamber was installed. Its function was threefold. First, it was equipped with a water spray system to quench the test rig exhaust gases down from 2500°F average temperature to a minimum of 600°F before discharging across the back pressure valve. Second, it was equipped with a traversing mechanism which was used to translate a pressure and a temperature probe across the burner exit for profile measurements. Third, it was equipped with a window to allow visual observation of the burner and cascade exhaust gases.

All of the cell duct work was designed to withstand at least full plant air pressure of 90 psig at maximum expected operating temperatures. The quench chamber was designed to hold full pressure at 1500°F metal temperature in the event that the quench system failed.

Instrumentation

The design of the stationary instrumentation for the first phase of the program has been on conventional lines using ceramo thermocouples for metal and gas temperatures and stainless steel tubing for pressure tappings. The traversing probe used to investigate combustor exit conditions has been designed for more arduous duty utilizing ceramics and noble metal.

Static pressure was measured with square-edged tappings in the walls of the ducts and the primary combustor. No blockages or leakages have been found. The traversing probe was fitted with an alumina head with drilled passages for total pressure measurement.

Chromel/Alumel swaged wire thermocouples (MgO insulation in Inconel sheath) were used for wall and gas temperature measurements in the burner area and also for measurements of blade skin and spar temperatures in the cascade. Skin temperatures in excess of 2400°F were found in the center of the upper protective sheaf at the combustor exit. This thermocouple was mounted in an alumina block and secured with Astroceram cement (Figure 150), and the integrity of the installation was maintained. No other combustion-area thermocouples were subjected to unusual temperatures, and none failed. Thermocouples mounted in the blades of the cascade were of lighter construction (0.020 inch and 0.025 inch OD rather than 0.040 inch), but no failures were experienced other than during handling. Improvements in the method of securing these thermocouples are being introduced.

Traversing Probe

A probe driven by a conventional C-W yaw-probe actuator has been operated in the combustor outlet where three temperatures have been read (see Figures 150 and 151). Graphs of the temperatures found can be seen in Section 5.2.3. Pressure measurements have also been made and are reported in the following section. The probe head is supported in an Inconel X carrier and is held in position by means of a corrugated Inconel shim which has a spring-clip effect; Astroceram cement is packed around the probe lead to form a seal. The carrier rests on two rails and is driven by a tube which also carries the instrumentation leads out of the rig. A second tube passes through the wall of the rig opposite the probe actuator and serves to equalize pressure on the carrier, thus eliminating reaction against the actuator. Thermocouples mounted in the walls of both support tubes became detached due to lack of support, but not until after it had been established that the tubes were running cold. The material of the probe head has been the subject of much investigation, and no entirely satisfactory arrangement has yet been found. The first material chosen was boron nitride (BN), but very rapid oxidation in the hot stream occurred; no problems were experienced with this material due to its affinity for water in spite of its operation in a quench chamber. The material now in use is 99.9 percent alumina (Al_2O_3); severe thermal cracking and shattering of the probe head was encountered in early runs, but the thermocouples, ISA calibration "S" in platinum sheath of 0.040 inch diameter, continued to function after damage was sustained. Current efforts are aimed at refining the design of the alumina head to increase its resistance to the high thermal loads; discussions are taking place with the vendor and his supplier, General Electric. As a backup, Englehardt Industries has been approached to supply probe heads made from a rhodium-iridium high-temperature alloy. The probe actuator has been moved from its original position and is now attached directly to the quench chamber. This change was necessary because the movement of the rig during operation has a roll component and the actuator was lifted off of its support.

Pressures were read on gages and on mercury manometers. Temperatures were read on push-button and strip-chart recorders. Traversing probe position was measured on a strip-chart recorder. No problems have been encountered with any of this equipment. The pressure-measuring head on the traversing probe was read out on the strip-chart recorder via pressure transducers. This is a standard technique, and no difficulties are foreseen.

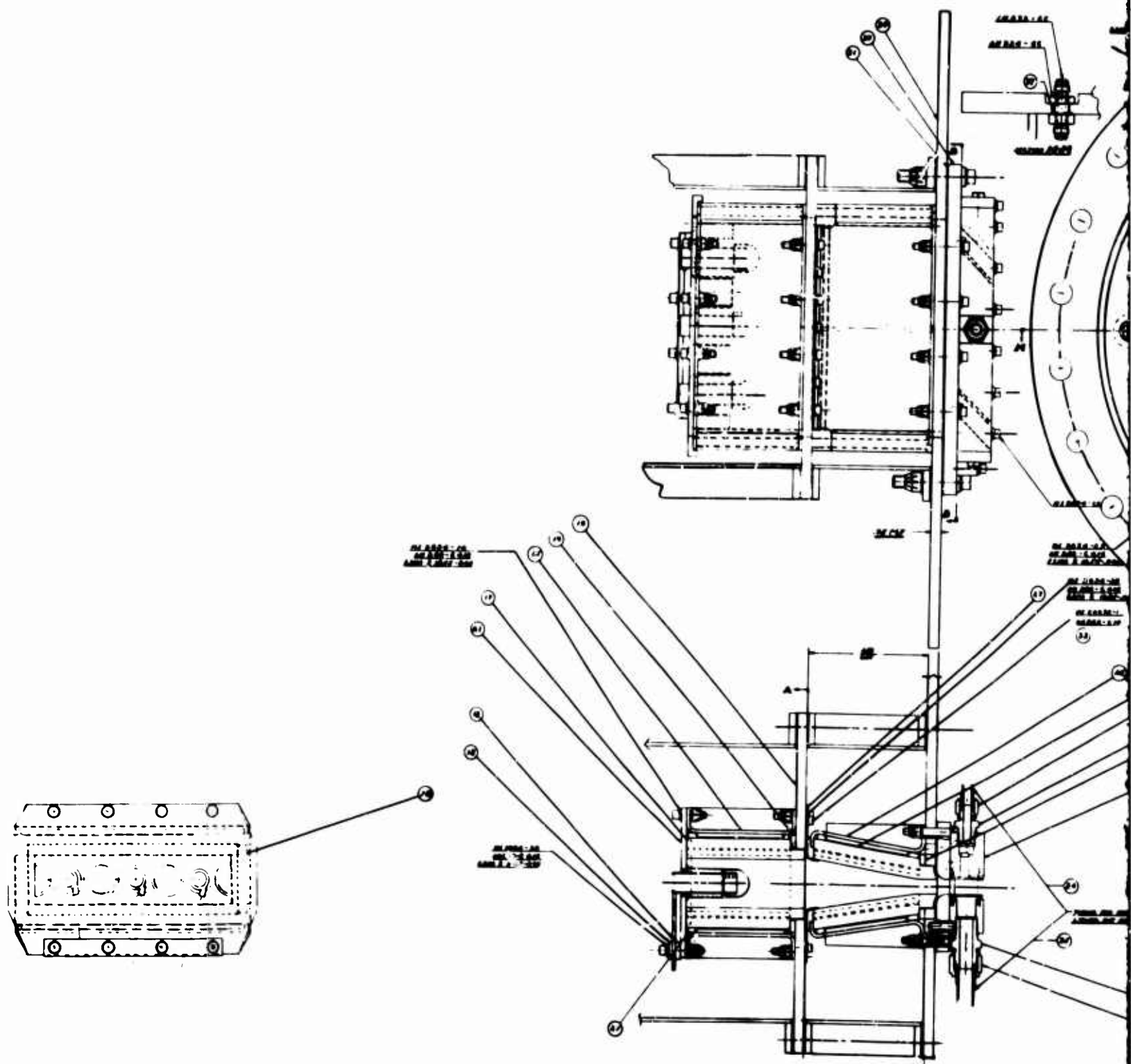
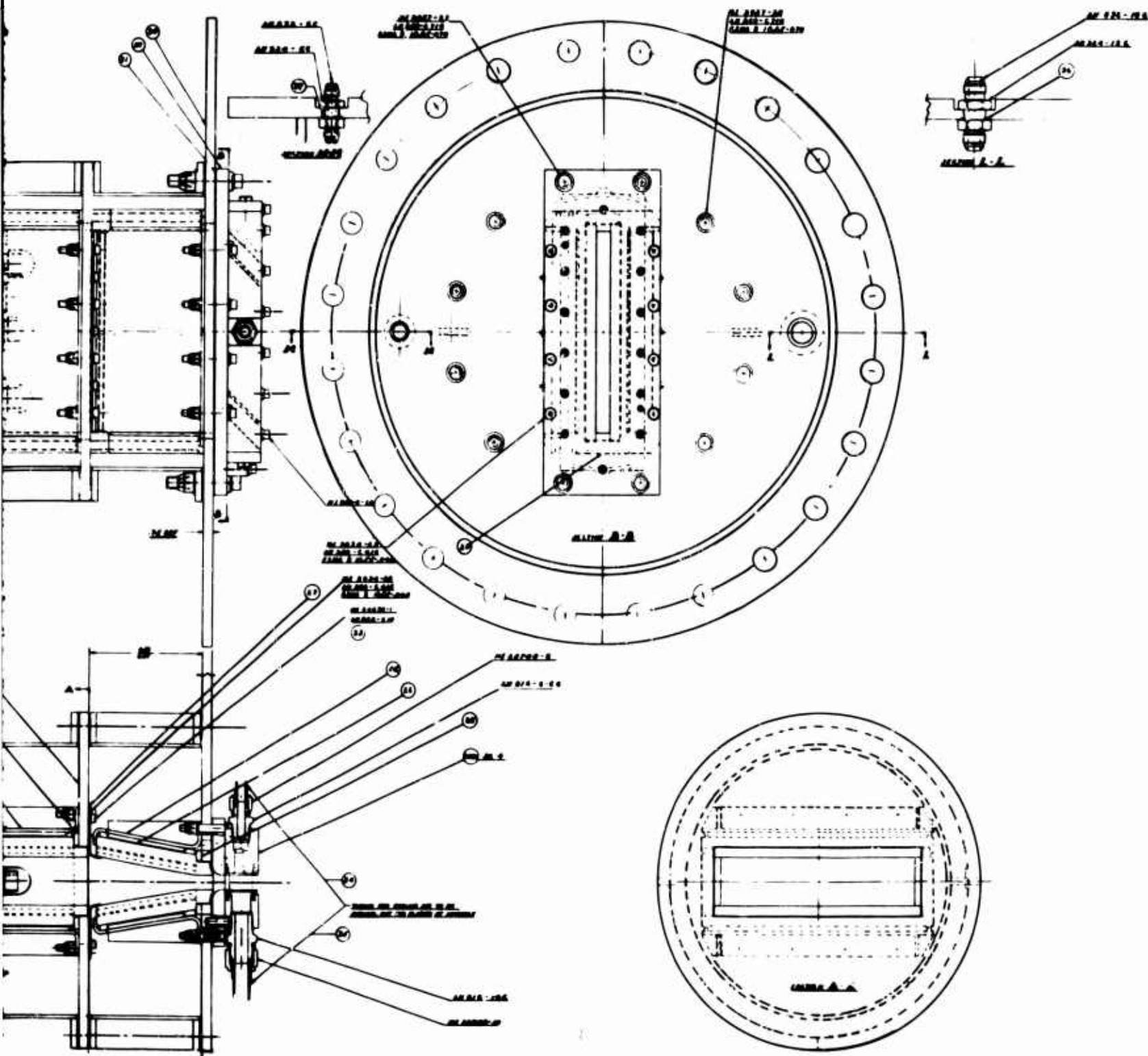


Figure 145. Cascade Rig Combustor Assembly.



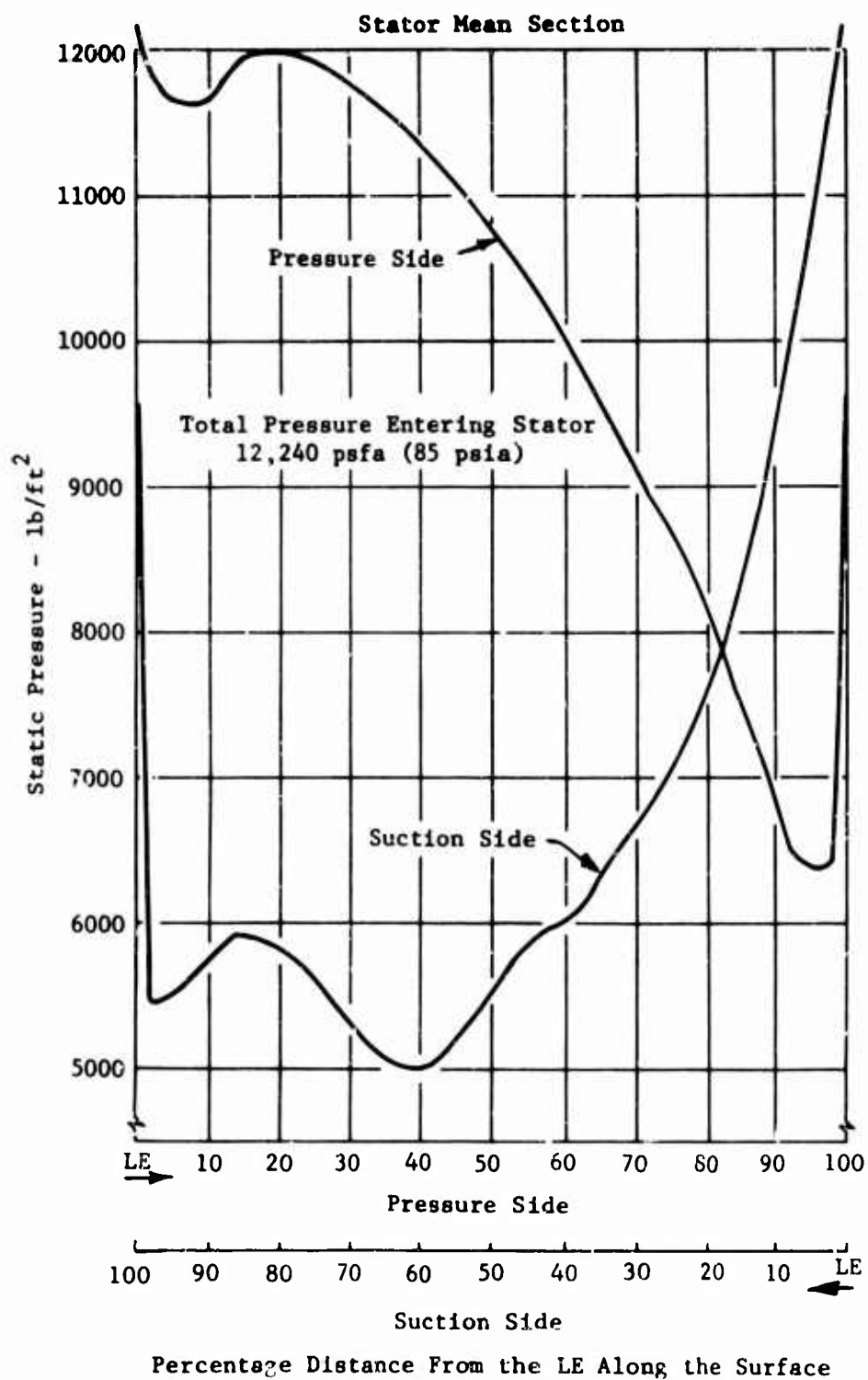


Figure 146. Turbine Cascade Static Pressure Distribution.

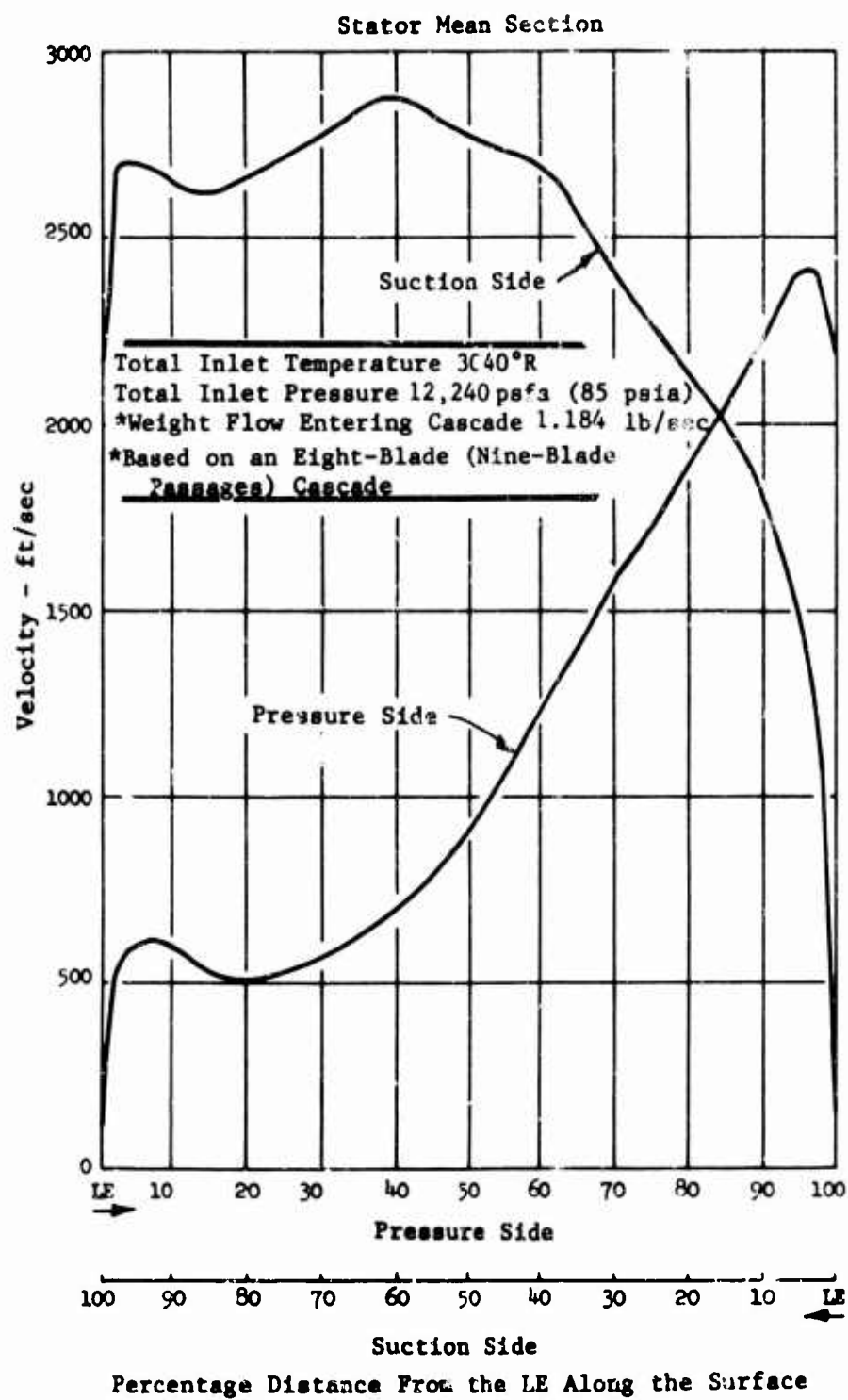


Figure 147. Velocity Distribution - Turbine Cascade.

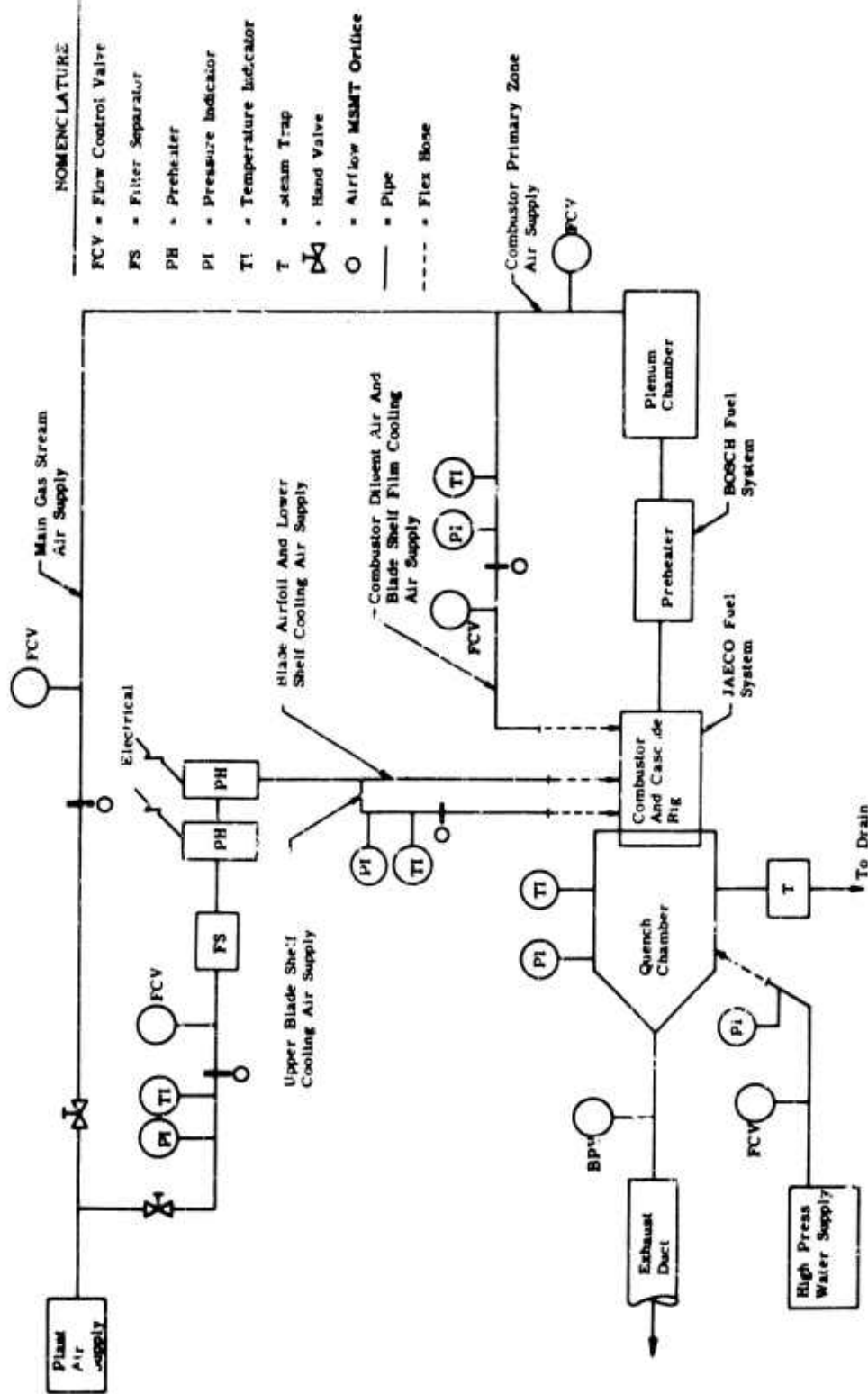


Figure 148. Cascade Rig Test Stand Schematic.

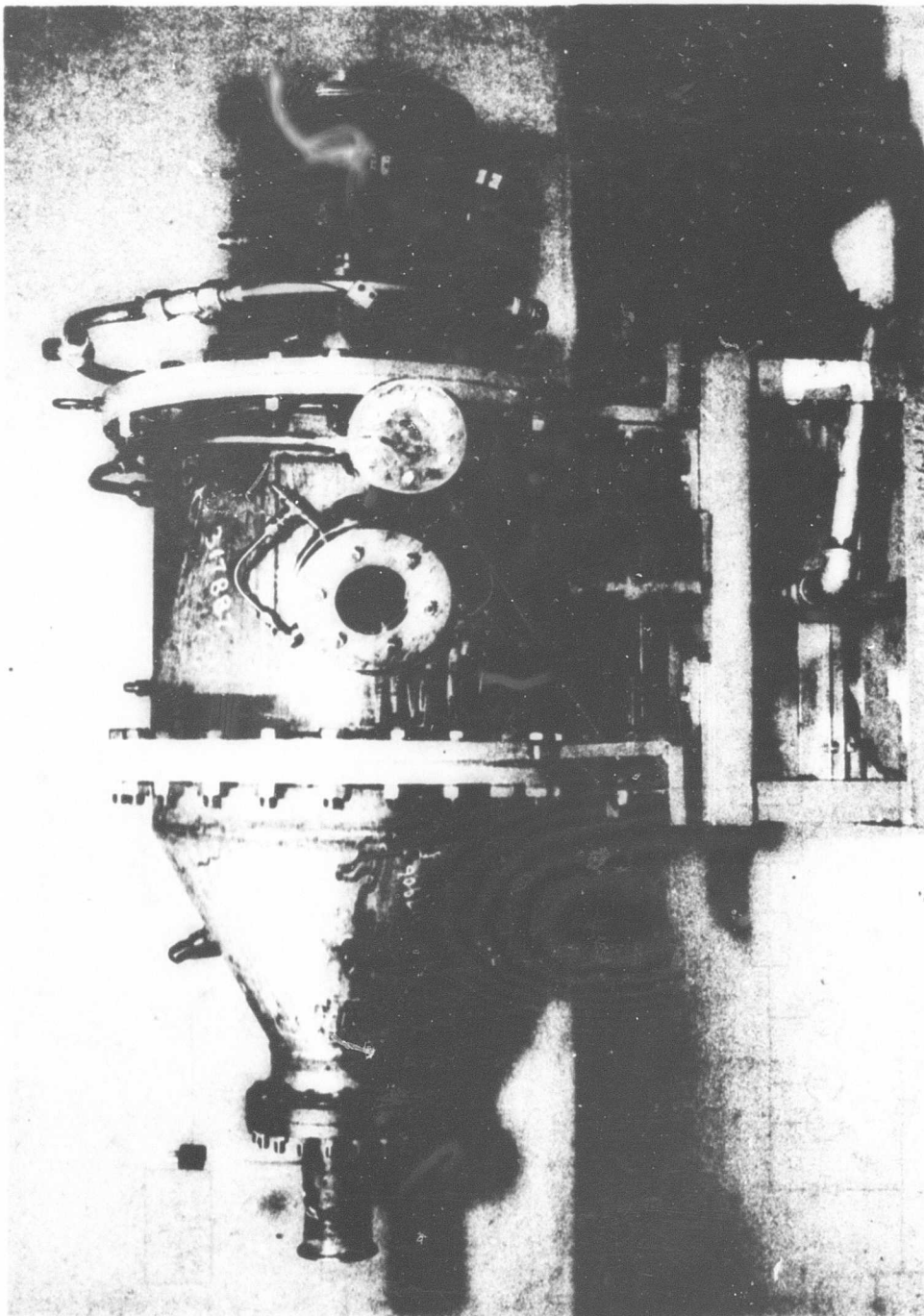


Figure 149. High Temperature Turbine Cascade Rig.

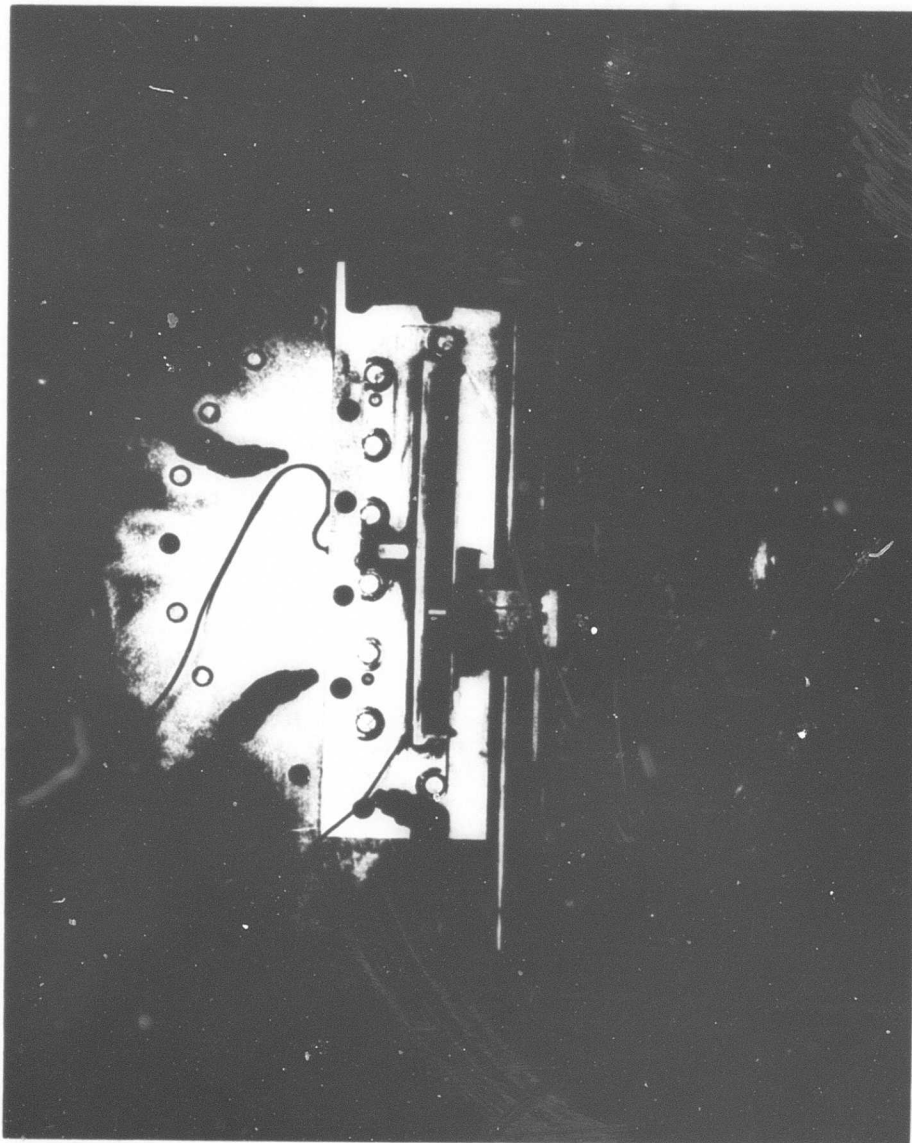


Figure 151. Temperature Traversing Probe Viewed From Quench Chamber.

5.3 Cascade Rig Test

The cascade rig was built to evaluate cooling effectiveness of the transpirationally cooled stator blades operating in a high-temperature atmosphere. The testing accomplished verified that the blade cooling concepts developed for larger engines were indeed applicable to the small gas turbine. Total burning time was 38:15 hours, with 14:00 hours accumulated on stator blades. Maximum gas temperature across a blade was as high as 2900°F for a duration of 1:35 hours.

Figure 145 is a drawing of the rig which is described in the previous sections. The burner technology for the headplate and aircups is similar to that for the full round rig. Silicon-carbide-coated RVC graphite uncooled liners were chosen for rig testing, since diluent cooling air could be adjusted to vary combustor exit conditions and profiles.

5.3.1 Transverse Temperature Profiles

Temperature profiles at the combustor exit were taken by means of a three-thermo probe of platinum/platinum 10 percent rhodium thermocouples in a boron nitride head (see Section 5.2.2). The uncooled boron nitride head could make about two complete traverses at temperatures varying from 2500° to 3000°F and then would deteriorate. This probe was replaced by one with an alumina head with a slight increase in durability at the higher temperatures. Shattering of the alumina head took place after a few traverses in the high-temperature field. Figure 152 illustrates a probe after shattering. It was suggested by the manufacturer that a probe of constant cross section would eliminate this problem.

The temperature profile was adjusted by means of the diluent baffles, Item 27 of I.S 29955, Figure 145. A total of five configurations were tried in an attempt to adjust the profile. The results of these tests indicate that the diluent baffles could adjust the profile only at lower temperatures than design, and then only modest adjustments were achieved. The major factor affecting the horizontal temperature profile is the headplate air slot and fuel vaporizing tube positions. As the temperature level is increased to the design temperature, the percentage of total air used as diluent is decreased, reducing the adjusting ability of the diluent air baffles and allowing headplate air slots to be the major influencing factor.

The first configuration tested was a baffle with no rework arrangement. This configuration yielded a horizontal profile which can be seen in Figure 153. The peaks were positioned in front of the headplate aircups. In order to reduce these peaks and raise the rest of the profile, the baffle rework consisted simply in welding the 1-inch by 0.030-inch-thick plates at the exit of the diluent air baffles in line with the low-temperature modes. Baffle rework No. 1 of Figure 154 illustrates this arrangement. As a result of this rework, the temperature profile in Figure 155 was obtained. This arrangement improved the profile, but there was a hot spot on the right side of the combustion chamber exit. This type of arrangement limits the film cooling and the resulting vertical profile. For this reason, baffle rework No. 2 (Figure 154) was instituted. The air slots cut

into the diluent baffles were to allow diluent air to penetrate the main gas stream in the high-temperature areas, causing mixing and temperature drop. Figures 156 and 157 show the improved temperature profiles obtained from this rework. These figures are modified to show only the midstream reading and blade cascade for use in later discussions.

In an attempt to improve the profile still further, baffle rework No. 3 (Figure 158) was used. This configuration proved to be a regression, allowing the effect of the aircups to dominate the profile again. The even distribution of the slots shown did not improve the mixing, and Figures 159 and 160 show the resulting temperature profiles. As a final attempt to improve the profile, the configuration shown in baffle rework No. 4 of Figure 158 was used, yielding the profiles of Figures 161 and 162.

An important consideration in the combustor exit temperature profile is the ratio of the maximum local temperature with the mean. This in effect is a measure of the maximum temperature of any peak compared to the mean. In the case of the cascade rig, this ratio was (Figure 159 and 161)

$$\frac{\text{maximum local } ^\circ\text{R}}{\text{mean } ^\circ\text{R}} = \frac{3200^\circ + 460}{2638^\circ + 460} = \frac{3660}{3098} = 1.180.$$

The design ratio was (Figure 36)

$$\frac{\text{maximum local } ^\circ\text{R}}{\text{mean } ^\circ\text{R}} = \frac{2990^\circ + 460}{2580^\circ + 460} = \frac{3450}{3040} = 1.135.$$

Again we see that the two-dimensional combustor was limited in equalizing the peak temperatures, with the result that the stators were subjected to a much greater range of temperature than anticipated. This fact, however, is encouraging since it indicates the ruggedness of the stator design. As mentioned above, the full round combustor offers a better circumferential temperature profile because of its annular vaporizer and flexibility in adjusting secondary airflows.

5.3.2 Radial Temperature Profiles

The vertical temperature profiles taken during the circumferential survey of Figures 161 and 162 are shown in Figures 165 and 166. It can be seen from the latter figure that the vertical profile is flatter than the design. Comparing the actual profile with the design shows this as follows:

Peak to mean radial total temperature ratio - $^\circ\text{R}/^\circ\text{R}$

$$\text{Design (Figure 36)} = \frac{2765^\circ + 460}{2580^\circ + 460} = \frac{3225^\circ\text{R}}{3040^\circ\text{R}} = 1.06.$$

$$\text{Actual (Figure 169)} = \frac{3200^\circ + 460}{3100^\circ + 460} = \frac{3660^\circ\text{R}}{3560^\circ\text{R}} = 1.03.$$

This flatter profile results in a more severe cooling requirement than design. In the full round (annular) rig, however, there is more latitude in the combustor design which makes it possible to adjust the radial profile closer to the desired 1.06 peak/mean ratio.

5.3.3 Pressure Profiles

Pressure profiles were taken of the last combustor configuration and yielded a steady trace across the exit. For the burner condition of Figure 161 ($F/A = 0.0284$, average temperature = 2120°F), the exit pressure profile varied as follows:

Top probe	=	67.5 - 68.5 psig
Mid probe	=	63.0 - 64.5 psig
Base probe	=	69.0 - 69.5 psig

For the burner condition of Figure 162 ($F/A = 0.037$, average temperature = 2638°F), the exit pressure profile was

Top probe	=	68.0 psig
Mid probe	=	60.0 - 62.0 psig
Base probe	=	68 psig

Location of the total pressure taps was the same as for the exit thermocouples which were positioned along the combustor exit span, as shown in Figure 165. The steady pressure traces attest to the stable combustion attained and indicate that there are no areas of instability.

5.3.4 Blade Cooling Air

As the turbine cascade testing proceeded, it became evident that further effort would be required on sealing the blade cooling air. Consequently, a series of tests was performed to determine the areas of leakage and to initiate means to minimize this on the component turbine rig.

As can be seen from Figure 145, the areas of potential leakage are at the stem seals under the blade shelves and at the lap joints between the blades. By adhering to the close machining tolerances in these areas, it is anticipated that the leakage will be materially reduced. This approach will be followed on the full round turbine rig. A more direct approach, however, was used on the cascade rig, in that the leakage paths were sealed by high-temperature sealants, by metal mesh, and finally by welding. Advantage can be taken of the metal mesh effectiveness in the turbine rig design by minor modifications if required.

In order to obtain a relation of the amount of leakage from the various areas, a cascade blade assembly (Figure 167) was flow checked in a static pressure environment. By blocking off the various leakage paths in sequence, the following results were obtained:

Blade plenum pressure	9 psig
Total airflow to cascade	0.1252 pps

Airfoil cooling flow (from calibration)	0.0173 pps
Total estimated seal leakage (upper and lower seals)	0.0756 pps
Estimated blade lap joint leakage (upper and lower)	0.0323 pps
Ratio of blade joint leakage to seal leakage	43 percent

To minimize the leakage paths, a set of blades was EB welded together at the blade joints and along the seals. This assembly was then inserted in the blade support and the remaining joints were closed with high-temperature flexible sealant. The static leakage check before and after test showed a leakage increase from zero to 35.3 percent at the 9-psig supply pressure.

A subsequent test with the welded blade assemblies was made in which an average gas temperature across the cascade was 2560°F with 2900°F maximum temperature across one blade (Figure 163). Cooling flow supplied to the blade plenum ranged from 0.1016 to 0.1106 pps. The calculated airfoil cooling air for this condition was 0.0540 to 0.0579 pps. This represents a 32.7 percent to 42.5 percent increase over the design flow. This occurred because cold cooling air was used so as to keep blade temperatures low in areas where gas temperatures peaked to as high as 3200°F. Maximum blade temperature recorded during this run was 1640°F.

The final test with the welded cascade assembly was made at a reduced average gas temperature which resulted in an estimated gas temperature over two blades of 2500°F (Figure 164). Cooling air was heated to the limit of the facility (445°F), and the resulting flow dropped to 84.8 percent of design. Maximum blade temperature recorded was 1645°F.

The above-mentioned tests verify the effectiveness of the transpirationally cooled blade in operating at severe gas temperatures. Further work is indicated to minimize leakage and to improve the combustor exit temperature profiles. Ample consideration has been given to both of these areas in the design of the forthcoming turbine test rig.

5.3.5 Stator Cascade Tests

Three series of stator cascades were tested and may be categorized as follows:

<u>Configuration</u>	<u>Total Time</u>	<u>Time at Max Temp</u>	<u>Max Avg Temp</u>	<u>Mean Temp</u>
1st Cascade	1:45	:55	2093°F	1793°F
2nd Cascade	7:45	4:15	2528°F	1956°F
3rd Cascade	4:30	1:35	2900°F	2560°F

Five of the blades from the 2nd cascade also ran in the 3rd, thus accumulating 12:15 hours total. The 3rd cascade was tested at a sustained high gas temperature to determine the high-temperature operational characteristics which would be encountered by the stators in the high-temperature testing of the turbine component rig. This testing showed that the blades suffered no detrimental effect, as noted by visual inspection and subsequent flow checks of the cooling air passage. It is to be noted that the maximum average temperature noted in the table above is the gas temperature averaged over one blade span. The mean temperature is the average over the entire cascade.

The stator cascade assembly is shown in Figure 167. The post-test condition of the 1st cascade can be seen in Figure 168, the condition of the 2nd cascade, in Figure 169; and the condition of the 3rd cascade, in Figures 170 and 171. The oxidation seen on the shelf and trailing edge of blade S/N 35 (Figure 170) is due to the excessive local average gas temperature of 2900°F. All other blades were in excellent condition. The time accumulated by the blades at the various gas temperatures is summarized as follows:

<u>Maximum Average Temp - °F</u>	<u>Number of Hours</u>
1600 - 2200	12:25
2200 - 2300	8:55
2300 - 2400	7:15
2400 - 2500	4:40
2500 - 2600	1:35
2800 - 2900	1:35

Detail listing of blade spar and gas temperatures over individual blades is given in Table XVIII. The applicable temperature profile over the blades (Figures 156 to 164) is noted in this table as a cross-reference. Preliminary heat transfer analysis of the test results shows good correlation between actual and computed values of blade spar temperatures. Average measured values of blade spar and gas temperatures are compared with computed values for the specific thermocouple locations shown in Figure 172. These average values with the actual test variations are shown below:

<u>Blade Section</u>	<u>Thermo Location</u>	<u>Computed Temp °F</u>	<u>Average Measured Temp °F</u>	<u>Measured Variation °F</u>
TIP	1st Land Suction Side	676	854	+ 81 -134
	1st Land Pressure Side	673	641	+239 -131
	Trailing Edge	1050	777	+193 -187
	Gas Temperature	1953	1953	+547 -588

Blade Section	Thermo Location	Computed Temp	Average	Measured
		°F	Measured Temp °F	Variation °F
MEAN	Leading Edge Land	863	669	+ 81 - 59
	Spar Center	707	710	+190 -135
	Gas Temperature	1936	1936	+554 -856
HUB	Trailing Edge	1180	1220	+625 -425
	Gas Temperature	1985	1985	+625 -425

A point of interest in the final cascade test was that the three new blades (S/N 42, 45, and 49) had Ni V Cb skin material. These blades showed a cooler temperature pattern on the cooling air inlet side of the shelf. This observation confirms results of the full-scale blade programs, indicating that the Ni V Cb material is more oxidation resistant than the N155 at elevated temperatures. In anticipation of this result, Ni V Cb was chosen as the initial skin material for the full round turbine test rig.

As a convenient reference, the following summary describes the cascade rig test activity after the initial rig startup and checkout:

<u>Date</u>	<u>Build No</u>	<u>Test Accomplishment</u>
3/12/65	5	Rig tested with silicon-carbide-coated RCV graphite combustion liners. Temperature profile of exhaust made. Average temperature 2193°F. Probe deteriorated from temperature and binding. Probe was replaced and traversing mechanism modified.
3/16/65	6	Temperature survey of combustion exhaust made at reduced average temperature of 1857°F. Combustion chamber liners in excellent condition. Probe head deteriorated; reworked track to allow probe to be removed from exhaust gas at end of travel.
3/19/65	7	Temperature survey made at 1750°F average exhaust temperature. Probe head intact. Diluent air baffles reworked with blanking plates to improve temperature profile.
3/23/65	8	Temperature survey made at same condition as previous test. Temperature profile improved. Rig removed to install stator blade cascade.

<u>Date</u>	<u>Build No</u>	<u>Test Accomplishment</u>
3/31/65	9	Hot cascade testing complete at same condition as previous test. Flow check made of blade leakage. Blades suitable for continued testing after blade thermocouple repair. Temperature paint on stator support assembly (see Figure 9) indicated temperature in film cooled passage sidewalls was less than 900°F.
4/7/65	10	Temperature survey of combustion exhaust made using an alumina probe head. Traverses made at two fuel-air ratios with average exhaust temperatures of 1753°F and 2134°F. The probe head deteriorated at the end of the last traverse. The traversing mechanism continued to bind. A shield was fabricated to protect the probe from thermal shock due to the quench water. This profile was made with a modified diluent air baffle (12 slots). Temperature profile improved.
4/13/65	11	Hot cascade test was performed under the condition of the previous low temperature profile test. The first set of stator blades was reinstrumented for this test, and the entire cascade was sealed using Dow Corning RTV 732 silicon rubber, which has an upper temperature limit of about 500°F. This seal was inadequate in areas of elevated temperature. Thermocolopaint indicated no excessive blade support temperatures.
4/19/65	12	The second set of stator blades were instrumented for a hot cascade test. Johns-Manville Plastiseal "F" was used as a sealant for the cascade. Upon shutdown, flow check indicated an increase in leakage.
4/20/65	12	Reran second set of stator blades. Could not establish design pressure drop across blade skin due to excessive leakage.
4/29/65	13	Temperature survey of combustion exhaust using second alumina probe head. Modified diluent air baffles (27 slots) used for this survey showed regression in profile improvement. F/A's of 0.021 and 0.027 established average gas temperatures of 1755°F and 1956°F, respectively. Probe mechanism bound and probe shattered while trying to establish a 2500°F profile.
4/30/65	14	Hot cascade testing using the same temperature conditions as above test. The first 45 minutes were at an F/A of 0.021 and an additional 4:15 hours were at an F/A of 0.0269. A positive blade plenum pressure was maintained during this test, assuring coolant flow. Bubble check made of blades showed them to be suitable

<u>Date</u>	<u>Build No</u>	<u>Test Accomplishment</u>
		for retest after cleaning. The silicon-carbide-coated RVC graphite combustor liners showed deterioration at culmination of testing. Replacements are in work.
5/17/65	15	Temperature survey of combustion exhaust with modified diluent air baffle (17 slots). F/A's of 0.0284 and 0.037. Peak temperature of approximately 3200°F was attained. Probe head shattered. Prepare for pressure profile traverse.
6/15/65	17	Hot cascade test was performed using F/A = 0.0284 (i.e., $T_{avg} = 2120^{\circ}\text{F}$). Cascade consisted of five previously tested N155 skin material blades and three new Ni V blades. Excessive blade cooling air leakage prevented higher turbine inlet temperatures.
6/16/65	17	Reran above conditions for photographic purposes.
6/22/65	18	Hot cascade test was performed with a modified blade plenum chamber construction. The combustion inlet temperature was reduced to run a 2580°F average temperature. Maximum blade temperature was 1640°F on blade S/N 40.
6/23/65	18	Ran hot cascade test with F/A of 0.0298 with a predicted average temperature of 2210°F. The purpose of this test was to allow the use of heated cooling air with several blades in gas environments of near design conditions. The maximum cooling air temperature was 445°F; with this, the maximum blade temperature was 1645°F on S/N 39.

TABLE XVIII
DETAIL SUMMARY OF BLADE TIME AND TEMPERATURE

Cascade No.	Blade No.	Temp Profile Fig No.	Date	Time Hr:Min	Avg Temp °F	Peak Temp °F	Temp Profile Fig No.	Time Hr:Min	Avg temp °F	Peak Temp °F
1	1		3/31/65	:55	1739	1970		:50	1760	1970
	2				1767	1875			1760	1970
	3				1813	2100			1660	1790
	4				1867	1815			1925	2030
	5		4/13/65		1833	1970			1963	2050
	6				2093	2400			1798	1940
	7				1717	2010			1853	1990
	8				1513	1945			1617	1900
2	16	156	4/19/65	2:35	1778	1980	157	:10	2269	2490
	23				1778	1980			2030	2220
	35				1660	1790			2127	2550
	39				1925	2030			2412	2630
	40		4/20/65		1963	2050			2253	2480
	44				1798	1940			2080	2190
	48				1853	1990			2035	2210
	29				1617	1900			1859	2170
2	16	159	4/30/65	:45	1747	1905	160	4:15	1832	2200
	23				1378	1807			1622	2050
	35				1809	1905			1996	2200
	39				1675	1905			1853	2140
	40				1652	2083			2047	2420
	44				2148	2295			2328	2550
	48				1880	2250			2020	2410
	29				1753	1880			1950	2150
3	35	161	6/15/65	1:15	2453	2620				
	39				1897	2535				
	45				2093	2280				
	42				2047	2175				
	49		6/16/65		2170	2370				
	40				2347	2565				
	44				2002	2235				
	48				1950	2090				
3	35	163	6/22/65	1:35	2900	3200	164	1:40	2550	2680
	39				2255	2480			1945	2180
	45				2582	2730			2232	2370
	42				2492	2700			2142	2350
	49		6/23/65		2535	2830			2185	2360
	40				2880	2915			2430	2480
	44				2379	2880			2029	2480
	48				2350	2500			2030	2200

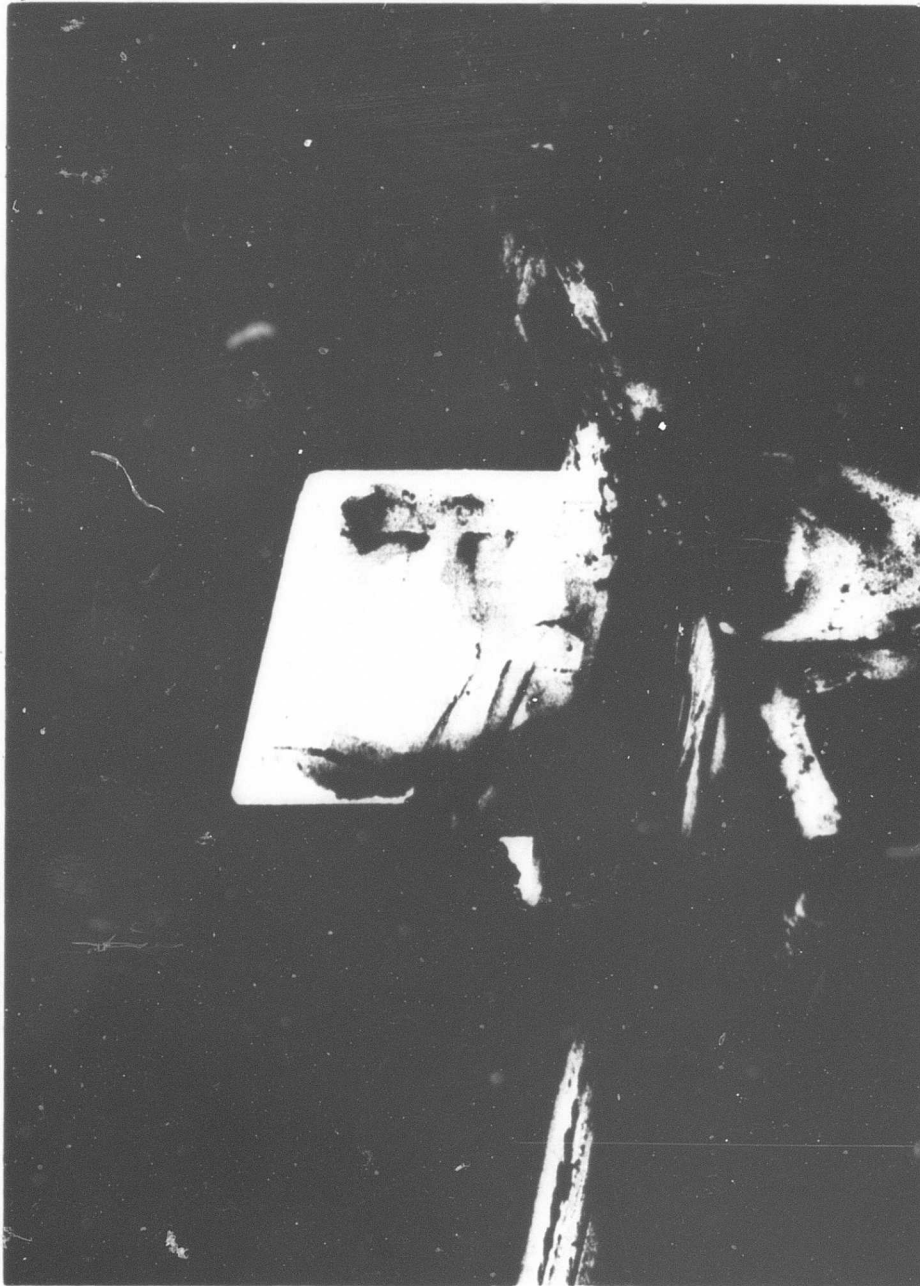


Figure 152. Alumina Temperature Traversing Probe in Post-Test Condition.

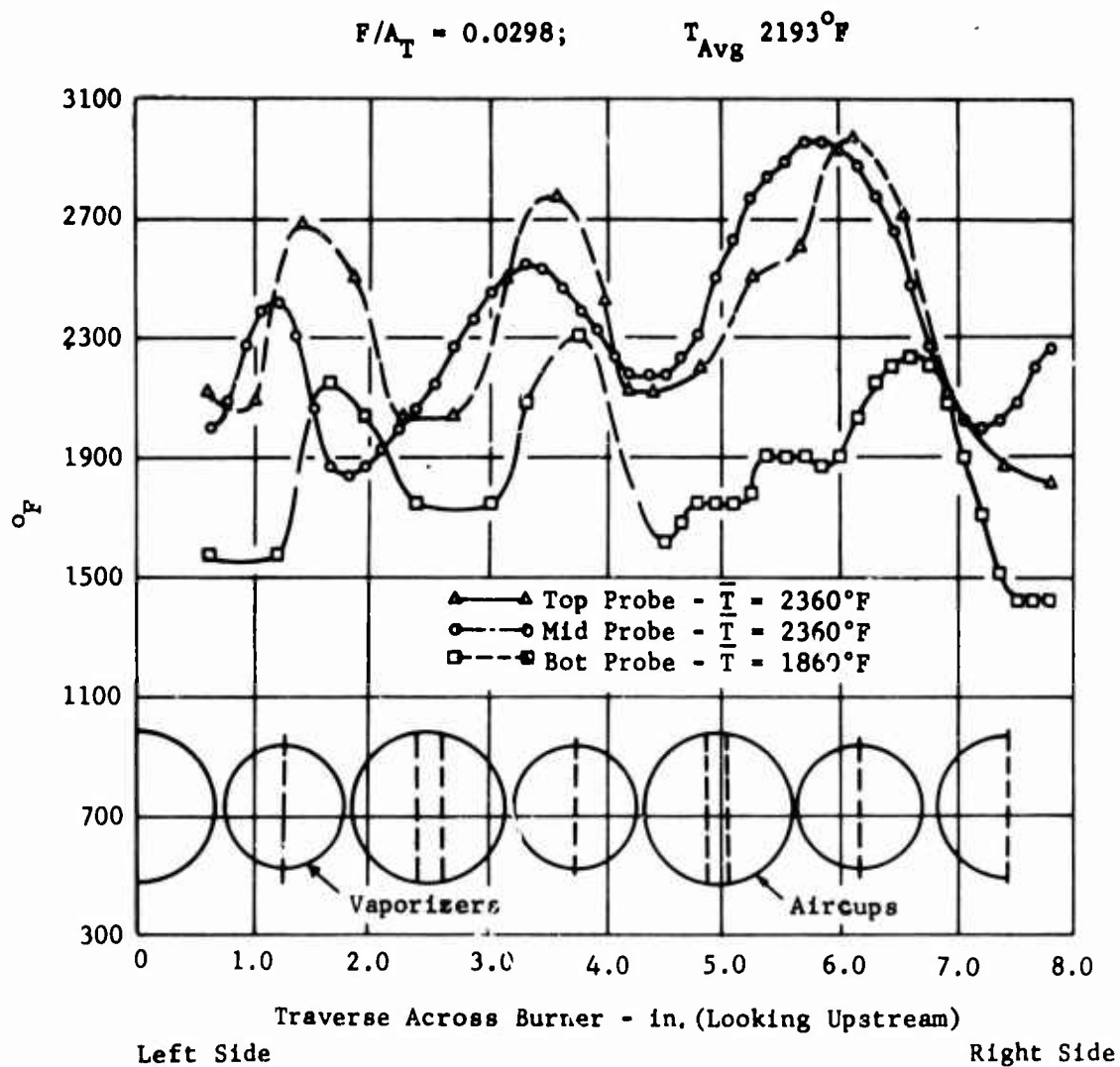


Figure 153. Temperature Profile at Burner Exit.

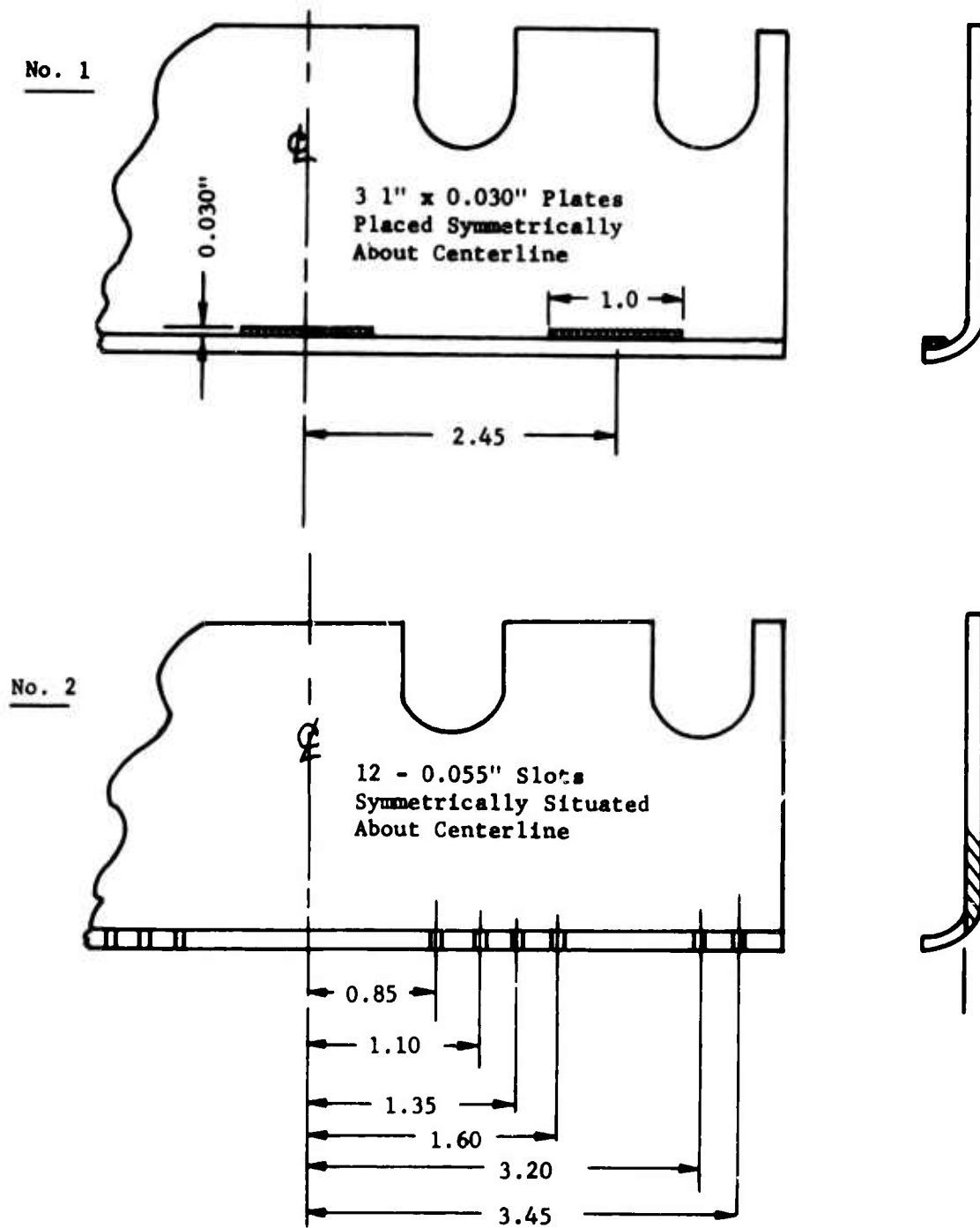


Figure 154. Baffle Rework.

After Diluent Air Baffle Rework - 3-23-65

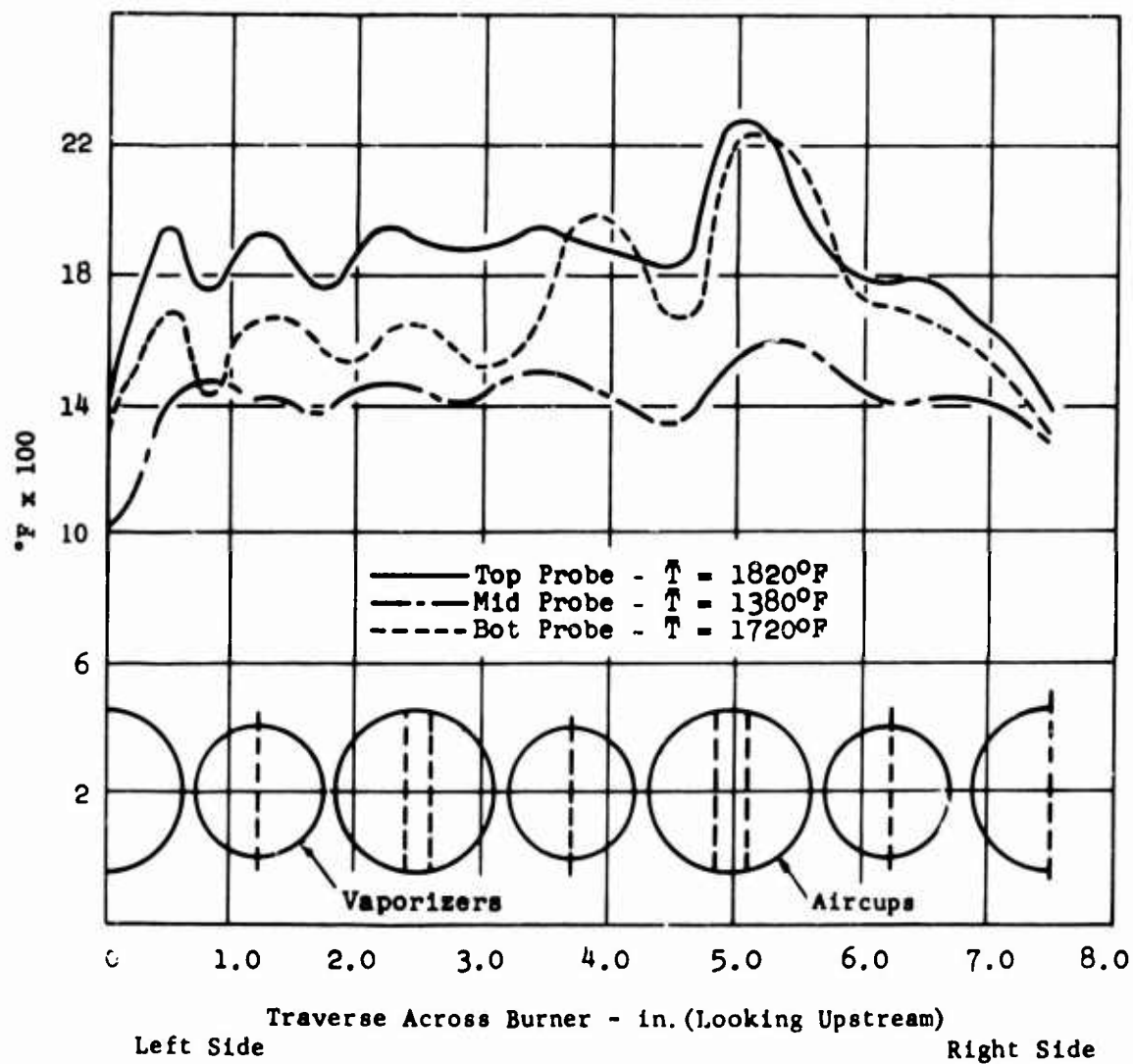


Figure 155. Temperature Profile at 0.022 Overall F/A Ratio.

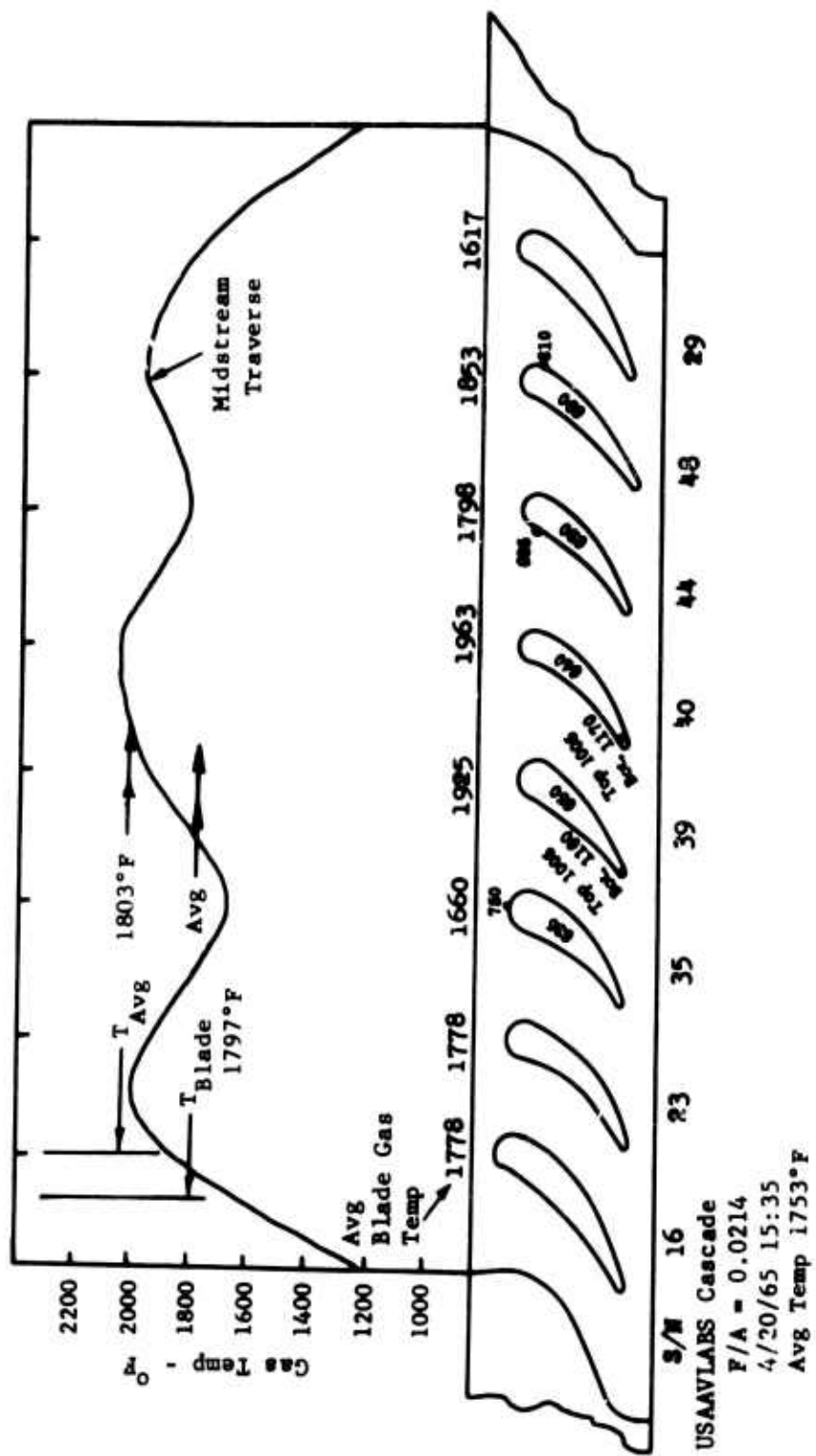
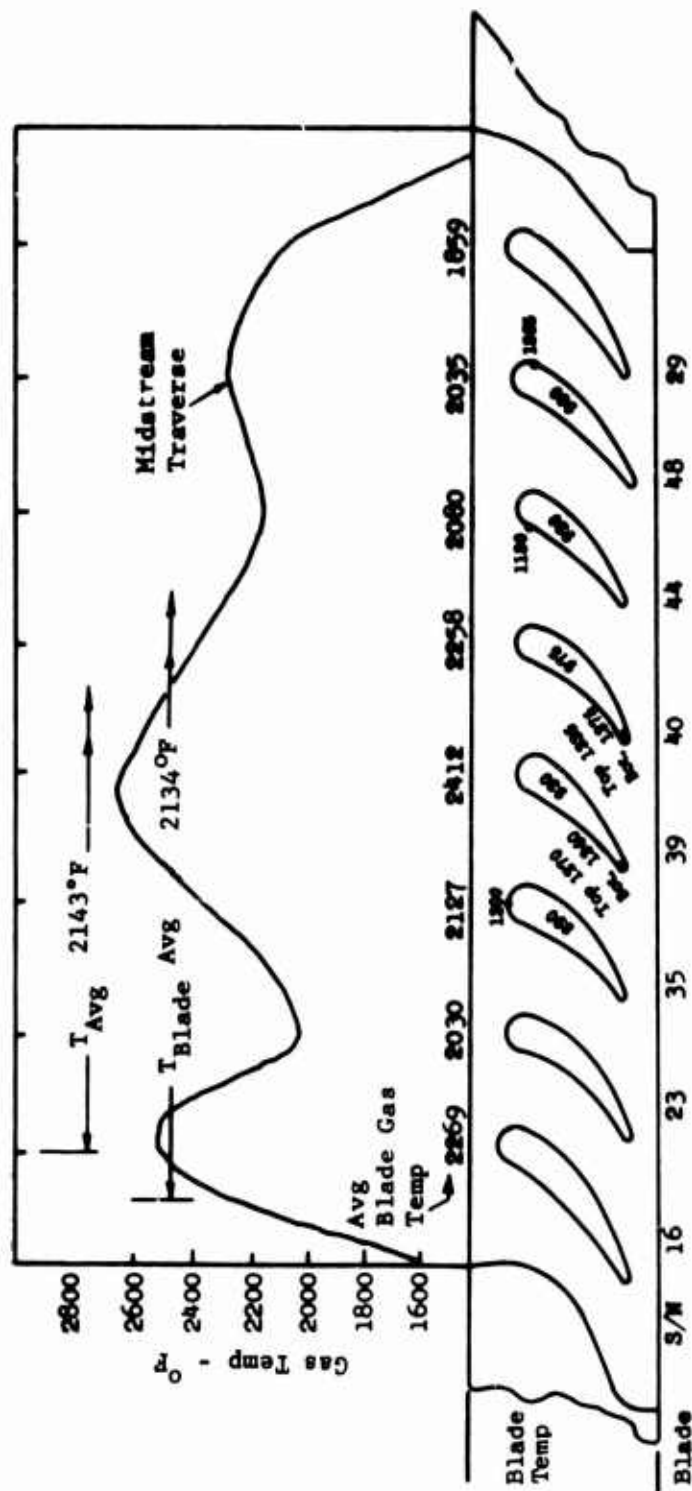


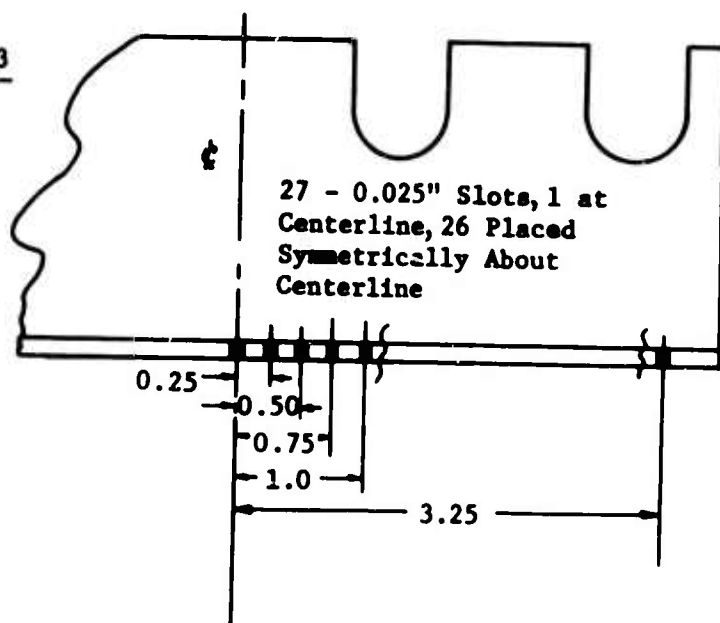
Figure 156. Schematic of Temperature Profile and Typical Blade Test Data.



Stator Cascade
 F/A = 0.0269
 4/20/65 15:45
 Avg Temp 2090°F

Figure 157. Schematic of Temperature Profile and Typical Blade Test Data.

No. 3



No. 4

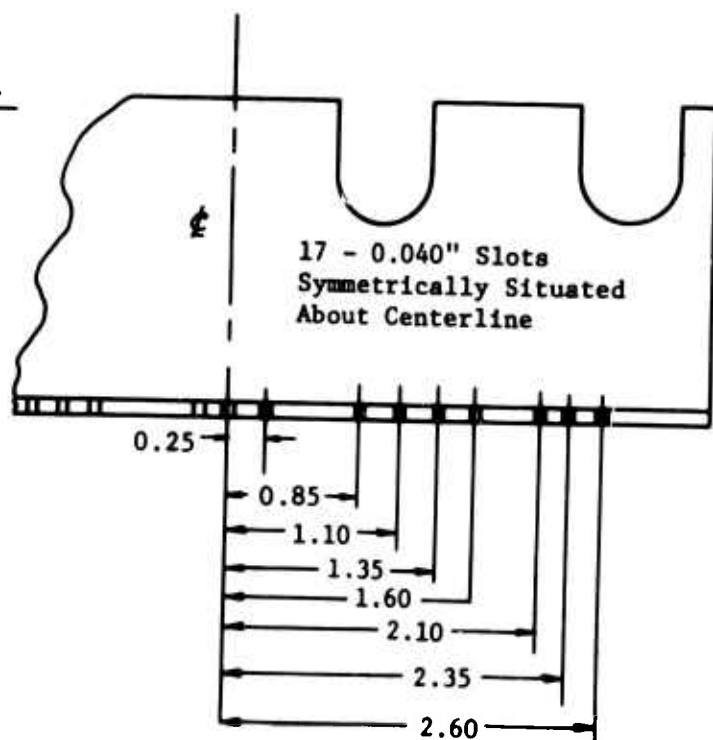


Figure 158. Baffle Rework.

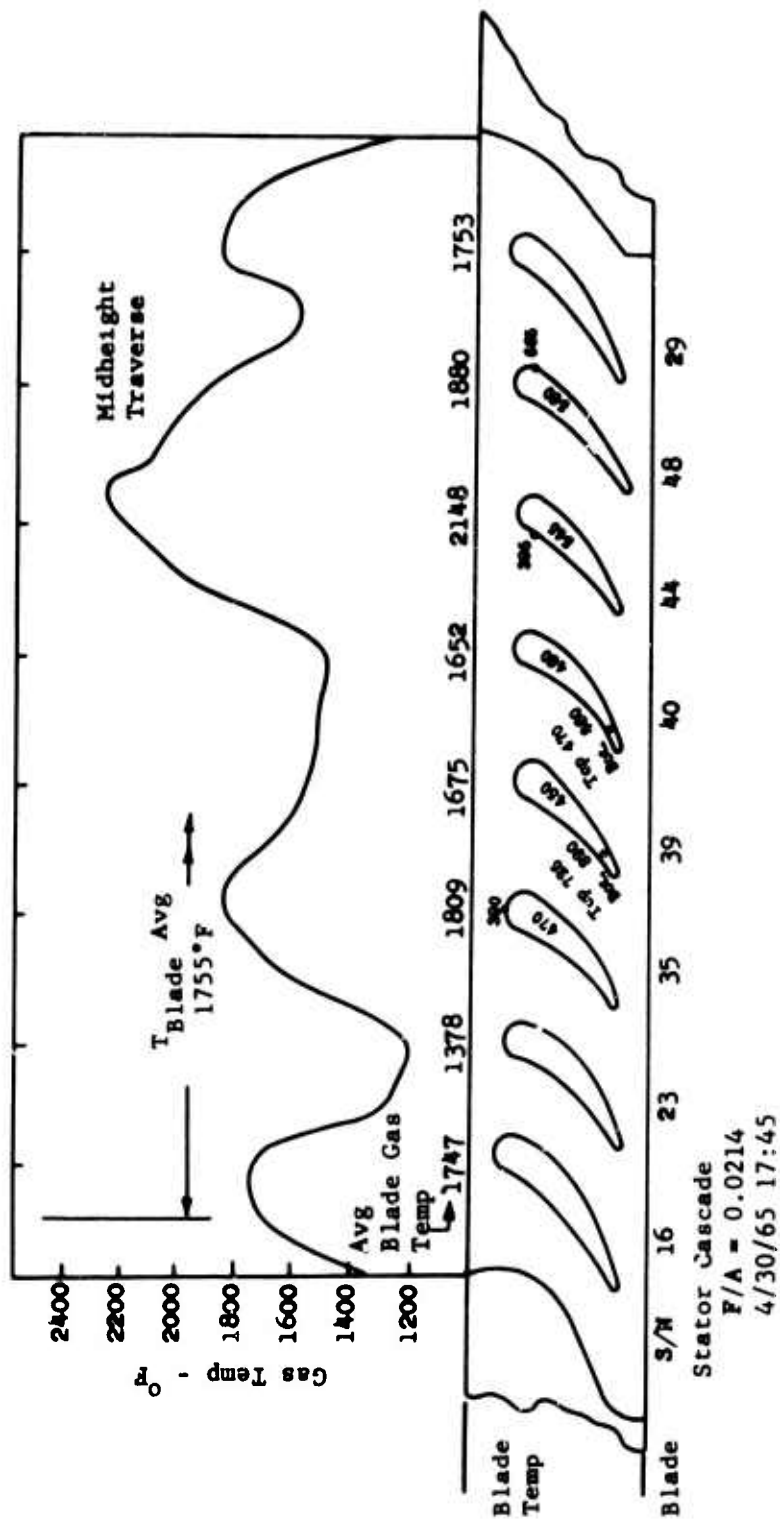


Figure 159. Schematic of Temperature Profile and Typical Blade Test Data.

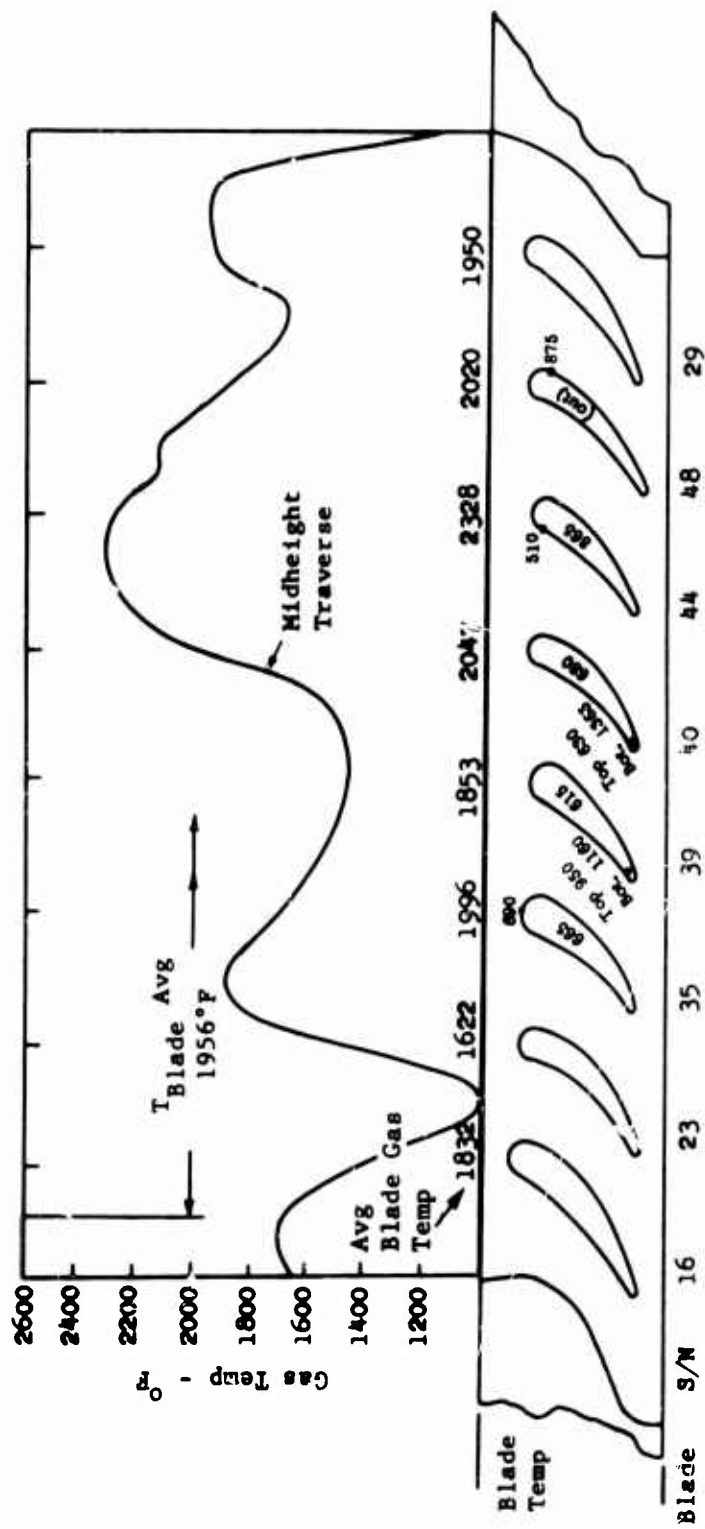


Figure 160. Schematic of Temperature Profile and Typical Blade Test Data.

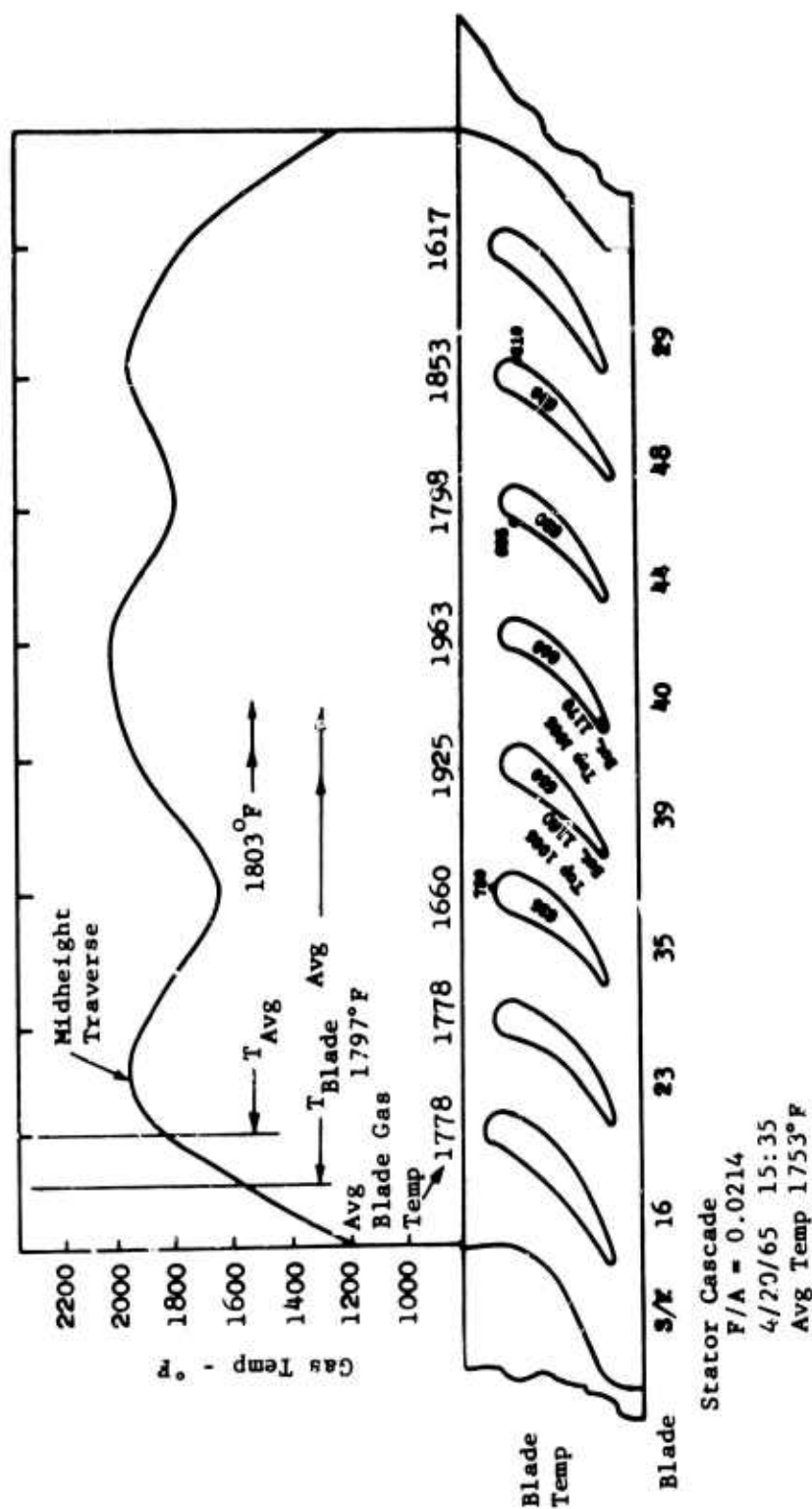


Figure 161. Schematic of Temperature Profile and Typical Blade Test Data.

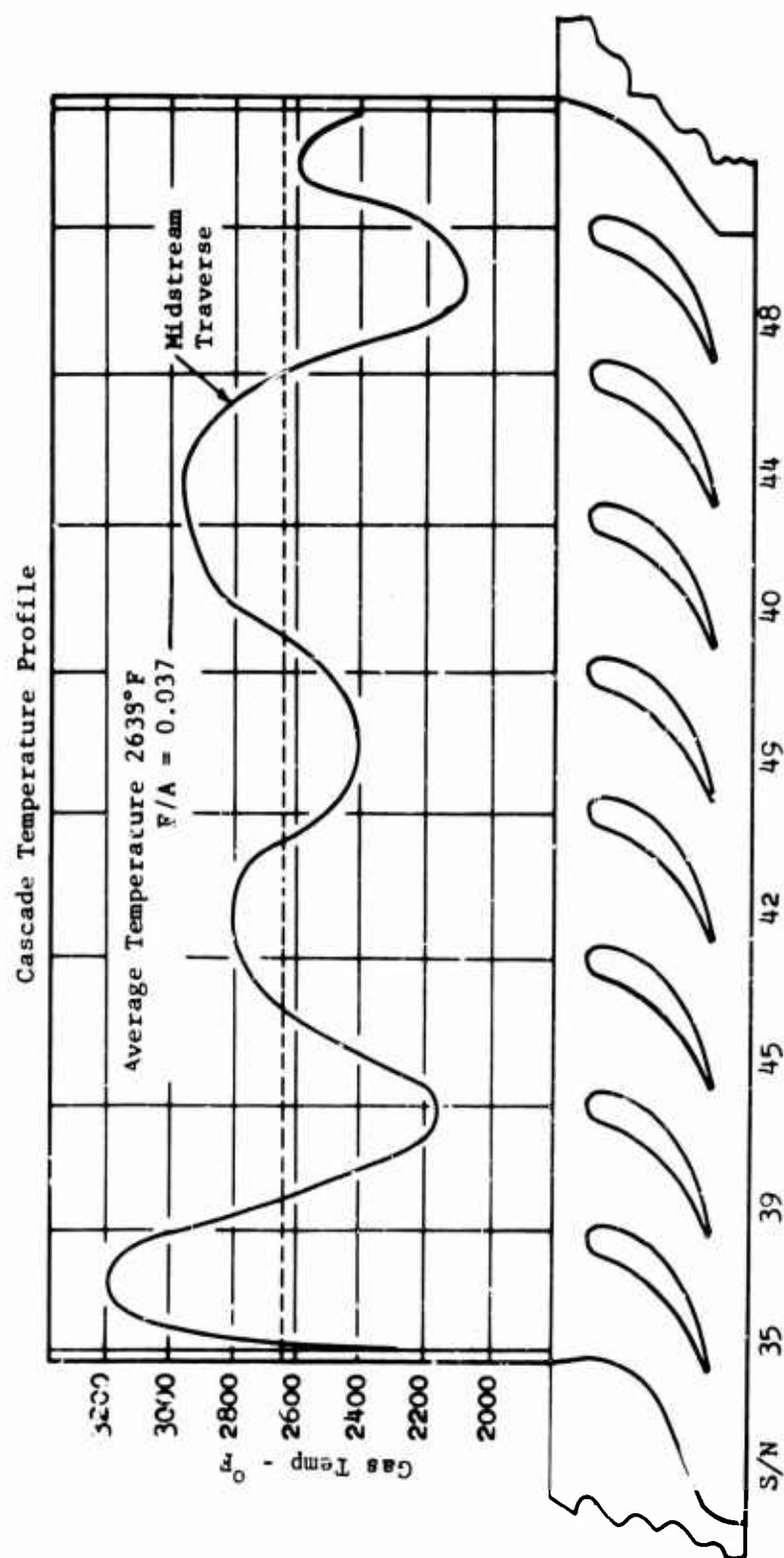


Figure 162. USAAVLABS Stator Cascade.

Cascade Temperature Profile

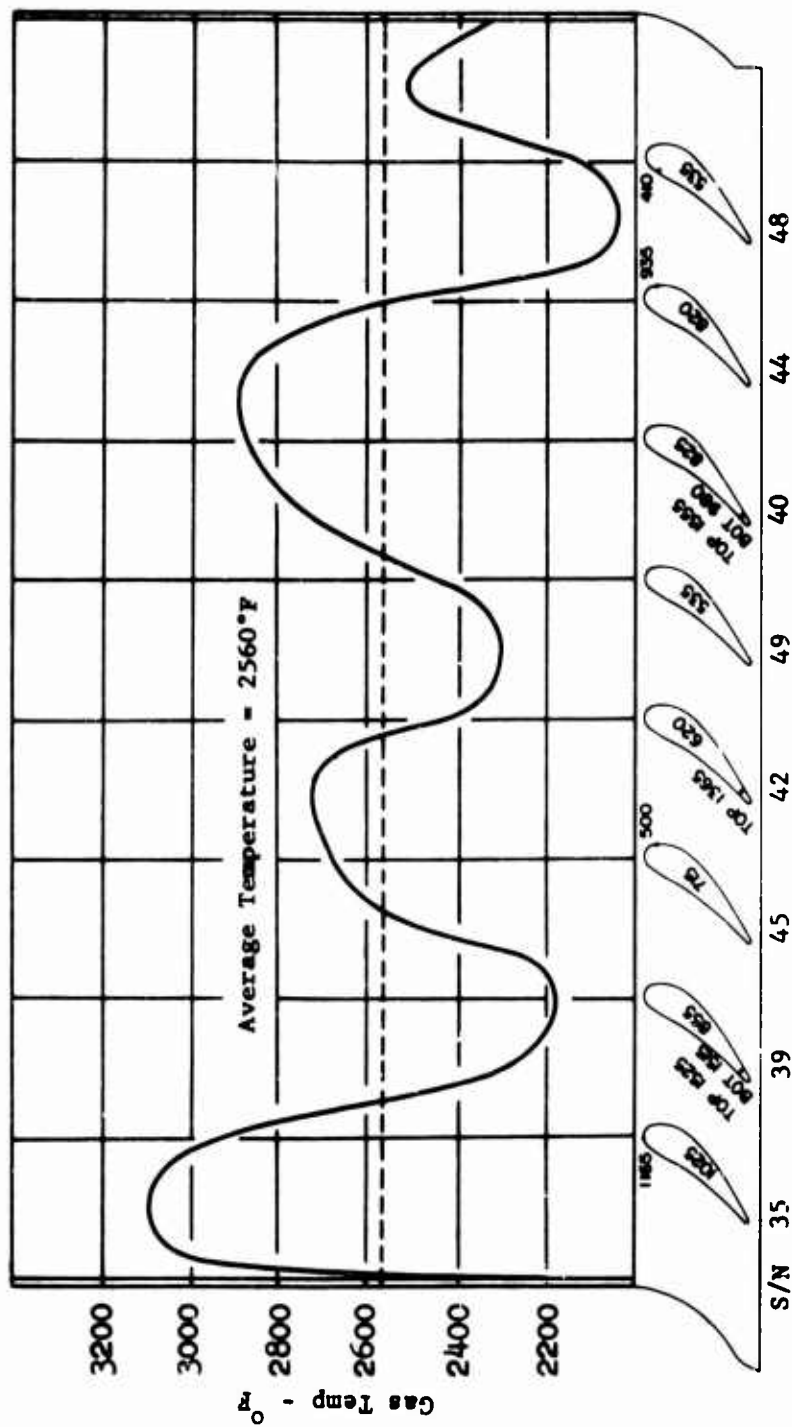


Figure 163. USAAVLABS Stator Cascade.

Cascade Temperature Profile

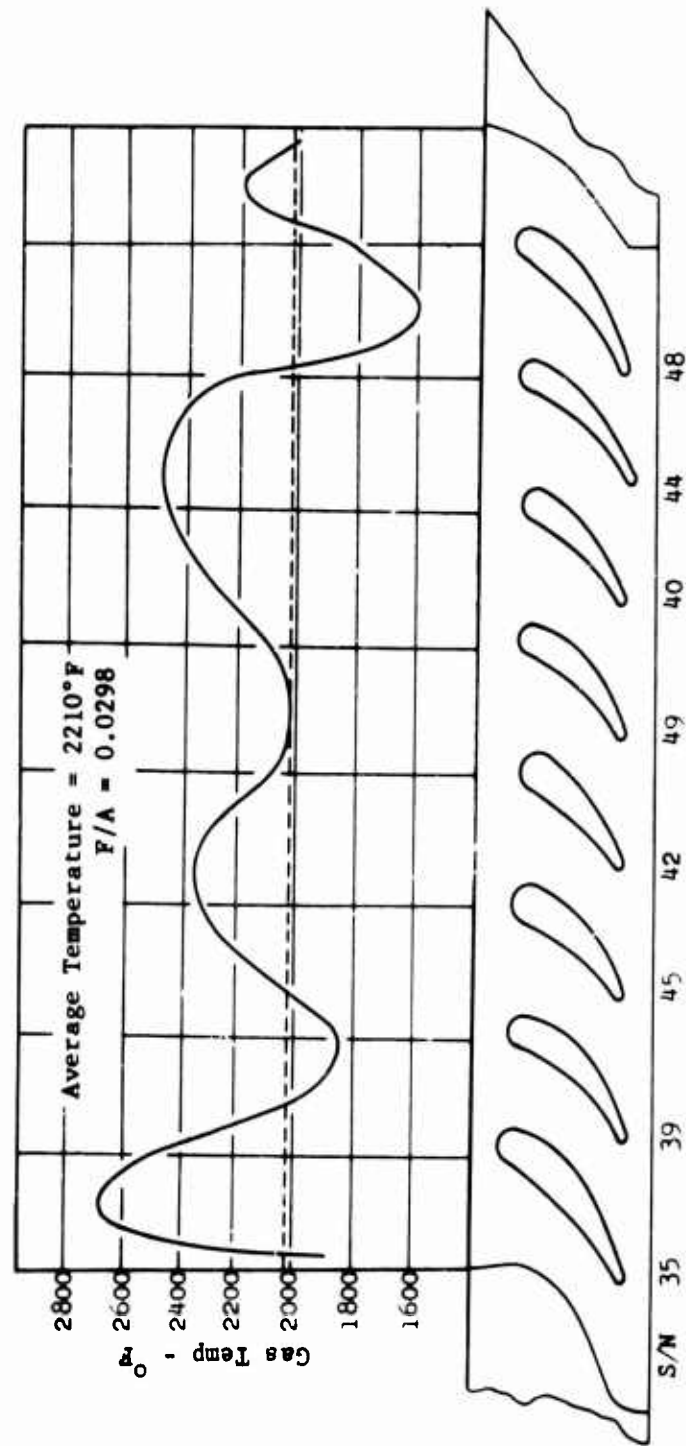


Figure 164. USAAVLABS Stator Cascade.

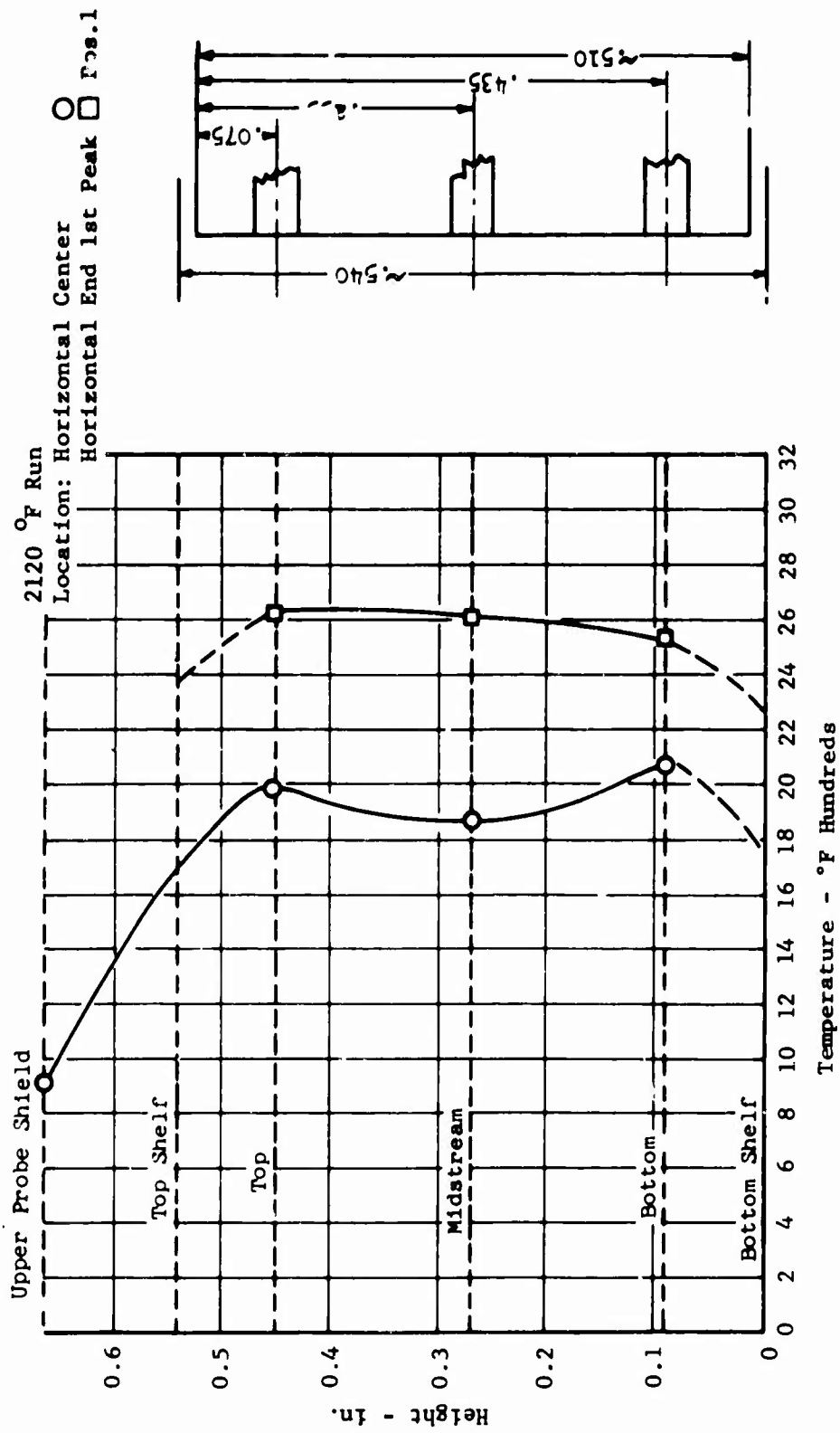


Figure 165. Vertical Temperature Profile Cascade Rig.

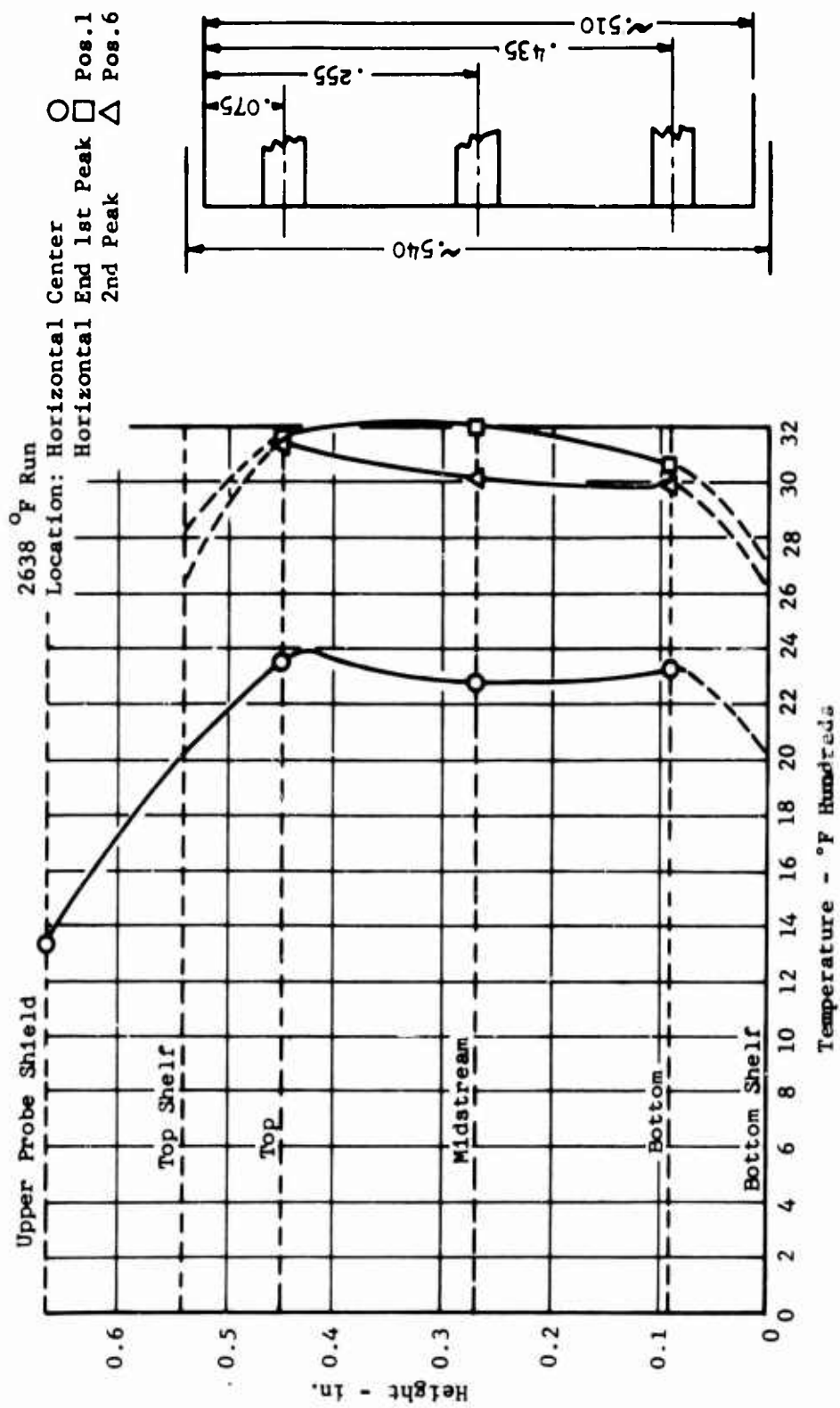


Figure 166. Vertical Temperature Profile Cascade Rig.

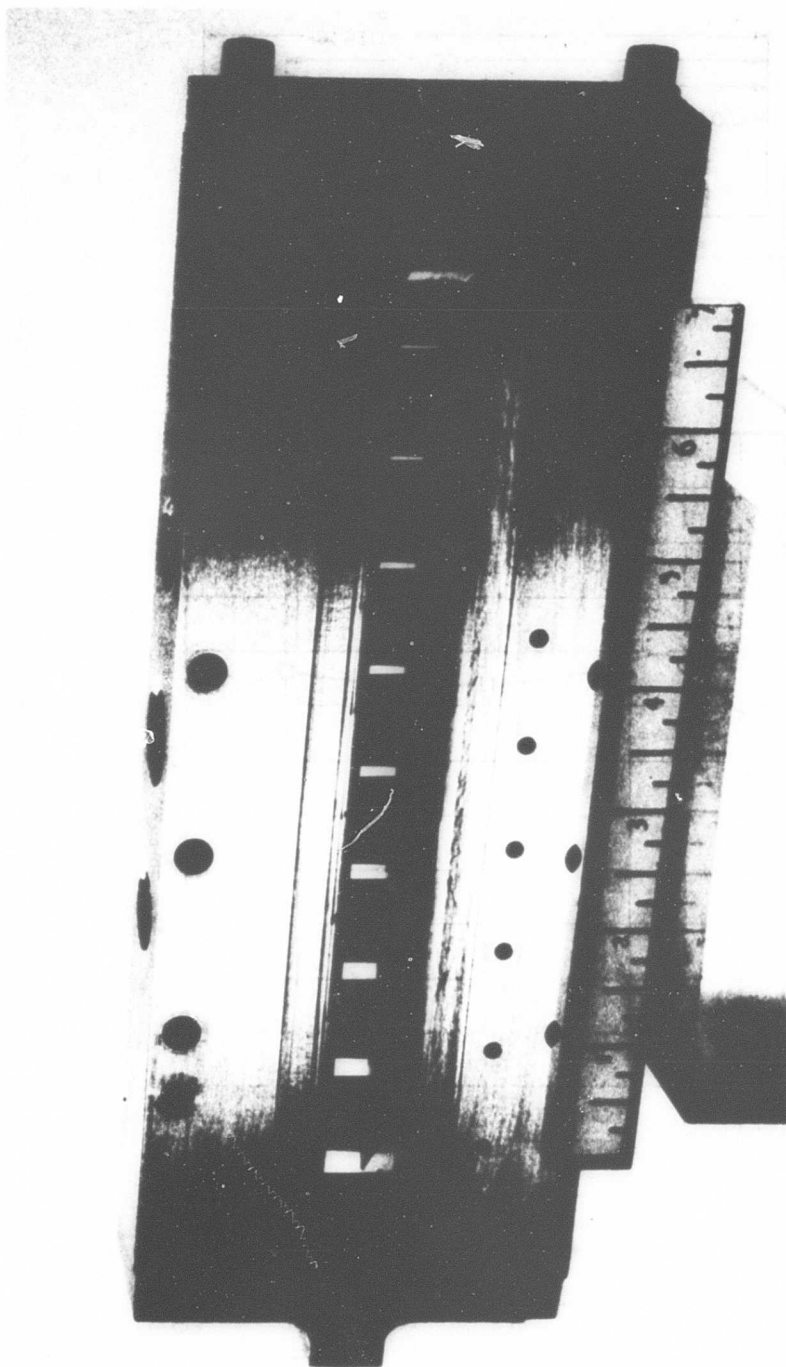
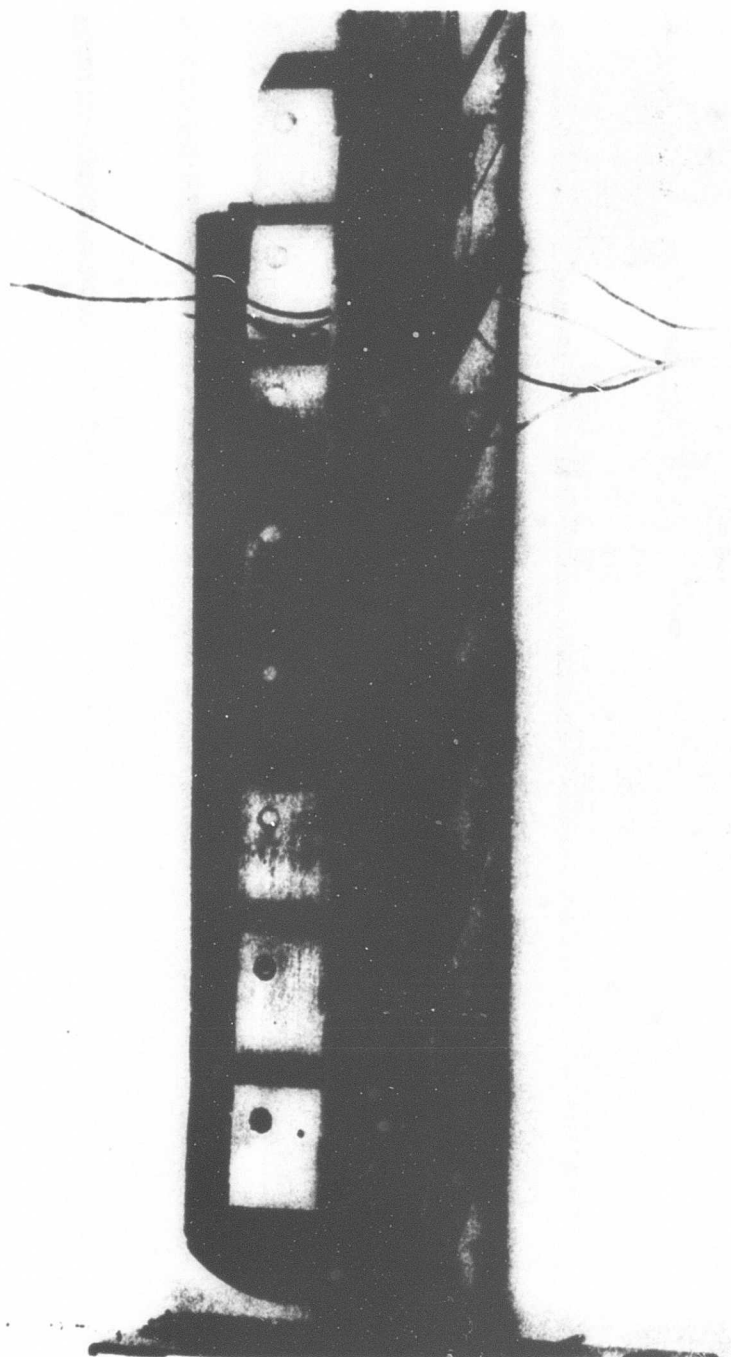


Figure 167. Stator Cascade Complete Assembly.



Blade S/N 1 2 3 4 5 6 7 8

Figure 168. Trailing Edge of 1st Cascade Stator Blades in Post-Test Condition.

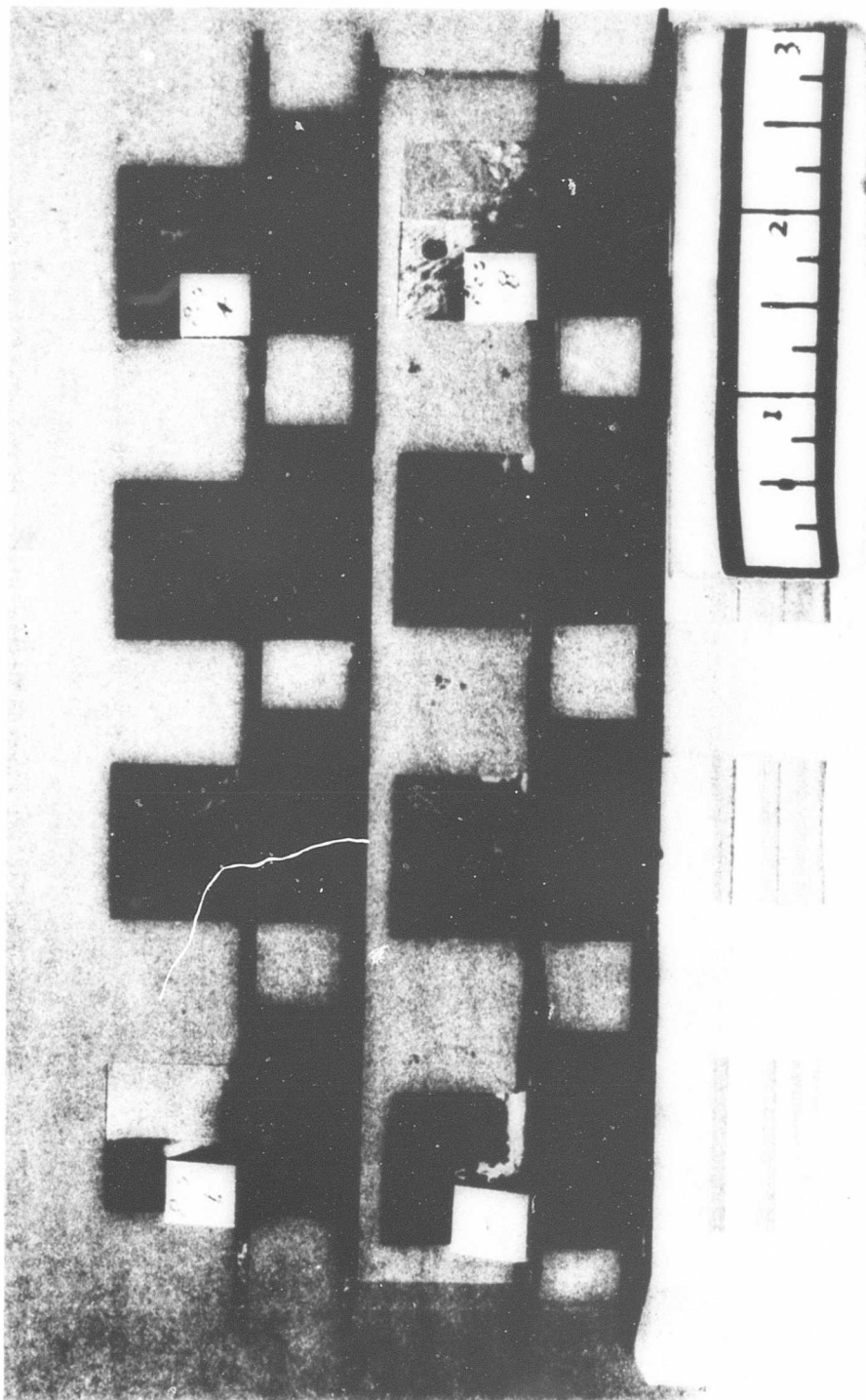


Figure 169. Pressure Side Of 2nd Cascade Blades in Post-Test Condition.

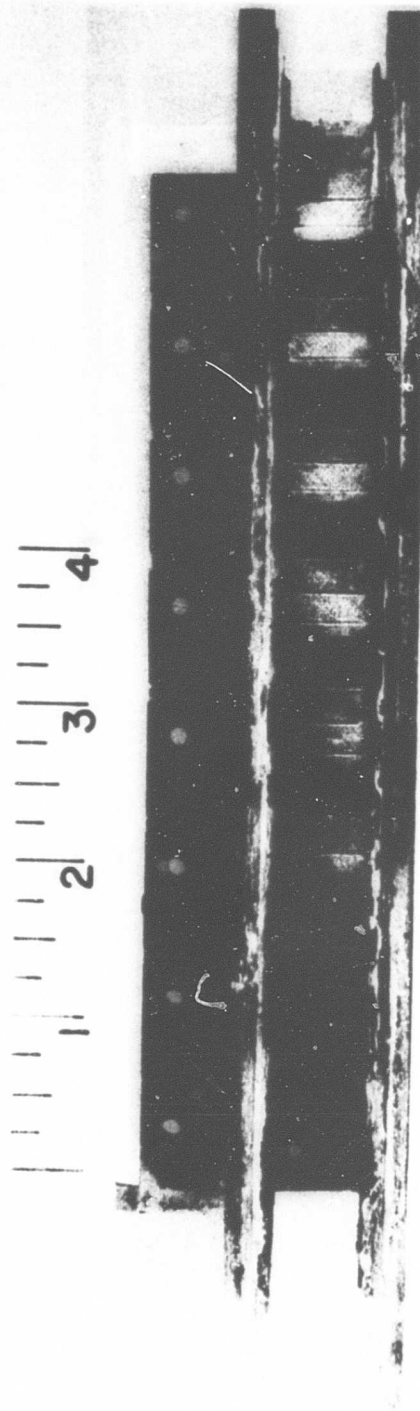


Figure 170. Leading Edge of 3rd Cascade Blades in Post-Test Condition.

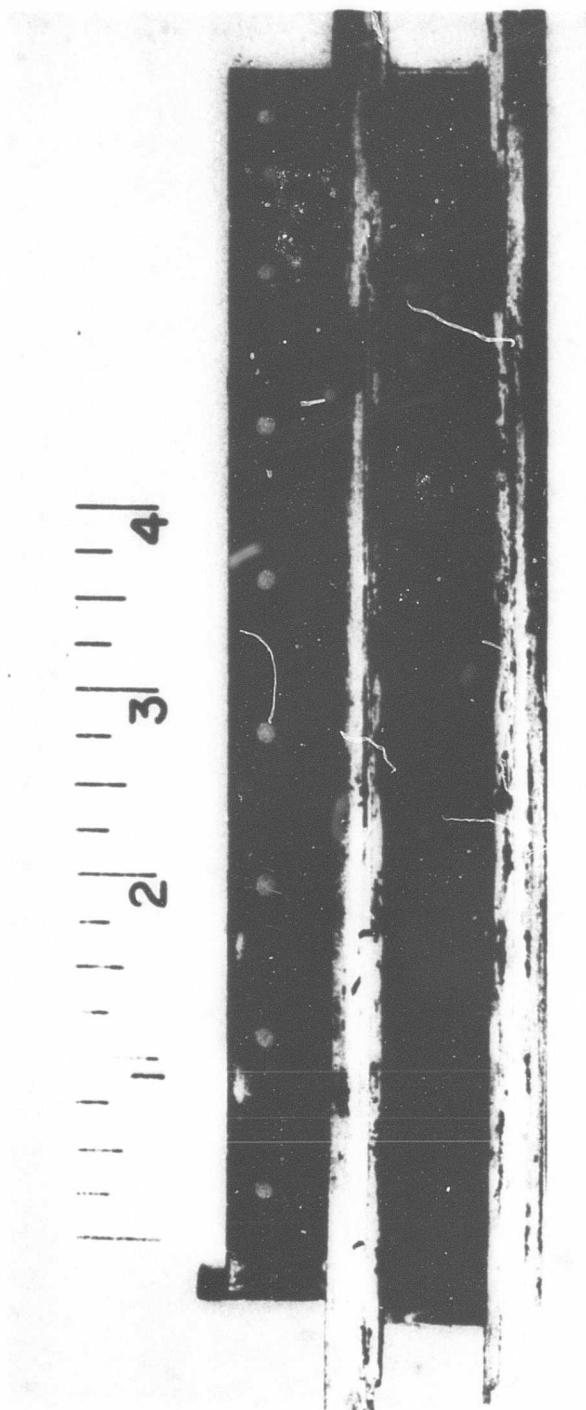


Figure 171. Trailing Edge of 3rd Cascade Blades in Post-Test Condition.

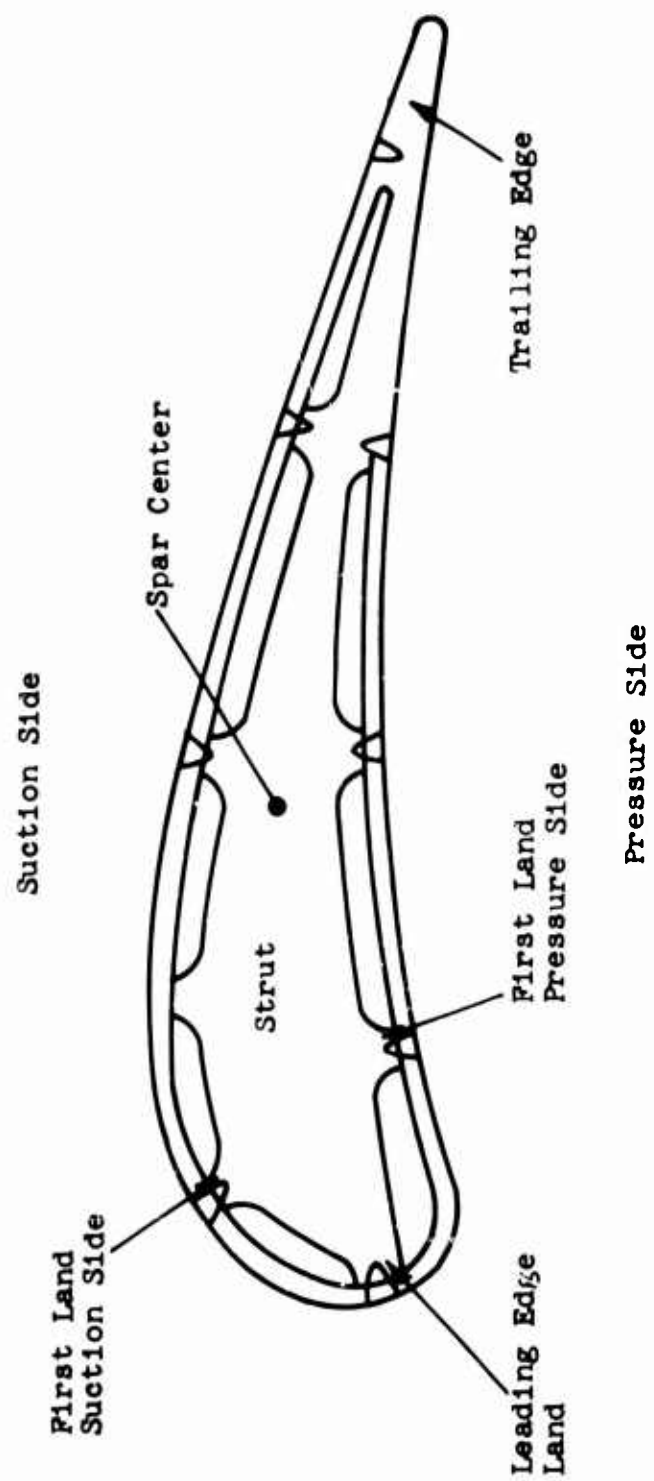


Figure 172. Cascade Stator.

5.4 FATIGUE PROPERTIES

The fatigue properties of the proposed turbine blades are well defined from test experience on similar blades and specimens. The information that follows was generated under separate contracts, AF 33(657)-9058 and NOW 64-0501-ci. This information is technically applicable to the small gas turbine and is presented here for easy reference. Fatigue tests demonstrated that the basic assembly of skin and strut results in a well damped structure and that the materials chosen have ample strength in the anticipated environment. Since the design of the proposed blade is based on optimization of elements from actual test evaluations, some of which are described below, the confidence level in the resulting design is understandably high.

5.4.1 Room Temperature Fatigue

The first evaluation described here concerns René 41, which is the material for the two-dimensional rig blades. This evaluation also investigated the initial point of fatigue failure.

Five spars of cast René 41 material were tested on the "beehive" rig to evaluate fatigue strength of as-cast specimens. The results of these tests were compared with previously established specifications for the blade material and found to be equivalent as shown:

<u>Spar No.</u>	<u>Freq - cps</u>	<u>Failure Stress psi @ Trailing Edge</u>
1577-1	847	57,000
1577-2	869	38,400
1577-3	891	48,000
1577-4	843	56,400
1577-5	850	55,300
	Avg	51,000

Fatigue strength of six specimens per C-W Heat Treat Spec 7813 were:

High	50,100 psi
Avg	42,600
Low	35,100

The "beehive" rig induces vibration by blowing air across the tip of the blade, causing it to flutter. The spar coupon was encased in plastic steel, and "beehive" step bending fatigue tests were initiated at a stress level of 10,000 psi. The stress was increased in increments of $\pm 2,500$ psi at the completion of each 4×10^6 cycle period. The stress level was increased until the fatigue limit was reached. Metallurgical inspection.

showed all failures nucleating from the trailing edge close to the blade shelf. In a few cases, the nucleus was along the horizontal length of the shelf and was probably due to stress concentration from the sharp edge.

Correlation of the various spar materials considered for use on turbine rotor blades can be made from the following test report. This test compared relative fatigue strength of wrought Inconel 700, cast René 41, cast Inconel 713, and cast Stellite 31 at room temperature. It also evaluated the effect of EB welding on the fatigue strength of wrought Inconel 700 material.

Results

1. Summarized below are the results of the bending fatigue tests which were conducted on four materials. Failure stress, in psi, and failure strain, in inch/inch, are tabulated. Test specimens were 1-inch slabs with Poroloy skin welded to ribs to simulate blade construction. The indicated failure stress and strain correspond to the values at the outer fiber of the spar rib.

<u>Specimen</u>	<u>No. of Test Specimens</u>	<u>Avg Failure Stress \pm psi</u>	<u>Standard psi Deviation \pm</u>	<u>Avg Failure Strain in./in.</u>
Cast René 41	6	42,600	7,500	0.00133
Wrought Inconel 700	6	45,400	3,440	0.00142
Cast Stellite 31	10	53,800	9,440	0.00165
Cast Inconel 713	4	54,100	6,300	0.00174

2. Summarized below are the results of the bending fatigue tests of sample spars of wrought Inconel 700 with and without Poroloy mesh. The values listed are at the outer fiber of the spar rib.

<u>Specimen</u>	<u>No. of Test Specimens</u>	<u>Avg Failure Stress \pm psi</u>	<u>Standard psi Deviation \pm</u>	<u>Avg Failure Strain in./in.</u>
Wrought Inconel 700	5	45,200	5,380	0.00141
(Spar Alone)	6	45,400	3,440	0.00142

3. Metallurgical failure analysis limited to the Stellite 31 specimens pinpointed the failure nuclei at the rib of the spar where the electron beam welding is performed. The sectional properties of the specimens are such that the highest stresses are located in this area, and thus the failure nucleating at this point is to be expected.

Conclusions

1. At room temperature, the fatigue strengths of both cast Inconel 713 and cast Stellite 31 are essentially the same.

2. At room temperature, the failure stress of both Inconel 713 and Stellite 31 is between 15 and 23 percent above that of René 41 and Inconel 700.
3. Electron beam welding does not significantly affect the fatigue strength of the wrought Inconel 700 material.

5.4.2 High Temperature and Thermal Fatigue

Applicable fatigue testing at elevated temperature was accomplished on turbine blades of Inco 700 spar material with an N155 Poroloy mesh airfoil electron beam welded to the spar ribs. These blade assemblies were tested on an electromagnetic shaker with a Lepel induction heater which raised blade temperatures to 1200°F. The conclusions drawn from this evaluation are as follows:

1. At 1200°F, it took 40 percent less strain to fail the blade in the trailing-edge mesh than was required to fail Poroloy mesh specimens at 75°F. (The proposed turbine rig blades are short and stiff, thus reducing entire strain level.)
2. These trailing-edge mesh failures occur in the widest unsupported span of mesh. (On the proposed turbine rig blades, the unsupported section of mesh is at least half of that for the blades tested.)
3. At 1200°F, the blade assembly trailing-edge spar failed at a 43 percent lower total tip amplitude than was required to fail the initial spar specimen at 75°F. (Tip amplitudes on the proposed turbine rig rotor blades are small by comparison.)

High-temperature testing was also accomplished on SST blades of similar configuration as above but with Stellite 31 strut material. Blade temperatures of 1400°F were achieved and failure strains were reached at 2.1×10^6 cycles and occurred during a fatigue step as in the previous test. It is interesting to note that in both cases, the fundamental blade frequency was about 8 percent lower at elevated temperatures than at room temperatures.

Thermal fatigue on Inco 713 turbine blades with N155 Poroloy mesh was evaluated during the 150-hour endurance test on a J65 rig engine. During this period there was a minimum of 100 starts and stops, thus providing a thermal cycle that is realistic and of a type actually encountered in a practical installation. Accelerations from one temperature condition to another also imposed thermal shocks on these blades, although to a lesser degree.

The excellent condition of these blades after test and detail inspection showed no sign of thermal fatigue. It is felt that the above-mentioned testing verifies the transpiration blade construction as sufficiently rugged for sustained operation at elevated temperatures.

6.0 TEST PLANS

Various tests are planned for the turbine component test rig, test equipment, and instrumentation designed during the Phase I period in order to adequately determine the turbine performance characteristics and to demonstrate its high-temperature operating capability. In general, these tests are divided into four categories culminating in the high-temperature demonstration. The four test periods planned are shown below in the sequence anticipated :

1. Combustor Tests
2. Turbine Stator Tests
3. Turbine Performance Tests
4. High-Temperature Tests

The test rig is designed so that the combustor can be tested independently in order to develop its performance characteristics before mating it with any of the turbine components. In this way, the combustor discharge conditions will be better understood and modified as necessary to minimize any deleterious effects on the downstream turbine blading.

The turbine stator blades will be added to the combustor rig next, to show their high-temperature capability and typical performance so that the operating characteristics of the complete stage will be more readily understood. The third step, operation of the complete stage, stator, and rotor, will be conducted at moderate temperatures (1000°F) to explore the full operating range of the turbine. Testing at the lower temperature will allow use of more conventional instrumentation in critical areas so that true performance will be more adequately defined.

The final objectives of this test period will be the demonstration of the turbine operating at an average turbine inlet temperature of 2500°F and the determination of cooling requirements at this operating condition. Further details of these tests are included in the following sections.

6.1 COMBUSTION TESTING

Independent testing of the combustor component of the high-temperature turbine test rig will be initiated in July in order to establish design performance and durability in advance of turbine testing. Combustor design goals have previously been set forth in Section 3.2 of this report. In brief, the combustor design goals are:

Operating F/A Range = 0.005 to 0.035
Combustion Efficiency = 99.0% at 0.032 F/A
Combustor Pressure Loss = 3.0% of Combustor Delivery Total Pressure
Combustor Exit Temperature Distribution = As shown in Figure 36
(Maximum Exit Temp = 1.135 of Mean Exit Temp, degree R)

The test setup for combustor testing will be similar to that shown for the turbine test rig in Figure 31, except that the turbine section aft of the combustor will be replaced by the rotating exhaust probe assembly shown previously in the test equipment description. The exhaust probe assembly includes separate probe heads for measurement of total temperature and total pressure. Each head contains three sensing elements located radially on the centers of three equal annular area sections of the exit annulus. The rotating probe assembly is capable of mapping both temperature and pressure over the full 360 degree arc of the combustor exit. Instrumentation will be provided at strategic locations in the combustor to establish internal flow distribution, combustor pressure loss, combustor exit pressure, temperature distribution both radially and circumferentially, combustion efficiency, and liner metal temperature distribution. A remotely operated back-pressure valve will be located downstream of the exhaust probe assembly in order to provide for adjustment of the operating pressure level from essentially atmospheric conditions to that of the turbine test rig operating design point.

Initial testing will be conducted at reduced pressure levels and fuel-air ratio. Emphasis during this period will be placed on evaluating and adjusting the stability range, combustion efficiency level, exit temperature distribution, and ignition procedures. Modifications to the combustor system will consist primarily of changes to the combustor air porting to adjust the internal flow distribution as required by test results. The severity of combustor operating conditions will gradually be increased to that of the design point as development of performance proceeds. It is anticipated that combustor testing will consist of approximately 5 rebuilds and 25 hours of burning time.

6.2 TURBINE STATOR TESTS

A series of turbine stators will be evaluated, incorporating the transpiration air-cooled blade concept, to establish preliminary aerodynamic data and to verify, experimentally, the metallurgical, mechanical, and heat transfer performance of various transpiration cooling design parameters. Blades of constant permeability will be operated at various gas temperatures and various levels of cooling airflow to determine metal operating temperature levels.

The hot turbine stator cascade program will allow correlation of the experimental results with the analytical thermal designs of turbine blade components and related coolant systems. This correlation will be made with the aid of computer programs.

Approximately 100 hours of testing will be accomplished with 10 rebuilds. The following combinations of blade material or configuration will be considered:

1. Inco 713 LC spar with N155 porous skin
2. Inco 713 LC spar with N1 V Cb porous skin
3. IN-100 with N155 skin
4. Mar-M-302 or 509 with N155 skin

Together with these combinations, the rotor blades offer additional variations; i.e., Mar-M-302 spar material or Mar-M-322 and N155 or N1 V Cb porous skin.

The stator cascade testing will evaluate the stator flow characteristics and establish outlet temperature profile. A parabolic profile was assumed in the design phase. This was used also to establish rotor cooling requirements. The traversing probe of the combustor test will be adapted to the cascade to measure circumferential patterns.

Testing of the annular cascade will initially follow the plan used on the two-dimensional rig, namely:

1. Cold flowing of blades to verify cooling flow characteristics.
2. Sealing checks and modifications to optimize sealing configurations.
3. Warm air checks on test stand using preheater on main air and using both cold and heated blade cooling air.
4. Main combustor in operation. Vary F/A ratio from low to high with control blade cooling flow to maintain blade spar at design temperature. Blade cooling air temperature will vary from ambient to 610°F. During this phase the minimum amount of cooling air to maintain design strut temperature will be determined.

5. Short endurance runs at discrete turbine inlet temperatures followed by metallurgical inspection to evaluate condition of airfoil mesh and struts.
6. Cyclic tests to evaluate thermal fatigue durability. Temperatures will be varied from low to high with main airflow in operation. Temperature cycling will also be achieved by a series of starts and stops.

Further testing to determine stator blade performance will be done once the initial blade cooling flows and sealing effectiveness are established. The tests contemplated in this phase of the program will include:

1. Establishing curves of main airflow versus turbine stator pressure drop at various gas temperatures and at various amounts of blade cooling air. The purpose will be to determine if the cooling airflow will reduce temperature in the main flow noticeably at a given pressure ratio and temperature condition.
2. Determining the flow direction of the air at the blade exit, by means of the traversing yaw probe. Of interest here will be the effect of varying amounts of blade cooling air on flow deviation.
3. Estimating the stator loss coefficient, Y , by measuring total pressures at the stator inlet and outlet ($P_{T_{in}}$ and $P_{T_{out}}$) and the outlet static pressure ($P_{s_{out}}$) and then evaluating the expression.

$$Y = \frac{P_{T_{in}} - P_{T_{out}}}{P_{T_{out}} - P_{s_{out}}}$$

6.3 PERFORMANCE TEST

The test program will be formulated in accordance with the basic test program described in the statement of work: This shall include approximately 40 hours of testing to establish the aerodynamic performance map.

The goal of the testing will be to determine two maps: (1) the map generated by the turbine with no secondary (cooling air) supplied to either stator or rotor, and (2) the map generated by the turbine with both stator and rotor operating with design or optimum percentage cooling flows. The map generated by the turbine with no cooling air will provide a performance baseline with which the turbine can be compared when operating "cooled".

To obtain these two maps will require approximately all of the allotted 40 hours of testing; nevertheless, two additional goals will be sought: one, determine the $\Delta h/T$ versus W/P characteristic over a range of speeds at design pressure ratio with only stator cooling air turned on, and two, determine the same characteristics with only rotor cooling air turned on. These will help provide answers, at design pressure ratio, to these questions: What is the effect of a transpiration-cooled stator operating with cooling air on turbine performance, and what is the effect of the rotor operating cooled on turbine performance? The test of cooling flow only to the stator has particular meaning for a multistage, high-temperature turbine in which the inlet temperature is such that only the stator requires cooling. The second test adds an additional flow consideration to the already complicated main flow in the rotor and already complicated secondary and boundary layer flows of the rotor. Appreciable radial flows of low velocity may occur and produce unforeseen choking, separation, and flow deviation phenomena, all of which could prevent attainment of the design or reference map condition. Approximately 200 test points will be run.

The rig has been designed to facilitate expeditious removal and replacement of stator blades, the rotor disc assembly, the exhaust housing, and instrumentation without the removal of the basic test rig and within the period of one working shift. Two rotor discs are available to permit replacement in the event any difficulties develop.

The test program and basic procedure to be followed will be the same for each map. In general, the test plan outline has been established to experimentally develop program information in terms of the following:

1. Establish the mechanical integrity of the turbine test rig.
2. Establish the effects of a range of cooling airflow rates on design point performance in order to select the cooling airflow rates for the map at off-design conditions.
3. Establish the overall turbine performance map over a range of speeds from 40 percent to 110 percent design speed and pressure ratios from those corresponding to 50 percent of design ideal enthalpy drop to those corresponding to limiting loading with and without blade-cooling airflows.

4. Establish the turbine performance ($\Delta h/T$ vs WN/P) over a range of speeds at design pressure ratio: (1) with only stator cooling air turned on, (2) with only rotor cooling air turned on.
5. Compare the overall performance of each configuration with respect to a baseline turbine.

During the initial test period, a shakedown of the turbine test rig will be conducted to verify that the rig operation is free of critical speeds throughout the entire operating range and that the mechanical integrity of the rig and the instrumentation satisfy the requirements of the program. After this period, the program will start in the low speed (about 20,000 rpm) low pressure ratio (about 1.4) range.

Incremental changes in pressure ratio and subsequently in speed toward the design point will be effected in a carefully planned approach to search for unexpected critical operating zones for the rig or the instrumentation and equipment. Exit surveys will be accomplished during this period to familiarize personnel with the test techniques and to evaluate data reduction methods which have been formulated to analyze the test measurements. Following the shakedown, the test rig will be operated at the design point. The design test point will be set initially without blade cooling airflow. Total pressure, absolute flow angle, total temperature, and specific mass flow will be measured. Primary airflow will be carefully monitored because testing by NASA and Curtiss-Wright has indicated that there is the tendency for transonic turbines to fail to pass the design weight flow.

Following the design point survey, a complete performance map will be generated by setting a total-to-total pressure ratio of approximately 1.4 and entrance total temperature of 610°F and varying speed from 50 to 110 percent rpm in 10 percent rpm increments. Each speed point will be run without cooling airflow at ambient temperature, as applicable. Subsequently, the same procedure will be repeated at higher pressure ratios in pressure ratio increments of 0.1 until the limit-loading condition is reached, estimated to be in the neighborhood of 2.7 pressure ratio. This limit-loading condition is determined when no additional shaft work is produced with increasing pressure ratio. At each point, data to be obtained include turbine weight flow, rotative speed, torque, inlet total temperature, inlet, interstage and exit static pressures at the hub and tip, exit absolute flow angle, exit total pressure, and exit total temperature. Test stand plots of shaft output (dynamometer horsepower), primary and secondary airflow, and interstage static pressures as functions of rpm will be maintained.

Next, the test will be repeated with both stator and rotor cooling airflows operating and set to design percentages and the ratio of cooling air supply pressure (stator and rotor) to turbine inlet total pressure noted. It is intended that the cooling airflow rate for off-design points will be determined by maintaining this same ratio of cooling-to-primary-air-supply pressure ratio. By so doing, it is felt that this simulates operation of such a turbine in the actual engine where compressor bleed would be the cooling air source.

At each point, data to be obtained include turbine weight flow, rotative speed, torque, inlet total temperature, inlet, interstage and exit static pressures at hub and tip, exit absolute flow angle, exit total pressure, exit total temperature, secondary airflows, and secondary air inlet pressure and temperature. Test stand plots will be maintained as before.

It is, in order to detail some of the operating techniques and test procedures, to be used for the test settings and for measurement and collection of performance test data. For test operation, the primary external air supply will be manipulated through the use of a waste-gate bleed arrangement and an indirect-fired preheater to set the turbine entrance conditions. The rotor speed will be set by means of the water brake dynamometer. The map will be generated along lines of constant pressure ratio. This survey may be repeated for duplicate conditions, but with a flow rate of cooling air above and below the design rate to examine the influences of cooling flow at selected off-design operating conditions. To ensure representative flow survey data, extreme care will be taken to provide steady-state and constant inlet and exhaust conditions at the turbine.

Prior to assembly of the turbine as a unit, it is planned to flow check the components in the following manner. Individual stator blades will be flow checked to a nominal value to minimize blade to blade flow deviations. Next the complete stator ring annulus assembly will be flow checked to establish its corrected flow versus pressure ratio characteristics. All the preceding tests will be carried out at ambient static external conditions. This stator testing may be a new assembly or may be the stator used in the testing of Section 6.2.

In a similar manner, the individual rotor blades will be tested and then the entire rotor assembly flow tested after it is welded together. This will be done in "free air" and within the turbine casing. Flow testing (non-rotating) within the casing will be in conjunction with establishing typical pressures within the various passages that supply air to the rotor and labyrinths. These tests are all directed toward establishing the pressure-flow-leakage characteristics of the system.

These tests provide technical information as to the flow characteristics of the system, provide information for heat transfer analysis and studies, and provide data to which recourse can be made during rotating tests. For example, a high stator blade metal temperature reading during hot running could be discounted, if during the cascade testing it was shown the metal ran cool for the same pressure and airflow.

6.4 HIGH-TEMPERATURE TEST

Ten hours of testing are allotted to demonstrate turbine operation at the following conditions:

<u>Avg TIT °F</u>	<u>Test Hr</u>
1600-2200	5
2200-2400	4
2400-2500	1

The initial running will be with design blade cooling airflows modified by the experience gained during the turbine stator test. Experience gained in the previous performance testing will assist in setting specific design points. During this test, the main combustion chamber will be in operation to achieve the above-mentioned turbine inlet temperatures, and the rotor will be turning at speeds up to 55,000 actual rpm.

Once the blade cooling has been established and the power absorption equipment checked out to the maximum speed condition, the turbine will be operated to demonstrate: (1) turbine inlet temperature of 2500°F, (2) percent cooling airflow required, and (3) 140 Btu/per pound/per second actual Δh . This testing will take place after test experience has been gained at the lower temperature points.

Two rebuilds are anticipated for this phase of the test evaluation. The instrumented turbine rotor disc will be installed on the second rebuild. During this testing, the rotor cooling air effectiveness can be evaluated and possibly modified to optimize the flow requirement.

At the completion of the demonstration run, an alternate blade material may be tested. The evaluation of alternate materials will be at maximum conditions for a stabilized time period to assure steady-state temperature soak conditions. It is anticipated that turbine parts will be available to continue short endurance tests even after the 10 hours allotted have been completed. If so, these parts will be evaluated at high temperatures and speeds, temperature cycling, and endurance demonstrations so as to increase the accumulated hot time on parts. Frequent inspection of parts and careful monitoring of instrumentation will minimize the risk of major damage occurring during test.

Metallurgical inspection of the blades and discs after test, as well as static cooling airflow checks, will attest to the turbine condition. Areas of particular concern to be inspected will include the turbine disc at the weld joint to the blades and also the turbine exit housing and the high speed turbine bearings. There are adequate spares to assure that testing can proceed at a minimum of down time for parts.

REFERENCES

No.

- 1 Zweifel, O., The Spacing of Turbo-Machine Blading, Especially with Large Angular Deflection, the Brown Boveri Review, Baden, Switzerland, December 1945.
- 2 WAD Serial Report No. MRE.00-281, Detailed Analysis of the Turbine for Application to MBT Vehicles, February 25, 1964.
- 3 Bagg, S.L., and Holliday, S.B., The Influence of Altitude Operating Conditions on Combustion Chamber Design, AGARD Selected Combustion Problems II, Liege, Belgium, December 1955.
- 4 Langer, B.F., Design of Pressure Vessels for Low-Cycle Fatigue, ASME D Vol. 84 (1962) p389.
- 5 Gerard, G., and Becker, H., Handbook of Structural Stability, NASA TN 3738, August 1957.
- 6 Clark, J., and Jackson, S., General Considerations in the Design of Combustion Chambers for Aircraft and Industrial Gas Turbines, presented at the 1962 SAE International Congress, Detroit, Michigan.
- 7 Curtiss-Wright Corporation, Wright Aeronautical Division, Specification No. XDS-8001, Specification for Power Absorber System, March 30, 1965.
- 8 Curtiss-Wright Corporation, Wright Aeronautical Division, Specification No. XDS-8002, Specification for Direct Drive Power Absorber, March 30, 1965.
- 9 Curtiss-Wright Corporation, Wright Aeronautical Division, Specification No. XDS-8003, Specification for High-Speed Reducer, March 30, 1965.
- 10 Hatch, J.E., and Papell, S.S., Use of a Theoretical Flow Model to Correlate Data for Fluid-Cooling or Heating on Adiabatic Wall by Tangential Injection of Gases of Different Fluid Properties, NASA TN D-130, November 1959.
- 11 Curtiss-Wright Corporation, Wright Aeronautical Division, Proposal 517, Determination of Thermal Stress Cracking in Turbine Blades, March 1, 1965.
- 12 Porray, M.J., Newman, M., Switzky, H., Thermo-Structural Analysis Manual, United States Air Force Wright Aeronautical Development Division, Technical Report No. WADD-TR-60-517, Wright-Patterson Air Force Base, Ohio, August 1962.

REFERENCES - Continued

No.

- 13 Supplement to ASME Power Test Code Bulletin PTC 19.5:
4-1959.

Unclassified

Security Classification

DOCUMENT CONTROL DATA - R & D		
(Security classification of title, body of abstract and indexing annotation must be entered when the overall report is classified)		
1. ORIGINATING ACTIVITY (Corporate author) Curtiss-Wright Corporation Wood-Ridge, New Jersey		2a. REPORT SECURITY CLASSIFICATION Unclassified
		2b. GROUP
3. REPORT TITLE SMALL GAS TURBINE ENGINE COMPONENT TECHNOLOGY - TURBINE VOLUME I - PHASE I SUMMARY REPORT		
4. DESCRIPTIVE NOTES (Type of report and inclusive dates) Final Report		
5. AUTHOR(S) (First name, middle initial, last name) W. Franklin T. Schober		
6. REPORT DATE October 1968	7a. TOTAL NO. OF PAGES 335	7b. NO. OF REFS 13
8a. CONTRACT OR GRANT NO. DA 44-177-AMC-182(T)	8b. ORIGINATOR'S REPORT NUMBER(S) USAAVLABS Technical Report 68-50A	
9. PROJECT NO. 1G162203D14413		
10. DISTRIBUTION STATEMENT This document has been approved for public release and sale; its distribution is unlimited.	11. OTHER REPORT NO(S) (Any other numbers that may be assigned this report) R-419-F	
11. SUPPLEMENTARY NOTES Volume I of a two-volume report		12. SPONSORING MILITARY ACTIVITY US Army Aviation Materiel Laboratories Port Eustis, Virginia
13. ABSTRACT This report describes the aerodynamic, thermal, and mechanical design and analysis, fabrication, and experimental evaluation of a transpiration cooled, single stage axial-flow turbine component capable of operation at 2500° F average inlet temperature. Combustor design and development and test rig design are described, as well as stator vane hot thermal and cold aerodynamic cascade testing. The objective of the program was to advance and demonstrate high turbine inlet technology for use in a gas generator with a compressor pressure ratio of 8 to 10 and an airflow of 4 pounds per second. Additional objectives included turbine work of 140 Btu per pound of airflow at a high level of turbine efficiency. Phase I report presents the design and analysis, and Phase II report gives the details of manufacture and results of test evaluations. One hundred hours of complete stage testing were accomplished with 2 hours at 2500° F. The cascade rig was tested for 87 hours which included 1.2 hours at 2650° F. All blading was in excellent condition after the tests and confirmed the efficacy of the thermal design and transpiration cooling as applied to small size blading. A work of 133 Btu per pound was achieved at a low level of efficiency, attributable to stator profile shape and low aspect ratio. One hundred thirty-seven hours of combustor testing at an average exit temperature of 2500° F was accomplished with operating characteristics consistent with the turbine requirements. It was concluded that the advanced technology incorporated in the turbine design relative to blade cooling and turbine mechanical integrity are practical and can be applied to the design of advanced small gas turbines.		

DD FORM 1473

REPLACES DD FORM 1473, 1 JAN 64, WHICH IS OBSOLETE FOR ARMY USE.

Unclassified

Security Classification

Unclassified

Security Classification

1a. KEY WORDS	LINK A		LINK B		LINK C	
	ROLE	WT	ROLE	WT	ROLE	WT
Axial Flow Turbine Aerodynamic Design Mechanical Design Test, Development Analysis Cascade Test Combustor Design Thermal Design and Test Cooling, Transpiration High Temperature High Work Manufacture Rig Design Performance Stator Vanes Rotor Blades Efficiency Turbine Map Temperature Profile Blade Profile Dynamometer Test Equipment						

Unclassified

Security Classification

11492-68